University of Dundee

DOCTOR OF PHILOSOPHY

A Qualitative and Quantitative Analysis of the Juvenile Ischium

Maclean, Stephen J.

Award date:
2017

Link to publication
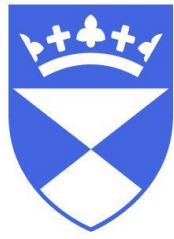
A Qualitative and Quantitative Analysis of the Juvenile Ischium

Stephen J. Maclean

PhD in Anatomy and Forensic Anthropology

Centre for Anatomy and Human Identification

School of Science and Engineering

University of Dundee

May 2017

Contents

Appendices

All appendices associated with this doctoral thesis are presented as a separate electronic attachment, or on-disc with physical copies of the thesis.

Appendix	Description
4.1	Copy of Maclean *et al.*, 2014 paper
4.2	Summary of macroradiography details
4.3	Summary of digital radiography details
5.1	Summary of microcomputed tomography details
5.2	Allometry raw data and descriptive statistics
5.3	Noise reduction raw data
5.4	Noise reduction statistical results
5.5	VOI placement guide
5.6	Intra-observer raw data
5.7	Intra-observer statistical results
6.1	Raw histomorphometric data, Phase 1
6.2	Raw histomorphometric data, Phase 2
6.3	Raw histomorphometric data, Phase 3
6.4	Phase 1 statistical summaries
6.5	Phase 2 statistical summaries
6.6	Phase 3 statistical summaries
6.7	BV/TV interphase statistical summaries
6.8	Tb.Th interphase statistical summaries
6.9	Tb.N interphase statistical summaries
6.10	Tb.SP interphase statistical summaries
6.11	SMI interphase statistical summaries
6.12	DA interphase statistical summaries
6.13	P.C.Th interphase statistical summaries
6.14	A.C.Th interphase statistical summaries
6.15	Pelvic v Lateral Thickness statistical summaries
R1	Copy of reference: Skyscan (N.D.) – Structural Parameters Measured by SkyScan CT-analyser

List of Abbreviations

Abb.	Full Description	Abb.	Full Description
μCT	Micro-computed tomography	MRI	Magnetic resonance imaging
2D	Two-dimensional	NO	Nitric oxide
3D	Three-dimensional	OCS	Optimum customary strain
AIIS	Anterior inferior iliac spine	P.C.Th	Pelvic cortical thickness
ANOVA	Analysis of variance	PGE_2	Prostaglandin E_2
ASIS	Anterior superior iliac spine	PIIS	Posterior inferior iliac spine
BFA	Bone functional adaptation	PPMC	Pearson's product-moment correlations
BMC	Bone mineral content	PSIS	Posterior superior iliac spine
BMD	Bone mineral density	PTH	Parathyroid hormone
BMU	Basic multicellular unit	PVA	Partial volume averaging
BV	Bone volume	RANK-Ligand	Receptor activator of nuclear factor Kappa-β ligand
BV/TV	Bone volume fraction	ROI	Region of Interest
C.Th	Cortical thickness	RSD	Relative standard deviations
cAMP	Cyclic adenosine monophosphate	S	Surface area
CCD	Charged couple device	S'	Surface area following dilation
CT	Computed tomography	SD	Standard deviation
CTan	Ct-Analyser	SEM	Scanning electron microscopy
DA	Degree of anisotropy	SMI	Structural model index
DKK-1	Dickkopf-1	SS	Sum of Squares
DXA	Dual-energy X-ray absorptiometry	Tb.D	Trabecular distribution
FEA	Finite element analysis	Tb.N	Trabecular number
i.u.	Intra-uterine	Tb.Sp	Trabecular separation
L.C.Th	Lateral cortical thickness	Tb.Th	Trabecular thickness
MB	Maximum breadth	TGF-β	Transforming growth factor - β
MD	Maximum depth	TV	Total volume
MIL	Mean intercept length	VEGF	Vascular endothelial growth factor
ML	Maximum length	VOI	Volume of Interest
MPC	Multiple pairwise comparisons		

List of Tables

List of Figures

Acknowledgements

I would like to express my most sincere thanks to my supervisors, Dr Craig Cunningham and Professor Dame Sue Black, to whom I owe a great deal of gratitude. The enthusiasm they have shown for my work, and the many keen insights they provided, has been instrumental in shaping not only this project, but also my skills as a researcher and an academic. In particular, the constant support and calm wisdom Craig has provided, on an almost daily basis at times, has prevented many nervous breakdowns along the way.

I would also like to thank the following people, who have directly aided the completion of this research project:

> Professor Michael Fagan and Ms Sue Taft, CMET, University of Hull, for providing micro-computed tomography facilities.
>
> Ms Margaret Low, Ninewells Hospital, for assistance with radiographic procedures.
>
> Dr Luca Albergante and Professor Steve Hubbard, University of Dundee, for providing advice on my statistical methods and their interpretation.

I am grateful to the University of Dundee for accepting me on the Greenhouse Scholarship, which funded the latter three years of my research, and to my parents, who very generously funded the first.

On a more personal note, thanks also go to my parents, my siblings and my extended family for the endless amounts of love, support and patience they have shown over the past 4 years: it has been a long road and they have had to endure more than their share of moans and frightfully dull (and often unsolicited) explanations of what I'm getting up to.

Last, but most certainly not least, I owe everything and more to my partner Lauren, who has been a beacon of support and understanding during this process. She has provided encouragement when progress was slow, consolation and compassion when things were going wrong, and shared in my happiness as goals were achieved. My debt to her can never truly be expressed in writing; it is safe to say however that without her, this endeavour would not have been a success. I look forward to our future puppy-filled adventures together now this chapter of our lives has been put to bed.

Declaration

The candidate, Stephen James Maclean, is the author of the thesis. Unless otherwise stated, all references cited have been consulted by the candidate. The work, of which the thesis is a record, has been completed by the candidate. No portion of the work referred to in this thesis has been submitted in support of an application for another degree or qualification at this or any other university, or other institute of learning.

Stephen James Maclean

Copyright

Statement

We certify that Stephen Maclean has spent four years of research under our supervision. Stephen has fulfilled the conditions of Ordinance 39 and is qualified to submit the accompanying thesis in application for the degree of Doctor of Philosophy.

Professor Dame Sue Black   Dr. Craig Cunningham

Summary

There is little debate that mechanical feedback is a key factor in the regulation and maintenance of adult bone structure, following the principles of the mechanostat hypothesis. The factors that drive early ontogenetic change in skeletal microarchitecture are less easily discerned, however, and appear to include not only functional interactions, but also genetic and epigenetic components that may form a blueprint for future development.

The increasingly sophisticated capabilities of imaging technologies provide a platform through which ontogenetic patterns in skeletal development can be studied. When these patterns are considered in conjunction with major physiological, motor and sociological milestones, it may be possible to identify the factors that drive specific phases of development. In particular, digital radiography and micro-computed tomography are regarded as the gold standard imaging modalities for respective qualitative and quantitative studies of skeletal architecture. In this research, these techniques were applied to a sample of juvenile ischia across a developmental spectrum to identify changes in structure with increasing maturity.

The human ischium presents a suitable region for early ontogenetic investigation. During post-natal maturation, it develops load-bearing functions associated with bipedal locomotion and is primarily responsible for weight transmission through the pelvis in a seated posture. However, it reportedly experiences less pronounced mechanical strains and may therefore allow a greater exploration of the non-mechanical stimuli involved in early skeletal development.

The qualitative investigation of ischial development between the late fetal period and 14 years of age, identified 6 progressive phases of ischial development. In the fetal and perinatal period, bone intensity was found to increase rapidly to form a robust, radiopaque structure. Between 5 months and 2 years of age, there was a substantial decrease in the radiographic intensity of the ischium. This early period of bone loss may be linked to the dual action of the infant growth spurt, a period of enhanced growth of both the trunk and limbs, and the weaning period, which may restrict the availability of ingested dietary calcium and therefore demand the release of stored

skeletal calcium to facilitate growth. Beyond this period, however, this pattern of loss reversed and radiopacity was found to increase, with the most pronounced increases seen in the regions associated with the acetabulum and ischial spine.

To further explore the period of apparent bone accrual and subsequent loss that characterised the infant developmental period, micro-computed tomography was used to document the perinatal trabecular and cortical architecture and investigate changes in the internal structure with increasing maturity, up to 3 years of age.

Analysis of the perinatal ischium revealed statistically significant differences in regional trabecular bone characteristics and cortical thickness. The metaphyseal regions were defined by relatively immature bone indicative of modelling activities, regions of growth, while the central body of the ischium contained a more mature trabecular architecture that was consistent with accommodating the presence of a proliferating vascular centre.

It was subsequently confirmed that the loss of bone intensity observed qualitatively was the result of a significant decrease in bone volume fraction and cortical thickness across the ischium between 5 months and 2 years of age. Associated architectural changes included a significant decrease in trabecular number and an incremental increase in trabecular thickness. These changes suggest that there is a paradigm shift during infancy which prompts a rapid resorption of mineralised tissue within the ischium, perhaps to release sufficient stored calcium to facilitate the rapid growth of the child which is characteristic of this period. However, the changes are not exclusively deleterious, as the trabecular tissue which remains appears to undergo remodelling to increase trabecular thickness and perhaps prevent mechanical failure during routine use.

The identification of a period of skeletal overproduction and subsequent constructive regression may be of great significance in understanding early bone development at a whole-bone level and any subsequent failure. It is further proposed that the end of this transitory period may signal a biological switch between genetically-programmed skeletal growth *in-utero* and a functionally adaptive growth guided primarily by biomechanical stimuli.

Chapter 1: Introduction

1.1 Outline of thesis

Despite much interest and a growing body of literature, the mechanisms that underpin and direct the growth, maturation and maintenance of the human skeleton remain poorly understood. It is generally acknowledged that there are three potential classes of stimuli that may control skeletal architecture (Ruff *et al.*, 2006; Skedros *et al.,* 2007). The first is heritable genetic information that provides an evolutionary blueprint for bone morphology and position that is believed to be particularly important in the early development of the skeleton. The second are epigenetic factors that are external stimuli that alter bone development or adaptation by either increasing or decreasing the expression of an encoded, heritable, genetic trait. The third class of factors are extragenetic factors: external (environmental) stimuli that induce non-inheritable bone adaptation, such as the application of mechanical strains and the bioavailability of nutrients.

The extent to which these factors influence bone architecture, and the stages of development during which they are each most prevalent, is currently unknown. In the adult, the primary factors that regulate and maintain bone mass and architecture appear to be mechanical in nature, following the principles established by the theory of bone functional adaptation and the Utah paradigm, also known as the mechanostat model (Frost, 1990; Ruff *et al.,* 2006). In simple terms, these principles state that a bone can detect changes in local mechanical loading and will adapt its microarchitecture in response to this change. In regions that are subjected to increased loading, the structure of the bone will be reinforced by the addition of mineralised tissue and the optimisation of trabecular structure. Regions that are chronically under-loaded, i.e. subject to reduced mechanical strain, will be resorbed due to disuse. These changes in mechanical loading are detected by osteocytes within the bone matrix, which subsequently effect change through the regulation of osteoclastic resorption and osteoblastic formation of bone.

The factors influencing skeletal development are more difficult to elicit as the juvenile human passes through several developmental milestones, including physiological, nutritional and motor milestones that may each alter the development of the skeleton. The pelvis in particular represents a uniquely complex arrangement, as it is the junction through which the load of the trunk is ultimately transmitted to the lower limb. It will therefore experience variable loading conditions through ontogeny as a child transitions from a supine position, to upright sitting, through hands-and-knees crawling to an upright posture, with further changes likely accompanying the refinement of an adult gait pattern. In addition, genetic and hormonal influences prompt the development of clearly defined sexually dimorphic characteristics in the pelvis at puberty that may interact with the mechanical stimuli derived from ambulation.

Previous research has explored the architecture of the ilium during early development, including the neonatal (Cunningham, 2009; Cunningham and Black 2009a,b,c, 2010) and early post-natal periods (Glorieux *et al.*, 2000; Parfitt et al., 2000; Rauch *et al.*, 2006). No previously published data exists regarding the development of the ischium and the pubis. The internal architecture of the ischium in particular is of interest as it has been reported to contain trabecular bundles associated with weight bearing in a seated position (Aiello and Dean, 1990). It also comprises two fifths of the acetabulum, and a number of trabecular pathways which originate in the ilium have been described to pass inferior into the ischium before terminating, although their presence has not been confirmed previously (Macchiarelli *et al.*, 1999).

This project aimed to investigate the potential driving factors in the early post-natal development of the ischium through qualitative and quantitative analysis of skeletal architecture. This was achieved using two key imaging modalities, radiography and micro-computed tomography, in two consecutive investigative phases.

The qualitative investigation presented a radiographic description of the developmental morphology of the ischium from the late fetal period to adolescence, ceasing prior to the fusion of the acetabulum. The radiographs were processed using a colour gradient map and the resulting intensity patterns were considered in relation to potential factors that may influence the growth and maturation of the ischium.

Emphasis was placed on the perinatal and infant period (< 3 years of age) due to the combined interactions of weaning activities and the onset of the development of upright locomotor behaviours.

The data obtained from the radiographic study and the patterns that were revealed were used to guide subsequent quantitative analysis of the ischium. A key developmental period was identified in the first three years of life, where radiographic patterns revealed a trend involving the apparent loss of bone mass at 5 months – 1.5 years of age. A grid system was devised to allow the quantification of regional trabecular architecture and cortical thickness across the ischium, allowing comparison of individual regions within a single developmental cohort and also the comparison of a single region between phases. This enabled regional and developmental patterns to be established, and the potential driving factors behind these patterns were discussed.

1.2 Motivation and significance

Historically, the investigation of skeletal architecture was achieved using sectioned bones or histological techniques to qualitatively and quantitatively describe trabecular trajectories and document local variations in structure. The emphasis of these studies has traditionally been on the long bones, and in particular the femur. This was perhaps in part due to an informal convention, as trabecular arches of the proximal femur described by von Meyer (1867) and Wolff (1870) formed the basis around which one of the earliest forms of bone functional adaptation was created (Wolff, 1892), although the position of the femur and its role in weight-bearing also provides ample opportunity to study skeletal architecture in relation to mechanical loading.

The advent of high resolution three-dimensional medical imaging technologies, most notably micro-computed tomography, has allowed an expansion of the field of trabecular and cortical bone analysis which has prompted the incorporation of a greater diversity of skeletal elements, including the ilium (Cunningham and Black, 2009a,b,c, 2010), sacrum (Yusof, 2013), scapula (O'Malley, 2013), humerus (Cambra-Moo *et al.*, 2014), tibia (Gosman and Ketcham, 2008; Gosman *et al.*, 2013), calcaneus (Maga *et al.*, 2006) and vertebrae (Nuzzo *et al.*, 2003; Rapillard *et al.*, 2006).

Perhaps the greatest advantage presented by micro-computed tomography however, is the non-invasive nature of the technique: rare specimens, for example juvenile skeletal elements, which would previously have been unavailable for destructive testing techniques can now be analysed. The digital nature of this technology has also presented a number of advantages to histological approaches: a more expansive list of skeletal parameters can be investigated, including two- and three-dimensional parameters, the opportunities for data visualisation have been increased with three-dimensional surface- and volume-rendering software, and the potential for observer error in calculations has been reduced. This has facilitated the detailed investigation of ontogenetic change in histomorphometric parameters utilising irreplaceable juvenile skeletal populations where they are available.

The potential importance of analysing developmental trends in skeletal microarchitecture cannot be overstated: it provides a platform to quantify trabecular and cortical changes before and after developmental milestones are reached. For example, the investigation of pelvic architecture before the onset of bipedalism and during the maturation of gait will provide information regarding the effects of changing biomechanical pressures on trabecular architecture and they in turn relate to the attainment of the adult architectural arrangement. Such information may then be used to support current theories in skeletal development and the functional adaptation of bone, or lead to the investigation of alternative theories should conflicting information be revealed.

In addition to furthering the understanding of the factors that guide the development of mature skeletal architecture, a greater understanding of the development of the pelvis specifically may be applicable to a number of scientific fields.

While there is a relative wealth of information with regards to the structure and development of the human ilium (e.g. Cunningham and Black 2009a,b,c, 2010; Laurenson, 1964a,b; Macchiarelli *et al.*, 1999; Rauch *et al.*, 2006; Volpato *et al.*, 2008), including comparative studies looking at evolutionary trends, studies which consider the development of the ischium are relatively few. Typically, these focus on the development of gross features, such as the ischial spine (Abitbol, 1988) or the timings of pelvic and epiphyseal fusion events (e.g. Cardoso, 2008; Cardoso *et al.*, 2013;

Cunningham *et al.*, 2016; Flecker, 1932; Rissech *et al.*, 2003). The qualitative and quantitative analysis of the growth and maturation of the ischium may therefore supplement the present understanding of the development of this bone. It may also provide additional information with regards to the role the ischium plays in the structural integrity of the pelvis as it contributes to the transfer and distribution of applied loads within the pelvis (Dalstra and Huiskes, 1995; Kapandji, 2011; Phillips *et al.*, 2007).

An increased understanding of pelvic development may have applications in fields beyond pure anatomical science. In the first instance, an improved understanding of normal skeletal development may have implications for a number of clinical sub-specialties, perhaps most notably orthopaedics and paediatric medicine. An understanding of the developmental processes underlying mature skeletal architecture may help us to further understand the mechanisms and cause of bone failure, and provide an insight into potential therapeutic practices to assist in the repair mechanism.

The orthopaedic practitioner is concerned with the health of the musculoskeletal system, including the bones, joints and associated soft tissues such as muscles and ligaments (Adams and Hamblen, 2001), while paediatric medicine is concerned with the health of the child. Disorders of the pelvis and hip are not uncommon in both children and adults: the incidence of developmental dysplasia of the hip (DDH), which is characterised by instability or malformation of the hip leading to dislocation or subluxation, is estimated to be approximately 1 per 1000 births (McCarthy *et al.*, 2005). This number varies depending on geographic location and classifications used to diagnose the condition: Peled *et al.* (2005) suggested that the incidence of hip dysplasia in neonates might be as high as 5%, although less than 0.5% required subsequent correction or intervention.

The interventions for hip conditions are also numerous, and may range from orthopaedic braces and supports to correct positional abnormalities and DDH, to surgical interventions such as a pelvic osteotomy, to correct late diagnoses of DDH, and hip replacements (Adams and Hamblen, 2001). An understanding of the skeletal architecture and associated biomechanics is of great importance therefore in both

fields to monitor typical growth and determine effective corrective procedures that do not compromise skeletal health and development. Therefore, any additional information that can be provided with regards to the development of the juvenile pelvis may augment these clinical practices.

The results of the present study may also contribute to anthropological and archaeological interests. The architecture of the pelvis is considered a site of importance in comparative anatomy and osteology, as the presence of specific structural trajectories may allow researchers to infer locomotor behaviour: for example, iliac trabecular trajectories have been shown to be highly specific to locomotor mode and may identify early Hominin species which had evolved a bipedal gait and posture (Macchiarelli *et al.*, 1999; Martinón-Torres, 2003; Rook, 1999; Volpato *et al.*, 2008).

The ischium is not often considered in such studies due to its inferior position and limited role in the direct transfer of weight. However, it is suggested that the human ischium carries trabecular bundles associated with load transfer in a seated posture and collateral trajectories which assist in the distribution of ground reaction forces at the hip (Kapandji, 2011), in addition to providing attachment for several muscles and ligaments which have an increased role in a bipedal posture (Abitbol, 1988; Aiello and Dean, 1990). As such, there may be structural adaptations of the ischium that could be used to infer locomotor mode or posture in cases where fragmented remains are recovered, or where analysis of the ilium alone is not conclusive.

Finally, the adult pelvis is a site of particular forensic significance: it is the most highly sexually dimorphic region of the skeleton, and is also used in a variety of age-estimation methods. An assessment of pelvic maturation may also be used to estimate the age of sub-adult individuals through metric analyses and morphological appraisals of skeletal development. The discovery of developmental trends that either appear mature or disappear within a specific temporal window may lead to the identification of new methods of age estimation that could be applied following the recovery of fragmented skeletal remains. In particular, radiographic trends may be of interest for potential forensic applications due to the prevalence of radiographic facilities, the speed and non-invasive nature of data acquisition and the low costs involved.

1.3 The Scheuer Collection

This study utilised skeletal material from the Scheuer Collection of juvenile skeletal remains, which is housed in the Centre for Anatomy and Human Identification at the University of Dundee. This is believed to be the only active repository solely for juvenile skeletal remains, and presents a unique and invaluable opportunity to study the development of the human skeleton at different ages. The collection arose through the accumulation of material to produce a series of texts by Scheuer and Black (Cunningham *et al.*, 2016; Schaefer *et al.*, 2008; Scheuer and Black, 2004).

The Scheuer Collection is comprised of the remains of over 150 sub-adult individuals obtained from several sources, including archaeological, historic anatomical and forensic contexts. The collection contains complete and partial skeletons in addition to single isolated bones. Only a small number of the individuals are of known provenance with recorded age-at-death and sex available. All other individuals have been assigned an estimated age utilising dental age assessment where possible, and/or skeletal age assessment using metric or morphological indicators of age. This presents a potential limitation as inaccuracies in age assessment, or errors introduced due to geographical disparities or secular change, may influence the results of the study. It is also acknowledged that in most cases details of cause of death and associated morbidity are not known; therefore, it is not possible to exclude any effects of this on skeletal development.

Due to the variable origins of the skeletal remains, the state of preservation differs between individuals, which may impact negatively on skeletal analyses. Only those specimens which exhibited a good to excellent state of preservation were included in the study. Specimens that exhibited extensive damage or indicators of potential pathologies were excluded from the study. Examples of exclusion criteria are: fracturing and displacement of the cortical surfaces; erosion of cortical surfaces across a broad area to expose underlying trabecular bone, loss of anatomical features (e.g. ischial ramus) due to fracturing.

Despite the potential limitations introduced by the limited documentation available for the Scheuer Collection, it remains an invaluable resource that can provide insight into

the gross development of the skeleton and, in combination with modern imaging modalities, an opportunity to examine the architecture of individual skeletal elements at various stages of development.

1.4 Objectives

The objective of this study was to investigate the trabecular and cortical bone architecture of the juvenile ischium at key intervals during ontogenetic growth using qualitative and quantitative imaging techniques. To achieve this, observed patterns were discussed in relation to potential drivers of skeletal development and maturation, including functional relationships related to gait and possible systemic influences on bone development.

In addition, this study aimed to further build on the established volume of interest grid method devised for the quantification of skeletal architecture in the neonatal ilium (Cunningham, 2009). Investigation of data handling techniques and data visualisation methods were completed to ensure the method was suitable for examining developmental changes in the juvenile ischium, including intra-observer testing. This aided the establishment of a framework to guide future skeletal analyses.

The specific objectives outlined at the commencement of this project were:

i.   To document, using radiographic techniques, variations in the intensity pattern of the ischium during the juvenile period.

ii. To identify, a developmental period of interest for analysis using quantitative techniques (i.e. micro-computed tomography), based on the results of the qualitative study.

iii. To develop and utilise a research protocol to allow the quantification and comparison of trabecular and cortical structure at each stage of the identified developmental window of origin.

The results of the radiographic study conducted to achieve objective i revealed an unexpected pattern of development, which occurred between the perinatal period and 3 years of age. This developmental period was therefore selected to fulfil objective ii,

the period of interest for quantitative analysis. Objective iii was consequently redefined to focus on this developmental window.

I. To create and validate a grid method of analysis which allows the collection of comparable volumes of interest between ischia from the perinatal period to 3 years of age.

II. To document the trabecular and cortical structure of the perinatal ischium and to relate this structure to temporal forces acting on the bone at this age

III. To document the regional changes in trabecular and cortical structure of the ischium between the perinatal period and 3 years of age to identify potential driving factors for the radiographic changes observed, and to comment on any specific architectural changes which occur.

Chapter 2: Bone Structure and Development

2.1 Structural composition of bone

The human postcranial skeleton is comprised of two distinct structural arrangements: cortical (compact) and trabecular (cancellous) bone. Both types of bone are similar in their basic structure, being comprised of units called osteons, however their morphology, distribution and biomechanical role in the skeleton differ greatly (Schwartz *et al.*, 1998).

Cortical bone is found in the diaphyses of long bones, the continuous outer covering of the epiphyses of long bones and the outer shell of irregular shaped skeletal elements such as the ischium. Cortical bone is comprised of many tightly interlocking cylindrical osteon structures called Haversian canals [Figure 2.01]. At the core of each Haversian system is a canal containing blood capillaries and a nerve, around which a series of concentric layers of bone, or lamellae, are arranged (Clarke, 2008). The Haversian capillaries are connected to neighbouring osteons and the external blood supply by smaller perpendicular canals called Volkmann canals. There is limited porosity and few voids within cortical bone, typically less than 5% (Clarke, 2008). This has been shown to increase with age however, with increased cortical porosity reported as a key factor contributing to the fragility of osteoporotic bones (Brandi, 2009; Sundh *et al.*, 2015).

Small lacunae exist between each concentric lamella, which are occupied in life by osteocytes. These are the most numerous cells within the bone matrix, making up 90 – 95% of the adult bone cell population (Schaffler *et al.*, 2014). Each lacuna is connected directly to neighbouring lacunae by a three-dimensional network of canaliculi, through which extend the dendritic processes of the osteocytes. These processes allow osteocytes to communicate with each other, and with the osteoblast-derived bone lining cells found on the bone surface (Huiskes *et al.*, 2000). The network of osteocytes is thought to be of vital importance in mechanosensation and the control of bone modelling and remodelling (Marotti, 2000; Schaffler *et al.*, 2014) (see Chapter 2.4.1).

Figure 2.01. Magnified histological section of a Haversian osteon in adult cortical bone, stained using von Kossa's method. Adapted from Kerr, 1999.

Conversely trabecular bone is a network of interconnected struts of bone, called trabeculae, formed from avascular osteons called trabecular 'packets' (Clarke, 2008; Schwartz *et al.*, 1998). It is found in the epiphyses of long bones, the vertebral centra and the core of many flat and irregular bones, including the three component bones of the innominate. The arrangement of trabecular bone is typically described as being comprised of either rod- or plate-like structures that are separated by macroscopic spaces (Schwartz *et al.*, 1998). In place of a central vascular canal, osteocytes within trabecular packets are connected to their external environment exclusively by canaliculi, which drain directly into the marrow sinusoids between trabeculae (Burger and Klein-Nulend, 1999).

The trabecular microarchitecture is highly adaptable to external mechanical forces, and as such the precise arrangement of trabeculae is site specific, both within a single bone and between different skeletal elements (Huiskes *et al.*, 2000; Schwartz *et al.*, 1998). In the adult, the trabecular network is typically oriented in the direction of principal mechanical loads and is responsible for the distribution of forces within a skeletal element (Ruimerman and Huiskes, 2005).

The resulting structural union of cortical and trabecular bone forms a unit that is sufficiently light to facilitate efficient movement, but also stiff and strong enough to function without fracture under normal loading conditions (Huiskes, 2000). Through the processes of modelling and remodelling, a bone is capable of both adapting to a changing environment and repair following fracture and failure, and also to function as a store of important minerals such as calcium and phosphorus (Raggatt and Partridge,

2010). Bone modelling [see Section 2.5] is a cellular response which alters the size and shape of a bone through the formation of new osseous tissue (anabolic) or the removal of previously-established bone (catabolic). Bone remodelling [see Section 2.6] conversely is characterised by the sequential resorption and deposition of bone at a single location, which acts to renew and redistribute pre-existing skeletal regions (Clarke, 2008).

2.2 Bone development

The initial formation and development of human bone may occur through one of two processes: intramembranous ossification and endochondral ossification. Intramembranous ossification occurs though the direct mineralisation of mesenchymal tissue, while endochondral ossification involves the transformation of a cartilaginous precursor to bone (Cunningham *et al.*, 2016).

Intramembranous ossification is considered to be a primitive form of bone growth that has been linked to a requirement for early support and protection (Cunningham *et al.*, 2016). Bones formed through intramembranous ossification include the bones of the facial skeleton and some bones of the vault of the skull.

Endochondral ossification involves the formation of a cartilaginous anlage (template) from mesenchymal condensations, which is then subsequently replaced with bone. Endochondral bones in the human skeleton include the long bones and the bones of the girdles, including the ilium, ischium and pubis.

2.2.1 Intramembranous ossification

The initial formation and mineralisation of bone in intramembranous ossification has been described as arising through one of two possible pathways. The first, termed *de novo* mineralisation, occurs through the formation of numerous small ossific nodules within microenvironments called matrix vesicles (Boyan *et al.*, 1990). These vesicles are released from chondrocytes, and act to attract and absorb calcium (Ca_{2+}) and phosphate (PO_4) ions. In the presence of phosphatase enzymes, which metabolise phosphate ions, these precursor molecules form calcium hydroxyapatite crystals ($CH_{10}[PO_4]_6[OH]_2$), the inorganic component of bone. As these crystals increase in size,

they rupture the matrix vesicle membrane and project into the mesenchymal tissue. As they continue to accumulate minerals, neighbouring nodules fuse to form larger seams of woven bone (Marvaso and Bernard, 1977).

It has also been demonstrated that intramembranous ossification can occur in the absence of matrix vesicles however, through the direct differentiation of mesenchymal cells into osteoblasts (Arsenault and Ottensmeyer, 1984). The osteoblast cells secrete osteoid, the collagenous bone matrix, and the phosphatase enzymes that promote the mineralisation of the osteoid and the formation of the primary ossification centre. The concurrent growth of blood capillaries and differentiation of osteoblasts within the mesenchyme is regulated by vascular endothelial growth factor (VEGF), a growth factor which stimulates angiogenesis in hypoxic conditions, and also the recruitment and differentiation of osteoblasts within mesenchyme (Yang *et al.*, 2012).

In intramembranous elements, the primary spongiosa forms first through the growth of thin bone spicules between adjacent mesenchymal cells, which ultimately expand and thicken via surface apposition to encompass the network of blood vessels. Bone is also accumulated on the free ends of these spicules, which facilitates radial growth of the spongiosa. As the rudimentary trabecular core expands, the surface of the developing bone condenses to form the fibrous periosteum, and it is on the inner layer of this structure that the preliminary layers of cortical bone are deposited, enclosing the expanding trabecular cavity (Cunningham *et al.*, 2016).

Periosteal ossification: a precursor to endochondral ossification

In addition to facilitating the formation of entire bones, the formation of an intramembranous ossification centre may be an important precursor to endochondral bone formation in some circumstances. Prior to the commencement of endochondral ossification, an intramembranous ossification centre may be observed in the perichondrium of the cartilaginous anlage. In long bones, this occurs via proliferation and differentiation of mesenchymal cells in the midshaft perichondrium to form osteoblast cells. These cells secrete osteoid matrix in close proximity to the perichondral capillaries, which is ossified rapidly due to the presence of matrix vesicles in the vicinity of this condensation (Cunningham *et al.*, 2016). This 'bony collar'

encircles the cartilaginous anlage and begins to extend proximally and distally to cover the surface of the diaphysis, ultimately forming cortical bone. Initially this is laid down as woven bone by mesenchymal osteoblasts, although this is later remodelled to form mature lamellar bone (Shapiro, 2008).

2.2.2 Endochondral ossification

Chondrogenesis

Endochondral ossification is, by necessity, preceded by chondrogenesis: the formation of a cartilaginous precursor. Chondrocyte precursor cells are recruited by transcription factors released from nearby mesodermal cells. These cells condense quickly and differentiate to form chondrocytes, or cartilage cells, which proliferate to adopt the shape of the future bone (Karsenty, 2001). These chondrocytes are responsible for the secretion and maintenance of the cartilaginous extracellular matrix that forms the precursor to bone.

Ossification

Following the establishment of the bony collar via intramembranous ossification, the core chondrocytes within the cartilaginous anlage cease dividing and increase in size, becoming hypertrophic chondrocytes (Blair *et al.*, 2002). These hypertrophic chondrocytes degrade their local extracellular matrix, altering surface receptors to make it increasingly sensitive to calcium phosphate mineralisation, and they also begin secreting angiogenic stimulators such as VEGF which attract developing capillaries (Maes *et al.*, 2002). Ultimately the hypertrophied chondrocytes undergo apoptosis, leaving a thin lattice of cartilaginous matrix surrounding the chondrocyte lacunae (Roach, 1997; Sasaki *et al.*, 1996). A vascular bud then penetrates the bony collar in response to the angiogenic stimulators, creating an interruption canal and allowing osteoblasts access to the modified matrix to commence ossification. The longitudinal septae of the cartilaginous matrix become ossified to form trabecular struts, while the interconnecting transverse septae are largely resorbed (Sasaki *et al.*, 1996). While in long bones the endochondral trabeculae formed in the diaphysis are largely resorbed during later development (with the exception of those in the extremity of the

diaphysis), in atypical bones such as the three pelvic elements the endochondral trabeculae are retained and remodelled to form the cancellous core of these bones.

Bone growth and the growth plate

Two processes facilitate the continued growth of a bone: periosteal apposition allows for circumferential (or diametric) growth through cortical drift, while the proliferation of the specialised cartilaginous growth plate allows longitudinal growth.

The periosteum which lines the outer surface of bones is comprised of two layers: an outer fibrous layer and an inner cambium layer, which is highly cellular and contains mesenchymal cells, osteogenic progenitors and differentiated osteoblasts (Burr and Guillot, 2012; Dwek, 2010; Roach, 2007). It is this cambium that facilitates the apposition of bone on the periosteal surface, providing the necessary osteogenic cells and a rich vascular supply. The thickness of the cambium decreases with increasing age, which is concurrent with a decrease in the rate of periosteal apposition (Burr and Guillot, 2012).

The longitudinal growth of an endochondral bone is dependent on the action of a growth plate, a transitional region of cartilage that encapsulates proliferation, hypertrophy and ossification sequentially. A growth plate is a highly organised structure that can be divided into a number of morphologically distinct layers (or 'zones') when viewed in cross-section (Mackie *et al.*, 2008) [Figure 2.02]. The layer furthest from the primary centre of ossification is termed the resting or germinal zone, in which chondrocytes are small and unevenly distributed (Abad *et al.*, 2002). These cells have been suggested to be stem-like cells that are responsible for the formation and alignment of the chondrocytes of the subsequent layers (Abad *et al.*, 2002). Adjacent to the germinal zone is the proliferative zone, in which active cell division occurs (Abad *et al.*, 2002; Mackie *et al.*, 2008). During proliferation, chondrocytes align in a series of columns along the longitudinal axis of the bone, with cell division occurring at the base of each column (Burdan *et al.*, 2009).

The proliferative zone transitions into the zone of transformation, which can be further subdivided into a hypertrophic layer and a degenerative layer (Burdan *et al.*, 2009). Throughout this layer there is a progressive transformation as the chondrocytes

differentiate terminally to form hypertrophic chondrocytes (Abad *et al.*, 2002). The cells cease dividing, enlarge, and begin to produce alkaline phosphatase, which in turn will facilitate hydroxyapatite deposition via matrix vesicles (Burdan *et al.*, 2009). It has also been suggested that the hypertrophic cells release angio-attractant signals that attract blood vessels to further invade the cartilaginous matrix (Abad *et al.*, 1999), perhaps through the release of VEGF, in a manner similar to angiogenesis during primary ossification (Maes *et al.*, 2002). In the final zone of ossification, osteoblasts invade the mineralised matrix and form a layer of new bone on the longitudinal matrix spicules (Abad *et al.,* 1999).
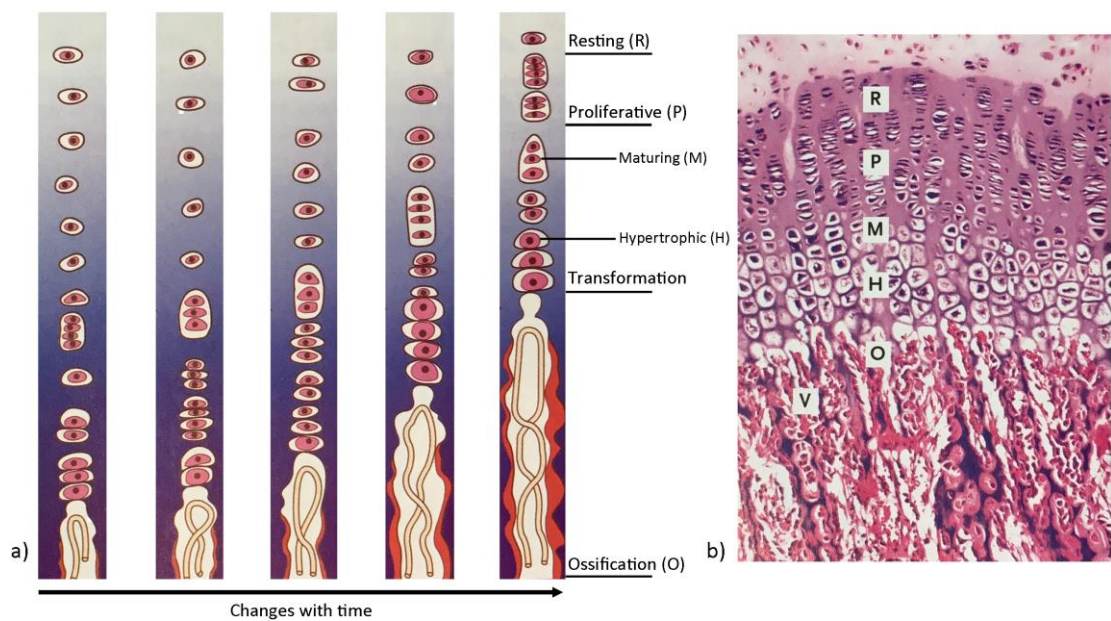
Figure 2.02. The growth plate. a) Diagrammatic representation of temporal changes in the growth plate. b) Longitudinal section of a growth plate, showing chondrocytes in designated areas of rest (R), proliferation (P), maturation (M), hypertrophy (H) and ossification (O), with vascular invasion occurring inferiorly (V). Adapted from Kerr (1999).

Growth plate closure

The closure of the growth plate, or epiphyseal union, occurs when the growth of bone surpasses the growth of cartilage (Mackie *et al.*, 2008). This closure is driven primarily by a decrease in the proliferative potential of chondrocytes within the proliferative zone of the growth plate, although the underlying mechanisms are poorly understood (Shim, 2015). The physical manifestation of fusion is evident when the subchondral surfaces of the diaphysis and epiphysis begin to thicken, forming dense parallel plates

(Cunningham *et al.*, 2016). The two plates advance further with the mineralisation of the intervening cartilage, and small vessels are observed to pierce through the cartilage and unite the metaphyseal and epiphyseal vessels. Osteoblasts migrate with the blood vessels and establish thin bridges of bone between each plate, which then expand to entirely replace the remaining cartilage (Cunningham *et al.*, 2016).

Oestrogen is known to be an important systemic factor in controlling senescence of the growth plate (Nilsson and Baron, 2004; Weise *et al.*, 2001), although its precise actions have not yet been determined. Relatively high concentrations of oestrogen have been shown to suppress growth, although physiological concentrations are linked to the onset of the pubertal growth spurt (Weise *et al.*, 2001). It has been suggested that oestrogen does not stimulate fusion directly, but rather acts through an unknown signalling mechanism to increase the programmed senescence pathway that leads to the exhaustion of the proliferative capacity of the resting zone chondrocytes.

2.3 The adaptation of bone

2.3.1 Overview

Bone is a complex, metabolically active tissue that is continually renewed, restructured and redistributed in response to a number of external stimuli (Hadjidakis and Androulakis, 2006; Roberts *et al.*, 2004). In particular, bone has been found to be highly responsive to its mechanical environment, increasing bone strength through increased bone mass and architectural optimisation in response to increased loading, and conversely losing bone mass in regions where loading is decreased (Huiskes *et al.*, 2000; Ruff *et al.*, 2006).

However, the structure and modification of bone is not informed by biomechanical stimuli alone, and a number of variables have been identified which may influence bone form. These include genetic programming, for example skeletal patterning and the regulation of cell signalling, and epigenetic and extragenetic factors such as health, nutritional status and homeostatic mechanisms (in particular calcium homeostasis) (Lovejoy *et al.*, 2003; Prentice, 2001; Ruff *et al.*, 2006; Skedros *et al.*, 2007).

2.3.2 Historical context of mechanical adaptation

The relationship between skeletal form and function and the influence of biomechanical interactions is perhaps most commonly referred to as 'Wolff's Law', after the work of anatomist and orthopaedic surgeon Julius Wolff in the late 19th century (Huiskes, 2000). This 'law', known as bone functional adaptation (BFA) in its present usage, refers to the concept that the form of bone reflects its mechanical loading history, and will adapt to its mechanical environment during life (Ruff *et al.*, 2006).

The origins of Wolff's Law lie first in the work of Georg Hermann von Meyer, who published a manuscript outlining the observed similarities between the orientation of trabecular architecture in a number of skeletal elements and their hypothetical loading conditions (von Meyer, 1867). For example, he noted that the trabeculae of the distal tibia were primarily arranged in line with the longitudinal axis of the bone, directed towards the talar articular surface, which is consistent with unidirectional weight transfer from the knee to the ankle [Figure 2.03]. The proximal tibia also exhibited longitudinal trabecular bundles, but with oblique trabeculae that crossed from each condyle to the opposing diaphyseal surface which was suggested to provide increased multi-directional reinforcement due to the greater range of loading conditions at the knee (von Meyer, 1867).
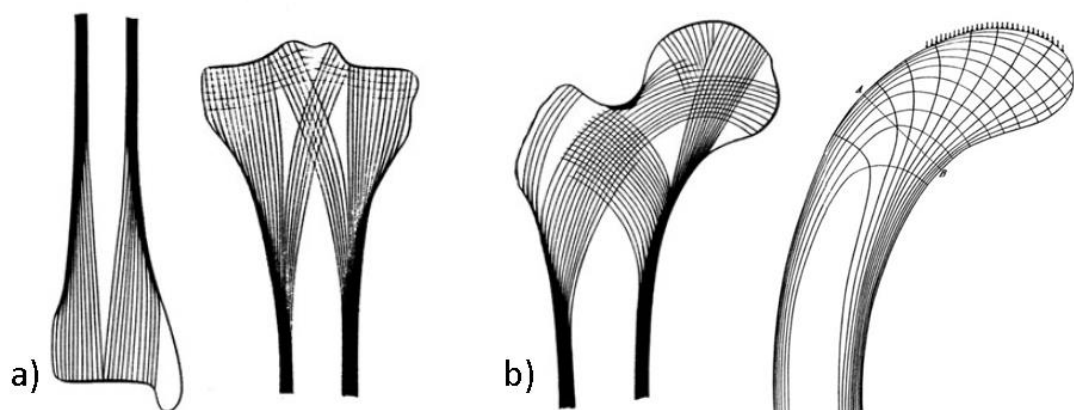
Figure 2.03. Schematic diagrams of the a) principal trabecular arrangements of the distal and proximal tibia and b) the correspondence between trabecular organisation in the proximal femur and the stress distribution in a Culmann bridge. Adapted from von Meyer, 1867.

Of perhaps greater importance however were the observations of the proximal femur. Von Meyer noted distinct similarities between the general appearance of the trabecular architecture of the proximal femur and the theoretical stress distribution in a curved Culmann bridge, after diagrams produced by Carl Culmann [Figure 2.03]. There was agreement between both the arcing compressive trajectory emanating from the femoral head, and also the reciprocal tensile trajectory crossing from the greater trochanter to the medial aspect of the diaphysis. In conclusion, von Meyer observed that *"…through more detailed investigation…one sees an apparently well-intended architectural arrangement closely interdependent with the statics and mechanics of the bone"* (von Meyer, 1867).

It was this intersection of anatomy and engineering which was subsequently explored by Julius Wolff, who described the observations of von Meyer as *"one of the most extraordinary discoveries of physiology, one of the most meaningful, actually, to which the study of bones has led until today"* (Wolff, 1870). Following extensive study of the proximal femur in particular, Wolff proposed that the architecture of bones may not only be optimal for their specific biomechanical environment, but that that environment may itself be involved in the formation of the bone (Wolff, 1870). Wolff described instances of fracture healing and noted that repair did not simply involve the reattachment of free trabecular ends, but rather the formation of new trabeculae in response to the altered dynamics of the bone (Wolff, 1873).

The studies of Wolff culminated in the publication of the renowned treatise 'The Law of Transformation of Bone' (originally '*Das Gesetz der Transformation der Knochen*'), which outlined a mathematical model describing the relationship between mechanical stress and bone architecture (Wolff, 1892). The "law" stated that any changes to the internal architecture, and indeed changes to the external morphology of a bone, occurred as a consequence of "*primary changes in the shape and stressing of the bones*", following strict mathematical rules (Wolff, 1892). It should be noted that the changes in shape and stress suggested by Wolff were primarily pathological in nature, for example altered biomechanics following fracture, rather than temporal and functional fluctuations in loading.

The implications of this monograph led to great debate, both within the contemporary literature at the time of publication and in the present day (Huiskes, 2000; Ruff *et al.*, 2006; Skedros and Baucom, 2007). It has been observed that the theory proposed by Wolff was based on several incorrect assumptions. The Culmann Bridge model around which Wolff based his theory was derived for a homogenous and isotropic structure, rather than the interactions of cortical bone and complex trabecular networks to which his model was applied (Huiskes, 2000). It was also noted that the depictions of trabecular structures presented and used were somewhat simplified, in a manner that tended to overstate the orthogonal nature of the trabecular trajectories (Hammer, 2015).

Shortly before the seminal publication of Wolff, a second author, Wilhelm Roux, proposed an alternative theory to Wolff's Law that explained the phenomenon of trabecular organisation following two important principles: that organisms possess the capacity to adapt to a changing environment, and that bone cells have the capacity to detect and respond to local mechanical stimuli (Ruff *et al.*, 2006). The colloquially applied 'Wolff's Law' as it appears in current literature is perhaps best described as an amalgamation of the principles of both Wolff and Roux. The mathematical basis of Wolff's Law as it was written have been largely dismissed due to the inaccuracies in the model on which they were based (Huiskes, 2000; Ruff *et al.*, 2006). What remains is the 'general' version of Wolff's Law, which suggests that the structure of bone is informed and directed by its biomechanical environment. It has been suggested that the term Wolff's Law is indeed a misnomer, as this generalised version bears greater similarity to the hypotheses of Roux than Wolff, and so to become distinct from the historical mathematical Wolff's Law, the adaptation of bone in response to mechanical stimuli is now more commonly referred to as bone functional adaptation (BFA) (Ruff *et al.*, 2006).

2.3.3 Bone functional adaptation and the mechanostat hypothesis

In simple terms, the action of bone functional adaptation can be viewed as a negative feedback loop, in which the deviation of bone strain from a physiological set point (the

optimum customary strain; OCS) will invoke a change in either bone modelling or remodelling (Lanyon, 1982) [Figure 2.04a]. This mechanical stimulus is strain, the physical deformation of bone in response to a load, rather than stress, the force or load that is applied (Ehrlich and Lanyon, 2002). This strain-adaptive feedback loop is perhaps best known as the 'mechanostat', after the theory outlined by Frost (1996).

In its most basic form, the mechanostat predicts that an increase in mechanical loading will increase local strain above the optimum customary strain. This will trigger the formation of new bone to reinforce the atypically loaded area, which will distribute the load and reduce the strain back to the OCS (Ruff *et al.*, 2006). The opposite occurs when loading is reduced and the strain falls below the OCS: extraneous bone will be resorbed to increase the local strain and restore the set point. An important caveat to the mechanostat model is the acknowledgement of possible extraneous variables that may also influence modelling and remodelling, termed 'non-mechanical agents' by Frost (1996) [Figure 2.04b]. These agents include systemic agents such as hormones and local signalling factors such as cytokines.
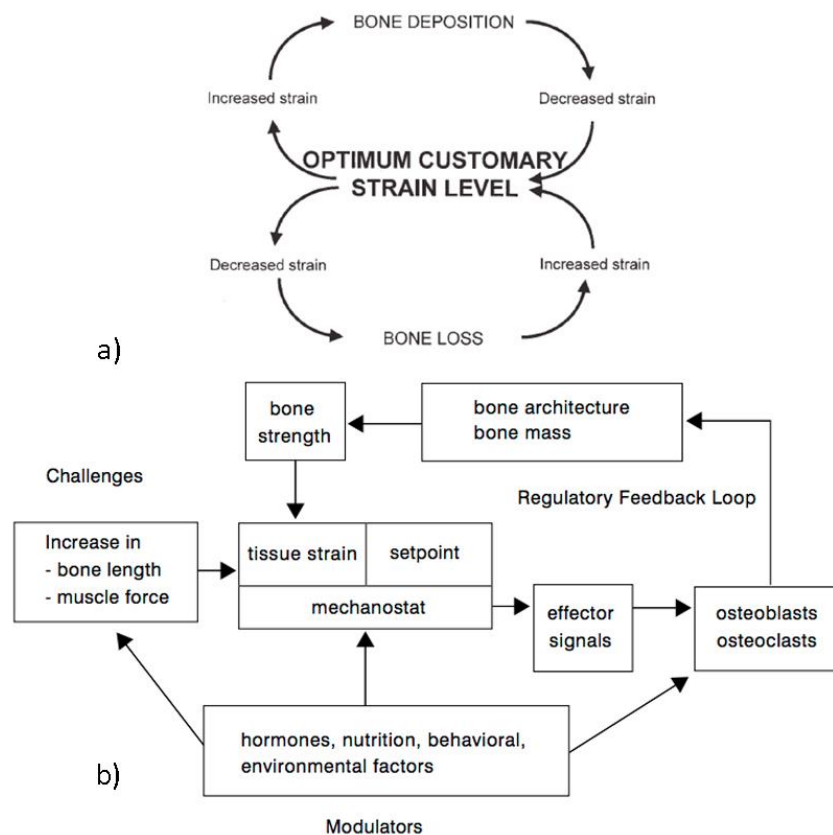
Figure 2.04. a) A simple negative feedback model describing mechanical bone adaptation. From Lanyon, 1982. b) A functional model demonstrating the mechanostat comparison with the set point centrally and non-mechanical agents which may modulate the mechanostat or its response. From Schoenau, 2005.

The type of response that is initiated, either modelling or remodelling, is dependent on the relative magnitude of the strain detected (Standford and Brand, 1999) [Figure 2.05]. The physiological loading that is represented by the OCS is typically described as approximately 50 – 200 microstrains (Skedros *et al.,* 2001; Standford and Brand, 1999).

Strains within this magnitude typically produce what is considered normal remodelling of bone: renewal of the present bone mass and structure with minimal net change or reorganisation, assuming an optimal structure has been achieved previously. With deviation in loading to below 50 – 200 microstrains, bone will undergo disuse atrophy which results in a loss of bone mass. Excessive loading above 2500 microstrains will create physiological overload which initiates a modelling response to increase bone mass and strength in the regions of high strain, and this will continue until the strain has decreased to the physiological level. Skedros *et al.* (2001) noted that above approximately 4000 microstrains, woven bone is produced rather than mature lamellar bone, and therefore may be better considered a repair mechanism than either modelling or remodelling.
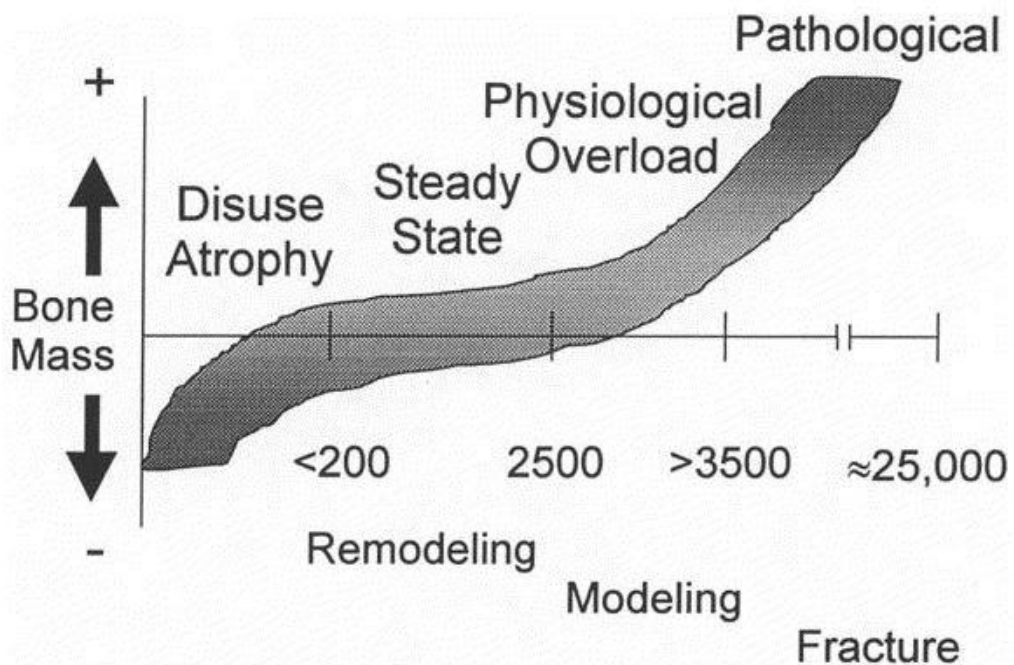
Figure 2.05. The influence of mechanical strain on bone mass. The shaded area represents change in bone mass associated with loading. From Stanford and Brand, 1999.

2.4 Mechanosensation

Although a great deal of research has been traditionally directed at understanding the actions of the effectors of change in bone architecture, osteoblasts and osteoclasts, it has become increasingly apparent that it is the osteocyte cells which are primarily responsible for directing the activities of both effector cell types (Marotti, 2000; Schaffler *et al.*, 2014). Osteocytes are capable of communicating with osteoblasts and bone lining cells directly through cell-to-cell gap junctions and by extracellular signalling pathways (Schaffler *et al.*, 2014). Osteocytes are also believed to be involved in signalling pathways involving osteoclast recruitment and differentiation, although these pathways are poorly understood (Heino *et al.*, 2002; Schaffler *et al.*, 2014).

2.4.1 Mechanotransduction

Osteocytes are the most numerous cells within the bone matrix, making up 90 - 95 % of the adult bone cell population (Schaffler *et al.*, 2014). They are derived from osteoblasts that have become entrapped in the ossified bone matrix during bone formation. The lacunae in which they reside are connected directly to their neighbouring osteocytes by dendritic processes which extend through the three-dimensional network of canaliculi, and also to the osteoblast-derived bone lining cells (Huiskes *et al.*, 2000).

It has been largely accepted that osteocytes act as a central control system that directs the response to mechanical stimuli (Marotti, 2000) through mechanotransduction, the conversion of mechanical inputs to electrical or biochemical signals. Physiological loading induces two primary changes: a physical deformation of the bone matrix and a change in the interstitial fluid flow dynamics, which introduces shear stresses to osteocyte membranes (Schaffler *et al.*, 2014; Skedros *et al.*, 2001; You *et al.*, 2000). Despite much interest in the process however, the mechanisms that underlie this function remain contested (Bonewald, 2007; Heino *et al.*, 2002; Ruimerman and Huiskes, 2005; Schaffler *et al.*, 2014).

While it has been demonstrated that osteocytes are capable of detecting physical deformation, as are most cell types, it would appear unlikely that this direct sensory

mechanism is responsible for mechanotransduction. You *et al.* (2000) demonstrated that while osteocyte cell cultures did increase signalling following the application of mechanical strains, the level of strain required to induce a significant increase in signalling was in excess of 5,000 microstrains. This exceeds the levels of normal physiological loading, rather representing physiological overload and potentially resulting in osteocyte apoptosis through microfracturing (Schaffler *et al.*, 2014).

In light of the relatively high physical strains necessary to stimulate osteocytes directly, the influence of extracellular fluid flow is now considered the most likely pathway by which osteocytes detect strain *in-vivo* to initiate modelling or remodelling (Schaffler *et al.*, 2014; You *et al.*, 2000).

Numerous studies have indicated the importance and mechanics of fluid flow in osteocyte mechanosensation. In the study by You *et al.* (2000), it was found that while mechanical strains only stimulated osteocyte activity at levels far in excess of physiological conditions, osteocytes were highly responsive to oscillating fluid flow which mimicked that expected during routine loading, thereby significantly increasing cell signalling.

These results have been supported by further studies that have examined the effects of fluid flow on bone resorption and formation. Tan *et al.* (2007) demonstrated that osteocyte cell cultures subjected directly to a pulsating fluid flow acted to inhibit osteoclastogenesis and bone resorption, and suggested that this was related to the up-regulation of a nitric oxide (NO) signalling pathway. Vezeridis *et al.* (2006) reported that osteocytes exposed to a similar pulsating fluid flow released signalling factors that inhibited osteoblast proliferation, but resulted in increased differentiation into mature, bone-forming osteocytes. Although the signalling pathways were not clearly identified, it was suggested that this might also be a result of NO production.

The unique three-dimensional environment of the osteocyte, confined within lacunae and connected by canaliculi, have been the subject of some discussion with regards to mechanosensation as it has been noted that the relatively voluminous lacunae would exhibit different fluid flow pressures to the more restrictive canaliculi (Verbruggen *et al*, 2012). The dendritic processes that extend through the canaliculi are therefore the

most likely to receive adequate stimulation to trigger an osteogenic response due to the amplifying effect of the narrow spaces (Burra *et al.*, 2010; Verbruggen *et al.*, 2012).

2.4.2 Activation of bone modelling

Osteoclast communication

The nature of osteoclast recruitment by osteocytes remains poorly understood, although it appears that it is linked intrinsically to osteocyte apoptosis (Jilka *et al.*, 2013; Schaffler *et al.*, 2014). It has been recognised both in the clinical and experimental literature that physiological underloading or disuse through immobilisation will result in an increase in osteocyte apoptosis and an increase in bone resorption (Aguirre *et al.*, 2006; Basso and Heersche, 2006; Demirbag *et al.*, 2005; Mann *et al.*, 2006). For example, Mann *et al.* (2006) demonstrated a significant increase in the rate of osteocyte apoptosis in *in-vitro* trabecular bone cores following periods of disuse, which appeared to be redressed by the subsequent application of mechanical stimuli. Termed 'disuse atrophy', this increase in apoptosis typically occurs where the local strain falls below 200 microstrains (Stanford and Brand, 1999).

The mechanism through which apoptosis is triggered and how this subsequently affects osteoclast activity remains contentious, as no definitive signalling pathways have been identified as yet. The increase in osteocyte apoptosis was linked in mice to a decrease in the release of nitric oxide and expression of nitric oxide synthedases (Basso and Heersche, 2006). High levels of nitric oxide have been shown to favour the formation of bone, and are released from osteocytes in response to mechanical loading (Zaman *et al.*, 1999). With regards to increased resorption, Heino *et al.* (2002) identified that, at rest, osteocytes secrete Transforming Growth Factor-β (TGF-β), a cytokine signaller which inhibits osteoclastic bone resorption. The mechanism which underlies this inhibitory action is unclear, although it may involve an interaction with the stimulatory RANK-ligand / OPG pathway [See Section 2.6.1]. A decrease in the secretion of TGF-β following osteocyte apoptosis would reduce or remove the inhibitory effects demonstrated by this cytokine, allowing bone resorption to occur.

Osteoblast communication

In addition to either promoting or preventing the recruitment of osteoclast cells, osteocytes also appear to play a role in the control of osteoblastogenesis and bone formation. In addition to the release of the osteoclast-inhibiting TGF-β, osteocytes have also been shown to secrete two proteins, sclerostin and dickkopf-1 (DKK-1), which inhibit osteoblast action through the disruption of the Wnt signalling pathway (Schaffler *et al.*, 2014), which is known to promote osteoblast differentiation and bone formation (Moester *et al.*, 2010).

The expression of the Sost gene and the release of sclerostin in particular has been considered to be of importance in regulating osteoblast activity. Robling *et al.* (2008) demonstrated that the release of sclerostin is inversely proportional to mechanical strain in mice: an increase in strain decreases the release of sclerostin, removing its inhibitory effects and allowing osteoblast differentiation. This highlights the potential importance of sclerostin, and osteocytic mechanosensation, in bone formation.

Osteocyte cells have also been shown to secrete paracrine signalling factors in response to mechanical stimulation, including factors such as cyclic AMP (cAMP), nitric oxide and prostaglandin E_2 (Schaffler *et al.*, 2014), although the latter is more often linked to the activation of the basic multicellular unit in bone remodelling [See Section 2.6.1]. The intermittent release of cAMP has been shown to increase osteoblast differentiation in the presence of parathyroid hormone (PTH), leading to an increase in bone formation (Kao *et al.* 2012). Nitric oxide signalling is conversely believed to be influential in both osteoclast inhibition (Tan *et al.*, 2007) and osteoblast differentiation and bone formation (Vezeridis *et al.*, 2006; Zaman *et al.*, 1999).

2.5 Bone modelling

The process of modelling drives changes in the size and shape of a bone in response to physiological influences, for example during growth, and in response to mechanical loading and failure (Clarke, 2008; Roberts *et al.*, 2004). Modelling is an uncoupled process: it is characterised by the resorption and deposition of mineralised tissue at spatially distinct sites (Raisz, 1999; Roberts *et al.*, 2004; Schnitzler *et al.*, 2009).

Bone modelling is often described as occurring through lamellar or cortical 'drifts' (Frost, 1990). Formation drifts, or anabolic modelling events, are characterised by the deposition of new circumferential lamellae across a region of bone surface, while resorption drifts, or catabolic modelling events, act to remove regions of bone through osteoclastic action (Frost, 1990; Roberts *et al.*, 2004).

While the emphasis of literature examining bone modelling is typically on cortical change, it has also been suggested that smaller-scale modelling events occur on trabecular bone surfaces (Frost, 1990). These 'mini-modelling' activities were proposed to be a mechanism by which trabeculae increase in thickness in response to mechanical loading. The distinction of a mini-modelling event from a trabecular remodelling event is based on the morphology of the cement line between new and old bone: in remodelling, deposition is preceded by resorption which creates a scalloped surface, while in modelling no resorption has occurred so the cement line appears smooth and uninterrupted (Jee *et al.*, 2007; Kobayashi *et al.*, 2003) [Figure 2.06]. The occurrence of these events in adult and elderly populations appears to be very low, covering less than 1 % of the trabecular bone surface (Kobayashi *et al.*, 2003), but it may be more prolific in juvenile individuals who also demonstrate a higher rate of cortical modelling than adults.
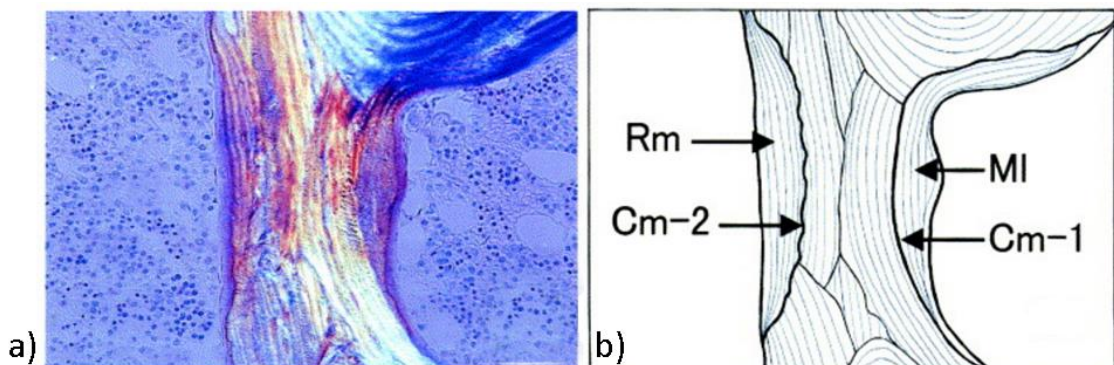
Figure 2.06. Minimodelling and remodelling as observed in human iliac trabecular bone. a) Polarised light micrograph of a trabecula which exhibits characteristics of remodelling (left) and minimodelling (right) activity; b) schematic of representation of a). MI: minimodelling; Cm-1: smooth, uninterrupted cement line; Rm: remodelling; Cm-2: Scalloped cement line. Adapted from Kobayashi et al., 2003.

Modelling may result in the deposition of various types of bone, the selection of which is dependent on the magnitude of loading that drives the depositional event. Low levels of strain may permit the deposition of mature lamellar bone, while higher levels

of strain may require the more rapid deposition of woven or composite bone which can then be remodelled to form mature lamellar bone (Roberts *et al.*, 2004). As noted previously, it is debated whether this deposition should be considered a function of bone modelling or repair (Skedros *et al.*, 2001).

2.6 Bone remodelling

Bone remodelling, in contrast to modelling, is a coupled process characterised by the sequential resorption and deposition of osseous tissue at a single location in a carefully controlled series of events. Remodelling acts throughout life, actively removing discrete regions of older bone and replacing it with new bone. In addition, it provides a mechanism by which pre-existing structures can be modified in response to biomechanical loading. Remodelling can result in either the conservation of total bone tissue or, particularly later in life, a reduction in bone tissue as resorption exceeds deposition, but it is not typically associated with a net increase in bone mass as is associated with anabolic modelling (Frost, 1994; Morgan *et al.*, 2010).

Remodelling occurs through a synchronised series of events at a single location, although no agreement has been reached on the number or nomenclature associated with each remodelling phase. Parfitt (1984) defined a series of five stages: a period of quiescence during which no remodelling activity occurs; activation of bone remodelling followed by resorption, reversal and formation, before returning to a period of quiescence. Clarke (2008), Jilka (2001) and Raggatt and Partridge (2010) also described five stages, but removed 'quiescence' in favour of a final 'termination' phase. Hadjidakis and Androulakis (2006) described only three stages, resorption, reversal and formation, excluding the quiescent period and a specific activation phase. Feng and McDonald (2011) suggested four stages, combining formation and the termination / quiescence phases into a single event. Kini and Nandeesh (2012) instead described six stages, with the addition of a 'mineralisation' phase following formation, and a restoration of the 'quiescence' terminology. Despite the disagreement, each author describes the same pattern of events, allowing for writing focus and available knowledge. For the purposes of this project, the nomenclature of the five stages as described by Parfitt (1984) will be utilised.

2.6.1 The basic multicellular unit

Bone remodelling is completed through the action of a basic multicellular unit (BMU), a collaboration of osteoclasts and osteoblasts that acts to remove and replace discrete packets of bone, termed 'bone remodelling compartments' (Hadjidakis and Androulakis, 2006). The bone remodelling compartment is contained by the persistent presence of bone lining cells derived from the osteoblast lineage covering the surface of the compartment (Parfitt, 1984). A single BMU consists of a number of cell lineages that are supported by connective tissues and a blood supply, typically in the form of a capillary (Jilka, 2001). In cortical bone, a small number of multi-nucleated osteoclasts form the anterior 'cutting cone' which tunnels through the bone, followed by a large number of osteoblasts which deposit new osteoid matrix and direct its conversion into new lamellar bone and the formation of a new osteon (Hadjidakis and Androulakis, 2006; van Oers *et al.*, 2008). In trabecular bone, the process is similar but in place of tunnels, osteoclasts traverse the surface of the trabeculae and create a shallow trench called a Howship lacuna. Osteoblasts then fill this trench to create a hemi-osteon (Figure 2.06b, marker Rm) (van Oers *et al.*, 2008).

The rate of bone turnover of trabecular bone is greater than cortical bone, with a replacement of 2 – 5% of cortical bone per year, compared to an annual renewal of 25% of trabecular bone. While this has been described as an increase in the remodelling rate of trabecular bone when compared with cortical bone (e.g. Clarke, 2008; Morgan *et al.*, 2010), Parfitt (2010) urged caution for this interpretation. Bone remodelling is a surface response and therefore bone turnover is dependent on the surface to volume ratio of the tissue in question. As trabecular bone possesses a much greater surface-volume ratio than cortical bone, it may not be the rate of remodelling *per se* that is increased, but rather the number of BMU activations on the surface that contribute to the increased turnover of trabecular bone.

Activation of the BMU via RANK-ligand and OPG pathway

The first phase of remodelling is *activation*, and while this is perhaps the most significant factor driving skeletal maintenance and modification, it is also perhaps the least well understood. In practical terms, activation involves the recruitment of

osteoclasts, which then migrate towards, and bind with, the mineralised surface to be resorbed (Parfitt, 1984). There are several pathways that can trigger this phase, including the repair of microdamage, the influence of mechanical loading and hormonal signalling.

Following the detection of a mechanical strain, osteocytes release a number of signalling factors including prostaglandins. In particular, the release of prostaglandin E_2 (PGE$_2$) is reported to trigger the initial activation of the BMU (Ajube *et al.*, 1999; Klein-Nulend *et al.,* 1995; Tian *et al.*, 2008). PGE$_2$ recruits osteoblast progenitor cells to the site of remodelling, which in turn enlist mononuclear osteoclast precursors through the regulation of cytokine concentrations (Clarke, 2008). Release of the osteoclast-inhibiting osteoprotegerin (OPG) is down-regulated while the release of receptor activator of nuclear factor kappa-B (RANK) ligand, an up-regulator of osteoclastogenesis, is increased (Roodman, 1999). The osteoclast precursors accumulate and enter beneath the bone lining cells, and multiple mononuclear cells then fuse to form large multinucleated osteoclasts (Feng and McDonald, 2011; Raggatt and Partridge, 2010).

Systemic regulation of BMU activation

The initial activation of the BMU may also be controlled by hormonal signals in response to systemic signals. Parathyroid hormone, Vitamin D_3 and calcitonin are each known to have an influence on bone remodelling (Raisz, 1999; Raggatt and Partridge, 2010).

Parathyroid hormone (PTH) is a regulator of serum calcium concentrations: it is released by the parathyroid glands in response to low blood serum calcium levels. PTH will bind to osteoblasts and stimulate the release of cytokines which will recruit osteoclastic cells through the RANK-ligand system, up-regulating RANK-ligand and down-regulating OPG (Carter and Schipani, 2006). Interestingly the effects of PTH appear to be temporally controlled: the intermittent release of PTH will stimulate osteoblast mediated bone formation rather than resorption (Kroll, 2000). A decrease in PTH secretion due to increased serum calcium concentrations will result in a decrease in bone turnover and lead to an increase in bone volume (Carter and Schipani, 2006).

Vitamin D_3 is also involved in calcium homeostasis: most notably, it regulates the intestinal absorption of calcium, and its reabsorption in the kidneys, where an increase in vitamin D_3 concentration will increase absorption. A decrease in vitamin D_3 will decrease calcium absorption, creating a hypocalcaemic environment that will trigger the release of PTH to increase bone resorption (Raisz, 1999). A vitamin D_3 deficiency has been linked to the failure of bone development and mineralisation, leading to rickets, osteomalacia and growth plate anomalies (Li *et al.*, 1998).

Eisman and Bouillon (2014) noted that the regulatory effects of vitamin D_3 express a similar temporal relationship as PTH: it may introduce either a catabolic (resorptive) or anabolic (depositional) change in bone remodelling. However, the mechanism underlying this action is not fully understood. Vitamin D_3 metabolites have been found to stimulate the release of OPG directly from mature osteoblasts, which will inhibit bone resorption (Baldock *et al.*, 2006). However, it has also been shown to stimulate immature osteoblasts to trigger osteoclast differentiation, which would increase bone resorption (Suda *et al.*, 1999). Calcitonin, a hormone secreted by the thyroid gland, has also been described as an important factor in bone remodelling. It has been demonstrated that serum calcitonin concentrations are typically low, but increase dramatically during pregnancy, along with vitamin D concentrations (Whitehead *et al.*, 1981). This, it was suggested, was a response to protect the maternal skeleton from excessive resorption during pregnancy: vitamin D increases intestinal calcium absorption and osteoclast-mediated bone resorption, while calcitonin inhibits osteoclast activity.

In-vitro studies have confirmed that calcitonin binds to a receptor on osteoclasts, which prevents the migration and differentiation of the cells and blocks the osteoclastogenic action of RANK-ligand (Carter and Schipani, 2006; Davey and Findlay, 2013). The absence of calcitonin has been shown to increase the responsiveness of osteoclasts to PTH administration in mice, rather than directly increase resorption (Hoff *et al.*, 2002), further reinforcing the action of this hormone as being primarily protective in nature, preventing excessive bone resorption and moderating the activity of osteoclast-stimulating factors.

It has also been suggested that calcitonin may have an inhibitory effect on bone formation, as mice that were modified to lack the calcitonin gene displayed an increase in trabecular bone volume at approximately 3 months of age, with a subsequent increase in cortical bone porosity occurring at 12 months of age (Huebner *et al.*, 2006). The pathway that facilitates this apparent dual action has not yet been identified, although it is unlikely to be a direct influence on osteoblast cells but rather an indirectly mediated response (Davey and Findlay, 2013). This dual action might explain why calcitonin deficiency, for example following thyroidectomy, does not increase bone resorption substantially, and similarly an overproduction of calcitonin does not lead to an increase in bone mass (Carter and Schipani, 2006; Davey and Findlay, 2013).

2.6.2 Resorption

The resorption phase of the remodelling cycle typically persists for 2 – 4 weeks and begins with the formation of multinucleated osteocytes, which secrete metalloproteinase (MMP) enzymes which degrade the un-mineralised osteoid lining the surface of the bone (Raggatt and Partridge, 2010). This allows the osteoclasts direct access to their binding sites on the mineralised matrix, to which they bind by creating small isolated microenvironments referred to as 'sealed zones'. The pH of the sealed zone is lowered by the injection of hydrogen ions (H^+) which mobilises the matrix adjacent to the osteoclast (Raisz, 1999). The osteoclasts then secrete low-pH lysosomal and collagenolytic enzymes which will degrade both the mineral and organic components of the bone matrix (Raisz, 1999). The resulting scalloped regions of demineralisation are called Howship's lacunae.

2.6.3 Reversal

The resorption phase is immediately followed by a period of reversal, which remains poorly understood despite its vital importance for the coupling of bone resorption and formation (Delaisse, 2014). Huiskes *et al.* (2000) suggested that, at least in trabecular bone, the coupling mechanism might be mechanical in nature. The creation of a resorption cavity may elevate local strain causing the release of recruitment stimuli by

osteocytes [Figure 2.07]. This phase can last a number of weeks following resorption (Delaisse, 2014).

During reversal, several flattened, mononuclear cells of uncertain lineage are evident on the eroded bone surface. Although originally thought to be phagocytic, the most recent literature suggests that these reversal cells share surface markers with osteoblasts (Anderson *et al.*, 2013; Delaisse, 2014). Indeed, it has been suggested that these reversal cells may ultimately differentiate into mature osteoblasts, which then contribute to the formation phase of remodelling (Delaisse, 2014). The reversal cells act in the first instance to phagocytose the remnants of the bone matrix following resorption. They then deposit the collagenous matrix that will form the cement lines on the resorbed surface, the substrate on which osteoblasts will subsequently deposit the new bone matrix (Anderson *et al.*, 2013; Raggatt and Partridge, 2010).
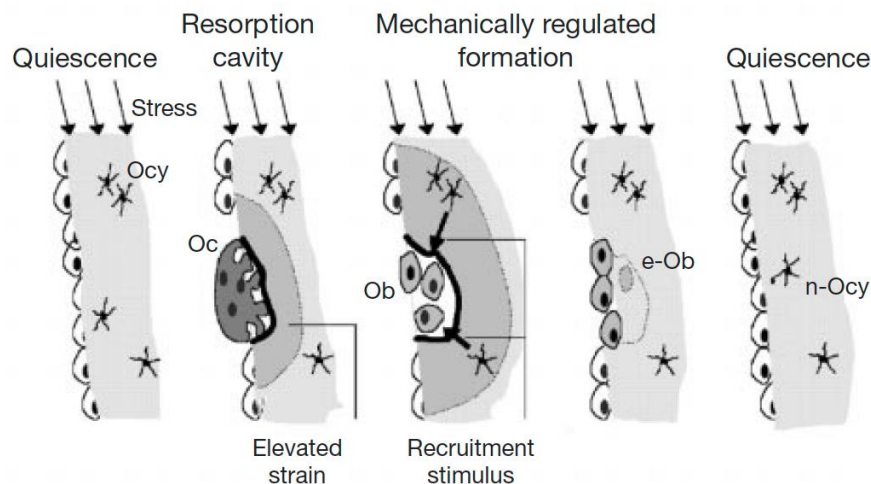
Figure 2.07. Proposed mechanical coupling of bone resorption and deposition in remodelling. The formation of a resorption cavity causes elevated strain in the remaining bone, resulting in the recruitment of osteoblasts by neighbouring osteocytes. Ocy: osteocyte; Oc: osteoclast; Ob: osteoblast; e-Ob: entrapped osteoblast; n-Ocy: new osteocyte formed by differentiation of e-Ob. From Huiskes et al., 2000.

2.6.4 Formation

During formation, successive waves of osteoblasts secrete molecules that comprise the organic matrix of new bone, including collagen Type I and a number of non-collagenous proteins (Clarke, 2008; Raggatt and Partridge, 2010; Raisz, 1999). The osteoblasts also secrete alkaline phosphatase, the enzyme necessary to precipitate

hydroxyapatite crystal formation, and matrix extracellular vesicles which contain sufficient calcium and phosphate ions for mineralisation to occur (Clarke, 2008). The process of formation and mineralisation can take 4 to 6 months to complete (Clarke, 2008; Hadjakis and Androulakis, 2007).

The underpinning mechanisms that coordinate the precise deposition of bone by osteoclasts remain unconfirmed (Raggatt and Partridge, 2010). It was initially believed that the signalling factors were bound within the bone matrix itself and were therefore released on resorption. However, this was disproved as osteoblast bone formation remains coupled to osteoclast presence even where the osteoclasts are defective and cannot resorb bone (Martin and Sims, 2005). One pathway which promotes bone formation during remodelling is Wnt signalling, a glycoprotein that promotes osteoblast differentiation (Moester *et al.*, 2010). The Wnt receptors on the surface of osteoblasts are inhibited by the presence of sclerostin, which is secreted by resting osteocytes. However, when subjected to mechanical strain or PTH stimulation, sclerostin production is reduced allowing Wnt signalling to occur (Moester *et al.*, 2010; Raggatt and Partridge, 2010).

2.6.5 Termination and a return to quiescence

The completion of a remodelling cycle in cortical bone is indicated by the formation of a new osteon, and in trabecular bone by the restoration of trabeculae through the formation of a new hemi-osteon (Clarke, 2008; Raisz, 1999; van Oers *et al.*, 2008). It is unclear what physiological trigger signals the end of remodelling, although it is believed to involve the resumed secretion of sclerostin by osteocytes (Raggatt and Partridge, 2010). In addition to the inhibition of Wnt signalling, sclerostin is also known to induce osteoblast apoptosis, and this might explain why approximately 50 – 70 % of active osteoblasts undergo apoptosis at the conclusion of remodelling. The remaining osteoblasts differentiate further, either to become osteocytes trapped within the bone matrix, or new bone lining cells on the surface of the remodelled bone (Clarke, 2008).

2.7 Genetic influences on bone

The second prevailing theory in bone development is that the direction and regulation of ossification are primarily under genetic control, with systemic regulation guiding the construction and maintenance of whole bone morphology, with negligible local effects due to mechanical loading (Lovejoy *et al.*, 2002, 2003). Following the discovery of increased femoral size in mice bred selectively for increased physical activity over a control group, Wallace *et al.* (2010) suggested that bone morphology may be, to some extent, heritable and indicative of ancestral or evolutionary behaviour.

The genetic and epigenetic control of bone development, that is those features which are either directly inheritable, or are the result of a genetic trait which is modifiable by environmental factors (Skedros *et al.*, 2007), has received much interest. The relevance of genetic programming is clear when considering pathologies of bone development that involve gene pathways. For example, osteogenesis imperfecta, or brittle bone disease, is caused by a mutation in genes controlling collagen synthesis (Roach and Glorieux, 2004); fibrodysplasia ossificans progressiva, which causes spontaneous *de novo* mineralisation in non-skeletal tissues, is a result of a specific mutation in the ACVR1 pathway which controls progenitor cell fate and bone formation (Shore, 2012); and achondroplasia, the most common form of human dwarfism, is the result of a genetic mutation which prevents the proliferation and differentiation of growth plate chondrocytes (Horton *et al.*, 2007).

Skeletal patterning, the process by which cell differentiation establishes the basic position and form of the embryonic limb, has also been established to be of great importance in skeletal development (Cohn *et al.*, 2002; Mariani and Martin, 2003). Although no definitive model has been formulated to explain the process fully, it is accepted that primary control is regulated by gene expression and the sequential release of various signalling factors (Hentschel *et al.*, 2004; Marian and Martin, 2003). As described above, the later processes of modelling and remodelling are dependent also on gene expression, albeit gene expression which appears to be modulated in a variety of ways by mechanical stimulation [see Chapter 2.5, 2.6].

Perhaps the greatest limitation in the present literature with regards to the regulation of bone development and maintenance is the insistence of separating the importance of genetic and mechanical influences, rather than attempting to understand the manner in which one may inform or modify the other. Although the basic skeletal morphology and pattern of the human skeleton may be genetically predefined, the variation present between individuals is more likely a product of both genetic and environmental influences (Ruff *et al.*, 2006). The contentious nature of this debate is perhaps best illustrated by Lovejoy *et al.* (2003) where they express that *"we obviously take an opposite view – that more is now known (or at least rationally suspected) about skeletal genetics than about the 'mathematical laws' by which bones hypothetically model themselves (…) despite a long tradition of heroic attempts to define such laws."*

However, the importance of the interplay between genetic factors and mechanical stimuli has been historically recognised. Early experiments on avian embryos by Hall and Herring (1990) demonstrated a retention of basic bone morphology in the long bones of the limbs following paralysis, although overall growth was diminished. However, the morphology and growth of the sternum was severely retarded, leading to collapse of the thorax. These results therefore suggested that genetic patterning preserved the rudimentary formation of the more linear skeletal elements, but also that the absence of mechanical stimulation detrimentally affected growth. More recent literature has supported these findings, with an overall trend towards diminished bone development the absence of mechanical stimulation (e.g. Osborne *et al.*, 2002; Sawamura *et al.*, 2006).

Overall, it would appear that the mechanisms which control bone formation and adaptation are inexorably complex, and rely on not one parameter or stimulus, but the interaction of genetic programming with epigenetic and extragenetic stimuli, such as mechanical strain or homeostatic mechanisms (Ruff *et al.*, 2006; Skedros *et al.* 2007).

Chapter 3: Structure, Function and Development of the Pelvic Girdle

3.1 Introduction

The pelvis is perhaps one of the most complex regions of the human post-cranial skeleton. The morphology of the pelvic girdle reflects its functions: provision of a biomechanically stable structure capable of supporting an upright posture and bipedal locomotion in the male, and a compromise between locomotor demands and the provision of a safe pathway for the passage of a fetal head during parturition in the female (Hogervorst *et al.,* 2009).

The pelvis is the key junctional complex that unites the trunk, via the lumbosacral region of the vertebral column, and the lower limb, via the femoral head, therefore serving as an important biomechanical gateway (Cunningham and Black, 2009a). The gross morphology and architecture of the pelvis is highly adapted for load transmission and the attachment of numerous muscles and ligaments which support the pelvic girdle and effect movement of the lower limb (Aiello and Dean, 1990).

The demands placed on the pelvis with regards to parturition are emphasised by the extent of sexual dimorphism evident in the human pelvis: indeed, the pelvis is considered to be the most sexually dimorphic region of the skeleton (Christensen *et al.*, 2014; Cunningham *et al.*, 2016). Sex-dependent differences in both size and shape can be identified in the post-pubertal pelvis, leading to a broader pelvic girdle with a wider pelvic inlet and outlet in the female form than the male equivalent (Correia *et al.,* 2005). The most pronounced, and reliable, sexually dimorphic traits emerge in relation to the dimensions of the pubis: in the female, the pubertal pubis grows at a more rapid rate than the male, increasing the diameter of the completed pelvic ring (Rissech and Malgosa, 2007).

The pelvis also provides support and protection for the viscera of the lower abdomen, provides insertion for the abdominal muscles supporting the body wall and houses the internal organs associated with the urinary and reproductive systems. Further, the

pelvis also acts as a neurovascular interchange as the nerves, arteries and veins that are necessary for the function and maintenance of the lower limbs typically arise or branch forth from within the pelvic cavity.

3.2 Adult osteology

3.2.1 Overview

The pelvic complex is typically considered to be formed from three separate skeletal elements: the paired, irregularly shaped innominate bones (*Os coxa)* and sacrum and coccyx collectively [Figure 3.01a]. The sacrum occupies the midline posteriorly, articulating with the vertebral column via the fifth lumbar vertebra. The laterally directed auricular surfaces of the sacrum articulate with the medially directed auricular surface of each innominate to form the sacro-iliac joint, a junction consisting of both fibrous and synovial joint components between axial and appendicular elements. Each innominate then passes anteriorly and inferiorly as the superior pubic rami, which articulate with their antimere in the midline at the pubic symphysis. The completed pelvis is then connected to the lower limb through the hip joint, between the anterolaterally oriented acetabulum and the head of the femur.

The innominate is formed from three separate bones that develop from individual centres of ossification and later fuse in the region of the acetabulum [Figure 3.01b]. Most superiorly lies the broad, flat ilium, which extends inferiorly to form the upper two fifths of the acetabulum. The inferior aspect of the innominate is formed from the union of the wedge-shaped ischium posteriorly and the narrow, angular pubis anteriorly. Each of these elements will ultimately unite with each other in the region of the acetabulum. The ischium and pubis also fuse together inferiorly at the ischiopubic ramus, a relatively thin bar of bone which forms the inferior border of the obturator foramen, a large aperture which exists within the inferior aspect of the innominate. In life, the majority of this foramen is sealed by the presence of the obturator membrane, a fibrous sheet which inserts around the obturator margin anteriorly, posteriorly and inferiorly, with only the small obturator canal left open superiorly. This canal allows the obturator vessels and nerves to exit the pelvic cavity and enter the medial compartment of the thigh.
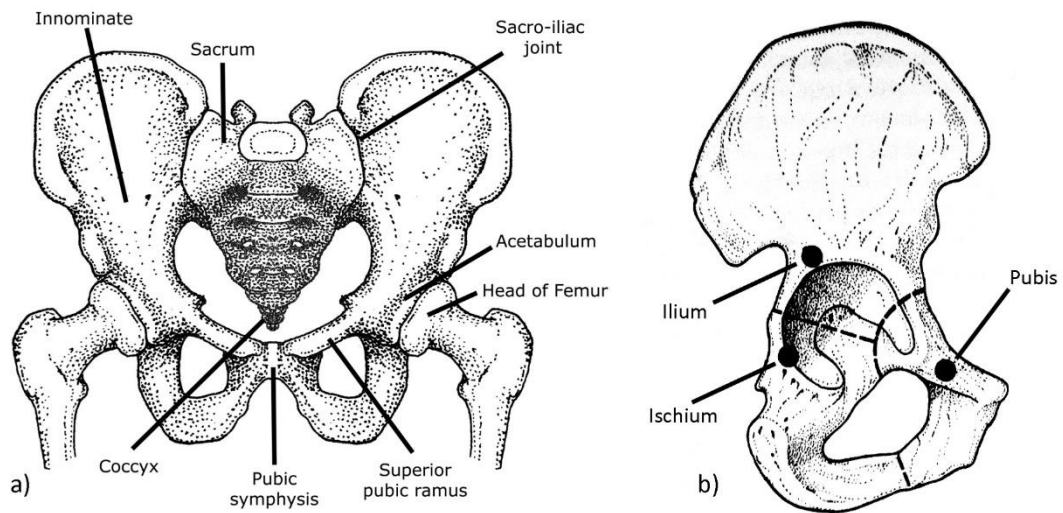
Figure 3.01. a) Components of the pelvic girdle. b) The three bones forming the right innominate, with initial centres of ossification indicated (black circles). Dashed lines represent the approximate boundaries of the ilium, ischium and pubis at the acetabulum and ischiopubic ramus. Adapted from Cunningham et al., 2016.

In its articulated form, the pelvis is divided into two distinct anatomical regions: the true pelvis and the false pelvis. These two regions are separated by the pelvic inlet (or brim), an oblique ellipse that is formed between the alae and promontory of the sacrum posteriorly and the pubic crest and symphysis anteriorly (Cunningham *et al.*, 2016). The lateral margins of the ellipse follow the iliopectineal lines across the ilium and superior pubic ramus to complete the inlet. The false pelvis is considered to extend from the pelvic inlet inferiorly to the level of the fifth lumbar vertebra superiorly, while the iliac fossae and abdominal muscles form the anterior and lateral walls of the cavity. The true pelvis conversely lies inferior to the pelvic inlet and houses the distal components of the urinary system and the internal reproductive organs. It is bordered inferiorly by the pelvic outlet, a quadrangular plane lying between the coccyx, ischial tuberosities and inferior aspect of the pubic symphysis. This quadrangular plane is also the approximate level of the pelvic floor (diaphragm), which separates the true pelvis from the perineum.

3.2.2 Musculoskeletal system

Due the complexity of the interactions in which the innominate is involved, there are many morphological landmarks associated with this bone. Many of these landmarks

are specific to the individual developmental centres, while a more limited number cross multiple elements.

As the features of the innominate are typically linked to ligamentous or muscular insertions, where relevant the key topographical features will be discussed in relation to the structures which attach at that location.

Ilium

The ilium is the largest of the three skeletal elements that form the innominate, and is typically described as a broad, flat bone with a more protuberant region inferiorly at the acetabulum [Figure 3.02]. On the medial aspect of the ilium lies the rugose articular surface of the sacro-iliac joint, called the auricular surface. In the adult, the auricular surface demonstrates a characteristic curved 'l' shape that is often described as forming two limbs: a shorter superior (cranial) limb (or demifacet) and a longer inferior (caudal) limb which projects posteriorly and caudally. Inferior to the caudal limb of the auricular surface, the margin of the ilium demonstrates a pronounced concavity, transitioning from its anterior path to curve inferiorly and posteriorly to meet with the posterior aspect of the ischium. This curvature, the greater sciatic notch, is completed posteriorly by the presence of the sacrospinous ligament in life to form the greater sciatic foramen (Standring, 2008), an aperture that allows important neurovascular structures (and the piriformis muscle) to exit the pelvic cavity and enter the gluteal region. These structures include the sciatic nerve, the inferior and superior gluteal neurovascular bundles, the pudendal nerve and internal pudendal vessels and several cutaneous and muscular nerve branches (Standring, 2008).

The iliac crest forms the most superior extremity of the ilium and constitutes the raised and rugose superior border of the bone. When viewed superiorly, the profile of the crest is approximately s-shaped with a concave anterior curvature and convex posterior curvature. The iliac crest is a significant site of muscle attachment, providing attachment for the muscles of the abdominal wall, quadratus lumborum, erector spinae and latissimus dorsi (Standring, 2008).
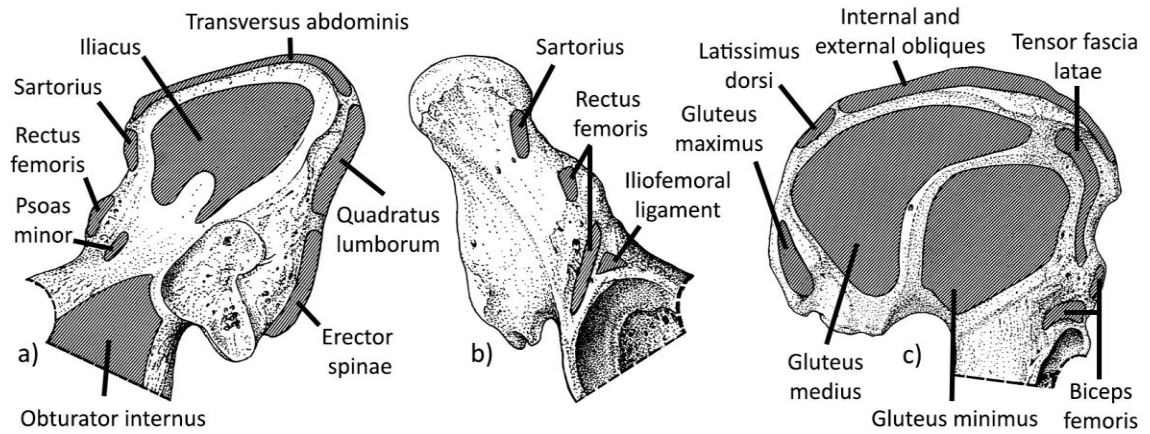
Figure 3.02. Muscle attachment sites on the ilium. a) medial (pelvic) view; b) lateral view; c) posterior (gluteal) view. Adapted from Cunningham et al., 2016.

The outer aspect of the iliac crest also provides attachment for the tensor facia latae and the iliotibial tract. The crest terminates anteriorly at the anterior superior iliac spine (ASIS) and posterior at the posterior superior iliac spine (PSIS), with each providing further sites for muscle attachment. The inguinal ligament and the sartorius muscle insert on the ASIS, while the PSIS provides attachment for the posterior sacroiliac ligament and the thoracolumbar fascia.

Inferior to the ASIS is a second, smaller protuberance, the anterior inferior iliac spine (AIIS), which provides attachment for the rectus femoris muscle, a flexor of the thigh, and also the iliofemoral ligament, one of the components of the hip joint capsule (Cunningham *et al.*, 2016).

The posterior aspect for the ala of the ilium is also rugose, with a series of three defined ridges on its surface. These are the anterior, posterior and inferior gluteal lines, which demark the attachment sites for the gluteus muscle group. Gluteus minimus, the smallest and deepest muscle, inserts on the ilium between the inferior and anterior gluteal lines, while gluteus medius can be found inserting between the anterior and posterior gluteal lines. Together these muscles act to flex and abduct the lower limb at the hip, and also to help secure the position of the pelvis during the stance phase of the gait cycle (Standring, 2008). Gluteus maximus, the largest and most superficial muscle in the gluteal region, inserts directly on the ilium, posterior to the posterior gluteal line. Gluteus maximus is primarily responsible for extension of the thigh at the hip and also acts to stabilise the hip and knee through its insertion into the iliotibial tract.

Conversely, the anterior, or pelvic, aspect of the ala of the ilium is relatively smooth and concave. This region forms the iliac fossa and superiorly provides a broad area of attachment for the iliacus muscle, a flexor of the hip (Standring, 2008). Inferiorly it also allows the attachment of the most superior fibres of obturator internus.

Ischium

The posteriorly- and laterally-positioned ischium is an irregular wedge-shaped bone that curves inferiorly to form a prominent anterior projection, the ramus of the ischium. The adult form can be described as possessing three discrete surfaces: an inner pelvic surface, which forms the lateral wall of the true pelvis; a laterally-directed femoral surface on which the ischial contribution of the acetabulum is located; and a dorsal surface, which faces posteriorly and is predominantly formed for the expanded, medially-projecting ischial spine and the posterior surface of the ischial tuberosity inferiorly [Figure 3.03].
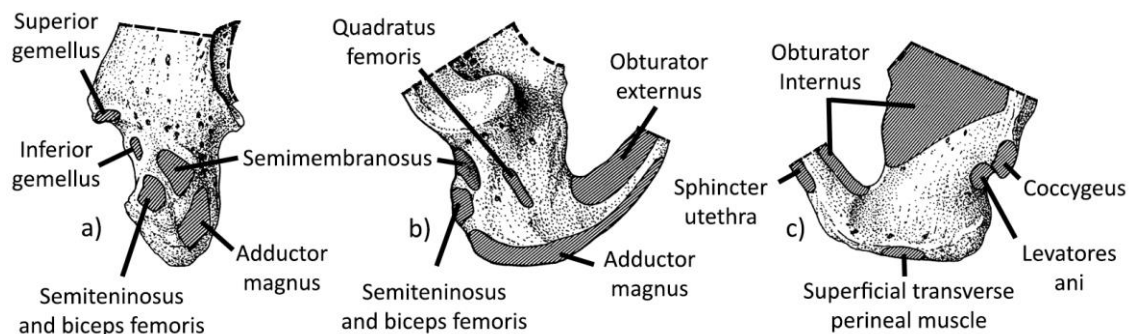
Figure 3.03. Muscle attachments of the ischium. a) Dorsal view; b) femoral (lateral) view; c) pelvic (medial) view. Adapted from Cunningham et al., 2016.

The dorsal surface of the ischium is continuous with the ilium in the adult, forming the lower aspect of the greater sciatic notch most superiorly [Figure 3.03a]. At approximately the level of the lower aspect of the acetabular margin, the dorsal surface of the ischium projects medially and inferiorly as the ischial spine, a significant site of ligamentous and muscular insertion (Standring, 2008) [Figure 3.04]. The sacrospinous ligament, which inserts to the most prominent point of the ischial spine, is partly responsible for resisting anterior rotation of the sacroiliac joint, in conjunction with the sacrotuberous and sacroiliac ligaments (Cunningham *et al.*, 2016), and as a result generates high tensile forces between the ischium and sacrum (Tardieu *et al.*,

2013). The tendinous arch of the pelvic fascia also inserts directly onto the ischial spine, and many of the muscles of the pelvic floor either insert directly onto the ischial spine or one of these two ligamentous structures (Abitbol, 1988) [Figure 3.02]. This includes the iliococcygeus and pubococcygeus muscles of levator ani and coccygeus. On the gluteal aspect, the gemellus superior muscle inserts onto the inferior aspect of the ischial spine (Standring, 2008).

Inferior to the ischial spine lies a second smaller concavity, the lesser sciatic notch, which is closed posteriorly by the continuation of the sacrotuberous ligament to form the lesser sciatic foramen. The tendon of obturator internus exits the pelvis through this foramen to run with the superior and inferior gemelli muscles to insert onto the greater trochanter of the femur.
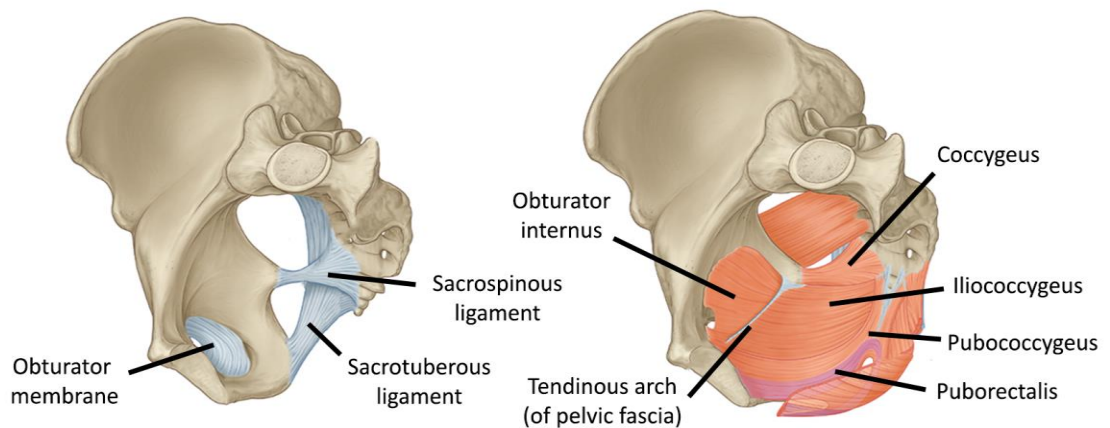
Figure 3.04. Pelvic view of the ligaments (left) and muscles (right) of the pelvic floor and their relations to the ischial spine. Adapted from Drake et al., 2010.

In addition to allowing the exit of the tendon of obturator internus, the lesser sciatic notch allows the pudendal nerve and internal pudendal arteries and veins to enter the ischioanal fossa, inferior to the pelvic floor, after they had previously existed the pelvic cavity through the greater sciatic notch. As a result, each of these three structures can be found traversing the lateral aspect of the ischial spine and sacrospinous ligament.

The dorsal surface of the ischium ends inferiorly with the presence of the ischial tuberosity, a large, protuberance that provides attachment for a number of muscles. The tuberosity is divided into superior and inferior surfaces by a raised transverse ridge. The medial aspect of the superior surface provides attachment for the long head of biceps femoris and semitendinosus as a single conjoined tendon, while the

semimembranosus tendon inserts laterally (Beltran *et al.*, 2012). The hamstring group act together to extend the thigh at the hip and to flex the leg at the knee during bipedal locomotion. Semimembranosus and semitendinosus also act to internally rotate the leg at the knee due to their medial insertion distally, while the oblique biceps femoris acts to externally rotate the leg (Koulouris and Connell, 2005).

The inferior surface of the ischial tuberosity curves anteriorly to become continuous with the ischial ramus. The lateral aspect of this inferior surface is the origin for a portion of the adductor magnus muscle, which also attaches to the inferior aspect of the ischiopubic ramus. The portion of the muscle that inserts onto the ischial tuberosity is often referred to as a 'mini-hamstring', or the hamstring part of adductor magnus due to its innervation via the sciatic nerve rather than the obturator nerve, and also its role in extending the hip (Barrett and Arthurs, 2010). The medial aspect of the inferior surface is covered by the ischial bursa, which lies between the ischial tuberosity and the fibres of gluteus maximus (Kreder and Jerome, 2010). It is this medial aspect of the ischial tuberosity that is reported to contact the ground and transfer the weight of the body when sitting (Standring, 2008).

In addition to the hamstring muscles, gemellus inferior is also reported to insert on the ischial tuberosity, occupying a position on the uppermost aspect (Standring, 2008). This muscle, along with obturator internus and gemellus superior, acts to laterally rotate the thigh at the hip during extension and abduct the thigh at the hip during flexion.

It should be noted that some literature sources also suggest that the quadratus femoris muscle may insert on the anterior margin of the ischial tuberosity (Aiello and Dean, 1990; Bano *et al.*, 2010; Kassarjian *et al.*, 2011; Palastanga and Soames, 2011). However, other sources suggest that this insertion occurs anterior to the ischial tuberosity in the tubero-acetabular sulcus (Cunningham *et al.*, 2016; Standring, 2008; White *et al.*, 2005). No direct anatomical studies could be identified which explored and depicted the origins of this muscle, leaving it unclear which description should be treated as the most accurate, or indeed whether this discrepancy may be due to anatomical variation.

Finally, the ischial tuberosity is also the distal site of attachment for the sacrotuberous ligament, one of the principal stabilising ligaments of the pelvic girdle (Aiello and Dean, 1990; Woodley and Kennedy, 2005). It passes from a broad insertion which incorporates the PSIS and the dorsal surface and lateral margin of the sacrum, which may in part incorporate the posterior aspect of the sacroiliac joint to insert on the lower medial aspect of the ischial tuberosity, with some fibres passing inferiorly onto the ramus itself (termed the falciform ligament) (Standring, 2008; Woodley and Kennedy, 2005). In addition to its role in stabilising the pelvis, it is also considered to provide a portion of the proximal attachment for muscles of the hip and thigh, including gluteus maximus, piriformis and the long head of biceps femoris.

The femoral, or lateral, surface of the ischium [Figure 3.03b] contains the ischial component of the acetabulum, which constitutes approximately two-thirds of the total acetabulum. The outer margin of the acetabulum is raised and protrudes laterally from the surface, and curves from the superior edge of the ischium inferiorly and then anteriorly towards the articulation with the pubis. The margin terminates before this union at the acetabular notch, an inferior deficiency in the acetabular margin which gives rise to the typical horseshoe like shape of the acetabulum. The acetabular notch in life is bridged by the transverse acetabular ligament, which acts to complete the acetabular margin inferiorly and supports the hip joint (Löhe *et al.*, 1996). The acetabular margin itself provides attachment for the ligaments of the hip joint, with the ischium contributing the proximal attachment for the ischiofemoral ligament. The structure of the acetabulum is further explored in Section 3.2.3.

Inferior to the acetabulum, the femoral surface is reported to provide attachment for the quadratus femoris muscle and also the obturator externus muscle, which inserts across the obturator membrane and the adjacent bone, including the superior aspect of the ischiopubic ramus and the posterior bony border of the obturator foramen (Standring, 2008). The tendon of obturator externus passes posteriorly through the tubero-acetabular fossa, the depressed area between the acetabular margin and anterior border of the ischial tuberosity, to form a conjoined tendon with the piriformis muscle that inserts on the lateral wall of the trochanteric fossa. Due to its unusual path, passing inferior to the femoral neck and posteriorly to the hip joint,

obturator externus will effect lateral rotation of the thigh at the hip (Solomon *et al.*, 2010).

In contrast to its dorsal and femoral surfaces, the pelvic (medial) surface of the ischium is relatively smooth and featureless [Figure 3.03c]. Superiorly it adopts an approximately quadrangular shape with a slight concavity, termed the quadrangular plate, which tapers and curves inferiorly towards the ischiopubic ramus. Excluding the pelvic floor muscles associated with the ischial spine, only a single muscle inserts on the pelvic surface: obturator internus. Obturator internus inserts on the internal surface of the obturator membrane the surrounding bony margins of the obturator foramen. It also inserts superiorly along the superior pubic ramus and anterosuperior aspect of the quadrangular plate of the ischium (Solomon *et al.,* 2010). Scheuer and Black (2000) noted that, although the fibres of obturator internus cover the majority of the pelvic surface of the ischium, they do not insert across this surface entirely: they are separated from the bone by the presence of a synovial bursa. The tendon for obturator internus passes posteriorly and exits the pelvic cavity through the lesser sciatic foramen, after which it runs between the bellies of the superior and inferior gemelli to insert on the greater trochanter of the femur.

The ischium is completed inferiorly by the ischial ramus, a relatively thin, elongated protrusion that is fused in the adult and continuous with the inferior pubic ramus to form the ischiopubic ramus. The superior aspect of the ramus provides insertion for the obturator membrane, and the obturator externus and internus muscles of the femoral and pelvic surfaces respectively (Cunningham *et al.*, 2016). Inferiorly the pelvic surface is also associated with the insertion of the urogenital diaphragm and smaller pelvic floor structures including the erectile tissues and their associated muscles. The inferolateral aspect of the ramus also provides the ischial part of the broad attachment for the adductor part of adductor magnus, which extends anteriorly to the inferior pubic ramus (Standring, 2008).

Pubis

The pubis is comprised of four main elements: the body of the pubis, its associated symphyseal face and the superior and inferior pubic rami. As with the ilium and

ischium, the pubis demonstrates a smooth, posteromedially oriented pelvic surface and more rugose anterolaterally directed outer surface [Figure 3.05].

The superior pubic ramus projects posteriorly and laterally, and at its extremity expands from the iliopectineal eminence to form the anterior fifth of the acetabulum and fuses with the ilium. The inferior pubic ramus projects inferiorly to meet the advancing ischial ramus and fuses to form the ischiopubic ramus.

The pectineal line can be found on the superior aspect of the superior pubic ramus, beginning at the iliopubic eminence. This line provides attachment for the pectineus muscle from the medial compartment of the thigh. This line terminates anteriorly at the pubic tubercle, a protuberance that provides the distal attachment of the inguinal ligament medially. Between the pubic tubercle and the raised margin of the pubic symphysis lies a second ridge, the pubic crest, which along with the tubercle provides attachment for the rectus abdominis and pyramidalis muscles of the anterior body wall (Standring, 2008).
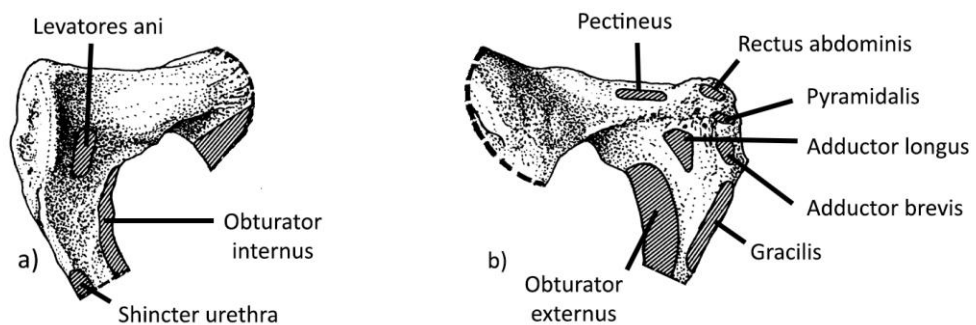
Figure 3.05. Muscle attachments of the pubis. a) Pelvic (medial) view; b) lateral view. Adapted from Cunningham et al., 2016.

The inferior surface of the superior pubic ramus bears a deep sulcus, the obturator sulcus (or groove) that marks the approximate position of the obturator canal. Overlying this groove on the pelvic aspect is the obturator internus muscle, which inserts on the pelvic surface of the pubis along the superior pubic ramus, the posterior aspect of the pubic body and the inferior pubic ramus (Aung *et al.*, 2001; Cunningham *et al.*, 2016). The most anterior fibres of the pubococcygeal component of levator ani also insert on the pelvic aspect of the pubis, slightly lateral to the symphyseal face.

The lateral aspect of the obturator margin of the pubis provides a broad attachment area for the obturator externus muscle. As the ischium and pubis are fused in the adult, the pubic attachment of this muscle in continuous with the attachment to the ischial portion of the obturator margin. In addition, the ventral surface of the pubic body provides the proximal attachment of several muscles from the medial compartment of the thigh, including adductor longus, adductor brevis and gracilis, and posteriorly a small region for the insertion of the most anterior fibres of adductor magnus, continuing its attachment from the inferolateral aspect of the ischial ramus. Together in association with pectineus, these muscles of this compartment act primarily to adduct the thigh at the hip, with a smaller contribution to flexion and rotation.

3.2.3 Joints

As previously described, the adult innominate is involved in three separate joints: the posterior junction with the sacrum at the sacroiliac joints, in the midline anteriorly at the pubic symphysis and laterally with the head of the femur at the hip joint. Each of these joints is supported by a complex arrangement of ligamentous structures that reinforce the joint capsules. As each of these joints fulfil an important role in the biomechanical stability of the pelvis, a brief outline of the structure and mechanics of each joint is provided below. Emphasis is placed on the hip joint, which is the only joint of the pelvis in which the ischium is directly involved.

Sacroiliac joint

The sacro-iliac joint is an atypical synovial articulation between the L-shaped auricular surfaces of the ilium and sacrum. The anterior aspect of this joint demonstrates the typical features of a synovial joint: surfaces covered with hyaline cartilage, separated by a synovial cavity and contained within a fibrous capsule (Forst *et al.*, 2006). However, it has been reported that the posterior aspect of the joint is fibrous in nature, providing reinforcement and restricting movements (Vleeming *et al.*, 2012; Yusof, 2013).

The sacro-iliac joint is reinforced posteriorly by the interosseous sacroiliac ligament (sometimes divided into superior and inferior components), which adheres tightly to

the post-auricular space of the ilium and the sacral tuberosity (Standring, 2008). The joint is further supported by the anterior sacroiliac ligament, which covers the pelvic surface of the sacrum and inserts on the anterior margin of the iliac auricular surface, and the stronger and more expansive posterior sacroiliac joints which lie superficial to the interosseous sacroiliac ligament (Palastanga and Soames, 2011). The posterior ligaments act to resist the anterior displacement and rotation of the sacrum (nutation) against the ilium in response to the anteriorly positioned load from the lumbar vertebrae. The joint is further reinforced by a number of accessory ligaments, the most notable of which are the sacrotuberous and sacrospinous ligaments. Both of these ligaments resist the rotation of the sacrum by anchoring it inferiorly to the posterior aspect of the innominate (Standring, 2008).

The sacroiliac joint represents a junction between the axial and appendicular skeleton and is the region through which the weight of the trunk is allegedly transmitted to the pelvic girdle and lower limbs. It is not considered to be a mobile joint, as no muscles act directly on this joint: although slight movement is possible, these are a result of forces imposed during pelvic movements (Standring, 2008). It is also, more surprisingly, not presently considered to be truly load-bearing, as the vertical orientation, posterior position and anomalous growth pattern of the auricular surfaces do not lend themselves to this role (Palastanga and Soames, 2011; Yusof *et al.*, 2013). It is rather the strength of the ligaments reinforcing the sacroiliac joint posteriorly that most likely support the weight of the body and hold the auricular surfaces in place.

Pubic symphysis

The pubic symphysis (sometimes symphysis pubis) is a secondary cartilaginous joint formed between the opposing symphyseal faces of the left and right innominate. A fibrocartilaginous disc, the interpubic disc, separates the irregular symphyseal faces throughout life. Although a small cavity may be present in the joint, this is not synovial in nature (Standring, 2008).

Four key ligaments support the pubic symphysis. The thick anterior pubic ligament inserts on the ventral aspect of the rim of each symphyseal face and is reported to be the strongest ligament of the symphysis (Becker *et al.*, 2010). The superior pubic

ligament supports the anterosuperior aspect of the joint, attaching to the pubic tubercle and crest on each innominate (Palastanga and Soames, 2011). Inferiorly the joint is reinforced by the thick inferior, or arcuate, pubic ligament which is comprised of two fibre bundles. The most inferior fibres attach to the inferior pubic rami, while superiorly the fibres are transverse and blend with the inferior aspect of the interpubic disc (Becker *et al.*, 2010). The dorsal surface of the symphysis is supported by the very thin posterior pubic ligament, which has a similar orientation to the anterior pubic ligament.

As with the sacroiliac joint, the pubic symphysis is not typically considered to be a mobile joint but rather a supportive union of two skeletal elements, although some movement is possible (Palastanga and Soames, 2011). Due to the position of the symphysis and the cyclic nature of human locomotion, the loading conditions at the pubic symphysis are variable. A single gait cycle includes the application of compressive, tensile and shearing stresses across the pubic symphysis, each of which must be resisted by the ligaments supporting the joint (Becker *et al.*, 2010).

The hip joint

The hip joint is a synovial ball and socket joint formed by the articulation of the acetabulum of the innominate and the head of the femur. It is arguably the most complex joint of the innominate as it has the dual requirements of great stability to support the transmission of the load from the trunk to the lower limb, but also mobility to facilitate efficient bipedal locomotion.

The acetabulum is a large, approximately hemispherical depression visible on the lateral aspect of the innominate at the junction of the ilium, ischium and pubis [Figure 3.06]. It features a raised non-articular margin that superiorly is an expansion of the inferior extremity of the ilium and the posterior aspect of the pubis but which posteriorly becomes a defined projection from the femoral surface of the ischium. The inferior aspect of the margin is deficient inferiorly at the acetabular notch.

The internal surface of the acetabulum is divided into two distinctive regions: the lunate surface and the acetabular fossa. The lunate surface is the articular surface of the joint and is therefore lined with hyaline cartilage and contacts with the reciprocal

surface of the femoral head. The lunate surface is approximately horseshoe shaped, and is deficient inferiorly at the acetabular notch (Aiello and Dean, 1990). Conversely the acetabular fossa, which forms the medial wall of the acetabulum, is non-articular in nature and in life is covered by a fibroelastic pad (Standring, 2008).
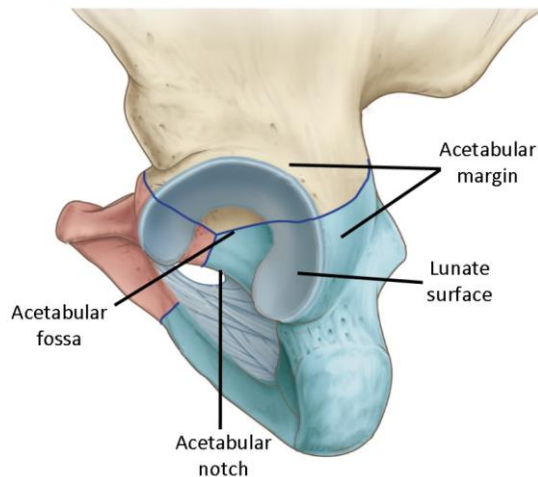
Figure 3.06. Diagram of the major surface features of the acetabulum. Adapted from Drake et al., 2010.

The acetabulum is slightly deepened by the presence of the acetabular labrum, a fibrocartilage structure that encircles and attaches to the acetabular margin (Bsat *et al.*, 2016). It is attached at its base to the hyaline cartilage that lines the lunate surface and inferiorly provides attachment for fibres of the transverse acetabular ligament [Figure 3.07]. Together these structures form a single continuous structure which increases the depth of the acetabulum to extend beyond the 'equator' of the femoral head laterally, acting to seal the femoral head within the joint capsule and thus increase the stability of the joint (Bsat *et al.*, 2016; Grant *et al.*, 2012).
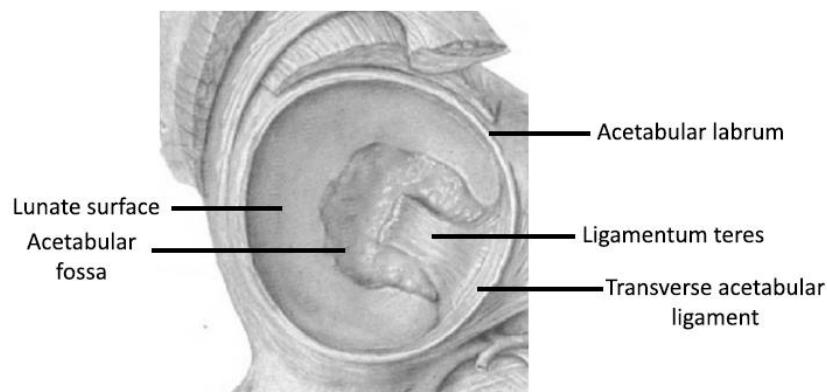
Figure 3.07. The acetabular labrum and its anatomical relations. Adapted from Grant et al., 2012.

The labrum also acts as a seal for the synovial capsule, preventing the egress of fluids from the joint (Ito *et al.*, 2009), although due to its circumferential position, it does not appear to play a substantial role in the direct transmission of force across the joint (Henak *et al.*, 2011).

The capsule of the hip joint is comprised primarily of four extracapsular ligaments: the iliofemoral ligament, the ischiofemoral ligament, the pubofemoral ligament and the zona orbicularis [Figure 3.08]. The iliofemoral, ischiofemoral and pubofemoral ligaments are primarily comprised of longitudinal fibres which pass from the acetabulum and surrounding structures to the proximal femur, while the zona orbicularis is a circumferential structure which is located at the distal aspect of the femoral neck.
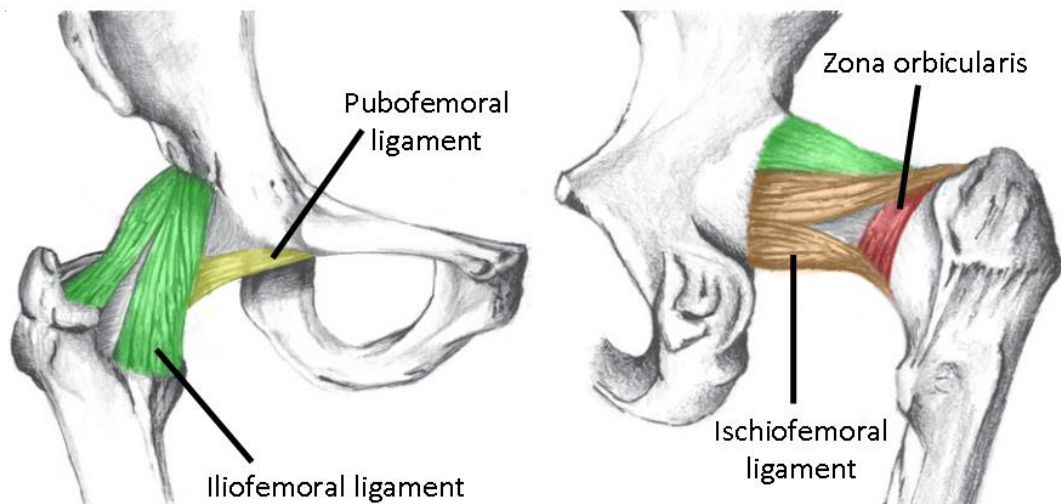
Figure 3.08. Extracapsular hip ligaments. Adapted from Wagner et al., 2012.

The iliofemoral ligament lies anteriorly, attaching proximally to the AIIS and iliac acetabular margin and distally to the intertrochanteric line of the femur (Wagner *et al.*, 2012). It is most often described as possessing an inferior band, inserted on the lower part of the intertrochanteric line, and a superior band, inserted on the upper aspect of the line, which are connected by a thinner central region. The inferior band is responsible for the restriction of extension of the hip, while the superior band primarily restricts external rotation.

The ischiofemoral ligament forms the posterior aspect of the hip capsule and arises from the ischial component of the acetabular margin. It passes anteriorly and

superiorly to insert on the superior base of the greater trochanter, posterior to the position of the superior band of the iliofemoral ligament. A smaller inferior band also passes inferiorly to blend with the circumferential zona orbicularis, which reinforces the synovial membrane of the joint (Wagner *et al.*, 2012). This ligament is reported to resist internal rotation at the hip, and prevent adduction and dislocation posteriorly during flexion of the hip (van Arkel *et al.*, 2015).

The pubofemoral ligament reinforces the inferior aspect of the joint capsule, and contributes to the support of the anterior aspect (Palastanga and Soames, 2011). It originates from the superior pubic ramus and the iliopubic eminence and inserts on the lower region of the intertrochanteric line, along with the inferior band of the iliofemoral ligament (Wagner *et al.*, 2012). The pubofemoral ligament is suggested to primarily resist abduction and lateral rotation (Palastanga and Soames, 2011).

The zona orbicularis does not cross the hip joint with the previous three longitudinal ligaments, but rather circumnavigates the narrowest point of the femoral neck (Malagelada *et al.,* 2015). Although not directly contributing to the resistance of hip movements, the zona orbicularis is reported to act as a locking mechanism to prevent dislocation of the hip laterally (Ito *et al.,* 2009).

In addition to the extracapsular ligaments, two intra-capsular ligaments also support the hip joint: the transverse acetabular ligament and the ligamentum teres [Figure 3.07].

The transverse acetabular ligament forms the inferior aspect of the acetabular labrum and acts to bridge the acetabular notch. A small foramen is created between the floor of the acetabular notch and the transverse acetabular ligament, through which neurovascular structures can enter the hip joint (Palastanga and Soames, 2011). It is also responsible for the maintenance of the joint integrity during loading of the acetabulum, for example standing upright. The transverse acetabular ligament is placed under tension by the widening of the acetabular notch in response to acetabular deformation (Löhe *et al.,* 1996).

The ligamentum teres, or ligament of the head of the femur, originates from the inferior aspect of the acetabular fossa, the margins of the acetabular notch and the

transverse acetabular ligament, and inserts at the fovea capitis (Bardakos and Villar, 2009). Although sometimes dismissed as a vestigial structure in the adult, contemporary literature indicates that the ligamentum teres is of biomechanical significance (Bardakos and Villar, 2009; Cerezal *et al.*, 2010). The ligament tenses during external rotation, while absence or damage of the ligamentum teres leads to hip instabilities, indicating a direct role in the stability of the hip joint. Further, the presence of nerve fibres within the ligament has resulted in the postulation that this ligament is involved in prevention of damage through excessive movement by activating reflexive contractions of the hip muscles (Dehao *et al.*, 2015).

3.3 Arterial system of the pelvis

3.3.1 Arterial network of the pelvic cavity

The pelvis is not only an important biomechanical junction, but is also a key physiological gateway between the trunk and the lower limb. As such, many key vascular structures can be found traversing between the two anatomical regions.

The major arterial system of the pelvis arises from the common iliac artery, which branches from the abdominal aorta in the false pelvis, at the level of L4 / L5. The common iliac artery quickly divides into the external and internal iliac arteries at approximately the level of the first sacral vertebra [Figure 3.09]. The external iliac artery exits the false pelvis (and abdominal cavity) beneath the inguinal ligament, entering the femoral triangle as the femoral artery. From here, it provides arterial supply to the anterior compartment of the thigh and the posterior compartment of the thigh, the leg and the foot through branches.

The internal iliac artery demonstrates a complex branching pattern that supplies the structures of the pelvis, including the floor, viscera and reproductive organs, and compartments of the lower limb. The anterior trunk of the internal iliac artery [Figure 3.09a] gives rise to a number of branches, including those that supply the viscera of the pelvis. It branches to form the obturator artery, which exits the pelvis through the obturator canal to supply the medial compartment of the thigh, and the inferior gluteal artery, which supplies the gluteus maximus muscle. It also gives rise to the

internal pudendal artery which exits the pelvic cavity via the greater sciatic notch and then enters the perineum through the lesser sciatic notch. A variable number of smaller arteries also branch from the anterior trunk to supply the urinary bladder, female reproductive structures and rectum. Typical direct branches include the umbilical artery, uterine artery, inferior vesical (or vaginal) artery and the middle rectal artery. The posterior trunk provides fewer branches [Figure 3.09b] which include the superior gluteal artery, which completes the supply to the gluteal region, and the iliolumbar and lateral sacral arteries.

The primary venous systems of the pelvis adopt a similar pattern and nomenclature to the arterial system.
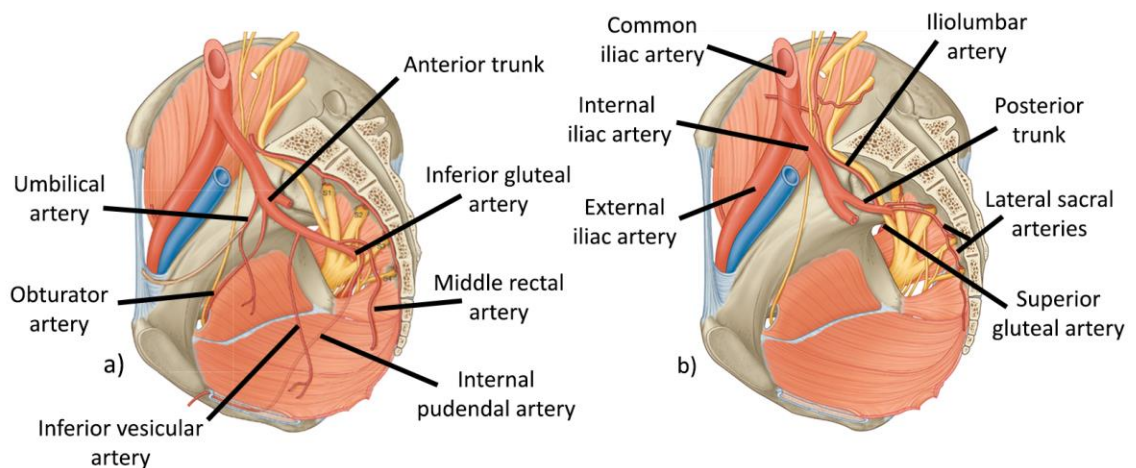
Figure 3.09. Divisions and branches of the common iliac artery, including branches of a) the anterior trunk; and b) the posterior trunk. Adapted from Drake et al., 2010.

3.3.2 Blood supply to the ischium

As with all skeletal elements, the ischium requires a supply of blood to provide nutrients and regulating factors to the cells within, and an associated venous system to remove waste products (Marenzana and Arnett, 2013). Angiogenesis and the pattern of arterial invasion have also been demonstrated to be of great importance when discussing the early development and ossification of skeletal elements (Cunningham and Black, 2010), and indeed the initial arrival and differentiation of osteoblast cells during primary ossification is inextricably linked to vascular invasion of the cartilaginous anlage (Maes *et al.* 2010). Typical models of bone vascularisation

promote the presence a single dominant nutrient artery and foramen which pierces the bone, with the presence of smaller periosteal and epiphyseal vessels.

Adult supply

Dissection-based studies following the arterial supply to the innominate (Yiming *et al.*, 2002) and hip (Beck *et al.*, 2003) both described the observed distribution of vessels [Figure 3.10]. Yiming *et al.* (2002) [Figure 3.10a] described the ischial supply as arising predominantly from the obturator branch of the internal iliac artery, providing supply directly as it crossed the pelvic surface of the ischium and also through a series of anastomosing branches encircling the obturator foramen. Additional branches were identified on the pelvic surface from the internal pudendal artery as it approximated the ischiopubic ramus, and on the lateral surface from what the authors named the artery of the ischium. This branched from the inferior gluteal artery and progressed around the inferior aspect of the acetabular margin.
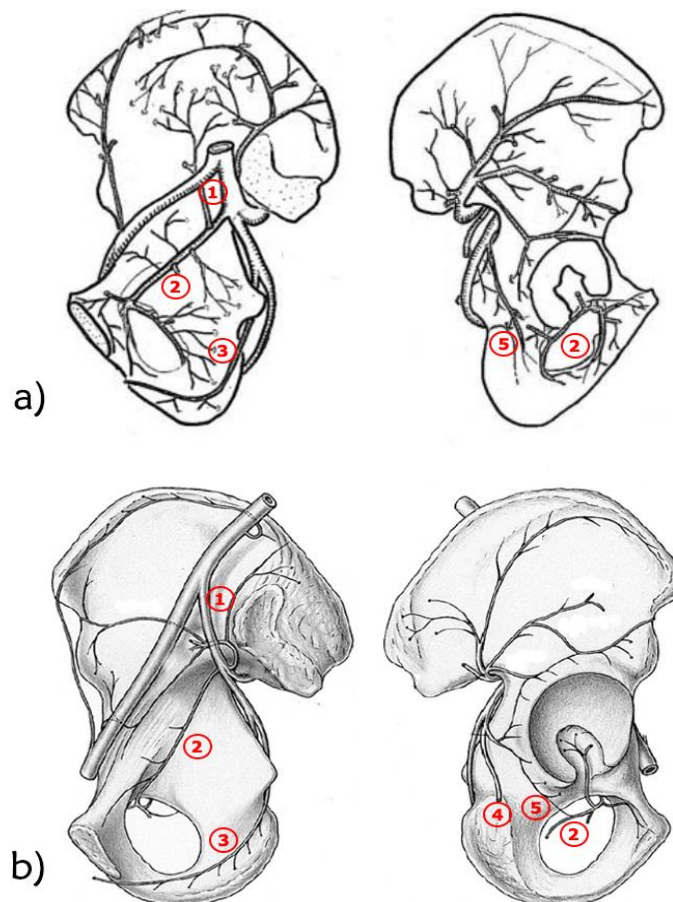
Figure 3.10. Diagrams of arterial distribution to and around the innominate as described by a) Yiming et al., 2002 and b) Beck et al. 2003. 1) Internal iliac artery; 2) Obturator artery; 3) Internal pudendal artery; 4) inferior gluteal artery; 5) acetabular branch of the inferior gluteal artery.

Beck *et al.* (2003) [Figure 3.10b] provided an account which was largely consistent with this view, although some discrepancies were noted. In their approach, they described the artery of the ischium as the acetabular branch of the inferior gluteal artery as it supplied not only the inferior acetabular margin, but was also continuous with supply superiorly to the iliac component of the acetabulum. Further, a much less extensive series of anastomoses were observed from the obturator nerve, with no major branches exiting along its course on the pelvic aspect of the ischium to provide the dominant arterial supply. These discrepancies may be a result of the focus of each study: Yiming *et al.* were specifically investigating the blood supply to the innominate bone, where Beck *et al.* (2003) were studying the hip and its surrounding soft tissues. Additionally, Yiming *et al.* (2002) appraised the distribution of identifiable nutrient foramina on dry bone specimens to supplement their dissection, allowing some contingency against the loss of some vessels during the dissection process. Beck *et al.* (2003) did not observe a similar procedure, only utilising dissection specimens.

Juvenile supply

In the developing ischium, and particularly in the early stages of growth, the principal ischial blood supply is suggested to originate primarily from the obturator artery (Cunningham *et al.*, 2016; Lierse, 1987). The primary nutrient artery is described as piercing the pelvic surface of the ischium at approximately the level of the ischial spine, which can be confirmed through dry bone observations [Figure 3.11]. Additional nutrient foramina, possibly metaphyseal or periosteal in nature, can also be observed on the lateral aspect of the ischium, most notably surrounding the acetabular margin. The placement of these foramina is consistent with the descriptions of the acetabular branch of the inferior gluteal artery and the obturator artery in the adult (Crock, 1996).
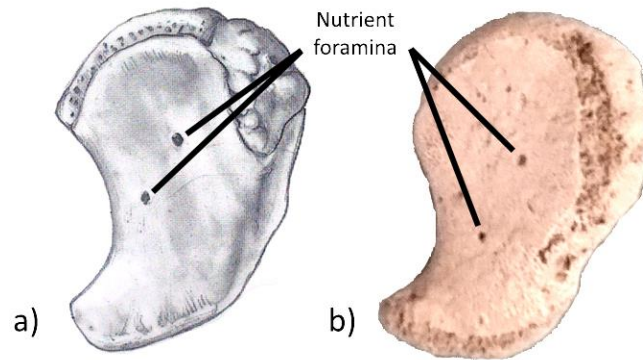
Figure 3.11. Large nutrient foramina identifiable on the pelvic aspect of the perinatal ischium. a)
Diagrammatic representation; b) photograph of perinatal specimen. Diagram adapted from Cunningham
et al., 2016.

3.4 Nerves of the pelvis

In addition to the rich vascular network, a number of major nerves enter and branch
within the pelvis in close proximity to the skeletal framework [Figure 3.12]. Indeed, the
major nerves of the lower limb, the femoral, obturator and sciatic nerves, are
established in advance of the precursor tissues of the innominate and are believed to
influence its morphology as a result, for example informing the shape of the greater
sciatic notch (Laurenson, 1963).
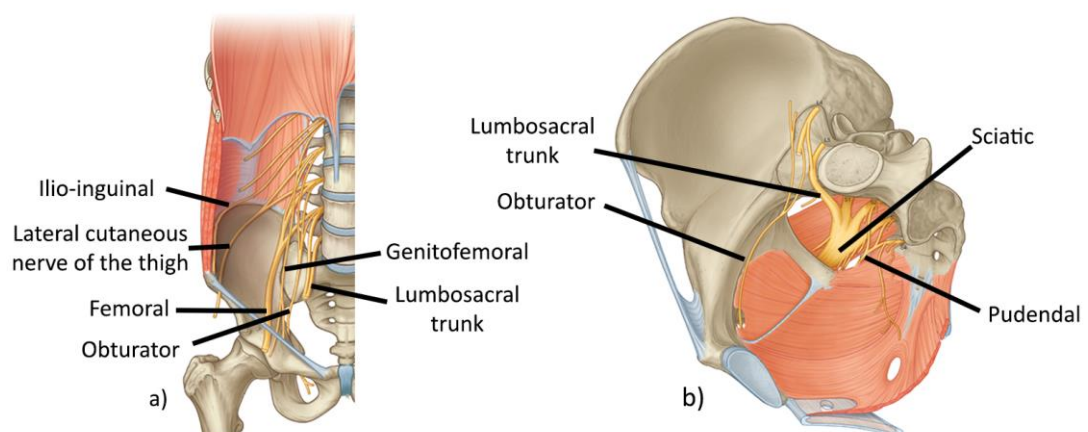
Figure 3.12. Nerves of the lumbo-sacral plexus. Adapted from Drake et al., 2010.

The nerves of the pelvic cavity originate primarily from the anterior rami of the lumbar
and sacral spinal nerves and are considered to form the lumbar and sacral plexuses, or
more simply the lumbosacral plexus. Perhaps the most noteworthy nerves are the
femoral, obturator and sciatic nerves which together are responsible for motor control

of the lower limb. The femoral nerve arises from nerve roots L2 – L4 and crosses the pelvis lateral and deep to iliopsoas. It exits the pelvic cavity alongside the femoral artery, passing beneath the inguinal ligament to enter the femoral triangle. The obturator nerve, which also arises from roots L2 – L4, travels laterally on the pelvic aspect of the superior pubic ramus to the obturator canal, through which it reaches the medial compartment of the thigh. The sciatic nerve, the largest of the nerves of the lumbosacral plexus, is formed from the nerve roots of L4 - L5 (via the lumbosacral trunk) and S1 – S3, which come together to form a single structure on the anterior surface of piriformis. It exits the pelvis through the greater sciatic foramen, passing into the gluteal region and then the posterior compartment of the thigh to provide motor innervation to the posterior thigh and the entirety of the leg and foot. Upon exiting the pelvis, the sciatic nerve can be found passing lateral to the ischium between the long head of biceps femoris and quadratus femoris.

The pudendal nerve also exits the pelvis through the greater sciatic foramen after forming from the anterior rami of S2 to S4. It follows the path of the internal pudendal vessels in crossing the lateral aspect of the ischial spine and sacrospinous ligament to enter the perineum via the lesser sciatic notch. It then provides motor and sensory fibres to the pelvic floor.

3.5 Development of the pelvis

3.5.1 Early development

The hard and soft tissues of the lower limb and pelvic girdle develop directly from the lower limb buds, which first appear at approximately 28 – 29 days of intra-uterine development (Moore and Persaud, 1998; Sadler, 2010). The limb buds develop in response to signalling from the adjacent somites (pairs 24 – 29) and initially present as visible outpouchings from the ventrolateral body wall (Cunningham *et al.*, 2016). They are comprised of an ectoderm shell, from which the integumentary system of the limb will develop (Lee and Eberson, 2006) and an internal mesenchymal condensation (Moore and Persaud, 1998). This mesenchyme forms the precursor of the musculoskeletal tissues of the innominate and hip joint (Rooker, 1979) and is derived from the somatic lateral plate mesoderm (Sadler, 2010).

The embryonic pelvic complex first appears as a condensation of mesoblast cells in the most cranial region of the lower limb buds towards the end of the 5th week of development (Cunningham *et al.*, 2016). This condensation occurs in the region of the major nerves of the lower limb, which develop earlier in the 5th intra-uterine week (Moore *et al.,* 2013). The early presence of these nerves dictates the subsequent shape and position of the components of the pelvis as they are forced to develop around these relatively linear neurological structures (Laurenson, 1963). The condensing mesenchyme extends in three processes that separate these nerves: a superior iliac process extending superiorly, a poster-inferiorly oriented ischial projection and an antero-inferiorly positioned pubic projection. At the centre of these three processes, a shallow depression forms in association with the presence of the condensation for the mesenchymal femur, marking the future position of the acetabulum (Lee and Eberson, 2006). By the beginning of the 6th week, the mesenchymal pelvis begins to approach completion as the ischial and pubic processes fuse around the obturator nerve to form a primitive obturator foramen. The iliac processes fuse superiorly with the developing costal processes of the upper sacral vertebrae whilst the two pubic processes meet ventrally to form a precursor to the pubic symphysis (Cunningham *et al.*, 2016). As this mesenchymal condensation progresses, the musculature of the pelvis and associated motor nerves from the lumbar plexus begin to establish (Moore *et al.* 2013).

3.5.2 Chondrification

Chondrification of the mesenchymal template for the pelvis begins in the 6th week of development with the formation of hyaline cartilage in the iliac mesenchyme mass, superior to the level of the greater sciatic notch (Laurenson, 1964a). The ischium and the pubis have begun chondrification in the 7th intra-uterine week, separated by the obturator nerve (Cunningham *et al.*, 2016). As the 7th week progresses, chondrification advances towards the acetabulum in all three pelvic elements, quickly leading to their fusion in the region of the acetabulum (Lee and Eberson, 2006). The ilium and ischium anlagen are the first to fuse together, occurring by the end of the second month (Cunningham *et al.*, 2016). The pubis quickly unites with this to form a single cartilaginous anlage by the 8th week (McAuley and Uhthoff, 1990). Even at this early stage of development the shape and depth of the acetabulum is defined by the

presence of the cartilaginous head of the femur, as evidenced by the congruence between these two structures at this stage (Delaere and Dhem, 1999; Rooker, 1979). At this stage, chondrification of the pubic symphysis is also complete, with each cartilaginous innominate fused centrally (Gamble *et al.,* 1986). This region will subsequently cavitate to form the pubic symphysis, differentiating into the hyaline cartilage and fibrocartilage disc of the symphysis.

With the position and shape of each cartilaginous anlage determined, chondrification of the innominate expands to further define the structure of the pelvis. By the beginning of the third intra-uterine month, chondrification is nearing completion, and structures such as the anterior superior iliac spine (ASIS), ischial spine and ischial tuberosities are all well-defined (Cunningham *et al.*, 2016).

3.5.3 Cavitation of the hip joint

As chondrification progresses in the innominate, the joints of the pelvis also begin to develop. The cavitation of any synovial joint, including the hip, occurs when a region of arrested chondrogenesis forms between two cartilaginous structures (Decker *et al.* 2014; Sadler, 2010). A dense region of mesenchymal cells develops in this region of arrested development, termed an 'interzone', which will subsequently undergo programmed cell death (apoptosis) to create a fluid-filled cleft which separates the developing cartilages (Lee and Eberson, 2006). The peripheral cells of the interzone do not apoptose, rather they concurrently differentiate to form the supporting capsular tissues of the joint (Moore and Persaud, 1998).

The presence of the hip joint can be identified in the sixth intra-uterine week, in the site where the developing ilium, ischium and pubis meet (Delaere and Dhem, 1999; Uhthoff and Carey, 1990). At this stage, the future joint is represented by an interzone separating the cartilaginous femur from the acetabulum (Rooker, 1979; Sadler, 2010). This interzone enlarges quickly through an elongation of the blastemal cells, such that by the 7th week the joint is readily identifiable histologically (Uhtoff and Carey, 1990).

At the conclusion of the 8th week of intra-uterine life, all elements of the hip joint are developing including the capsular tissues, acetabular labrum, ligamentum teres and transverse acetabular ligament (Delaere and Dhem, 1999; Lee and Eberson, 2006). By

week 11, the hip joint becomes recognisable macroscopically, with a maturation of the joint position and the structures associated with the capsule and labrum. By 16 weeks, the hip joint space is fully formed, including the presence of articular hyaline cartilage and functional muscular structures (Lee and Eberson, 2006).

3.5.4 Ossification

Literature which discusses the ossification of the bones of the pelvis often focuses on the development of the ilium, with less attention paid to the ischium and the pubis. As a result, the developmental minutiae of these bones is not well understood and only milestone developments are chronicled. This imbalance is likely due to the biomechanical and functional significance of the ilium: it is a primary component in both the sacro-iliac joints and the acetabulum, while the inferior elements of the pelvis are perceived to perform a predominantly supportive role. In addition, the ilium begins to ossify many weeks in advance of the ischium and pubis, providing a larger window for investigation, and indeed a larger element to investigate.

Ossification of the bones of the pelvis begins towards the end of the 8th week of intra-uterine development, mimicking the pattern and order established during chondrification. The first pelvic centre of ossification appears in the perichondrium of the ilium in the roof of the acetabulum, close to the greater sciatic notch (Laurenson, 1964b). This expands in a cranial direction to establish the gluteal and pelvic cortices prior to vascular invasion of the underlying cartilaginous template (Laurenson, 1964b). This invasion begins in the 10th and 11th weeks of development with the formation of pores in the cortical bone, allowing osteoblasts access to the cartilage within.

During the fourth month of intra-uterine development, as ossification advances rapidly in the ilium, the first centre for the ischium appears in the perichondrium (Delaere and Dhem, 1999). This centre is said to form posterior to the acetabulum (Cunningham *et al.*, 2016), although a more precise location does not appear to be defined in the literature. It is likely that, given the documented osteogenic nature of neurovascular tissues that this approximates to the position of the lesser sciatic notch, although in the absence of further study, this will remain an unverified hypothesis. Ossification progresses quickly following its onset and the ischium is readily identifiable by the 7th

intra-uterine month. At this stage, the ischium is represented by a comma-shaped element with convex superior and posterior borders, a pointed end anteriorly at the ramus and a slightly concave anterior border, which forms the posterior border of the obturator foramen. The medial, or pelvic, surface of the ischium is smooth and relatively unremarkable and the medially projecting ischial spine has yet to develop. The lateral, or acetabular, surface is more rounded in topography, bearing a slight crest in the midline of the body and a flattened region anterosuperiorly in the position of the future acetabular fossa.

The pubis is the final ossification centre to appear, between the fifth and sixth intra-uterine month (Delaere and Dhem, 1999). This centre is located in the superior pubic ramus anterior to the acetabulum, in close proximity to the obturator and femoral nerves. Unlike the ilium and ischium, some reports exist of multiple centres of ossification for the pubis, although these remain localised to the superior ramus and coalesce quickly. As with the ischium, there is little information that documents the immediate development of the pubis, save to establish that it is readily identifiable by birth.

By birth, each of the bones of the pelvis has adopted a morphology consistent with its adult form, and ossification of each element has reached the walls of the acetabulum (Delaere and Dhem, 1999; Cunningham *et al.*, 2016). The ilium bears its most distinctive feature even at this early age, with the anterior and posterior superior iliac spines evident and the curvature of the greater sciatic notch well defined.

The morphology of the ischium at birth has changed relatively little from that of its fetal counterpart. It remains comma-shaped, although the ramus forms a more prominent projection inferiorly [Figure 3.13]. The most notable feature by birth in the ischium is the development of a raised articular surface on the lateral surface of the ischium to form the posterior margin of the acetabulum. This is located posterior to the flattened acetabular fossa, which remains evident at this stage.

The pubis at birth is identifiable as an asymmetric v-shaped bone comprised of two projecting pubic rami connects anteriorly by the developing symphyseal surface. The superior ramus is club-like in shape proximally at the acetabulum, while the shorter

inferior ramus is pointed and projects inferiorly and posteriorly towards the ramus of the ischium.
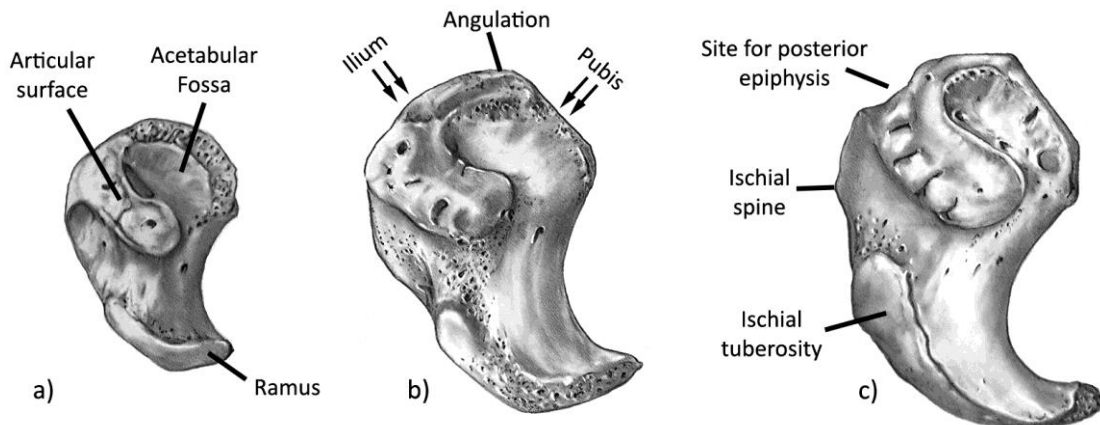
Figure 3.13. The early development of the ischium. a) birth; b) 6 months; c) 1 year. Adapted from Cunningham et al., 2016.

3.5.5 Fusion of the bones of the pelvis

These three bones, although similar to their adult morphology and position, remain separate from each other by persisting cartilaginous intersections. The complex, three-flanged triradiate unit separates each bone in the acetabulum, with the ischium and pubis also separated inferiorly at their rami. The acetabulum remains separate throughout much of juvenile development, with the first appearance of ossification centres in the triradiate cartilage not developing until 9 – 10 years of age, while the fusion of the ischial and pubic rami to form the singular ischiopubic ramus will occur earlier.

These growth fronts, the acetabulum and the ischiopubic ramus, are the regions where the greatest changes will occur in the pelvis prior to the formation of secondary centres of ossification.

Ischiopubic fusion

Ischiopubic fusion at the ramus is the first fusion event to occur in the pelvis, and will do so between the approximate ages of 5 and 8 years of age (Cunningham *et al.*, 2016), although this timing is variable. Cawley *et al.* (1983) stated that ischiopubic fusion typically occurred between 4 and 12 years. Based on a dry-bone study of 148 juvenile individuals, for whom age and sex data was available, Cardoso *et al.* (2013)

observed that non-fusion may persist until 8 (male) or 11 (female) years of age, while complete fusion was observed at 7 years (males) or 5 years (female).

As the time of fusion approaches, the extremities of the pubic and ischial rami begin to expand and flare to adopt a 'heaped' appearance, indicating the onset of fusion at the ischiopubic synchondrosis. Although now known to be a feature of typical development, this appearance of swelling was first considered to be a pathological change, termed osteochondritis ischiopubica (Cawley *et al.,* 1983; Herneth *et al.,* 2000). The synchondrosis develops a callous-like radiographic appearance prior to fusion, and although typically diminished by 10 years of age, this expanded region may persist beyond fusion until the early teenage years (Herneth *et al.*, 2000). The pattern of fusion at this synchondrosis appears variable, with reports of fusion first appearing either on the internal or external surface (Cunningham *et al.*, 2016). Furthermore, individual bilateral fusion patterns for this junction may not be symmetric, with greater flaring observed unilaterally on the side of the dominant foot in physically active children (Herneth *et al.*, 2004). The duration of fusion once commenced appears short; Cardoso *et al.* (2013) noted that only two of 148 individuals were found to display partial fusion of the ischiopubic ramus. This may be exacerbated by the relative fragility of this region, although the authors noted no individuals possessing evidence of bridging that had been damaged post-mortem.

Acetabular fusion

The fusion of the acetabulum is a complex series of events that involves the ossification of the triradiate unit, the closure of the acetabular growth plates and the appearance and fusion of three secondary centres of ossification.

The triradiate unit is comprised of the triradiate cartilage and the cup-shaped acetabular cartilage. The triradiate cartilage is formed from three epiphyseal cartilage flanges that are fused centrally and separate the bones of the pelvis: these are the anterior (iliopubic), posterior (ilioischial) and vertical (ischiopubic) flanges (Portinaro *et al.*, 2001) [Figure 3.14]. The junction between these flanges and their corresponding skeletal elements are comprised of growth cartilage, which allows the triradiate area to function as a growth front in much the same manner as a long bone growth plate.

The acetabular cartilage is located within the acetabulum, lining the developing articular surface. It is important to note that this is distinct from the acetabular labrum, the fibrocartilaginous structure that encircles and deepens the acetabulum (Portinaro *et al.*, 2001).
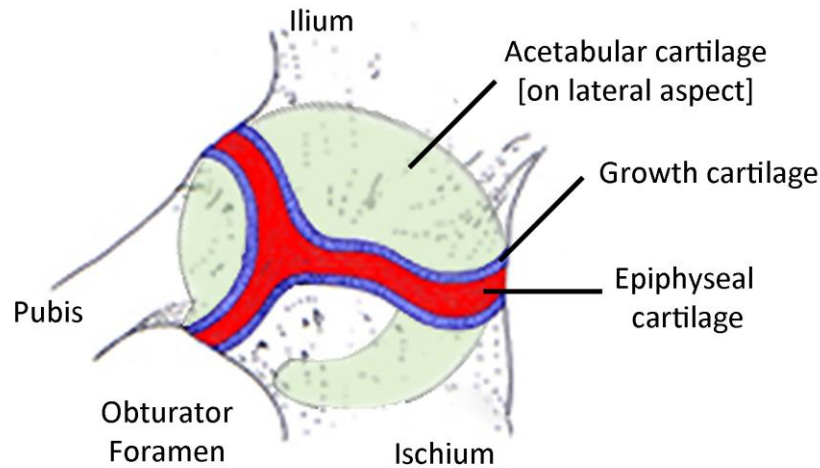
Figure 3.14. Triradiate unit in the developing acetabulum, as viewed from the medial aspect of the innominate. Adapted from Cunningham et al., 2016.

Portinaro *et al.* (2001) examined the growth plates of the triradiate cartilage histologically and determined that they consisted of four specific growth plates per bone. The first (GP1) was directed towards the articular surface of the acetabulum, and the second (GP2) were directed towards the centre of the triradiate cartilage, while the third and fourth (GP 3 and 4) were directed towards the flanges of the triradiate cartilage [Figure 3.15]. Each growth front presented different rates of growth; for example, the central growth plate of the ischium advanced at the greatest rate when compared with the same front of the ilium and pubis, while growth of the ischiopubic flange was noted to be the slowest of the three flanges.

Despite their close proximity, the triradiate cartilage and the acetabular cartilage ossify from separate centres of ossification. The acetabular cartilage ossifies through the development of three separate ossification centres which appear in the acetabular margin (Cunningham *et al.*, 2016).
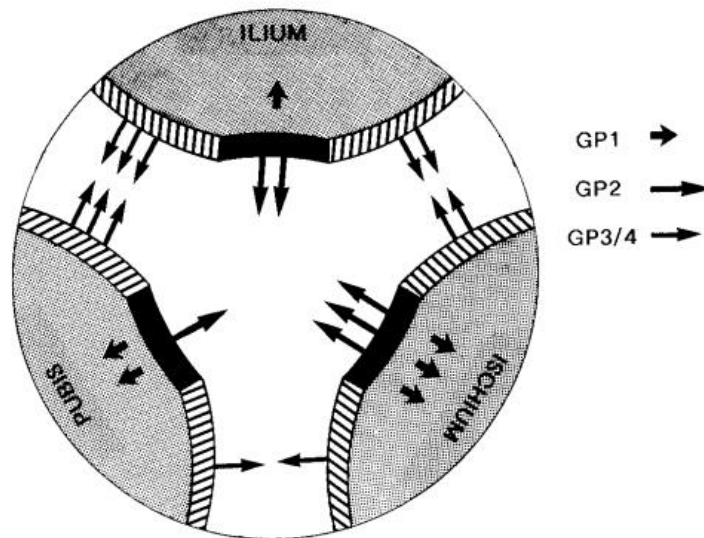
Figure 3.15. Microanatomy of the triradiate cartilage demonstrating the position of each growth plate. The magnitude of growth is indicated by the size and number of arrows. Adapted from Portinaro et al. 2001.

The first of the epiphyses of the acetabular cartilage to form is the 'os acetabuli', or the anterior acetabular epiphysis [Figure 3.16. This centre first develops in the cartilage of the acetabulum adjacent to the pubis at approximately 9 – 10 years of age (Cunningham *et al.*, 2016). The os acetabuli ultimately expands to form the anterior aspect of the acetabular rim, including the articular surface of the pubis and the anterior aspect of the iliac articular surface. It also extends medially towards the anterior flange of the ossifying triradiate cartilage and superiorly towards the superior acetabular epiphysis.
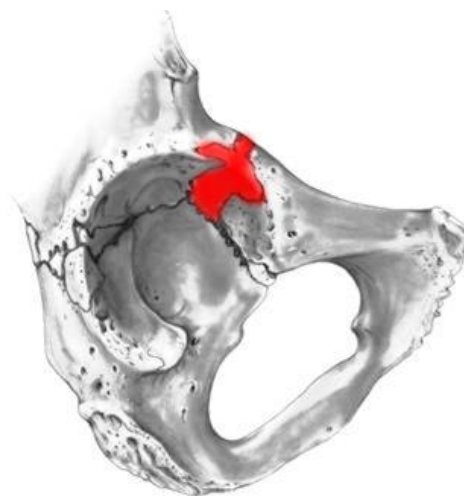
Figure 3.16. Acetabulum of individual approximately 15 years of age, highlighting the position of os acetabuli. Adapted from Cunningham et al., 2016.

The second acetabular epiphysis to form is the os marginalis superior acetabuli, or posterior acetabular epiphysis, which develops in the posterior aspect of the acetabular cartilage at the superior margin of the ischium [Figure 3.17]. It is described as appearing at 10 – 11 years of age, slightly later than the os acetabuli, and may form from a number of smaller ossicles which unite to form a larger centre (Cunningham *et al.*, 2016). The posterior epiphysis expands to form the superior and posterior rim of the acetabulum, the articular surface of the ischium and the posterior aspect of the iliac articular surface. As with the os acetabuli, the posterior epiphysis will extend medially to ultimately fuse with the ossified posterior flange of the triradiate cartilage.
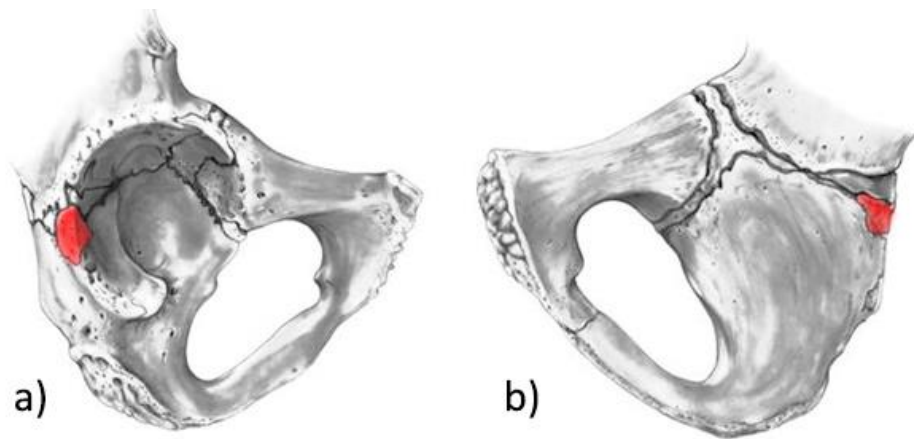
Figure 3.17. Acetabulum of individual approximately 15 years of age, highlighting the position of the posterior acetabular epiphysis. a) Lateral view; b) Pelvic (medial) view. Adapted from Cunningham et al., 2016.

The third epiphysis of the acetabulum is the superior acetabular epiphysis, which appears in the superior margin of the acetabulum at 12 – 14 years of age [Figure 3.18]. This epiphysis is unique in its position as it is not associated with a flange of the triradiate cartilage. It forms the superior aspect of the acetabular rim and the roof of the articular surface of the acetabulum (Cunningham *et al.*, 2016). It may also extend superiorly to cover the lower region of the anterior inferior iliac spine [Figure 3.18c]. If this occurs, fusion at the AIIS may not complete until 16 – 17 years of age (Cunningham *et al.*, 2016).
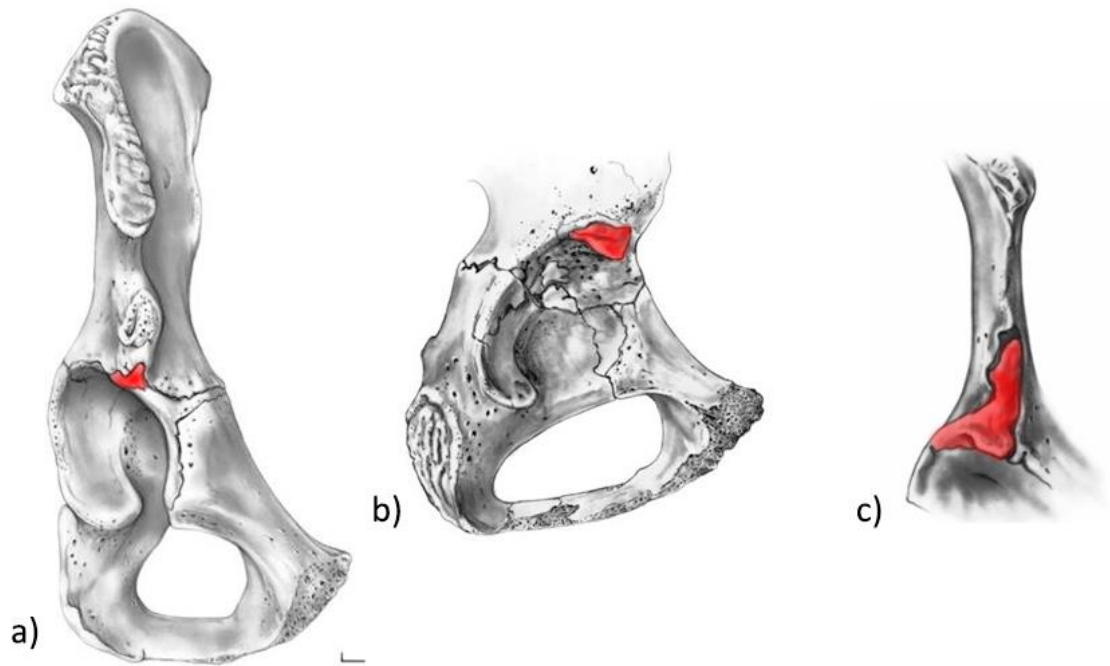
Figure 3.18. Three presentations of the superior acetabular epiphysis. a) approx. 15 years of age; b) female, 12 years of age; c) female, 14 years of age, showing prolongation to inferior iliac spine. Adapted from Cunningham et al., 2016.

Ossification of the true triradiate cartilage begins with the formation of a variable number of ossific nodules within the flanges from approximately nine years of age (Cunningham *et al.*, 2016). These islands enlarge and eventually encompass the entirety of the triradiate cartilage, in addition to uniting with the developing acetabular epiphyses and the borders of each of the pelvic bones. Fusion of these elements to form a single structure begins at approximately 11 years in females and between 11 – 14 years in males (Cardoso, 2008). The pelvic region of the triradiate cartilage typically fuses slightly in advance of the acetabular aspect. Completion of the acetabulum typically occurs by 16 years of age in females and 18 years in males (Cardoso, 2008).

3.5.6 Pelvic epiphyses

In addition to the epiphyses associated with the acetabulum, there are a further five secondary centres of ossification associated with the peripheral borders of the ischium: three which are associated with the ilium, one associated with the ischium and one with the pubis.

Ilium

The first peripheral epiphysis is reported to appear for the anterior inferior iliac spine between 10 and 13 years of age (Cunningham *et al.*, 2016). It is possible that this centre may form as an extension of the superior acetabular epiphysis, rather than a separate centre, due perhaps to these regions both providing the attachment site of the iliofemoral ligament [Figure 3.18c]. Due to the presence of this ligamentous structure, and the proximal attachment of rectus femoris, avulsion of this epiphysis has been reported in individuals between 14 and 17 years of age, typically following strenuous physical activity (Serbest *et al.*, 2015). Fusion of this epiphysis is typically reported as occurring by 20 years of age (Cunningham *et al.*, 2016).

The iliac crest is formed from two separate centres of ossification, one each for the anterior and posterior aspects of the iliac crest. The centres for the iliac crest appear at approximately 12 – 13 years of age, with the anterior forming slightly in advance of the posterior (Cunningham *et al.*, 2016). The centres fuse posterior to the highest point of the crest, with the anterior epiphysis passing forward to the ASIS and the posterior epiphysis ending with the formation of the PSIS [Figure 3.19]. As with the AIIS epiphysis, avulsion of the iliac crest epiphyses in the juvenile has been noted in the clinical literature, most often associated with abrupt contraction of the abdominal muscles which insert on the crest (Mortati *et al.*, 2014). Fusion of the iliac crest to the ilium typically occurs between 14 – 23 years of age, with the youngest reported complete fusion occurring at 17 years in males, or 18 years in females (Webb and Suchey, 1985). Fusion in all individuals was noted after 23 years of age.
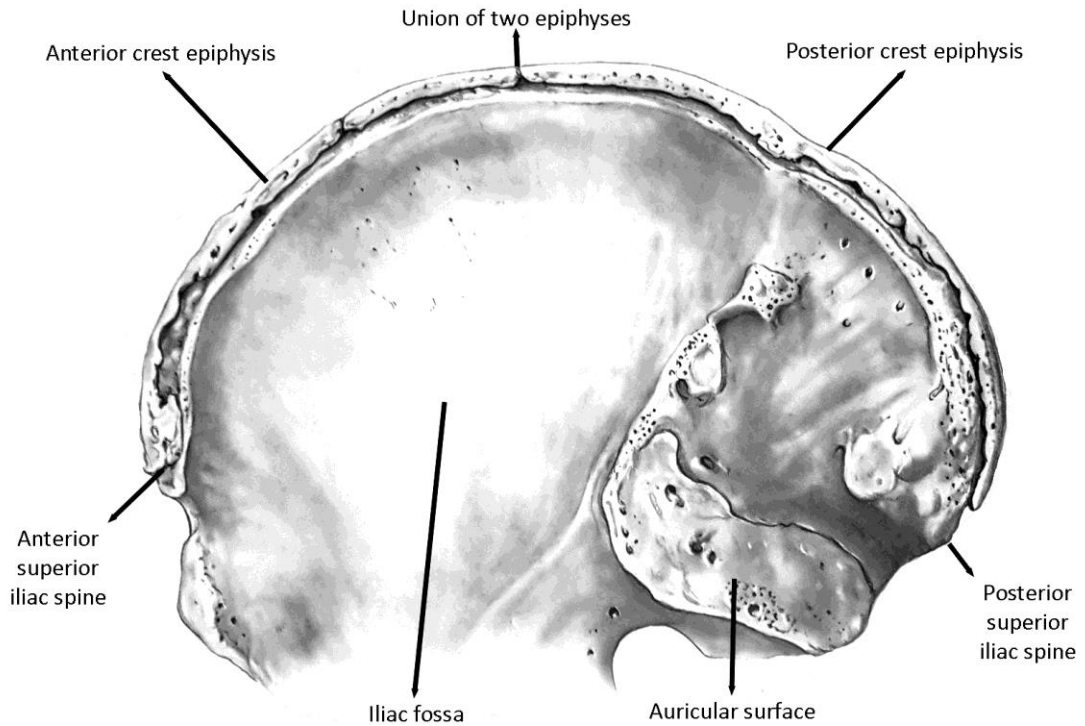
Figure 3.19. Development and fusion of the iliac crest epiphyses (approx. 16 years). Adapted from Cunningham et al., 2016.

Ischium

There are two epiphyses typically associated with the developing ischium, described as the ischial epiphysis and the ramal epiphysis (Figure 3.19). The ischial epiphysis, which will ultimately form the adult ischial tuberosity, is first observed forming as a small flake on the superior aspect of the ischial tuberosity at 13 to 16 years of age (Flecker, 1932; Cunningham *et al.*, 2016). It is reported to commence fusion to the ischium shortly after its appearance, fusing first at the superior margin (Figure 3.20a). The centre for the tuberosity then extends inferiorly to 'cap' the metaphyseal surface, progressing to the most inferior aspect of the tuberosity before curving anteriorly towards the ramus of the ischium [Figure 3.20b]. The anterior continuation of this centre is then termed the ramal epiphysis, perhaps in part due to its more prolonged existence as the true ischial epiphysis is typically considered to fuse to the ischium between 16 – 18 years (Cunningham *et al.*, 2016). The ramal epiphysis progresses anteriorly along the ramus, extending to the posterior aspect of the inferior pubic ramus, and active fusion may persist until 20 – 23 years of age [Figure 3.20c] (Cunningham *et al.*, 2016).
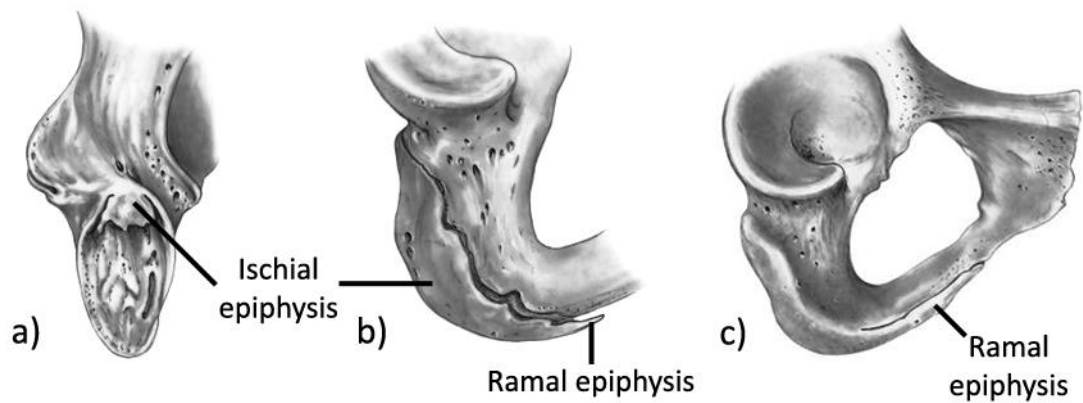
Figure 3.20. Development of the ischial and ramal epiphyses. a) Formation and fusion of flake-like epiphysis (female, age 14); b) Fusing cap-like ischial epiphysis extending to form ischial epiphysis (male, age 17); c) Fused ischial epiphysis with fusing ramal epiphysis (female, 19). Adapted from Cunningham et al., 2016.

Flecker (1932) described fusion of the 'tuber ischii' epiphysis as occurring by 20 – 24 years of age based on radiographic observations, although it is unclear whether this included a distinction between the ischial and ramal epiphyses. Schaefer (2008) more recently documented the fusion of the ischial tuberosity as occurring between 16 and 20 years of age, based on a Bosnian male population, without reference to the ramal epiphysis component. Cardoso (2008) reported similar results from a modern Portuguese population, with fusion typically commencing between 14 – 15 years of age in females and 15 – 16 years in males. Fusion of the ischial tuberosity component was found to be complete between the ages of 16 – 20 years in females and 17 – 22 years in males. Complete fusion of the ramal epiphysis was found to have occurred in all individuals by 23 years for both males and females (Cardoso, 2008).

As the ischial tuberosity provides attachment for the hamstring muscle group, powerful extensors of the thigh and flexors of the knee, it is perhaps not surprising that avulsion of the ischial epiphysis has been noted in the clinical literature, particularly in young athletes (Salvi *et al.,* 2006; Schlonsky and Olix, 1972).

Pubis

The development and maturation of the pubic symphysis is a process which has been studied extensively due to its importance in the assessment of age (Brooks and Suchey, 1990; Cunningham *et al.,* 2016; Hanihara and Suzuki, 2005). This process occurs over a prolonged period of time, with the first changes from an immature ridge-

and-furrow surface beginning between 15 – 23 years of age, and completion of the mature symphyseal face often not achieved until 35 – 40 years of age. The complexity of this process is such that a brief summary would be insufficient to document and describe the series of morphological changes which occur and their implications.

3.6 Gait

3.6.1 The gait cycle

The locomotor behaviour of humans, that is the adoption of a habitual bipedal posture and gait, is perhaps one of the most immediately identifiable traits of modern humans (Hogervorst *et al.*, 2009). It requires the coordinated action of a number of muscles across the hip, ankle and joints of the foot, in addition to reciprocal changes in the vertebral column, upper limb and head to ensure balance is maintained. As a result, a great deal of emphasis is placed on the analysis of the hip and its component structures in the biomechanical, neurological, clinical and evolutionary literature.

Although the specific gait of an individual is an idiosyncratic motion, there is an established series of phases that are followed during the standard gait cycle (Keen, 1993). This cycle is traditionally defined as "the period of time between any two identical events in the walking process" (Ayyappa, 1997; Magee, 2008), although an informal consensus typically lists the beginning of the cycle as the right heel strike, also referred to as initial contact. A new cycle begins when this event is next repeated on the same side.

There are several possible descriptors that can be applied to the gait cycle [Figure 3.21]. In the first instance, the phases of gait can be defined as being part of either a stance period or a swing period, based on the presence or absence of ground contact respectively (Ayyappa, 1997). Each leg spends approximately 40% of each gait cycle in its swing period between its toe-off and subsequent heel strike, and 60% of the cycle in a stance period before the next toe-off (Magee, 2008). There is by necessity an overlap in the stance phase of each leg, for example between the heel strike of the right foot and the toe-off of the left, which creates a brief period of double support (Racic *et al.,* 2009). Double support therefore occurs twice during a single gait cycle:

once at the beginning and once in the middle between each leg's swing period. The cyclical nature of gait results in a variable biomechanical environment, as the pattern of loading and resulting strains differ at each stage of walking [See Chapter 3.7.2].
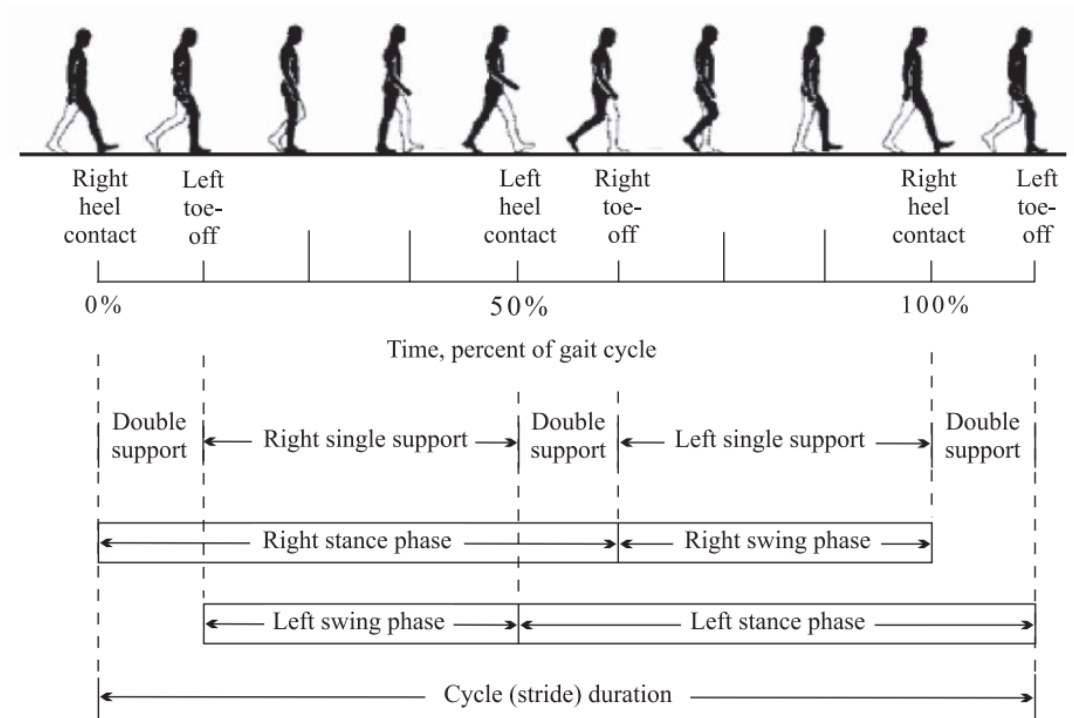
Figure 3.21. The phases of gait, as described by Racic et al., 2009.

3.6.2 Gait maturation

The development of gait is a gradual process that evolves over a period of years, combining learned motions with reflexive actions (Keen, 1993). The methods and terminology used to describe the development of gait vary, as does the age at which each stage is attained. Figure 3.22 summarises two separate classifications of gait development.

The first indicators of bipedalism are identifiable following birth. In the early post-natal period, when held upright, infants will display what is termed the 'stepping reflex', a series of coordinated lower limb movements that bear a similarity to the adult gait cycle (Thelen and Fisher, 1984; Thelen et al., 2002). It has been noted however that although the motions are similar to adult gait, they are irregular and lack several key postural characteristics (Lacquaniti et al., 2012). This reflex typically disappears after approximately two months, although it has been demonstrated that this primitive walking response can be retained if its use is promoted by repeated stimulation

(Zelazo *et al.*, 1972) or by submerging the lower limbs in water (Lacquaniti *et al.*, 2012). This suggests that the loss of this reflex is at least in part caused by the increasing muscular strength required to mobilise the lower limb
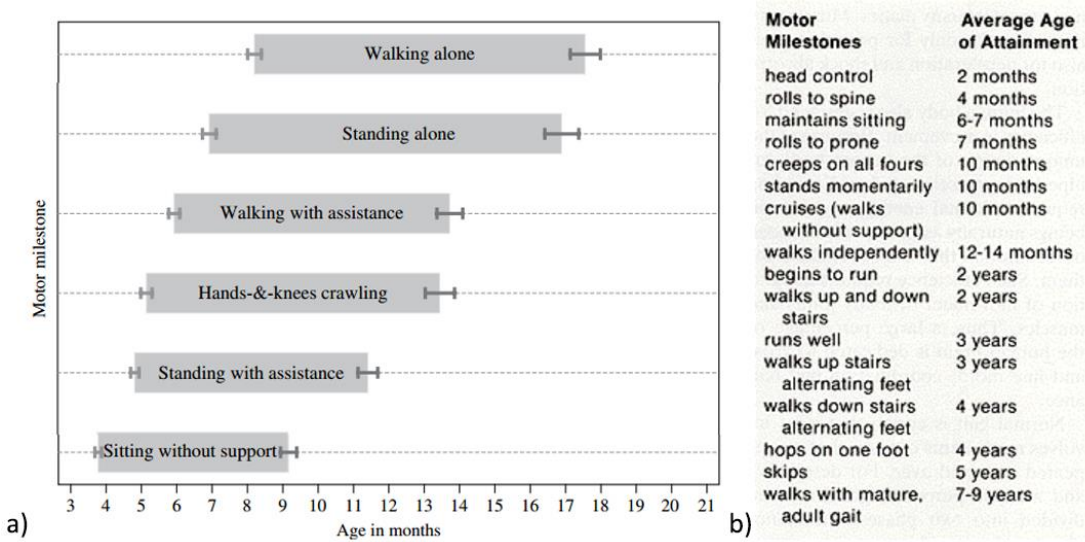
Figure 3.22 a) Descriptions of gross motor development stages and their age of appearance. Adapted from WHOMRSG, 2006. b) Developmental motor milestones as described by Keen, 1993.

Over the first 12 – 14 months of life, the human infant transitions from an obligate supine position to independent sitting, to a transitional period of hands-and-knees crawling which is reminiscent of the locomotor behaviours of quadrupedal primates (Righetti *et al.*, 2015). This is followed by the progressive development and maturation of an upright posture and bipedal locomotion which, although initially requiring support and assistance, is an independent movement by approximately 12 – 14 months of age (Keen, 1993; Lacquatini *et al.*, 2012).

Only limited information is available regarding the crawling phase of human locomotor development, which begins at approximately 9 months of age (Goldfield, 1989). The development of crawling is preceded by an increase in lower and upper limb movements, with increased co-ordination of contralateral limb movements (Goldfield, 1989). In the early stages of crawling, weight is distributed between the upper and lower limbs through hand and knee or, less commonly, foot ground contact. As crawling progresses however, weight distribution is gradually shifted posteriorly to the lower limbs as the head is lifted and the upper limb is utilised more frequently for prehensile functions in a 'tripod' balance (Goldfield, 1989).

Following the crawling phase, human infants begin to adopt an upright stance and bipedal locomotor behaviours. These become independent at approximately 12 months of age, although this can vary from 9 to 18 months (Lacquatini *et al.*, 2012; WHOMGRS, 2006). There are five determinants which are used to define gait development, including; duration of single limb stance, walking velocity, step cadence (frequency) and length, and the breadth of the support base (Sutherland *et al.*, 1980). Each of these individual characteristics develops from an immature form to a mature presentation over time, and at different rates, following this transition to independent upright walking.

In the early stages of walking, step cadence is high with relatively limited duration swing phases and prolonged double-stance support (Lacquatini *et al.*, 2012). The hip is typically externally rotated and the knees remain flexed, creating a wide base of support, and foot contact is typically flat-footed (Keen, 1993). Over the next six months, a more mature heel strike develops, as does a reciprocal arm swing, and the base of support narrows. By approximately two years old, the position of the lower limb conforms more closely to the adult form, including less external rotation and pelvic tilt than was seen in the early stages of gait maturation. By three years of age, the basic mechanics of adult gait have been established: the ratio of swing phase to stance phase approximates that of adults, the base of support is proportional to body size and movements have become more regular (Keen, 1993), although there remain differences in joint movements when compared to adult gait. The adoption of adult cadence, velocity and step length does not truly occur until sufficient growth has occurred as they are each related to limb length (Beck *et al.*, 1981; Keen, 1993).

3.7 Biomechanics of the pelvis

3.7.1 Overview of adult pelvic architecture

The human pelvis is a responsible for the transfer of the weight of the body from the lumbar vertebrae and sacrum to the ilium via the sacroiliac joints, and to head of the femur through the ilium and the roof of the acetabulum at the hip joint (Rook, 1999; Macchiarelli *et al.*, 2001). In addition, each innominate is also subjected to the ground reaction forces transmitted into the innominate from the head of the femur which can

be far in excess of the forces generated by the downward transfer of weight. It has been demonstrated that during 'normal walking' (4 km / h on a level surface), peak forces generated at the acetabulum may be greater than 250% of body weight, which may be further increased by atypical loading conditions such as stair climbing (Bergmann *et al.*, 2001).

The architecture of the innominate must be capable of withstanding these forces without failure, a goal that is achieved through the organisation of the trabecular and cortical bone structure of the innominate (Macchiarelli *et al.*, 1999; Martinón-Torres, 2003; Rook *et al.*, 1999). The basic structure of the innominate is commonly referred to as a 'sandwich', comprised of two cortical shells separated by a core of relatively low-density trabecular bone (Dalstra and Huiskes, 1995; Cunningham and Black, 2009b; Macchiarelli *et al.*, 2001). The majority of the loading in the pelvis is typically reported to be carried by the cortical bone, while the trabecular core acts as a spacer to separate the two shells and disperse sheer stresses (Dalstra *et al.*, 1993; Rook *et al.*, 1999). However, despite being attributed with a diminished responsibility for load transfer, the trabecular bone architecture of the innominate has been found to vary between primates with differing locomotor behaviours to an extent where locomotor behaviour can be inferred with relative confidence from the observed architecture (Rook *et al.*, 1999; Macchiarelli *et al.*, 1999). The adoption of an evolutionarily atypical locomotor behaviour has also been found to substantially alter pelvic microarchitecture: for example, when trained to walk upright in a bipedal posture, the trabecular structure of the Japanese Macaque has been shown to transition from a quadrupedal form to one which mimics the human trabecular system (Volpato *et al.*, 2008).

On a gross scale, the human pelvis is most often described as possessing three primary trabecular systems in relation to locomotor forces: the superior auriculo-acetabular pathway, the inferior auriculo-acetabular pathway and the sacro-ischial pathway (Aiello and Dean, 1990; Cunningham *et al.*, 2016; Kapandji, 2011) [Figure 3.23]. These bundles are each ascribed a specific function with regards to posture and locomotion. The inferior auriculo-acetabular trajectory pathway is reported to transmit compressive forces between the auricular surface and the iliac component of the acetabulum; the superior auriculo-acetabular trajectory pathway resists shearing

stresses and the sacro-ischial trabecular trajectory is proposed to transmit compressive forces from the auricular surface to the ischial tuberosities while seated.
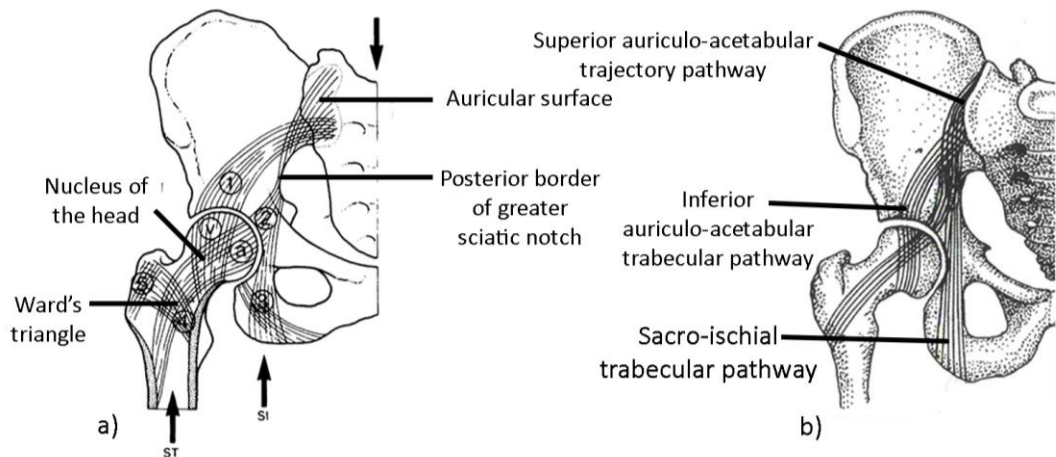
Figure 3.23. The trabecular systems of the adult pelvis after a) Aiello and Dean, 1990 and b) Cunningham et al., 2016. The bundles described as 1, 2 and 3 by Aiello and Dean (1990) correspond with the inferior auriculo-acetabular trajectory pathway, the superior auriculo-acetabular trajectory pathway and the sacro-ischial trajectory pathway respectively.

In addition to these locomotor and load-bearing functions, the anterior pelvic arch, comprised of the superior pubic rami and pubic symphysis, is also considered to be under compressive loading, providing an anterior 'brace' against medial displacement of the innominate, and also transmitting reactive hip forces away from the acetabulum (Macchiarelli *et al.*, 1999). A trabecular trajectory has also been described passing posteriorly from the symphyseal face of the pubis to the ischial tuberosity, traversing the ischiopubic ramus, along with perpendicular trabeculae passing from the inferior border of the obturator foramen and the inferior margin of the ramus (Holm, 1980).

In the anthropological literature, the trabecular architecture of the innominate, in particular the ilium, has been further subdivided into a number of smaller, interconnected bundles, each associated with locomotor forces (Macchiarelli *et al.*, 1999; Martinón-Torres, 2003) [Figure 3.24]. The primary bundles associated with an upright gait are the sacropubic (spb) and ilioischial (iib) bundles, which cross in a region of increased trabecular volume termed the trabecular chiasma (tc), which lies superior the acetabulum and anterior to the greater sciatic notch (Rook *et al.*, 1999). The sacropubic bundle appears to correlate closely to the described inferior auriculo-acetabular trabecular pathway, and assists in the transmission of compressive forces between the auricular surface and the acetabulum. The ilioischial bundle is reported

to be responsible for the dispersion of tensile forces generated by compression of the spb, preventing the buckling of the iliac blade (Macchiarelli *et al.*, 1999).

Supplementary trajectories around the acetabulum have also been reported passing concentrically (pericotyloid bundle; pcb) and radially (radial trabeculae; rt) around the acetabulum, likely acting to disperse reactive forces passing into the ilium from the hip joint (Kapandji, 2011; Macchiarelli *et al.*, 1999). Additional trajectories are associated with the AIIS (anterior bundle; ab), body of the ischium (posterior bundle; pb) and the iliac crest (superior bundle; spb) (Macchiarelli *et al.*, 1999). Each of these regions correspond with sites of muscular or ligamentous attachment, and it is therefore likely that these less pronounced trabeculae are associated with the forces generated by musculoskeletal interactions at these locations.
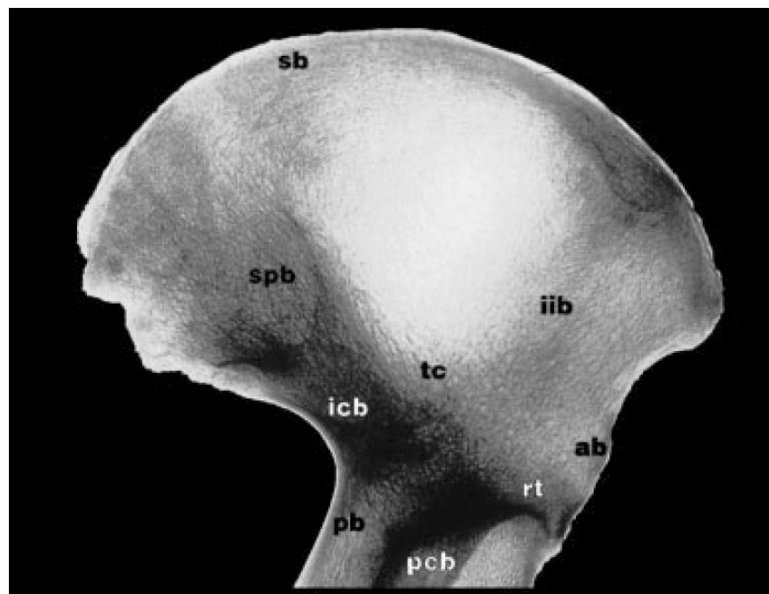
Figure 3.24. Trabecular architecture of the human ilium. ab: anterior bundle; icb: iliocotyloid bundle; iib: ilioischial bundle; pcb: pericotyloid bundle; pb: posterior bundle; rt: radial trabeculae; sb: superior bundle; spb: sacropubic bundle; tc: trabecular chiasma. From Macchiarelli et al., 1999.

It should be noted that, while the presence of these structural features are often referred to with regards to their mature form and role in load transmission, it has also been reported that these 'adult' trajectories are also present during skeletal development and in advance of habitual bipedalism. Cunningham and Black (2009a) demonstrated rudimentary regions of increased radiopacity in regions corresponding to the trabecular chiasma, sacropubic trajectory and ilioischial trajectory in the late fetal period, which were found to be well established by the neonatal period. The early

establishment of these high intensity regions mimicking the adult form have been attributed to the retrograde forces associated with reflexive *in-utero* lower limb movements (Cunningham and Black, 2009), which may suggest that the ground reaction forces in the adult play a greater role in the maintenance of the adult architecture than is often presented. It was also observed that the increase in radiopacity in these regions was primarily driven by increased cortical thickness, rather than trabecular volume as, while trabecular thickness in the neonatal chiasma was found to be relatively high, the bone volume was reduced (Cunningham and Black, 2009b,c). This is consistent with the proposed 'sandwich' arrangement of the innominate, where the cortical shells rather than the underlying trabeculae carry the majority of stresses. The trabeculae within these regions were found to align more closely with the axes of these proposed trajectories with increasing age, with the sacropubic trabeculae in particular maintaining congruence with both the auricular surface and lunate surface of the acetabulum (Abel and Macho, 2011). Due to the relatively broad categorisation of age presented, based on permanent molar eruptions, it was unclear if this increased anisotropy could be directly linked to milestones in gait development.

3.7.2 Load transmission in the pelvis

The nature of load transmission within the pelvis has been studied primarily through the use of finite element analysis (FEA) to simulate strains in models based on current knowledge of pelvic architecture and loading scenarios, typically based on the stages of gait.

Dalstra and Huiskes (1995) examined the distribution of the forces applied at the acetabulum during 8 stages of the gait cycle, including single support, double support and the raising and lowering each leg. Only those forces that originated in the acetabulum were considered and from the surrounding musculature were considered, excluding the load associated with the trunk passing inferiorly from the sacroiliac joints and the reinforcement provided by the ligaments of the hip, pubic symphysis and SI joint. The results of this study were broadly consistent with expectations: due to the sandwich construction of the innominate, the strains placed on the cortical shells were predicted to be much greater than those experienced by the underlying trabecular

bone. During weight bearing, high cortical strains were predicted in the ilium, particularly along trajectories similar to the spb and iib, with increased strains also present across the pubic symphysis. Strains in the ischium were found to be minimal during weight bearing, although strains were predicted to increase in the region posterior to the acetabulum during lifting and lowering of the corresponding leg. This is likely due to the activation of the muscles inserting on the ischium rather than the transmission of a compressive force, although the authors make no note of the type of strain incurred (i.e. compressive, tensile, shearing etc.). The predicted trabecular strains were primarily located in the regions superior to the acetabulum, the greater sciatic notch and the superior pubic ramus, with some strain also predicted in the region of the ischial spine during raising and lowering of the lower limb.

Further finite element analyses have built upon the stress model presented by Dalstra and Huiskes (1995), incorporating additional elements to address limitations in the earlier study. Phillips *et al.* (2007) addressed one of the principal limitations: the use of a fixed boundary model where the auricular surface was represented by an anchored point. A recreation of this original fixed boundary model was compared with a 'muscular and ligamentous boundary condition' (ML) model which included computed elements representing the ligaments around the sacroiliac joint and pubic symphysis to allow a degree of movement and pliability in response to simulated loading. Only a single loading condition was presented however: a single leg stance (i.e. while weight-bearing). As was observed following the inclusion of the acetabular articular cartilage, the magnitude of strains described in the ilium were reduced in both the trabecular and cortical components of the model, with a particularly pronounced decrease in the loads experienced by the lateral cortical shell [Figure 3.25a]. The cortical stresses around the ischial spine, posterior ischial body and the central aspect of ischiopubic ramus were increased however, likely caused by the inclusion of the strong sacrospinous and sacrotuberous ligaments. Trabecular stresses were found to increase in the superior aspect of the ischium, underlying and surrounding the acetabulum, and also in the region inferior to the most inferolateral angulation of the obturator foramen [Figure 3.25b].

Ghosh *et al.* (2015) also recreated the model and parameters established by Dalstra and Huiskes (1995), but with the inclusion of an anatomically accurate model of the

femoral head and the cartilaginous layer covering the lunate surface. This modification was found to reduce the overall magnitude of the stress distributed within the pelvic cortex, although the trajectories were similar to those reported previously [Figure 3.25c]. The stresses experienced in the underlying trabecular bone were also reported to decrease in the modified model, although the distribution of stress within the trabecular bone volume was not presented graphically for any case (Ghosh *et al.*, 2015).
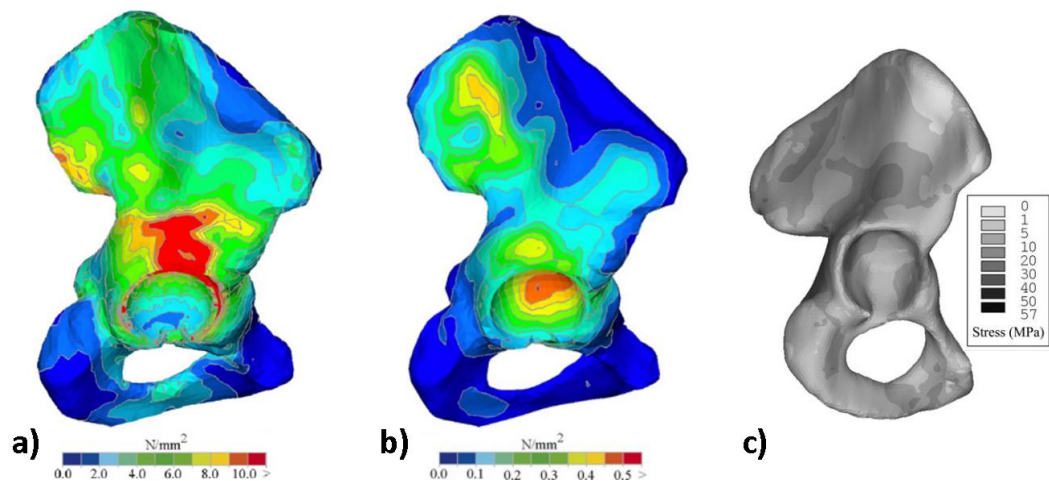
Figure 3.25. FEA stress distributions modelled in a hemi-pelvis, loaded in single stance. a) Cortical and b) trabecular bone stresses calculated using ML boundary conditions (Phillips et al., 2007); c) Cortical bone stresses calculated using a fixed boundary but with the inclusion of the acetabular articular cartilage (Ghosh et al., 2015).

It should be noted that the accuracy of the predicted strains in a finite element analysis is dependent on a number of variables; for example the number and type of elements, the prescribed material properties and the loading and boundary constraints which are used to create the model (Watson *et al.*, 2017). The level of anatomical detail and simulated biomechanical environment should be examined in detail, as this can affect the applicability of results: each model is specific to its formulation. While no 'complete' finite element analyses could be identified, i.e. those constructed with an ML boundary model including loading at both the sacroiliac joint and the acetabulum and a full complement of muscular and ligamentous structures, the observed stress distribution appeared to mirror gross changes in architecture as described radiographically (Macchiarelli *et al.*, 1999; Martinón-Torre *et al.*, 2003).

3.7.3 Structure and biomechanics of the ischium

Considering that the sacro-ischial trajectory is considered to be one of the primary load-bearing trajectories of the pelvis, there is a remarkable paucity in the literature regarding either the architecture or biomechanics of the ischium, at any developmental stage. Indeed, although seminal texts refer to the existence of the sacroischial trajectory, at present no papers which either qualitatively or quantitatively demonstrate its presence could be identified within the literature.

However, structural adaptations to bipedalism have been described in the ischium, particularly with regards to gross morphological developments. The prominence of the human ischial spine, typically diminished or absent in quadrupedal species has been linked to the evolution of the supporting ligaments and the pelvic floor as a result of an upright posture (Abitbol, 1988). The prominence of the ischial spine may be accompanied by underlying architectural adaptations to reinforce this region against tensile stress, perhaps in the form of increased cortical thickness.

Aiello and Dean (1990) also suggested that the development of an increasingly prominent and superiorly flared ischial tuberosity in humans may be due to the altered strains associated with bipedalism, as the ischial tuberosity in non-bipedal apes has been described as distinctly wider, lower and possessing less well defined muscular insertions than the human equivalent. This flaring, described as 'pulling-up', may be a result of increased strains generated between the sacrum and ischium as the sacrotuberous ligament resists anterior rotation of the sacrum. Woodley and Kennedy (2005) indirectly disputed this assertion however, citing the numerous small coccygeal vessels and nerves which pierce the sacrotuberous ligament as an indicator that this ligament is unlikely to be subjected to high loads as this would create the potential for damage to these structures.

In their treatment of the architecture of the innominate, Macchiarelli *et al.* (1999) described a small number of trabecular systems which are purported to traverse the ischium, although their accompanying images did not extend below the iliac component of the acetabulum [Figure 3.24]. The inferior bundle is described as traversing the ischiopubic ramus, including both the ischial and pubic components. The

posterior bundle (pb) is described as running through the posterior margin on the innominate, traversing the ilium and ischium to enter the ischial tuberosity. Joining this is the ilioischial bundle (iis), which is described as passing from the anterior iliac crest to the ischial tuberosity, passing posterior to the acetabulum. The description of the posterior bundle corresponds closely with the described position of the sacroiliac bundle (Aeillo and Dean, 1990), and therefore may be responsible for the transmission of compressive forces between the auricular surface and the ischial tuberosity.

Further trabecular bundles which may be identifiable in the ischium include the pericotloid and radial trabeculae, which are described as radially and concentrically surrounding the acetabulum to assist with force dissipation (Macchiarelli *et al.*, 1999). Although they have not been described explicitly as occurring within the ischium, the ischium supplies 2/5th of the lunate surface and features a relatively protuberant acetabular margin, therefore it is likely they are identifiable. A final trabecular bundle has also been described, the ischiocotyloid bundle, which are derived from both the inferior and posterior bundles, and pass between the ischial tuberosity and the lunate surface. These trabeculae may also be involved in the dissipation of the ground reaction force from the acetabulum, as their described position is similar to the location where an increase in strain during single-leg weight bearing is predicted during ML boundary FEA (Phillips *et al.*, 2007) [Figure 3.25b].

Chapter 4: Qualitative Analysis of the Juvenile Ischium

4.1 Aims

The qualitative analysis of the juvenile ischium was achieved using digital radiographs which were processed using a colour-map function to visualise gross variations in radiographic intensity, both within single specimens and between specimens of different ages.

In the first instance, the aim of the project was to document qualitative changes in the radiographic appearance of the ischium during growth and development and relate these to the structure and function of the ischium.

Secondly, this project aimed to determine whether there was evidence of specific architectural changes which could provide information regarding the factors influencing the pattern of growth and development, for example changes in the biomechanical environment associated with gait maturation.

4.1.1 Macro-radiographic investigation

Prior to the use of digital radiographs, a similar investigation was undertaken using hard-copy macro-radiographs which were obtained during a previous PhD project, but which did not ultimately form a part of that earlier project (Cunningham, 2009).

The macro-radiographic investigation was published as an original research paper (Maclean *et al.*, 2014). A copy of this publication can be found in Appendix 4.1.

The content of this publication will not be reproduced here as it was noted that all primary observations from the macro-radiographic study were found to be mirrored in the subsequent study which utilised digital radiographs, with the addition of specific findings from this second analysis cohort. For the specific data regarding the macro-radiographic investigation please refer to appendices 4.1 and 4.2.

4.2 Background

4.2.1 Principles of radiography

Radiography is an imaging technique that is used to visualise the structure of a specimen based on the variable attenuation of the x-ray beam by different tissue types and thicknesses.

To capture an image, a heterogeneous beam of x-ray photons is directed towards a suitable detector (projected beam) through the specimen. As the photon beam passes through each tissue, a proportion of the photons will be absorbed or deflected. This causes attenuation (weakening) of the beam as it progresses through the specimen. The remaining photons (emerging beam) will exit the subject tissues and impact the chosen detection equipment that will react, to or measure, the varying photon intensities of the beam.

Modern radiographic apparatus utilises flat-panel digital detection plates that allow the instantaneous capture of intensity data in a digital format. These typically consist of a photosensitive layer that fluoresces when x-ray photons impact its surface. This fluorescence stimulates a photodiode layer to produce an electrical signal that is detected and translated into a digital image by a series of charged-couple devices (CCD). The final image is then available for transfer to a computer to be displayed.

Radiography provides an excellent preliminary method of investigation, both clinically and in research, as it allows the rapid collection of two-dimensional data that can be interpreted quickly. It is limited in its discriminatory capability however as the final radiographic image is a compressed two-dimensional representation of a three-dimensional object, where the plane of compression follows the direction of the x-ray beam. The strength of the emerging beam detected is representative of the total attenuation of all tissues in this plane, including any soft tissues, cavities, cortical bone and trabecular bone. In the ischium, this composite attenuation represents the sum of the lateral and pelvic cortical shells and the trabecular bone which separates the two.

Density vs intensity

The term 'density' is one that is frequently misused in clinical and osteological literature (Seeman, 1997), and may have multiple implied contextual meanings. In its purest form, the density of bone as a tissue is used to refer to the mass of mineralised tissue per unit volume (usually g / cm^3) minus non-mineralised structural components, other tissues and voids within the structure (Seeman, 1997).

The measurement of bone density can be used to assess bone quality, for example through clinical bone densitometry, also called dual-energy x-ray absorptiometry (DXA). DXA involves the transmission of two projected beams of different strengths: hard and soft tissues attenuate the first, while hard tissues only attenuate the second. The difference between the two resulting emerging beams indicates the specific intensity of hard tissues present in a patient or specimen. The final 'density' referred to is a calibrated translation of the emerging beam intensity which indicates the quantity of mineralised tissue present (g) across the specimen. Areal and/or volumetric corrections can then be applied to estimate the quantity of bone per unit volume, called bone mineral content (BMC; g / cm^2) and bone mineral density (BMD; g / cm^3) respectively. Both are considered measures of 'apparent density' as they do not necessarily reflect absolute values: structural variables are not well accounted for even in volumetric BMD calculations (Seeman, 1998).

The colloquial use of "density" is also sometimes associated with non-DXA radiography to refer to the emerging beam intensity; typically with the inflection that greater beam attenuation (or radiopacity) is indicative of greater density. While this statement is not untrue for a homogeneous structure of constant dimensions, in practice it is a simplification of complex series of variables. Beam attenuation may be influenced by true tissue densities, but also the physical size and composition of the specimen. Beam attenuation would also be increased by increasing the depth of tissue in the path of the beam, or the relative composition of the subject. Similarly, discussions of 'trabecular bone density' should be avoided as 'density' may be a function of trabecular number, thickness, spacing or depth of tissue.

In place of the potentially misleading term 'density' therefore, the term 'intensity' will be adopted to describe the final greyscale images produced. The highest 'intensity' tissues are represented by a white colour, indicating strong beam attenuation. The darkest regions represent 'low intensity' areas that exhibit the weakest beam attenuation.

4.3 Materials and methods

4.3.1 Specimen selection

Specimens were selected from the Scheuer Collection of juvenile skeletal remains, which is housed in the Centre for Anatomy and Human Identification, at the University of Dundee.

The records for the collection were inspected to identify all individuals from whom either a single or paired ischia were present and the bones were then examined to determine suitability for inclusion.

Specimens were excluded from the analysis if there was external evidence of pathology that may have influenced the development of the bone. Further, specimens which exhibited extensive post-mortem fracturing or were considered too fragile to handle were also excluded. As the collection includes bones of both archaeological and historical anatomical origin, it was not possible to exclude all bones with imperfections and cortical damage, but due consideration was given to the effects that wear or damage may have had on subsequent analyses.

Following assessment of the collection, ninety-six (96) ischia were selected for inclusion in the radiographic study. These represented 58 individuals (49 right, 47 left) and the individuals were aged between 28 intra-uterine weeks and 16 years of age. Full details of specimens including age and side are provided in Appendix 4.3. A summary of specimens and their age distribution is provided in Table 4.01.

For the purposes of data analysis, the ischia included within the study were identified by a unique reference number that was formed from their collection designation number and side only (e.g. SC-082-R). This permitted subsequent analyses to be

conducted based on the apparent morphological and radiographic maturation of each element without being influenced by the age (either estimated or documented) held on record for each specimen.

Table 4.01. Specimens included and recorded age distribution.

Age Category	Number of Specimens	Number of Individuals	Left	Right
Fetal (28 – 38 weeks)	10	5	5	5
Perinatal (birth – 1 month)	22	13	10	12
Infancy (5 months - < 2 years)	8	6	3	5
Early Childhood (> 2 -5 years)	19	12	10	9
Late Childhood (5 - < 9 years)	17	9	9	8
Adolescence (> 9 - 16 years)	20	13	10	10
Total	**96**	**58**	**47**	**49**

4.3.2 Specimen preparation

As the ischium matures, the three-dimensional shape of the element changes. Subtle curvatures develop in the orientation of the ramus, which projects increasingly medially with age, in addition to an increasing prominence of both the ischial spine medially and acetabular margin laterally. This limited the ability to image specimens in a standardised plane and therefore necessitated the creation of a supporting mechanism. A mounting system was devised to secure the orientation of the bone relative to the scanning plane.

Anhydrous Oasis 'wet' florists' foam was selected as the medium in which the ischia would be mounted due to its low-density structure and deformable nature: the ischium could be pressed into its surface with little pressure, reducing the risk of damage. To prevent any foam particulate from entering nutrient foramina, exposed regions of trabecular bone or macro-porosity a protective layer of ParaFilm biofilm was used to separate the bone from directly contacting the foam [Figure 4.01]. Each foam block was cut to 15 mm in thickness to ensure any effect on the detected radiopacity would be consistent between specimens. A single thickness of ParaFilm was then stretched across the surface of the foam block in the location in which the bone was to be inserted.
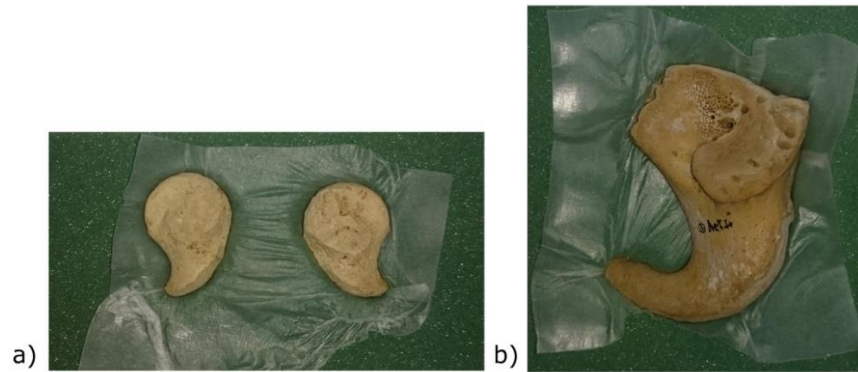
Figure 4.01. Specimens were mounted in florists' foam prior to scanning to allow a standard orientation. a) SC-084: perinatal; SC-010-L: 4 years.

The pelvic (medial) surface of the ischium was then gently pressed into the foam, ensuring that the acetabular fossa was positioned in the horizontal plane in each specimen. This enabled specimens to be positioned consistently throughout the developmental period of interest. To maximise efficiency, multiple individuals were placed into a single foam block, ensuring sufficient separation between each element to allow isolation during post-processing.

4.3.3 Imaging protocol

All radiographic imaging was completed in the Department of Clinical Radiology, Ninewells Hospital and Medical School, Dundee, using a Multix Tube and Table (Siemens). Exposure settings of 55 kV and 1.60 mA were used to generate each radiograph at a focal distance of 100 cm. Each foam block was radiographed separately and the resulting intensity data was collected digitally as an 8-bit greyscale JPEG image. No magnification was necessary during the capture of radiographs as the digital detectors provided an image of sufficiently high resolution to document the required information at 100 % scale. The digital nature of these images allowed images to be magnified using the 'zoom' function available in image viewing software programs.

4.3.4 Post-processing

Data handling

The radiograph produced for each foam block was imported into Adobe Photoshop CS5 for processing. Each bone in the radiograph was highlighted individually using the

freeform 'Lasso' selection tool, ensuring that the entirety of the element was contained within the selection area with an encircling region of background. This selection was then copied and transferred into a new Photoshop document to create a separate file for each specimen included in the study. The default background of each new document was set to black to mimic the background of the radiographic image: this designation was for aesthetic purposes only and ensured consistency between the radiograph background and canvas background following further processing.

Gradient map application

The greyscale digital radiograph for each individual bone was then processed using a four-colour 'gradient map' adjustment mask to create a colour coded image which highlighted gross variations in radiopacity.

This gradient map function allows the user to divide the greyscale spectrum into a series of coloured 'blocks', each with a defined range of grey levels. The software then examines the recorded grey level for each pixel in the original image and allocates it automatically to the appropriate colour block. The final image mask was comprised of only four colours which indicate the relative intensity of the grey levels throughout the image. This technique has previously been employed in the analysis of developmental patterns in the juvenile ilium (Cunningham, 2009; Cunningham and Black, 2009a), sacrum (Yusof, 2013), scapula (O'Malley, 2013) and ischium (Maclean *et al.*, 2014).

To allow the addition of a colour-based gradient map, the image was converted from an 8-bit greyscale image to an RGB image colour format. A 'yellow, violet, orange, blue' gradient map adjustment mask was then superimposed onto the image [Figure 4.02].

The 'gradient editor' control panel was used to redistribute the sectioning points of the gradient map mask to determine at what grey level the transition between colours would occur [Figure 4.03]. In all cases, a 'baseline' was first established by setting the 'yellow' slider to a level that produced a consistent yellow background to the image.
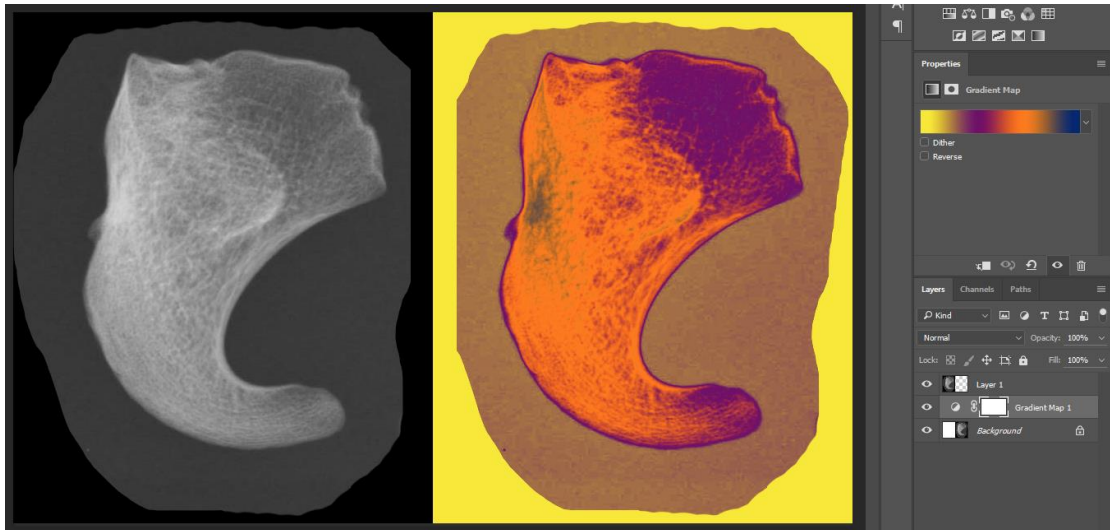
Figure 4.02. Radiograph of SC-010-R (left) and SC-010-R with applied 'yellow, violet, orange, blue' gradient map adjustment map (right). Yellow border represents pure black background, darkened periphery around specimen represents 'background' intensity of the radiograph.

This colour group represented the background levels of colour intensity, and typically fell between 15 % and 30 % of the greyscale spectrum. The remaining spectrum was then divided equally between the three remaining colours in the gradient map. For example, if the background slider was set at 24%, the remaining greyscale spectrum was divided into its respective colours at intervals of 19 %.
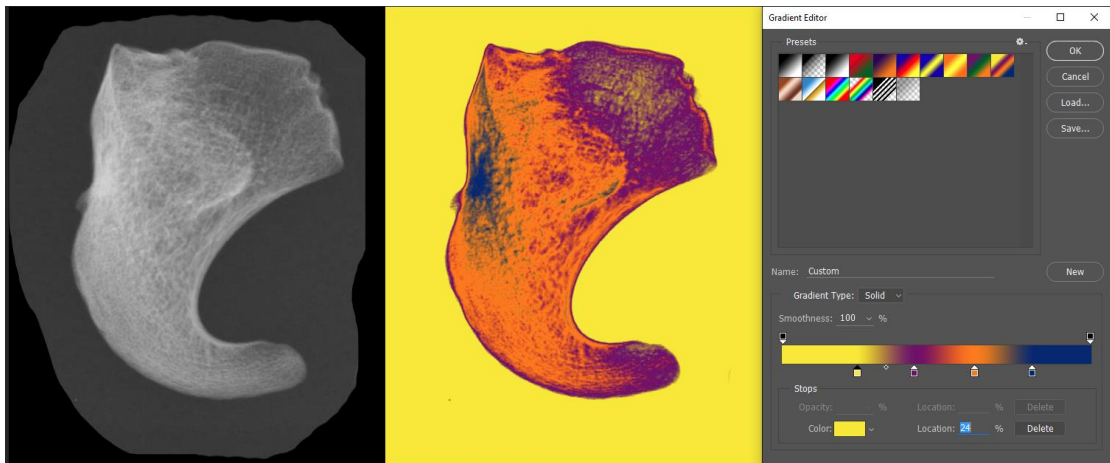
Figure 4.03. Division of greyscale spectrum into respective colour blocks using sliders.

The completed gradient mapping process divided the juvenile ischium into a colour map comprised of four colours, each representing a different relative intensity of bone. The yellow regions represented the background levels of exposure, transitioning through violet and orange, at low and intermediate intensities respectively, to blue,

which represented the most radiopaque regions [Table 4.02]. It should be noted that due to the absence of a phantom, no direct relationship can be drawn between the radiopacity and BMD/BMC; the colour maps instead indicate relative intensity.

Table 4.02. Intensity gradient levels and their corresponding colours, radiopacity ranges and grey levels.

Relative Intensity Level	Colour	Approximate Radiopacity (%)	Equivalent Grey Levels (0 – 256)
Very Low	Yellow	0 – 30	0 – 76
Low	Violet	31 – 53	77 – 136
Intermediate	Orange	54 – 77	137 – 196
High	Blue	78 - 100	197 – 256

4.3.5 Maturity analysis

All gradient mapped radiographs were printed to create a hard-copy dataset that could be examined more easily as a complete group of individuals. Each individual radiograph was examined to identify the gross morphology of the element and the intensity patterns present.

Specimens were first arranged into broad categories based on identifiable similarities in intensity patterns between radiographs, e.g. the presence of a high intensity region in the posterior aspect of the ischium. With consideration to both the radiographic and morphological changes visible, these broad categories were then arranged into a sequence which best described the apparent maturation of the ischium throughout the developmental period analysed. Specimens demonstrating low intensity levels, smaller size and / or poor definition of external landmarks were considered to be less mature, progressing to the more mature specimens which demonstrated higher intensity levels and more advanced morphological development.

4.4 Results

Arranging the gradient mapped ischia into order of perceived maturity allowed a progressive pattern of development to be identified, transitioning the ischium from a poorly-defined and immature structured specimen to a mature morphology [Figure 4.04]. The identification of specific, consistent variations in radiographic intensity

pattern allowed the developmental spectrum to be subdivided into a number of discrete phases. The age ranges and number of individuals for each phase is provided in Table 4.03.
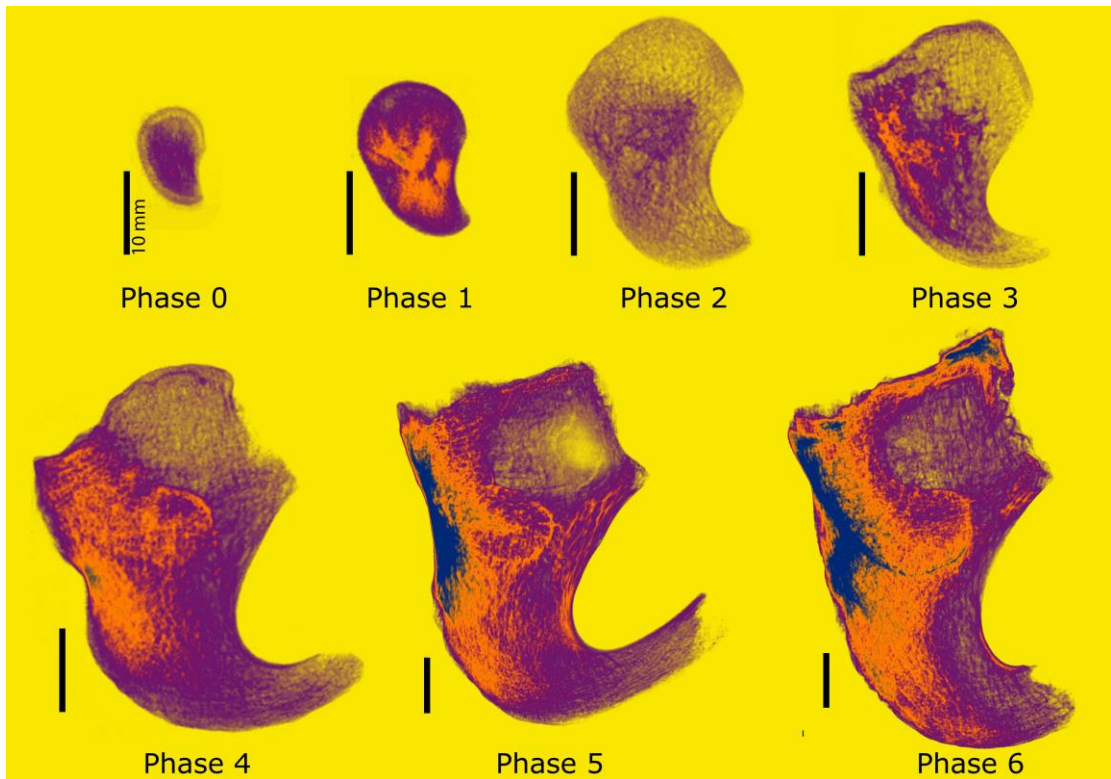
Figure 4.04. Exemplar specimens from each maturity phase demonstrating overall transition. Phase 0 – 4 are shown at 100% scale, Phase 5 and 6 shown at 60% scale.

Table 4.03. Designated phases of development based on results of maturity analysis, including associated age range and number of individuals. Note that paired elements from a single individual may not be placed in the same phase.

Phase	Age Range	Number of specimens	Number of Individuals
0	28 - 38 i.u. weeks	10	5
1	Perinate	22	13
2	5 months - 2 years	5	3
3	1 - 3 years	4	4
4	2 - 8 years	13	8
5	3 - 16 years	19	13
6	4 - 14 years	23	16
	Total	96	

4.4.1 Phase 0 (n = 10)

Phase 0 contained all pre-natal specimens included in the study [Figure 4.05]. This included individuals ranging from 28 to 38 intra-uterine weeks. This phase was characterised by a relatively uniform preponderance of violet colouration, indicating a low intensity of bone present. It was noted that the borders and central mass of each element were typically represented by a consistent low-intensity colouration with a combination of very low and low intensity areas separating these regions. The external morphology of the ischium became increasingly elongated and defined throughout this phase due to the development of the superior margin and the ischial ramus.
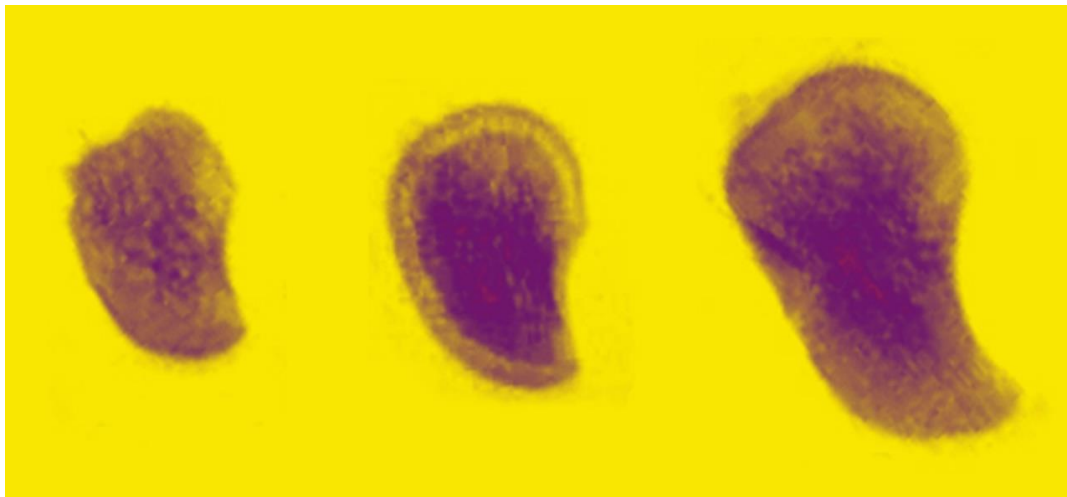
Figure 4.05. Developmental progression within Phase 0, from least mature (left) to most mature (right).

4.4.2 Phase 1 (n = 22)

All specimens identified as occupying Phase 1 were perinatal. The transition from Phase 0 to Phase 1 was marked most notably by the appearance of regions of orange intermediate intensity within the central body of the ischium and the developing acetabular margin [Figure 4.06].

In all specimens included in this phase, it was noted that the region representing the future acetabular fossa and a variable region in the superior border of the ischium was of a distinctly lower relative intensity than the acetabular margin inferiorly and posteriorly. Similarly, although the body and acetabular margin of the ischium were typically of similar intensity level, a band of decreased intensity was evident between these two regions corresponding to the more inferior aspect of the acetabulum.
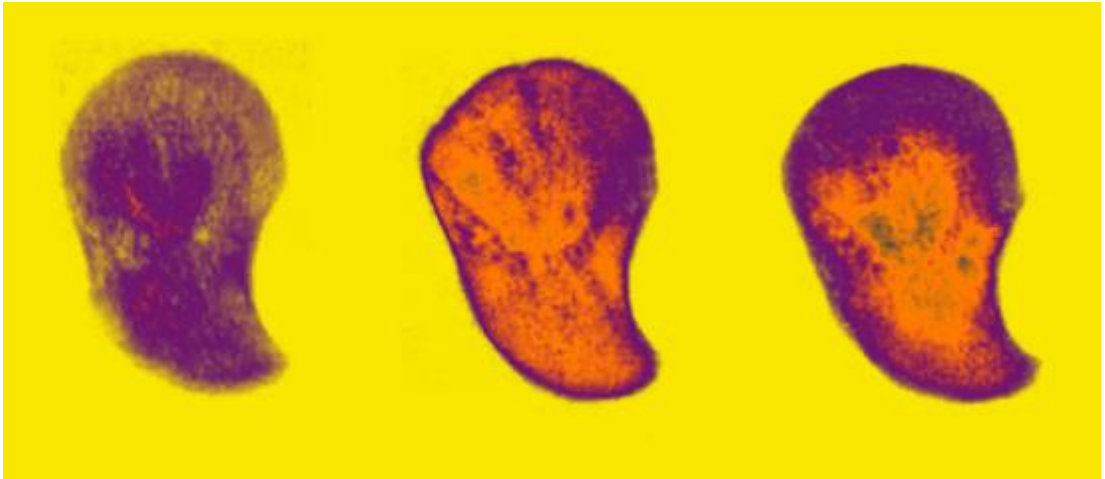
Figure 4.06. Developmental progression within Phase 1, from least mature (left) to most mature (right).

A small region of relatively lower intensity was also identifiable posteriorly on the body of the ischium in seventeen specimens, inferior to the acetabular margin. This approximated the position several small nutrient foramina on the dry bone specimens.

It was noted that there was some discrepancy between the absolute intensities of the specimens in this group. Thirteen specimens were predominantly violet in colouration with small regions of both lower intensity levels, approximating the yellow background level, and orange intermediate intensity levels. The remaining nine specimens revealed a similar pattern, however the intensity levels across the ischium were increased by one band (i.e. patterns which were of purple colouration previously were of intermediate orange colouration, while orange regions were instead represented by high-intensity blue colouration) [Figure 4.07]. As a result of the striking consistency in *pattern* rather than absolute intensity these were considered to represent a single phase.
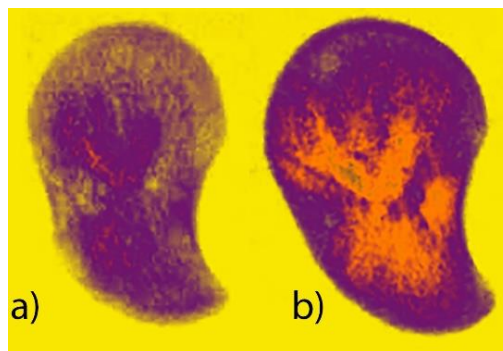
Figure 4.07. Comparison of relatively a) low- and b) high-intensity Phase 1 specimens. Note the similarity in patterning despite absolute colour differences.

4.4.3 Phase 2 (n = 5)

Five specimens were identified as occupying Phase 2, aged between 5 months and two years of age [Figure 4.08]. The specimens included within this group were noted to be approximately twice the size of the specimens in Phase 0 and 1.
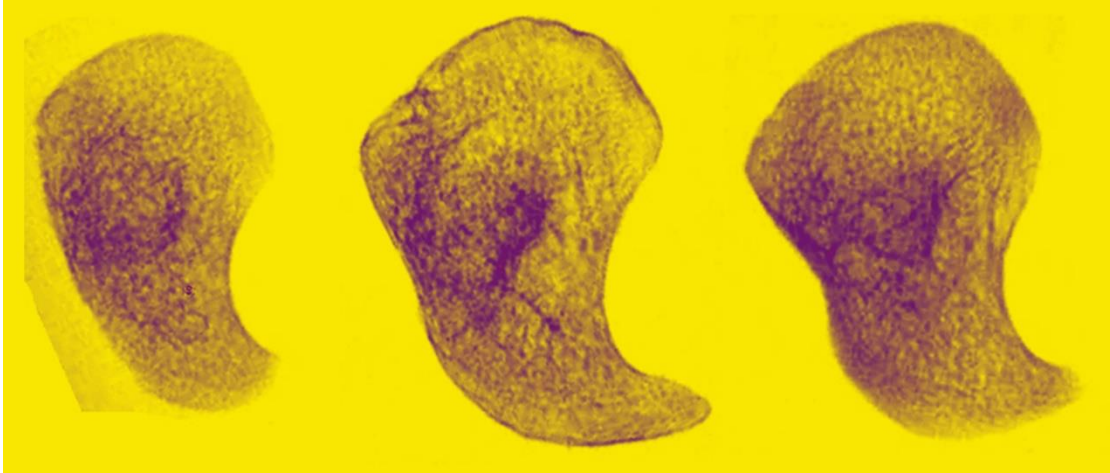
Figure 4.08. Developmental progression in Phase 2, from least (left) to most (right) mature.

The most striking feature of the Phase 2 individuals was a universal reduction in the intensity of bone present in the gradient mapped radiographs. Each specimen was characterised by a uniformity of very low intensity which approximated the background levels of intensity. In contrast to the preceding phase, no intermediate (orange) or high (blue) intensity regions were identified in any member of this group. Due to the very low intensity of bone present, it was not possible to further distinguish structural features in this group.

4.4.4 Phase 3 (n = 4)

Four specimens aged between 1 and 3 years of age were identified as occupying Phase 3 [Figure 4.09]. Consistent with Phase 2, this cohort continued to be defined by an overall relative lack of intensity in comparison with Phase 1 specimens, despite their increased size.
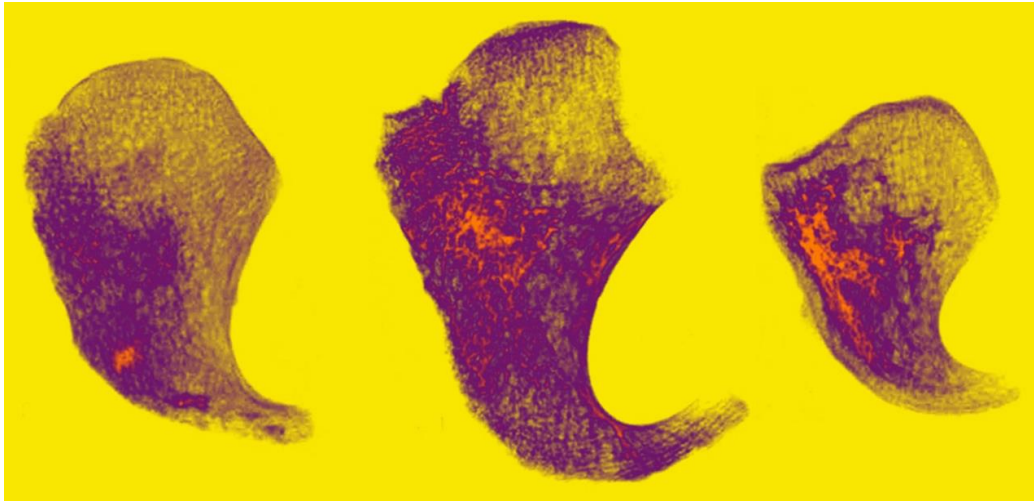
Figure 4.09. Developmental progression in Phase 3, from least (left) to most (right) mature.

In contrast to Phase 2 however, Phase 3 was characterised by the renewed presence of small regions of intermediate intensity. This was localised to the posterior aspect of the body of the ischium in particular, which was consistently defined by a combination of low and intermediate intensity regions. The acetabular fossa and anterior half of the body of the ischium were defined by a very low intensity of bone which approximated the background intensities. No regions of high intensity were observed in the specimens occupying Phase 3.

4.4.5 Phase 4 (n = 13)

Phase four comprised thirteen bones between 2 and 8 years of age. Specimens in this cohort were identified by an increase in intensity when compared with previous groups [Figure 4.10].
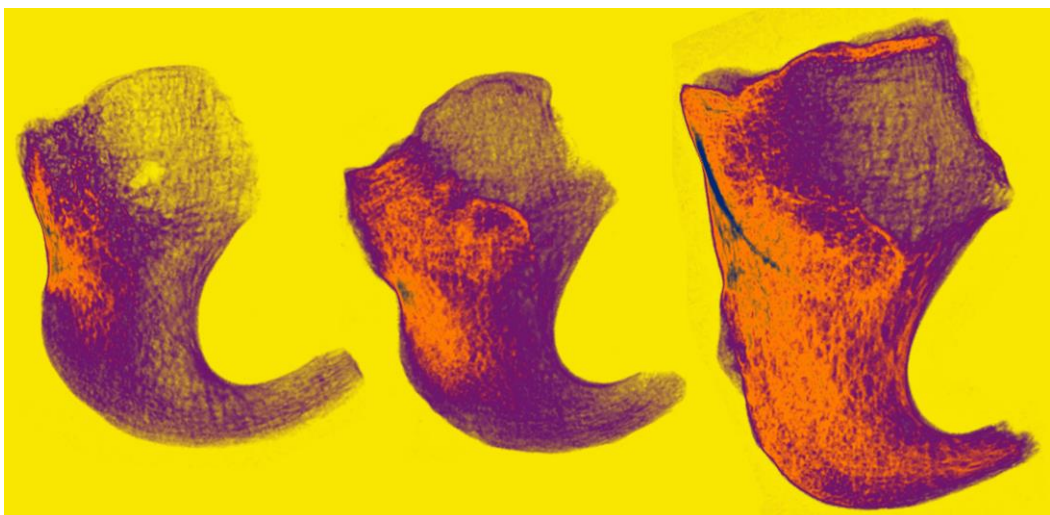
Figure 4.10. Developmental progression in Phase 4, from least (left) to most (right) mature.

In the less mature specimens in this phase, a defined region of orange colouration was identifiable in the posterior aspect of the ischium, with a smaller blue high intensity region contained within its margins. This high intensity region corresponded with the approximate location of the lesser sciatic notch. Conversely, the acetabular fossa, ramus and anterior aspect of the body continued to be represented by a lower intensity of bone.

With increasing maturity, the orange and blue regions of colouration expanded to occupy a greater proportion of the ischium. The orange intermediate intensity colouration entered the acetabular margin and progressed into the ramus in the most advanced specimens. The high intensity region however was confined to the posterior body and most posterior edge of the acetabular margin.

It was also noted that this was the final phase in which no evidence of ischiopubic ramus fusion was present on any of the specimens. In the majority of specimens (n = 8) this distal aspect of the ramus was sufficiently preserved to ascertain that fusion had not yet occurred: the surface was rounded with no evidence of billowing, and a smooth face was identifiable on the anterior aspect. Post-mortem damage to the ramus in all remaining specimens prevented definitive identification of fusion.

4.4.6 Phase 5 (n = 19)

Phase 5 contained nineteen specimens from 3 to 16 years of age, incorporating the oldest specimen in the study [Figure 4.11]. This included both ischia from the individual of greatest maximum age, estimated to be 10 – 16 years, while the second oldest individual in the group was estimated to be 13 – 14 years of age.
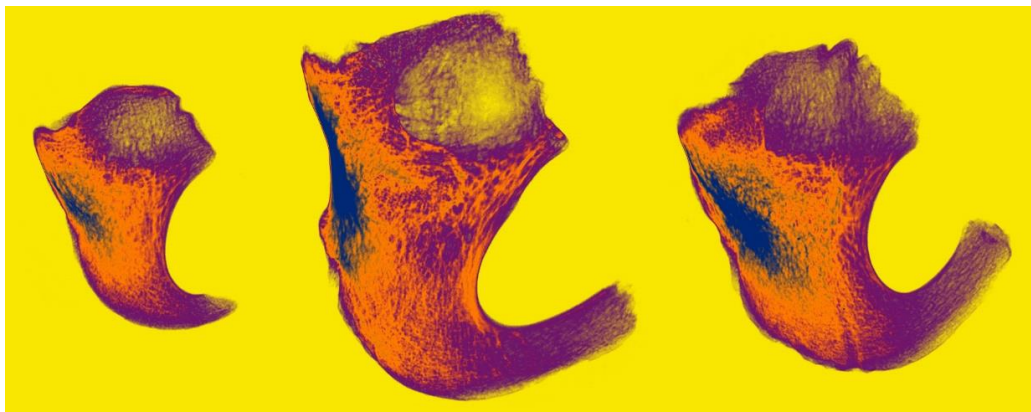
Figure 4.11. Developmental progression in Phase 5, from least (left) to most (right) mature.

This developmental cohort was predominantly defined by an increasing intensity of bone across the surface of the ischium. The orange intermediate intensity of bone progressed further anteriorly into the body of the ischium, with a concurrent increase in blue high intensity bone posteriorly that extended around the region of the lesser sciatic notch. The acetabular margin was predominantly defined by an orange colouration, with some high-intensity colouration developing in the posterior aspect of the margin. In this phase a high intensity of bone was not identified anteriorly in the acetabular margin.

4.4.7 Phase 6 (n = 23)

Twenty-three specimens were identified as occupying Phase 6, with an age range of 4 to 14 years of age [Figure 4.12].
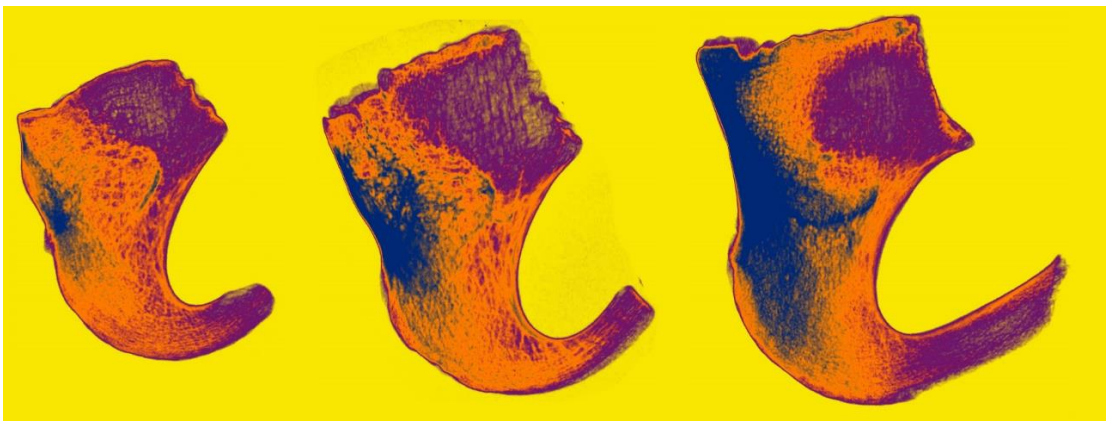
Figure 4.12. Developmental progression in Phase 6, from least (left) to most (right) mature.

This phase represented a continuous expansion of the patterns identified in Phase 5, including an overall increase in intensity across most of the surface of the bone. Most notably the high intensity associated with the posterior aspect of the ischium expanded to encompass a greater proportion of the body of the ischium and acetabular margin. The transition used to segregate these specimens from those of Phase 5 was the development of a curved region of high intensity bone along the anterior periphery of the acetabular margin which was not visible in earlier phases. As with all previous groups, the acetabular fossa region remained a site of low to very-low intensity bone in this group, although some regions of intermediate and high intensity bone were identified in the superior margin of the ischium.

4.5 Discussion

The results of the radiographic analysis of the developing ischium revealed an unexpected pattern of development during which the radiographic intensity of the ischium fluctuated between high and low intensities. The pre- and peri-natal ischium demonstrated an increase in radiographic intensity towards the time of birth, which was followed by a period of substantial, generalised loss of radiopacity in infancy. At 1 -2 years, a localised return of intensity was noted in the posterior aspect of the ischium, followed by a more widespread increase in intensity beginning after 3 years of age which marked a transition to a more defined pattern of intensity similar to that of the adult form.

4.5.1 Fetal and perinatal development

It has been suggested that *in-utero* development and early post-natal growth, and in particular the accumulation of bone mass, are important precursors to post-natal development and bone health (Holroyd *et al.*, 2012). Ay *et al.* (2011) demonstrated positive associations between birth weight and weight and BMD at six months of age, while Cooper *et al.* (1997) reported a similar correlation between recorded weight at 1 year of age and BMC in the elderly. Although the underpinning mechanisms driving this relationship are not yet fully understood, an understanding of the early development of an element may be of great importance when interpreting later development and especially in understanding ontogenetic change when a structure might fail.

The fetal ischia included within this study were found to occupy a single developmental cohort, termed Phase 0, which was defined by a preponderance of relatively low intensity bone across the surface of the ischium. These low overall intensities may in part be due to the very small size of the ischium in this period, and also the low level of mineralisation at this stage (Walker, 1991). The most intense regions were identified near the site of the primary ossification centre, below the acetabular margin (Cunningham *et al.*, 2016), and in the periphery of the bone – although it should be noted that in this group 'most intense' refers to the consistent

appearance of only low intensity bone in place of the very low intensity bone which is present elsewhere in specimens from this cohort.

Information regarding the pattern of ossification in the ischium is scarce, beyond an approximate position for the primary ossification centre (Cunningham *et al.*, 2016). The ischium is preceded by a cartilaginous anlage and it is believed that it follows the 'typical' pattern of endochondral ossification: the initial formation of an intramembranous bony shell on the perichondrium followed by the vascular invasion, cartilage disintegration and the formation of underlying trabecular bone (Cunningham *et al.*, 2016). Due to its atypical, relatively flattened shape and its close proximity to the ilium, it is likely that ossification proceeds in a manner similar to the ilium via the formation of two cortical bone 'plates' which extend across the pelvic and lateral aspects of the anlage rather than the bony collar associated with long bone development (Laurenson, 1964).

The central region of increased intensity corresponds closely with the documented position of the initial centre of ossification, and may therefore be indicative of the bone tissue which has had the longest time to form both cortical and trabecular bone mass. The decreased intensity progressing outwards from this point may in turn represent bone which has been more recently laid down and is therefore less well established. At the periphery of the advancing cortical front, intensity may also be increased by the orientation of the cortical shell. As the cortex aligns with the direction of the photon beam, the thickness of bone through which the beam must pass would be at its greatest, resulting in increased radiopacity.

The perinatal ischium was found to present a higher relative intensity than that seen in the fetal period, with intermediate intensity regions developing in the body of the ischium and the acetabular margin. Although initially present primarily near the acetabular margin, the intermediate intensity areas were observed to extend superiorly and inferiorly to occupy the majority of the bone's surface in more mature specimens. The acetabular fossa was a notable exception to this, demonstrating consistently lower intensity than the neighbouring regions of bone. The intensity distribution did not appear to adopt a specific pattern or orientation, but was rather a more generalised increase in intensity across the body of the ischium.

The generalised increase in bone intensity in the perinatal period may in part be due simply to the increased volume of the ischium relative to the fetal size. It may also however reflect an early accumulation of calcium stores prior to birth, in preparation for subsequent development. During fetal development, nutrients are supplied directly via placental exchange and are therefore dependent on maternal health and nutritional status (Mathews *et al.*, 1999; Specker, 2004). Through the third trimester, fetal blood serum calcium levels peak (Schauberger and Pitkin, 1979), providing high calcium availability during a concurrent period of rapid calcium accretion (Kovacs, 2009). The combined action of an increase in size and also proportion of mineralised tissue present, whether in trabecular bone volume or cortical thickness, would increase the radiopacity of the ischium.

The small regions of decreased radiopacity evident around the acetabular margin correspond with several small foramina on the lateral surface of the ischium [Figure 4.13]. Arterial invasion precedes bone formation, and has previously been linked to the presence of vascularised spaces within the bone (Eriksen *et al.*, 2007). It is therefore likely that the decreased intensity observed near these nutrient foramina reflects spaces necessitated by a confluence of vessels. These vessels are most likely small nutrient supply branches arising from the inferior gluteal artery, as similarly positioned vessels have been identified in the adult (Beck *et al.,* 2003). Without three-dimensional visualisation however, it is not possible to definitively attribute these small decreases in intensity to the presence of vascular structures.
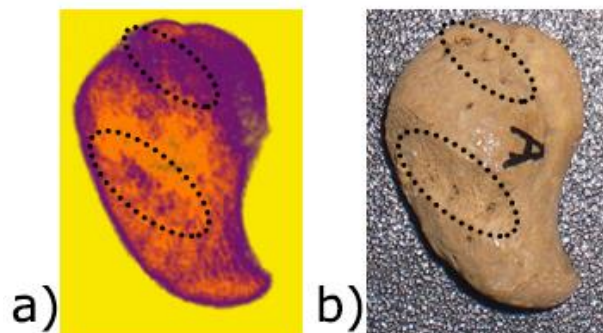
Figure 4.13. Corresponding areas of a) decreased radiographic intensity and b) nutrient foramina superior and inferior to the acetabular margin.

Despite increasing intensity, the perinatal ischium retains a relatively non-descript radiographic appearance without evidence of structural organisation. This is in

contrast to previous observations of the developing ilium, which displays a precocious and progressive pattern of development from early in the fetal period (Cunningham and Black, 2009a). Evidence of rudimentary buttressing was identifiable at 23 – 30 *intra-uterine* weeks, passing anteriorly and inferiorly in trajectories which were comparable with the weight-bearing trabecular pathways of the adult ilium. In the adult, these trajectories are typically attributed to the transfer of weight between the auricular surface of the ilium and the femoral head at the acetabulum (Aiello and Dean, 1990; Cunningham *et al.*, 2016; Kapandji, 2011) and the distribution of associated tensile stresses around the acetabulum (Macchiarelli *et al.*, 1999). The observation of corresponding, although relatively immature, regions of increased radiopacity in the fetal ilium prompted questions regarding the cause of such an early establishment. The pelvis is not typically considered a weight-bearing structure prior to birth (Walker, 1991) and, as discussed previously, traditional models suggest that adult trabecular structure is primarily formed and maintained in response to mechanical stimuli (Huiskes, 2000; Wolff, 1892). Alternative influences were proposed, including the influence of a genetic directive for trabecular architecture to be laid down in key trajectories to ensure biomechanical competency, perhaps reinforced by reaction forces generated by fetal movements (Cunningham and Black, 2009a,b). Subsequent publications also stressed the likely importance of vascular invasion and patterning in the development of iliac trabecular architecture (Cunningham and Black, 2010). The absence of similar precocious development in the fetal or perinatal ischium, despite common embryological origins and their close approximation, perhaps reflects a disparity in the biomechanical significance of the ilium and ischium.

Although no clear evidence of precocious development was noted, it is possible that the increase in intensity observed in the acetabular margin may be influenced by mechanical stimulation. Portinaro *et al.* (2001) observed that, although studies on the subject were scant, any forces associated with fetal movements would likely be transmitted to the posterior aspect of the acetabulum due to the flexed position of the fetal lower limb. It was suggested that this could explain the increased rate of growth observed in the ischial portion of the acetabulum, and assist in the formation of a competent joint by increasing anteversion of the socket. Only after extension of the hips following parturition would reactive forces be primarily directed towards the roof

of the acetabulum. However, no other literature sources were available to support this postulation. In the absence of a quantitative investigation of the microarchitecture of the acetabular margin and surrounding bone, it is not possible to assert that this may be a significant factor in the early development of the ischial structure.

4.5.2 Phase 2: a reduction in bone intensity

The specimens classified as occupying Phase 2, aged between 5 months and 1 -2 years of age, expressed a marked decrease in radiopacity in comparison with the intermediate levels of intensity observed in the most mature perinatal specimens. Each specimen included in Phase 2 presented a very low bone intensity across the entirety of the ischium, such that the observed radiopacity approximated that of the yellow background calibration level in each image. As each specimen was imaged using the same equipment and calibration settings, and was subsequently gradient mapped following the same protocol, it is highly unlikely that this stark transition in colouration can be attributed to experimental procedures. Rather, it is suggestive that a true difference exists between individuals occupying Phases 1 and 2.

A re-examination of each specimen included in Phase 2 did not reveal any outwardly apparent indicators of this reduced bone intensity, and it was confirmed that no identifiable signs of pathology were present. It was noted however that the Phase 2 specimens were considerably larger than their Phase 1 equivalents. Subsequent metric analyses confirmed that the mean length, width and depth of Phase 2 individuals were between 30 and 50 % larger than the Phase 1 specimen [see Section 5.7.3]. The physics of radiographic imaging and beam attenuation would suggest that if two objects which are of different size but proportional composition are imaged, the larger of the two will present a greater radiopacity because the beam must pass through a larger quantity of substrate before reaching the detector. The converse was observed in the ischium: the larger Phase 2 individuals presented a substantially lower radiopacity, perhaps indicating a greatly reduced quality or quantity of mineralised bone tissue.

The scapular 'reboot'

The phenomenon of a period of growth occurring simultaneously with a decrease in bone intensity (as viewed radiographically) has been documented only once previously

in the developing human (O'Malley, 2013). This period of apparent bone resorption was identified in the juvenile scapula between the ages of 4 months and 5 years of age. As in the ischium there was a general reduction of radiopacity throughout the scapula, although it was most pronounced in the infraspinous fossa and medial border of the scapula [Figure 4.14].
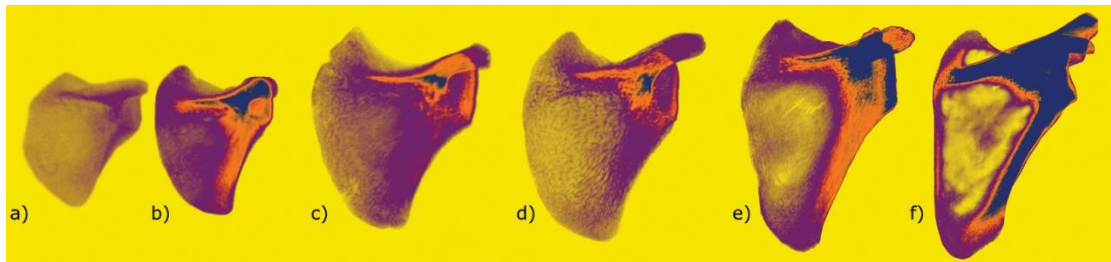
Figure 4.14. Representation of the scapular reboot as documented by O'Malley (2013). a-b) Minimum and maximum pre-reboot specimen; c - d) minimum and maximum reboot specimen; e - f) minimum and maximum post-reboot specimens. Adapted from O'Malley (2013).

Termed the 'scapular reboot', this transitional period was suggested to be a possible "conflict between modern and ancient": a developmental dispute between the phylogenetic origins of the scapula as a site of weight transfer to a quadrupedal forelimb and the prehensile nature of the modern human upper limb (O'Malley, 2013). It was suggested that the initial robusticity observed was driven by the anticipation of a weight-bearing role after birth, a role which is not fulfilled in the human child. In the post-natal period therefore, there is an ontogenetic drive to remodel and adapt the architecture of the scapula rapidly to adopt a morphology more representative of its realised biomechanical environment as part of a prehensile limb. This transitory period coincides with the descent of the thorax and pectoral girdle, the development of prehensile upper limb functions and the attainment of a bipedal gait which added support to this hypothesis.

In addition to this evolutionary conflict, the changing nutritional environment through infancy was suggested as a possible contributing factor to this newly identified developmental pattern. This was considered a secondary driver as this phenomenon had not previously been identified elsewhere in the human skeleton, indicating the cause was likely to be specific and local to the scapula. However, the discovery of a similar transitory period in the human ischium occurring in a comparable temporal

window, an element with greater phylogenetic stability, suggests that the primary driver may be systemic in origin. Phylogenetic interactions with the ontogenetic role may indeed play a supporting role in this transition in the scapula, but with regards to a systemic influence the importance of growth patterns and nutritional status may be of greater significance than was previously recognised.

Infancy: a period of nutritional change

While the prenatal period is characterised by a relative abundance of nutrient availability, dependent on maternal health, the post-natal environment is constrained by physiological availability. Placental nutrient transfer is removed at birth and is replaced by a dependency on dietary intake via intestinal uptake (Kovacs, 2006). This typically takes the form of a milk-based diet utilising human milk or a suitable alternative (e.g. infant formula) depending on availability. This is then followed by a transitional period of weaning where a diet based on solid food is introduced gradually (Golden and Abrams, 2014).

The transition to intestinal calcium uptake causes a dramatic reduction in serum calcium levels following birth (Jain *et al.*, 2010), reducing the availability of calcium for new bone creation. With regards to breast-fed infants, it should be noted that where mother and child are both healthy, the dietary calcium available is considered to be sufficient to sustain an infant (Golden and Abrams, 2014; Power *et al.*, 1999), but this may not necessarily be optimal for the accrual of bone tissue. Studies of the effects of calcium supplementation during milk feeding suggests that additional calcium will increase BMD and BMC in the short term (Prentice *et al.*, 2006; Zhu and Prince, 2012), although it is unclear whether this also presents long-term benefits to bone health as it has been suggested that the effects are not sustained into adulthood (Butte *et al.*, 2000; Jones *et al.*, 2000). The positive short-term effects of supplementation suggest that the potential peak rate of bone mineralisation is not realised during this dietary stage. This 'lost potential' may be influential in the observed loss of skeletal radiopacity in infancy in the present study.

In the modern developed world, it is recommended that this period of exclusive milk feeding persist for the first six months of life (World Health Organisation, 2002).

Following this, the infant enters into a period of weaning where the milk component of the diet is supplemented and gradually replaced by solid foods. It is recommended that this process is completed by approximately 2 years of age (World Health Organisation, 2002). Weaning practices vary culturally and are linked geographically and temporally, which therefore makes it difficult to define the likely nutritional status of the individuals included in this study, and whether weaning had started. However, it was noted in a review of documented feeding practices in non-industrial populations through the late 19th and 20th centuries that cultural behaviours were remarkably similar to current medical recommendations (Sellen, 2001), suggesting that this optimal practice has, where possible, been informally recognised and approximated.

Regardless of the onset or duration of weaning, it is important to note that the transition to a diet which is not human milk based presents opportunity for poor nutritional practices to restrict nutrient availability (Glinsmann *et al.* 1996). To compound this, there is a complex interaction between nutrients which will affect bioavailability (i.e. the ability to extract and absorb present nutrients) if inappropriate meals are provided (Bosscher *et al.*, 2002; Greer and Krebs, 2006): for example, increasing protein levels have been shown to reduce calcium bioavailability from the diet which may subsequently reduce bone mineral apposition (Bosscher *et al.*, 2002).

The availability of vitamin D is also of great importance in the accrual of bone mass as it regulates the absorption of calcium, among other nutrients, from the intestines and also influences osteoclast activity, which will influence maternal calcium availability during *in-utero* development (Cooper *et al.*, 2005). A deficiency in vitamin D will present with the symptoms of hypocalcaemia, while chronic deficiency leads to the development of rickets, a condition characterised by decreased bone mineralisation and, in severe cases, the development of atypical curvatures of the spine and long bones (Wagner and Greer, 2008). No evidence of rickets was observed in any of the individuals in the present study, suggesting that chronic vitamin D deficiencies did not occur. It has been observed that even in the developed world however, acute vitamin D deficiencies remain prevalent due to limited dietary sources and inadequate sunlight exposure, therefore fortification and supplementation are recommended to ensure adequate intake (Holick, 2007; Wagner and Greer, 2008). As with calcium supplementation, it is unlikely that the individuals included in the present study had

access to any form of vitamin D supplementation and therefore maternal or dietary deficiencies may have influenced the accrual of bone mass.

The complicated and culturally dependent nature of infant nutrition does not lend itself to clear interpretation. However, while not of obvious pathological impact, it is likely that insufficiencies, and perhaps deficiencies, of key nutrients may have influenced bone mass accrual during this period of nutritional turmoil.

The effects of rapid growth

In addition to the potential effects of decreased calcium and vitamin D availability, infancy is also characterised as a period of rapid growth. In particular, elevated growth rates are described for the first three years of life, leading to rapid increases in both body length and weight (Ay *et al.,* 2011; World Health Organisation, 1994). In the first six weeks of life, body weight has been shown to increase by up to 45%, and by six months this has become 133% of the birth weight (Ay *et al.,* 2011). There are also increases in body mass index (BMI) and lean muscle mass through the first two years of life (Ylihärsilä *et al.,* 2008), and an increased rate of skeletal development which persists through the first three years of life (Prentice *et al.*, 2006).

The relationship between the higher growth rates associated with infancy and skeletal development and mineralisation is not well documented. Parallels with this period can perhaps be drawn with the better-documented pubertal, or adolescent, growth spurt, where the peak post-natal growth rates are observed (particularly with regards to stature). There is a consensus in the literature that there is a discrepancy between growth and mineralisation during the pubertal growth spurt, with peak increase in height occurring in advance of peak rates of BMC acquisition (Bachrach, 2001; Bonjour *et al.,* 1994). The duration of this period of lagging mineralisation is debated, with cross-sectional information suggesting a duration of 14 – 19 months (Matkovic *et al.,* 1994) contrasting with longitudinal studies which reduce this period to 6 – 9 months (Bailey *et al.,* 1999). Regardless of its duration, this discrepancy between growth and bone deposition results in the formation of poorly-mineralised bone tissue, leading to a period of fragility which corresponds with an increasing incidence of fractures (Cooper *et al.,* 2004; Goulding *et al.,* 1998; Landin, 1983; Parfitt, 1994). This interaction

is site-specific, and exact growth rates and BMC acquisition rates varies across the body (Heaney *et al.,* 2000). In the pubertal period, the emphasis is on long bone growth, therefore the associated fragility (and concurrent increase in fracturing) occurs in the extremities (Cooper *et al.*, 2004).

This transient period of lowered bone quality can be viewed as a necessary compromise between quantity and quality (Bonjour and Chevalley, 2014). The rapid deposition of tissue in an effort to expand volume precludes immediate architectural optimisation. Rather, the temporary increase in calcium demand to facilitate rapid growth requires the release of calcium from bone already established, in an action described by Parfitt (1994) as akin to physiological osteoporosis.

Although such an effect in infancy is not specifically documented in the literature, there are similarities between the described effects of rapid growth during puberty and the observed resorption of bone intensity in the infantile ischium. Averaged fracture data from Cooper *et al.* (2004) indicates a slight peak in fracture incidence at around 2 years of age, which may be consistent with a reduced bone strength during growth in infancy. It was not considered to be of significance by the authors, but the relative lack of mobility, and presence of supervision, in this age group may prevent the accidental injuries which are commonly the cause of fractures during the pubertal growth spurt. In the absence of abundant calcium and the physiological capability to pair increased physical growth and optimal bone deposition, the observed decrease in intensity would be consistent with a temporary selection for increased tissue volume over tissue strength.

4.5.3 Phase 3: biomechanically-guided recovery

The termination of the resorptive phase of development becomes apparent between 1 – 3 years of age with a gradual return of bone intensity in key regions of the ischium. Defined as Phase 3, this recovery of intensity is first identifiable in the posterior aspect of the body of the ischium as vertical streaks of mid-level intensity bone. As this phase progresses, these orange regions expand within the body of the ischium but remain localised to this region.

This group corresponds with the age at which the more rapid infant growth rates are observed to decline, reducing the demand for free calcium for growth. This may in turn facilitate more widespread remodelling processes to supplement the rapidly-deposited bone already present. This localised recovery of bone intensity coincides temporally with the onset and development of locomotor milestones. By the age of 1 – 2 years it would be expected that a child would have developed the ability to sit upright without support and crawl on their hands and knees, and be in the process of developing the ability to stand and walk upright (Keen, 1993; Sutherland *et al.*, 1980; WHOMGRS, 2006). Passing through each of these milestones will create a change in the habitual biomechanical environment of the pelvis and therefore may result in subsequent modification of the bone structure to adapt to this purpose (Keen, 1993).

The act of sitting upright is perhaps the most significant milestone with regards to ischial development, as this will represent the first adoption of direct weight-bearing through the ischium. The transmission of weight in a seated positon is facilitated through the proposed sacro-ischial trabecular pathway, which begins at the auricular surface of the ilium, passes posterior to the acetabulum to terminate at the ischial tuberosity (Aiello and Dean, 1990; Cunningham *et al.*, 2016; Kapandji, 2011). This position corresponds closely with the regions observed to first increase in intensity during the recovery of the ischium [Figure 4.15]. The similarity between the proposed trajectory and observed changes in radiopacity suggests that the drive behind this initial recovery may be biomechanical in origin. That this region of increased intensity develops following the age at which unassisted upright sitting is achieved lends support to this suggestion, as this transition would begin to establish more mature biomechanical requirements.

While the sacro-ischial pathway has been referred to in anatomical and osteological texts, no direct qualitative or quantitative evidence confirming the presence of architectural reinforcement of the ischium can be found in the contemporary literature. The cause of this may be twofold. As described previously, studies examining the development and architecture of the ischium are few in number, unlike sites perceived to be of greater importance in bipedal locomotion such as the ilium and proximal femur.
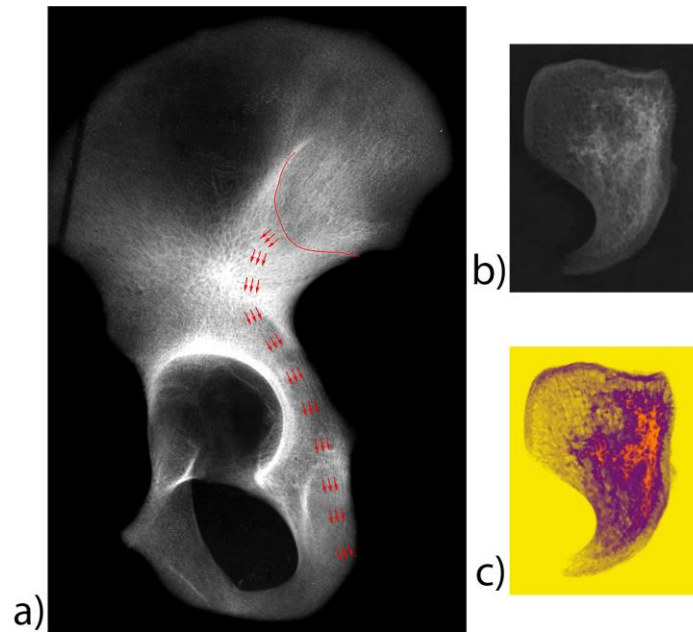
Figure 4.15. a) Proposed sacro-ischial pathway superimposed on radiograph of innominate (arrows). b) Radiograph of Phase 3 specimen showing original greyscale intensity pattern; c) gradient mapped specimen highlihighting intensity pattern.

Tangential support for the presence of a sacroischial bundle can be found in literature which discusses the radiographic appearance of the adult ilium. There are references to an ilioischial bundle which can be identified passing posteriorly and inferiorly from the anterior aspect of the iliac crest to the ischial tuberosity, and also to a posterior bundle which can be found running along the posterior aspect of the ilium and ischium (Macchiarelli *et al.*, 1999). However, these are not visualised in the works provided as the authors only presented images of the ilium and upper third of the acetabulum, so their correspondence with the described sacroischial pathway can only be inferred.

Further, the forces associated with sitting, a largely static force, would likely be less than those of the dynamic motions of bipedalism, and the soft tissues of the posterior thigh and gluteal region provide a greater contact surface which may aid in the distribution of these forces beyond the ischium. Static forces do not generate a strong remodelling response in comparison to dynamic forces (Robling *et al.*, 2001) and this combined with the diminished level of force may not be sufficient to produce pronounced skeletal reinforcement, unlike those observed in the ilium and femur. As a result, the force-transmitting pathways may not be readily identified through radiographic analyses. Quantitative investigation of the trabecular structure of the

ischium using high-resolution imaging techniques such as micro-CT are necessary to observe architectural changes associated with this bundle in the adult.

The prominence of the proposed sacro-ischial remodelling in the present study may therefore be a fortunate result of the preceding phase of resorption reducing overall bone density in the ischium. Even limited remodelling and reinforcement of the ischium during this period would be more easily discerned in this reduced intensity environment than in the intermediate-intensity ischium identified later in childhood and adolescence.

This period also coincides with the first development of the ischial spine, which begins to protrude medially at approximately 1 year of age (Cunningham *et al.*, 2016). The ischial spine is a macroscopic indicator of human locomotor behaviour, as it is believed to have evolved to meet the demands of the ligaments and musculature supporting pelvic orientation and the pelvic diaphragm (Abitbol, 1988). The transition to an upright posture would establish greater forces in the sacro-ischial ligaments to prevent rotation of the pelvis at the sacroiliac joint, and also require a pelvic floor capable of supporting the pelvic and abdominal viscera. It should be noted therefore that the appearance of the ischial spine may also contribute to the increased bone intensity posteriorly, but the observed regions of increasing intensity expand beyond the boundary of the ischial spine alone.

It is perhaps interesting to note that the recovery of bone intensity was observed first in the ischium, in advance of the scapula. The ischium demonstrated a recovery period between 1 - 3 years of age and a more typical cumulative development recognisable from 2 years at the earliest. Scapular development demonstrated a recovery in bone intensity beginning at 3 years of age at the youngest and proceeding through childhood (O'Malley, 2013). This temporal discrepancy is slight, and may be influenced by the use of additional stages to classify distinct periods of ischial development, and differences in specimen selection. Although the scapulae and ischia were drawn from the same skeletal collection, the available skeletal elements varied between individuals and therefore the sample populations were not identical. However, the implications may also be important as general skeletal development in the upper limb typically precedes that of the lower limb, from the earliest embryological derivation of the limb

buds through chondrification and ossification, to the closure of epiphyseal growth plates (Cunningham *et al.*, 2016). That a marked recovery in intensity should therefore occur first in the pelvic girdle rather than the pectoral girdle reinforces the possibility that ischial recovery may be guided by a newly-arisen biomechanical imperative in this period.

4.5.4 A return to cumulative growth patterns

The conclusion of the resorptive and recovery phases of ischial development is indicated by a generalised increase in bone intensity across the ischium, with a reduction in the proportion of very low intensity bone present. Three discrete phases of further development have been identified based on the presence and progression of specific intensity patterns. In all phases, the regions previously characterised as being of very low intensity in previous groups were found to transition to higher gradient levels, except for the acetabular fossa and small regions in the ramus. The designated Phase 4 is characterised by the progressive development of an area of intermediate intensity in the posterior aspect of the body and most posterolateral aspect of the acetabular margin, with a small region of high intensity bone localised to the posterior aspect. Phase 5 specimens were defined as those specimens which had a more expansive intermediate intensity present across the body of the ischium and the development of discrete areas of high intensity bone in both the posterior aspect of the body and the posterolateral aspect of the acetabular margin. When a high intensity colouration was evident across a greater proportion of the acetabular margin, progressing anterior to outline the posterior border of the acetabular notch, this was considered to represent Phase 6.

It should be noted that, while progressive levels of increasing intensity in each cohort have led these to be denoted as consecutive phases, there is a great degree of overlap between each of the phases in terms of age ranges and generalised appearance. This makes it difficult to state definitively whether these phases are truly a developmental progression (i.e. an element progresses sequentially through Phases 4, 5 and 6 during development) or represent three alternative patterns of intensity which are influenced by individual ontogenetic circumstance. When presented as a grid organised vertically by phase and horizontally by increasing maturity within a phase, the complicated

nature of this progression becomes clearer: horizontal, vertical and diagonal projections could each be interpreted as increasing maturity [Figure 4.16].

Only Phase 4 appears to present a distinctly separate morphological progression as increases in intensity are confined to the posterior aspect of the ischium and contained minimal blue high intensity bone. A smaller age range, 2 – 8 years of age, attributed to this phase in comparison to Phase 5 and 6 may also indicate a more cohesive grouping for this phase.

With regards to macroscopic development, the ischial spines became increasingly prominent as the juvenile period progressed, and projected more medially towards the sacrum (Abitbol, 1988). This may influence the radiopacity posteriorly as the spine volume increases as this will increase the quantity of bone which lies in the plane of the photon beam during radiography. These phases also introduced the potential occurrence of ischiopubic ramus fusion, which typically occurs in individuals between the ages of 5 to 8 years (Cunningham *et al.*, 2016). In Phase 4, no evidence of ischiopubic fusion was identifiable. In nine of the thirteen specimens, the ramus was well preserved and the pre-fusion rounded morphology was discernible. In the remaining four specimens, damage to the extremity of the ramus prevented definitive determination of fusion status, as fusion may have begun and subsequently broken post-mortem. However, an absence of completed ischiopubic fusion in this group may also further serve to reinforce its cohesive nature and explain the more constrained developmental pattern observed in this group compared with Phases 5 and 6.

The ischial body: ischial spine and lesser sciatic notch

Perhaps the most distinct changes in intensity during Phases 4, 5 and 6 are associated with the posterior aspect of the ischium. The intensities observed here increased progressively with maturity, transitioning from a low to intermediate intensity to a consistent intermediate intensity with high intensity trajectories located in the posterior margin of the body.

This trajectory is likely a development of the previously-described biomechanical influences arising from the sacroischial trabecular pathway and the muscular and ligamentous attachments acting on the ischial spine. With the continuing development

of bipedal locomotion, which would be expected to be reaching a stable, though immature, presentation after the age of 3 (Keen, 1993), the strength and activation frequency of the muscles inserting on the posterior aspect of the ischium would increase. This would reinforce any mechanical signals which were responsible for driving the increase in intensity observed in Phase 3.
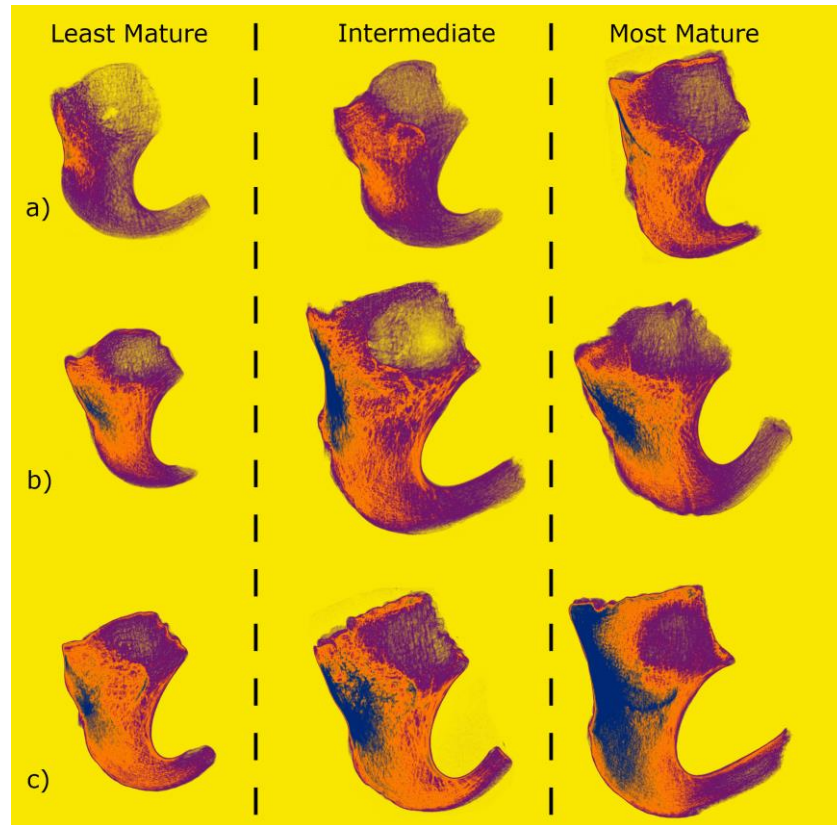
Figure 4.16. Exemplar specimens demonstrating the intensity patterns within each phase following recovery of intensity from least to most mature. a) Phase 4; b) Phase 5; c) Phase 6.

In addition to providing attachment for several muscular and ligamentous structures, the posterior aspect of the ischium is also associated with the passage of the pudendal nerve and internal pudendal artery, which exit the pelvic cavity through the greater sciatic foramen, pass over the sacrospinous ligament and ischial spine and then enter the ischioanal fossa via the lesser sciatic notch. The proximity of major nerves has been previously associated with the initial ossification of regions such as the greater sciatic notch (Laurenson, 1964), and has been suggested to be involved in the persistent increase in radiographic intensity in this area through the fetal and perinatal period (Cunningham and Black, 2009a). It is therefore possible the very close proximity of the pudendal nerve, and perhaps the slightly more distant sciatic nerve, in this region has

an extended influence in the adjoining regions of the ischium. However, due to the relatively late development of the increased intensity in the ischium, it is unlikely to be a primary factor in this pattern as the position of these nerves is established early in development (Cunningham *et al.*, 2016).

The obturator border

The anterior body of the ischium was often found to present a lower intensity, with the variable presentation of low and intermediate bone intensity throughout each of the developmental phases identified. It is possible that this contrast with the posterior aspect of the body is a function of the dimensions of the wedge-shaped ischial body, which narrows anteriorly to a blunted point at the border of the obturator foramen. Such a reduction in the depth of bone in the plane of the photon beam may be sufficient to present a diminished radiopacity due to diminished beam attenuation. The absence of any ascribed load-bearing in the anterior aspect of the ischium may also contribute to this reduction in intensity as substantial architectural optimisation may not be necessary for the competency of the element.

Only the posterior border of the obturator foramen, and in some specimens the superior aspect of the ischial ramus, consistently presented a slight increase in intensity in more mature specimens [Figure 4.16]. It is possible that, as was suggested in the earlier stages of development, that this is a consequence of the orientation of the cortex at the periphery of the bone aligning with the photon beam, thus increasing the thickness of bone tissue through which the beam must pass.

It is possible that the observed increase in intensity in the border of the obturator foramen and ischial ramus is influenced by musculoskeletal interactions. The location of the increased intensity corresponds with the ischial attachments of the obturator membrane and the obturator internus and externus muscles (Standring, 2008). The tensile stresses associated with the action of these muscles may be sufficient to prompt remodelling and reinforcement of the cortical bone at these locations. Interestingly there does not appear to be a similar increase in intensity inferiorly associated with the ischial tuberosity and inferior aspect of the ramus, which provide attachment for the hamstring muscles and adductor magnus. This may be a

phenomenon associated with the absence of the associated epiphyses at this stage of development, resulting in continued outward growth and maturation of the tuberosity. No such epiphyses are present in the obturator border, perhaps facilitating remodelling rather than extending growth.

It is possible, though perhaps unlikely, that the presence of the obturator neurovascular bundle is also responsible for the increased intensity observed in the obturator border. However, these vessels do not exist in close proximity to the ischium, but rather the soft-tissue obturator foramen, formed by an aperture in the obturator membrane, is associated with the inferior aspect of the superior pubic ramus. The passage of each of these structures similarly appears to follow the inferomedial aspect of the superior pubic ramus, avoiding direct contact or relative proximity to the ischial component of the acetabular border. Further, as with the sciatic nerve the pathway of these vessels is established early in development, in advance of the ossification of the ischium (Cunningham *et al.*, 2016), therefore it would be expected that evidence of this action would be identifiable prior to 4 years of age.

Acetabular development

Differentiation of the position of the acetabular margin and acetabular fossa became increasingly pronounced with increasing maturation. The acetabular fossae in each Phase, including Phases 1 – 3, were consistently amongst the least dense regions of bone, while the acetabular margin showed an increase in relative intensity with increasing maturity in Phases 4 – 6.

The low intensity observed in the acetabular fossa may be partially attributed to the relatively shallow cross-sectional depth of the ischium at this point, particularly relative to the steady increase in size and maturity observed in the acetabular margin. Further, the acetabular fossa is not typically associated with substantial biomechanical interactions. The acetabular fossa forms the non-articular floor of the acetabulum, separated from the femoral head by a fibroelastic pad (Standring, 2008), and is therefore not directly involved in weight-bearing associated with locomotion (Daniel *et al.*, 2005). Rather these forces are directed through the articular lunate surface, where

the direct contact with the femoral head occurs. Several authors have further indicated that the principal contact between the lunate surface and femoral head during weight-bearing occurs in the iliac portion of the acetabulum (Chuckpaiwong *et al.*, 2009; Daniel *et al.*, 2005; Greenwald and Haynes, 1972; Ipavec *et al.* 1999). The forces transmitted through the ischial and pubic components of the lunate surface are typically less intense and vary depending on the type and phase of movement occurring (Ipavec *et al.,* 1999). For example, when walking there is intermittent load-bearing contact during the swing phase (Greenwald and Haynes, 1972). The minimal level of force in the ischial component of the acetabulum may explain the relatively low intensity of bone observed in this region in comparison with the early establishment of high intensities in the developing ilium (Cunningham and Black, 2009a).

4.6 Limitations and future advancements

Despite rapidly advancing imaging technologies and the refinement of three-dimensional imaging modalities such as CT and MRI, digital radiography remains an important tool for skeletal analysis. Obtaining radiographic images is rapid, inexpensive and readily available, and the processing and interpretation of data does not require sophisticated software packages or computational skill. The present studies expand on a growing literature base utilising gradient mapping to qualitatively assess structural variations and developmental patterns within the juvenile skeleton (Cunningham, 2009; O'Malley, 2013; Yusof, 2013). This can provide valuable information regarding the mechanisms of skeletal development and highlight periods that are of interest for further study.

It is important to have an appreciation of the limitations that apply to any methodology, as this will inform the confidence of results and any potential confounding factors that must be accounted for during interpretation.

The principal limitation of any imaging study that uses radiography is the two-dimensional nature of the data and, more significantly, the superimposition of all structural information into a single plane. As a result, all bone in the plane of the x-ray beam is compressed into a single intensity value, with no other indication of the

composition of the tissue. This excludes information about the ratio of cortical and trabecular bone and the physical depth of bone in the plane of the beam, each of which may have an influence on the interpretation of data. An independent in-plane increase in the cumulative thickness of cortex, the quantity of trabecular bone or increases in physical size (while preserving the other parameters) may increase the radiopacity of a region of bone. From a radiograph alone it is not possible to determine definitively which of these factors may cause observed changes, whether in isolation or combination, or indeed whether a more complex cause drives the change, such as variations in trabecular bone microarchitecture.

As it is not possible to determine the bone tissue composition from radiographs alone, no attempt was made to differentiate between the effects of cortical and trabecular bone variations on the intensity pattern: rather changes were considered holistically to best represent the available data. Exceptions to this were made where the literature supported suggestions of specific cortical or trabecular interactions affecting the intensity pattern. However, where such suggestions were made, they were accompanied by the caveat that it is not possible to confirm these suggestions without further investigation of cortical and trabecular structure using a three-dimensional imaging modality.

The in-plane depth of bone during imaging required some consideration, as variations in specimen size may influence intensity in a similar manner to architectural changes. At each stage of analysis therefore, radiographs were examined alongside the pertinent specimens to assist in differentiating between potential structural variations and dimensional changes. Where increases in intensity corresponded closely with qualitative variations in in-plane tissue depth, this was highlighted as a potential cause for the intensity observed. For example, in Phase 6 it was noted that the region of high intensity approximating the acetabular notch mirrored the shape of the acetabular margin in this region, which became increasingly pronounced with increasing maturity. This change therefore is unlikely to reflect intricate trabecular or cortical development, but rather the presence of a more protuberant region of bone. A stringent control for these changes in depth was beyond the capacity of this project due to technological and temporal constraints.

In addition, calibration phantoms were not available at the time of scanning, which prevented any possible quantification of bone density associated with each colour level in the gradient maps. However, the inability to differentiate between cortical and trabecular bone would not have been resolved by the inclusion of calibration phantoms, and the difficulties and dangers of incorrectly quantifying or interpreting changes in bone density, bone mineral density and bone mineral content are well documented (Seeman 1997; 1998).

However, the negative influence of in-plane depth and its interpretation may be an area which can be improved future studies, particularly when analysing irregularly shaped bones such as the ischium. The derivation of a control for depth would therefore allow more confident extraction of relevant structural information.

Several possible options exist for creating this control. A rudimentary control could be achieved by taking a discrete series of linear measurements of depth across the surface of the bone to quantify broad variations in size. Digital or manual callipers would be suitable for this, but this method would be limited both by their precision and also their ease of use. The more irregular the surface, the more difficult it would be to ensure a representative measurement was achieved.

A more comprehensive control could be tested using a three-dimensional data capture method in place of dry bone measurements. Medical imaging technologies such as (micro)CT could be used for this purpose, but other systems such as 3D laser scanning could also be utilised to create a three-dimensional model of the bone. This could then be orientated correctly in the plane of the scan and the depth of the bone mapped graphically. Similar topographic thickness maps have been utilised to map thicknesses of long bones (Bondioli *et al.* 2010) and the temporal bone in preoperative planning (Wimmer *et al*. 2015).

The topographic thickness map could then be compared with the gradient mapped radiographs to establish where similar thickness and intensity patterns intersect. This would provide a more robust method of isolating the effects of physical size from those of architectural change.

A measure of the size of the areas represented by each intensity level in each specimen might allow for a more quantitative approach to the analysis of development. This was however discounted as such a rudimentary measurement would detract from the importance of the simple but effective nature of this analysis. Its strengths lie in the detection of generalised trends which can inform regarding developmental influences and identify deviations from expected patterns, such as the resorptive development found in the ischium. These patterns can present at different absolute intensity levels, as highlighted in Phase 1 specimens in particular, and reliance of an area-based quantification may result in an inaccurate interpretation of developmental patterns.

4.7 Conclusion

The radiographic analysis of the juvenile ischium revealed a series of phases each characterised by a distinctive pattern of bone intensity.

The fetal period is characterised by a generalised increase in bone intensity in advance of birth. Following this early period of acquisition, the ischium then undergoes a period of simultaneous volumetric expansion and bone resorption, resulting in an ischium characterised by very low bone intensity during infancy and in advance of habitual bipedalism.

As locomotor milestones are passed, most significantly sitting upright, intensity returned to the posterior aspect of the ischium in the proposed location of the sacro-ischial trabecular pathway, indicating a biomechanical imperative driving remodelling in this area. From 4 years of age, the ischium demonstrated a general increase in intensity which replaced the majority of the regions of very low intensity bone with a low or intermediate colouration, with the notable exception of the acetabular fossa. The regions of higher intensity associated with the posterior body, ischial spine and acetabular margin continued to increase in intensity with age, reinforcing the patterns established during the initial recovery phase.

The identification of a period of resorption in the ischium closely mirrors a similar period of resorption in the juvenile scapula and sacrum, also occurring during infancy, and is similar to reports of fragility and poor mineralisation of long bones during the

pubertal growth spurt. This suggests that infancy may be a time of systemic calcium insufficiency that requires the release of calcium from regions of bone already established to facilitate further growth. This period ends of insufficiency appears to end at the conclusion of the infantile growth spurt, and in conjunction with the growing biomechanical demands associated with locomotor behaviour promote local remodelling.

Chapter 5: Quantitative Analysis of the Juvenile Ischium

5.1 Introduction

The results of the radiographic analysis of the developing juvenile ischium revealed a period which was characterised by a temporary decrease in radiopacity, indicating a loss of bone with increasing age.

To further explore this period of reduced radiopacity, four phases were initially selected for quantitative analysis using micro-computed tomography (μCT). The use of a three-dimensional imaging technique, which was designed specifically for the analysis of bone, allowed the measurement of cortical thicknesses and the calculation of trabecular histomorphometric parameters to identify differences in bone microarchitecture. This included comparisons of regional architecture within specimens from the same developmental phase, and also a comparison of specific volumes between phases.

Prior to analysis, it was necessary to ensure that the methodology employed was capable of extracting the necessary structural information in a manner which was reliable and repeatable. During the design of the final method, three pilot studies were conducted to validate individual components of the process, the results of which are outlined herein sequentially.

5.2 Principles of micro-computed tomography

The first computed tomography (CT) was designed, built and tested in the late 1960's by engineer Godfrey Newbold Hounsfield and physicist Allan MacLoed Cormack (Cierniak, 2011). The principles of computed tomography are similar to those of radiography, utilising the differential attenuation of an x-ray photon beam by various tissues. However, where a radiograph is the result of a single planar exposure, a CT dataset is formed from the collation of a large number of exposures collected through a 360° rotation of the specimen. When reconstructed, these exposures create a single

slice which contains detailed information regarding the internal structure of the specimen. The combination of multiple parallel slices in sequence facilitates three-dimensional reconstruction.

Micro-computed tomography is a modified form of CT imaging which was first developed in 1989 with the specific purpose of creating high-resolution images of the internal structure of bone (Boyd, 2009; Feldkamp *et al.*, 1989; Genant *et al.*, 1999). Modern µCT systems typically achieve scan resolutions of < 10 µm which allows the visualisation and analysis of complex three-dimensional trabecular networks (Boyd, 2009). Micro-computed tomography addresses many of the deficiencies of histological examination, as it is non-invasive and non-destructive, and also allows for an investigation of three-dimensional structures.

A µCT system utilises the same radiographic principles as plane-plate radiography. The object or specimen to be scanned is mounted on a rotating stage located between an x-ray source and a detector, both of which are connected to a computer controller (Holdsworth and Thornton, 2002). The x-ray source is typically a micro-focus x-ray tube, while the detector is a high-resolution solid-state charged couple device (CCD) camera covered in a phosphorescent layer. This layer reacts to the impacting photon beam, converting the beam to visible light which is detected by the CCD and can be recorded digitally (Stauber and Müller, 2006). A typical µCT system is demonstrated in Figure 5.01.

During data acquisition, a beam of x-ray photons is directed through the object towards the detector to capture a single projection image. The specimen stage is rotated through a regular series of intervals and a projection is captured in each position (Boyd, 2009; Stauber and Müller, 2008). The resulting two-dimensional projections are then digitally reconstructed using complex back-projection algorithms which cross-reference fluctuations in beam attenuation as the x-ray beam is directed through different series of structures, and at different angles, to create a volumetric dataset describing the external and internal appearance of the object (Holdsworth and Thornton, 2002; Stauber and Müller, 2006). This three-dimensional dataset is then segmented into a series of two-dimensional images, or 'slices', along a single axis,

which can then be exported as a variety of conventional digital image formats (Holdsworth and Thornton, 2002).
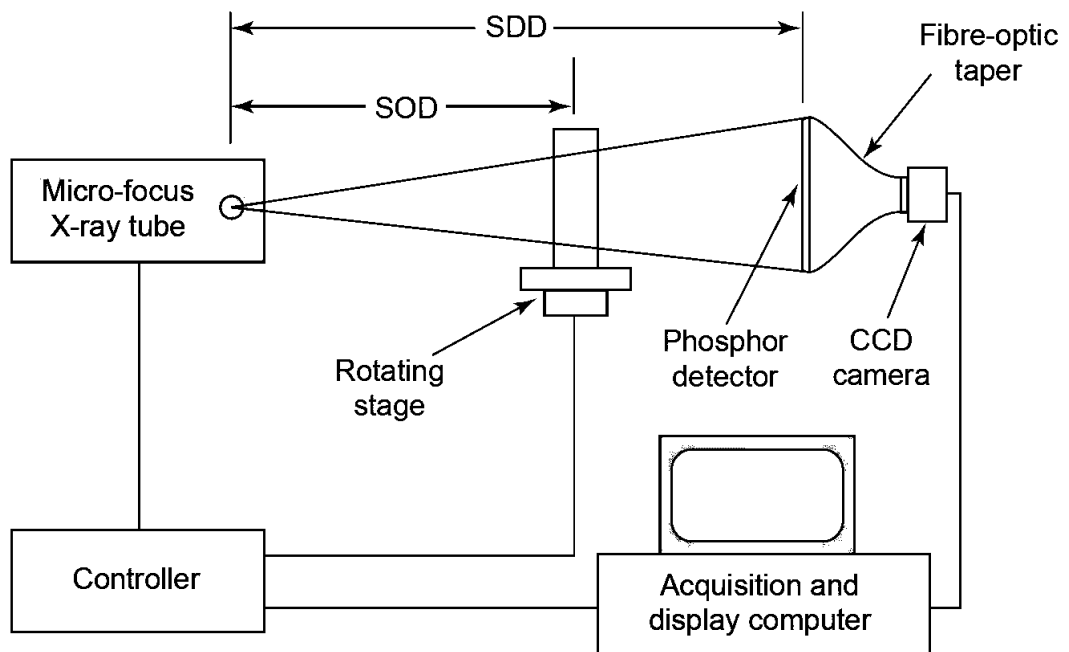
Figure 5.01. An example of a µCT system. SOD: source-object distance; SSD: source-detector distance. Adapted from Holdsworth and Thornton, 2002.

5.3 Quantifying bone micro-architecture

To quantify the micro-architecture of a skeletal element from a µCT dataset, the parameters of interest must first be defined. Due to the number of software packages available and differing research interests, there are a number of potential parameters which may be selected (MacNeil and Boyd, 2007). As the first study quantifying the cortical and trabecular architecture of the juvenile ischium, a series of seven parameters of interest were selected to investigate, based on those parameters most commonly encountered in the relevant literature. These included four parameters describing the trabecular morphology (bone volume fraction, trabecular thickness, trabecular number and trabecular separation) and two parameters describing the structure of the trabecular network (structural model index and degree of anisotropy), in addition to linear measurement of cortical thickness. The method of calculation for each of these parameters in the SkyScan CT Analyser (CTan) software package is outlined below.

5.3.1 Quantifying trabecular architecture

Bone volume fraction (BV/TV)

In mathematical terms, bone volume fraction is the most basic trabecular bone parameter that is calculated by the CTan software. However, it is also arguably one of the most important when considering bone quality, as BV/TV alone has been found to have strong correlations with trabecular bone strength (Maquer *et al.,* 2015; Nazarian *et al.*, 2008; Ulrich *et al.*, 1999), explaining between 53 % and 84 % of the stiffness and elasticity of the trabecular network.

Bone volume fraction represents the proportion of a volume of interest (VOI) which is occupied by binarised 'solid' objects, i.e. trabeculae (Skyscan, N.D.) against the total tissue volume. It is expressed as a percentage (%) and is calculated using the following formula;

$$BV/TV = (BV / TV) \times 100$$

Where BV is the bone volume, or the number of voxels that are binarised to white within a VOI, and TV represents the tissue volume, the total volume represented by all voxels within the VOI.

When quantifying BV/TV, and all subsequent structural parameters, it is important that the volume selected for analysis contains only trabecular bone tissue and does not include any cortical bone which may neighbour the selection (SkyScan, N.D.). Any cortical bone that is present within a selected VOI will be considered along with the trabecular bone volume with regards to the calculation of parameters and would therefore alter trabecular indices and invalidate results.

Trabecular thickness (Tb.Th)

Trabecular thickness is a descriptor which denotes the average thickness of each binarised solid object (i.e. trabecula) present within a VOI. This can be calculated in one of two ways: model dependent and model independent. Model dependent calculations of Tb.Th rely on two-dimensional measurements of local trabecular thickness which are subsequently inserted into one of three separate calculations

based on the perceived structure of the data – either rod-like, plate-like or spherical (Parfitt *et al.*, 1987). However, it has been demonstrated that model-dependent calculations using the rod equation consistently underestimate trabecular thickness while the plate model consistently overestimate thickness (Ding and Hvid, 2000; Hildebrand *et al.*, 1999). Trabecular bone presents as a mixture of rod-like and plate-like structures in differing proportions and therefore simple assumptions do not describe the possible variations adequately. However, with advances in three-dimensional imaging, a voxel-based model-independent calculation has been devised to eliminate the need for structural assumptions (Hildebrand and Rüegsegger, 1997a).

The model-independent calculation of Tb.Th involves the determination of local thickness for each voxel which represents a binarised solid (SkyScan, N.D.). This local thickness is defined as the diameter of the largest sphere which meets two requirements [Figure 5.02]:

1. The sphere encloses the specific voxel which is to be measured, though it need not be the central voxel of the sphere.
2. The sphere is entirely contained within the surfaces of the object.
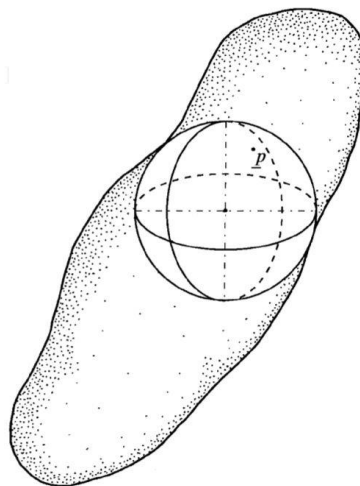
Figure 5.02. Diagrammatic representation of local trabecular thickness. The local thickness at the defined point (p) is the equivalent to the diameter of the largest sphere that fits inside the object and encloses p. This process is repeated for each 'solid' (i.e. bone) pixel in the selected region. Modified from Hildebrand and Rüegsegger, 1997a.

Following calculation, each of these local thicknesses are averaged to produce an overall trabecular thickness value for the VOI analysed. In addition to this single value, it is also possible to obtain information regarding the range of values obtained (including maximum and minimum) and standard deviations. Trabecular thickness values are presented in micrometres (µm).

Trabecular number (Tb.N)

Trabecular bone number is a calculation of the number of trabeculae present in a volume, typically presented as a number per unit of measurement. Historically, the derivation of Tb.N was model-dependant, based on either a parallel plate or cylindrical rod model. Model-specific equations were used to calculate Tb.N from the previously calculated BV/TV and Tb.Th.

CTan instead uses a model-independent calculation based on the direct 3D measurement of trabecular thickness, using the following equation (SkyScan, N.D.):

$$Tb.N = (BV / TV) / Tb.Th$$

It should be noted that the 'BV / TV' here refers not to bone volume fraction as a percentage, but the ratio which is first derived by the division of bone volume and tissue volume.

Trabecular number is calculated as the number of trabeculae per micrometre (μm^{-1}). However, this produces values that are typically represented by values less than 0.01 which do not lend themselves to clear presentation. Therefore, Tb.N values are presented as number of trabeculae per millimetre (mm^{-1}).

Trabecular separation (Tb.Sp)

Trabecular separation provides a measure of the average distance between binarised solid objects (trabeculae) in a volume. With respect to its calculation, Tb.Sp is the inverse of Tb.Th and is the "thickness of the spaces defined by binarisation" (SkyScan, N.D.). The method of calculation is conducted in three dimensions using a model-independent method that mirrors that of Tb.Th. The local separation is calculated for

each voxel as described for Tb.Th, where the sphere created is entirely bounded by binarised non-bone (i.e. space) [Figure 5.03]. Trabecular separation values are presented in micrometres (μm).
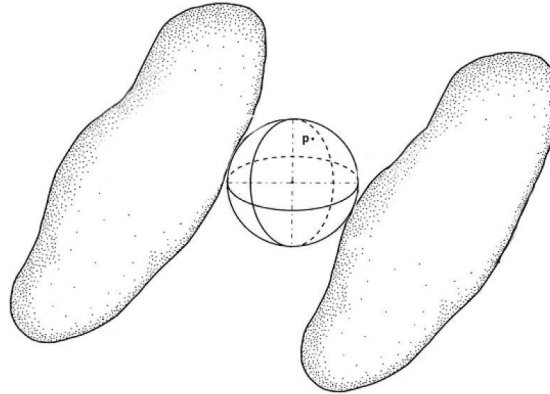
Figure 5.03. Diagrammatic representation of local separation. The local separation at the defined point (p) is equivalent to the diameter of the largest sphere that fits between objects and encloses p. This process is repeated for each non-bone pixel in the selected region. Modified from Hildebrand and Rüegsegger, 1997a.

Structural model index (SMI)

The structural model index is a non-metric parameter that indicates the relative presence of cylindrical rods and parallel plates in a trabecular bone volume through the assessment of surface convexity [Figure 5.04] (SkyScan, N.D.). It was first proposed by Hildebrand and Rüegsegger (1997b) as a method of quantifying the historically ambiguous classifications of 'rod-like' and 'plate-like' trabecular bone formations.
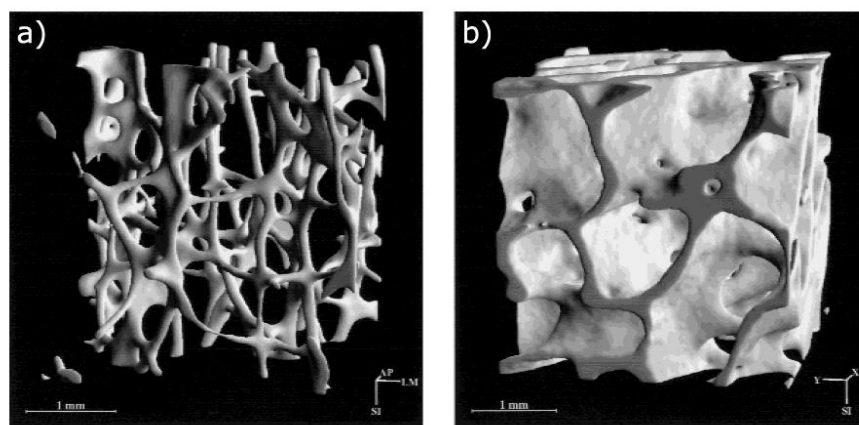
Figure 5.04. Examples of trabecular bone structures demonstrating a) rod-like morphology (SMI = 2.5) and b) plate-like morphology (SMI = 0.16). Adapted from Hildebrand et al., 1999.

To calculate SMI, the total surface area (S) of all objects in a volume (V) is determined based on 'exposed' voxel surfaces. The original surfaces are then artificially dilated by a single voxel to create an expanded surface in three dimensions and a new dilated surface area is calculated (S') [Figure 5.05]. These values can then be used to calculate the SMI in the following formula:

$$SMI = 6 \times [(S'xV) / S2)]$$

The typical SMI values for an ideal plate, cylinder (rod) and sphere are 0, 3 and 4 respectively, although with regards to trabecular architecture the classification of 'spherical' is a theoretical construction. Trabecular bone volumes are likely to be comprised of a mixture of plates and rods, in practice SMI values would be expected to fall between 0 and 3. Due to the method of calculation, values less than 0 and greater than 3 are possible but unlikely. Negative values indicate the presence of small enclosed cavities, as the dilation of these surfaces will lead to a reduction in their surface area (and perhaps their complete removal). Therefore, regions of bone with a BV/TV greater than 50% may return negative SMI values (SkyScan, N.D.). In addition, this can be affected by digital noise which introduces small holes, perforations or pitting.
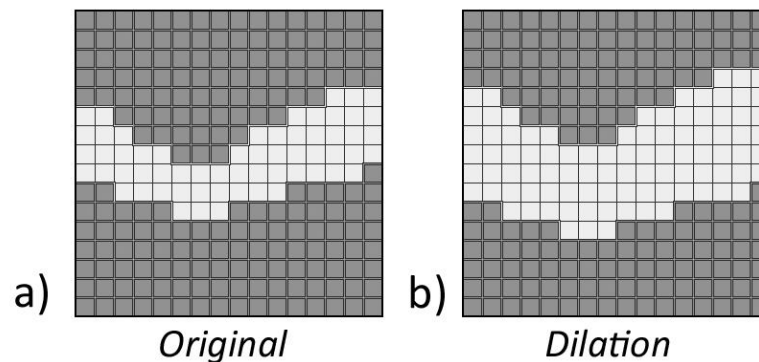
Figure 5.05. Two-dimensional representation of surface dilation. Dark squares represent non-bone pixels; light squares represent bone pixels. a) original surface; b) dilated surface.

Degree of anisotropy (DA)

Where SMI describes the prevailing structure of individual trabeculae, the degree of anisotropy describes the three-dimensional structure and organisation of a trabecular volume as a whole. An idealised isotropic structure is one in which there is no

directional preference: all structures are arranged in a symmetrical pattern that extends equally in all directions (Feldkamp *et al.*, 1989). As structures begin to align in a particular direction, or are predominantly gathered in a single region of a given volume, the level of anisotropy will increase, indicating this directional orientation. With regards to trabecular bone, anisotropy is typically related to organisation of trabeculae into discrete pathways, most often linked to biomechanical influences within that region of bone (Keaveny *et al.*, 2001).

The derivation of DA is perhaps the most complex parameter to be addressed with regards to those investigated during this project. The first stage requires the creation of a sphere of best fit within the volume of interest (if it is not already spherical). A grid of 'test lines' is then projected through this sphere through a wide range of three dimensional angles [Figure 5.06], with the centre of the grid aligning with the centre of the sphere. The number of intersections that each line makes with the binarised solid phase objects (i.e. bone) is counted and for each angle projection a mean intercept length (MIL) is calculated.
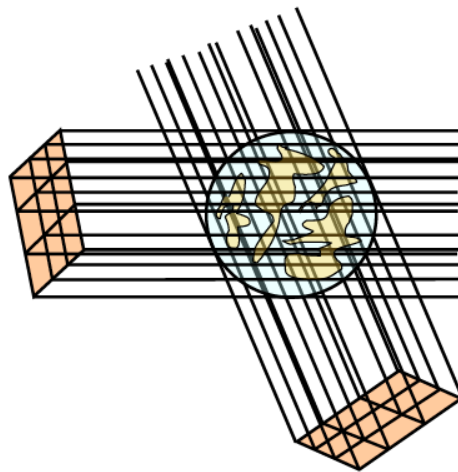
[Figure 5.06]. Demonstration of MIL grid projection through a spherical volume of interest. MIL is calculated as a single value representing all lines in a single grid. Adapted from SkyScan, N.D.

Following this, a polar plot of MIL is created. This is achieved by plotting each MIL as a line projecting at the angle of collection from a central point, creating a 'pin-cushion' plot [Figure 5.07]. An ellipsoid is then fitted around this three-dimensional plot that describes the shape and orientation of the data. Three vectors are then defined which describe the 3D axes of the ellipsoid: the longest orientation of the ellipsoid and the length and width of the ellipsoid at right angles to the longest axis. The degree of

asymmetry reflects the level of anisotropy, where an isotropic volume would be represented by a sphere. Three eigenvalues are then defined for the ellipsoid that represent an index of the relative MIL in each of the three axes. To derive DA, the maximum eigenvalue is divided by the minimum eigenvalue. This presents a scale from 1 (fully isotropic) to infinity (fully anisotropic), which does not lend itself to presentation or interpretation. Therefore an index is created using the following equation:

$$DA = (\ 1 - [min\ eigenvalue\ /\ max\ eigenvalue]\ )$$
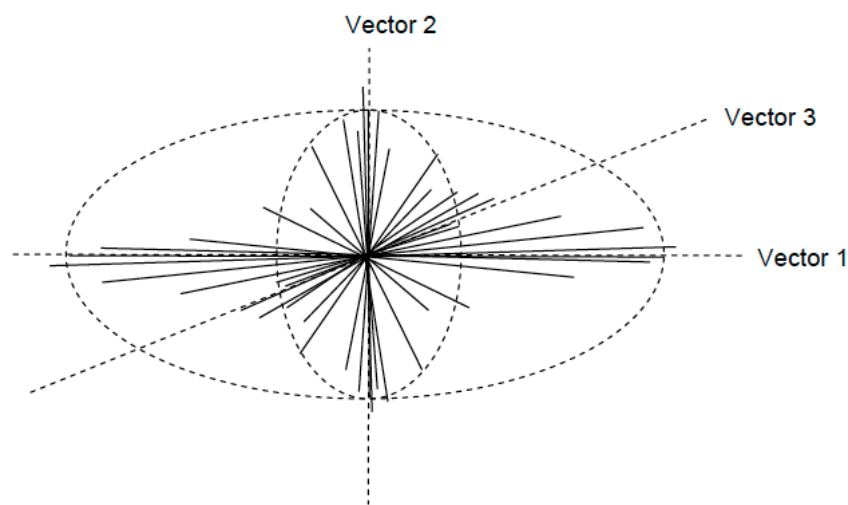
Figure 5.07. Simplified representation of the polar plot of the Mean Intercept Lengths. The statistically-derived ellipsoid fitted to this arrangement is also demonstrated. Adapted from SkyScan (N.D.)

This will create a scale from 0 (perfect isotropy) to 1 (perfect anisotropy). It is this latter indexed scale which is typically utilised in trabecular bone analysis. It should also be noted that while in mathematical terms, an isotropic structure would be considered 'organised' and an anisotropic volume would be considered 'disorganised', the opposite holds as it refers to trabecular bone.

Rather, an anisotropic DA value would suggest the presence of a stimulus (e.g. a specific loading pattern) which has caused an adaptation to the trabecular network: i.e. an organised response. Conversely, a trabecular network which is diffuse and lacking in directionality would be expected in a region which does not require a specific structure to achieve its role, or is subjected to a wide array of stimuli which preclude a specific change in directionality: i.e. a disorganised response.

5.3.2 Quantifying cortical thickness

While μCT analyses typically focus on the quantification of trabecular bone volumes alone, an understanding of cortical bone structure is also important when discussing bone development (Cunningham and Black, 2009c, 2010; Gosman *et al.*, 2013; Tanck *et al.*, 2006) and function (Holzer *et al.*, 2009; Schnitzler *et al.*, 2009; Seeman, 2002) of skeletal elements. Documenting the cortical thickness (C.Th) within a VOI can be achieved through linear measurements between the endosteal and periosteal surfaces on μCT images, producing a value in μm [Figure 5.08]. This process can be used to document overall C.Th circumferentially, or to compare different cortical surfaces within a single element (e.g. the pelvic and lateral surfaces of the ischium) for comparison, and multiple measurements can be taken to provide a representative mean for a given volume.
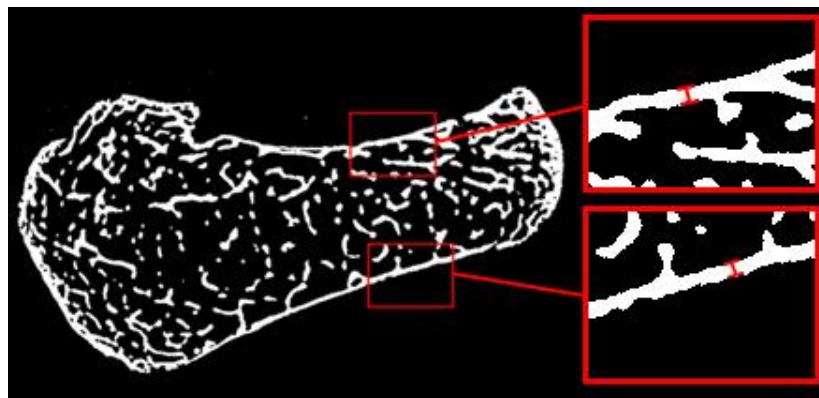
Figure 5.08. Position and orientation of cortical thickness measurements from the lateral (upper inset) and pelvic (lower inset) surfaces.

Caution must be exercised when taking cortical thickness measurements on two-dimensional slice data, as the plane orientation of the slices can have a marked influence on recorded measurements. An out-of-plane 2D measurement may represent a more oblique line passing through the bone in three-dimensional space, thus increasing the recorded thickness value for that site (Treece *et al.*, 2010). Standardisation is essential to ensure comparable measurements between sites, individuals and groups of individuals. Further, it is important to ensure that the sites selected for measurement do not contain the anchorage for trabecular struts on the endosteal surface as the inclusion of these regions will also inflate cortical thickness values artificially (Cunningham and Black, 2009c).

5.3.4 Factors which may influence data analysis

Image resolution

Of particular benefit to trabecular and cortical bone analysis are the high resolutions that can be achieved using µCT (Stauber and Müller, 2008). The resolution utilised for any investigation must be considered carefully, as the resolutions achieved during a scan may impact on the resulting analyses.

'Resolution' as it applies to µCT can be broken down into two discrete classifications of resolution with different implications for research. The spatial resolution (or scanning voxel size) describes the ability of a system to detect the edges of physical objects, or more precisely the distance that must exist between two objects in order for them to be recorded as separate entities (Boyd, 2009; Kim *et al.* 2004). This is dependent on the sensitivity of detectors and the number of photons produced by an x-ray source, with a two-fold increase in resolution requiring approximately 16 times the number of photons to preserve the original signal-noise ratio (Boyd, 2009).

The reconstructed voxel resolution documents the dimensions of each voxel within the three-dimensional dataset created at the conclusion of a µCT scan. These voxels are comprised of three dimensions, x, y and z, which can be used to describe each unit of the final image in space: when exported in a two-dimensional dataset, the final value (z) becomes synonymous with 'slice thickness'. This voxel resolution can be calibrated to a range of values during the back-projection reconstruction as suits the needs of the user, where the maximum resolution possible is equal to the spatial resolution of the equipment used. However, it is advised that the highest practical output should be limited to 1.5 times the spatial resolution to reduce noise and artefacts within the exported dataset (Boyd, 2009). For example, a µCT system achieving a spatial resolution of 10 μm^3 would have a recommended reconstructed voxel resolution of 15 μm^3. Where possible, data should also be exported in an isometric format (i.e. x = y = z) as increasing slice thickness independent of the pixel dimensions has been shown to cause an overestimation in BV/TV and Tb.Th when compared to isometric data of the same pixel dimensions (Kothari *et al.* 1998).

Where 'resolution' is discussed further, it is the voxel resolution which is being referred to unless it is stated otherwise.

Partial volume averaging

Concerns regarding attained resolutions extend beyond ensuring that data is isometric in nature, as the specific resolution achieved is also of great importance when analysing μCT datasets. Perhaps the most limiting artefact to be found in μCT is the phenomenon of partial volume averaging (PVA).

Partial volume averaging occurs when the space represented by a single voxel (the smallest available unit of detection and / or display) is not wholly occupied by a single tissue / material of constant density, but rather by a number of densities (e.g. a mixture of bone and air) (Abel *et al.*, 2013). As this space can only be represented by a single value, this final output will be a mean which represents the proportions of bone and space within the defined voxel – an intermediate between 'bone' and 'non-bone' [Figure 5.09] (Abel *et al.*, 2013; Barrett and Keat, 2004; Kothari *et al.*, 1998). This is a fundamental limitation of all forms of digital imaging that can cause a loss of information around the periphery of objects (Goodenough *et al.*, 1981).
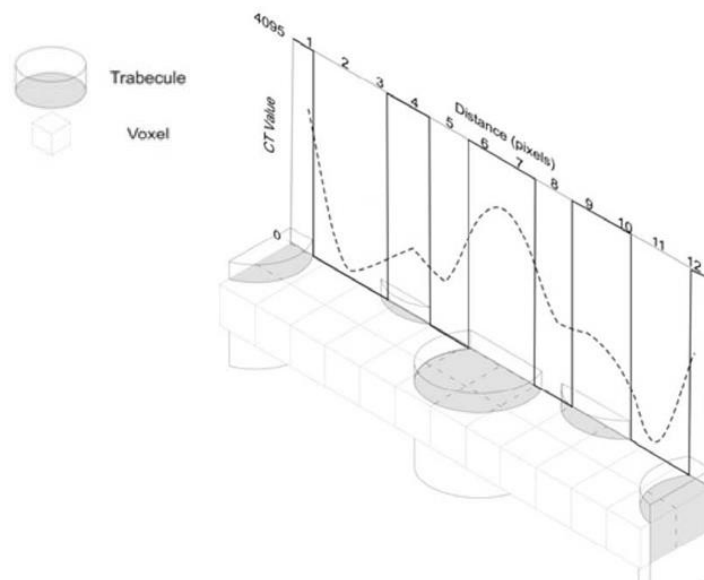
Figure 5.09. Diagrammatic representation of partial volume averaging. When tissues of different densities (i.e. bone and air) occupy a single voxel, the grey level assigned to the voxel represents an average of both tissue values (solid line) rather than the true intensity profile (dashed line) Adapted from Abel et al., 2013.

If the resolutions achieved are not sufficient to resolve individual trabeculae, PVA can result in the complete loss of these structures (Bruker, N.D.a), therefore the prospective resolution should be higher than the smallest expected object. As typical values for human trabecular thickness are cited as approximately 100 – 200 μm, depending on the region analysed (Bouxsein *et al.*, 2010; Frost, 1999; Kothari *et al.*, 1998), using resolutions of less than 100 μm^3 is inadvisable, particularly with the capabilities of modern μCT systems, as this will greatly increase the effect that PVA will have on a dataset. Although PVA remains unavoidable at the periphery of trabeculae, the higher the resolution achieved, the smaller the PVA will become, as the edges of objects are increasingly well defined by the available pixels.

Influence of image resolution on trabecular bone stereology

The precise influence of resolution on the quantitative analysis of bone micro-architecture has been investigated extensively with regards to μCT (Cooper *et al.*, 2007; Kim *et al.*, 2004; Kothari *et al.*, 1998; Liu *et al.*, 2011; Müller *et al.*, 1996; Sode *et al.*, 2008). Early studies were limited in the resolution that was possible, but described a scenario consistent with the effects of PVA. A resolution dependency was demonstrated for both BV/TV and Tb.Th, which were increasingly over-estimated as resolution was lowered (Majumdar *et al.* 1996; Müller *et al.*, 1996), although trabecular number and spacing were maintained with greater accuracy up to resolutions of 175 μm (Müller *et al.*, 1996). The preservation of Tb.N is likely due to its derivative nature – this value is a function of both BV/TV and Tb.Th, so if these increase proportionally the resulting calculation of Tb.N would not alter significantly. The consistency observed in Tb.Sp conversely is likely due to the relative size difference between Tb.Th and Tb.Sp. The larger regions of non-bone pixels would be less likely to be influenced by PVA than the smaller groupings of trabeculae pixels.

More recent studies of bone stereology have taken advantage of the higher resolutions now attainable to conduct similar tests of resolution dependency (< 100 μm). Liu *et al.* (2011) examined the relationship between resolution and typical morphometric parameters using 25 μm^3 scan data that was 'coarsened' to provide further resolutions of 40 μm^3, 60 μm^3 and 80 μm^3 for analysis. This coarsening process involves artificially combining and averaging voxels to create larger voxel sizes and

therefore lower resolutions. The authors noted that with decreasing resolution, significant differences were introduced to measures of trabecular thickness, separation and the number of rod-like trabeculae present, while the number of plate-like trabeculae and BV/TV were conserved. However, it was also demonstrated that although the absolute values varied, resolutions of 40 µm3 and 60 μm^3 showed significant correlations with structural parameters imaged at 25 μm^3. At 80 μm^3, the strength and significance of correlations decreased however. This suggests that although absolute values obtained may vary with changing resolution, the relationship between parameters is maintained at 60 μm^3 and below.

Sode *et al.* (2008) conducted a similar study to examine the effects of resolution on non-metric parameters used to describe trabecular architecture, including SMI and DA. Scanning resolutions of 16 μm^3 and 20 μm^3 were achieved during the initial scan and data was subsequently coarsened to create a range of lower resolution datasets. It was found that with a decrease in resolution, the structure of the trabecular architecture adopted a more rod-like conformation, i.e. an increase in SMI value. This is likely a result of the influence of pixilation whereby rod-like shapes will be exaggerated by the pixilation effect of coarsening, while plates (with sharp angles) will be less susceptible, and therefore may not be replicated were the scanning resolution altered rather than the reconstructed voxel resolution. Degree of anisotropy did not differ significantly between each of the resolutions examined, indicating that this non-metric parameter was conserved. However, although the coarsening of data may affect the curvature of structures, it may not necessarily alter the number of structures and therefore may not alter the MIL during DA calculation. It should be noted that caution has been advised when interpreting the results of datasets that utilise 'coarsening' to lower resolution artificially. The spatial resolution of the initial scan has been shown to have a greater impact on subsequent analyses than coarsening the reconstructed voxel resolution of a single scan (Cooper *et al.,* 2007; Kim *et al.,* 2004). Prospective scanning at each designated resolution would therefore allow for a more representative analysis of resolution-dependent changes.

Using prospective scanning however, Kim *et al.* (2004) compared a number of resolutions, including 21 μm^3, 50 μm^3 and 110 μm^3. It was observed that, consistent with previous studies, BV/TV, Tb.Th and Tb.Sp values all increased as the resolution

was lowered while Tb.N was found to decrease. The authors suggested that this was most likely due to a loss of definition of features, where smaller spaces between trabeculae were not recorded and two trabeculae therefore 'merged' to form one larger structure, and where smaller regions of bone were lost altogether [Figure 5.10]. It was also noted that, in contrast with 'coarsened' studies, fewer correlations between parameters at each resolution were observed indicating a greater importance of scanning resolution than reconstructed voxel resolution. It was also noted that care should be taken when comparing data that has been obtained at different scanning resolutions, particularly in clinical and diagnostic settings, as results may not be directly comparable.
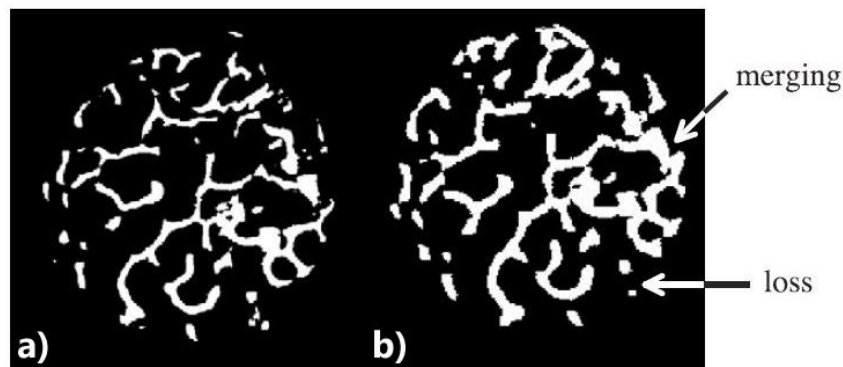
Figure 5.10. A comparison of matched µCT data at resolutions of a) 21 µm³ and b) 50 µm³, highlighting regions of merging and loss of bone data. Adapted from Kim et al., 2004.

Despite a number of investigations, due to conflicting methodologies and interests, a consensus has not been reached on the 'ideal' resolutions that should be used for µCT analyses, nor the precise effects of resolution on stereological analyses. However, it is apparent that the higher the resolution, the more limited the potential impact of PVA and the more clearly resolved objects will become within the resulting dataset. Caution should be exercised when comparing the results of studies completed at different resolutions and direct numerical comparisons should be avoided where possible as resolution has been demonstrated to affect absolute values. Care should also be taken when artificially coarsening datasets through resampling; rather the spatial resolution of the scan should be adjusted in place of the reconstructed voxel resolution.

Importance of image segmentation

Prior to quantitative analysis, a µCT dataset must be transformed from a series of greyscale images representing a spectrum of intensities to a binary format which can be interpreted by the software selected. This process, called segmentation or binarisation, relies on the application of a threshold to define the greyscale intensity level above which voxels will be considered to be a solid object (i.e. bone), and below which level voxels can be considered to be 'space' (i.e. non-bone).

Two threshold values are required for binarisation– a lower contrast limit and an upper contrast limit. The lower contrast limit establishes the base level of the scan, and should not be increased from zero (0) as this may affect the resulting images (Bruker, N.D.a). The upper contrast limit then defines the point of segmentation: any voxels above this level will become white while any voxels below this level will become black [Figure 5.11]. When threshold values are reported, it is this upper contrast limit that is typically stated in the literature. This upper limit can be determined visually using the histogram slider and should be set following the first peak (non-bone) at the bone-air interface.
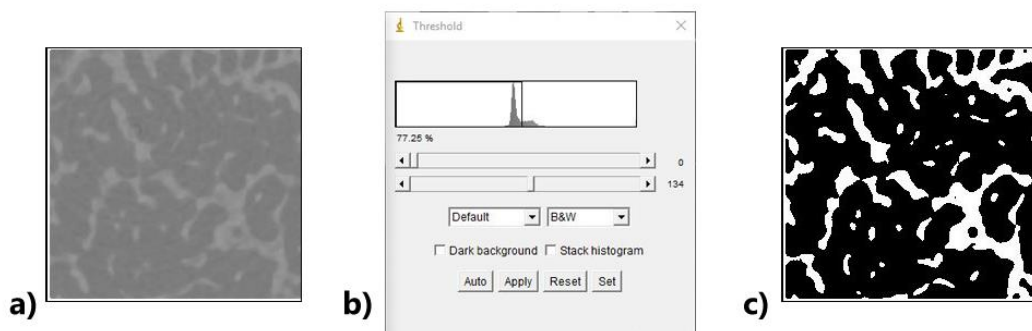
Figure 5.11. Example of trabecular bone segmentation. a) Greyscale µCT image; b) Threshold selection options in ImageJ; c) Final binarised image showing bone (white) and non-bone (black) regions.

It has been noted that the selection of an appropriate threshold value may influence the results of histomorphometric analysis. Using a threshold value that is too high will result in the exclusion of bone tissue at the periphery of the object, and indeed some smaller trabeculae, while setting the threshold value too low will result in the inclusion of non-bone as perceived 'bone' (Hangartner, 2007). It has been demonstrated that relatively minor changes in threshold value may alter BV/TV significantly, which may in

turn influence connectivity and descriptive parameters relating to this data (Ding *et al.*, 1999), therefore care must be taken in selecting an appropriate threshold value. Hara *et al.* (2002) demonstrated that even very small changes of 5 'grey levels' in a threshold value will alter the results of histomorphometric analyses, although statistical testing was not applied to determine whether these variations were significant.

Some debate has been presented regarding the application of either global or local thresholds to datasets. A global threshold is the use of a single value to binarise a complete dataset prior to analysis, while a local threshold is the *ad-hoc* application of a specific threshold to a single region or volume of interest. A simple global threshold is simple to apply, control and document but leaves some risk of accentuating artefacts such as beam hardening, noise and PVA (Waarsing *et al.*, 2004). A local threshold technique offers advantages of potentially accounting for small variations in local architecture, intensity and noise more precisely, although the more complicated application increases the opportunity for error (Burghardt *et al.*, 2007; Chang *et al.*, 2013). Ultimately, the selection of local or global segmentation appears to depend on the structure of the data presented and compromises necessary to ensure optimal data collection.

5.4 Aims and objectives

The quantitative analysis of the developing juvenile ischium using μCT was undertaken with the aim of documenting the structure of the juvenile ischium in the early post-natal period. An emphasis was placed on describing the trabecular and cortical bone structure of the perinatal ischium and identifying any changes in architecture associated with the resorptive period of development identified during radiographic analysis [Chapter 4].

This aim was achieved through the following objectives:

- Establish a repeatable and reliable method suitable for data collection from µCT datasets representing the juvenile human ischium.
- Establish data handling and noise reduction protocols which can be followed to ensure accurate data collection.
- Complete intra-observer testing to validate data collection
- Analyse the juvenile ischium quantitatively using three-dimensional histomorphometry and linear measurements throughout the period of interest.

5.5 Specimen selection

Four phases identified during the radiographic analysis were initially selected for further study: Phase 1 (perinatal), Phase 2 (resorption), Phase 3 (recovery) and Phase 4 (resumption). These phases were selected as their analysis allowed the quantification of architectural changes during the post-natal developmental pattern which has not been documented quantitatively previously.

Details of the number of specimens in each phase that were selected for inclusion in the quantitative study are presented in Table 5.01. Two specimens, the left and right ischia from SC-020, were excluded from the Phase 1 population at this time due to their fragility, as they were perceived to be at risk of damage during transit for µCT image acquisition. Due to time constraints, it was not possible to include all specimens from Phase 4, therefore 11 right ischia were selected to represent the sample population. For full details of specimens included, please see Appendix 5.1.

Table 5.01. Summary information for specimens which underwent µCT scanning.

Phase	Age Range	Number of Specimens	Number of Individuals	L	R
1. Perinatal	Perinate	20	12	9	11
2. Resorptive	5 months – 2 years	5	3	2	3
3. Recovery	1 year – 3 years	4	4	2	2
4. Resumption	2 years – 8 years	11	11	0	11

5.6 Volume of interest selection

The characterisation of bone architecture requires the designation of a number of volumes of interest (VOI) which can be designated within analysis software to allow data collection. Prior to the collection and analysis of μCT datasets, it was necessary to create the mechanism by which specific volumes of interest could be captured repeatedly and reliably between specimens and age ranges. This would allow statistical comparison of pooled data from across a developmental cohort to characterise the structure of the ischium at each stage of development.

Several approaches to VOI selection exist within the literature. For studies interested in specific sites and the changes that may be occurring within these, a single or limited number of VOI may be utilised. These are typically aligned proportionally or according to specific morphological landmarks.

This format is typically restricted to studies that involve the use of elements too large to be scanned in current-generation μCT systems (at the time of study) and therefore require the extraction of bone cores for analysis (Lai *et al.*, 2005; Nicholson *et al.*, 2001; Stauber and Müller, 2006), or for studies that are investigating a very specific region within the bone (Gosman and Ketcham, 2008; Judex *et al.*, 2004; Maga *et al.* 2006; Ryan and Krovitz, 2006). Whilst this focussed methodology allows specific research questions to be assessed regarding architectural changes, it limits the potential for unexpected discoveries in the surrounding bone.

For more comprehensive investigations of bone architecture, and where it is possible to scan the entire bone in a single scan, a grid-based analysis system has been demonstrated to be very successful in quantifying and comparing micro-architecture across an entire element (Cunningham, 2009; Cunningham and Black 2009b,c; 2010; O'Malley, 2013; Yusof, 2013).

The specific grid in this study was first devised using the morphology of the perinatal ischium as a guide to VOI positioning. Five external morphological landmarks were identified on the bone that would also be identifiable in the μCT datasets [Figure 5.12a], which were utilised sequentially to create a rectangular perimeter for the ischium [Figure 5.12b].

The most superior (A) and inferior (B) points of the developing obturator margin were first identified, and a straight line transecting both of these points was drawn: this created the anterior border of the rectangle. The inferior border was then created by projecting a line perpendicular to line AB that contacted the most inferior aspect of the ischium, located on the base of the ischiopubic ramus (C). This procedure was repeated superiorly to create the upper border, which contacted a metaphyseal plateau superiorly (D). The posterior border of the rectangle was then created parallel to the line AB that contacted the most posterior aspect of the body of the ischium (E).
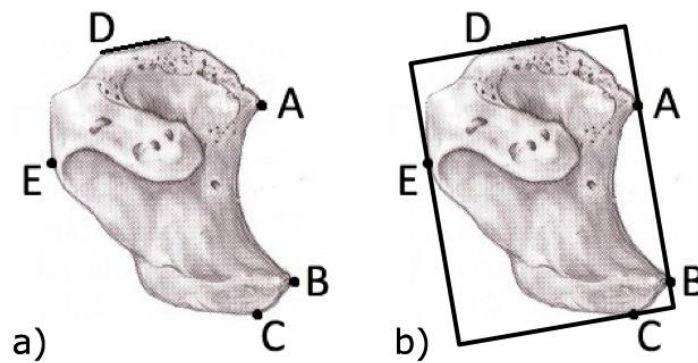
Figure 5.12. a) Points of reference used for the creation of the analysis grid; b) Super-imposed outer rectangle. A: most superior projection of obturator margin; B: most inferior projection of the obturator margin; C: most inferior point of the ischium; D: superior metaphsyeal plateau; E: most posterior projection of ischium.

Once the rectangle was established in the correct orientation and position, the remaining grid lines were inserted to divide this single space into a number of smaller discrete volumes. This was achieved by inserting a series of three equidistant grid lines parallel to the long axis of the rectangle and a further four equidistant grid lines perpendicular to the long axis. This subdivided the volume into twenty rectangular two-dimensional regions of interest (ROI) of equal size that together defined the entirety of the rectangle. These regions could then be extrapolated through the depth of the ischium to create volumes of interest suitable for analysis. Four of these twenty VOI were subsequently discounted from the analysis phase (i – iv). VOI i and ii were discounted as they contained insufficient bone to provide a suitable analysis. ROI iii and iv were also discounted on receipt and appraisal of the μCT data as this border of the obturator foramen did not occupy a significant proportion of the three-dimensional space and was predominantly composed of a thickened, curved region of

cortical bone absent sufficient trabecular bone for analysis. The remaining sixteen volumes of interest were then numbered 1 – 16 to allow identification [Figure 5.13].

Following the completion of the grid for use in the perinatal age cohort, it was then necessary to investigate whether the same grid system could be utilised in subsequent phases of interest and facilitate the statistical comparison of data obtained.
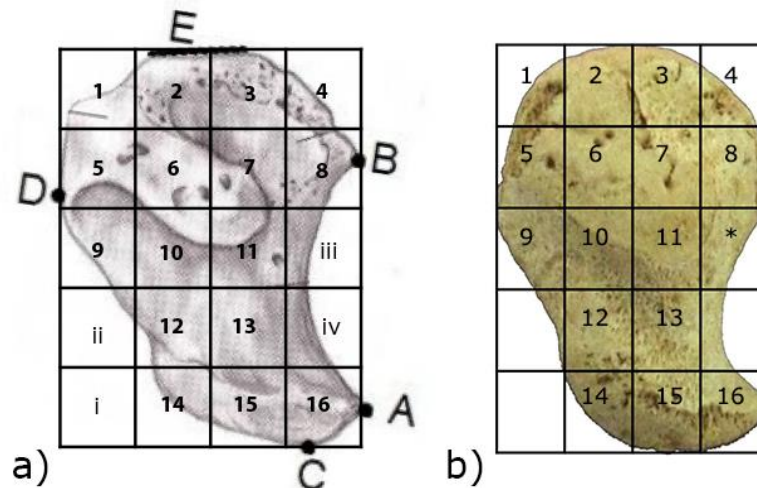
*Figure 5.13. a) Completed analysis grid denoting each VOI, including those discounted, as derived using images from Cunningham et al., 2016. b) Analysis grid as applied to specimen SC-085-R. * Discounted VOI iii appears to contain more bone than the representative 3D VOI as realised in the µCT datasets due to the orientation of the photograph.*

5.7 Allometric analysis of the juvenile ischium

5.7.1 Background

"Allometry can be defined as the study of the relationship between size and shape." (Small, 1996).

Allometry is a very broad subject area which is used to describe growth relationships, ecological interactions or the consideration of morphological traits, and is a term which was first introduced to refer to the phenomenon of proportionate and disproportionate biological scaling (Shingleton, 2010; Small, 1996).

Allometric growth is not uncommon in biological systems, perhaps best illustrated in the size of the human head relative to overall body size during development. Due to the precocious nature of neurological development *in-utero*, the head grows more

rapidly than the rest of the body before birth. At birth this is represented by a large head relative to overall body length. As development progresses the head develops more slowly while limb and trunk development advances, altering the overall proportions of the body [Figure 5.14].
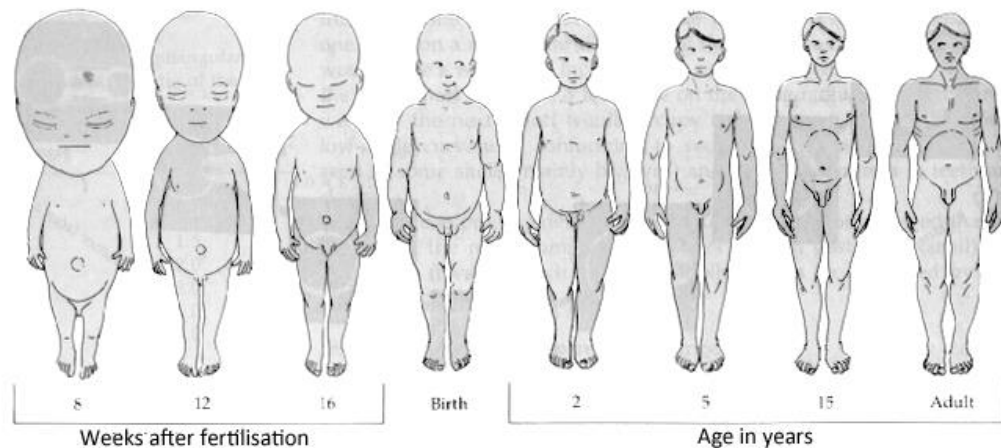
Figure 5.14. Diagrammatic representation of body proportions during development, highlighting change proportions with age (Moore, 1983).

There are three classifications defined for proportional relationships between morphological traits (Shingleton, 2010). Growth is said to be isometric when two features develop in perfect proportion to each other throughout development. This does not require the magnitude of this growth to be equal for both measures, but rather that they retain their relative sizes. Hyperallometric growth occurs when one feature develops more rapidly than the other, resulting in an increase in relative size of this feature when compared with the second. Hypoallometric growth is the inverse of this, where one feature develops more slowly than the other, resulting in a disproportionately smaller first feature

When considering allometric studies, there are several potential tests which can be investigated. The study of proportional growth is at its core a study of ratios and covariance, asking questions of how two measurements compare at any given stage of development, and how this relationship changes over time. To this end, comparing simple ratios may be sufficient to determine whether two parameters may be isometric if discrete groupings or categories are available for one parameter – such as 'age in years'. To further this with statistical analysis, correlations have been applied to

anthropometric measurements to determine whether two or more metric measurements are related (Rissech and Black, 2007).

There also exist specific equations which refer to allometric analyses, designed originally in relation to evolutionary biology by Huxley and Tessier (Gayon, 2000). The relationship between two parameters has been described as a power law which takes the form:

$$y = bxk$$

Where y and x represent the two measurements being compared (x is typically an 'independent' variable (e.g. body length), while y is the dependent variable (e.g. head length)), k represents the differential growth ratio between each measure and b represents the origin index (value of x where y = 0) (Gayon, 2000). The relationship can be also expressed more simply as a logarithmic equation (Gayon, 2000; Shingleton, 2010):

$$Log\ y = k\ log\ x + log\ b.$$

The use of the logarithmic form allows for the visualisation of this data, where the differential growth ratio (k), also described as the 'allometric coefficient' (α) equals the gradient of a line of best fit in the data plots, and log b is the intercept on the logy axis.

Allometry in the juvenile ischium

It was intended that this project utilise a grid-based method of analysis fixed to, and scaled by, the extremities of the ischium. However, statistical comparison of the data obtained between specimens and groups would be appropriate only if it can be demonstrated that the grid can capture the same regions of bone within each volume of interest, both within a single age cohort and also between age cohorts. If the horizontal and vertical growth of the ischium is not proportionate, the volumes of interest would be distorted when the grid was aligned to each new specimen and would therefore not be comparable.

While metric standards exist for the estimation of age in the juvenile ischium (Fazekas and Kósa, 1978), limited literature exists which explores growth rates and allometric relationships between these measurements. Rissech *et al.* (2003) investigated the

growth rates of three metric measurements of the ischium, ischium length, vertical acetabular diameter and horizontal acetabular diameter, across an age range of 0-97 years on documented individuals from four skeletal collections. The results demonstrated that the growth rate for each of these measurements was linear until the cessation of growth, with the exception of the horizontal acetabular diameter for females, which showed a slight decrease in the rate of growth in the earlier years. However, the authors explored only a single combination of parameters: the horizontal and vertical diameters of the acetabulum, a measurement which does not influence the grid proposed for the present investigation. In addition, the large age range appraised somewhat obscures the data obtained directly from younger years, as only 39 of the 327 ischia analysed (0-9 years) correspond with the age ranges of interest to this project (perinatal – 8 years).

This allometric investigation therefore aims to further explore the relationship of basic metric measurements obtained from the ischium, with specific focus on the developmental cohorts previously identified for quantitative analysis via micro-computed tomography. This will inform the appropriateness of applying and comparing a uniform grid between cohorts of increasing age. A secondary consideration is the comparison of methods of appraising allometry, including ratios, correlations and logarithmic allometry equations to determine the most useful method of comparing metric measurements.

5.7.2 Materials and methods

Forty isolated ischia were selected for analysis, which were the same specimens selected for µCT analysis following the qualitative radiographic studies. These specimens represent the perinatal, resorptive, recovering and resumption groups identified previously, with the precise specimen numbers per group defined in Table 5.01.

Measurements

Three measurements were identified for inclusion in this study, illustrated in Figure 5.15:

- Maximum length of the ischium (ML): Maximum distance between the superior metaphyseal surface of the acetabulum (A) and the inferior border of the ischium on the ischiopubic ramus (B).

- Maximum breadth of the ischium (MB): Maximum distance between the posterior margin of the ischium (C) and the anterior border of the ischium (D), crossing the acetabular surface (Schaefer *et al.*, 2008).

- Maximum depth of the ischium (MD): Maximum distance measured between the lunate surface (E) and the inner pelvic surface of the ischium (F) perpendicular to the measurements of length and breadth.

All measurements were taken using Duratool digital callipers, with readings taken in millimetres, accurate to 0.01mm. All measurements were repeated three times per specimen and a mean value obtained to represent the final measurement.
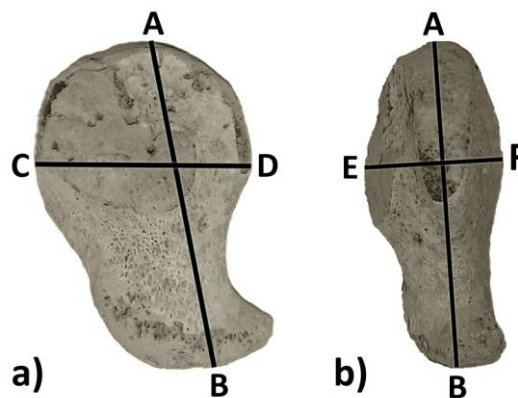
Figure 5.15. Measurements used for data collection. a) Maximum length (ML) is represented by line AB; maximum breadth (MB) is represented by line CD; b) Maximum length represented by line AB; maximum depth (MD) is represented by line EF.

Analysis

Data was collated in Microsoft Excel and was analysed statistically using the analysis package R. Three methods of analysis were employed. MS Excel was used to calculate simple mean ratios for each combination of parameters: ML : MB, ML : MD, MB : MD.

Pearson's product-moment correlations (PPMC), calculated and visualised in R, were used to identify trends within the data between each of the three parameters. This analysis measured the strength of a linear association between two variables, producing an r value and a p value for each comparison. An r value of 1 denotes a

perfect linear relationship, where an increase in one variable is met by an equivalent increase in the second, while an r value of -1 indicates a perfect inverse relationship, where an increase in one parameter leads to an equivalent decrease in the other. An r value of 0 indicates no linear relationship is present between the two variables, although it does not exclude the possibility that a non-linear relationship exists. The associated p value indicates the significance of the r value – i.e. whether this relationship is likely to have arisen by chance.

The logarithmic equation described previously was also used to calculate the allometric coefficient for each possible pair of measurements using a modified log script in R, whereby a logarithmic plot was created from the data for each specimen, a line of best fit was determined and the equation of that line extracted. On a graph of logx against logy, the gradient of the line is equivalent to the allometry coefficient. When $\alpha = 1$, the two measures are considered to increase in perfect proportions: i.e. they are isometric. When $\alpha < 1$, the measure plotted on the y axis is increasing at a disproportionately slower rate than that of the x axis, or that growth of that measure is hypoallometric. Conversely, when $\alpha > 1$, the measure plotted on the y axis is increasing at a disproportionately higher rate to that of the x axis: in other words, the relationship is considered to be hyperallometric.

5.7.3 Results

Mean results and descriptive statistics for each group are presented in Table 5.02. Full data regarding linear measurements is presented in Appendix 5.2.

The metric results showed that, with each increasingly mature phase there was a concurrent increase in each of the mean measurements. Standard deviations in phases 3 and 4 showed an increase in comparison to phases 1 and 2, likely a result of the increasingly broad age ranges ascribed to these groupings of specimens.

Variable ratios

In the first instance, simple ratios were created to show the potential relationship between pairs of measurements. This was achieved by dividing all values by the smallest measurement obtained. This created ratios which can be described as x : 1.

Three specific ratios were calculated, including ML : MB, ML : MD and MB : MD. Table 5.03 records the mean ratios for each group.

Table 5.02. Descriptive statistics for measurements of maximum length, maximum breadth and maximum depth at acetabulum for each phase.

Phase	N	Maximum Length (mm)				
		Mean	S.D.	Min	Max	Range
1. Perinate	20	18.03	1.09	16.24	20.23	3.99
2. Resorption	5	27.78	1.60	25.74	29.47	3.73
3. Recovery	4	36.05	5.66	28.31	43.61	15.30
4. Resumption	11	45.87	4.16	38.27	54.14	15.87
Phase	**N**	**Maximum Breadth (mm)**				
		Mean	S.D.	Min	Max	Range
1. Perinate	20	12.14	0.69	10.93	13.55	2.62
2. Resorption	5	18.97	1.64	16.82	20.35	3.53
3. Recovery	4	24.51	2.71	21.28	28.63	7.35
4. Resumption	11	33.53	2.67	28.70	37.84	9.14
Phase	**N**	**Maximum Depth at Acetabulum (mm)**				
		Mean	S.D.	Min	Max	Range
1. Perinate	20	7.32	0.42	6.56	8.12	1.56
2. Resorption	5	10.86	0.25	10.43	11.21	0.78
3. Recovery	4	13.21	2.10	10.95	16.43	5.48
4. Resumption	11	18.14	1.67	15.06	20.38	5.32

The ratios obtained for ML : MB for each phase were found to be the lowest of the three ratios calculated in all cases, with observed values between 1.368 : 1 and 1.486 : 1. The ratio of ML : MD conversely was consistently the largest ratio observed for all phases, with ratios ranging from a minimum of 2.464 : 1 to 2.729 : 1. The ratio of MB : MD exhibited intermediary values of between 1.658 : 1 and 1.855 : 1.

Table 5.03. Ratios obtained for pairs of metric measurements.

Phase	ML : MB	ML : MD	MB : MD
1. Perinate	1.486	2.464	1.658
2. Resorption	1.465	2.558	1.747
3. Recovery	1.471	2.729	1.855
4. Resumption	1.368	2.528	1.848

Correlation of measurements

Pearson's Product-Moment correlations were calculated for each possible pair of measurements. The results of these correlations are presented in Table 5.04. These have been represented graphically below in Figure 5.16.

Table 5.04. Pearson's correlation coefficients for possible correlation coefficients, with confidence intervals and the p-value indicating the significance of the correlation (P < 0.05 = significant).

Correlation	R Value	95 % Confidence Interval		P Value
		R min	R max	
ML MB	0.993542	0.9877339	0.9966046	2.20E-16
ML MH	0.9913437	0.9835749	0.9954464	2.20E-16
MB MH	0.9927049	0.9861493	0.9961637	2.20E-16

Each of the three measurement combinations was found to be strongly positively correlated, with a minimum r value of 0.9913437 between maximum length and depth, and a maximum r of 0.993542, between maximum length and breadth. All correlations were found to be very highly significant (P < 0.001); therefore, these correlations are unlikely to have arisen as a result of random chance.

Allometric equations

The logarithmic equations described by Huxley and Tessier (1936) promoted the use of logarithmic scales to compare factors to assess allometry.

$$Log\ y = \alpha\ log\ x + log\ b$$

The allometric coefficient (α) obtained for each combination of measurements is presented in Table 5.05. The associated logarithmic graphs of these combinations are presented in Figure 5.17.

Table 5.05. Allometry coefficients for each measurement combination.

Comparison	Allometry coefficient (α)
ML MB	1.0688
ML MH	0.9499
MB MH	0.885

Figure 5.16. Scatter plots of each parameter combination with associated regression line. The gradient of the regression line, R, represents the correlation coefficient.

Allometric Assessment of Maximum Length vs Maximum Breadth
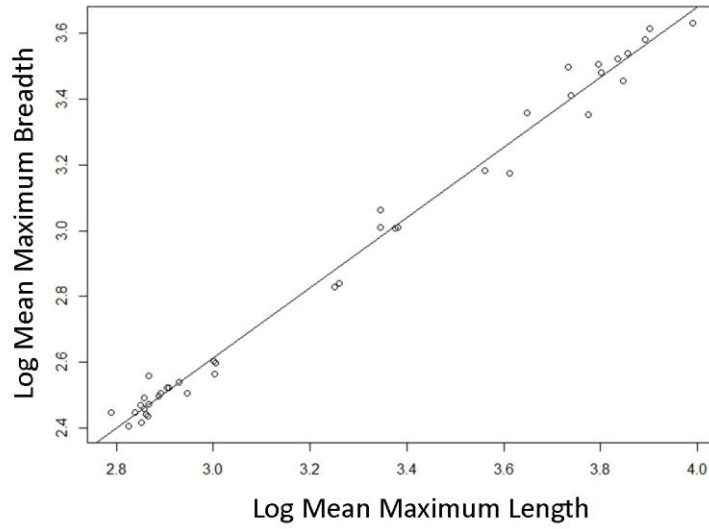
Allometric Assessment of Maximum Length vs Maximum Depth
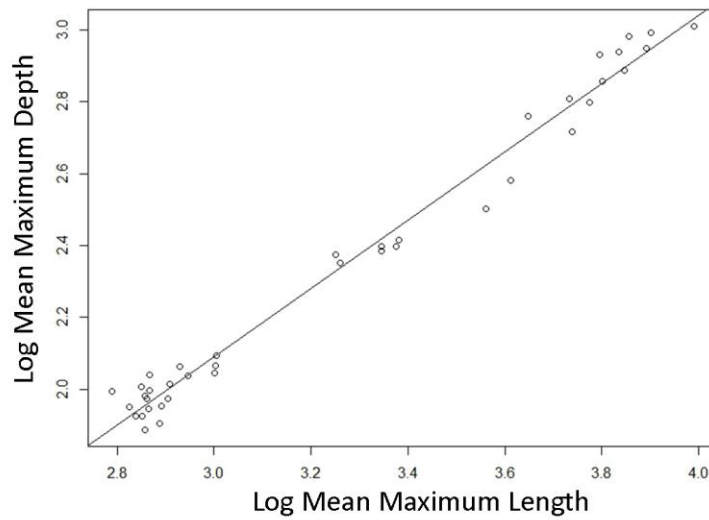
Allometric Assessment of Maximum Breadth vs Maximum Depth
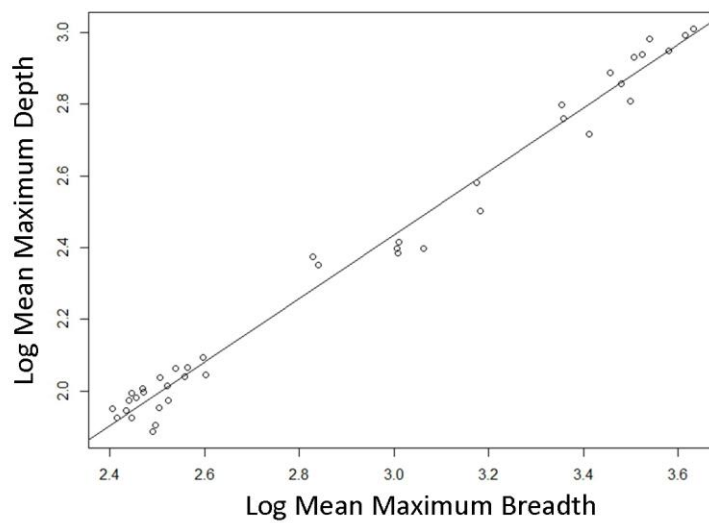
Figure 5.17. Logarithmic plot of each parameter combination with line of best fit. The gradient of the line, α, represents the allometric coefficient.

The α values obtained varied between each combination of measurements. The plot of maximum length against breadth revealed a coefficient of 1.0688, indicating that breath has a very slightly hyperallometric relationship to length. A coefficient of 0.9499 was obtained for the comparison of maximum length and depth, indicating a slightly hypoallometric relationship between depth and length. The lowest coefficient was observed between maximum breadth and depth, where α = 0.885. This indicates a hypoallometric relationship also exists when height is compared to breadth.

5.7.4 Discussion

The results of this study demonstrate that there is a high degree of isometry in the development of the ischium with regards to increasing length and breadth with age. Achieving an allometric coefficient of 1.0688, which very closely approximates perfect isometry, 1, for maximum breadth with maximum length demonstrates that the increase in length with age is proportional to the increase in width: in other words, the relative size of the bone is preserved during development. The α values observed for ML against MD and MB against MD both present hypoallometric values which less closely approximate isometry indicating a weaker preservation of these proportions during growth. However, these are also indicative that there may be a somewhat proportional increase in size between length, breadth and depth.

This preservation of proportions is of importance when applying a grid-based analysis protocol. When applying any method of analysis, it is important that it be fit for purpose, reliable and repeatable. With respect to the ischium, the maximum length and breadth of the ischium are used to identify the outer edges of the grid which is superimposed over the bone [see Section 5.6]. Were the proportions of these dimensions to vary with increasing age, it would result in a skewed grid which would not consistently measure the same volume between specimens of different ages. This in turn would prevent any statistical analysis of inter-phase differences and restrict the potential output of the project. However, as the α obtained for ML : MB for this population very closely approximates 1, the use of a single fixed grid for analysis is supported between groups of increasing age, provided the landmarks identified for use remain identifiable in the μCT data obtained for older cohorts.

It is important to note that the sample population used here is small (n=40), and the individuals within groups are not evenly dispersed. This may have influenced the α values obtained, with a high number of closely-associated individuals in the perinatal group (n=20) and a more diverse range of measurements in the older phase cohorts (n=20), although the value being so closely approximated with isometry (α = 1) is reassuring. This imbalance in specimen distribution could not be avoided due to the material available for study, and the specific grouping requirements following the radiographic analysis. This makes the output data specific to this sample alone, and it is recommended that these results not be applied to datasets beyond this study without first increasing the sample size and redressing the distribution to make the results more widely applicable.

The use of several potential methods of defining proportional growth has presented an interesting contrast in the information which can be gleaned from various types of analysis. Although each of the ratios appraised showed limited variation between each phase, the use of ratios proved too simplistic for anything beyond an estimate of relative growth between metric measurements due to the absence of appropriate statistical testing. Ratios may prove useful where there is a very clear difference between groups at this stage, as it provides a quick and accessible overview of the data. It is however strongly advised that further exploration using statistical means is pursued wherever possible if ratios are indicative that a relationship may be present.

Correlations have been used previously as an indication of proportionality in juvenile skeletal remains (O'Malley, 2013), specifically for identifying the constancy of proportions in the perinatal scapula. Strong positive correlations were found between several key metric parameters, where the author indicated 'strong' correlations as possessing a correlation coefficient (r) greater than 0.9. This provides a comparison to the r values obtained herein, where all r values were greater than 0.99, with a minimum r value of observed between ML and MD and a maximum between ML and MB. However, when these were then converted to a logarithmic form to assess allometry directly, the α values obtained did not follow this order. While ML and MB continued to present the coefficient which most closely approximated 1, ML MD proved to have an α closer to isometry than ML MB, despite their correlations adopting the opposite order. Also, the observation that a correlation of 0.993, which is

both strong and positive, can produce a α value of only 0.885, which is hypoallometric indicates that great care should be taken when extrapolating correlations to proportional growth, as the two are not necessarily directly comparable.

5.7.5 Conclusions

The attainment of allometric coefficients which closely approximated isometry, $\alpha = 1$, demonstrates that increases in length and breadth of the juvenile ischium occur proportionally during phases 2, 3 and 4 as identified through radiographic analysis. This conservation of proportions supports the use of a single fixed grid across each age group, and also the use of statistical methods of comparison between each phase provided external landmarks are readily identifiable in each group.

The simplistic data presented through the use of metric ratios prevents them from being useful in anything but an initial investigative tool, proving hard to extrapolate to a definitive conclusion. Instead it is strongly recommended that the α value obtained from the logarithmic equation described for use in allometric equations be utilised. Due to the discrepancies between the results of these prescribed allometric coefficients and correlation coefficients obtained from the same dataset, it cannot be recommended that r values be used as a substitute for α values.

5.8 Micro-CT data acquisition

5.8.1 Micro-CT imaging

Micro-CT imaging was undertaken at the Centre for Medical Engineering, University of Hull, using an X-Tek HMX 160 micro-computed tomography scanner (X-Tek Systems Ltd., Tring, UK) with a 0.1mm copper filter and a beryllium target. The University of Hull was informed of the purpose of the scans and were requested to generate the scans at the highest appropriate resolution to facilitate visualisation of the internal architecture. A request that the bones be positioned consistently during each scan was also included, but due to the remote nature of the scanning process this could not be ensured with great precision. Previous studies within CAHID have utilised this facility to capture CT data (Cunningham, 2009, O'Malley, 2013; Yusof, 2013).

Specific scanning parameters for each specimen per phase can be found in Appendix 5.1.

Scan data for each specimen was then exported as a complete series of 16-bit Tagged Image File Format (.tiff) images, saved under their unique specimen number. This data was saved to a Seagate Expansion Portable Drive (250 GB) which was returned to the University of Dundee for analysis.

Upon receipt of each completed set of μCT data was backed up to a secure network drive to preserve the original data.

5.8.2 Software selection

The handling and analysis of three-dimensional μCT data requires the use of specific software designed for this purpose. The software selected for this analysis was the SkyScan CT-Analyser. Due to the limitations this software presented with regards to the visual representation and reconstruction of the data, the open-source software package ImageJ was also utilised.

CT-Analyser [v 1.9.1.0] (SkyScan, Belgium).

The SkyScan CT-Analyser (CTan) is a proprietary software specifically designed for the quantitative analysis of μCT data, allowing "accurate and detailed study of micro-CT datasets for morphometry and densitometry" (Bruker, N.D.b). This software offers a number of options for the selection of two-dimensional regions of interest (ROI) and three-dimension volumes of interest (VOI) and the subsequent quantification of these selections. A number of functions are available, including the calculation of a range of standard scientific and bone morphometry calculations and the measurement of linear distances and angles. The parameters of interest to this study are outlined below.

Two features of this software made this the optimal selection for architectural analysis. All calculations CTan performs are 'model-independent'. This means they do not rely on assumptions regarding the structure of the data to inform the calculations performed (model dependent): all calculations are a representation of the voxel structures analysed. Of further benefit, the software provides an extensive selection of ROI and VOI tools. This includes a number of fixed shapes ('square', 'rectangle' 'circle'),

a polygon selector and a freehand drawing option for ROI selection in addition to tools for saving, copying and pasting selections. Where multiple shaped selections are made at stages throughout the VOI, clear interpolation of the connection space, and therefore the final volume, is also provided to ensure the desired volume can be achieved.

ImageJ [v 1.48v] (National Institutes of Health, USA).

ImageJ is an open-source image-editing software package which has a wide array of functionalities relating to the reading, processing and analysing of digital image data. It can be expanded through user-created 'plug-in' extensions that increase this range of functionality. This program was used for all post-processing stages that were applied to the μCT data (discussed below). In addition to post-processing functions, the orthogonal viewer tool and volume rendering tools were used for the visualisation of data to provide a guide when selecting volumes of interest using CTan.

Further information and download links are available here: http://imagej.nih.gov/ij/

A single plug-in was utilised during this project: 3D Viewer (created by the Virtual Insect Brain Project, University of Würzburg, Germany). This allows for the three-dimensional visualisation of image stacks. Further information and download links can be found here: http://3dviewer.neurofly.de/

5.8.3 Data handling

The CTan software has a restricted number of compatible image file types, which does not include the 16-bit .tiff files provided by the University of Hull. This therefore required the data to be converted to a compatible file type prior to analysis, a process which was completed using the ImageJ software package.

Each dataset was imported into ImageJ and opened as a single stack of images. It was noted at this time that the datasets contained a large area of non-bone 'background' surrounding the bone contained centrally in each image. This included the periphery of each slice and a variable number of slices at the beginning and end of each series that contained no bone. In order to minimise storage space required and decrease data-

handling times this excess background area was also decreased when the file format was changed.

To achieve this, a rectangular region selection was applied to the first slice found to contain bone data, which encompassed the entirety of this data. The dataset was then examined sequentially, expanding the selected region as necessary to ensure that all bone data from the scan was captured, but excess background regions were excluded from the region. In addition, note was taken of the first and last image where bone data was present. The 'Duplicate' function was then used to create an identical copy of the data contained within the selection area for all slices containing bone data, and a buffer of 5 'empty' slices on each end. This created a new, smaller dataset which contained minimal extraneous scan regions. These new datasets were then saved as BITMAP image series (.bmp), a file-type which is compatible with both ImageJ and Skyscan.

It was observed during these data handling stages that the datasets from Phase 1 specimens appeared to contain a relatively high level of noise throughout, which may have the potential to disrupt the planned stereological analyses. As a result, a study was devised to evaluate the likely impact of noise within a dataset and the potential to reduce this effect using post-processing algorithms was investigated.

5.9 Algorithmic approaches to noise reduction in micro computed tomography data

5.9.1 Background

Micro-CT studies are primarily limited by the resolution and clarity of the scan data available: large voxel sizes, image artefacts or a preponderance of noise within a scan can have a detrimental effect on data obtained from stereological analyses. The noise within a scan typically arises during the capture and reconstruction of data and is tied to spatial resolution: therefore, with increasing resolutions, an increase in noise is unavoidable (Buzug, 2008). This noise, which can be loosely defined as "any unwanted information that contaminates an image" (Jamil *et al.*, 2008) will be represented in segmented datasets as voxels which are erroneously classified – either as non-bone

regions which are segmented as bone ('positive noise') or bone region which are segmented as non-bone ('negative noise'). There are three sub-sets of noise in relation to μCT: quantum noise, electronic noise and artefacts.

Quantum noise (also referred to as photon or Poisson noise) is caused by fluctuations in the number of x-ray quanta that are detected during each imaging stage, even where identical parameters are set for the scan (Buzug, 2008). This number varies naturally during the quanta counting process, forming an inherent limitation in x-ray radiographic systems such as CT scanners (Hanson, 1981). Typically, this will present as random bright and dark streaks through slices along axes of greatest attenuation (Boas and Fleischmann, 2012). This type of noise can be reduced in relative terms by increasing the radiation dose; by increasing the total number of quanta directed at the object, the fluctuation in those numbers will become a smaller proportion of the total detections in a scan. However, in a low-energy scan environment, such as is required for μCT, this can be difficult to control. Increasing the number of repeats at each imaging stage may also help to reduce this effect.

Electronic noise originates from the x-ray detection itself, as data passes through analogue components of the detector circuitry (Duan *et al.*, 2013), although this typically has a negligible effect on most modern μCT systems as they are designed to minimise this interference.

The more expansive category of 'artefacts' can include a number of forms of noise and typically represent a disruption of 'normal' scanning procedures. The predominant of these artefacts are ring artefacts, which appear as a series of concentric circles imposed throughout a dataset. Ring artefacts are typically caused by technical problems, such as faulty detectors, incorrectly calibrated equipment (Anas *et al.,* 2011), or indeed any form of high-density particulate matter that may have built up inside the specimen chamber (Bruker, N.D.a). Beam hardening may also introduce artefacts into a μCT dataset, which occurs when the lower-intensity photons in a beam are absorbed more readily than higher-intensity photons (Barrett and Keat, 2004; Boas and Fleischmann, 2012). This typically presents in the form of streaks and dark bands appearing between dense objects, or 'cupping' artefacts that cause an increase in average beam intensity through the centre of rounded or cylindrical objects.

More generalised sources of noise may also affect scan clarity. Small variations in the scanning environment, such as temperature fluctuations, may also disturb the scanning process and generate noise within a scan (Kyriakou *et al.* 2009). Round-off errors also occur where the raw data collected by the scanner system is 'translated' to a digital form with a finite number of grey levels (Hanson, 1981).

While an intrusive level of noise, regardless of source, may be detrimental to the data collected from µCT datasets, the digital nature of such data presents a number of potential methods to compensate for the effects of this noise. In the case where noise is limited, a simple adjustment to the threshold level during segmentation may be sufficient to improve the results of stereological analyses. The adoption of local thresholds for individual volumes enhances this, allowing from either higher or lower thresholds regionally as required by the dataset. However, with increasing noise levels, a threshold which removes noise pixels adequately may risk impinging on the quantity of 'true bone' in the final image, particularly where the intensity of 'noise' pixels closely approximate the most appropriate threshold level.

Established literature which utilises computer-based analyses rarely mention noise reduction, although instances exist within the literature of the use of algorithms to reduce or remove noise without justification or referencing to support their use (Buie *et al.*, 2007). There are studies that do discuss methods of noise-reduction, which typically focus on qualitative approach to noise reduction (Anas *et al.*, 2011; Kyriakou *et al.*, 2009; Prell *et al.*, 2009) or generalised discussions of sources of noise and methods by which they can be limited (Barrett and Keat, 2004; Buzug, 2008; Stauber and Müller, 2008). This may be in part due to the diagnostic uses of CT technologies, where the mathematical impact of noise, or its reduction, is less important than its aesthetic implications (in terms of image clarity). Stauber and Müller (2008) recommended the use of a Gaussian filtration (or Gaussian blur) algorithm, which filters a greyscale dataset and reduces noise present. However, it is acknowledged that this reduces the contrast of objects in the dataset, which may itself complicate segmentation, and no quantitative data was presented to support its appropriateness for stereological analyses.

Prell *et al.* (2009) and Kryiakou *et al.* (2009) both present methods specifically designed for removing ring artefacts from clinical CT and μCT datasets respectively using complex processing steps in an unidentified software package. The complex method involves the use of a median filter to identify the ring artefacts, followed by a transformation to polar coordinates, filtration to correct for the ring artefact and then subsequent back-transformation into Cartesian coordinates to create the final dataset. Visually the ring artefacts were removed from the datasets with some success, both from water phantom scans and a CT scan of a skull respectively, and some quantification was provided to indicate there were fewer variations in the phantom analyses. However, these quantitative investigations were conducted on the water phantom alone. No consideration was given to the possible effects on bony structures, so the impact of this extensive series of post-processing stages on subsequent architectural analyses remains unknown.

5.9.2 Influence of noise on bone stereology

As a result of this absence of focus on the quantitative assessment of noise in μCT scans, limited information exists regarding the specific effects of noise on the analysis of trabecular bone. However, an awareness of the nature of noise and an understanding of the computational process for the calculation of standard trabecular bone parameters of interest to this study allows for a theoretical contemplation of the effects of incorrectly segmented pixels. The derivations discussed below are based on the CTan methods for calculating each parameter as described previously [See Chapter 5.3.1].

Bone volume fraction

Bone volume fraction is a direct measurement of the quantity of bone present within the scanned VOI, expressed as a percentage of the total region analysed. With regards to the influence of noise therefore, it is important to note that only a net change in bone and non-bone pixels will be detected: i.e. a single negative noise voxel will be countered mathematically by a corresponding positive noise voxel within the analysed volume. As noise does not typically demonstrate a bias towards either negative or positive noise, the net change in pixels due to incorrect segmentation is likely to be a

very small proportion the total number of voxels within a volume. Therefore, it is not expected that noise will significantly influence BV/TV.

Structural model index

The SMI value is an indication of the prevailing three-dimensional structure of trabeculae within a volume of interest. As SMI is calculated based on surface convexity, the presence of both positive and negative noise may have an influence on SMI, and in opposing manners. A typical trabecular strut will have approximately a quarter to a third of its voxels forming the external surfaces of a trabecula, therefore each voxel will contribute only a small proportion of the overall surface of the trabecula. Isolated noise pixels will have all surfaces exposed and will therefore skew the calculated surface area disproportionately after dilation – this will be expanded by a single voxel on each surface. This will increase the value of S' and therefore positive noise is likely to increase the SMI.

Conversely, negative noise voxels within a region of otherwise intact bone will act to create small perforations in the structure which will be interpreted as small enclosed voids. When these small voids are 'dilated', the addition of voxels to these surfaces will eliminate these voids thus reducing surface area locally. This will in turn lead to a decreased S' value and, in the presence of extreme perforation, may lead to the achievement of a negative SMI value. Such a value would suggest that, rather than an interweaving network of connected struts, the morphology of the structure more closely resembled a finely perforated sheet. This is unlikely in a trabecular volume, therefore a negative SMI value would imply the presence of artificial spaces or negative noise within a dataset.

Degree of anisotropy

As the most complex parameter mathematically, the effects of noise on the degree of anisotropy are more difficult to estimate. As the calculation of DA is based on mean intercept lengths of trajectories through a sphere, it would be expected that the more 'random' distribution of noise in comparison to true bone data would act to increase isotropy (i.e. reduce the DA value). This would be dependent on the position of the sphere of best fit inside the selected VOI and is likely to be influenced by the precise

structure of the volume in question. A theoretical VOI with a low BV/TV and Tb.N value would likely be adversely affected by noise as the errant pixels (particularly positive noise) would create much higher number of intercepts with the solid phase proportionally, while in a VOI with a higher BV/TV and a higher Tb.N the influence of noise would be decreased as 'noise intercepts' would thus form a smaller proportion of these intercepts. It is therefore expected that while noise is likely to decrease the DA for a volume, the magnitude of this effect will likely vary greatly between VOIs.

Trabecular thickness

As trabecular thickness is calculated based on an analysis of ALL voxels within an image segmented as bone, this will include noise voxels without discrimination. Positive noise represented by isolated (or small groups of) white 'noise' voxels will therefore be recorded as having a very low trabecular thickness (likely < 50 μm). As the reported thickness of human trabeculae typically falls between 100 – 150 μm (Kim *et al.*, 2011; Nuzzo *et al.*, 2003; Salle *et al.*, 2002), even a small number of these 'false trabeculae' recorded within a volume would act to lower the mean trabecular thickness substantially. In addition, the spheres used to calculate Tb.Th may not contain non-bone regions, therefore where even single voxels of negative noise disrupted a trabecula this single object would be divided into multiple smaller trabeculae for the purposes of measurement, once again reducing Tb.Th.

Trabecular distribution

A non-standard histomorphometric parameter was included in the noise-reduction study, termed trabecular distribution (Tb.D), to describe the percentage of binarised solid objects which were of 1-3 voxels in average thickness. This measurement is provided as standard by CTan, which outlines the distribution of trabecular sizes that comprise the final mean trabecular thickness (Tb.Th).

As a spatial resolution of < 16 μm was achieved for all Phase 1 specimens in this study, an object with an average thickness of 3 voxels or less would translate to a physical size of no greater than 48 μm. This is less than 50% of the typical trabecular thickness values expected, and such objects can therefore be reasonably considered to represent a region of noise rather than true trabeculae. A higher percentage of these

objects would therefore represent a preponderance of noise, which would have a negative impact on the mean trabecular thickness as described previously. In the event of successful noise reduction, it would be expected that this value would decrease substantially to reflect a diminished number of isolated pixel groups. Should Tb.Th decrease significantly but Tb.D remain relatively constant, this may indicate that the applied algorithm is not only affecting 'noise' voxels, but also true trabecular voxels.

Trabecular number

As the Tb.N of a given volume is calculated as a function of the measured Tb.Th values, it would be expected that noise would have an opposite and proportionate effect on Tb.N calculations (i.e. it will act to increase the number of trabeculae). This is consistent with the interpretation of positive noise as a series of smaller isolated trabeculae, and indeed with negative noise causing single objects to be divided into multiple smaller objects.

Trabecular separation

As trabecular separation value is, in essence, the inverse of trabecular thickness, the effects of noise would correspond with those described for Tb.Th. The presence of single voxels (or small groups thereof) of negative noise would be interpreted as unnaturally small spacing, while positive noise within regions of space would act to 'break up' larger regions of true space between trabeculae into multiple smaller spaces. This would results in an increased number of smaller spaces in place of a more limited number of larger spaces, therefore decreasing the mean Tb.Sp value calculated for a given volume.

5.9.3 Materials and methods

Specimen selection

Four juvenile ischia were selected from the Phase 1 cohort for processing with prospective noise-reducing processes [Table 5.06]. These specimens were selected specifically to represent variation in resolutions present in Phase 1.

Table 5.06. Spatial resolutions and threshold values for noise reduction specimens.

Specimen	Resolution (µm³)	Control Threshold	'Altered Threshold'
SC-082-R	12.6000	132	139
SC-085-R	14.6472	97	102
SC-092-L	15.4057	106	111
SC-158-L	13.5325	113	119

Algorithm selection

Four potential noise-reducing algorithms were identified from the standard functions of ImageJ, based on descriptions of their mode of action (Ferreira and Rasband, 2012). These were 'Close', 'Despeckle', 'Median' and 'Remove Outliers'. A graphical representation of their mode of action is presented in Figure 5.18.
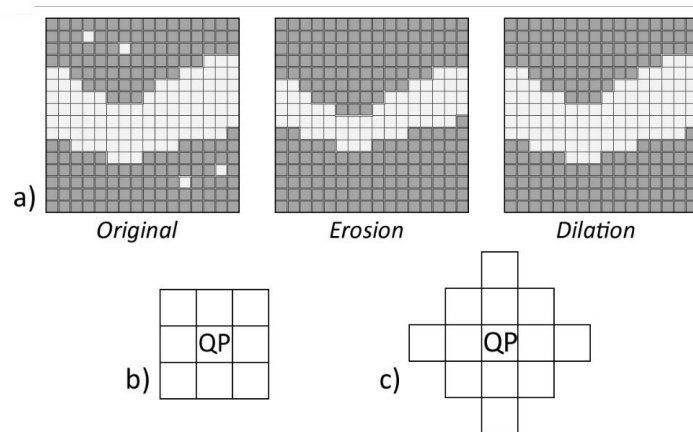
Figure 5.18. Diagrammatic representation of each image processing technique. a) Stages involved in the action of 'close'; b) Area of action for 'despeckle' algorithm; c) Area of action for 'median' and 'remove outliers' algorithms. QP = questioned pixel.

In addition to these algorithms, a comparison was made between a conservative control threshold value and a higher threshold value ('altered threshold') which removed a greater proportion of noise, but also potentially affected the quantity of true bone visible.

The 'close' algorithm acts in two stages. An erosion operation is first applied to remove a single layer of pixels from each edge of binarised objects (i.e. 'white' pixel conglomerations). This is followed by a dilation operation which adds a single layer of pixels to the surfaces created by the erosion [Figure 5.18a]. Any objects which are less

than two pixels in width, indicative of noise, will be removed entirely by the erosion operation and will therefore not be present after the dilation operation.

The 'despeckle' algorithm is a form of median filter which evaluates a 3 x 3 square of pixels and replaces the central 'questioned' pixel (QP) with the median value of this square [Figure 5.18b]. This is repeated for all pixels in the image. As a result, any white pixels which are surrounded by four or more white pixels will remain white, while those bordered by 5 or more black pixels will be converted to black. This also applies in reverse to black pixels. Each comparison is conducted using the original image composition as a reference, eliminating any potential for error due to appraisals including previously reattributed pixels.

The 'median' algorithm is described as a pure median filter which utilises a circular region of pixels (kernel) to appraise the central QP. This radius can be calibrated by the user, however for this study, the default radius of two pixels was selected [Figure 5.18c]. This process is repeated for all pixels within the image as described above, with the threshold for conversion of pixels being 7 or more pixels of the opposing colour in the appraised area.

The 'remove outliers' algorithm is a further variation of the median filter kernel, which can be calibrated through three options. The radius is user-defined (default = 2 pixels), and for non-binary images the threshold for replacement can also be defined. Further, this algorithm acts on only a single class of outlier – specifically altering either 'bright' or 'dark' (i.e. white or black) pixels. As erroneous white pixels were noted to be visually the most pervasive and had the greatest potential to disrupt stereological analyses, 'bright' outliers were selected for replacement. The area of action for this process is represented by Figure 5.18c.

Image processing

Each complete dataset was imported into ImageJ as a single series of slices for processing. The raw greyscale data was duplicated to create two identical datasets. Each dataset was segmented using different threshold values, as determined visually by the investigator using a histogram. The first, which was to become the control, was segmented at a relatively low threshold value which preserved the maximum visual

quantity of 'true' bone pixels at the cost of excessive noise. The second dataset was segmented with a higher threshold value which compromised between minimising noise and preserving bone data. This became the 'altered threshold' data and was not subjected to further enhancement prior to analysis. The threshold values used for each dataset can be found in Table 5.06.

The control dataset was used as the base for each algorithmic enhancement. The duplicate function was used to create identical datasets which were then processed using a single algorithm as described above. Three series of 100 slices were then extracted from each processed dataset to act as test datasets, including slices 250 – 349, 600 – 699 and 1050 – 1149.

Image analysis

A visual comparison of each dataset was conducted to examine the qualitative effect of each process when compared with the control. Subsequently, a quantitative stereological analysis was conducted using CTan to assess the effects of each process on the stereological parameters of interest to the larger project. These included BV/TV, Tb.Th, Tb.N, Tb.Sp, SMI and DA. In addition to these parameters, the percentage of trabeculae which were of 1 – 3 pixels in average thickness (Tb.D) was recorded as a measure of the treatment of the smallest objects in the scan.

The copy – past ROI function of CTan was used to highlight the desired VOI in each comparable slice series, ensuring identical spatial volumes were scanned. Therefore, any change in output data can be attributed directly to the action of the processing applied rather than an inherent variation in the trabecular bone present within a volume.

Analysis of Variance was used to test for significant differences between the control and processed data, conducted in the SigmaPlot statistical package. When significant differences were identified for a parameter, Dunnett's method for multiple pairwise comparisons was applied to compare each algorithm's action to the control alone. This identified the algorithms which significantly altered each of the trabecular bone parameters analysed.

5.9.4 Results

Qualitative assessment

Each noise reducing process introduced a qualitative change in the µCT datasets when compared with the control [Figure 5.19]. In the example dataset below, a slight ring artefact is evident in the upper left of the raw and control image.

Control dataset: no algorithm

Figure 5.19a presents a comparison of the original (raw) µCT data (left) with the binarised control data, which highlights the consistency of the trabecular structure prior to and following segmentation. The binarised control data contains a relatively high level of visual noise, including both positive noise and negative noise. Each subsequent image is a comparison between this control data (left) and the processed data (right).
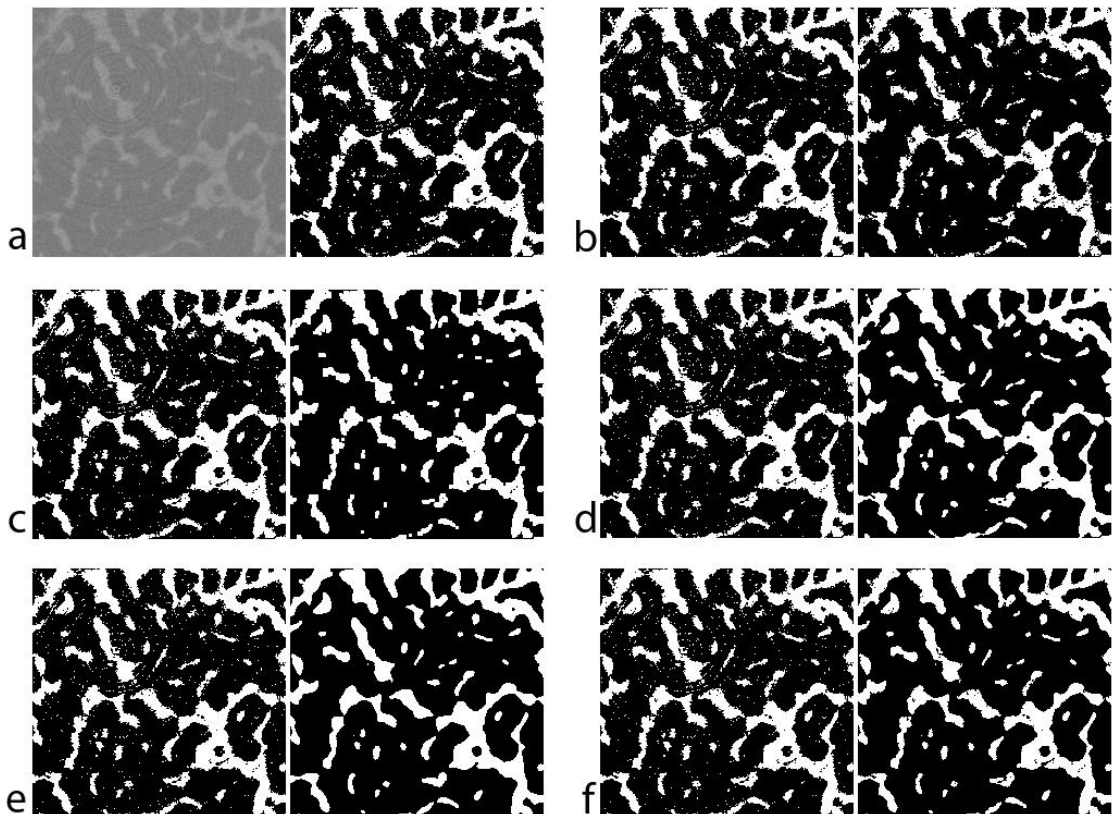
Figure 5.19. a) Comparison of the raw µCT dataset (left) and the binarised control data (right). b-f) Comparison of the control data (left) against data processed with each noise-reducing protocol. [b) Altered threshold; c) close; d) despeckle; e) median; f) remove outliers.

'Altered threshold'

Increasing threshold value used for segmentation acted to reduce the visible appearance of positive noise in the scan data [Figure 5.19b]. However, there was also an increase in negative noise within the boundaries of the trabeculae, and the edges of these structures also appeared diminished. This created a 'thinned-out' and porous appearance to the trabeculae, absent some of the smaller features and bridging regions between larger structures.

'Close' algorithm

A comparison of the control data with the 'close' series, it was observed that there was a substantial change to the visual bone quality. While there was an apparent reduction in the number of noise pixels after processing, there was also an increase in the pixilation of the data: where previously relatively smooth surfaces were evident, the 'close' algorithm had created sharper edges and corners [Figure 5.19c].

'Despeckle' algorithm

The datasets processed with the 'despeckle' algorithm revealed a pronounced reduction in both positive and negative noise when compared with the control data [Figure 5.19d]. The ring artefact was also indistinguishable, although some errant white pixels were identifiable on the periphery of trabeculae.

'Median' algorithm

The results of the 'median' algorithm presented data which was visually similar to those of the 'despeckle' algorithm. Both positive and negative noise was reduced in the datasets and the ring artefact was removed [Figure 5.19e]. However, some of the smaller bridging regions of trabecular bone appeared slightly thickened when compared with the control while others were removed entirely depending on their thickness.

'Remove outliers' algorithm

A comparison of the 'remove outlier' algorithm with the control dataset revealed a considerable reduction in the presence of positive noise [Figure 5.19f]. However, due to the persistence of negative noise, a subtle porous appearance was retained.

Quantitative assessment

The mean data and standard deviations obtained from the stereological analyses are presented in Table 5.07. The raw data generated for each parameter of interest is presented in Appendix 5.3. The statistical test reports produced by SigmaPlot are presented in Appendix 5.4.

Variations were observed between each algorithmically processed dataset and the control, with each algorithm producing a different set of stereological results when compared with the control.

Table 5.07. Descriptive statistics for each stereological parameter.

	BV/TV (%)		SMI		DA	
	Mean	S.D.	Mean	S.D.	Mean	S.D.
Control	29.32	13.21	3.83	2.21	0.36	0.12
Altered Threshold	25.86	12.12	1.35	1.25	0.39	0.12
Close	27.56	12.92	1.06	1.14	0.37	0.10
Despeckle	29.00	13.32	1.53	0.63	0.38	0.12
Median	28.87	13.56	1.49	0.64	0.40	0.11
Remove Outliers	27.60	12.99	0.69	1.45	0.38	0.13

	Tb.Th (µm)		Tb.D (%)		Tb.N (mm^{-1})		Tb.Sp (µm)	
	Mean	S.D.	Mean	S.D.	Mean	S.D.	Mean	S.D.
Control	130.42	28.18	2.77	1.54	2.3	1.0	165.47	49.81
Altered Threshold	118.74	29.04	0.50	0.29	2.2	1.1	245.65	70.55
Close	132.93	28.78	0.70	0.35	2.1	0.9	346.56	153.40
Despeckle	146.25	31.80	0.63	0.26	2.0	0.8	324.88	134.29
Median	151.95	33.10	0.40	0.19	1.9	0.8	348.38	152.52
Remove Outliers	133.22	28.97	0.70	0.30	2.1	0.1	348.22	152.12

Each of the algorithms ('close', 'despeckle', 'median' and 'remove outliers') acted to reduce BV/TV, Tb.N, SMI, DA and Tb.D values while increasing both Tb.Th and Tb.Sp. The magnitude of variation observed in each parameter was dependent upon the algorithm used. The altered threshold sample demonstrated a reduction in BV/TV, Tb.Th, Tb.N, SMI and Tb.D whilst increasing Tb.Sp and DA. High standard deviations

were observed for most mean values, which is predominantly a result of variations in trabecular bone structure between each individual VOI analysed.

The data obtained for each parameter was found to be non-parametric following Sharipo-Wilk tests of normality, conducted as standard by SigmaPlot. As a result of this, analysis of variance on ranks was used to test the significance of the variations observed in each parameter before and after processing [Table 5.08]. Highly significant differences were observed in all seven parameters ($P < 0.001$). Each parameter was subsequently subjected to Dunnett's method for multiple pairwise comparisons (MPC) to determine where significant differences existed between the control dataset and processed datasets [Table 5.09].

The MPC results for the 'altered threshold' datasets showed significant differences in BV/TV, DA and SMI, while the trabecular descriptors (Tb.Th, Tb.D, Tb.N and Tb.Sp) did not vary significantly from the control.

Table 5.08. Results of analysis of variance on ranks.

Parameter	Chi-square	Degrees of Freedom	P
BV/TV	54.429	5	< 0.001
SMI	42.333	5	< 0.001
Tb.Th	58.714	5	< 0.001
Tb.N	46.444	5	< 0.001
Tb.Sp	55.810	5	< 0.001
DA	20.667	5	< 0.001
Tb.D	54.381	5	<0.001

The datasets created using the 'close' algorithm revealed significant differences from the control for BV/TV, SMI, Tb.D, Tb.N and Tb.Sp, but not for DA or Tb.Th. The 'despeckle' dataset demonstrated significant differences in SMI, Tb.Th, Tb.D, Tb.N and Tb.Sp when compared with the control, while no significant differences were observed for BV/TV and DA. The 'median' algorithm introduced significant differences in the values obtained for all parameters with the exception of BV/TV. The 'remove outlier' algorithm introduced significant differences in all parameters except DA.

*Table 5.09. Studentised range (q) for each protocol when compared against the control series using Dunnett's method for MPC procedures. *Result was **not** significantly different from the control (P > 0.05). Critical value: 2.68 - q values above this are statistically significant (Dunnett, 1964).*

ImageJ Protocol	BV/TV	DA	SMI	Tb.Th	Tb.D	Tb.N	Tb.Sp
Altered Threshold	7.359	3.744	4.389	1.549*	1.291*	1.291*	1.807*
Close	5.035	0.387*	5.035	1.936*	4.906	3.421	4.906
Despeckle	1.549*	0.258*	3.357	4.648	5.035	3.744	2.840
Median	1.936*	2.840	3.098	6.197	7.617	7.230	6.713
Remove Outlier	5.035	2.066*	7.359	2.711	3.615	4.454	6.971

5.9.5 Discussion

The stereological data obtained from each μCT dataset processed with a potential noise-reducing algorithm provides a means for appraising the effectiveness of each process through a comparison of predicted change in values based on their method of calculation and the variation observed in each parameter.

Altered threshold

The use of a stricter threshold level, whilst visually reducing the level of noise apparent, also acted to decrease the BV/TV without significantly affecting any of the descriptive trabecular parameters significantly (Tb.Th, Tb.D, Tb.N and Tb.Sp). This indicates that true bone pixels are also being lost as a result of this segmentation process, consistent with an observed overall 'thinning' of the trabecular bone regions as the threshold is increased. As a result, the simple manipulation of the segmentation threshold is not recommended as a method for reducing noise.

'Close' algorithm

The 'close' algorithm, although introducing a significant decrease in Tb.N, Tb.D and SMI, and a significant increase in Tb.Sp, also created a concurrent decrease in BV/TV. Such a significant decrease in BV/TV indicates that, in addition to removing noise voxels, there was a marked net loss of white voxels which could not be attributed to noise alone. This is also supported by the absence of a significant change in the mean thickness of trabeculae, as the loss of noise would be expected to increase Tb.Th.

Visually, the data also presented with a very pixelated appearance after being processed using the 'close' algorithm further reinforcing the unsuitability of this process. The combination of these detrimental changes to the bone architecture in the µCT datasets strongly indicates that the 'close' algorithm should not be used to reduce noise as it also alters the true bone represented within the dataset significantly.

'Despeckle' algorithm

A visual comparison of the 'despeckle' algorithm with the control dataset showed a marked loss of noise without any apparent changes on the true trabecular data. The quantitative analysis of the effects of this algorithm support this observation as no significant variation in BV/TV occurred, while all other descriptive trabecular parameters showed significant positive change. This included a concurrent increase in Tb.Th and Tb.Sp and a decrease in Tb.N. and SMI, indicating that smaller structures which may be attributable to noise were removed from the dataset. The degree of anisotropy was observed to increase in the 'despeckle' datasets when compared with the control, although this did not reach a level of statistical significance. This is consistent once again with the predicted effects of noise, as changes to DA may not be pronounced but would be expected to show some level of increase to anisotropy.

These results therefore support the use of the 'despeckle' algorithm as it does not appear to significantly alter the true bone data represented in the datasets. Whilst a minimal level of noise remained in the datasets, this is preferable to both the interference of noise on stereology, and the artificial alteration of trabeculae through inappropriate processing. The despeckle algorithm can therefore be considered to be a conservative method of noise reduction.

'Median' algorithm

The 'median' algorithm had, both visually and quantitatively, a very similar effect on the µCT data as the 'despeckle' algorithm. However, the algorithms did have a more significant influence on Tb.Th, Tb.D, Tb.Sp and Tb.N values and, unlike the 'despeckle' algorithm, did increase the degree of anisotropy significantly. This is likely a result of the 'median' algorithm using a larger kernel size to appraise the median value when

compared to the 'despeckle' algorithm, which may allow for more effective noise reduction in regions where larger clusters of noise exist.

Based on the quantitative and qualitative appraisals conducted, it is apparent that the use of the 'median' algorithm can be recommended for use in the reduction of noise. Due to the larger area used to calculate the 'median', and its potential for calibration, where larger groupings of erroneous pixels or more invasive artefacts are present, the 'median' algorithm may yield better results than the 'despeckle' algorithm.

'Remove outlier' algorithm

Visually, the 'remove outlier' algorithm appeared to remove a substantial proportion of the positive noise pixels from the images in each dataset, to a level visually comparable with the action of the 'median' and 'despeckle' algorithms. However, as 'remove outlier' did not have any effect on the negative noise, the trabeculae evident presented with a relatively high level of apparent porosity. The prevalence of this persistent negative noise also affected the stereological analysis of the data, causing a significant decrease in BV/TV and also a significant decrease in the SMI value. The decrease in SMI was so extreme in some cases that the final values were negative figures, representative of the trabecular 'porosity' noted in the qualitative assessment. As a result of these features alone, it is clear that the 'remove outlier' algorithm is not suitable in the removal of noise in μCT datasets as both positive and negative noise will influence subsequent analysis.

5.9.6 Conclusions and recommendations

The data presented in this study represents one of, if not the, first attempt to quantify the effects of noise, and of noise reduction, on trabecular bone stereology. These results provide a grounding for researchers for whom this may be a limitation to begin redressing this problem. It is acknowledged that, given the multitude of software programs available, the variety of possible algorithms and indeed the ever-increasing number of 'plug-in' extensions for ImageJ itself, the number of test conditions appraised is not exhaustive. Future studies directed at more extensive and increasingly refined testing are important in appraising potential differences in between pre- and

post-segmentation treatment and the use of more complex three-dimensional algorithms.

It is also acknowledged that an ideal control to this study would be the creation of a dataset with minimal noise present in the initial scan which could then have noise artificially introduced to test the hypothesised mathematical effects of the presence of noise. Unfortunately, as a result of the capacity and capabilities of the remote scanning facilities available at the time of this project it was not possible to include this at this stage.

However, the mathematical basis of this study is sufficiently robust that it can be stated with confidence that the 'median' and 'despeckle' algorithms carry potential for improving scan clarity and thus the validity of data obtained from analyses of the trabecular architecture. Analysis of their actions revealed comparable changes in the μCT datasets which was consistent with the removal of noise without significantly influencing trabecular architecture. While both of these may be suitable, the more conservative 'despeckle' algorithm was selected to be taken forwards as the method of reducing noise in this study.

5.10 Experimental procedure

5.10.1 Application of noise reduction algorithm

Following the selection of the 'despeckle' algorithm as a method for reducing noise, a protocol for the application of this algorithm was devised.

Each μCT dataset was imported individually into ImageJ as an image sequence. To identify whether noise reduction was necessary, a global threshold was used to segment bone and non-bone into white and black voxels respectively, eliminating the grayscale created during acquisition. This threshold was determined for each specimen in comparison with a non-segmented duplicate of the dataset to prevent undue loss of bone volume. The value selected fell in the bone-air interface depicted as a trough in the grayscale histogram. A global threshold was necessary at this stage because it was impractical to extract VOI at this stage, a function which ImageJ is not best suited to

perform, and the use of differential local thresholds followed by the 'despeckle' algorithm may lead to discrepancies in the structure and connectivity of a specimen.

The dataset was then examined visually to determine the degree to which noise was present and therefore whether application of a noise reducing algorithm was necessary. A specimen was selected for noise reduction if a preponderance of false white voxels were evident in regions of non-bone, or if there were small voids identified within bone regions.

It was concluded that all specimens contained within the Phase 1 required the application of the 'despeckle' algorithm to reduce noise. However, no individuals from the remaining phases (2 – 4) required such a procedure be applied as no noticeable noise was present in these specimens. It is unclear whether this discrepancy in contrast levels seen in the perinatal specimens and the older individuals was a result of a difference in the bone tissues themselves or a function of the temporal separation between scans. There were approximately 18 months between the data capture for the Phase 1 cohort and subsequent data capture for the later phases, which is sufficient time for hardware and software upgrades to occur.

Following binarisation with a global threshold, each Phase 1 dataset was processed as a single image sequence using the 'despeckle' algorithm to ensure consistent enhancement throughout a single dataset. The resulting image stack was then exported as a series of BITMAP images and stored as the final test dataset.

The specimens included in Phase 2 – 4 were also processed using a single global threshold value as described above despite not requiring the application of the 'despeckle' algorithm. This ensured consistent data handling of all specimens included for quantitative analysis. Each segmented dataset was then also exported as a series of BITMAP images and stored.

5.10.2 Quantitative analysis protocol

VOI grid and orthogonal viewer

The analysis grid designed for use in this study was developed on a lateral view of the ischium in order to subdivide the bone into VOI for analysis. Due to the remote

processing and scanning of each ischium however, it was not possible to dictate the precise orientation of the resulting two-dimensional scan data obtained from the Centre for Medical Engineering, University of Hull. Although the 2D slices were always exported through the shortest axis of the ischium (approximating a transverse section), the precise degree of rotation varied between each scan [Figure 5.20]. As a result, the geometry of the bone visible in each slice varied presenting a challenge for successfully applying a grid-based analysis protocol.

To navigate the two-dimensional slice data successfully and ensure the accurate placement of the grid therefore, a two-step process was developed which utilised an orthogonal viewer (multi-planar reconstruction) in conjunction with the CTan software to define each VOI [Appendix 5.5].
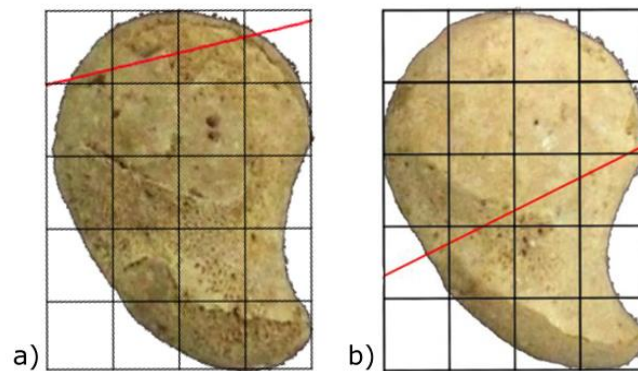
Figure 5.20. Comparison of differing slice orientation [red line] between two perinatal ischia. a) SC-083-L: 13.5º from horizontal; b) SC-084-L: 25.9º from horizontal.

Histomorphometric Analyses

Cortical thickness measurements were taken from the acetabular and pelvic cortices at this stage as the depiction of each VOI extended beyond the cortex. A C.Th measurement was defined as a line that extended from a point on the periosteal surface, perpendicular to that surface, until it reached the corresponding endosteal surface. Care was taken to ensure that this line did not include the anchorage points of trabecular struts on the endosteal surface. CTan displayed the linear distance between these two points in micrometres. This process was completed at five randomly selected locations on each surface throughout each VOI to provide mean values representative of the acetabular and pelvic cortex of that VOI.

Once all C.Th measurements were collected, it was necessary to redefine the VOI to exclude all extraneous space and cortical bone. To achieve this, each placed rectangular ROI selection was converted into a polygon of the same dimensions using the ROI shape tools provided by CTan. The corners of these polygons were then repositioned to a point within the trabecular compartment of the bone, closely approximating the cortical surface. The vertical axes of the selected regions were preserved to ensure the correct volume was incorporated. These changes were then interpolated through the VOI creating a new VOI in the same position that incorporated only trabecular bone. Each slice within the VOI was then examined to ensure that the boundaries of the VOI at that level did not include any cortical bone and, where necessary, additional ROI selections were placed to correct deviations.

Following correct definition of the trabecular VOI, the analysis of the trabecular architecture could then be conducted. As the data was segmented in ImageJ prior to noise reduction, specific binarisation was not necessary in CTan. The 'binarise' option was applied and it was ensured that the bone and non-bone phases were correctly classified as white and black respectively. This was then confirmed by progressing to the 'processed images' tab to finalise the selected volume. The '3D analysis' tool was then selected to begin the architectural analysis. When prompted, all available analysis parameters were selected for calculation and the software was instructed to automatically save the output data.

5.11 Intra-observer study

Following the creation of the grid system, an appraisal of the repeatability of grid alignment was necessary to validate the method of analysis. To achieve this, an intra-observer error study was conducted to determine whether the grid could be defined repeatedly within a single specimen and produce consistent results for each of the histomorphometric parameters.

5.11.1 Materials and methods

Four specimens were selected from the Phase 1 cohort for analysis to undergo intra-observer error analysis. Details of the specimens selected are summarised below [Table 5.10].

Table 5.10. Details of specimens for intra-observer study.

Specimen No.	Age	Voxel Size (μm^3)
SC-082-R	Perinate	12.6000
SC-083-L	Perinate	13.6325
SC-097-L	Perinate	15.4057
SC-161-R	Perinate	15.1509

Data was collected in CTan following the procedures outlined previously [Section 5.10.2]. Values were recorded for trabecular parameters (BV/TV, Tb.Th, Tb.N, Tb.Sp, SMI and DA) and lateral and pelvic cortical thicknesses (L.C.Th and P.C.Th respectively). Measurement protocols were repeated four times for each VOI per bone. To best replicate a conventional analysis, a single series of data was collected for VOI 1 to 16 for a single specimen, followed by three further cycles of collection. This ensured no two repeats of a VOI were conducted concurrently, preventing VOI placement being biased.

The resulting data was collated into Microsoft Excel prior to statistical analysis. Analysis of variance was used to investigate whether statistically significant differences existed within the data collected for each of the four specimens. Where data exhibited normal distribution, the parametric Kruskal-Wallis ANOVA was used. Where data was not normally distributed, an ANOVA on ranks was used in place of the parametric test. Individual tests were used per parameter per specimen to prevent any differences between specimens from influencing the results of the ANOVA testing.

5.11.2 Results

The raw data and descriptive statistics obtained for the intra-observer investigation are presented in Appendix 5.6. The statistical test reports produced by SigmaPlot are presented in Appendix 5.7. A summary of the results of each ANOVA test is outlined in Table 5.11.

*Table 5.11. Results of intra-observer analysis of variance. * Analysis completed using parametric ANOVA.*

Parameter	Specimen	H / F*	DoF	P
BV/TV	SC-082-R	0.318	3	0.957
	SC-083-L	0.028	3	0.999
	SC-097-L	0.131	3	0.988
	SC-161-R	0.001	3	1.000
Tb.Th	SC-082-R	0.030	3	0.999
	SC-083-L	0.012*	3	0.998
	SC-097-L	0.001	3	1.000
	SC-161-R	0.133	3	0.988
Tb.N	SC-082-R	0.661	3	0.882
	SC-083-L	0.019	3	0.999
	SC-097-L	0.085	3	0.994
	SC-161-R	0.002	3	1.000
Tb.Sp	SC-082-R	0.068	3	0.995
	SC-083-L	0.119	3	0.989
	SC-097-L	0.103	3	0.991
	SC-161-R	0.101	3	0.992
SMI	SC-082-R	0.787	3	0.853
	SC-083-L	0.924	3	0.820
	SC-097-L	0.143	3	0.986
	SC-161-R	0.269	3	0.966
DA	SC-082-R	0.279*	3	0.840
	SC-083-L	0.521*	3	0.669
	SC-097-L	0.241	3	0.971
	SC-161-R	0.391	3	0.942
P.C.Th	SC-082-R	0.485	3	0.922
	SC-083-L	0.131	3	0.988
	SC-097-L	0.035	3	0.998
	SC-161-R	1.717	3	0.633
L.C.Th	SC-082-R	0.970*	3	0.413
	SC-083-L	1.036*	3	0.383
	SC-097-L	1.353*	3	0.266
	SC-161-R	2.540	3	0.468

No significant differences were detected in any of the intra-observer test conditions analysed (P > 0.05). The results obtained for trabecular bone stereology demonstrated very high P values (P > 0.8) in all cases except the analysis of DA for SC-083-L, which revealed a lower P value (P = 0.669). The analysis of intra-observer error for pelvic cortical thickness demonstrated very high P values for SC-082-R, SC-083-L and SC-097-L (P > 0.900) and a lower P value for SC-161-R (P = 0.633). Though the lateral cortical thickness ANOVA did not demonstrate significant differences, they demonstrated the

lowest P-values observed when compared to the other parameters analysed. P values fell between 0.468 (SC-161-R) and 0.266 (SC-097-L).

5.11.3 Discussion

When devising any analysis protocol, it is of vital importance that it be fit for purpose. With regards to this study, this required that the placement of the grid be demonstrated to be repeatable with a high degree of accuracy. The collection of trabecular bone would be expected to be the most likely to present difficulty as local variations in trabecular architecture may be sufficient to introduce statistically significant differences between VOI should the grid not be aligned correctly. For example, a grid which is offset by 100-150 microns (approximately 10 voxels) may fail to capture entire trabeculae on the periphery of a VOI, which may be substituted with predominantly non-bone regions from the adjoining VOI, which would not only affect Tb.N, but also all other descriptive parameters assessed. It could be reasoned that C.Th measurements may be more robust than trabecular analyses in this respect as these may be selected away from the immediate vicinity of VOI boundary. This will ensure that no thickness data is incorrectly collected from an adjacent VOI.

The intra-observer study also acts to validate the collection of thickness measurements from both the acetabular and pelvic cortices, as there has been no published investigation into the number of linear measurements required to describe the cortex of a single VOI appropriately. The original method from which this cortical thickness protocol is derived utilised four randomly selected measurements to describe the C.Th in each VOI (Cunningham, 2009; Cunningham and Black, 2009c). Due to the perceived size of each VOI in the present study, this was expanded to five random linear measurements. The absence of any significant differences between repeats for each of the four specimens analysed supports the use of this measurement protocol: five measurements are sufficient to describe each cortex within the ischial VOI. Had significant differences been detected for C.Th measurements, but not for the trabecular bone histomorphometry, this would have suggested that perhaps additional linear measurements would be required within each VOI to better explain the variations in thickness within.

The relatively low P values obtained for the lateral cortical thickness parameter initially caused some concern as, while a minimum P value of 0.266 is not statistically significant, it does not lend itself to a high degree of confidence. However, when the raw data for cortical thickness was appraised more closely, it became apparent that the low P values were likely a result of the very low cortical thickness values observed in this region, where small deviations between each repeat may present as statistically significant, particularly if one series of repeats was consistently slightly higher than the others. This was supported by the observation that the lowest L.C.Th measurements corresponded with the lowest calculated P value, while the highest L.C.Th measurements corresponded with the highest P value.

5.11.4 Conclusion

The absence of significant differences observed when utilising the described grid system to analyse the juvenile ischium supports the use of this method for the quantification of architectural parameters. Further, the results obtained from the C.Th analyses for both the acetabular and pelvic cortices reinforced the use of five linear measurements to describe each VOI.

Following the absence of significant differences in four repeats of each specimen, it was decided that only a single collection per volume would be taken as a representative value for that volume. Furthermore, for each of the specimens included in the intra-observer study, the fourth and final intra-observer measurement for each parameter was taken forwards to represent that specimen in the main data analysis phase.

5.12 Principal data collection

Following the completion of intra-observer testing, data was collected for parameters of interest as outlined in Chapter 5.10.2. Data was collected and recorded for all VOI's sequentially within a single specimen before progressing to the next specimen. In addition, all data for a single specimen was collected in a single session to prevent any movement of the grid or software windows, minimising potential errors due to

disruption of VOI alignment. In addition, it removed the risk of calibration errors being introduced between sessions.

Data was collected from each phase in order, i.e. beginning with Phase 1 specimens, followed by Phase 2 and 3.

5.12.1 Exclusion of phase 4

While the allometric study [Section 5.7] demonstrated that the gross proportions of the ischium were preserved with increasing age through all individuals included within this study, difficulties were encountered when applying the fixed VOI grid to the older specimens represented by the Phase 4 cohort.

These difficulties were not caused by a direct change in proportion *per se*, as the grid could be aligned with the identified external landmarks without difficulty. However, a change was identified in the curvature associated with the posterior border of the obturator foramen, and the angle and thickness of the ramal projection inferiorly. A transition was identified from the constrained 'comma-shaped' appearance of the ischium in younger specimens to a more pronounced 'hook-shape' in the older specimens which distorted the contents of VOI 10 – 16.

As a result of this distortion, it was not possible to ensure that the trabecular architecture analysed in the Phase 4 specimens would be equivalent to the corresponding volumes in Phases 1 – 3, therefore Phase 4 was entirely discounted from further analysis.

5.12.2 Exclusion of specific volumes of interest

Due to the nature of the collection studied, specimens exhibited varying states of preservation and, in some cases, minor cortical damage and exposure of the underlying trabecular compartment. Those specimens which exhibited substantial damage – e.g. wear and fracturing of cortical surfaces and damage and potential loss of trabeculae – were previously excluded from the radiographic study.

Due the increased sensitivity of quantitative analysis using μCT imaging however, minor localised damage in a specific volume of interest presented the risk of

generating data which was not representative of cortical or trabecular structure at that location. It was necessary therefore to exclude specific volumes of interest where the structural integrity of either the cortical or trabecular bone could not be ensured. Damage or erosion of cortical bone as viewed from the periosteal surface was deemed a criterion for exclusion of cortical bone from the affected VOI(s). Lesions that penetrated the cortex and exposed the underlying trabeculae also required the exclusion of trabecular analysis at the affected VOI.

During the analysis of the µCT datasets, it was noted that the internal trabecular architecture of specimen SC-299-L, included in Phase 3, was anomalous in appearance. An ellipsoid void was present in the central region of the ischium in close proximity to the pelvic cortical surface. A very small number of thickened bone-binarised objects were observed to cross this void to anchor on a large central mass [Figure 5.21]. All other trabeculae were excluded from this central region and were instead clustered around the periphery of the bone. This trabecular morphology demonstrated morphology similar to descriptions of an aneurysmal bone cyst [Figure 5.22], a benign osteolytic tumour which is prevalent in the juvenile period and may affect any bone, including the pelvic elements (Hetaimish and Alshaya, 2016; Soma et al., 2013). Due to the potentially pathologic nature of this trabecular region, the specimen was excluded from further analysis.
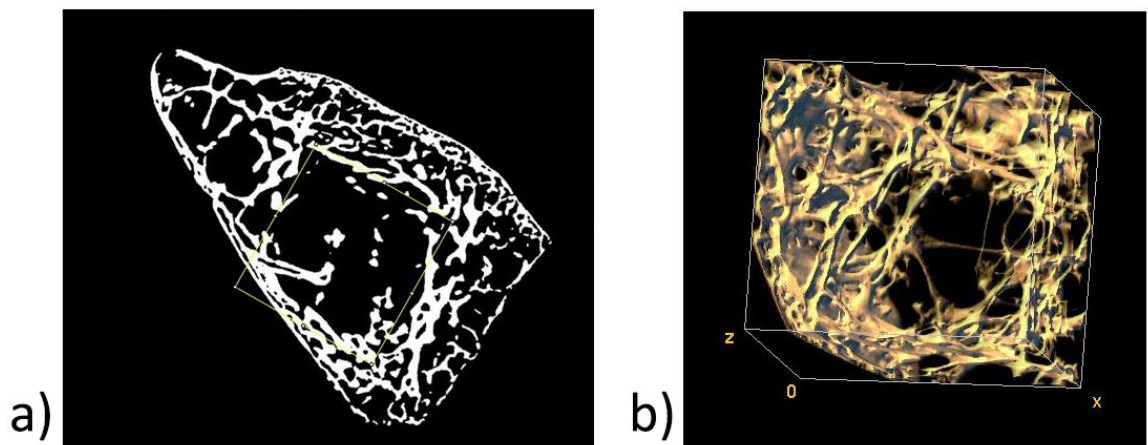
Figure 5.21. a) Two-dimensional view of the irregular elliptical void in the central region of SC-299-L. Yellow ROI denotes position of volume reconstructed in 3D. b) 3D volume rendering of the central region of trabecular architecture at 160% magnification.
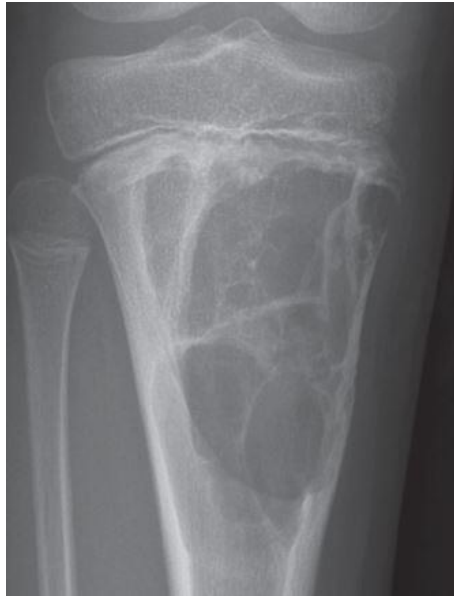
Figure 5.22. Radiograph of an aneurysmal bone cyst in the right proximal tibia of a female aged 11 years. Adapted from Soma et al. 2013.

Table 5.12 presents the final number of data points collected for all analyses, trabecular, lateral cortex and pelvic cortex, in each phase.

Table 5.12. Number of data points collected for trabecular bone histomorphometry (trab.), lateral cortical thickness (L.C.Th) and pelvic cortical thickness (P.C.Th) at each VOI per phase. N = total number of individuals. ▪ highlights absent data point(s).

	Phase 1 [N = 20]			Phase 2 [N = 5]			Phase 3 [N = 3]		
VOI	Trab.	L.C.Th	P.C.Th	Trab.	L.C.Th	P.C.Th	Trab.	L.C.Th	P.C.Th
1	20	20	19▪	5	5	5	2▪	1▪	1▪
2	20	20	20	5	5	5	3	3	3
3	20	19▪	19▪	5	5	5	3	3	3
4	20	20	20	5	5	5	3	3	3
5	20	20	20	5	5	5	2▪	2▪	2▪
6	20	20	20	5	5	5	3	3	3
7	20	20	20	5	5	5	3	3	3
8	20	20	20	5	5	5	3	3	3
9	20	20	20	5	5	5	2▪	2▪	2▪
10	20	20	20	5	5	5	3	3	3
11	20	20	20	5	5	5	3	3	3
12	20	20	20	5	5	5	3	3	3
13	20	20	20	5	5	5	3	3	3
14	20	20	20	5	5	5	2▪	2▪	2▪
15	20	20	20	5	5	5	2▪	2▪	2▪
16	19▪	19▪	19▪	5	5	5	2▪	2▪	2▪

5.13 Statistical analysis protocols

All statistical tests, with the exception of Pearson product-moment correlations (PPMC) [see Section 5.7.2 for further details] were performed in the SigmaPlot statistical package, which facilitated the analysis of trabecular and cortical bone histomorphometric results in an efficient and comprehensive manner. The selected software provides a number of step-wise analysis operations which include automated tests of distribution and variance, and the option for further *ad-hoc* analysis in the event a significant result is returned. Only tests which are suitable for application on the selected data are presented by the program, allowing the most appropriate tests to be identified and applied.

Analysis of variance (ANOVA) was selected for use to calculate the significance of differences identified between the volumes of interest analysed. Where an overall significant difference was found within a dataset, a multiple pairwise comparison procedure was applied to determine whether this significant difference could be localised to specific pairs of VOI.

The first stage of analysis applied tests of distribution and variance to the data to determine whether the data was parametric or non-parametric in nature. The Shapiro-Wilk test of distribution was used to determine normality, where a p value greater than 0.05 indicates the data passed the test: the data is normally distributed. Levene's test of equal variance was then applied, where a P value greater than 0.05 indicates that data displays homogeneity of variance. If both tests were passed, the data was considered parametric. If either test was failed, the data was considered to be non-parametric.

5.13.1 Analysis of variance (ANOVA)

Two forms of ANOVA were used to investigate significant differences, dependent on whether the data was found to be parametric or non-parametric.

Parametric data

Parametric data was tested using a one-way analysis of variance, which assumes samples are drawn from populations which are normally distributed and exhibit equal variance. The null hypothesis for this test is that there are no significant differences between the populations from which the samples are drawn. A parametric ANOVA provides a descriptive summary of the dataset analysed, including the source of the data; number of observations per group (n), and any missing observations; and the mean, standard deviation (SD) and standard error of the means (SEM) for each group. SigmaPlot then calculates the sum of squares (SS), which indicates the variability of average differences between sample groups, and the mean squares of the groups, providing two estimates of the population variances.

The level of statistical significance of this test is demonstrated by the F statistic and its corresponding p value. Where F is very low, approximating 1, it denotes that the data is consistent with the null hypothesis, i.e. that there are no significant differences between the groups. Conversely, in the F statistic is large, this indicates that the differences observed between samples are greater than would be expected as a result of random variation in the population.

The p value compliments the F statistic, presenting the probability of incorrectly rejecting the null hypothesis. A smaller p value indicates a lower probability of falsely rejecting the null hypothesis, therefore demonstrating a greater probability that true differences exist between the groups. Consistent with contemporary literature, the value of $p = 0.05$ was used as the threshold below which a difference was considered to be statistically significant.

Non-parametric data

Data which was found to be non-parametric was not suitable for analysis using a parametric analysis of variance, therefore the non-parametric equivalent was used. The test selected for this was the Kruskal-Wallis one-way ANOVA on ranks, which does not require assumptions of normality or equal variance. The null hypothesis for this test is that there is no difference in the distribution of values between the experimental groups.

Analysis of variance on ranks provides a summary of the number of observations (n), a count of missing observations, the median and percentiles for each group. The H statistic is calculated for the data by ranking all observations from smallest to largest and comparing the average values. As with the F statistic in a parametric ANOVA, a lower H statistic indicates that the distribution of values is consistent between groups and the null hypothesis cannot be rejected. However, where H is found to be large, the variability among the average values can be said to exceed that expected from random variation. From this it can be concluded that samples were drawn from different populations.

As with the parametric ANOVA, the p value represents the probability of falsely rejecting the null hypothesis. It was accepted that a significant difference existed where $p < 0.05$.

5.13.2 Multiple pairwise comparisons (MPC)

When a significant difference was found to exist among volumes of interest, multiple pairwise comparison procedures were applied to compare pairs of volumes. This allowed significant differences between specific volumes and regions to be identified. As with the ANOVA tests, parametric and non-parametric analysis methods were required to assess the data obtained as appropriate.

Parametric data

The parametric MPC test followed was the Holm-Sidak method, which is a series of t-test procedures with a power correction to offset the increased risk of falsely rejecting the null hypothesis. This method first calculates the difference of means for each possible comparison and ranks them from largest to smallest. The difference of means is used to calculate the t statistic for each comparison, which indicates the size of the difference relative to the variation in the sample. A high t value indicates that a true statistical difference exists between the volumes analysed. The associated p value is then calculated based on the significance level of the test, the total number of comparisons made and the rank of the comparison. The p values are then compared to the critical value ($p < 0.05$): if the p value for a comparison is below this value it can be

concluded that a statistically significant difference is present between the two volumes.

Non-parametric data

For non-parametric pairwise comparison procedures, two comparison methods were used. The most frequently utilised test, Dunn's method, was conducted on data where one or more observations were found to be missing. This applied to all non-parametric MPC procedures conducted on Phase 1, Phase 3 and inter-phase datasets. Where no observations were missing, as viewed in Phase 2 non-parametric MPC procedures, Tukey's Test was instead applied as the recommended test.

As with the parametric test, both non-parametric MPC procedures use the difference of ranks observed for each comparison to calculate either a Q (Dunn's method) or a q (Tukey's test) statistic for each possible pairwise comparison. The greater the value calculated, the larger the detected difference between the volumes compared.

In each of these tests, the comparison with the largest Q / q value is identified and placed at the top of the list. All subsequent comparisons for the volume in this comparison with the highest median value are then computed sequentially. This process is then repeated, where the next selected volume is the volume which was found to be most similar to the first (i.e. presented the lowest difference of ranks). Each Q value is then used to determine the corresponding p value which is compared to a critical value $P < 0.05$ to establish the significance of the result. When a comparison is found to not be statistically significant, subsequent comparisons which present a Q / q value lower than the failed test return a result of Do Not Test.

Chapter 6: Results of Quantitative Analyses

6.1 Presentation of results

Full raw data and results of statistical analyses for each parameter and phase are provided in Appendices 6.1 – 6.3. The results of statistical testing are presented in full in Appendices 6.4 – 6.15.

To ensure the clarity of information presented, the results section is subdivided into discrete sections which detail the results of each individual measured parameter across the three phases analysed, followed by an analysis of the relationship between parameters in each phase.

Three thresholds of significance were defined based on the P-values returned from statistical analyses. A result was considered to be statistically significant where $P < 0.05$. When $P < 0.01$, results were said to be highly significant, and if $P < 0.001$, results were considered to be very highly significant. SigmaPlot does not resolve P values below 0.001 to additional decimal places, rather presenting them as '$P < 0.001$' at the conclusion of analysis.

To highlight statistical relationships between volumes of interest in each phase, colour coded figures using either a three- or four-colour system have been created. Volumes exhibiting similar patterns of pairwise significant differences are grouped based on whether they exhibit statistically higher values (green), lower values (red) or intermediary values (yellow) [Figure 6.01].

In a single comparison, that of Phase 1 Tb.Sp, a 3 colour system was not capable of describing the results of all MPC tests appropriately. A fourth colour was introduced in this situation to better characterise the pattern of significant differences observed, which required the inclusion of a low-intermediate group (orange) to highlight regional differences [Figure 6.02].
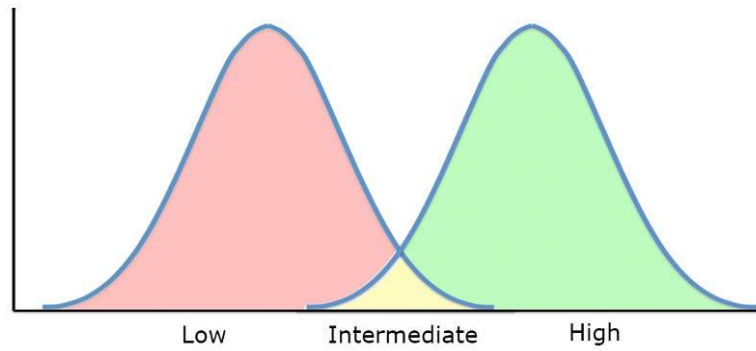
Figure 6.01. Visual representation of colour groups, where red and green colourations represent discrete populations, with a small intermediate group between these populations (yellow).

It should be noted that these descriptive systems are relative to the parameter and phase from which they are derived and describe overall trends for said parameter. It would be inappropriate to draw direct comparisons between either phases or parameters and imply statistical importance to the differences in colouration observed.
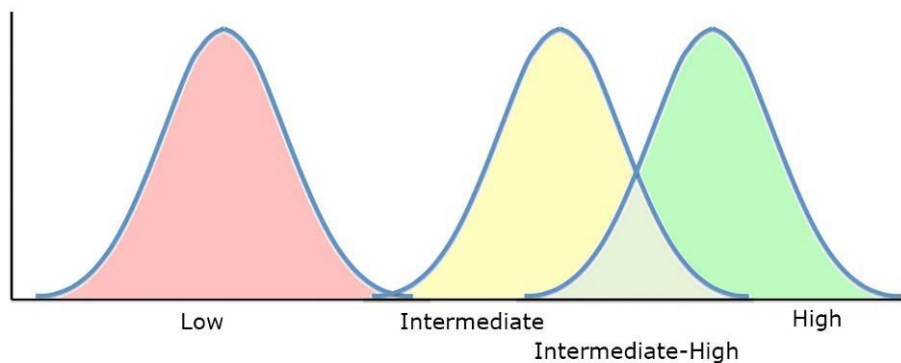
Figure 6.02. Representation of relationships between groups in the four-colour system applied in Phase 1 Tb.Sp.

If no statistically significant differences were identified, or the number deemed too few to permit a regional classification of the pattern observed, a single-colour coding system was instead presented. In addition, specific ischial maps localising regional parameter variations are only presented where either the three- or four-colour coding systems were applied.

6.2 Trabecular results

6.2.1 Bone volume fraction

Phase 1

The descriptive statistics for Phase 1 bone volume fraction in each volume of interest are displayed in Table 6.01.

The mean BV/TV values varied throughout the ischium, with a minimum mean BV/TV of 25.47 % (VOI 6) and a maximum mean of 51.30 % (VOI 16). In addition to local variation, the relative standard deviations (RSD) demonstrated a degree of variation between individuals, ranging between 15.18 % (VOI 16) and 30.36 % (VOI 1). It was noted however that the majority of RSD values fell below 25 % of the respective bone volume. This data is summarised graphically in Figure 6.03.

Table 6.01. Descriptive statistics (mean, range, standard deviation and relative standard deviations) for Phase 1 BV/TV for each volume of interest.

VOI	Mean	Range		SD (±)	RSD (±)
		Min	Max		
1	26.73	15.69	43.27	8.12	30.36
2	26.60	16.76	39.44	6.97	26.20
3	33.39	23.81	47.52	7.88	23.61
4	39.25	24.41	53.32	8.78	22.36
5	28.08	18.50	41.76	7.15	25.46
6	25.47	17.90	37.46	6.01	23.61
7	28.61	21.62	41.21	6.21	21.69
8	31.15	21.27	45.00	7.07	22.70
9	30.18	19.25	42.68	6.08	20.16
10	25.63	18.51	41.01	7.19	28.05
11	30.27	20.57	49.57	8.70	28.75
12	40.18	26.19	54.06	7.93	19.74
13	40.09	29.43	55.81	8.04	20.05
14	44.17	32.63	58.44	8.18	18.53
15	46.29	34.97	59.31	7.94	17.15
16	51.30	40.29	62.79	7.79	15.18

Phase 1 BV/TV (%)
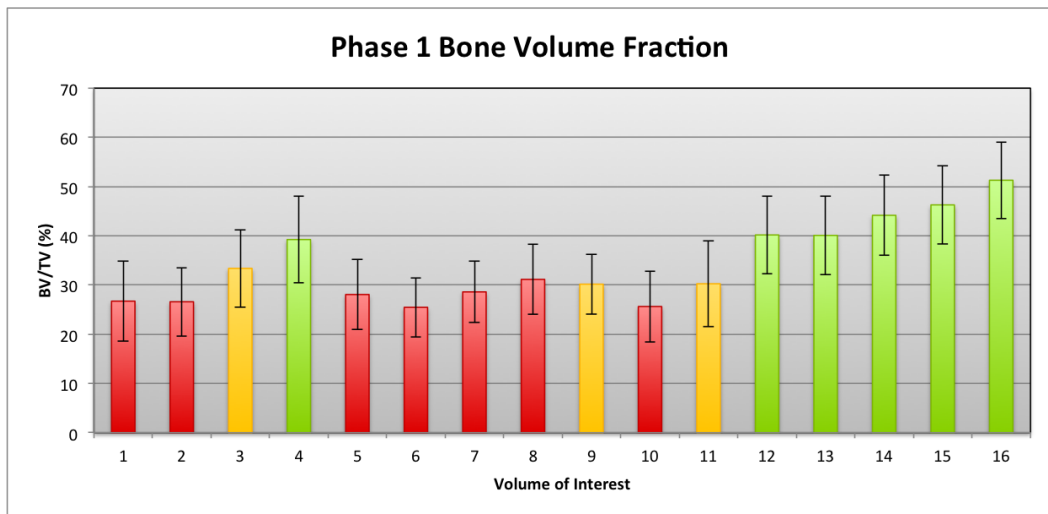
Figure 6.03. Graphic representation of mean (± SD) BV/TV per VOI for individuals in Phase 1. High (green), intermediate (yellow) and low (red) colouration applied based on MPC testing.

The data was found to be non-parametric (Sharipo-Wilk test: $p < 0.05$), therefore the Kruskal-Wallis ANOVA on ranks was used to test for significant differences. A very highly significant difference was found ($p < 0.001$) from an H-statistic of 162.089 with 15 degrees of freedom. Multiple pairwise comparisons were conducted following Dunn's method to determine whether this statistical significance could be localised to specific VOI pairs. Significant differences were found to exist between a number of VOIs [Figure 6.04].

An analysis of the patterns of pairwise significant differences revealed that this dataset could be defined by three groups, comprised of a high BV/TV group, a low BV/TV group and a small number of intermediary VOIs which did not align to either extreme [Figure 6.05].

The low BV/TV volumes (red) were located posterosuperiorly, including VOI 1, 2, 5 – 7 and 10. These volumes were found to be significantly different from the volumes identified as having high bone volume fraction, but did not exhibit significant differences from the intermediate volumes.
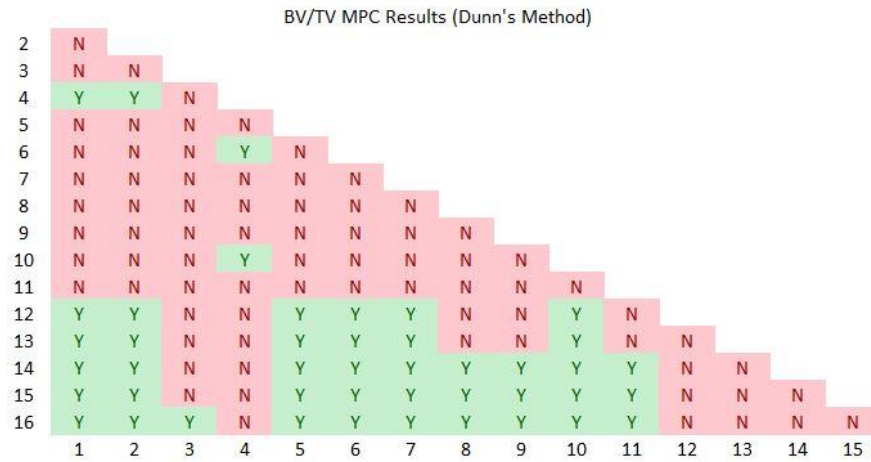
Figure 6.04. Multiple pairwise comparison results for Phase 1 BV/TV. Y = statistically significant difference (p < 0.05); N = no significant difference detected.

The mean BV/TV of each volume fell between 25.47 % and 28.61 % for this group. Each of the low volumes shared a minimum of one common border with the remaining members of this group, thus identifying a single combined region as having low bone volume fraction. This region defined the approximate position of the developing acetabular margin and articular surface.
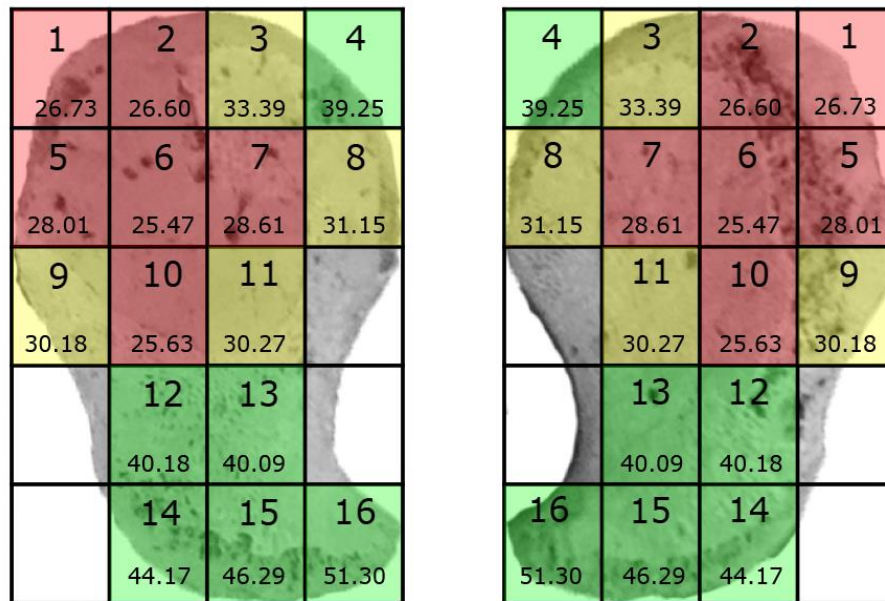
Figure 6.05. Bone volume fraction groups mapped to the perinatal ischium. Green: high BV/TV; yellow: intermediate BV/TV; red: low BV/TV. The values below the VOI number are the mean BV/TV for that volume (%).

The high bone volume fraction group (green) comprised volume 4 and the inferior volumes 12 – 16, and their mean values were found to be between 39.25 % and 51.30 %. As with the low group, the statistical similarity of VOI 12 – 16 created a larger region

which defined the developing ramus and lowest aspect of the body of the ischium, while VOI 4 was isolated anterosuperiorly. The high BV/TV VOI were found to be significantly different from all low BV/TV VOI, but only VOI 14 – 16 were significantly different from those classified as intermediate.

The four VOI classified as intermediate (yellow) displayed three or fewer statistically significant pairwise comparisons, in each case with the most inferior VOI from the high group, but did not demonstrate significant differences from the low BV/TV group or the other intermediate members. In each instance, these VOI were found to share borders with both low and high BV/TV volumes.

Phase 2

The descriptive statistics for Phase 2 BV/TV in each volume of interest are presented in Table 6.02.

The range of mean BV/TV values observed in Phase 2 was noted to be markedly smaller than that of Phase 1, with all mean values falling between 12.56 % (VOI 2) and 20.26 % (VOI 14). While the SD values observed were similar to those of Phase 1, the relative standard deviations were found to be greater than in Phase 1, ranging from 21.05 % to 57.92 %. It was noted however that although the RSD value for each VOI is typically higher in this phase, the magnitude of the standard deviation at each VOI was similar in both phases. This data is summarised graphically in Figure 6.06.

The Phase 2 bone volume fraction failed the test of distribution ($p < 0.05$) therefore the Kruskal-Wallis ANOVA on ranks was used to test for significant differences. The H-statistic was found to be 15.601 with 15 degrees of freedom, for which $p = 0.409$. This result was not statistically significant, therefore MPC testing was not required for this phase.

Table 6.02. Descriptive statistics for Phase 2 BV/TV at each VOI.

	Phase 2 BV/TV (%)				
VOI	**Mean**	**Range**		**SD (±)**	**RSD (±)**
		Min	**Max**		
1	14.21	10.08	18.28	2.99	21.05
2	12.56	10.39	17.83	3.01	23.97
3	14.63	10.75	22.94	4.20	28.72
4	19.43	10.46	38.13	8.82	45.40
5	14.43	11.18	18.67	8.36	57.92
6	12.81	9.15	17.04	2.84	22.14
7	15.13	10.03	20.75	3.46	22.89
8	16.86	10.10	25.11	4.73	28.03
9	16.79	10.10	24.76	5.36	31.93
10	17.31	13.49	22.39	4.49	25.92
11	14.97	10.54	23.11	4.29	28.67
12	17.38	8.45	31.69	6.76	38.90
13	18.45	12.37	25.23	6.87	37.23
14	20.26	13.29	36.75	7.34	36.23
15	17.95	13.43	27.36	7.38	41.10
16	19.89	15.71	25.10	4.51	22.66
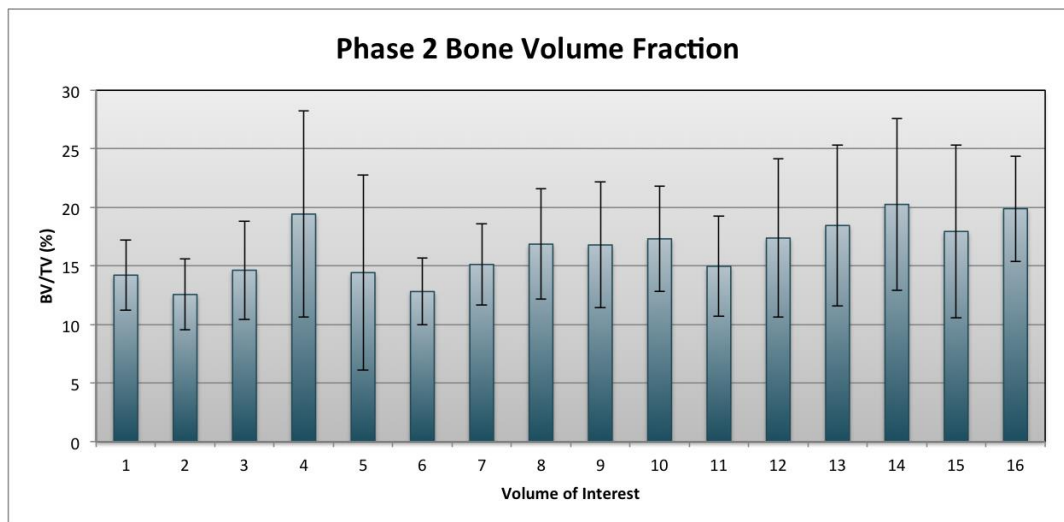
Figure 6.06. Graphic representation of mean (± SD) BV/TV per VOI for individuals in Phase 2. No BV/TV groups were identified; therefore, colour coding has not been applied.

Phase 3

The descriptive statistics for Phase 3 BV/TV at each VOI are displayed in Table 6.03.

Table 6.03. Descriptive statistics for Phase 3 BV/TV for each VOI.

VOI	Mean	Range		SD (±)	RSD (±)
		Phase 3 BV/TV (%)			
		Min	Max		
1	10.67	9.98	11.36	0.98	9.14
2	15.49	11.16	22.40	6.05	39.02
3	16.24	12.72	18.43	3.08	18.98
4	17.13	13.44	19.64	3.27	19.08
5	13.86	12.95	14.78	1.29	9.34
6	15.33	12.68	17.58	2.47	16.12
7	14.16	11.23	18.22	3.63	25.66
8	14.23	12.57	16.87	2.32	16.28
9	24.05	17.78	30.33	8.88	36.91
10	16.55	14.04	18.16	2.20	13.29
11	15.92	11.71	20.18	4.23	26.60
12	22.10	18.77	26.49	3.97	17.95
13	20.11	14.89	28.81	7.58	37.68
14	27.86	26.75	28.97	1.57	5.63
15	29.27	26.92	31.61	3.32	11.33
16	29.70	27.48	31.92	3.14	10.57

The mean values of BV/TV in Phase 3 were observed to vary by a larger degree than those of Phase 2, simultaneously presenting a lower minimum mean of 10.67 % (VOI 1) and a higher maximum mean of 29.70 % (VOI 16). The relative standard deviations in this group were decreased compared with Phase 2, falling between 5.63 % (VOI 14) and 39.02 % (VOI 2). This data is demonstrated graphically in Figure 6.07.

The Phase 3 BV/TV data was found to be normally distributed (Shapiro-Wilk $p = 0.507$) and of equal variance ($p = 0.552$), therefore a parametric one-way ANOVA was used to test for significant differences. A very highly significant difference ($p < 0.001$) was present between VOIs, with an F statistic of 4.348 with 15 degrees of freedom. As the data was parametric, the Holm-Sidak MPC procedure was used to investigate whether this overall difference could be localised to specific VOI pairs. Five pairwise comparisons were revealed to present statistically significant differences [Figure 6.08].
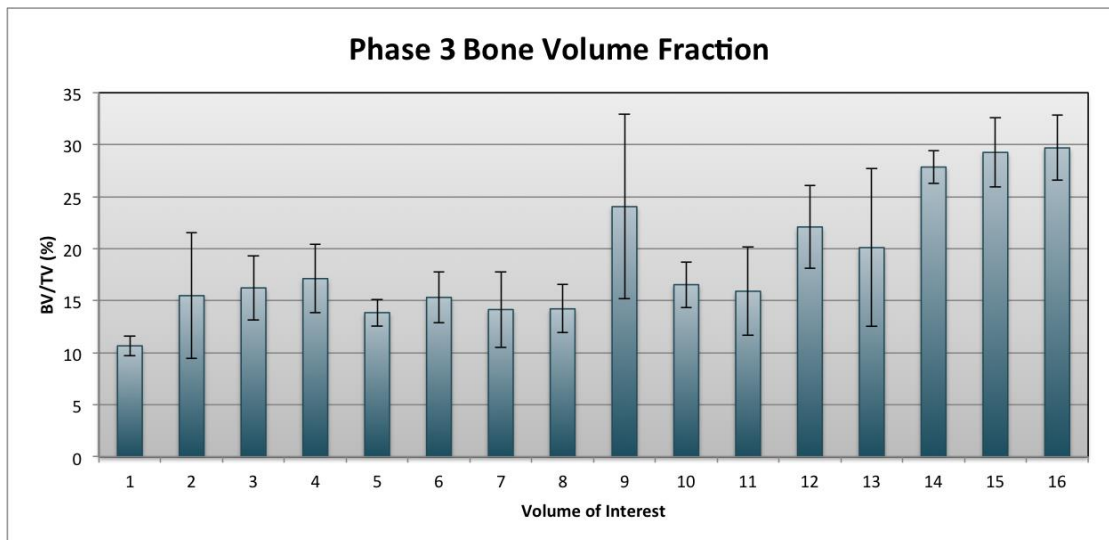
Figure 6.07. Graphical representation of mean (± SD) BV/TV per VOI for individuals in Phase 3.

The pairwise comparisons identified that BV/TV in VOI 1 was significantly lower than VOIs 14 – 16, and that VOIs 7 and 8 were also significantly lower than VOI 16. Several comparisons returned values which were greater than the significance threshold, but fell in close proximity to it, such as the comparisons of VOI 15 with volumes 7 and 8, and the comparison of VOI 16 with volumes 5 and 6. In each of these cases, p was found to be greater than 0.05 but less than 0.1. The limited number of significant differences was not sufficient to formulate designated VOI groupings for Phase 3.

Inter-phase variation by VOI

The mean values for bone volume fraction obtained for each phase independently indicated that there was a change in the quantity and distribution of bone in the ischium at each of these developmental stages [Figure 6.09].

It was noted that for all VOI's, Phase 1 presented the highest mean BV/TV values while the lowest values were distributed between Phase 2 and Phase 3. Most volumes exhibited the lowest BV/TV in Phase 2, with the exception of VOIS 1, 5, 7, 8 and 10 which were found to be lowest in Phase 3. In most cases, the magnitude of difference between mean BV/TV in Phase 2 and 3 was markedly lower than the difference between these two phases and Phase 1.
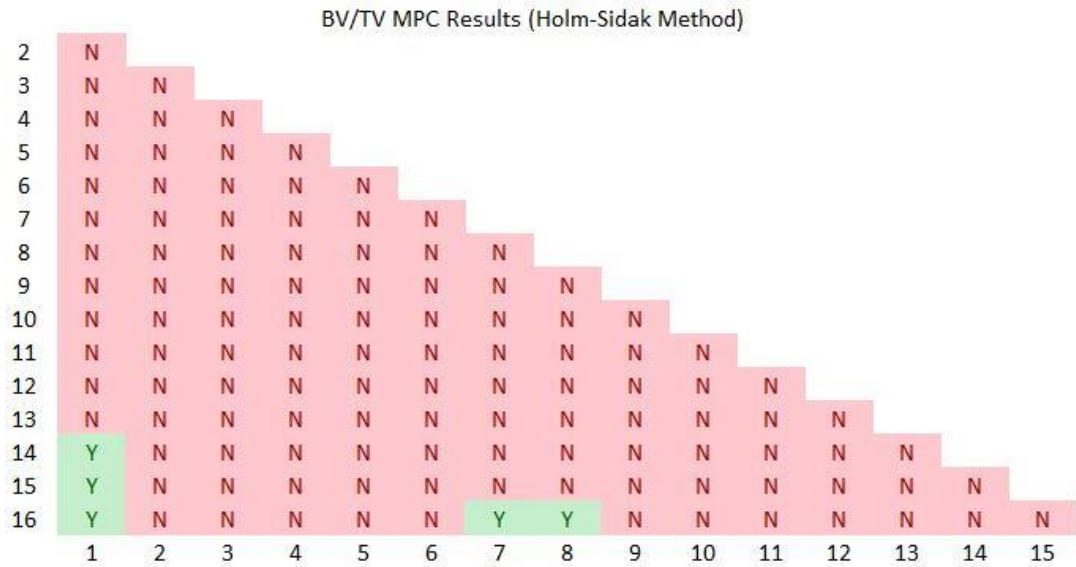
Figure 6.08. MPC results for Phase 3 BV/TV. Y = statistically significant difference (p < 0.05); N = no significant difference detected.
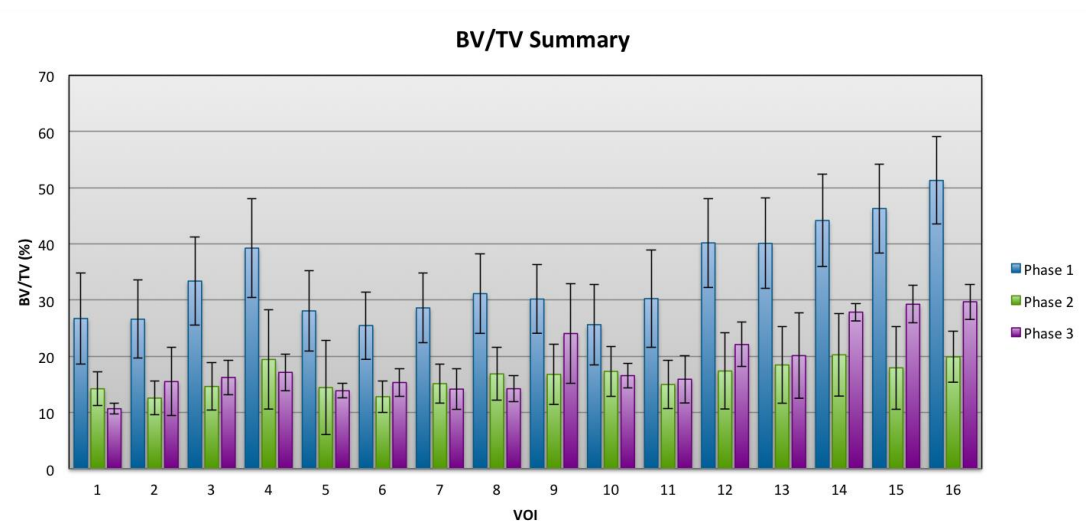
Figure 6.09. Summarised results for mean BV/TV ± SD at each VOI per phase.

To determine whether significant differences were present between phases for each VOI, individual ANOVA tests were conducted for each volume. Volumes 7, 10 and 11 were found to be non-parametric (Shapiro-Wilk p < 0.05) and were therefore analysed using the Kruskal-Wallis one way ANOVA on ranks. All other volumes expressed parametric data and were analysed using a parametric one way ANOVA. The results of the ANOVA (or ANOVA on ranks) for each VOI are outlined in Table 6.04.

*Table 6.04. Analysis of variance results for inter-phase comparisons of BV/TV in each volume of interest. ◊ indicates the test was non-parametric and the H statistic is presented in place of the F statistic. ** highly significant difference (p < 0.01); *** very highly significant difference (p < 0.001).*

VOI	F / H$^\diamond$	DoF	P
1	9.008	2	0.001**
2	11.746	2	< 0.001***
3	18.023	2	< 0.001***
4	15.192	2	< 0.001***
5	11.812	2	< 0.001***
6	13.577	2	< 0.001***
7	16.569$^\diamond$	2	< 0.001***
8	15.397	2	< 0.001***
9	9.762	2	< 0.001***
10	10.926$^\diamond$	2	0.004**
11	14.938$^\diamond$	2	< 0.001***
12	21.042	2	< 0.001***
13	21.553	2	< 0.001***
14	18.659	2	< 0.001***
15	31.113	2	< 0.001***
16	43.174	2	< 0.001***

Analysis of variance revealed that in all 16 volumes of interest there was a statistically significant difference present between phases. Volumes 1 and 10 expressed highly significant differences (p < 0.01), while all remaining VOI were found to be very highly statistically significant (p < 0.001). Multiple pairwise comparison procedures were then applied to all volumes to determine whether significant differences could be identified between specific phases for each VOI. The volumes determined to be parametric were processed using the Holm-Sidak method while the non-parametric volumes were analysed using Dunn's method. A summary of the significant differences identified for each VOI is presented in Figure 6.10.

In all 16 volumes of interest, the bone volume fraction was found to be significantly lower in Phase 2 than in the corresponding Phase 1 volume. In all VOIs except VOI 9, it was also identified that BV/TV was significantly lower in Phase 3 than in Phase 1. The pairwise comparison of VOI 9 in Phase 1 and 3 revealed the BV/TV to be statistically similar in both phases. No statistically significant differences were found to exist between the VOI in Phase 2 and those of Phase 3, indicating a greater consistency in BV/TV in these phases.
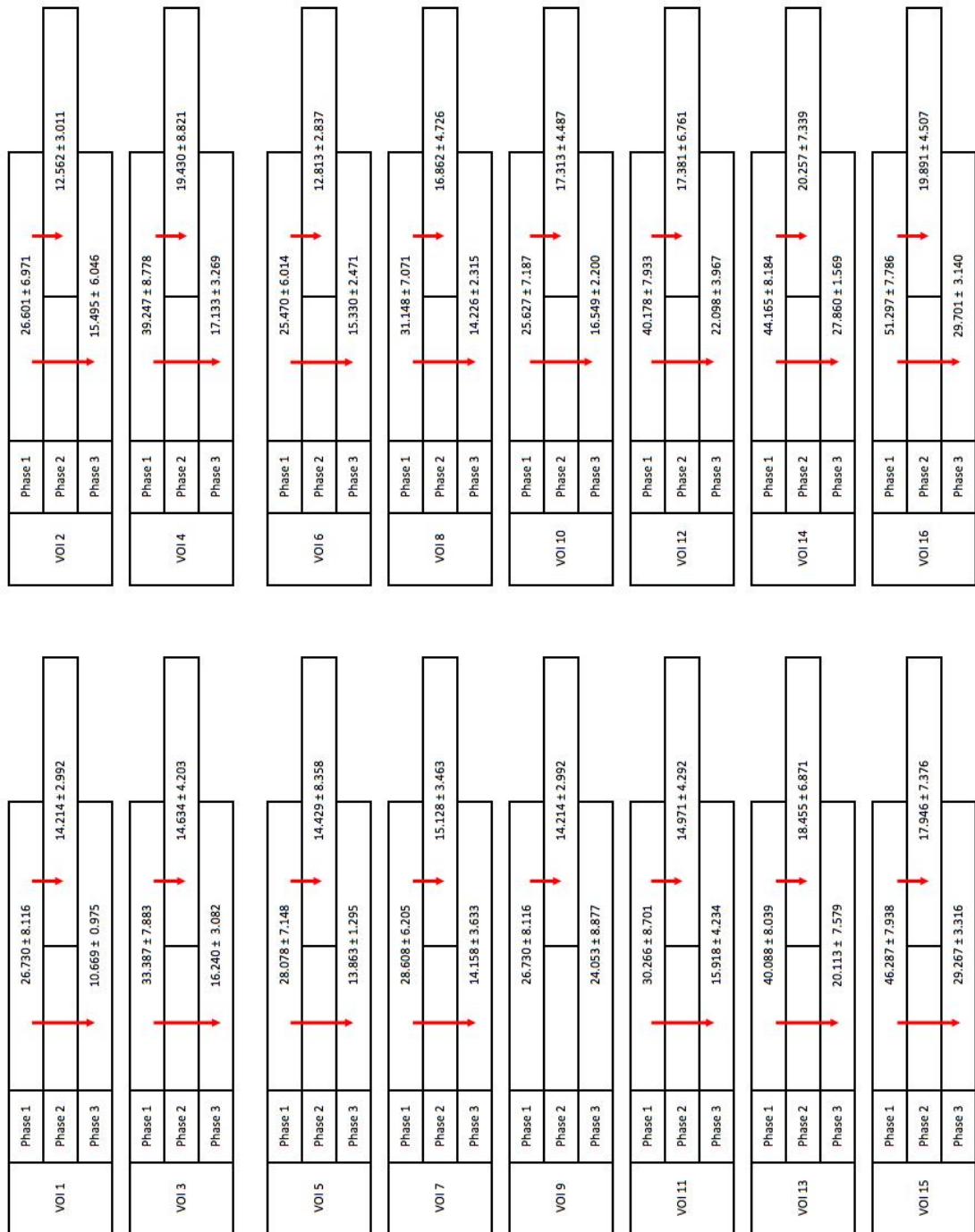
Figure 6.10. Multiple pairwise comparison results for inter-phase analysis at each volume of interest. Values are mean ± SD. Red arrow indicates significant difference exists between connecting phases (p < 0.05), arrow directionality shows decreasing BV/TV.

6.2.2 Trabecular thickness

Phase 1

The descriptive statistics for trabecular thickness are displayed in Table 6.05.

Table 6.05. Descriptive statistics (mean, range, standard deviation and relative standard deviations) for Phase 1 trabecular thickness in each volume of interest.

Phase 1 Tb.Th (µm)					
VOI	**Mean**	**Range**		**SD (±)**	**RSD (±)**
		Min	**Max**		
1	96.75	81.88	119.33	9.24	9.55
2	104.16	89.77	134.86	9.91	9.52
3	111.43	94.39	128.77	9.07	8.14
4	112.46	83.34	130.26	10.55	9.38
5	113.86	91.06	135.26	10.85	9.53
6	121.74	107.39	137.62	9.30	7.64
7	130.30	114.24	147.67	10.02	7.69
8	116.86	91.19	137.98	10.73	9.18
9	130.68	109.02	154.39	13.70	10.49
10	140.92	121.03	163.85	11.49	8.15
11	152.86	133.20	177.61	13.00	8.50
12	145.22	119.94	184.86	16.98	11.69
13	151.34	129.83	174.73	12.37	8.17
14	123.46	98.10	148.34	14.48	11.73
15	133.01	113.33	157.63	10.96	8.24
16	142.84	116.66	162.69	10.70	7.49

Mean trabecular thicknesses varied between each VOI in Phase 1, from a minimum mean of 96.75 µm (VOI 1) to a maximum mean of 152.86 µm (VOI 11). The standard deviations for Tb.Th displayed less variation than was observed for BV/TV, with RSD values falling within a maximum range of 7.49 % (VOI 16) and 11.73 % (VOI 14), with all VOIs except 9, 12 and 14 presenting RSD values below 10 %.The mean and standard deviations obtained for each VOI in this phase are displayed graphically in Figure 6.11.
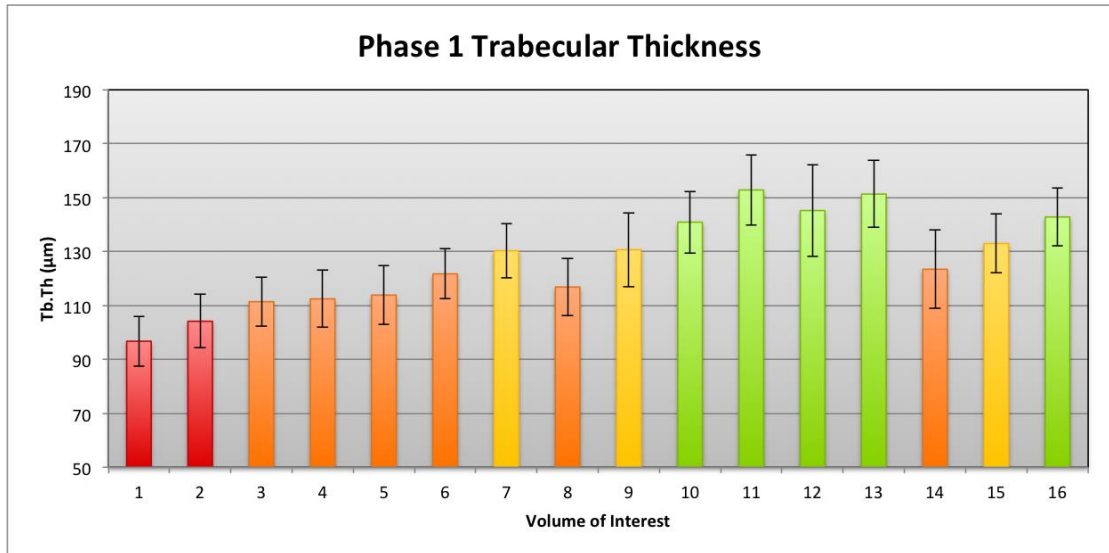
Figure 6.11. Mean trabecular thickness values and standard deviations observed at each VOI in Phase 1 individuals. High (green), intermediate (yellow), low-intermediate (orange) and low (red) colouration applied based on MPC testing.

The Phase 1 trabecular thicknesses were found to be parametric in nature (Shapiro-Wilk p = 0.551; equal variance p = 0.083), therefore a parametric one way ANOVA was used to test for significant differences within the data. A very highly significant difference was returned, with an F statistic of 42.131 with 15 degrees of freedom.

Multiple pairwise comparisons following the parametric Holm-Sidak procedure were applied to investigate whether significant differences existed between specific VOI pairs. The majority of these comparisons were found to be significantly different, with only 43 out of 120 comparisons returning a result which was not significant [Figure 6.12]. The distribution of these significant differences were mapped and it was determined that four groups were most suitable to describe the data, comprised of low, low-intermediate, intermediate and high Tb.Th groups [Figure 6.13].

The low Tb.Th group (red), comprised of VOI 1 and 2, were identified as being significantly lower than the majority of other volumes in this Phase. Indeed, the trabeculae of VOI 1 were significantly thinner than all other VOI except VOI 2, while those in VOI 2 were found to be thinner than all except VOIs 1, 3, 4 and 5. The values for these two VOI were 96.75 µm and 104.16 µm respectively.

The low-intermediate group (orange) was introduced for this parameter to describe VOI 3 -6, 8 and 14, which exhibited Tb.Th values that remained significantly thinner

than the majority of VOIs, but were also observed to be of significantly higher Tb.Th than the low-thickness group (specifically VOI 1).

Tb.Th MPC Results (Holm-Sidak)

	1	2	3	4	5	6	7	8	9	10	11	12	13	14	15
2	N														
3	Y	N													
4	Y	N	N												
5	Y	N	N	N											
6	Y	Y	N	N	N										
7	Y	Y	Y	Y	Y	N									
8	Y	Y	N	N	N	N	Y								
9	Y	Y	Y	Y	Y	N	N	Y							
10	Y	Y	Y	Y	Y	Y	N	Y	N						
11	Y	Y	Y	Y	Y	Y	Y	Y	Y	N					
12	Y	Y	Y	Y	Y	Y	Y	Y	Y	N	N				
13	Y	Y	Y	Y	Y	Y	Y	Y	Y	N	N	N			
14	Y	Y	N	N	N	N	N	N	N	Y	Y	Y	Y		
15	Y	Y	Y	Y	Y	N	N	Y	N	N	Y	Y	Y	N	
16	Y	Y	Y	Y	Y	Y	Y	Y	N	N	N	N	N	Y	N
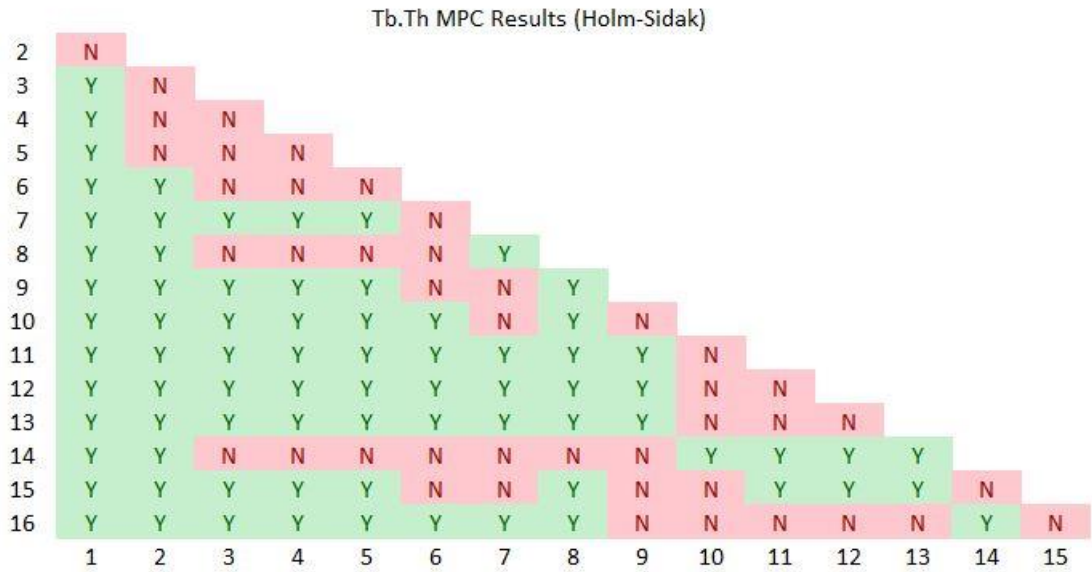
Figure 6.12. Multiple pairwise comparison results for Phase 1 Tb.Th. Y = statistically significant difference (p < 0.05); N = no significant difference detected.

Figure 6.13. Trabecular thickness groups mapped to the perinatal ischium. Green: high Tb.Th; yellow: intermediate Tb.Th; orange: low-intermediate Tb.Th; red: low Tb.Th. The values below the VOI number are is the mean Tb.Th (μm) of that volume.

None of the VOIs classified as low-intermediate differed significantly from each other. Values for this group fell between 111.43 μm and 123.46 μm.

The intermediate group (yellow) consisted of three isolated VOI, 7, 9 and 15, which were found to share boundaries with both the low-intermediate and high thickness groups. They were both numerically and statistically central within the data, with mean thicknesses between 130.30 µm and 133.01 µm, and demonstrated significant pairwise differences with volumes in each of low, low-intermediate and high thickness groups.

The high thickness group (green) was identified as primarily occupying the central region of the ischium, in VOI 10 – 13, in addition to VOI 16 distally in the ramus. The mean trabecular thicknesses were found to range between 140.92 µm and 152.86 µm, with the both extreme values found in neighbouring VOIs (10 and 11). As with previous groupings, no significant pairwise results were observed between members of the high thickness group, but mean thicknesses were significantly larger than the majority of VOIs that fell outwith this group, with the lowest rate being eight significant results out of eleven for VOI 10.

Phase 2

The descriptive statistics for Phase 2 trabecular thickness are presented in Table 6.06.

The mean values for trabecular thickness in Phase 2 were found to be more similar throughout the ischium than those of Phase 1, ranging between 127.91 µm (VOI 1) and 160.80 µm (VOI 11). Individual variation in this group remained low, with RSD values between 4.62 % (VOI 1) and 20.61% (VOI 4), although it should be noted that each of these values was notably distinct from their nearest neighbours. The second lowest and highest RSD values were found to be 8.88 % (VOI 2) and 16.77 % (VOI 8), which more closely delimited the remaining volumes. The means and standard deviations for this data are presented in Figure 6.14.

The Phase 2 Tb.Th data was not normally distributed (Shapiro-Wilk $p < 0.05$) therefore the non-parametric Kruskal-Wallis ANOVA on ranks was applied to test for significant differences. An H statistic of 18.999 was returned with 15 degrees of freedom, with an associated p value of 0.214. This result was not statistically significant ($p > 0.05$) therefore multiple pairwise comparisons were consequently not applied to this data.

Table 6.06. Descriptive statistics for Phase 2 Tb.Th at each VOI.

VOI	Mean	Range		SD (±)	RSD (±)
		Min	Max		
1	127.91	120.62	135.84	5.90	4.62
2	134.10	123.86	152.78	11.91	8.88
3	138.00	120.30	168.37	19.34	14.02
4	137.63	115.48	182.61	28.37	20.61
5	139.42	122.41	154.56	13.05	9.36
6	144.95	129.59	166.52	14.13	9.75
7	153.64	135.60	184.58	19.67	12.80
8	141.96	122.89	179.28	23.81	16.77
9	151.39	120.13	177.27	23.10	15.26
10	150.26	125.32	179.50	20.56	13.68
11	160.80	138.45	188.71	19.08	11.87
12	157.22	133.21	196.81	24.63	15.67
13	160.14	140.24	187.39	17.94	11.20
14	136.79	114.32	166.99	21.65	15.83
15	140.37	121.17	170.58	19.91	14.18
16	139.80	122.41	162.11	16.21	11.59
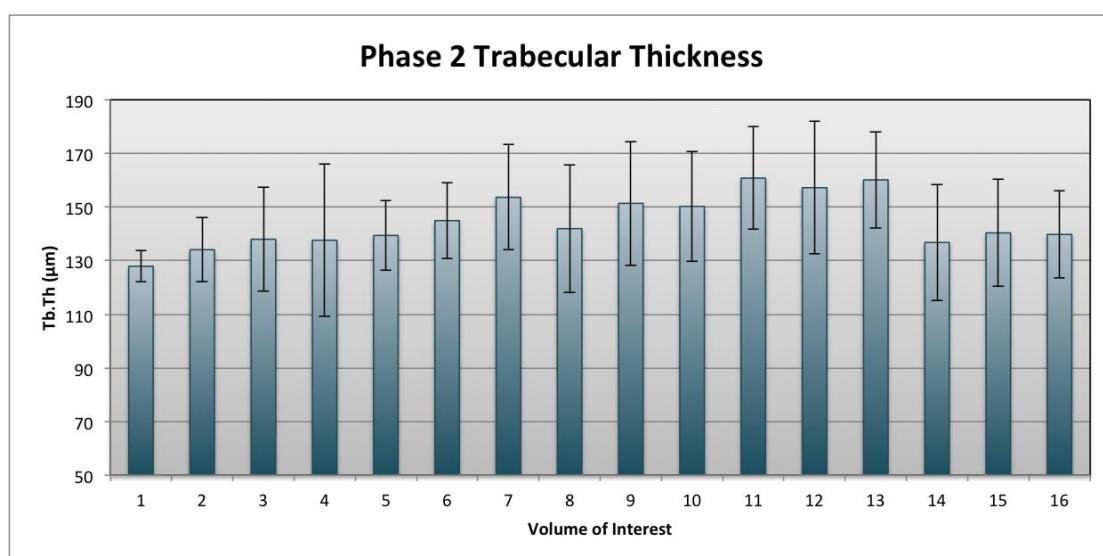
Figure 6.14. Graphical representation of the mean Tb.Th and standard deviations at each VOI in Phase 2.

Phase 3

The descriptive statistics documenting trabecular thickness in the ischium in Phase 3 are presented in Table 6.07.

The mean trabecular thickness values for Phase 3 across the ischium were noted to be greater than those observed in Phase 1 and 2 previously. The lowest mean thickness in

this group was found to be 163.47 μm (VOI 8), while the maximum mean thickness was 228.26 μm (VOI 9). Individual variation was also greater in this group, with a RSD range of 2.80 % (VOI 14) t0 27.06 % (VOI 9). The mean Tb.Th and standard deviations for this phase are summarised graphically in Figure 6.15.

Table 6.07. Descriptive statistics for Phase 3 Tb.Th at each VOI.

Phase 3 Tb.Th (μm)					
VOI	**Mean**	**Range**		**SD (±)**	**RSD (±)**
		Min	**Max**		
1	166.85	150.78	182.93	22.73	13.62
2	172.24	145.49	190.12	23.60	13.70
3	167.94	146.53	179.50	18.56	11.05
4	173.00	139.77	195.46	29.37	16.98
5	190.96	161.30	220.63	41.95	21.97
6	192.89	159.50	214.43	29.32	15.20
7	191.30	160.36	209.89	26.98	14.10
8	163.47	142.59	189.59	23.93	14.64
9	228.26	184.59	271.94	61.77	27.06
10	199.91	168.85	219.93	27.27	13.64
11	206.60	188.41	218.98	16.10	7.79
12	205.09	176.97	228.05	25.92	12.64
13	206.67	170.24	239.25	34.67	16.77
14	203.47	199.44	207.51	5.70	2.80
15	216.67	196.75	236.59	28.17	13.00
16	198.16	187.92	208.40	14.49	7.31

The Phase 3 Tb.Th data was found to be non-parametric (Shapiro-Wilk $p < 0.05$) therefore a Kruskal-Wallis ANOVA on ranks was applied to the data. The p values for this test was found to be 0.391, with an H statistic of 15.869 and 15 degrees of freedom, demonstrating that, as with Phase 2, no significant differences were identifiable in the Phase 3 trabecular thickness. Multiple pairwise comparisons were not conducted as there was no overall significant difference to investigate further.

Inter-phase variation by VOI

To facilitate a direct comparison of the trabecular thicknesses between each of the three phases, a summary of the mean Tb.Th ± SD in each volume are presented in Figure 6.16.
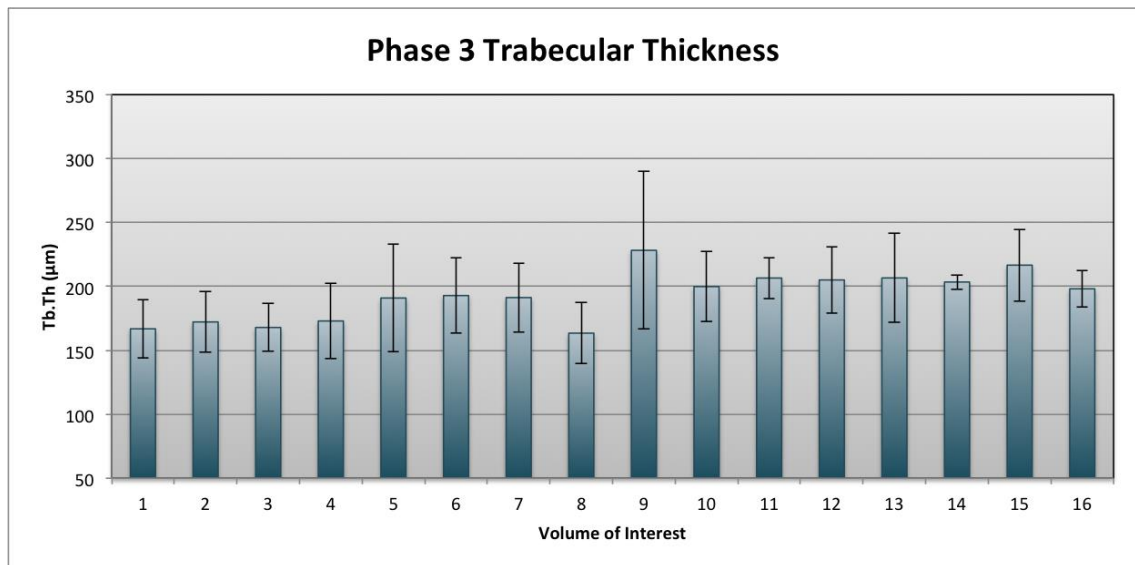
Figure 6.15. Summary of mean Tb.Th values and standard deviations for each VOI in Phase 3.

It was observed that in all volumes of interest, trabecular thickness was highest in Phase 3. Indeed, the lowest observed Phase 3 mean value was higher than the maximum Tb.Th observed in Phases 1 or 2. The lowest Tb.Th values were found in Phase 1 for VOI 1 – 15, while in VOI 16 Phase 2 Tb.Th was found to be slightly lower than that of Phase 1.
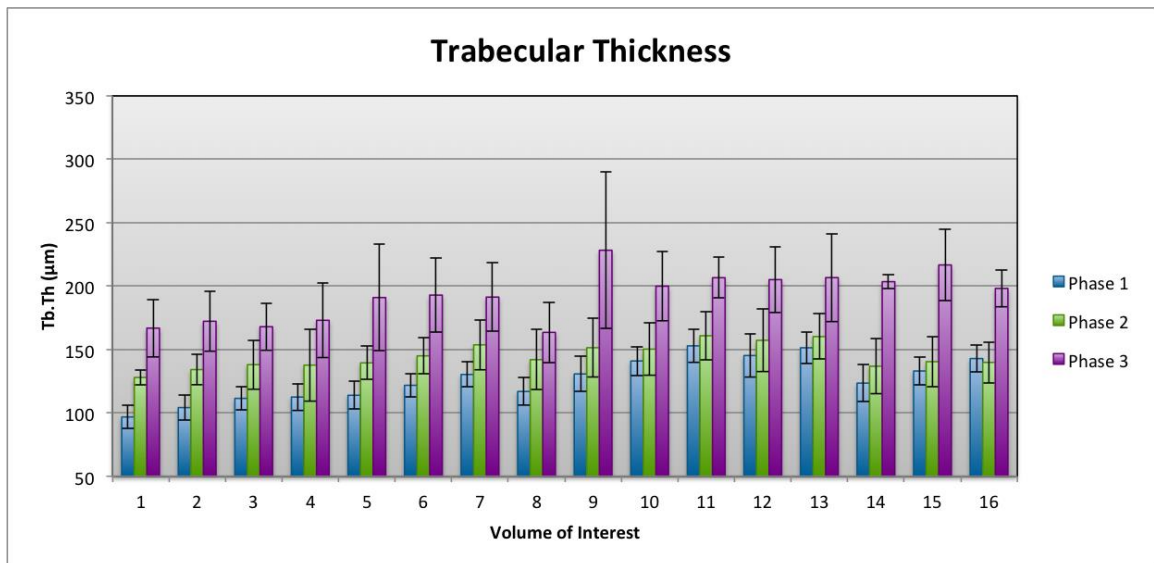
Figure 6.16. Summarised results for mean Tb.Th ± SD at each VOI per phase.

Analysis of variance was used to determine whether the observed differences between each parameter reached the level of statistical significance for each VOI. The data for volumes 1, 3, 11, 12, 14 and 16 were found to be parametric and were therefore analysed using a one-way ANOVA, while the remaining volumes failed the test of equal variance ($p < 0.05$) and were therefore processed using the Kruskal-Wallis one-way

ANOVA on ranks. Significant differences were identified for volumes of interest 1 – 14 and 16 (p < 0.05) [Table 6.08]. The differences in Tb.Th at VOI 15 did not reach the level of statistical significance, although the p value very closely approximated the threshold of significance (p = 0.052).

*Table 6.08. Analysis of variance results for inter-phase comparisons of Tb.Th in each volume of interest. ◊ indicates data was non-parametric, and therefore subject to ANOVA on ranks. * significant result (P < 0.05); ** highly significant difference (P < 0.01); *** very highly significant difference (P < 0.001).*

VOI	F / H$^{◊}$	DoF	P
1	60.232	2	< 0.001***
2	15.792$^{◊}$	2	< 0.001***
3	32.819	2	< 0.001***
4	11.376$^{◊}$	2	0.003**
5	13.040$^{◊}$	2	0.001**
6	14.766$^{◊}$	2	< 0.001***
7	12.747$^{◊}$	2	0.002**
8	12.597$^{◊}$	2	0.002**
9	8.040$^{◊}$	2	0.018*
10	8.054$^{◊}$	2	0.018*
11	18.178	2	< 0.001***
12	12.735	2	< 0.001***
13	7.333$^{◊}$	2	0.026*
14	24.010	2	< 0.001***
15	5.929$^{◊}$	2	0.052
16	20.147	2	< 0.001***

Following the identification of significant differences in VOI 1 – 14 and 16, multiple pairwise comparisons were conducted to determine whether statistical differences were present between specific phase pairs at each VOI. The Holm-Sidak MPC procedure was used for those volumes which were previously identified as parametric, while Dunn's method was used to appraise the non-parametric data. The results of these pairwise comparisons are summarised in Figure 6.17.

For each VOI which presented significant differences following ANOVA testing, the mean trabecular thickness was found to be significantly higher in Phase 3 when compared with that of Phase 1. In volumes 3, 11, 12, 14 and 16, the mean trabecular thickness of Phase 3 was also significantly higher than that of Phase 2, while in the remaining volumes there was no significant difference between Phases 2 and 3. The comparison of values between Phases 1 and 2 revealed that the mean trabecular

thickness of Phase 2 was significantly higher in VOIs 1 -3 and 5 – 8 than in Phase 1, while for the remaining volumes no significant differences were found.
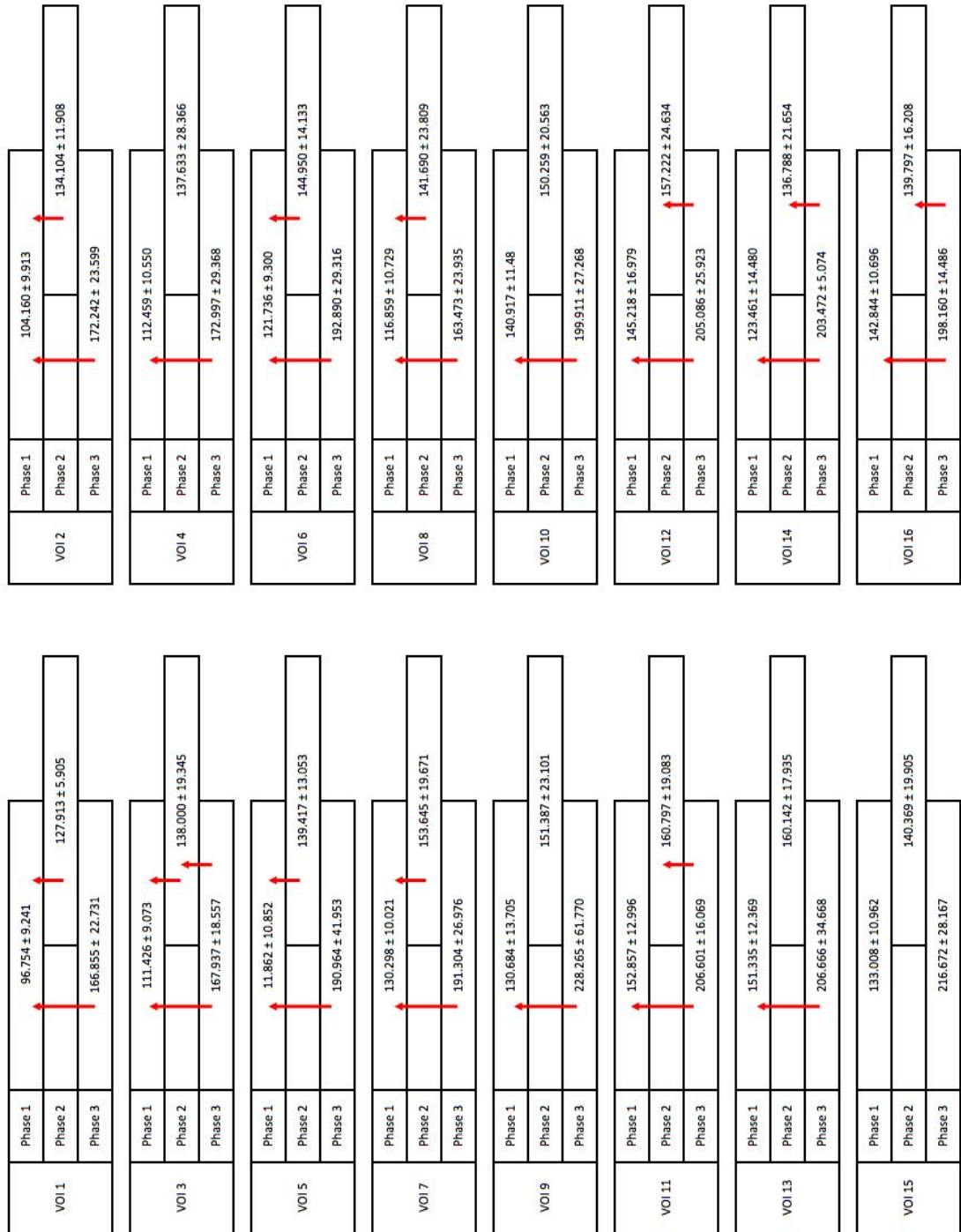
Figure 6.17. Multiple pairwise comparison results for inter-phase analysis at each volume of interest. Values are mean ± SD. Red arrow indicates significant difference exists between connecting phases (p < 0.05), arrow directionality shows decreasing Tb.Th.

6.2.3 Trabecular number

Phase 1

Table 6.09 summarises the descriptive statistics for trabecular number at each VOI in Phase 1.

Table 6.09. Descriptive statistics (mean, range, standard deviation and relative standard deviations) for Phase 1 trabecular number in each volume of interest.

		Phase 1 Tb.N (mm^{-1})			
VOI	**Mean**	**Range**		**SD (±)**	**RSD (±)**
		Min	**Max**		
1	2.74	1.82	3.92	0.67	24.51
2	2.57	1.63	3.50	0.63	24.38
3	2.98	2.27	3.94	0.60	20.21
4	3.47	2.48	4.36	0.62	17.87
5	2.45	1.71	3.39	0.51	20.94
6	2.09	1.30	2.85	0.45	21.69
7	2.20	1.46	2.87	0.45	20.43
8	2.66	1.83	3.68	0.52	19.40
9	2.33	1.40	3.50	0.49	20.98
10	1.83	1.18	2.87	0.53	29.13
11	1.98	1.24	2.90	0.54	27.07
12	2.77	1.92	3.44	0.47	16.79
13	2.65	1.72	3.40	0.48	18.10
14	3.58	2.98	4.50	0.50	14.11
15	3.47	2.70	4.28	0.48	13.70
16	3.60	3.00	4.15	0.38	10.68

The mean trabecular number was found to range between 1.83 mm^{-1} (VOI 10) and 3.60 mm^{-1} (VOI 16). The degree of individual variation remained consistent with values observed previously for BV/TV and Tb.Th, presenting RSD values between 10.68 % (VOI 16) and 29.10 % (VOI 10). This data is summarised in Figure 6.18.

The trabecular number data for Phase 1 was found to be non-parametric (Shapiro-Wilk $p < 0.05$), therefore a Kruskal-Wallis ANOVA on ranks was used to determine whether any significant differences were present for this parameter. An H statistic of 169.383 with 15 degrees of freedom was returned, for which the corresponding p value was very highly significant ($p < 0.001$).
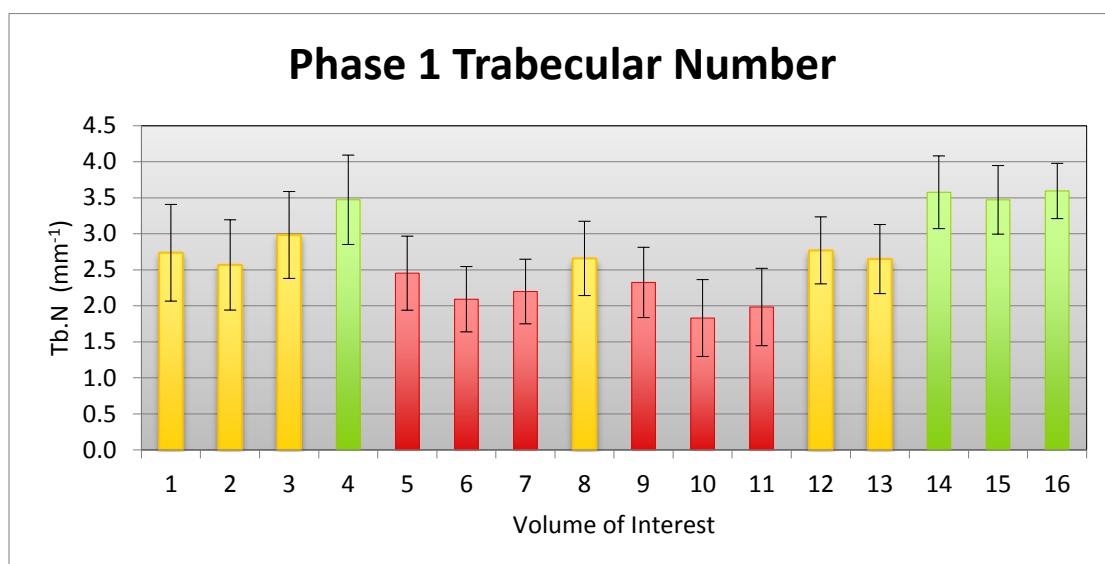
Figure 6.18. Bar chart representing mean Tb.N (± SD) per VOI for Phase 1 individuals. High (green), intermediate (lime), intermediate (yellow) and low (red) colouration applied based on MPC testing.

The identification of an overall significant difference between volumes for Tb.N in Phase 1 was further investigated using multiple pairwise comparisons to determine whether significant differences existed between specific VOI pairs.

Although the majority of volume pairs did not return significant results, significant differences were identified in approximately one third of comparisons [Figure 6.19]. The distribution of these differences was examined to identify whether any groups of volumes presented statistically similar values, and it was determined that the Phase 1 Tb.N data could be described adequately using 3 groups: a high (green), intermediate (yellow) and low (red) Tb.N group [Figure 6.20].

The low Tb.N group (red) was found to contain six volumes, including VOIs 5 – 7 and 9 – 11, with mean values between 1.83 mm^{-1} and 2.45 mm^{-1}. The trabecular number in each of these volumes were found to be statistically lower than each volume designated as having high Tb.N, and in addition in five comparisons were found to be significantly lower than the intermediate group. Members of this group were united by common borders, creating a central region defined by the low Tb.N values expressed.

The high Tb.N group (green) was found to contain four volumes of interest, the isolated anterosuperior VOI 4 and the inferior VOIs 14 – 16. The mean values for these volumes fell between 3.47 mm^{-1} and 3.60 mm^{-1}, thus incorporating all VOI which exceeded a mean of 3 mm^{-1}.

Tb.N Multiple Pairwise Comparisons (Dunn's Method)

	1	2	3	4	5	6	7	8	9	10	11	12	13	14	15
2	N														
3	N	N													
4	N	N	N												
5	N	N	N	Y											
6	N	N	Y	Y	N										
7	N	N	N	Y	N	N									
8	N	N	N	N	N	N	N								
9	N	N	N	Y	N	N	N	N							
10	Y	N	Y	Y	N	N	N	N	N						
11	N	N	Y	Y	N	N	N	N	N	N					
12	N	N	N	N	N	N	N	N	N	Y	N				
13	N	N	N	N	N	N	N	N	N	N	N	N			
14	N	Y	N	N	Y	Y	Y	Y	Y	Y	Y	N	Y		
15	N	Y	N	N	Y	Y	Y	N	Y	Y	Y	N	N	N	
16	Y	Y	N	N	Y	Y	Y	Y	Y	Y	Y	N	Y	N	N
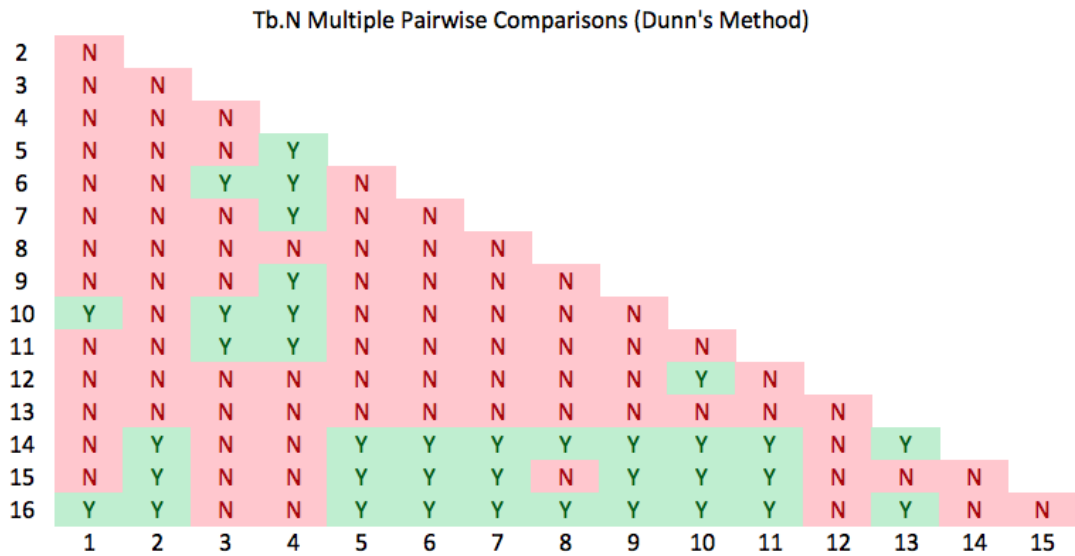
Figure 6.19. Results of multiple pairwise comparisons for Phase 1 trabecular number. Y = statistically significant difference (p < 0.05); N = no signficant difference.
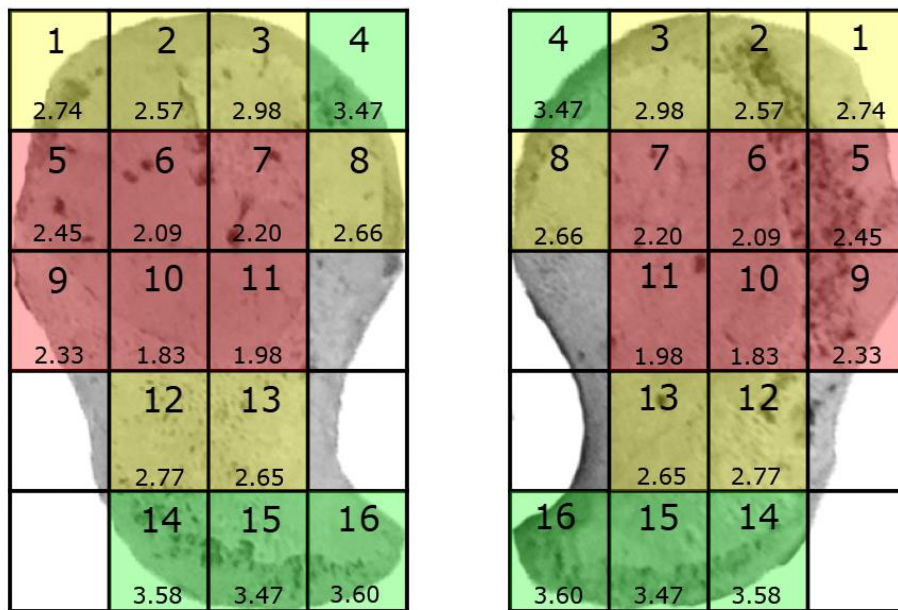
Figure 6.20. Diagrammatic representation of Tb.N groupings as indicated by multiple pairwise comparisons. Green: high Tb.N; Yellow: intermediate Tb.N; red: low Tb.N. The values below the volume number document the mean trabecular number for that VOI (mm⁻¹).

The trabecular number in each of these volumes was significantly higher than those of the low Tb.N group, and in addition VOI 14, 15 and 16 showed intermittent statistically significant differences from the intermediate group.

The remaining six VOIs presented intermediate values with no clear statistical alignment but rather appeared transitional volumes separating those designated as low and high. Volume 2 was found to be significantly lower than VOI 14 – 16 while VOI 8 and 13 were significantly lower than VOI 14 and 16 only. Conversely, VOI 3 was found to be significantly higher than VOIs 6, 10 and 11, while VOI 12 was significantly higher than VOI 10 alone. Volume 1 presented only two significant differences: one with VOI 10, the lowest observed Tb.N, and one with VOI 16, the highest Tb.N.

Phase 2

The descriptive statistics for Phase 2 trabecular number at each volume of interest are presented in Table 6.10.

The mean trabecular number in this phase fell between a minimum of 0.88 mm^{-1} (VOI 6) and a maximum of 1.41 mm^{-1} (VOI 16), in all cases lower than the mean values previously obtained for individuals in Phase 1. The relative standard deviations demonstrated values of 6.79 % (VOI 16) to 37.40 % (VOI 4), although only three VOI exceeded a RSD of 25 % (VOI 4, 11 and 14). This data is summarised in Figure 6.21.

Analysis of variance was used to determine whether any statistically significant differences were present within the Phase 2 Tb.N data. This dataset was found to be non-parametric (Shapiro-Wilk p < 0.05), therefore the Kruskal-Wallis one-way ANOVA on ranks was used. The results confirmed that there was a significant difference between the groups analysed (H = 30.359 with 15 degrees of freedom, therefore p = 0.011).

Following the positive identification of a significant difference, Tukey's multiple pairwise comparisons procedure was applied to determine whether individual volume pairs demonstrated significant differences. Only a single comparison was found to reach the level of statistical significance: VOI 6 was found to be of significantly lower Tb.N than VOI 16 [Figure 6.22].

As a significant result occurred exclusively between the maximum and minimum observed Tb.N values for this phase, it was not appropriate to divide the volumes into groups based on this result.

Table 6.10. Descriptive statistics for Phase 2 Tb.N in each volume of interest.

		Phase 2 Tb.N (mm^{-1})			
VOI	**Mean**	**Range**		**SD (±)**	**RSD (±)**
		Min	**Max**		
1	1.11	0.81	1.35	0.20	18.15
2	0.93	0.82	1.17	0.14	15.53
3	1.04	0.85	1.36	0.21	20.48
4	1.33	0.88	2.09	0.50	37.40
5	1.03	0.85	1.21	0.13	12.48
6	0.88	0.67	1.02	0.13	14.51
7	0.97	0.71	1.12	0.15	15.86
8	1.16	0.82	1.40	0.22	19.05
9	1.19	1.04	1.40	0.15	12.83
10	0.94	0.74	1.10	0.13	13.82
11	0.97	0.54	1.22	0.26	26.43
12	1.22	0.86	1.61	0.29	23.91
13	1.12	0.84	1.35	0.18	16.44
14	1.40	0.87	2.20	0.51	36.39
15	1.26	1.07	1.60	0.21	16.44
16	1.41	1.28	1.55	0.10	6.79
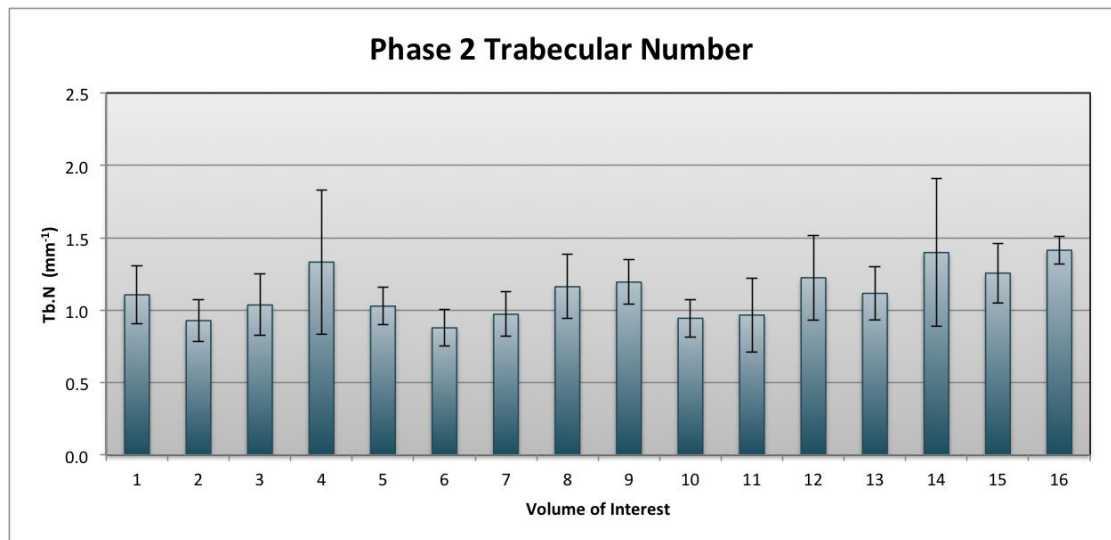
Figure 6.21. Graphical representation of mean Tb.N (± SD) per VOI for Phase 2 individuals.
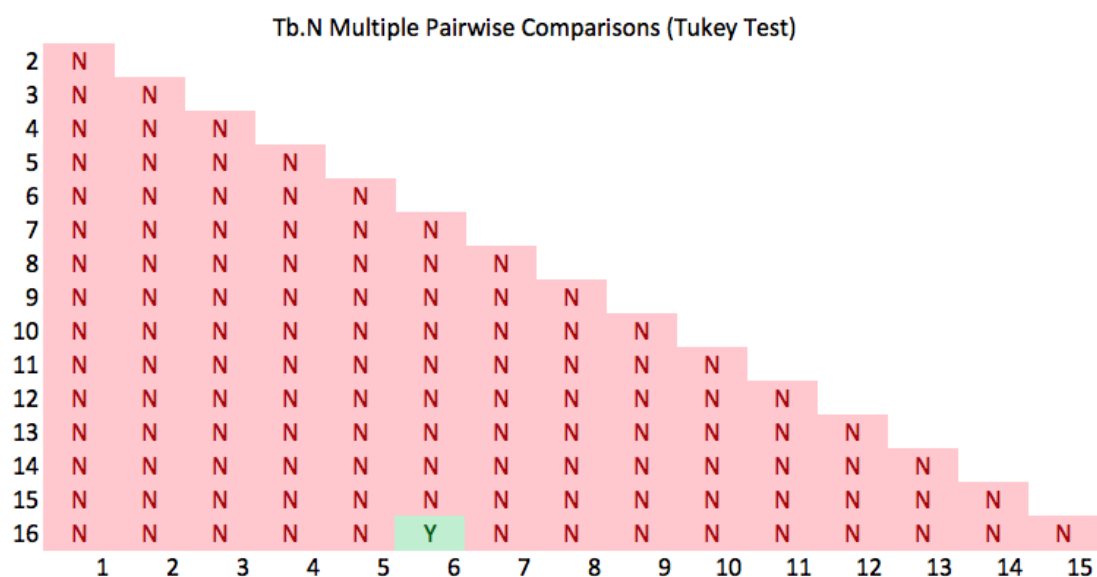
Figure 6.22. Results of MPC testing of Phase 2 Tb.N data. Y = significant difference (p < 0.05); N = no significant difference present.

Phase 3

The descriptive statistics for Tb.N in Phase 3 are presented in Table 6.11.

Table 6.11. Descriptive statistics for Phase 3 Tb.N in each volume of interest.

		Phase 3 Tb.N (mm^{-1})			
VOI	Mean	Range		SD (±)	RSD (±)
		Min	Max		
1	0.64	0.62	0.66	0.03	4.42
2	0.89	0.71	1.18	0.26	28.85
3	0.96	0.87	1.03	0.08	8.64
4	0.99	0.96	1.00	0.02	2.34
5	0.74	0.67	0.80	0.09	12.51
6	0.80	0.73	0.86	0.07	8.17
7	0.74	0.55	0.87	0.17	22.88
8	0.87	0.79	0.93	0.07	8.29
9	1.04	0.96	1.12	0.11	10.88
10	0.83	0.83	0.83	0.00	0.00
11	0.77	0.55	0.92	0.19	25.28
12	1.07	1.00	1.16	0.08	7.53
13	0.96	0.71	1.20	0.25	25.48
14	1.37	1.34	1.40	0.04	3.10
15	1.36	1.34	1.37	0.02	1.57
16	1.50	1.46	1.53	0.05	3.31

Mean values for Tb.N in this phase were found to range from 0.64 mm^{-1} (VOI 1) to 1.50 mm^{-1} (VOI 16), a wider range than was observed for Phase 2 Tb.N. Relative standard

deviations also varied between volumes, presenting values of 0 % for VOI 10, in which each of the 3 specimens returned the identical value of 0.83 mm^{-1}, to 28.85 % for VOI 2. The data for this phase is summarised graphically in Figure 6.23.

The trabecular number data was found to be parametric (Shapiro-Wilk p = 0.100; Equal variance p = 0.217), therefore a one-way ANOVA was used to determine whether an overall significant difference was present between VOIs. An F statistic of 7.547 with 15 degrees of freedom was returned, corresponding to a very highly significant difference (p < 0.001). Multiple pairwise comparison procedures following the Holm-Sidak method were applied to further investigate this difference. Twenty-six pairwise comparisons returned significant differences [Figure 6.24].
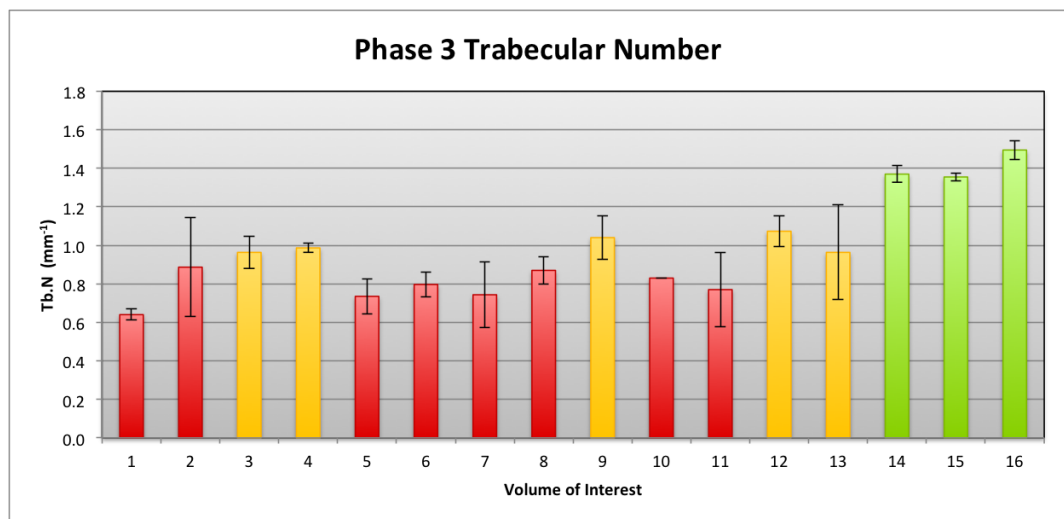
Figure 6.23. Phase 3 mean Tb.N ± SD per VOI. High (green), intermediate (yellow) and low (red) colourations applied based on MPC testing.

As with Phase 1 MPC results, the largest proportion of observed pairwise differences were found between the highest Tb.N regions located inferiorly in the ramus (VOIs 14, 15 and 16) and the lower values located centrally and postero-superiorly. The distribution of these pairwise significant differences facilitated the creation of three VOI groups, high (green), intermediate (yellow) and low (red) for Phase 3 Tb.N [Figure 6.25].

The low trabecular number group (red) in this Phase comprised of 8 volumes of interest (1, 2, 5 – 8, 10 and 11) with mean values of 0.64mm^{-1} to 0.89mm^{-1}. The mean value for each of these volumes, with the exception of VOI 2, was found to statistically lower than VOI 14 – 16 alone, while VOI 2 was found to be statistically lower than VOI

15 and 16 alone. These groups shared common borders, forming a conglomeration posterosuperiorly which extended anteriorly and inferiorly to occupy most volumes associated with the acetabular margin and fossa.
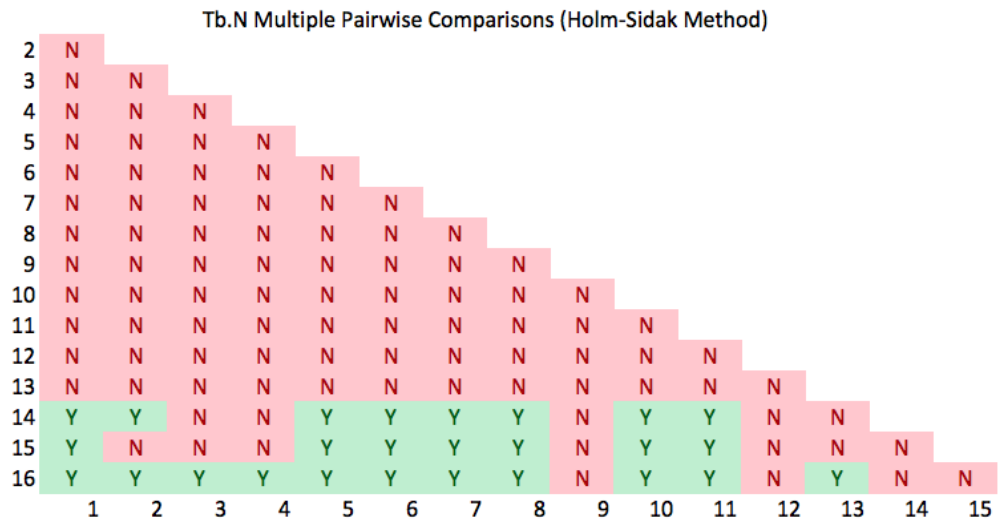
Figure 6.24. Multiple pairwise comparison results for Tb.N in Phase 3. Y = statistically significant difference (p < 0.05); N = no significant difference detected.
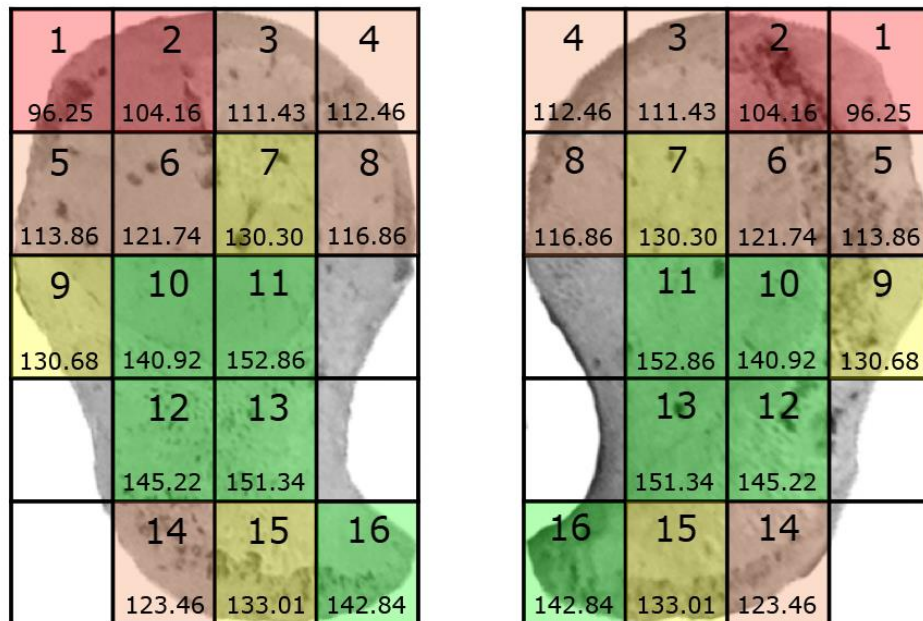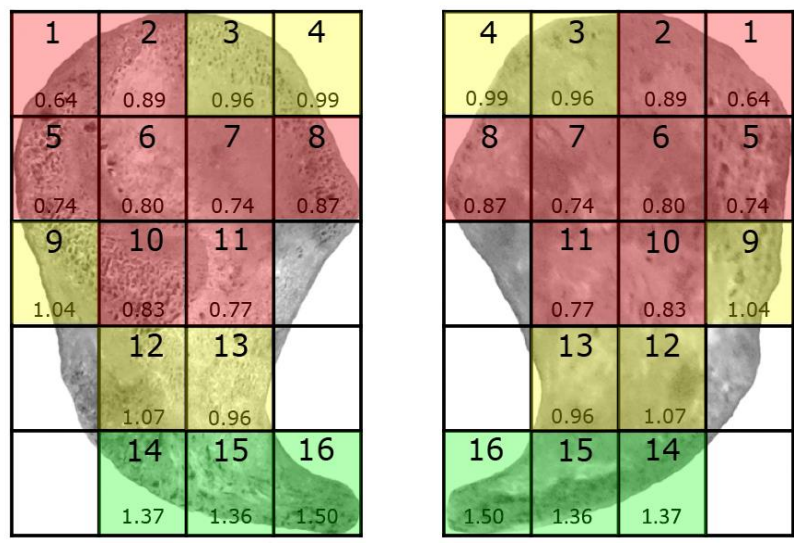

Figure 6.25. Trabecular number groups mapped to the Phase 3 ischium. Green: high Tb.N; yellow: intermediate Tb.N; red: low Tb.N. The lower value in the VOI is the mean Tb.N observed for that volume (mm^{-1}).

The high Tb.N group (green) in this phase consisted on VOI 14, 15 and 16 alone, with mean values ranging between 1.37 mm^{-1} and 1.50 mm^{-1}. These volumes exhibited significant differences with volumes included in the low group, and in 3 comparisons were also found to be significantly higher than intermediate volumes (comparisons of VOI 3, 4 and 13 with VOI 16). These adjacent volumes were found to define the most inferior aspect of the ischium, extending into the ramus.

Five volumes of interest were classified as intermediate in nature (yellow) and were found to contain one or fewer statistically significant differences with members of the high Tb.N group, and no statistically significant differences with the low Tb.N group. These volumes occur peripherally at VOI 3, 4 and 9, and also act to separate the high and low groups (VOI 12 and 13).

Inter-phase variation by VOI

The trabecular number data for each phase revealed differences between the distribution of trabeculae in each phase [Figure 6.26]. In all volumes, Tb.N was found to be markedly higher in Phase 1 volumes than those of either Phase 2 or Phase 3, while Phase 2 and 3 showed a similar expression of Tb.N. In the volumes of interest representing the ramus inferiorly (VOI 14 – 16) Tb.N was found to be either very similar or higher in Phase 3 than Phase 2, while in all other VOI Phase 3 contained the lowest mean trabecular number.
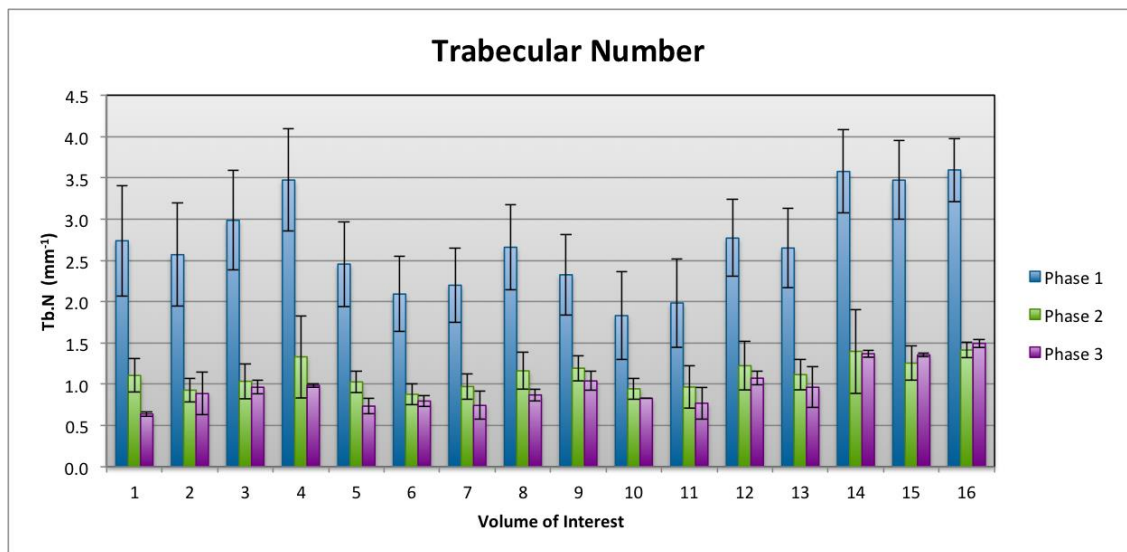
Figure 6.26. Summarised results for mean Tb.N ± SD at each VOI per phase.

Analysis of variance tests were applied to each VOI to determine whether the visual differences evident between each phase were of statistical significance. The data for VOIs 10 and 14 failed the Shapiro-Wilk test of normality ($p < 0.05$), while VOIs 1, 2, and 16 failed the test of equal variance ($p < 0.05$), therefore these tests were completed using the Kruskal-Wallis one way ANOVA on ranks. All other volumes were parametric

in nature and therefore could be analysed using the parametric one way ANOVA. The results of these tests are summarised in Table 6.12.

In all volumes, a very highly significant difference was found (p < 0.001) for trabecular number between phases. Multiple pairwise comparison procedures were then applied to each dataset to further investigate these significant differences. The parametric VOIs were processed following the Holm-Sidak method, while Dunn's method was used to analyse the non-parametric VOIs. A number of pairwise significant differences were identified [Figure 6.27].

Table 6.12. Analysis of variance results for inter-phase comparisons of Tb.N in each volume of interest. ◊ indicates data was non-parametric, and therefore subject to ANOVA on ranks. * significant result (P < 0.05); ** highly significant difference (P < 0.01); *** very highly significant difference (P < 0.001).

VOI	F / H$^\lozenge$	DoF	P
1	15.282$^\lozenge$	2	< 0.001***
2	16.601$^\lozenge$	2	< 0.001***
3	39.24	2	< 0.001***
4	44619	2	< 0.001***
5	28.149	2	< 0.001***
6	27.799	2	< 0.001***
7	31.183	2	< 0.001***
8	35.406	2	< 0.001***
9	18.665	2	< 0.001***
10	16.734$^\lozenge$	2	< 0.001***
11	14.783	2	< 0.001***
12	41.195	2	< 0.001***
13	39.198	2	< 0.001***
14	15.016$^\lozenge$	3	< 0.001***
15	66.617	2	< 0.001***
16	14.885$^\lozenge$	2	< 0.001***

When Phase 1 Tb.N values were compared to those of Phase 2, it was found in all 16 volumes that there was a statistically significant decrease into Phase 2. The comparison of Phase 1 with Phase 3 revealed that there was also a significant decrease from Phase 1 into Phase 3 in VOIs 1 – 13 and 15, while in VOI 14 and 16 no significant differences were identified between these phases. Despite the presence of Tb.N patterning within Phase 3 which was absent in Phase 2, there were no statistically significant differences found between mean trabecular number in Phase 2 and 3 at any VOI appraised.
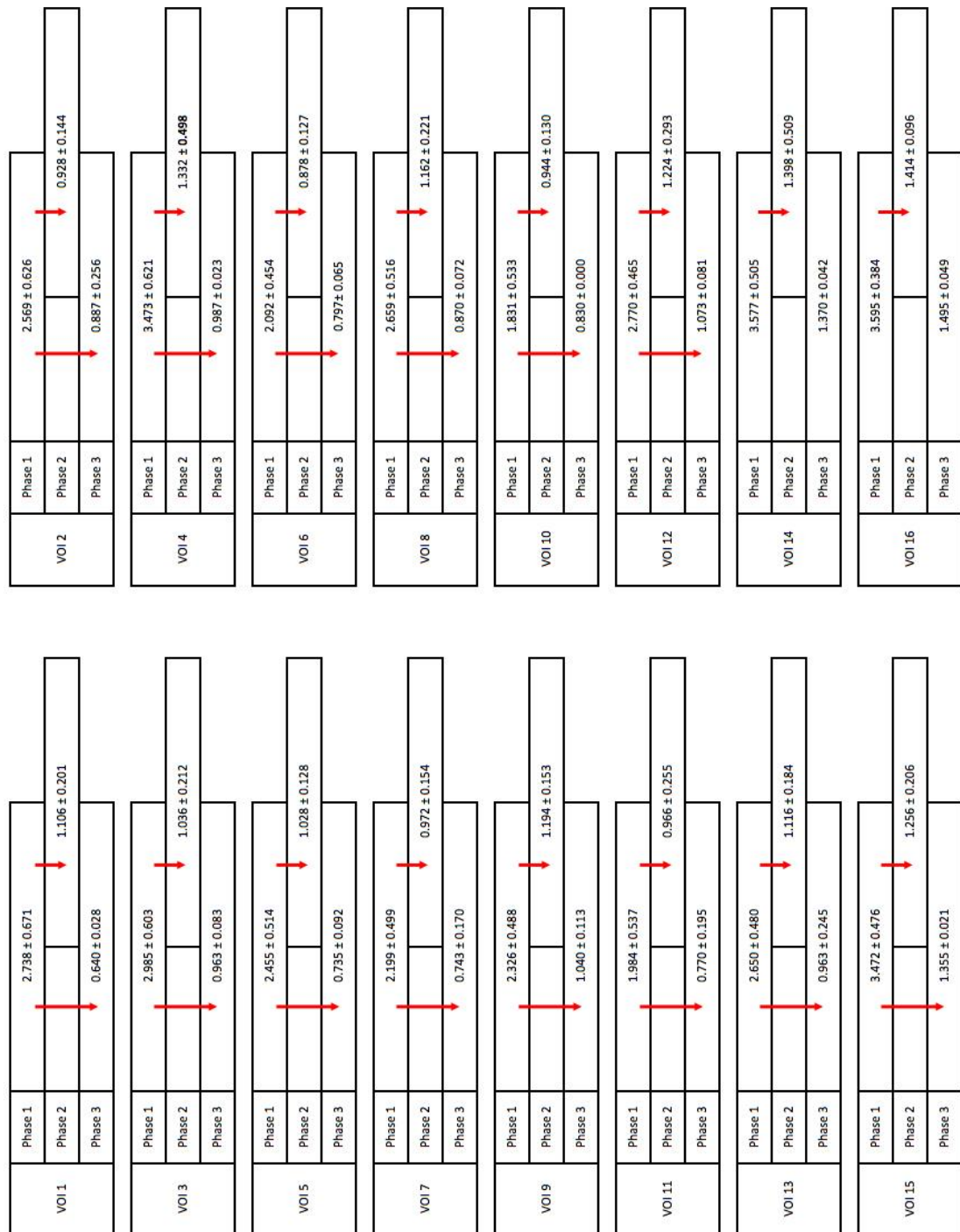
Figure 6.27. Results of multiple pairwise comparisons between phases at each volume of interest. Values listed are the mean ± SD; arrow indicates a significant difference exists between connected phases (p < 0.05), directionality shows decreasing Tb.N.

6.2.4 Trabecular separation

Phase 1

The descriptive statistics for Phase 1 trabecular separation are presented in Table 6.13.

Table 6.13. Descriptive statistics (mean, range, standard deviation and relative standard deviations) for Phase 1 Tb.Sp for each volume of interest.

		Phase 1 Tb.Sp (µm)			
VOI	**Mean**	**Range**		**SD (±)**	**RSD (±)**
		Min	**Max**		
1	221.25	153.20	290.56	35.84	16.20
2	239.29	181.54	332.14	44.20	18.47
3	212.67	156.78	253.06	35.45	16.67
4	174.64	132.73	252.13	33.44	19.14
5	256.77	192.81	356.25	42.45	16.53
6	308.24	221.86	485.57	60.47	19.62
7	300.26	213.13	400.33	53.17	17.71
8	231.75	169.73	318.40	38.27	16.51
9	331.30	179.55	589.30	85.88	25.92
10	403.39	224.05	595.93	106.27	26.34
11	370.96	196.45	514.63	94.19	25.39
12	248.26	172.43	479.61	67.22	27.08
13	247.77	187.84	329.76	45.65	18.42
14	170.38	120.38	208.10	28.16	16.53
15	175.31	117.22	234.06	32.37	18.46
16	160.55	118.66	199.58	25.58	15.93

The mean values for trabecular separation were found to lie between 160.55 µm (VOI 16) and 403.39 µm (VOI 10), with relative standard deviations for this parameter of 16.20 % to 27.08 %. This data is represented graphically in Figure 6.28.

When appraised using the Shapiro-Wilk test of normality, the data was found to be non-parametric ($p < 0.05$), therefore the Kruskal-Wallis one way ANOVA on ranks was used to determine whether there was a significant difference between the volumes of interest. A very highly significant difference was found (H = 207.415 for 15 degrees of freedom, therefore $p < 0.001$). Dunn's method for non-parametric multiple pairwise comparisons was employed to determine whether there were significant differences identifiable between specific VOI pairs.
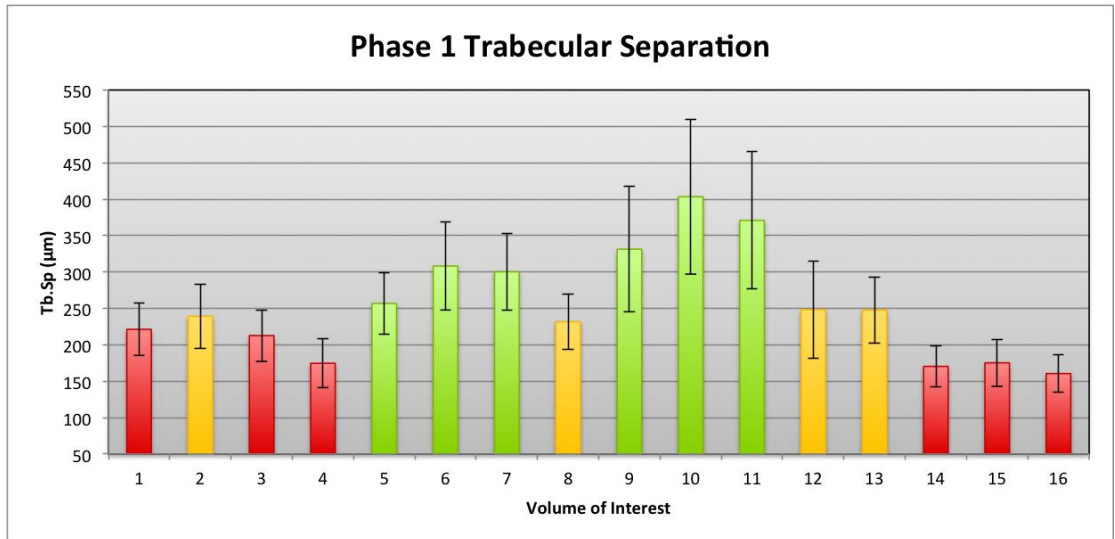
Figure 6.28. Bar chart depicting mean Tb.Sp (± SD) per VOI for Phase 1 individuals. High (green),

intermediate (yellow) and low (red) colouration based on MPC results.

Forty-six pairwise comparisons demonstrated significant differences [Figure 6.29].
These differences were found to primarily separate volumes 1 – 4 from 9 – 11, and
volumes 5 – 13 from 14 – 16. The precise distribution of these differences led to the
creation of three groups of related volumes [Figure 6.30].
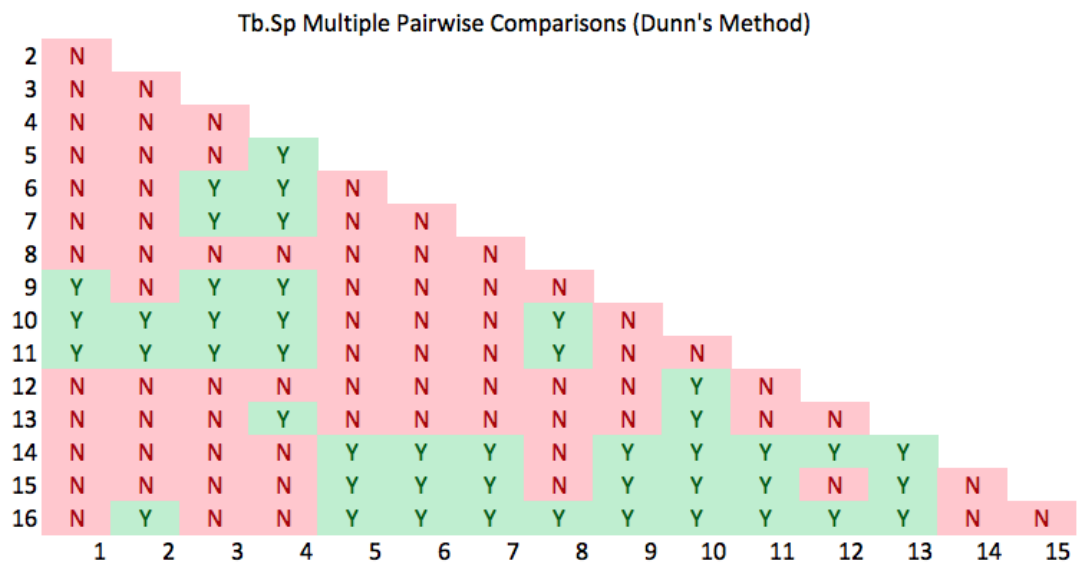
Figure 6.29. Results of multiple pairwise comparisons for Phase 1 Trabecular number. Y = statistically

significant difference; N = no significant difference detected.
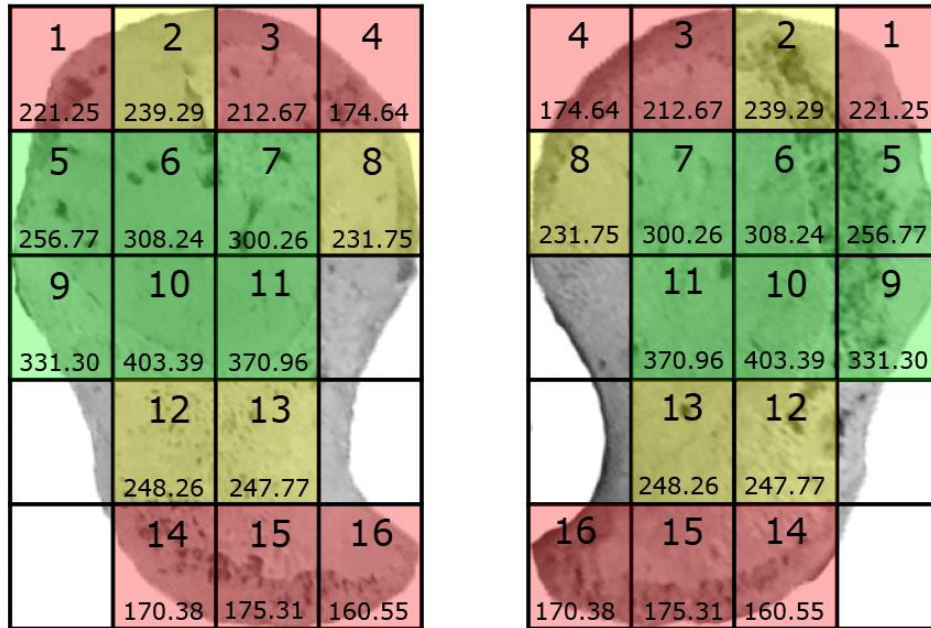
Figure 6.30. Trabecular separation groups as indicated by the results of multiple pairwise comparisons. Green: high Tb.Sp; Yellow: intermediate Tb.Sp; red: low Tb.Sp. The values presented are the mean value for each VOI (μm).

The low Tb.Sp group (red) comprised six volumes of interest (VOI 1, 3, 4 and 14 – 16) and ranged between 160.55 μm and 221.25 μm. Volumes included in this group were found to present a minimum of three statistically significant differences from the volumes categorised as having high Tb.Sp (VOI 1), and with a maximum of 10 significant differences; i.e. significantly different from all other volumes excluded from the low group (VOI 16). These volumes were not found to differ from any other low volumes, and were not significantly larger than any volumes.

Conversely, the high Tb.Sp group (green) were found to be significantly higher than volumes of the other groups, including VOIs 5 – 7 and 9 - 11. Mean Tb.Sp values for this group were observed to fall between a minimum of 256.77 μm and a maximum of 403.39 μm. Volume of interest 10 revealed the highest number of significant differences, 10, including all volumes beyond this group, while VOI 5 demonstrated only 4 significant pairwise comparisons. Of note, this group occupied the same position and identical volumes of interest as the group designated to have low trabecular thickness in this phase previously.

The intermediate volumes were identified as sharing boundaries with both the high and low groups, in volumes 2, 8, 12 and 13. They were characterised as being both significantly greater than volumes in the low Tb.Sp group and lower than volumes in the high Tb.Sp group, precluding them from joining either. The range of values observed in this group was narrower than in the preceding groups, falling between 231.75 μm and 248.26 μm.

Phase 2

The mean values and descriptive statistics for trabecular separation in Phase 2 are outlined in Table 6.14.

Table 6.14. Descriptive statistics (mean, range, standard deviation and relative standard deviations) for Phase 2 Tb.Sp for each volume of interest.

	Phase 2 Tb.Sp (μm)				
VOI	**Mean**	**Range**		**SD (±)**	**RSD (±)**
		Min	**Max**		
1	480.73	427.41	561.31	53.49	11.13
2	579.55	508.86	618.86	43.50	7.51
3	530.16	481.76	556.31	32.28	6.09
4	409.19	299.76	498.57	73.32	17.92
5	580.02	549.91	626.84	32.35	5.58
6	696.63	573.55	894.16	121.38	17.42
7	605.88	540.84	684.47	51.23	8.46
8	490.85	457.15	545.36	32.66	6.65
9	541.61	498.20	596.94	40.14	7.41
10	701.42	549.46	868.44	119.72	17.07
11	654.90	388.17	988.71	216.75	33.10
12	545.52	425.28	654.67	85.52	15.68
13	555.03	393.09	682.77	106.69	19.22
14	435.34	293.79	536.65	88.08	20.23
15	480.15	396.17	544.64	54.17	11.28
16	416.39	390.37	447.39	21.47	5.16

The mean values observed for trabecular separation in Phase 2 were found to be higher in all volumes than was previously observed in Phase 1. These ranged between 409.19 μm (VOI 4) and 701.42 μm (VOI 10). The relative standard deviations were predominantly lower than those found in Phase 1, for fifteen of the sixteen volumes these fell between 5.16 % (VOI 16) and 20.23 % (VOI 14), although VOI 11 was found to

have an atypically high RSD of 33.10%. The means and standard deviations are presented graphically in Figure 6.31.
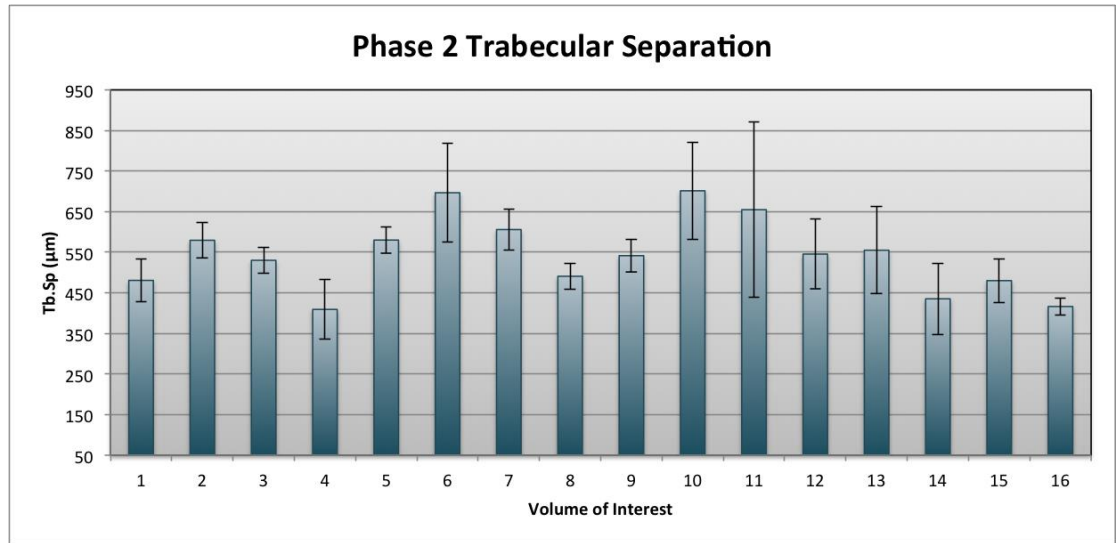
Figure 6.31. Bar chart demonstrating mean and standard deviations at each VOI for Phase 2 trabecular separation.

The Phase 2 trabecular separation data was found to be non-parametric (Shapiro-Wilk $p < 0.05$), therefore the Kruskal-Wallis one way ANOVA on ranks was used to test for significant differences. A very highly significant difference was found ($H = 50.430$ with 15 degrees of freedom, $p < 0.001$) therefore multiple pairwise comparisons were applied to test for significant differences between specific volumes of interest. As no data values were missing, Tukey's method for non-parametric MPC was applied, which revealed only five statistically significant pairwise comparisons [Figure 6.32].

These five pairwise comparisons occurred directly between the highest Tb.Sp regions (VOI 6 and 10) and the lowest Tb.Sp regions (VOI 4, 14 and 16). This limited expression of pairwise significance was not sufficient to further categorise trabecular separation in this phase.

Figure 6.32. Results of Tb.Sp multiple pairwise comparisons for Phase 2 volumes of interest. Y = significant difference (p < 0.05); N = no significant difference detected.

Phase 3

The descriptive statistics for Phase 3 trabecular separation are provided in Table 6.15.

The mean Tb.Sp values in this phase were found to be between 399.24 µm (VOI 16) and 833.63 µm (VOI 11), while the relative standard deviations typically fell between 2.07 % (VOI 16) and 21.12 % (VOI 11), although VOI 13 alone was found to have an atypically high RSD of 30.24 %. The mean and standard deviations of this data are presented graphically in Figure 6.33.

The Phase 3 Tb.Sp data failed the Shapiro-Wilk normality test (P < 0.05), therefore the data was considered to be non-parametric in nature. As a result, the Kruskal-Wallis one way ANOVA on ranks was used to establish whether a significant difference was present within the data. The H-statistic was found to be 32.481 with 15 degrees of freedom, which corresponded to a highly significant p value (p = 0.006). However, despite this overall highly significant difference, when multiple pairwise comparisons were applied using Dunn's method, there were no statistically significant results identified.

Table 6.15. Descriptive statistics (mean, range, standard deviation and relative standard deviations) for Phase 3 Tb.Sp for each volume of interest.

	Phase 3 Tb.Sp (µm)				
VOI	Mean	Range		SD (±)	RSD (±)
		Min	Max		
1	638.16	610.02	666.29	39.79	6.23
2	618.92	531.30	692.44	81.49	13.17
3	555.22	548.44	563.67	7.75	1.40
4	501.61	475.36	536.95	31.78	6.34
5	723.62	696.50	750.74	38.35	5.30
6	792.53	760.89	833.02	36.87	4.65
7	701.81	628.81	835.91	116.29	16.57
8	569.77	524.65	616.34	45.87	8.05
9	614.05	547.00	681.11	94.83	15.44
10	812.76	788.59	832.87	22.42	2.76
11	833.63	700.71	1033.31	176.06	21.12
12	592.13	524.24	675.89	77.06	13.01
13	682.76	505.79	909.62	206.49	30.24
14	447.99	427.64	468.33	28.77	6.42
15	452.98	443.25	462.71	13.76	3.04
16	399.24	393.39	405.09	8.27	2.07
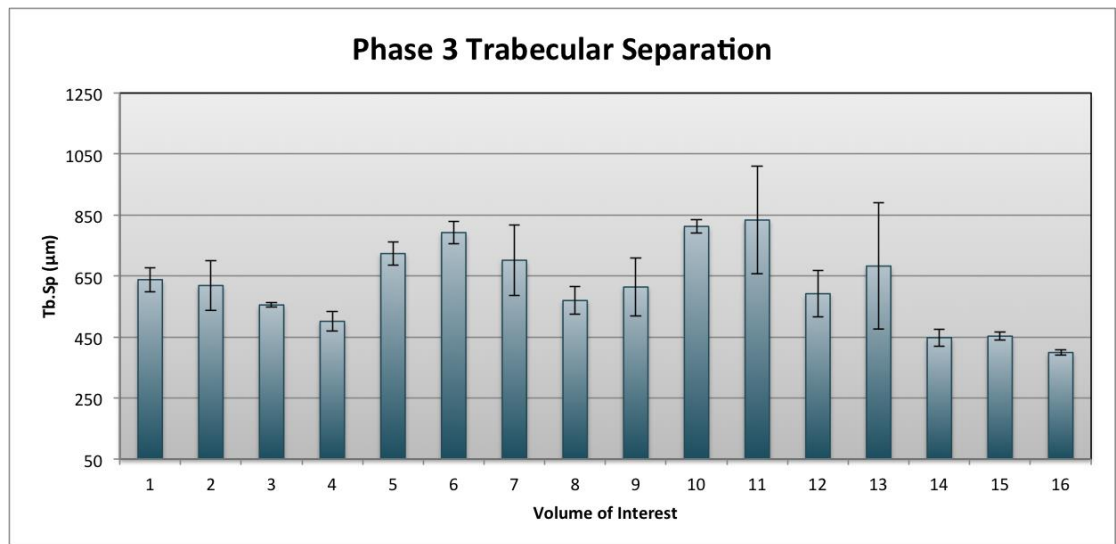
Figure 6.33. Bar chart demonstrating the mean Tb.Sp and standard deviation observed at each VOI in Phase 3.

Inter-phase variation by VOI

During individual phase analyses, it was noted that there was a trend towards increasing Tb.Sp in each progressive phase examined, with mean trabecular separation in Phase 1 notably lower than that observed in either Phase 2 or 3. In VOIs 1 – 14, Phase 3 demonstrated the highest separation values, while in VOIs 15 and 16 the highest values were found in Phase 2. This is summarised graphically in Figure 6.34.
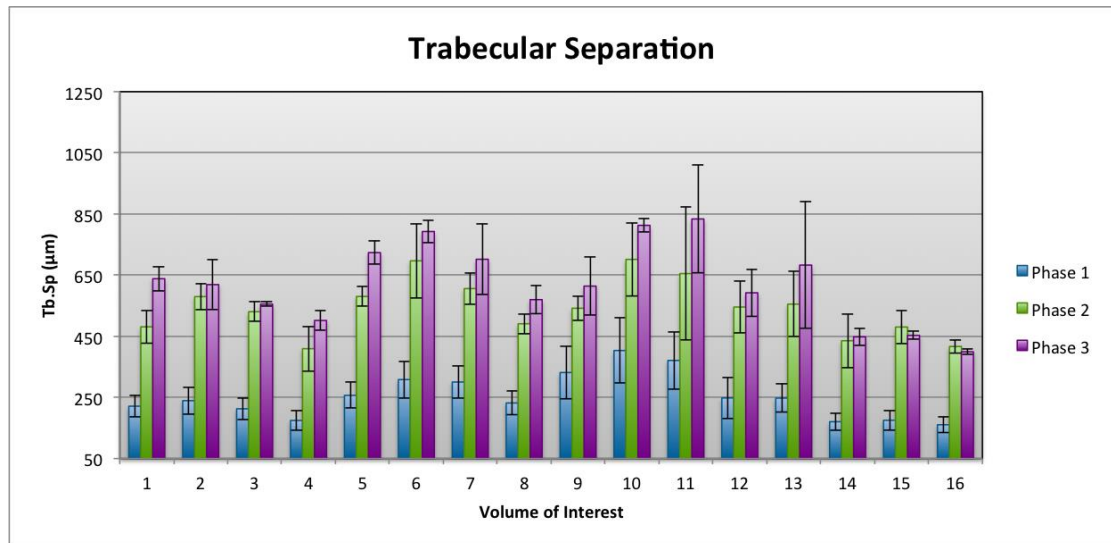
Figure 6.34. Summarised mean Tb.Sp ± SD at each VOI per phase.

Individual analysis of variance tests were conducted for the data obtained from each volume of interest to investigate whether significant differences existed between each phase [Table 6.16]. Volumes 1, 2, 5, 7, 8, 10, 11, 15 and 16 were found to be parametric and were therefore processed using a parametric one-way ANOVA. Volumes 3, 6, 9, 12 and 14 failed the Shapiro-Wilk test of normality ($p < 0.05$) and VOIs 4 and 13 failed the test of equal variance ($P < 0.05$) and were subsequently subjected to non-parametric Kruskal-Wallis analyses of variance on ranks.

Very highly significant results were observed in all phases analysed ($p < 0.001$), indicating that true statistical differences existed between the three phases at each site sampled. The data for each volume was subsequently analysed with MPCs using either the Holm-Sidak method or Dunn's method if the data was parametric or non-parametric respectively.

Table 6.16. Analysis of variance results for inter-phase comparisons of Tb.Sp in each volume of interest. ◊ indicates the test was non-parametric and the H statistic is presented in place of the F statistic. *** very highly significant difference (p < 0.001).

VOI	F / H$^◊$	DoF	P
1	165.403	2	< 0.001***
2	155.924	2	< 0.001***
3	16.648$^◊$	2	< 0.001***
4	16.790$^◊$	2	< 0.001***
5	215.84	2	< 0.001***
6	16.711$^◊$	2	< 0.001***
7	93.684	2	< 0.001***
8	168.030	2	< 0.001***
9	13.064$^◊$	2	< 0.001***
10	31.282	2	< 0.001***
11	22.813	2	< 0.001***
12	16.206$^◊$	2	< 0.001***
13	16.601$^◊$	2	< 0.001***
14	15.000$^◊$	2	< 0.001***
15	172.906	2	< 0.001***
16	270.879	2	< 0.001***

For each volume, a minimum of two significant results were found between phases [Figure 6.35]. In all volumes analysed, it was demonstrated that Tb.Sp was significantly higher in both Phase 2 and 3 than was observed in Phase 1. In addition, the values obtained in Phase 3 were found to be significantly greater than those identified for Phase 2 in volumes 1, 5, 7 and 8. No other statistically significant comparisons were identified for this parameter.

Figure 6.35. Multiple pairwise comparison results for inter-phase analysis at each volume of interest. Values are mean ± SD. Red arrow indicates significant difference exists between connecting phases (p < 0.05), arrow directionality shows decreasing Tb.Sp

6.2.5 Structural model index

Phase 1

The descriptive statistics for Phase 1 structural model index calculations are presented in Table 6.17.

Table 6.17. Descriptive statistics (mean, range and standard deviations) for Phase 1 SMI for each volume of interest.

		Phase 1 SMI		
VOI	**Mean**	**Range**		**SD (±)**
		Min	**Max**	
1	1.56	0.60	2.25	0.41
2	1.47	0.70	2.16	0.43
3	1.07	0.13	1.66	0.49
4	1.03	0.24	1.92	0.51
5	1.37	0.29	1.97	0.47
6	1.44	0.64	1.84	0.38
7	1.31	0.44	1.82	0.39
8	1.33	0.57	1.88	0.41
9	1.11	0.34	1.55	0.33
10	1.32	0.18	2.07	0.46
11	1.18	-0.24	2.36	0.62
12	0.66	-0.33	1.49	0.51
13	0.75	-0.09	1.98	0.63
14	0.89	0.19	1.44	0.41
15	0.50	-0.22	1.11	0.47
16	0.36	-0.52	1.18	0.55

The mean structural model index values in Phase 1 were found to lie between 0.36 (VOI 16) and 1.56 (VOI 1). Standard deviations for SMI were found to fall between 0.33 (VOI 9) and 0.63 (VOI 13), indicating that this parameter was more variable between individuals than those observed previously. As structural model index is not representative of a true rational number, but rather the relative proportions of rod-like structures to plate-like structures which may express negative values, the relative standard deviation is not an appropriate descriptor of variation for this parameter. For example, the calculated RSD for VOI 16 (0.55 / 0.36 * 100) was found to be 152.20 % as it failed to acknowledge that the base for SMI in this volume was not 0, but rather -0.52.

The range of values observed for volumes in Phase 1 indicated that the trabecular architecture was predominantly plate-like in the inferior VOIs 12 - 16 (SMI < 1), while superiorly a more balanced distribution of rods and plates was indicated in VOIs 1 - 11 (1 < SMI < 2). This data is presented graphically in Figure 6.36.
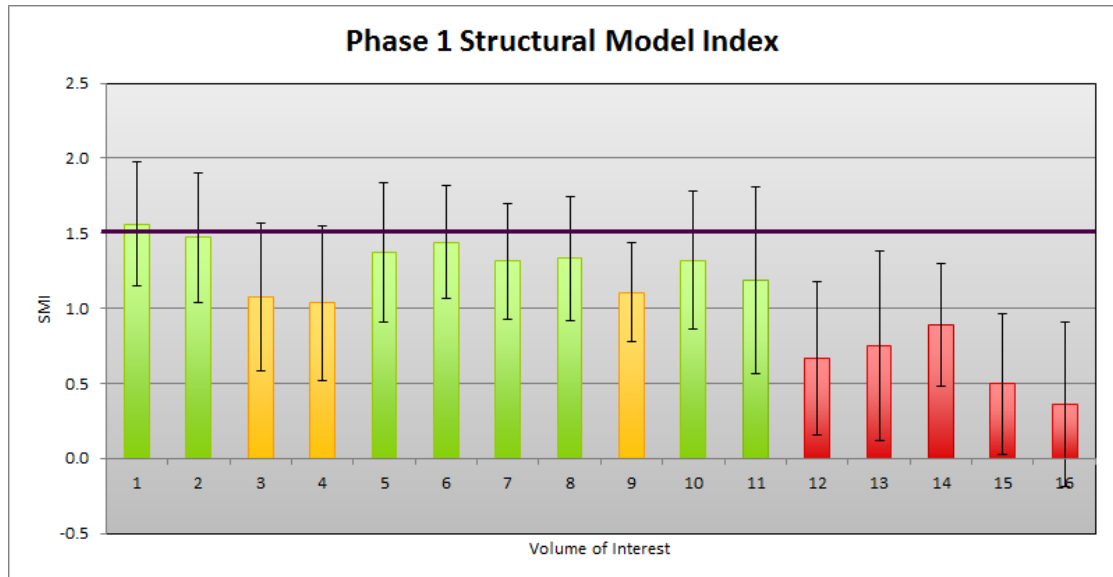
Figure 6.36. Bar chart depicting mean SMI (± SD) per VOI for Phase 1 individuals. High (green), intermediate (yellow) and low (red) colouration based on MPC results. An SMI value of 1.5 represents a precisely even distribution of rod-like and plate-like structures [purple line].

The data for SMI in Phase 1 was found to be non-parametric (Shapiro-Wilk $p < 0.05$), therefore a Kruskal-Wallis ANOVA on ranks was used to investigate whether any observed differences between volumes were of statistical significance. It was found that the variation in the data was very highly significant ($p < 0.001$), with an H-statistic of 110.539 with 15 degrees of freedom. Multiple pairwise comparisons following Dunn's method were then used to investigate whether significant differences exist between specific VOI pairs.

The results of the MPC procedure revealed that significant differences existed between 28 VOI pairs, predominantly separating VOIs 1, 2, 5 – 8, 10 and 11 from VOIs 12 – 16 [Figure 6.37]. The pattern of distribution of these significant differences was used to divide the ischium into three statistically comparable SMI groupings: high, intermediate and low SMI [Figure 6.38].

SMI Multiple Pairwise Comparisons (Dunn's Method)

	1	2	3	4	5	6	7	8	9	10	11	12	13	14	15
2	N														
3	N	N													
4	N	N	N												
5	N	N	N	N											
6	N	N	N	N	N										
7	N	N	N	N	N	N									
8	N	N	N	N	N	N	N								
9	N	N	N	N	N	N	N	N							
10	N	N	N	N	N	N	N	N	N						
11	N	N	N	N	N	N	N	N	N	N					
12	Y	Y	N	N	Y	Y	Y	Y	N	Y	N				
13	Y	Y	N	N	N	Y	N	N	N	N	N	N			
14	Y	Y	N	N	N	N	N	N	N	N	N	N	N		
15	Y	Y	N	N	Y	Y	Y	Y	N	Y	Y	N	N	N	
16	Y	Y	N	N	Y	Y	Y	Y	N	Y	Y	N	N	N	N
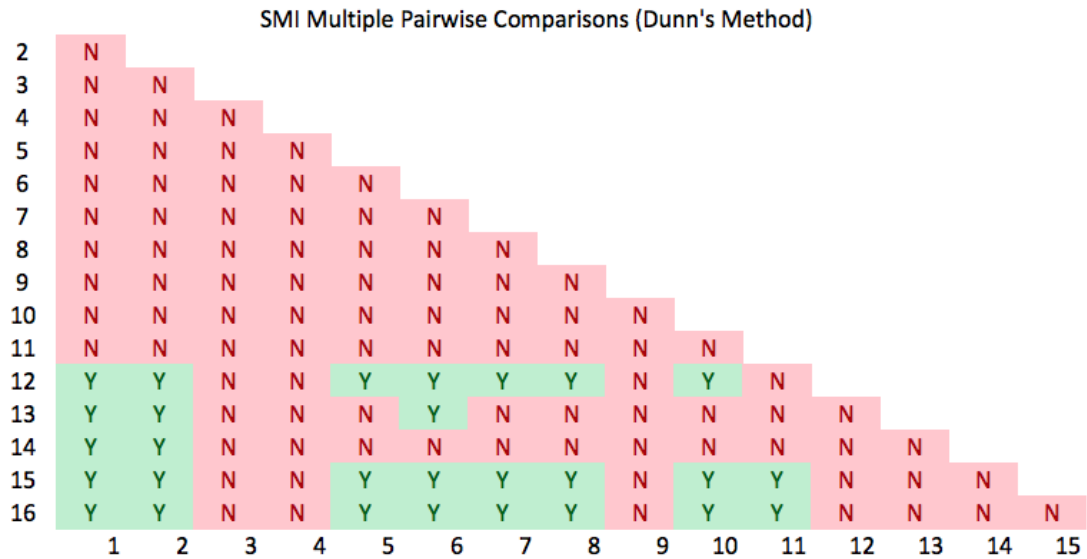
Figure 6.37. Results of Tb.Sp multiple pairwise comparisons for Phase 2 volumes of interest. Y = significant difference (p < 0.05); N = no significant difference detected.
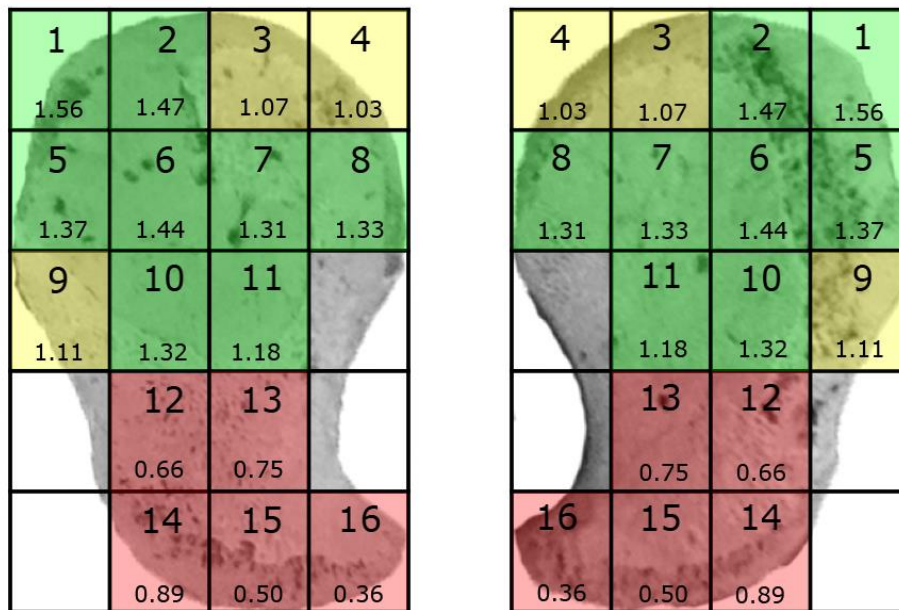
Figure 6.38. Structural model index groups as indicated by the results of multiple pairwise comparisons. Green: high Tb.Sp; Yellow: intermediate Tb.Sp; red: low Tb.Sp. The values presented are the mean value for each VOI.

The low SMI group (red) comprised of the inferiorly position VOIs 12 – 16, expressing mean values between 0.36 and 0.89. These volumes were each found to be statistically lower than the volumes characterised as having high SMI values, with a minimum of two significant differences at each VOI. This low SMI group included all volumes in

which it could be asserted that the predominant trabecular structure was plate-like in nature (SMI < 1).

The high SMI group (green) was formed the central and poster-superior VOIS, including 1, 2, 5 – 8, 10 and 11. Mean values for this group were observed to fall between 1.18 and 1.56. Each volume included in the high SMI group expressed a minimum of two significant differences from those indicated as low SMI. The SMI values for this group indicate that there is a relatively even distribution of rod-like and plate-like trabeculae in these volumes.

The intermediate volumes (yellow) included VOIs 3, 4 and 9. These volumes did not exhibit any significant differences with either the high or low groups, and had mean values ranging between 1.03 and 1.11. As with the high group, the SMI values for this group are indicative of the presence of rod-like and plate-like trabeculae, although there may be a greater tendency towards plate-like than is seen in the high SMI group.

Phase 2

The descriptive statistics for SMI in Phase 2 are presented in Table 6.18.

The mean SMI in Phase 2 was found to range between 1.57 (VOI 12) and 2.09 (VOI 11), with standard deviations falling between 0.09 (VOI 2) and an atypically high 0.81 (VOI 11), although in all other volumes SD was 0.51 or less.

The mean SMI values for VOI 1 – 10 and 12 – 16 fell between 1.57 and 1.94, indicating that a mixture of rods and plates was present (1 < SMI < 2), but tending towards a predominance of rod-like structures. VOI 11 demonstrated a stronger tendency towards rod-like trabeculae (SMI > 2). However, it should be noted that in VOI 11, which demonstrated the highest mean and SD, the maximum value obtained during analysis was 3.49. This indicated a mixture of cylinders (SMI 3) and spheres (SMI 4), the latter of which is not a possible conformation of trabecular bone. This may be suggestive of either an atypical region of trabecular bone within this volume or an artefact distorting the true structure. Neither was evident qualitatively within the scan data. The mean values and standard deviations are demonstrated graphically in Figure 6.39.

Table 6.18. Descriptive statistics (mean, range, standard deviation and relative standard deviations) for Phase 2 SMI for each volume of interest.

		Phase 2 SMI		
VOI	**Mean**	**Range**		**SD (±)**
		Min	**Max**	
1	1.94	1.83	2.12	0.12
2	1.95	1.83	2.05	0.09
3	1.88	1.59	2.08	0.19
4	1.88	1.25	2.29	0.42
5	1.72	1.59	1.89	0.11
6	1.91	1.74	2.34	0.26
7	1.79	1.66	2.00	0.15
8	1.74	1.45	2.12	0.26
9	1.58	1.41	1.67	0.11
10	1.82	1.55	2.34	0.31
11	2.09	1.62	3.49	0.81
12	1.57	1.35	1.86	0.18
13	1.88	1.52	2.76	0.51
14	1.71	1.26	2.10	0.34
15	1.75	1.57	1.93	0.13
16	1.69	1.55	1.89	0.15

The Phase 2 SMI data failed the Shapiro-Wilk test of normality ($P < 0.05$) and was therefore subjected to the Kruskal-Wallis ANOVA on ranks to determine whether significant differences could be identified within the dataset. It was found that no significant difference was present in the data ($H = 21.470$ with 15 degrees of freedom, therefore $p = 0.122$) indicating a statistical homogeny of SMI in this phase.
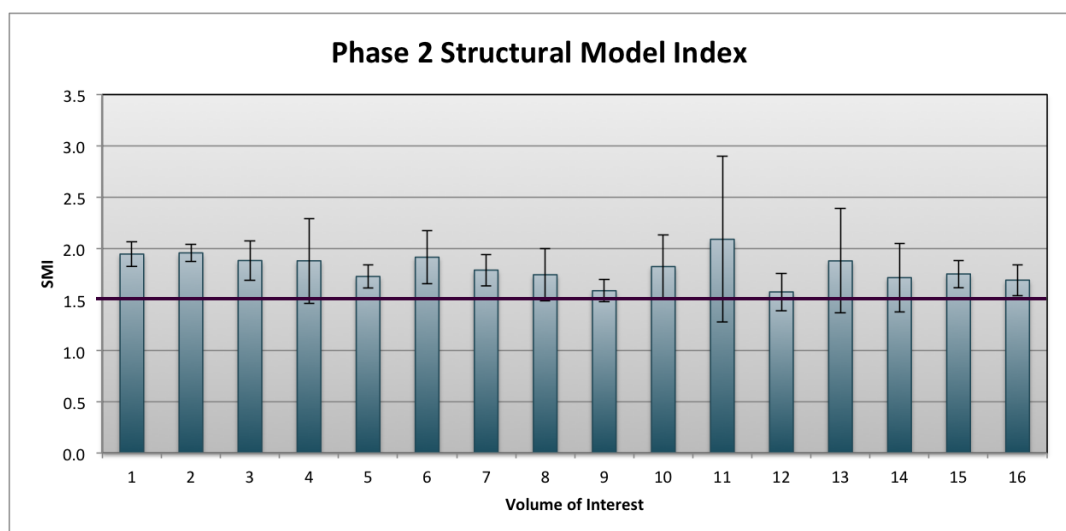
Figure 6.39. Bar chart depicting mean SMI (± SD) per VOI for Phase 2 individuals. An SMI value of 1.5 represents a precisely even distribution of rod-like and plate-like structures [purple line].

Phase 3

Descriptive statistics for the Phase 3 SMI data are displayed in Table 6.19.

Table 6.19. Descriptive statistics (mean, range, standard deviation and relative standard deviations) for Phase 3 SMI for each volume of interest.

		Phase 3 SMI		
VOI	**Mean**	**Range**		**SD (±)**
		Min	**Max**	
1	2.20	2.08	2.33	0.18
2	1.81	1.46	2.07	0.31
3	1.80	1.69	1.92	0.12
4	1.98	1.80	2.12	0.16
5	1.90	1.71	2.09	0.26
6	1.72	1.55	1.91	0.18
7	1.89	1.76	2.13	0.22
8	1.92	1.89	1.93	0.02
9	1.55	1.48	1.62	0.10
10	1.61	1.50	1.75	0.13
11	1.64	1.54	1.83	0.16
12	1.49	1.42	1.55	0.06
13	1.57	1.41	1.81	0.21
14	1.45	1.29	1.61	0.23
15	1.35	1.27	1.43	0.11
16	1.30	1.15	1.45	0.21

The mean values for SMI in this phase were found to fall between 1.30 (VOI 16) and 2.20 (VOI 1), with a smaller range of standard deviations, between 0.02 and 0.31. This mean data and associated standard deviations are presented graphically in Figure 6.40.

The structural implications of SMI in Phase 3 were found to be similar to those of Phase 2, with the majority of volumes (2 – 16) presenting a mixture of rod-like and plate-like structures. It was found that in volumes 14 – 16 this tended toward a greater number of plate-like structures, while in the remaining volumes there was a slightly elevated presence of rod-like structures, but neither of these tendencies were greatly pronounced (1 < SMI 2). VOI 1 however, presented a mean value of 2.20, which strongly indicated the presence of a greater proportion of rods than plates (SMI > 2), and no atypical results accompanied this observation as previously seen with VOI 11 in Phase 2. VOI 4 was also seen to very closely approximate this structure (SMI 1.98).
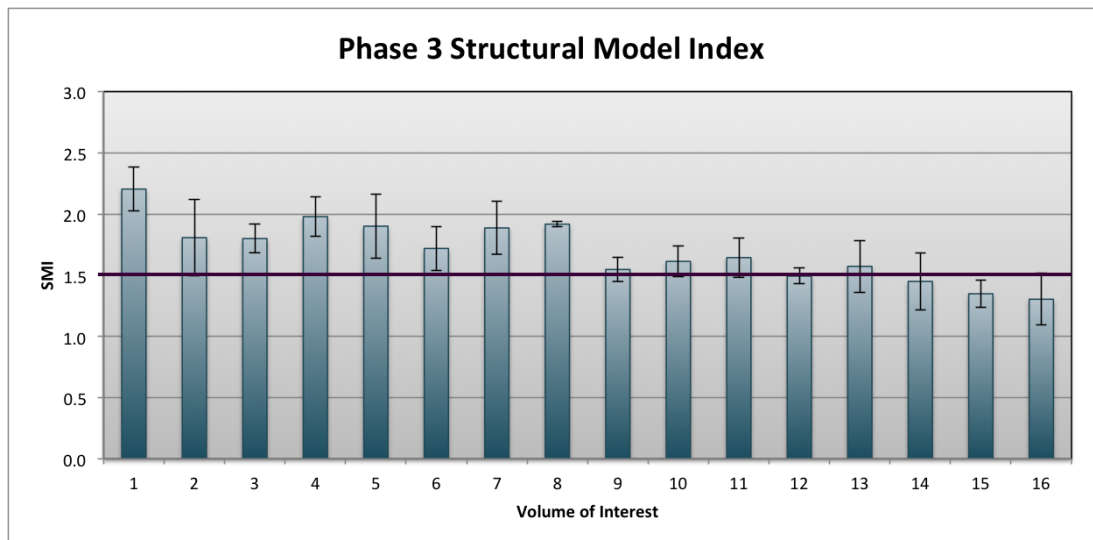
Figure 6.40. Bar chart depicting mean Tb.Sp (± SD) per VOI for Phase 1 individuals. High (green), intermediate (yellow) and low (red) colouration based on MPC results.

To determine whether any statistically significant differences were present in the Phase 3 SMI data, a parametric ANOVA was used (Shapiro-Wilk p = 0.251; equal variance p = 0.624). The results of this test revealed that a very highly significant difference was present within the data (F = 4.274 with 15 degrees of freedom, therefore p < 0.001). As a result, the Holm-Sidak parametric MPC procedure was applied to determine if this statistical significance could be localised to specific VOI pairs.

Five pairwise comparisons revealed statistically significant differences: VOI 1 compared with VOIs 12 and 14 – 16, and VOI 4 compared with 16 (Figure 6.41). As these significant differences were few in number and only occurred between the highest and lowest observed values, they did not allow the creation of Phase groups. The presence of these significant differences did however reinforce the transition through predominantly plate-like and rod-like trabeculae.

Inter-phase variation by VOI

A qualitative comparison of trends observed in the data for each of the three phases investigated indicated that the transition from Phase 1 to 2 was characterised by an increase in the proportion of rod-like trabeculae present in each volume. When Phase 2 and 3 are compared, trends are less clear: in the majority of VOIs, SMI decreases in Phase 3 however in VOI 1, 4, 5, 7 and 8 it is seen to increase in Phase 3. [Figure 6.42].
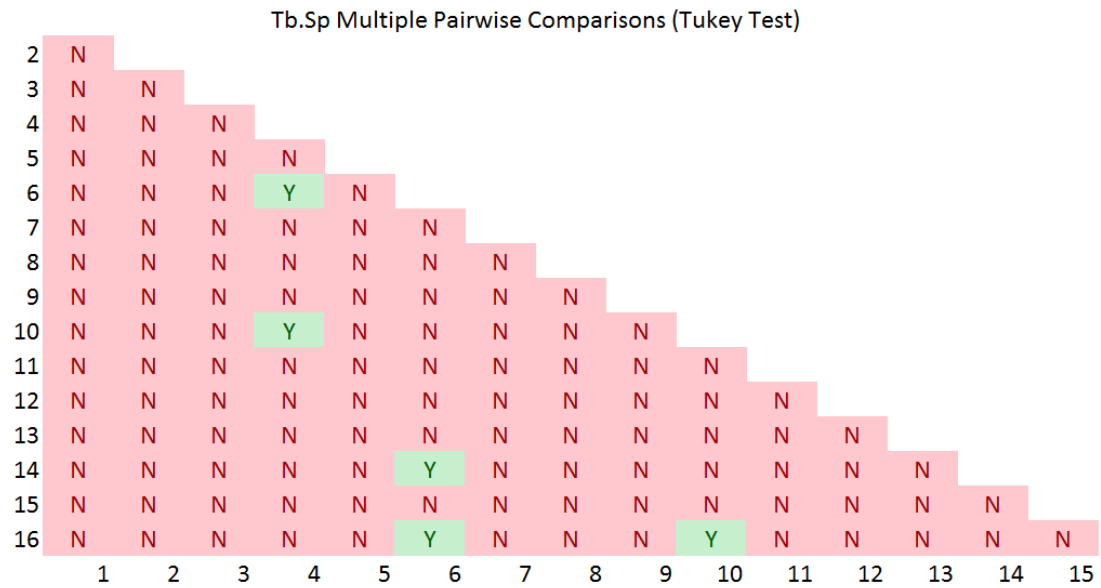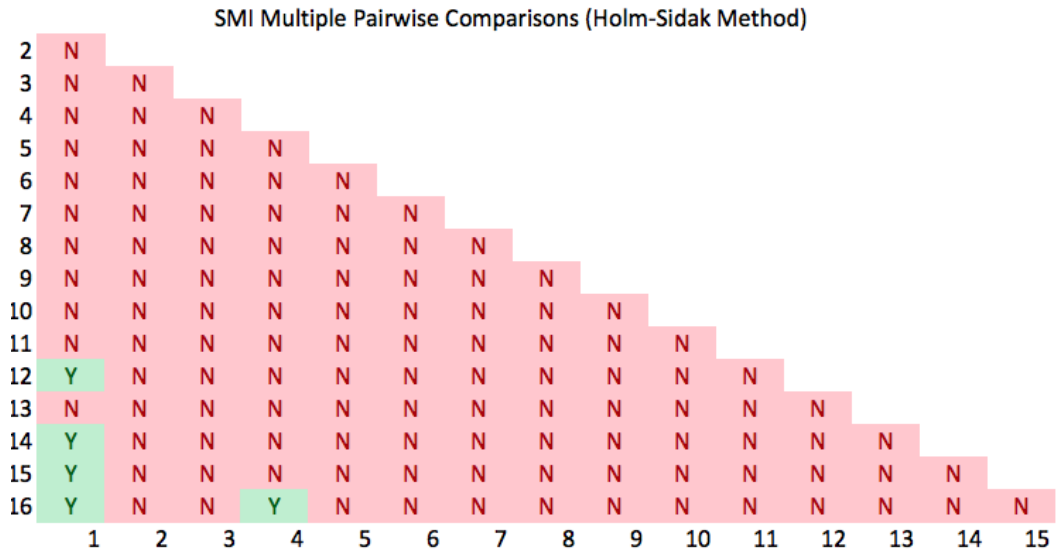
Figure 6.41. Results of Tb.Sp multiple pairwise comparisons for Phase 2 volumes of interest. Y = significant difference (p < 0.05); N = no significant difference detected.
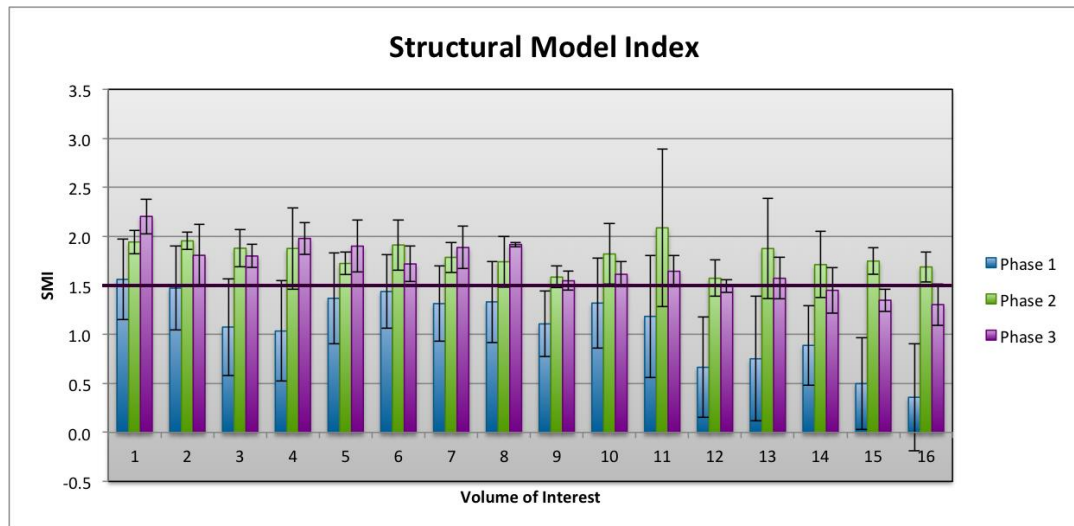
Figure 6.42. Summarised mean SMI ± SD at each VOI per phase.

Analysis of variance tests were applied to the combined data of all three phases per VOI to determine whether the trends observed between data were of statistical significance. Volumes 1 – 11, 13 and 14 were found to be parametric and were therefore processed using one-way ANOVA tests. VOI 12, 15 and 16 failed tests of equal variance (p < 0.05) and were therefore analysed using Kruskal-Wallis ANOVA on ranks.

A range of significant differences were observed [Table 6.20]. Volumes 4, 12, 14, 15 and 16 revealed very highly significant differences (p < 0.001) between phases. Volumes 3, 7, 9, and 13 presented highly significant differences (p < 0.01) while volumes 1, 2, 6, 8 and 11 demonstrated significant differences (p < 0.05). Volumes 5

and 10 did not reveal any statistically significant differences, but it was noted that the power of the test fell below that desired, so negative results should be treated with caution.

Table 6.20. Analysis of variance results for inter-phase comparisons of SMI in each volume of interest. ◊ indicates data was non-parametric, and therefore subject to ANOVA on ranks. ▫ indicates power of the performed test was below the desired power of 0.800. * significant result (P < 0.05); ** highly significant difference (P < 0.01); *** very highly significant difference (P < 0.001).

VOI	F / H$^◊$	DoF	P
1	4.209	2	0.027*
2	3.585	2	0.043*
3	8.917	2	0.001**
4	9.707	2	< 0.001***
5	2.549▫	2	0.099
6	4.092	2	0.029*
7	6.178	2	0.007**
8	4.759	2	0.018*
9	6.299	2	0.006**
10	3.087▫	2	0.063
11	4.319	2	0.024*
12	15.009$^◊$	2	< 0.001***
13	8.559	2	0.001**
14	9.939	2	< 0.001***
15	15.278$^◊$	2	< 0.001***
16	14.727$^◊$	2	< 0.001***

Following the identification of significant differences within volumes 1 – 4, 6 – 9 and 11 – 16, multiple pairwise comparisons were applied to determine whether significant differences could be identified between specific phases. Those VOI previously found to be parametric were analysed following the Holm-Sidak MPC method, while the non-parametric volumes were analysed using Dunn's non-parametric method.

Relatively few pairwise significant differences were found using MPC testing, as compared with previous parameters investigated [Figure 6.43]. As volumes 5 and 10 did not reveal significant differences during ANOVA, these were not tested for pairwise differences.

In VOIs 1, 2 and 8, no pairwise comparisons presented statistically significant differences despite presenting an overall statistical significance. Volumes 6, 9, 11 and 13 -16 demonstrated a statistically significant increase in SMI in Phase 2 compared

with Phase 1, indicating a relative increase in the proportion of rod-like trabeculae to plate-like trabeculae. No other pairwise significant differences were detected in these volumes. In VOI 3, 4, 7 and 12 it was noted that SMI was significantly higher in both Phase 2 and Phase 3 as compared to Phase 1. No volumes demonstrated a significant difference between Phase 2 and Phase 3 SMI values.
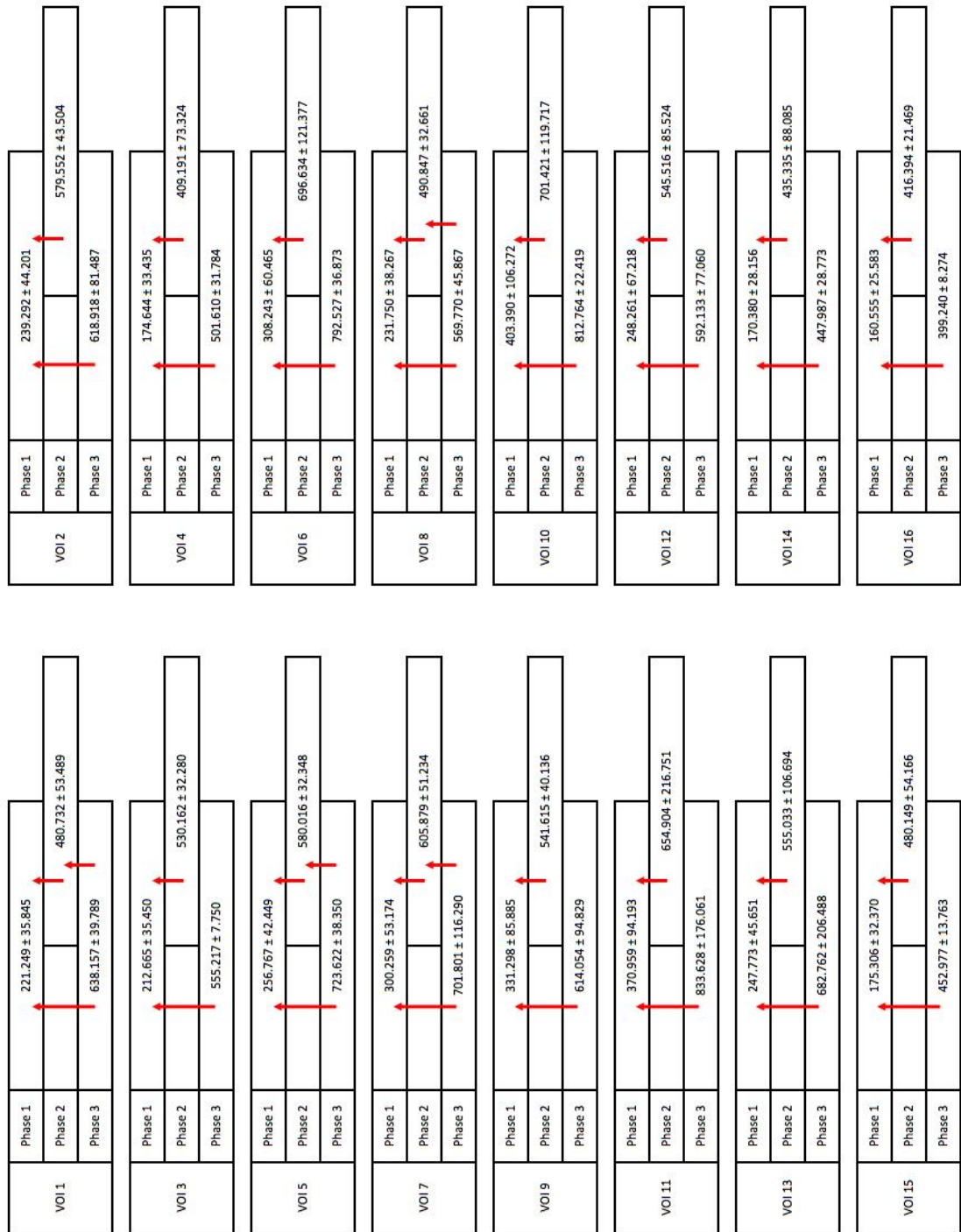

Figure 6.43. Multiple pairwise comparison results for inter-phase analysis at each volume of interest. Values are mean ± SD. Red arrow indicates significant difference exists between connecting phases (p < 0.05), arrow directionality shows decreasing SMI.

6.2.6 Degree of anisotropy

Phase 1

The descriptive statistics for degree of anisotropy are presented in Table 6.21.

Table 6.21. Descriptive statistics for Phase 1 DA in each volume of interest.

VOI	Mean	Range		SD (±)	RSD (±)
		Min	**Max**		
1	0.38	0.24	0.58	0.10	26.50
2	0.37	0.22	0.52	0.09	24.36
3	0.51	0.33	0.65	0.09	17.59
4	0.59	0.48	0.69	0.06	10.66
5	0.37	0.26	0.47	0.07	17.74
6	0.40	0.30	0.52	0.07	16.52
7	0.35	0.24	0.51	0.08	22.13
8	0.51	0.33	0.76	0.10	20.26
9	0.40	0.09	0.71	0.13	32.42
10	0.26	0.16	0.44	0.07	27.84
11	0.30	0.16	0.43	0.07	21.84
12	0.42	0.27	0.51	0.06	15.27
13	0.43	0.27	0.64	0.10	23.09
14	0.46	0.25	0.59	0.09	19.75
15	0.45	0.30	0.60	0.09	21.12
16	0.47	0.36	0.65	0.09	19.92

The mean values for DA in Phase 1 were found to fall between 0.26 (VOI 10) and 0.59 (VOI 4), with relative standard deviations between 10.66 % (VOI 4) and 32.42 % (VOI 9). The mean values and their standard deviations are summarised graphically in Figure 6.44.

Degree of anisotropy is an indicator of organisation that exists as a value between 0 [no trabecular alignment] and 1 [total trabecular alignment]. The DA values obtained for this phase did not show evidence of pronounced trabecular alignment, with the maximum observed DA being < 0.60. Indeed, the mean values for 13 of 16 volumes fell below 0.5, indicating a propensity towards non-alignment in these volumes.
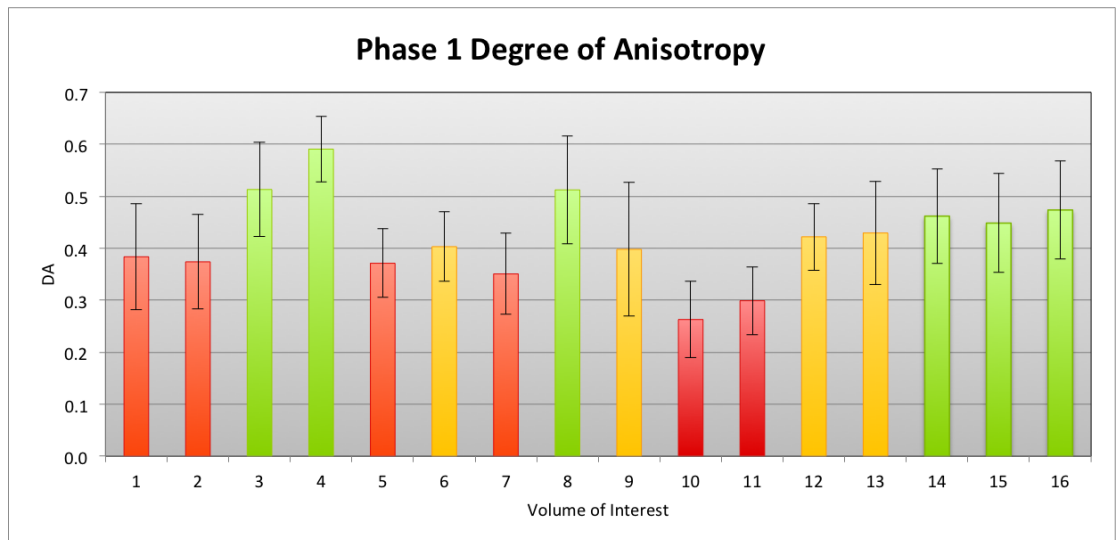
Figure 6.44. Graphic representation of mean (± SD) DA per VOI for individuals in Phase 1. High (green), intermediate (yellow) and low (red) colouration applied based on MPC testing.

The phase 1 DA data was found to be non-parametric (Shapiro-Wilk p < 0.05) therefore the Kruskal-Wallis one-way ANOVA on ranks was used to investigate whether significant differences were present within the dataset. A highly significant difference was observed (H = 144.918 with 15 degrees of freedom, therefore p < 0.001), indicating that a true difference was present between volumes of interest. Multiple pairwise comparisons were then applied following Dunn's method to determine whether significant differences were identifiable between specific volumes of interest.

Significant pairwise comparisons were found to exist between 33 pairs of volumes [Figure 6.45]. Volumes of interest 10 and 11 exhibited the greatest number of differences, demonstrating significantly lower mean DA values than volumes 3, 4, 6, 8, 9 and 12 – 16. When the overall distribution of significant differences was examined, it was possible to divide the Phase 1 ischium into 3 discreet groups of VOI [Figure 6.46].

The low anisotropy volumes (red) were found to demonstrate means of 0.26 to 0.38, indicating a structure with little discernable alignment. Each of these volumes were found to be statistically lower in DA than a minimum of two volumes included in the high DA group and, in the case of VOI 10 and 11, significant differences from the intermediate group.
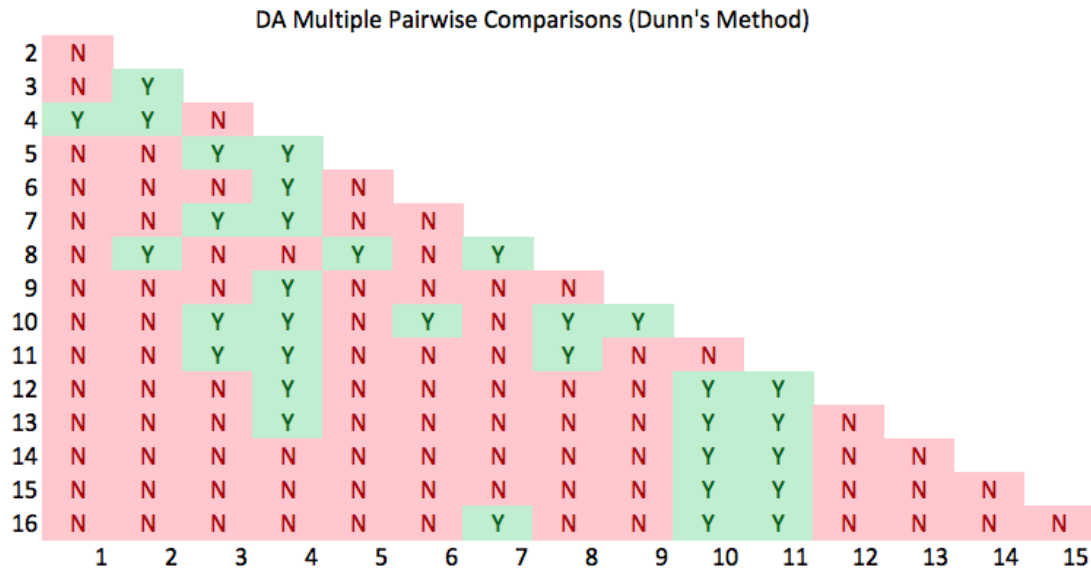
Figure 6.45. Results of DA multiple pairwise comparisons for Phase 1 volumes of interest. Y = significant difference (p < 0.05); N = no significant difference detected.
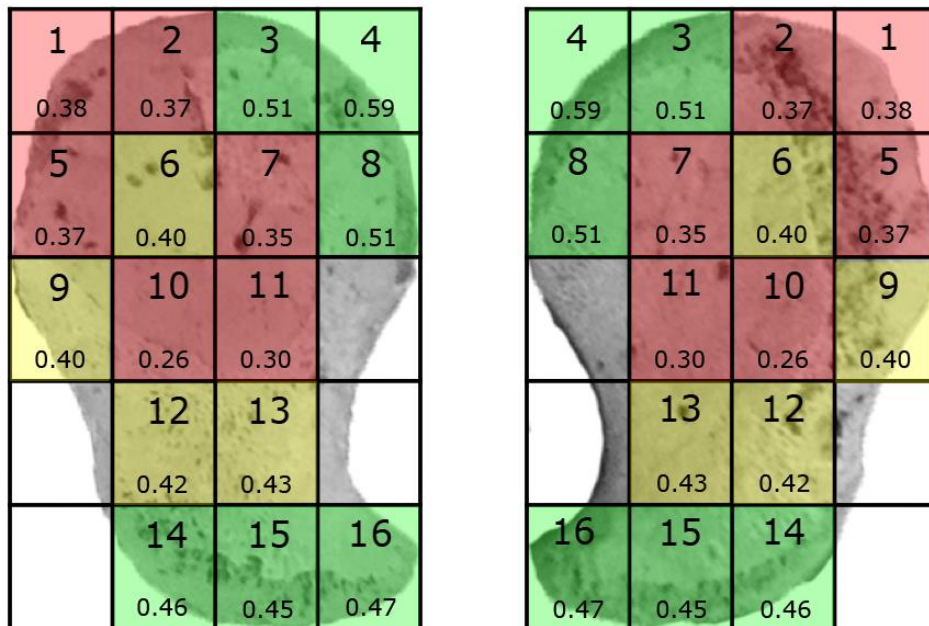
Figure 6.46. Degree of anisotropy groups as indicated by the results of multiple pairwise comparisons. Green: high DA; Yellow: intermediate DA; red: low DA. The values presented are the mean value for each VOI.

The high anisotropy group (green) were noted to fall between values of 0.46 and 0.59, including the inferior VOI which comprise the ramus and lower border of the ischium (14 – 16) and also the three volumes which comprise the anterosuperior aspect of the

ischium (3, 4 and 8). These volumes each exhibited a minimum of two significant differences from those designated to be of low anisotropy. VOI 4, the highest observed DA, was also significantly greater than the intermediate volumes. It should be noted that although this group is described as 'high' anisotropy this term is relative to the other volumes examined in this phase. With all DA values less than 0.6, these volumes do not indicate a highly anisotropic structure (perfect anisotropy = 1).

As above, the intermediate group of VOIs (yellow) were those found to be statistically significantly different from the volumes with both the highest (VOI 4) and lowest (VOI 10 and 11) anisotropy. The mean values for this group fell between 0.40 and 0.43.

Phase 2

The descriptive statistics for Phase 2 degree of anisotropy are presented in Table 6.22.

Table 6.22. Descriptive statistics for Phase 2 DA in each volume of interest.

		Phase 2 DA			
VOI	Mean	Range		SD (±)	RSD (±)
		Min	Max		
1	0.28	0.16	0.38	0.08	29.13
2	0.36	0.30	0.42	0.04	12.15
3	0.37	0.31	0.40	0.03	9.46
4	0.43	0.29	0.59	0.12	28.17
5	0.43	0.20	0.57	0.14	32.19
6	0.39	0.17	0.53	0.13	34.81
7	0.31	0.27	0.35	0.03	9.59
8	0.50	0.42	0.57	0.07	13.50
9	0.55	0.49	0.57	0.03	6.39
10	0.44	0.38	0.50	0.05	11.94
11	0.38	0.26	0.51	0.09	25.05
12	0.34	0.27	0.41	0.06	18.66
13	0.41	0.34	0.51	0.07	16.10
14	0.37	0.34	0.41	0.03	9.10
15	0.39	0.30	0.43	0.05	13.52
16	0.39	0.34	0.50	0.07	18.64

The DA values for Phase 2 were observed to be similar in range to those observed in Phase 1, with mean values falling between 0.28 (VOI 1) and 0.55 (VOI 9). The variation in relative standard deviations were found to be higher however, ranging between

6.39 % (VOI 9) and 34.81 % (VOI 6). The mean and standard deviations are demonstrated graphically in Figure 6.47.

The Phase 2 DA data was not normally distributed (Shapiro-Wilk p < 0.05), therefore a Kruskal-Wallis ANOVA on ranks was used to determine whether an overall significant difference was present between volumes. The results demonstrated that a highly significant difference did exist within the dataset (H = 36.072 with 15 degrees of freedom, therefore P = 0.002). Multiple pairwise comparisons using Tukey's Test were applied to investigate whether significant differences were detectable between specific volume pairs.
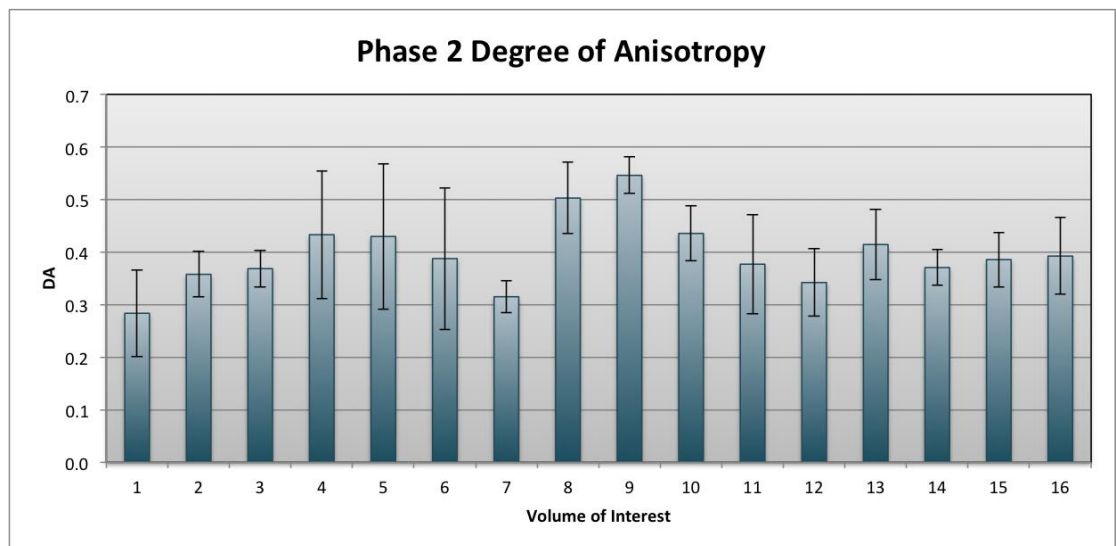
Figure 6.47. Graphic representation of mean (± SD) DA per VOI for individuals in Phase 2.

Only three pairwise significant differences were observed in this phase, occurring between the volumes with the highest (VOI 8 and 9) and lowest (VOI 1 and 7) levels of anisotropy Figure 6.48. No other comparisons revealed significant differences for this parameter in Phase 2.
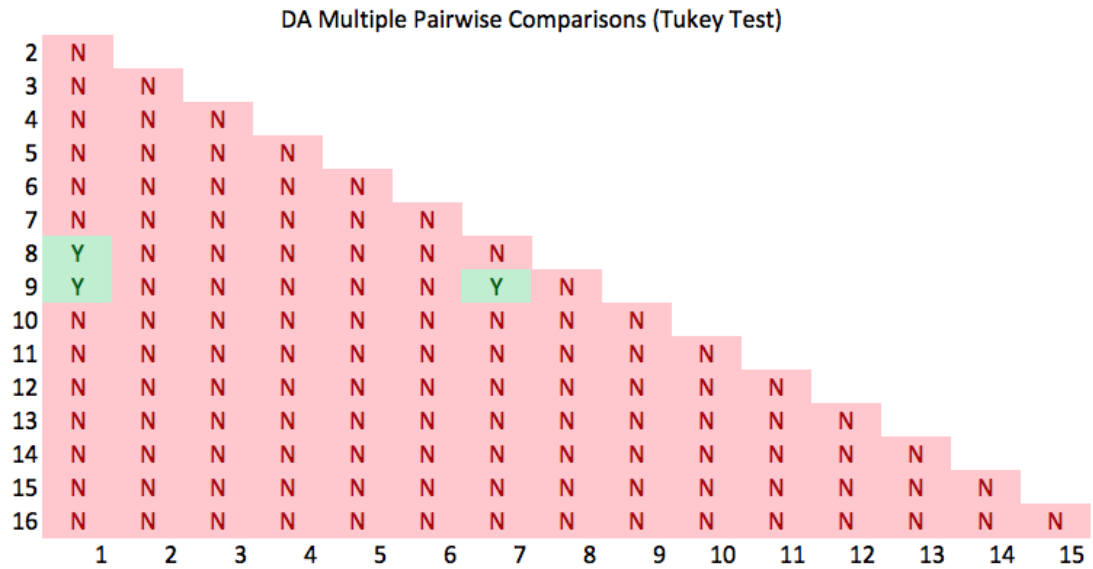
Figure 6.48. Results of DA multiple pairwise comparisons for Phase 2 volumes of interest. Y = significant difference (p < 0.05); N = no significant difference detected.

Phase 3

The descriptive statistics obtained for the degree of anisotropy expressed in Phase 3 are outlined in Table 6.23.

Table 6.23. Descriptive statistics for Phase 3 DA in each volume of interest.

VOI	Mean	Range		SD (±)	RSD (±)
		Min	Max		
1	0.34	0.30	0.39	0.06	18.10
2	0.29	0.20	0.42	0.11	39.30
3	0.41	0.25	0.50	0.14	33.99
4	0.42	0.35	0.50	0.08	18.31
5	0.52	0.47	0.57	0.07	14.18
6	0.39	0.31	0.47	0.08	19.85
7	0.36	0.28	0.43	0.08	20.90
8	0.55	0.54	0.57	0.02	2.74
9	0.66	0.59	0.74	0.11	16.88
10	0.30	0.25	0.34	0.05	15.38
11	0.41	0.31	0.51	0.10	24.61
12	0.35	0.27	0.43	0.08	22.85
13	0.50	0.40	0.58	0.09	17.58
14	0.22	0.14	0.30	0.11	51.24
15	0.33	0.29	0.37	0.05	15.38
16	0.61	0.56	0.66	0.07	10.95

The mean values observed for this phase were found to fall between 0.22 (VOI 15) and 0.66 (VOI 9), a slightly wider range than was previously observed in Phase 1 or 2. The relative standard deviations for this group were also wide however, ranging between 2.74 % (VOI 8) and 51.24 % (VOI 14). This data is presented graphically in Figure 6.49.

The data for degree on anisotropy in this phase was found to be parametric (Shapiro-Wilk p =0.201, equal variance p = 0.698), thus requiring the use of a parametric one-way analysis of variance to test for significant differences between volumes. The results of the ANOVA revealed that overall a very highly significant difference was present in this phase (H = 4.568 with 15 degrees of freedom, therefore p < 0.001). Following this significant result, multiple pairwise comparisons following the parametric Holm-Sidak method were used to test specific VOI pairs for significant differences. Six of these pairwise comparisons were found to return significant comparisons [Figure 6.50].
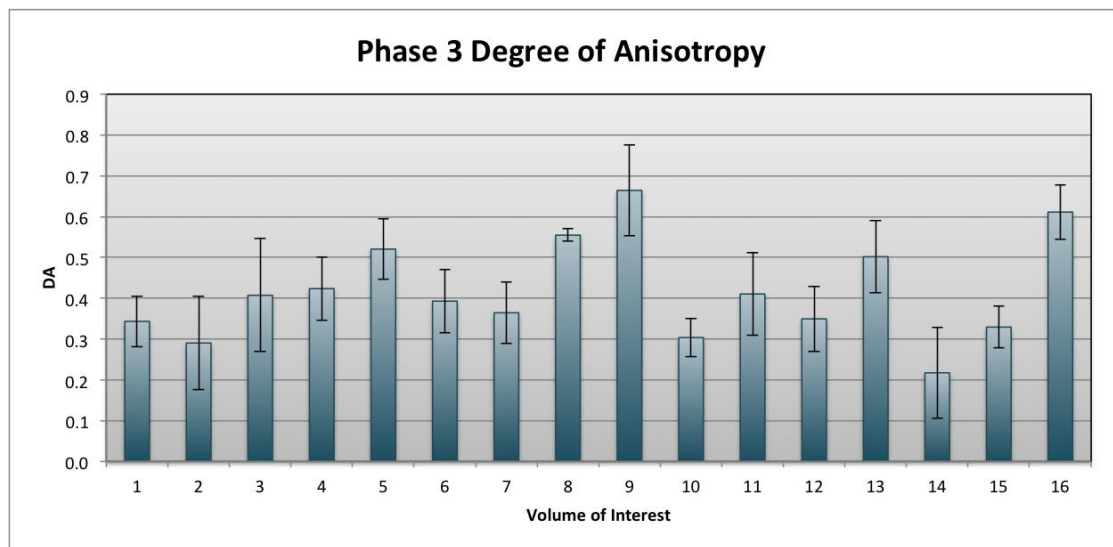
Figure 6.49. Graphic representation of mean (± SD) DA per VOI for individuals in Phase 3.

The statistically significant pairwise results were found to lie exclusively between the two extreme ends of the dataset. The most anisotropic volumes, 8, 9, and 16, were found to be significantly different from the least anisotropic volumes, including VOI 2, 10 and 14. This confirmed that there was a larger degree of difference evident within the structure of the ischium, but did not lend itself to groupings of volumes as very few comparisons were statistically significant. It was noted however, that VOI 9 was found

to be significantly higher than VOI 10, two volumes with a shared border. No other positional relationship was shared by the volumes showing significant differences.
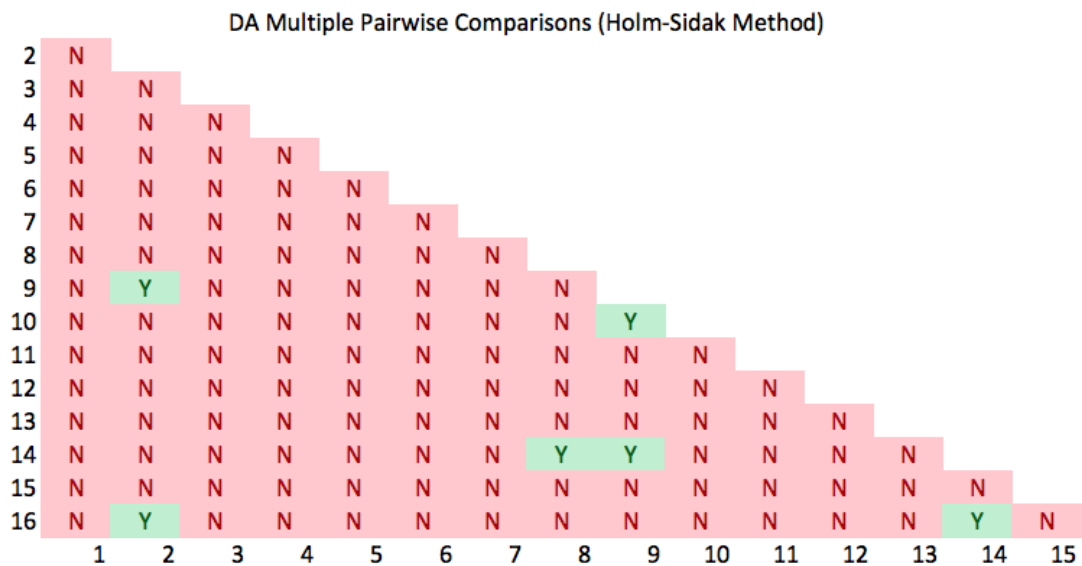
Figure 6.50. Results of DA multiple pairwise comparisons for Phase 3 volumes of interest. Y = significant difference (p < 0.05); N = no significant difference detected.

Inter-phase variation by volume

The variation between phases for degree of anisotropy was found to be the least predictable out of all trabecular parameters. No phase exhibited a predominance of either the highest or lowest values, and indeed in many volumes the mean values appeared relatively consistent between phases [Figure 6.51].

Analysis of variance was used to determine whether there was a significant difference between the degree of anisotropy in three phases at each volume of interest. The data for volumes 4, 10 and 16 were found to be non-parametric, therefore the Kruskal-Wallis one-way ANOVA on ranks was used to test for significance. The remaining volumes were found to be parametric allowing the use of a parametric one-way ANOVA. The results of each volume ANOVA are summarised in Table 6.24.

Degree of anisotropy presented the least number of statistically significant phase comparisons, with VOIs 1, 2, 6 – 8, 12 and 15 demonstrating no significant differences between each phase. These tests were all found to be of low power (power < 0.800), therefore the possibility of false negative results cannot be excluded. However, the

relatively small range of DA values and limited variability between these non-significant volumes support the suggestion that significant differences are unlikely.
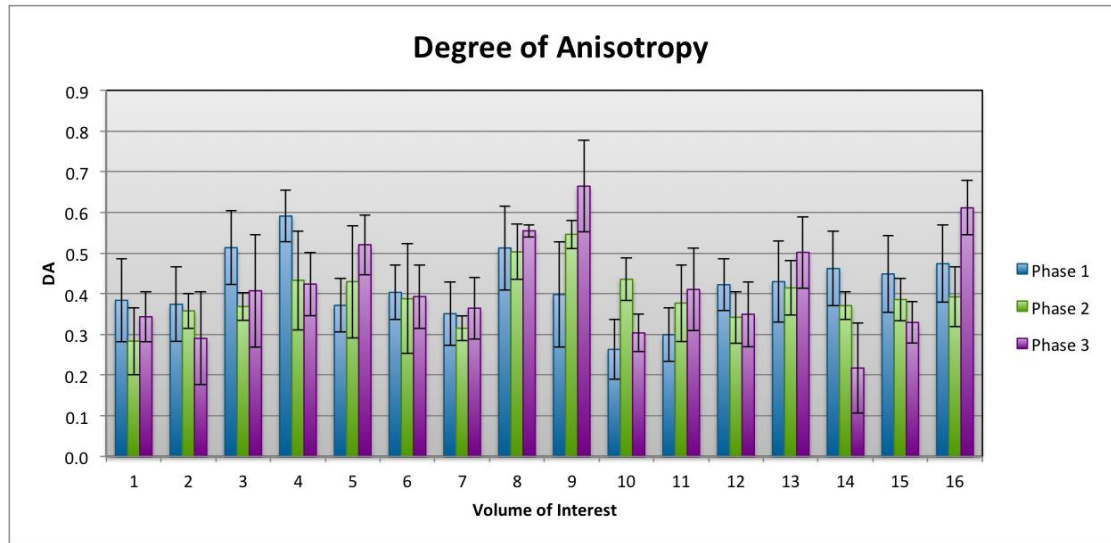
Figure 6.51. Summary of mean DA and standard deviations at each volume in Phases 1, 2 and 3.

Table 6.24. Analysis of variance results for inter-phase comparisons of DA in each volume of interest. ◊ indicates data was non-parametric, and therefore subject to ANOVA on ranks. ▫ indicates power of the performed test was below the desired power of 0.800. * significant result (P < 0.05); ** highly significant difference (P < 0.01).

VOI	F / H$^\lozenge$	DoF	P
1	2.158▫	2	0.138
2	1.207▫	2	0.316
3	6.289	2	0.006**
4	11.134$^\lozenge$	2	0.004**
5	3.549	2	0.045*
6	0.083▫	2	0.921
7	0.605▫	2	0.554
8	0.312▫	2	0.735
9	6.867	2	0.004**
10	11.084$^\lozenge$	2	0.004**
11	4.435	2	0.022*
12	0.911▫	2	0.415
13	3.969	2	0.032*
14	8.794	2	0.001**
15	2.404▫	2	0.112
16	6.861$^\lozenge$	2	0.032*

Of those volumes which did display statistically significant results, VOI 5, 11, 13 and 16 were found to only be significant at the level of p < 0.05. Volumes 3, 4, 9, 10 and 14

were found to be highly statistically significant (p < 0.01). No very highly significant differences were observed in this phase (p < 0.001).

The volumes which revealed statistically significant differences were subjected to multiple pairwise comparisons to identify whether this overall difference could be localised to specific phase pairs. The volumes found to be parametric were analysed using the Holm-Sidak MPC procedure, while the non-parametric data was appraised using Dunn's method for non-parametric MPCs.

Very few pairwise comparisons were found to be significant for this parameter, with a total of six volumes out of the nine analysed demonstrating a significant difference between at least one pair of phases [Figure 6.52].

Volumes 5, 12 and 13 did not demonstrate pairwise significant differences despite the significant result returned following analysis of variance. This indicates that while there is a difference between the mean values of each group, it is not great enough for the source of this difference to be stated conclusively.

In five VOIs (3, 4, 9, 10 and 14), it was found that anisotropy was significantly higher in Phase 1 than Phase 2. Volumes 4, 9 and 14 also demonstrated significantly higher anisotropy in Phase 1 when compared with Phase 3, although no differences were observed between the pairwise comparison of Phases 2 and 3. The only pairwise difference between Phase 2 and 3 was found in VOI 16, in which Phase 3 was found to have a statistically higher anisotropy.
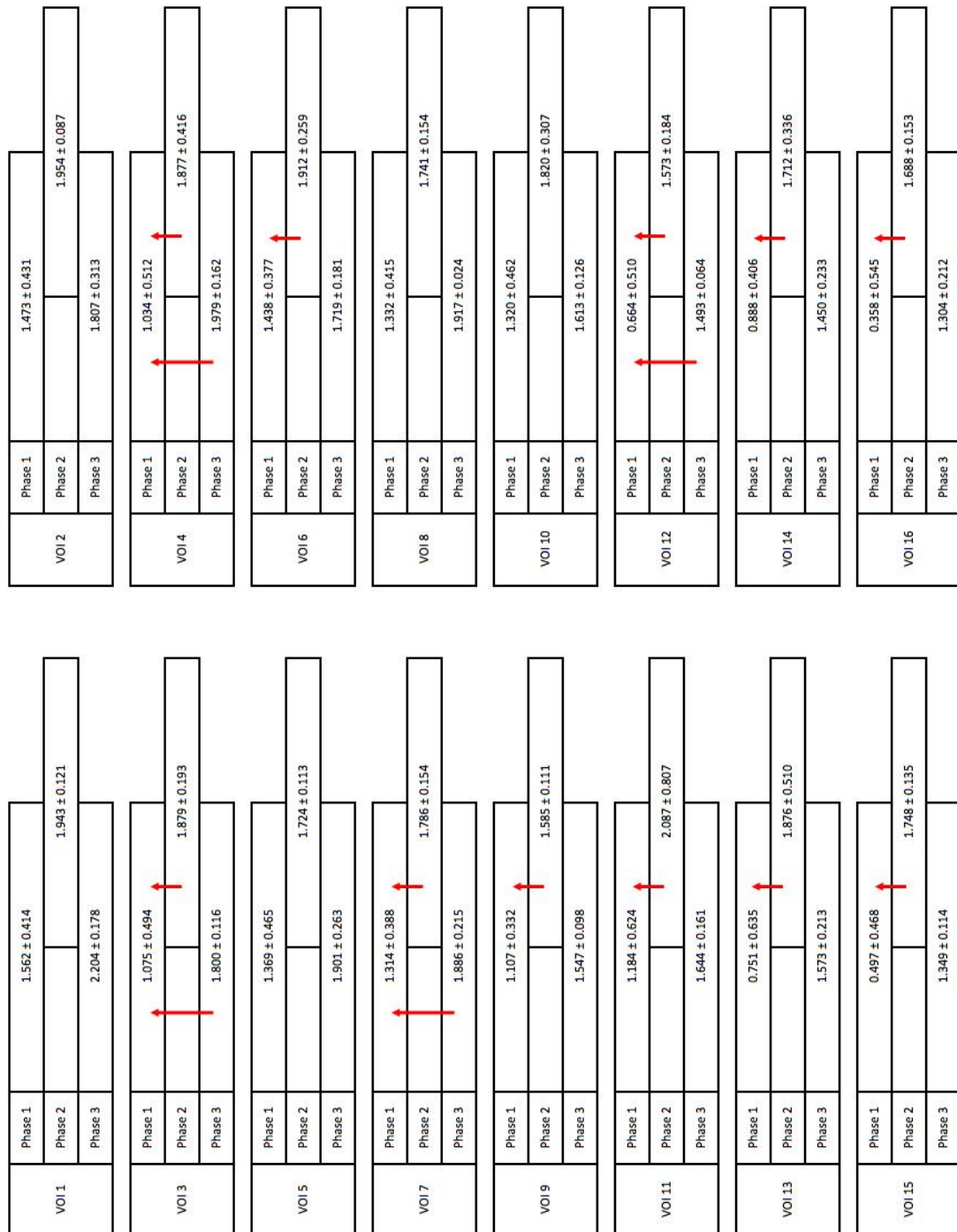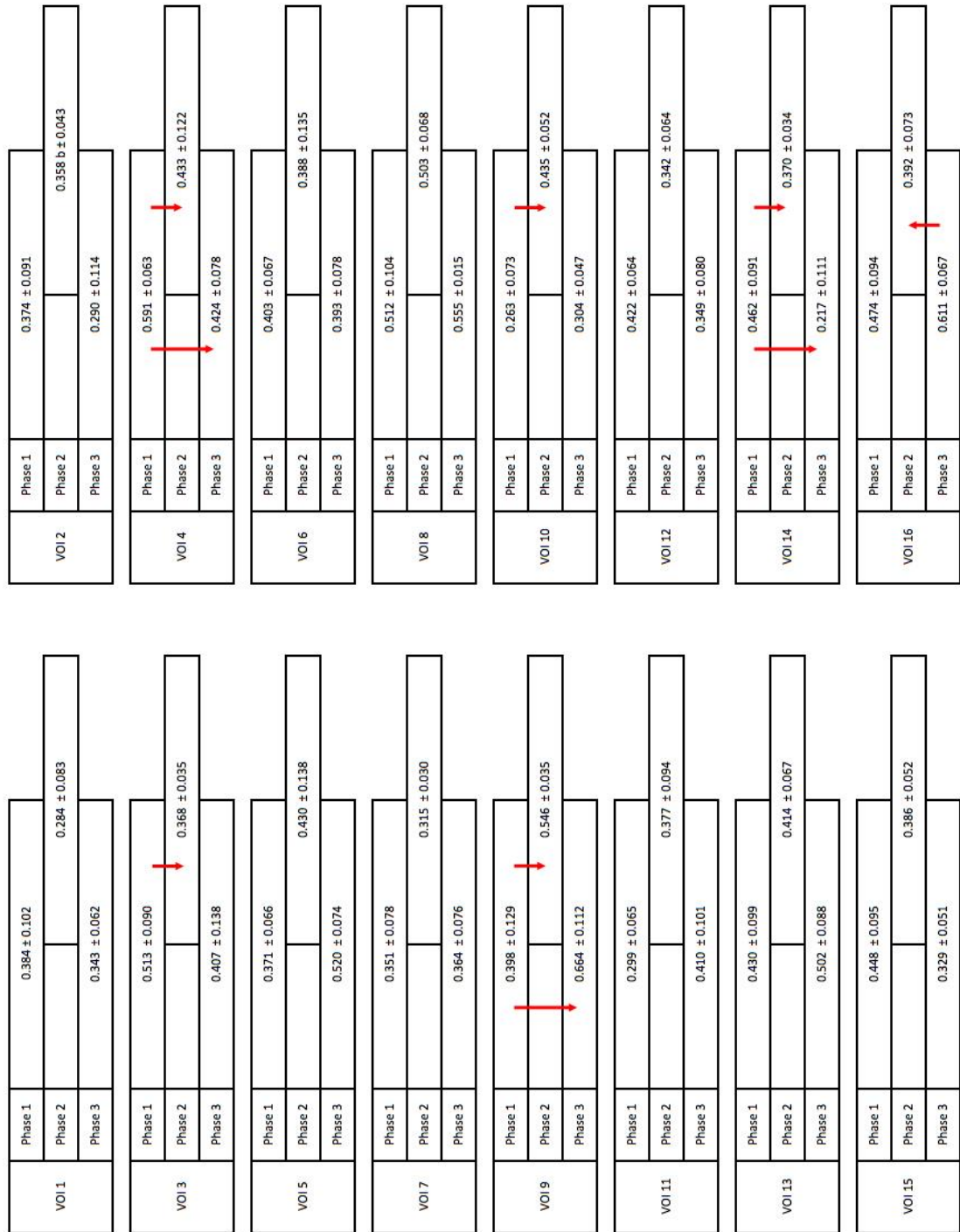
Figure 6.52. Multiple pairwise comparison results for inter-phase analysis at each volume of interest. Values are mean ± SD. Red arrow indicates significant difference exists between connecting phases (p < 0.05), arrow directionality shows decreasing DA.

6.2.7 Summary of regional trabecular architecture

Phase 1

The collation of the statistical analyses and inferred levels of structure for each VOI in the perinatal ischium provided a means to identify trends within trabecular architecture across the ischium [Figure 6.53].

Volume	BV/TV	Tb.Th	Tb.N	Tb.Sp	SMI	DA
1	L	L	I	L	H	L
2	L	L	I	I	H	L
3	I	LI	I	L	I	H
4	H	LI	H	H	I	H
5	L	LI	L	H	H	L
6	L	LI	L	H	H	I
7	L	I	L	H	H	L
8	I	LI	I	I	H	H
9	I	I	L	H	I	I
10	L	H	L	H	H	L
11	I	H	L	H	H	L
12	H	H	I	I	L	I
13	H	H	I	I	L	I
14	H	LI	H	L	L	H
15	H	I	H	L	L	H
16	H	H	H	L	L	H

L	Low
LI	Low-Intermediate
I	Intermediate
H	High

Figure 6.53. Summary of distribution for each parameter in the perinatal ischium.

Five trabecular regions were identified based on perceived architectural similarities between adjacent volumes of interest [Figure 6.54].

An initial distinction was apparent between the contained within the inferior aspect of the ischium, specifically volumes 12 – 16, and those of the superior aspect of the ischium, volumes 1 – 11. The inferior volumes were found to demonstrate consistently high BV/TV values (> 40 %), while the volumes in the superior ischium presented variable proportions of trabecular bone which were typically classified as either intermediate or low BV/TV.

The volumes located within the inferior ischium were further subdivided into two regions based on the presence of graduated changes between the ramal region [VOI 14 – 16] and the upper inferior region [VOI 12 – 13].
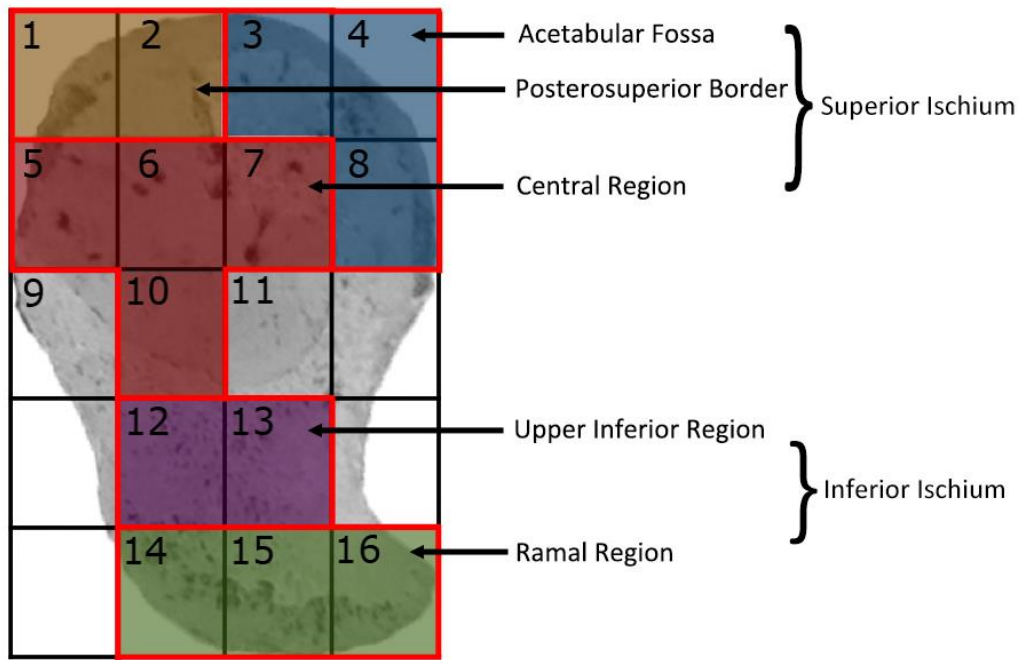
Figure 6.54. Regions of similar trabecular architecture in the perinatal ischium. Red borders separate each defined region.

The ramal region was characterised by a high BV/TV formed from a high number of tightly packed trabeculae of intermediate thickness. Structural model index was relatively low (< 1) indicating a predominantly plate-like morphology, while DA was relatively high (0.45 – 0.47) indicating a degree of alignment of trabeculae. The upper inferior region demonstrated a similar architecture, but with a decrease in trabecular number and an increase in trabecular thickness and separation compared to ramal volumes.

The superior ischium was divided into three discrete regions based on the dominant architectural patterns. The central region, including volumes 5, 6, 7 and 10, demonstrated a consistent trabecular morphology that was characterised by a low number of well-dispersed trabeculae of predominantly low-intermediate thickness. The exception to this was VOI 10, which demonstrated a higher mean thickness than the more superior volumes. The structural model index for this group indicated a relatively even distribution of rod-like and plate-like structures, with a slight tendency towards rod-like structures, while degree of anisotropy was relatively low.

The acetabular fossa, defined by volume 3, 4 and 8, were found to be broadly similar with regards to internal architectural composition to ramal region, with some minor exceptions. Bone volume fraction was elevated in comparison to the neighbouring

volumes, which include the proposed vascular centre. The architecture was defined by an intermediate number of thin, plate-like trabeculae. These volumes also demonstrated the highest degree of anisotropy observed in the ischium.

The volumes of interest which are present on the posterosuperior border (VOI 1 – 2) contained a low bone volume fraction, with a similar BV/TV to the central region. However, the trabecular architecture was characterised by a proliferation of relatively thin, intermediately spaced trabeculae. Indeed, the trabeculae in VOI 1 and 2 possessed the lowest mean thickness observed (< 105 µm). The mean SMI values indicated a region comprised of an even mixture of rod-like and plate-like trabeculae, while the degree of anisotropy was relatively low.

The trabecular architecture of VOI 9 and 11 did not present an architecture that was consistent with any of the adjacent volumes, preventing their incorporation into the established regional groupings. These volumes did show a degree of agreement in their architecture when compared to each other, therefore they were classified as peripheral volumes. The architecture of these peripheral volumes was defined by an intermediate BV/TV comprised of relatively few intermediate to high thickness trabeculae that were of an intermediate separation. SMI indicated that these trabeculae tended towards a plate-like morphology with a low – intermediate degree of anisotropy.

Phase 2 and 3: statistical structural homogeny

In contrast to the high number of pairwise significant differences observed in Phase 1, the data obtained from ischia in Phases 2 and 3 presented relatively few significant pairwise comparisons.

In Phase 2, a distinction between volumes of differing intensities was only possible in a single parameter, the lateral cortical thicknesses. The results for BV/TV, Tb.Th and SMI showed no significant differences between VOI pairs in Phase 2. Values for Tb.N, Tb.Sp and DA returned between 1 and 5 significant pairwise differences, which in each case existed between the highest and lowest mean values, while the ANOVA applied to L.C.Th revealed an overall statistical difference within the ischium, but this was too slight to be attributed to any specific VOI pairs during MPC testing.

In Phase 3, only Tb.N could be subdivided into regions of high, intermediate and low number based on MPC comparisons. No other groupings could be formed due to the low number of significant differences observed for each parameter. The data obtained for BV/TV, SMI and DA each revealed that significant differences were present, but too few pairwise comparisons returned significant results to allow segregation (n = 5, 5 and 6 respectively). Trabecular separation and lateral cortical thickness measurements were found to contain an overall significant difference, but no pairwise significant differences could be identified. Tb.Th and P.C.Th did not reveal any significant differences within the Phase 3 data, although it was noted that the power of the test applied to P.C.Th was low, and therefore the negative result should be treated with some caution.

As a result of this statistical homogeny, it was not possible to identify region-specific trabecular architectures in Phases 2 and 3.

6.2.8 Correlations between histomorphometric parameters by phase

The parameters used to define trabecular bone architecture are not isolated variables, but rather a set of interdependent characteristics that by their very nature share a degree of covariance. For example, in a fixed volume of bone, if mean trabecular thickness is increased the trabecular number must decrease, and therefore a change in trabecular separation may also occur. Variations in structure as detected by degree of anisotropy and structural model index may similarly influence the distribution of trabeculae and concurrently the separation between them.

To investigate whether any evidence of covariance exists between the trabecular bone parameters selected for inclusion in this study, the 'Pairs' function in the statistical package R was utilised. This function plots the all observations from two parameters against each other, independent of the volume in which the data was collected. The distribution of data in these plots can then inform as to the likely relationship between the two parameters. The 'cor.test' function was then used to determine the r^2 value of this relationship and the significance (p value) of the r^2.

A correlation was considered to be present where $r^2 > 0.7$ or < -0.7, and if the r^2 was shown to be statistically significant ($p < 0.05$). Further, a strong correlation was considered to be present where $r^2 > 0.8$ or < -0.8 and a very strong correlation was present if $r^2 > 0.9$ or < -0.9, in both cases only if the p values for the correlation was also found to be less than 0.05.

Phase 1

The 'pairs' plot and associated r^2 values for parameters included in Phase 1 are presented in Figure 6.55. From the 15 comparisons conducted, five were found to demonstrate correlations above the threshold of importance.

Bone volume fraction in this phase demonstrated the greatest number of correlations: was found to be strongly correlated with trabecular number, negatively correlated with trabecular separation and very strongly negatively correlated with structural model index. Trabecular number was also found to be negatively correlated with structural model index and strongly negatively correlated with trabecular separation values. In each of these comparisons, the r^2 was found to be very highly statistically significant.

Phase 2

The 'pairs' plot and associated r^2 values for trabecular bone data in Phase 2 is presented in Figure 6.56.

This phase presented a different arrangement of correlations that surpassed the threshold of importance ($r^2 > 0.7$ or < -0.7) to those in Phase 1: only three such correlations were observed for the Phase 2 data.

Bone volume fraction was again observed to be strongly correlated with trabecular number in this phase, but not with either trabecular separation or structural model index. A correlation was however observed between bone volume fraction and trabecular thickness ($r^2 = 0.723$). A negative correlation also persisted between trabecular number and separation, although it did not reach the threshold of a strong negative correlation ($r^2 < -0.8$). Each of these r^2 values were found to be very highly significant.

No other correlations were found to exceed the threshold of significance in this phase.

Phase 3

The 'pairs' plot and associated r^2 values produced for the trabecular bone data in Phase 3 is presented in Figure 6.57.

Four of the parameter comparisons in Phase 3 returned correlations above the threshold for significance, and demonstrated a similar distribution to Phase 1 correlations. Bone volume fraction was found to be very highly correlated with trabecular number in this phase, compared with the high correlations observed in both previous phases. In addition, a negative correlation was found to exist between bone volume fraction and structural model index ($r^2 = -0.765$).

In addition, negative correlations above the threshold of importance were also observed between trabecular number and trabecular separation ($r^2 = -0.798$), and also trabecular number and structural model index ($r^2 = -0.751$).

Each r^2 value above the threshold of importance was found to be very highly significant ($p < 0.001$), indicating that these correlations were not a result of random variation. No other correlations in this phase surpassed the threshold of importance.
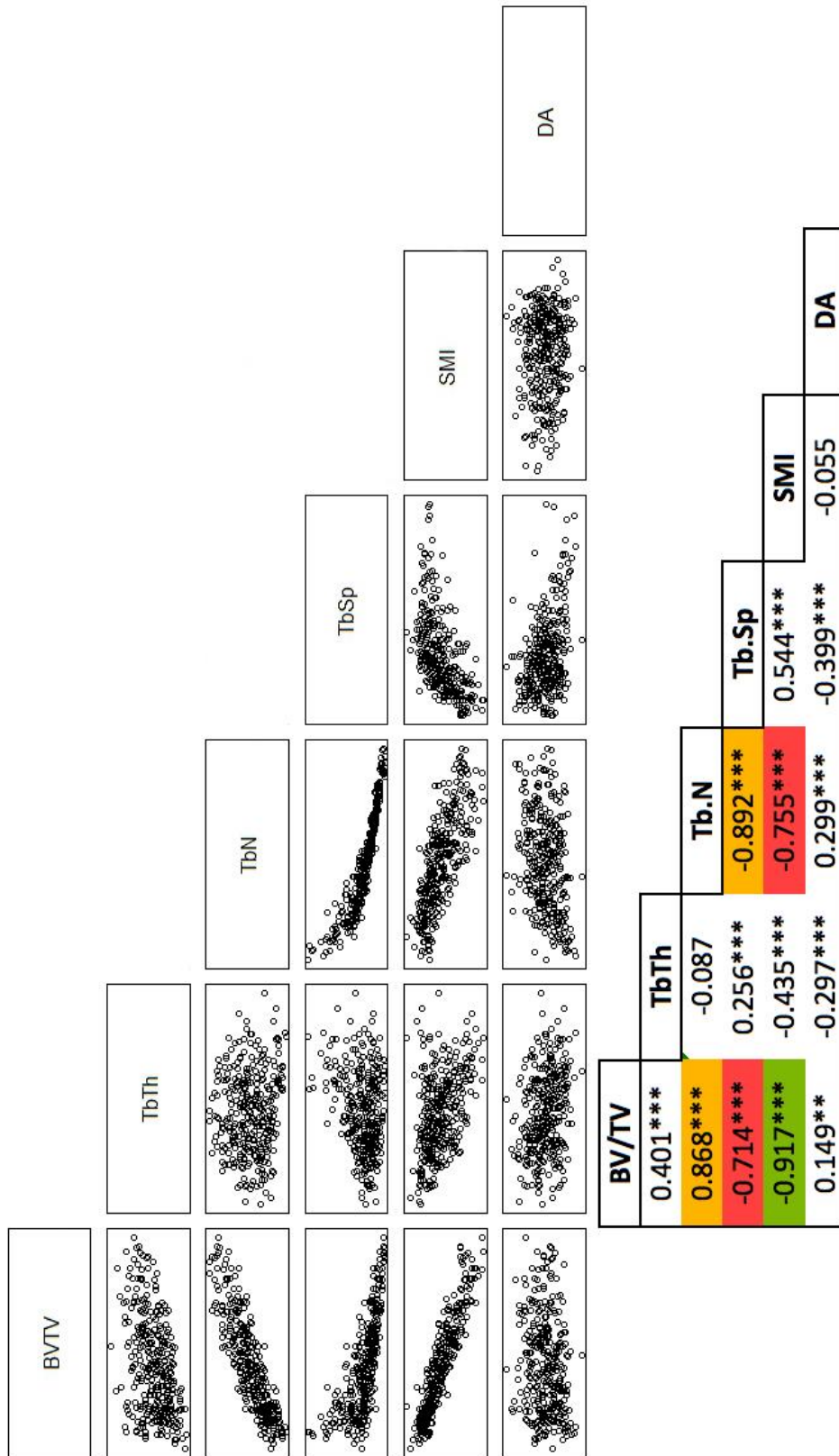
Figure 6.55. Pairs plot of trabecular bone parameters in Phase 1 and associated r^2 values. * r^2 significant (p < 0.05); ** r^2 highly significant (P < 0.01); *** r^2 very highly significant. Red: correlation (r^2 > 0.7 or < -0.7); yellow: strong correlation (r^2 > 0.8 or < -0.8); Green: very strong correlation (r^2 > 0.9 or < -0.9).
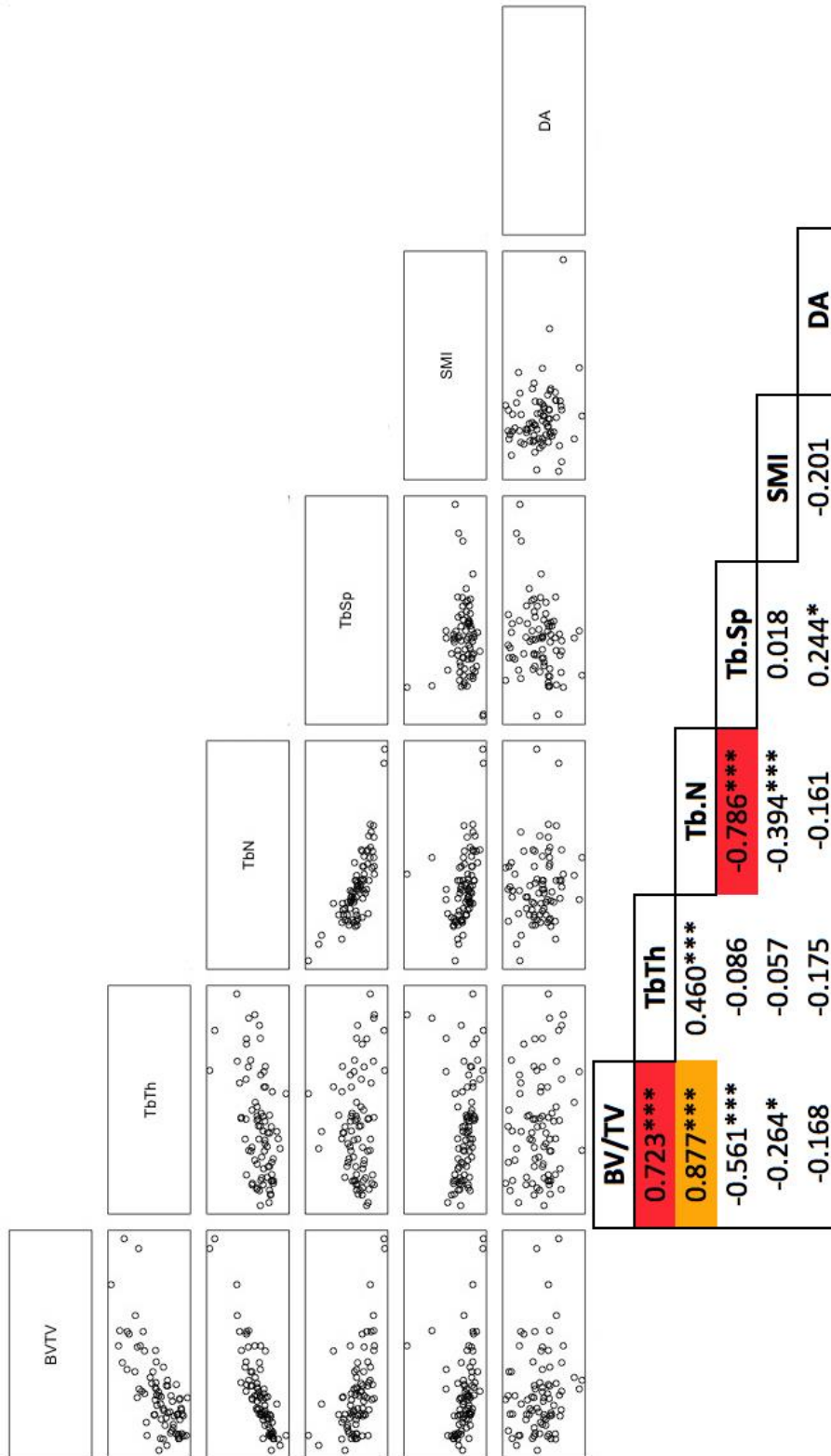
Figure 6.56. Pairs plot of trabecular bone parameters in Phase 2 and associated r² values. * r² significant (p < 0.05); ** r² highly significant (P < 0.01); *** r² very highly significant. Red: correlation (r² > 0.7 or < -0.7); yellow: strong correlation (r² > 0.8 or < -0.8); Green: very strong correlation (r² > 0.9 or < -0.9).
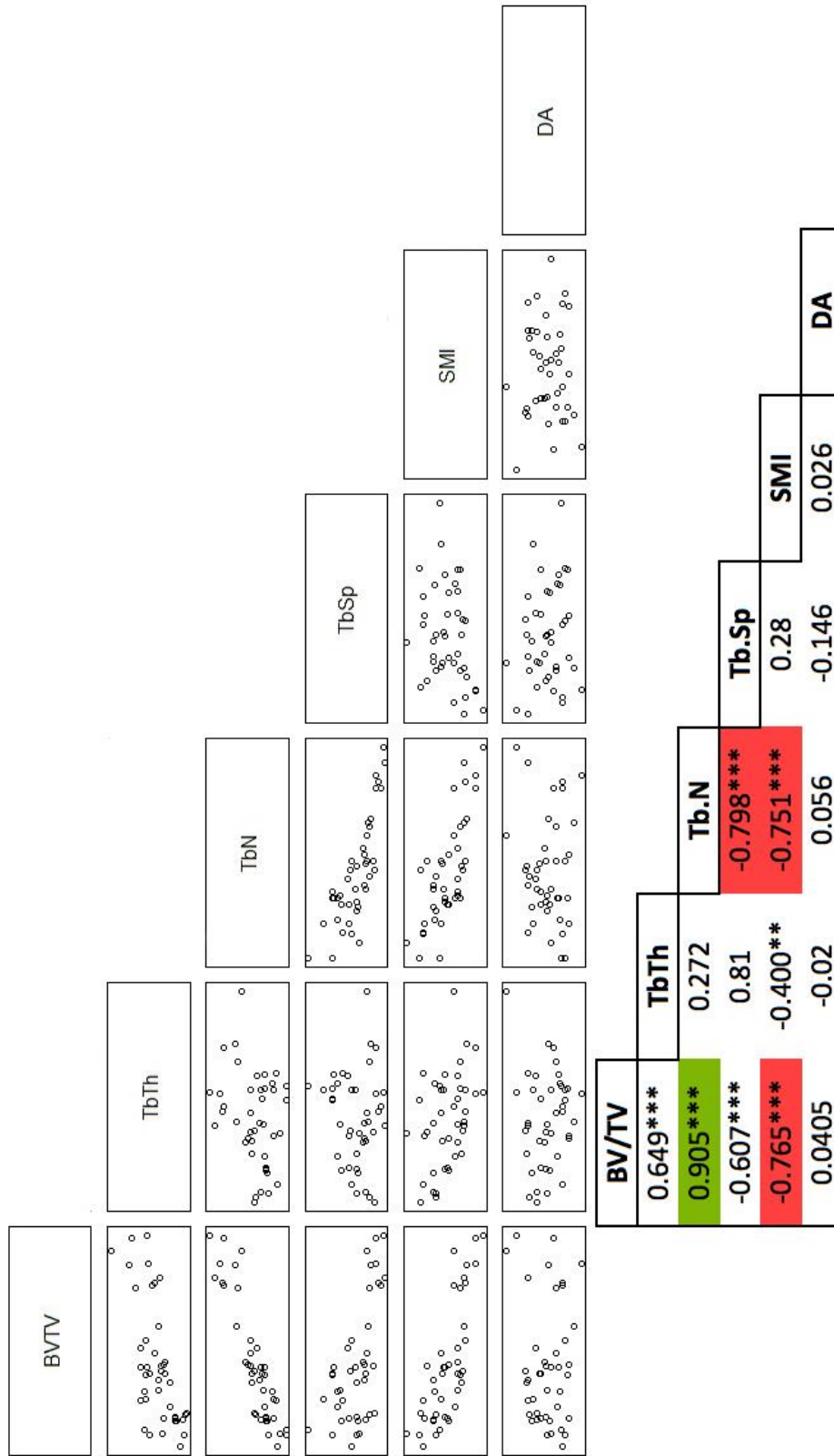
Figure 6.57. Pairs plot of trabecular bone parameters in Phase 3 and associated r² values. * r² significant (p < 0.05); ** r² highly significant (P < 0.01); *** r² very highly significant. Red: correlation (r² > 0.7 or < - 0.7); yellow: strong correlation (r² > 0.8 or < -0.8); Green: very strong correlation (r² > 0.9 or < -0.9).

6.3 Cortical results

6.3.1 Pelvic cortical thickness

Phase 1

The descriptive statistics for measurements of pelvic cortical thickness at each volume of interest are presented in Table 6.25.

A wide range of values was observed for the pelvic surface in this phase, with mean values ranging between 176.04 µm (VOI 1) and 782.18 µm (VOI 11). The relative standard deviations fell between 17.14 % (VOI 15) and 29.89 % (VOI 4) of the mean values. This data is summarised graphically in Figure 6.58.

Table 6.25. Descriptive statistics (mean, range, standard deviation and relative standard deviations) for Phase 1 P.C.Th for each volume of interest.

VOI	Mean	Range		SD (±)	RSD (±)
		Min	Max		
1	176.04	122.08	243.98	39.28	22.31
2	308.97	194.12	441.02	60.06	19.44
3	348.21	195.22	547.18	87.69	25.18
4	248.94	134.08	406.22	74.42	29.89
5	245.08	160.94	399.70	67.04	27.36
6	469.03	343.76	654.86	92.73	19.77
7	690.17	444.28	1091.88	178.74	25.90
8	481.59	308.76	776.70	111.90	23.24
9	333.41	204.04	544.88	82.52	24.75
10	572.74	376.22	1026.12	161.28	28.16
11	782.18	482.96	1235.78	171.19	21.89
12	536.74	339.44	767.62	101.40	18.89
13	557.34	404.94	979.52	149.00	26.73
14	244.27	163.70	418.58	57.31	23.46
15	252.40	193.74	348.38	43.25	17.14
16	190.82	130.60	244.48	35.42	18.56
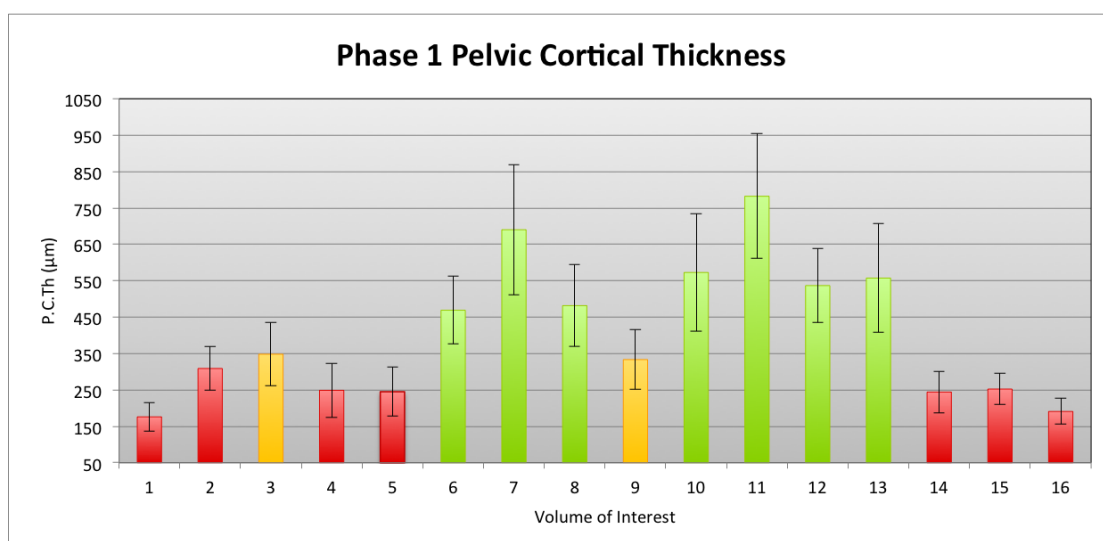
Phase 1 P.C.Th (µm)

Figure 6.58. Graphic representation of mean (± SD) P.C.Th per VOI for individuals in Phase 1. High (green), intermediate (yellow) and low (red) colouration applied based on MPC testing.

The Phase 1 P.C.Th data was found to be non-parametric in nature (Shapiro-Wilk $p < 0.05$), therefore the Kruskal-Wallis one way ANOVA on ranks was applied to determine whether a significant difference was present. The results confirmed that a very highly significant difference was present (H = 258.905 with 15 degrees of freedom, therefore $p < 0.001$) in the volumes analysed. Following this, non-parametric MPC procedures following Dunn's method were used to determine whether significant differences existed between specific pairs of volumes [Figure 6.59]. Fifty-four of these pairwise comparisons reached the level of statistical significance ($p < 0.05$), which were found to exist predominantly to separate the peripheral volumes superiorly (1 – 4) and inferiorly (14 – 16) from those located more centrally (6 – 13).

The distribution of these significant pairwise comparisons facilitated the creation of three cortical thickness groups which separated the low (red), intermediate (yellow) and high (green) cortical thicknesses observed in this phase [Figure 6.60].

The low P.C.Th group comprised of thicknesses if 176.04 µm to 308.97 µm and occupied volumes superiorly (1, 2, 4 and 5) and inferiorly (14 – 16) around the periphery of the bone. They were defined as being volumes in which the cortex was significantly thinner on average than the central high thickness group, with a minimum of five significant pairwise comparisons with volumes classified as high.
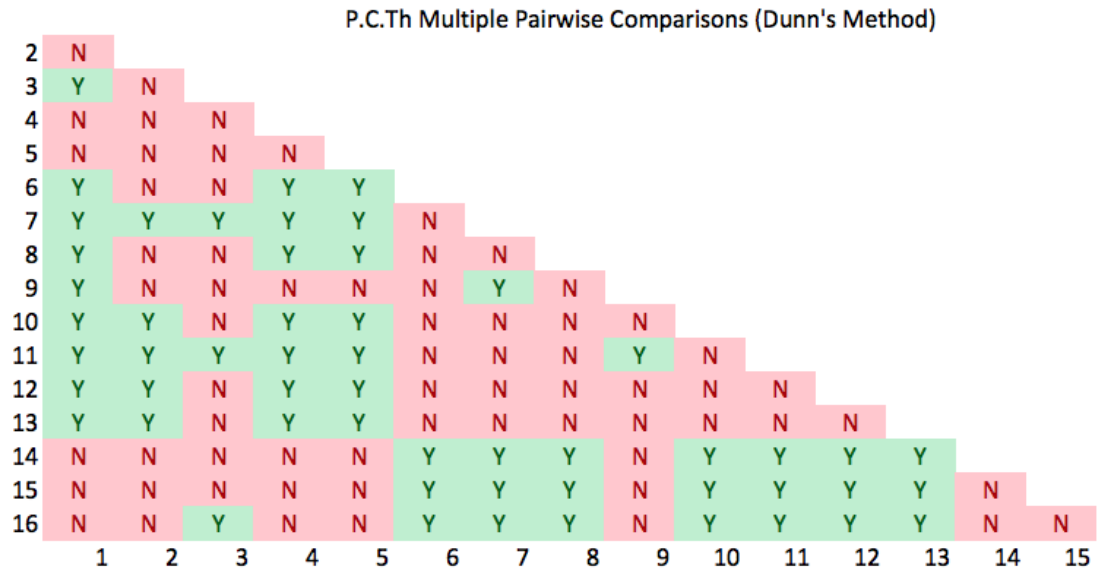
Figure 6.59. Multiple pairwise comparison results for Phase 1 P.C.Th. Y = statistically significant difference (p < 0.05); N = no significant difference detected.

Figure 6.60. Pelvic cortical thickness groups mapped to the perinatal ischium. Green: high P.C.Th; yellow: intermediate P.C.Th; red: low P.C.Th. The values below the VOI number are the mean P.C.Th for that volume (µm).

The high P.C.Th volumes concurrently were found to be statistically thicker on average than those defined as low thickness and included a centrally-located mass (VOIs 6 – 8 and 10 – 13). As these volumes shared borders, they established a single high thickness region. Values were observed to lie between 469.03 µm and 782.18 µm.

Volumes 3 and 9 were classified as intermediate between groups as they exhibited statistically significant differences from both the lowest thickness volumes (1 and 16) and the highest thickness volumes (7 and 11). Each of these volumes was found to exist peripherally, and also to share borders with both low and high thickness volumes.

Phase 2

The descriptive statistics for Phase 2 pelvic cortical thicknesses are presented in Table 6.26.

Table 6.26. Descriptive statistics for Phase 2 P.C.Th at each VOI.

		Phase 2 P.C.Th (µm)			
VOI	Mean	Range		SD (±)	RSD (±)
		Min	Max		
1	146.40	106.56	161.26	22.68	15.49
2	136.80	117.70	174.54	22.30	16.30
3	129.27	108.16	151.94	20.02	15.49
4	134.58	102.10	182.46	29.28	21.75
5	143.86	136.66	151.98	6.40	4.45
6	171.84	134.40	219.16	31.26	18.19
7	197.49	169.10	236.84	24.68	12.50
8	183.62	147.34	242.14	37.42	20.38
9	154.00	132.64	193.54	24.69	16.03
10	256.11	185.90	334.36	53.35	20.83
11	296.35	216.04	328.46	45.58	15.38
12	202.30	122.28	263.22	53.03	26.21
13	219.58	170.12	249.94	30.82	14.04
14	153.61	131.74	185.28	19.84	12.91
15	166.14	133.88	179.54	18.80	11.31
16	171.27	125.26	207.54	29.77	17.38

The range of mean thicknesses observed for the pelvic cortex in this phase was markedly narrower than that of the same cortex in Phase 1, with all values lying between 129.27 µm (VOI 3) and 296.35 µm (VOI 11). The relative standard deviations were also found to be smaller in this group with a range of 4.45 % (VOI 5) to 26.21 % (VOI 12). This data is summarised graphically in Figure 6.61.

The data obtained for this phase was found to be parametric in nature (Shapiro-Wilk p = 0.075; equal variance p = 0.734) therefore the parametric one-way ANOVA was applied to test for significant differences. The H-statistic was found to be 10.631 with

15 degrees of freedom, with a very highly significant p value of < 0.001. To determine whether significant differences were also present between specific VOI pairs, the Holm-Sidak MPC procedure was applied.
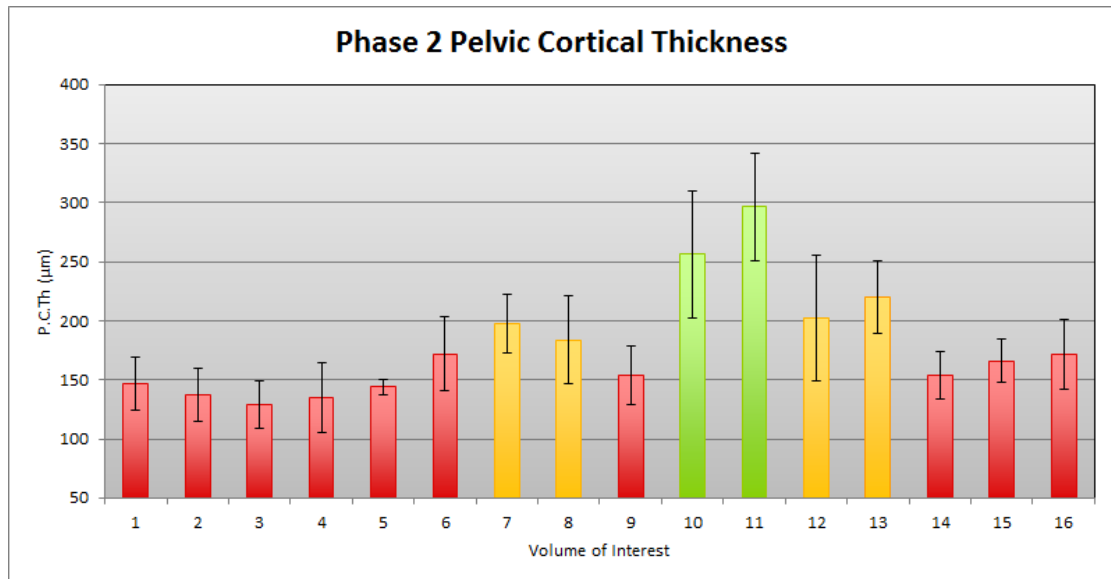
Figure 6.61. Graphic representation of mean (± SD) P.C.Th per VOI for individuals in Phase 2.

The results of the MPC test revealed that 28 pairwise comparisons demonstrated significant differences [Figure 6.62]. These differences were observed to occur in two distinct groups which indicated that volumes 10 and 11 were significantly different from the majority of volumes, excluding each other. VOI 13 was also found to be significantly higher than a more limited number of volumes.

The precise distribution of these significant differences indicated that the pelvic cortex could be divided into three groups; low, intermediate and high pelvic cortical thicknesses [Figure 6.63].

VOI 11 was found to be significantly thicker than all other volumes, with the exception of VOI 10. VOI 10 was then found to be significantly thicker than 10 volumes, excluding VOI 7, 8, 11, 12 and 13. The volume of differences these two alone presented allowed them to be classified as having a relatively high thickness (green), with mean values of 256.11 µm and 296.35 µm.

P.C.Th Multiple Pairwise Comparisons (Holm-Sidak Method)

	1	2	3	4	5	6	7	8	9	10	11	12	13	14	15
2	N														
3	N	N													
4	N	N	N												
5	N	N	N	N											
6	N	N	N	N	N										
7	N	N	N	N	N	N									
8	N	N	N	N	N	N	N								
9	N	N	N	N	N	N	N	N							
10	Y	Y	Y	Y	Y	Y	N	N	Y						
11	Y	Y	Y	Y	Y	Y	Y	Y	Y	N					
12	N	N	N	N	N	N	N	N	N	N	Y				
13	N	Y	Y	Y	Y	N	N	N	N	N	Y	N			
14	N	N	N	N	N	N	N	N	N	Y	Y	N	N		
15	N	N	N	N	N	N	N	N	N	Y	Y	N	N	N	
16	N	N	N	N	N	N	N	N	N	Y	Y	N	N	N	N
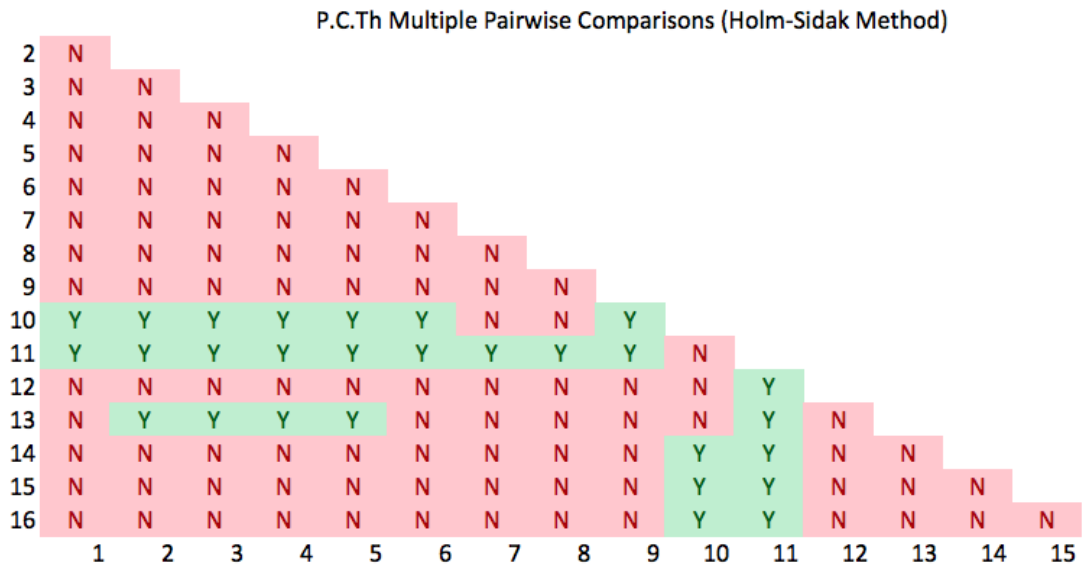
Figure 6.62. Multiple pairwise comparison results for Phase 2 P.C.Th. Y = statistically significant difference (p < 0.05); N = no significant difference detected.

4	3	2	1
134.58	129.27	136.80	146.40
8	7	6	5
183.62	197.49	171.84	143.86
	11	10	9
	296.35	256.11	154.00
	13	12	
	219.58	202.30	
16	15	14	
171.27	166.14	153.61	
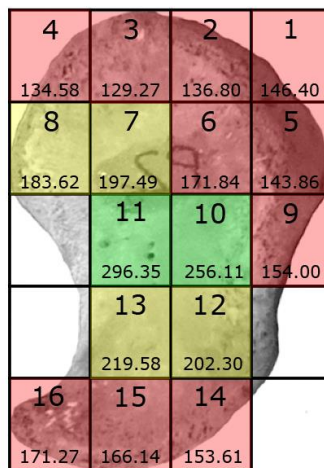
Figure 6.63. Pelvic cortical thickness groups mapped to the Phase 2 ischium. Green: high P.C.Th; yellow: intermediate P.C.Th; red: low P.C.Th. The values below the VOI number are the mean P.C.Th for that volume (μm).

Volumes 1-6, 9 and 14 – 16 were found to be significantly thinner than both VOI 10 and 11 which was used as a criterion to mark these volumes as being of relatively low cortical thickness (red). Mean values for this group fell between 129.27 μm and 171.27 μm.

Volumes 8, 9, 12 and 13 did not demonstrate the same patterns of significance as the remaining volumes: they were statistically lower than only VOI 11 and VOIs 8, 9 and 12 were not found to be significantly thicker than any other volumes. VOI 13 was found to

be significantly thicker in four pairwise comparisons, with volumes 2 – 5. However, as this was markedly fewer significant results than the high thickness group, and was itself significantly thinner than VOI 11, volume 13 was also incorporated in the intermediary group.

Phase 3

The descriptive statistics for pelvic cortical thickness in Phase 3 are documented in Table 6.27.

Table 6.27. Descriptive statistics for Phase 3 P.C.Th for each VOI. n/a indicates result was based on a single observation due to exclusion measurements in volumes exhibiting damage, and did not therefore have an associated standard deviation.

		Phase 3 P.C.Th (µm)			
VOI	Mean	Range		SD (±)	RSD (±)
		Min	Max		
1	119.76	119.76	119.76	n/a	n/a
2	166.98	144.58	208.36	35.88	21.49
3	191.28	162.72	226.16	32.19	16.83
4	172.41	126.18	215.06	44.55	25.84
5	181.98	140.20	223.76	59.09	32.47
6	272.53	203.64	344.98	70.74	25.96
7	277.35	205.16	381.48	92.40	33.31
8	272.05	163.34	426.30	137.27	50.46
9	271.23	141.50	400.96	183.47	67.64
10	347.79	189.30	437.04	137.62	39.57
11	347.14	212.30	446.84	121.15	34.90
12	293.84	199.64	347.66	81.86	27.86
13	301.38	147.64	409.56	136.77	45.38
14	222.90	211.26	234.54	16.46	7.39
15	341.42	284.12	398.72	81.03	23.73
16	257.87	250.94	264.80	9.80	3.80

The mean values for P.C.Th in this phase were wider in range than in Phase 2, with a minimum of 119.76 µm (VOI 1) and a maximum of 347.79 µm (VOI 10). It should be noted that the value obtained for VOI 1 was based on only a single specimen however: the lowest mean pooled from multiple specimens was found in VOI 2 (116.98 µm). Excluding VOI 1, which did not present standard deviations, the relative standard deviations fell between 3.80 % (VOI 16) and 67.64 % (VOI 9), showing a much greater

variation between individuals in some volumes than previously observed. This data is summarised in Figure 6.64.
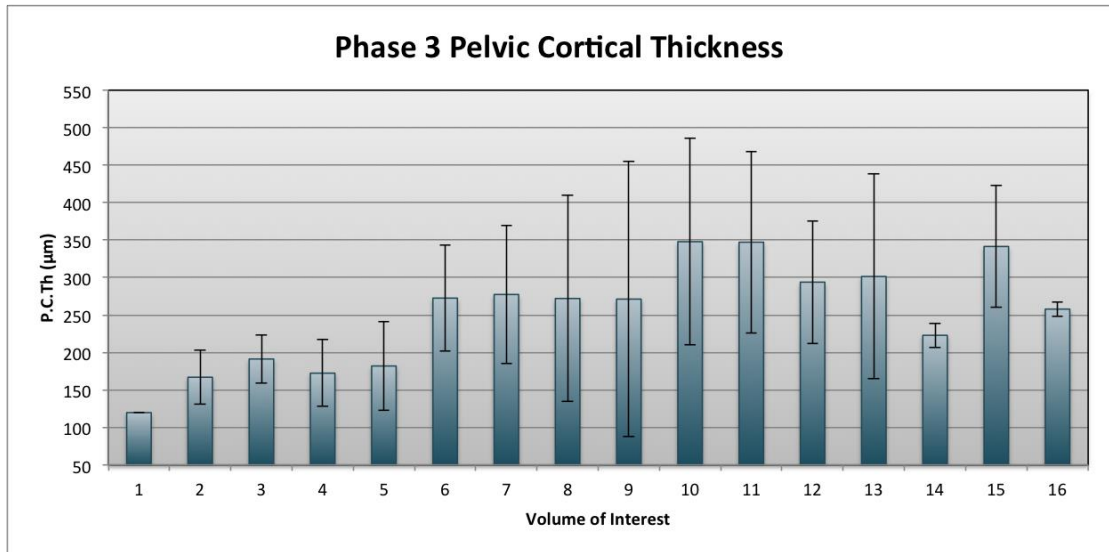
Figure 6.64. Graphical representation of mean (± SD) P.C.Th per VOI for individuals in Phase 3.

The phase 3 pelvic cortical thickness data was found to be parametric (Shapiro-Wilk p = 0.534; equal variance p = 0.594), therefore a parametric one-way ANOVA was applied to test for significant differences. The p value returned did not reach a level of statistical significance (F = 1.27 with 15 degrees of freedom, therefore p = 0.292), suggesting that the variation between volumes did not exceed that which may be expected as a result of random variation. As a result of the small sample size, low thickness values and relatively large standard deviations observed, the test fell considerably below the desired level of power (α = 0.055), indicating that the negative result obtained should be interpreted with caution.

Inter-phase variation by VOI

Differences were observed between the mean pelvic cortical thicknesses observed for each of the phases investigated, although the magnitude of these differences varied in each VOI. It was noted that although statistically there were relatively few significant differences beyond Phase 1, the pattern of means remained consistent between phases. VOI 7, 10 and 11 were consistently among the highest thicknesses observed, while the volumes positioned superiorly and inferiorly tended to present lower thicknesses.

However, despite similar trends occurring in each phase, it was observed that in all volumes except VOI 15 and 16, the mean P.C.Th values were highest in Phase 1 while Phase 2 and 3 were typically characterised by relatively low P.C.Th [Figure 6.65].
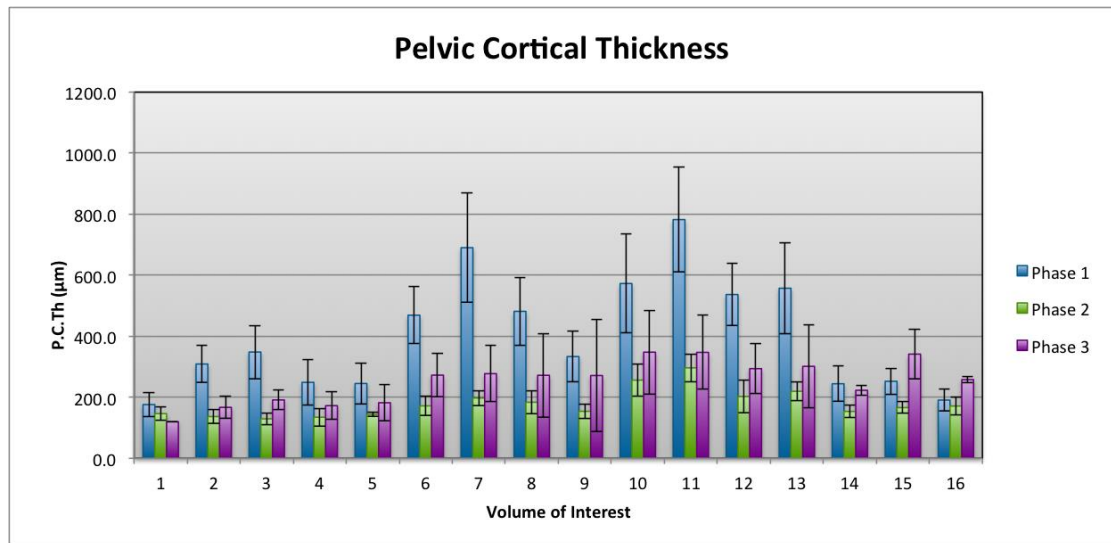
Figure 6.65. Summarised results for mean P.C.Th ± SD at each VOI per phase.

To determine whether the observed differences in mean values were of statistical significance, analysis of variance tests were conducted on the pooled phase data per VOI [Table 6.28]. Volumes 3, 5, 6, 7, 10 – 12 and 14 – 16 were found to be parametric and were therefore subjected to parametric one way ANOVAs. Volumes 1, 2, 4 and 9 were found to be not normally distributed (Shapiro-Wilk $p < 0.05$) while volumes 8 and 13 did not demonstrate equal variance ($p < 0.05$). These volumes were processed using non-parametric Kruskal-Wallis one-way ANOVA tests.

The results of the ANOVA tests revealed that in volumes 2 – 16, significant differences existed across the three phases analysed ($p < 0.05$). In volumes 4, 5, 9 and 14 these differences were found to be highly significant ($p < 0.01$), while in volumes 2, 3, 6 – 8, 10 – 13 and 15, the differences reached the threshold of very highly significant ($p < 0.001$).

Multiple pairwise comparison procedures were then applied to each volume which displayed overall significant differences, following the Holm-Sidak method for parametric data and Dunn's method for non-parametric data. A minimum of one pairwise significant difference was found for each parameter tested in this manner [Figure 6.66].

Table 6.28. Analysis of variance results for inter-phase comparisons of P.C.Th in each volume of interest. ◊ indicates the test was non-parametric and the H statistic is presented in place of the F statistic. ** highly significant difference (p < 0.01); *** very highly significant difference (p < 0.001).

VOI	F / H◊	DoF	P
1	4.363	2	0.048
2	25.571	2	< 0.001***
3	18.864	2	< 0.001***
4	6.663	2	0.005**
5	5.979	2	0.008**
6	28.459	2	< 0.001***
7	24.649	2	< 0.001***
8	18.464	2	< 0.001***
9	10.93◊	2	0.004**
10	14.893◊	2	< 0.001***
11	26.281	2	< 0.001***
12	30.135	2	< 0.001***
13	16.217◊	2	< 0.001***
14	11.35◊	2	0.003**
15	13.974	2	< 0.001***
16	4.759	2	0.019*

The results of these MPC tests confirmed that in VOI 2 – 15, Phase 1 pelvic cortical thicknesses were significantly higher than those of Phase 2, and in VOIs 2, 3, 6 – 8 and 11 – 13 P.C.Th was also higher in Phase 1 than Phase 3. Pelvic cortical thickness was not found to be higher in Phase 2 than any VOI in Phase 1, and volumes 2 -14 were statistically similar in thickness to values observed for Phase 3. However, in VOI 15 and 16 it was found that Phase 3 P.C.Th values were significantly higher than those of both Phase 2 and Phase 1.

Figure 6.66. Multiple pairwise comparison results for inter-phase analysis at each volume of interest. Values are mean ± SD. Red arrow indicates significant difference exists between connecting phases (p < 0.05), arrow directionality shows decreasing P.C.Th.

6.3.2 Lateral cortical thickness

Phase 1

The descriptive statistics for the lateral cortical thickness measurements (L.C.Th) obtained from Phase 1 individuals are summarised in Table 6.29.

Table 6.29. Descriptive statistics (mean, range, standard deviation and relative standard deviations) for Phase 1 L.C.Th for each volume of interest.

		Phase 1 L.C.Th (µm)			
VOI	**Mean**	**Range**		**SD (±)**	**RSD (±)**
		Min	**Max**		
1	152.05	115.68	222.96	35.73	23.50
2	162.84	112.84	249.06	38.93	23.91
3	169.81	111.14	244.50	37.38	22.01
4	166.17	123.90	230.40	35.11	21.13
5	183.59	122.14	267.44	50.06	27.27
6	181.63	111.10	263.14	43.16	23.76
7	188.36	123.84	280.60	44.86	23.81
8	208.29	146.08	287.56	44.47	21.35
9	243.45	132.20	476.22	86.70	35.61
10	216.61	129.16	349.14	67.72	31.26
11	194.57	119.76	311.38	49.60	25.49
12	185.56	122.46	279.10	44.80	24.14
13	199.29	117.74	329.38	48.14	24.16
14	169.67	115.00	284.54	44.00	25.93
15	158.05	115.36	250.00	32.47	20.55
16	150.19	98.32	221.22	32.74	21.80

The mean values for the lateral cortex were found to occupy a much narrower range than was observed for the pelvic cortex in the same phase. The mean values fell between 150.19 µm (VOI 16) and 243.45 µm (VOI 9), with relative standard deviations between 20.55 % (VOI 15) and 35.61 % (VOI 9). The mean and standard deviation for each volume is displayed graphically in Figure 6.67.

The data for this phase failed the Shapiro-Wilk test of normal distribution ($p < 0.05$), therefore a non-parametric Kruskal-Wallis ANOVA on ranks was used to determine if the differences between volumes demonstrated an overall significant difference. An H-statistic of 60.41 with 15 degrees of freedom was returned, with a corresponding p

value of < 0.001. Therefore, it was concluded that there was a very highly significant difference within the data.
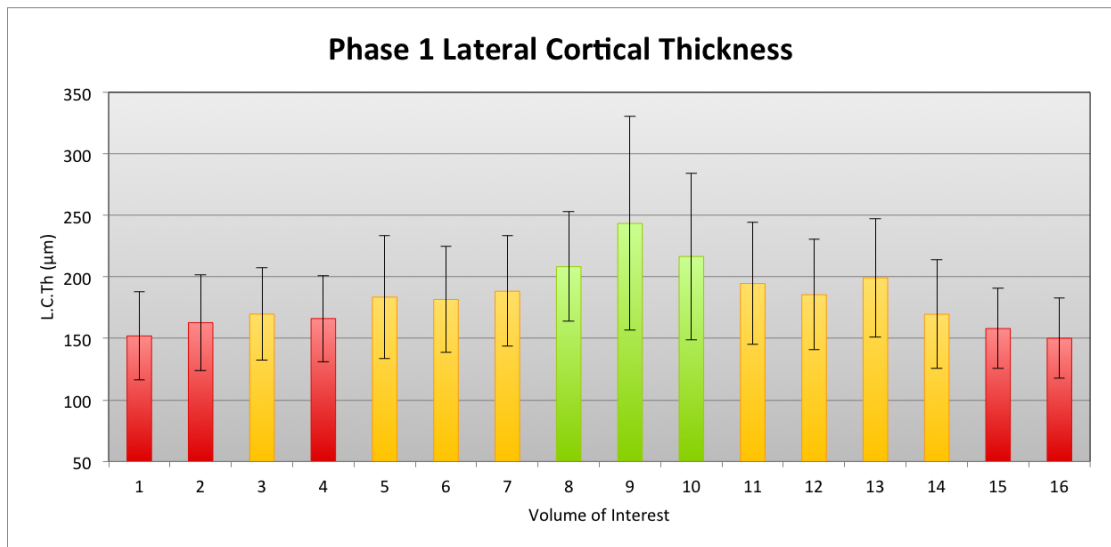
Figure 6.67. Graphic representation of mean (± SD) L.C.Th per VOI for individuals in Phase 1. High (green), intermediate (yellow) and low (red) colouration applied based on MPC testing.

The data for this phase failed the Shapiro-Wilk test of normal distribution (p < 0.05), therefore a non-parametric Kruskal-Wallis ANOVA on ranks was used to determine if the differences between volumes demonstrated an overall significant difference. An H-statistic of 60.41 with 15 degrees of freedom was returned, with a corresponding p value of < 0.001. Therefore, it was concluded that there was a very highly significant difference within the data.

Multiple pairwise comparisons were then conducted using Dunn's method [Figure 6.68]. Significant differences (p < 0.05) were found to exist in only 9 pairwise comparisons, including the comparison of VOI 1 and 16 with volumes 8 – 10, and also VOI 9 with VOIs 2, 4 and 15. Although few in number, when mapped to the ischium these revealed slight regional differences which separated the superior and inferior volumes from those located centrally [Figure 6.69].

Those volumes which were considered to exhibit low lateral cortical thickness included volumes 1, 2, 4, 15 and 16, with values between 150.19 μm and 166.17 μm. As with the pelvic cortex, these lower volumes occupied peripheral locations in the ramus inferiorly and along the superior margin. Statistically they were defined as those which were found to be statistically thinner than the high thickness group.
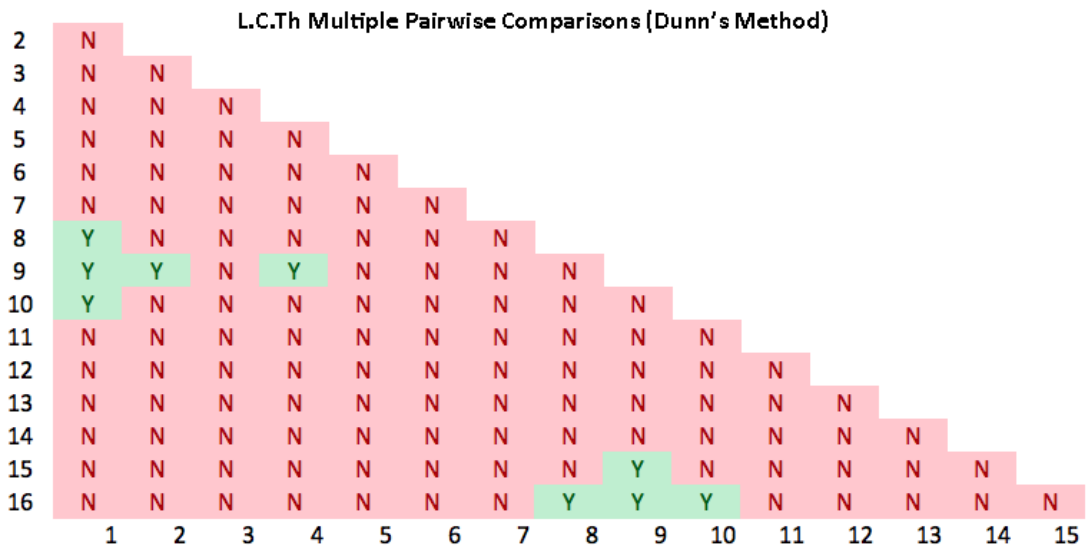
Figure 6.68. Multiple pairwise comparison results for Phase 1 L.C.Th. Y = statistically significant difference (p < 0.05); N = no significant difference detected.
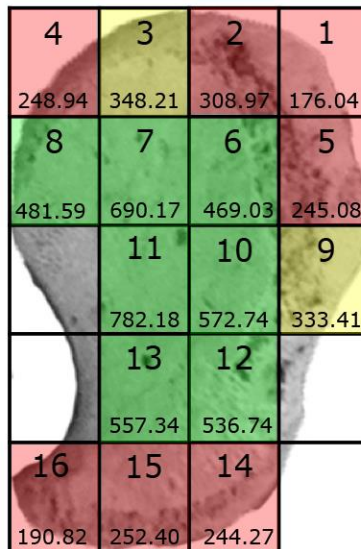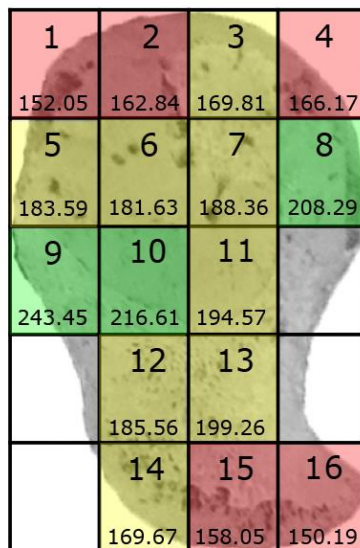

Figure 6.69. Lateral cortical thickness groups mapped to the perinatal ischium. Green: high L.C.Th; yellow: intermediate L.C.Th; red: low L.C.Th. The values below the VOI number are the mean L.C.Th for that volume (μm).

The high thickness volumes consisted of only VOIs 8, 9 and 10, each demonstrating thicknesses greater than 208.29 μm. Each volume was found to be significantly thicker than those designated as low thickness. It should be noted that although the lateral thicknesses in these volumes share a designation with their pelvic cortical thickness values, they were markedly lower in magnitude.

The remaining 9 volumes in this phase were designated as intermediate and did not return any statistically significant pairwise comparisons, either with each other or the

high and low thickness groups. This implied homogeneity is consistent with the very narrow range of values observed for the lateral cortical thicknesses in this phase, and provides further contrast with observations of the pelvic cortical thickness.

Phase 2

The descriptive statistics calculated for Phase 2 lateral cortical thickness are displayed in Table 6.30.

Table 6.30. Descriptive statistics for Phase 2 L.C.Th at each VOI.

VOI	Mean	Range		SD (±)	RSD (±)
		Min	**Max**		
Phase 2 L.C.Th (µm)					
1	137.83	113.78	166.32	20.95	15.20
2	124.73	119.56	141.14	9.28	7.44
3	124.70	111.40	147.66	14.15	11.35
4	141.02	112.94	220.04	45.11	31.99
5	143.67	126.16	168.80	21.87	15.22
6	131.68	110.32	151.82	16.17	12.28
7	149.19	137.28	177.54	16.13	10.81
8	157.96	137.20	202.80	27.87	17.64
9	129.99	104.32	157.48	19.55	15.04
10	145.66	124.02	168.70	19.35	13.29
11	169.97	129.84	214.52	34.73	20.43
12	151.22	126.46	209.16	33.26	22.00
13	194.64	158.72	247.54	38.05	19.55
14	133.18	102.70	191.18	35.69	26.80
15	147.21	116.24	211.34	37.13	25.22
16	128.06	114.06	162.36	19.87	15.52

As with Phase 1 L.C.Th, the range of values observed for this phase was found to be narrow, with a minimum mean thickness of 124.70 µm (VOI 3) and a maximum thickness of 194.64 µm (VOI 13). Relative standard deviations were found to be slightly smaller than those of Phase 1, with values falling between 7.44 % (VOI 2) and 31.99 % (VOI 4). This data is presented visually in Figure 6.70.
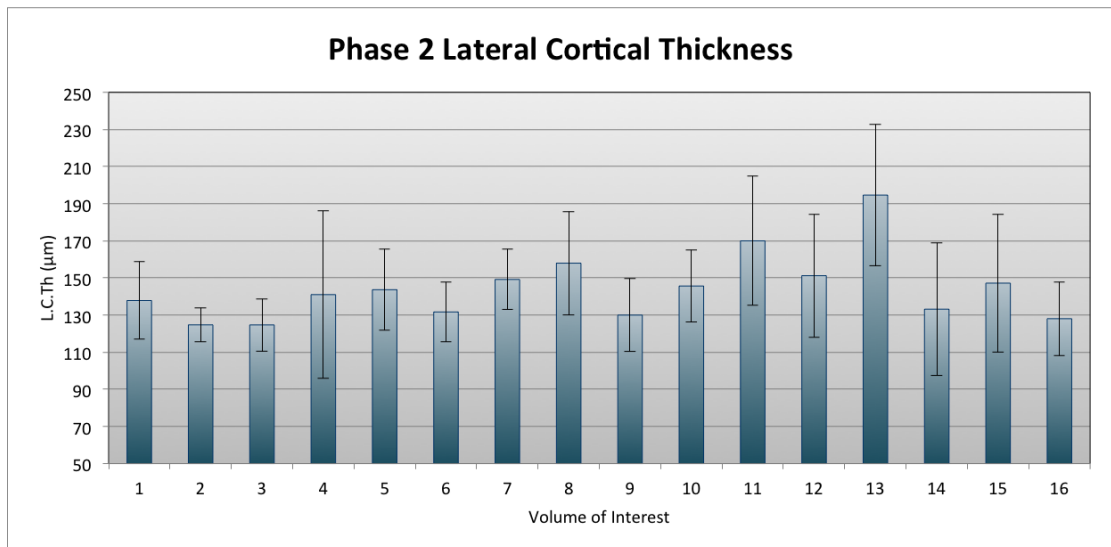
Figure 6.70. Graphic representation of mean (± SD) L.C.Th per VOI for individuals in Phase 2. No L.C.Th groups were identified, therefore colour coding has not been applied.

The data for this phase was also found to be non-parametric (Shapiro-Wilk $p < 0.05$), thus requiring the Kruskal-Wallis one-way ANOVA on ranks to investigate the presence of potential significant differences. A significant difference was found for this phase ($H = 28.112$ with 15 degrees of freedom, therefore $P = 0.021$). Multiple pairwise comparisons using Tukey's test were subsequently used to investigate whether this difference could be localised to specific pairs of volumes. However, no significant pairwise comparisons could be identified, indicating that while an overall significant difference was present it was not great enough to be expressed between specific volumes.

Phase 3

The descriptive statistics for lateral cortical thickness in Phase 3 are displayed in Table 6.31.

The mean values in this phase were found to fall between 123.52 µm (VOI 1) and 304.42 µm (VOI 13), although it should be noted that the value obtained for VOI 1 was based on only a single specimen. The lowest mean value based on multiple observations was found in the neighbouring VOI 2, with a mean thickness of 160.55 µm. Relative standard deviations for this phase ranged between 3.68 % and 47.32 %. This data is summarised in Figure 6.71.

Table 6.31. Descriptive statistics for Phase 3 L.C.Th for each VOI. n/a indicates result was based on a single observation and did not therefore have an associated standard deviation.

VOI	Mean	Range		SD (±)	RSD (±)
		Min	Max		
1	123.52	123.52	123.52	n/a	n/a
2	160.55	119.60	194.34	37.88	23.59
3	208.20	170.22	279.22	61.55	29.57
4	175.46	149.56	223.58	41.71	23.77
5	164.76	151.32	178.20	19.01	11.54
6	216.36	160.24	305.06	77.71	35.92
7	223.59	186.76	295.76	62.51	27.96
8	260.59	166.44	400.18	123.32	47.32
9	226.90	179.90	273.90	66.47	29.29
10	248.64	169.02	320.40	76.00	30.56
11	254.37	190.46	360.64	92.66	36.43
12	255.06	172.68	320.52	75.36	29.55
13	304.42	188.80	410.82	111.30	36.56
14	190.72	171.18	210.26	27.63	14.49
15	290.10	248.50	331.70	58.83	20.28
16	235.44	229.32	241.56	8.65	3.68
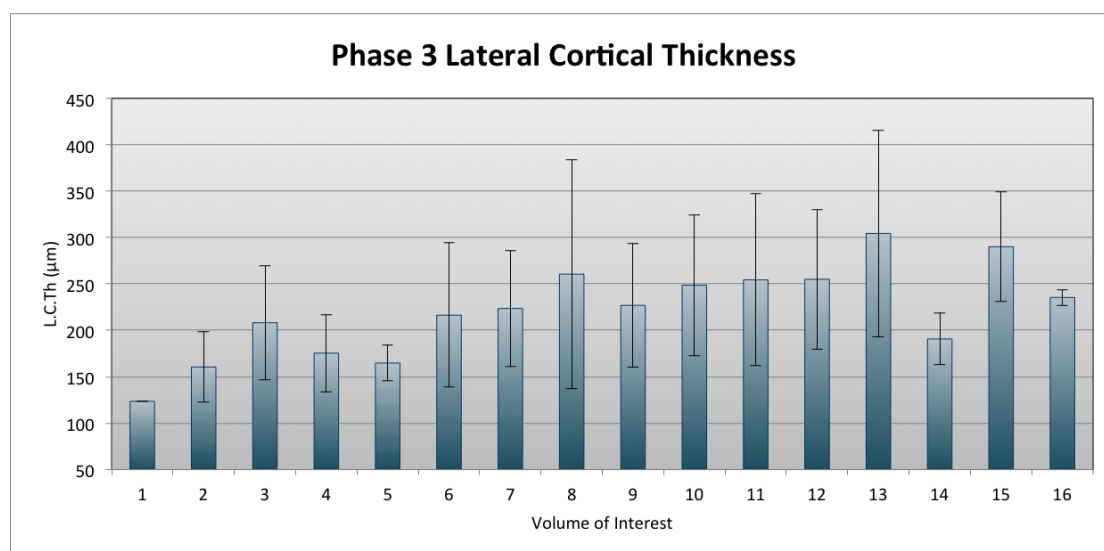
Phase 3 L.C.Th (µm)

Figure 6.71. Graphical representation of mean (± SD) L.C.Th per VOI for individuals in Phase 3.

The data for phase 3 L.C.Th was found to be parametric in nature (Shapiro-Wilk p = 0.534; equal variance p = 0.594), therefore a parametric one way analysis of variance was used to test for significant differences. No significant difference was found for phase 3 lateral cortical thickness in Phase 3 (F = 1.023 with 15 degrees of freedom, therefore p = 0.463)

Inter-phase variation by VOI

The range of values identified for L.C.Th in each phase were noted to be relatively low, particularly in comparison to those observed for P.C.Th previously, particularly in Phase 1. Only in Phase 3 did the mean L.C.Th value for a volume exceed 250 µm, and no volumes fell below 100 µm. The L.C.Th data for each phase is summarised graphically in Figure 6.72. Phase 3 appeared to present mean values that were typically greater than those of Phase 1 or 2, although this was not true in all volumes. In all volumes except VOI 1, Phase 2 was found to be of the lowest L.C.Th.
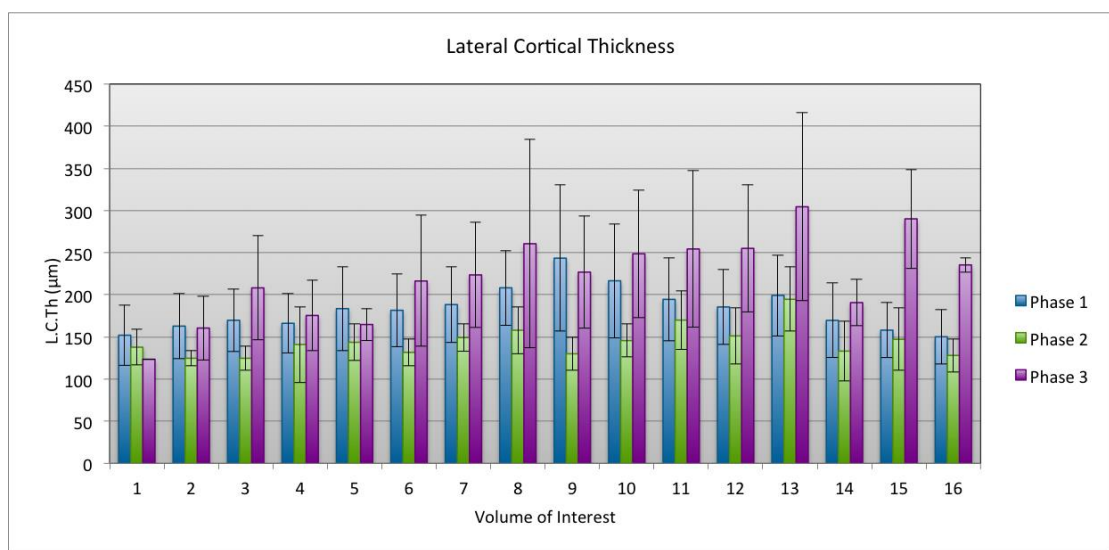
Figure 6.72. Summarised results for mean L.C.Th ± SD at each VOI per phase.

In order to determine whether any statistically significant differences were present between the phases at each volume, analysis of variance tests were conducted on the data for each volume [Table 6.32]. Volumes 3, 5 – 7, 10 -12 and 14 – 16 were found to be parametric and therefore a one way analysis of variance test was used for each of these volumes. Volumes 1, 2, 4 and 9 failed the Shapiro-Wilk test of normal distribution ($p < 0.05$), while VOI 8 and 13 failed the test of equal variance ($p < 0.05$). Each of these volumes were analysed using the non-parametric Kruskal-Wallis ANOVA on ranks.

Relatively few volumes were found to contain significant differences: only VOI 3, 6, 9, 12, 15 and 16 reached the threshold for significance ($p < 0.05$). Further, volumes 9 and 10 only reached were found to be highly significantly different ($p < 0.01$) while VOI 15 was found to be very highly significantly different between phases ($p < 0.001$). All

other VOIs, including 1, 2, 4, 5, 7, 8, 10, 11, 13 and 14, no significant difference was present between the three phases investigates. However, the ANOVAs for VOIs 5, 7, 10, 11 and 14 were observed to have a power below the desired level

Table 6.32. Analysis of variance results for inter-phase comparisons of L.C.Th in each volume of interest. ◊ indicates the test was non-parametric and the H statistic is presented in place of the F statistic. * Significant difference (p < 0.05); ** highly significant difference (p < 0.01); *** very highly significant difference (p < 0.001). ▫ indicates power of test was below desired level (< 0.800).

VOI	F / H$^{\diamond}$	DoF	P
1	0.862$^{\diamond}$	2	0.650
2	5.902$^{\diamond}$	2	0.052
3	5.068	2	0.014*
4	4.187$^{\diamond}$	2	0.123
5	1.586▫	2	0.225
6	3.951	2	0.032*
7	2.948▫	2	0.071
8	5.920$^{\diamond}$	2	0.052
9	10.973$^{\diamond}$	2	0.004**
10	3.227▫	2	0.057
11	2.48▫	2	0.104
12	4.716	2	0.018*
13	2.826$^{\diamond}$	2	0.243
14	1.917▫	2	0.169
15	13.992	2	< 0.001***
16	9.251	2	0.001**

(α < 0.800) and therefore these negative results should be interpreted with caution.

The six volumes that did exhibit significant differences were subsequently analysed using multiple pairwise comparisons to determine whether the observed overall difference existed between specific pairs of phases. The parametric volumes were processed using the Holm-Sidak MPC test, while the non-parametric volumes were analysed using Dunn's method.

In each of these volumes, a minimum of one significant pairwise difference was found [Figure 6.73]. In VOI 3, Phase 2 L.C.Th was found to be significantly less than both Phase 1 and Phase 3. In VOI 6, Phase 2 was found to be significantly thinner than Phase 3 only, while in VOI 7 Phase 2 was found to significantly thinner than Phase 1 only. In volumes 12, 15 and 16, Phase 3 was found to be of significantly greater thickness than

either Phase 1 or 2, between which no significant differences were found. No other significant differences were identified for these volumes.
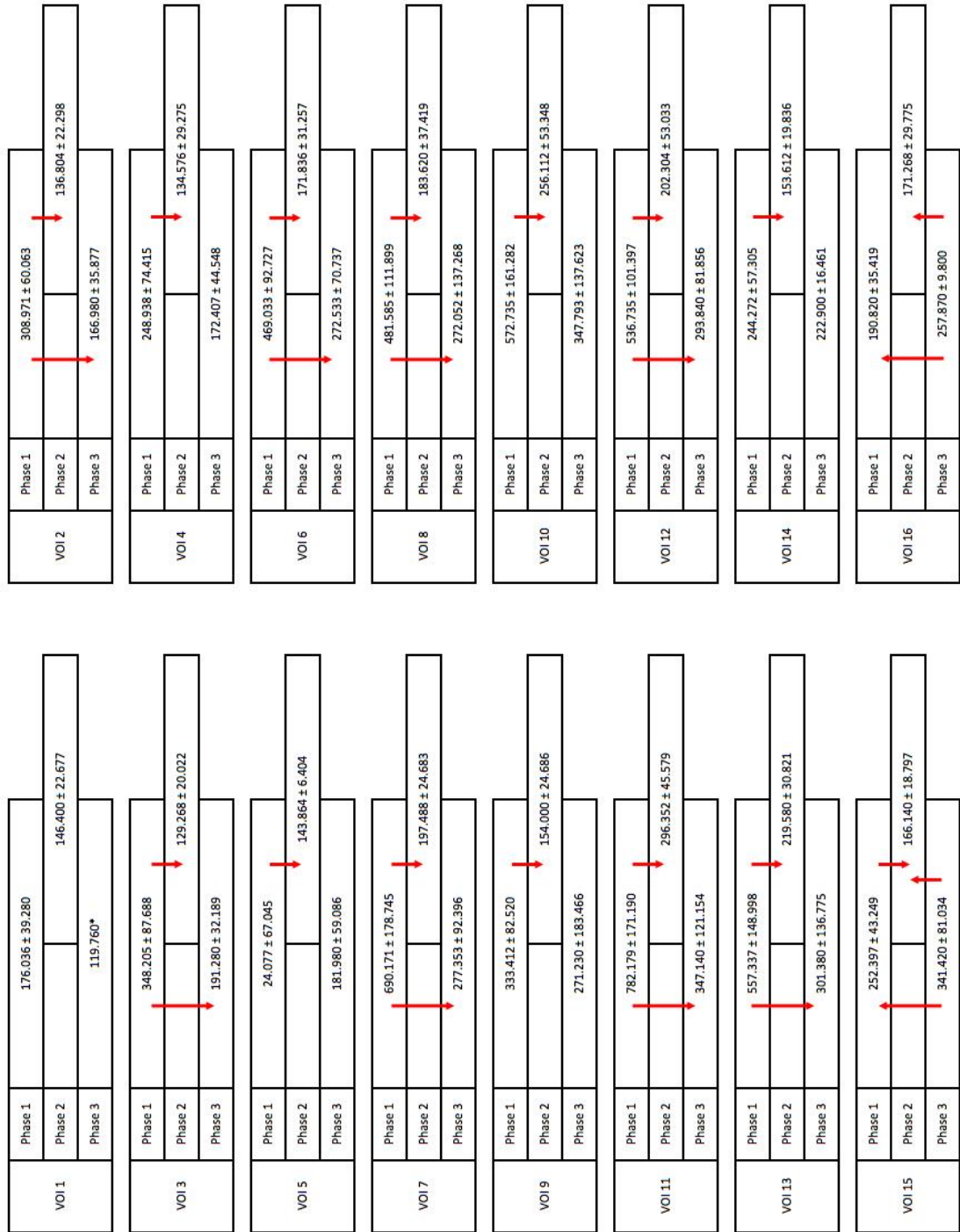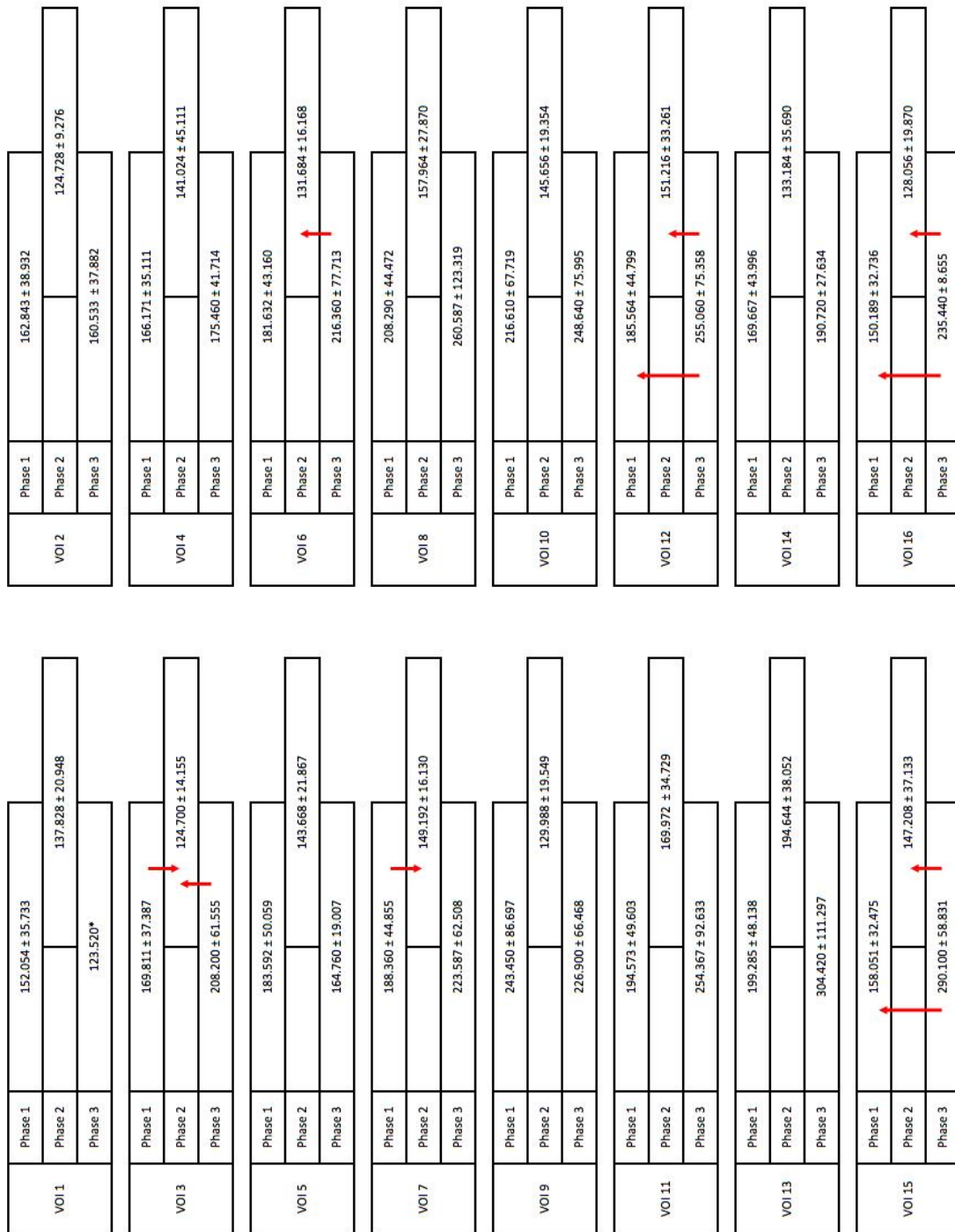

Figure 6.73. Multiple pairwise comparison results for inter-phase analysis at each volume of interest. Values are mean ± SD. Red arrow indicates significant difference exists between connecting phases (p < 0.05), arrow directionality shows decreasing L.C.Th.

6.3.3 Comparison of pelvic and lateral thicknesses

In addition to comparisons of cortical thicknesses across a single surface, analysis of variance tests were used to appraise the significance of differences between the pelvic and lateral cortices within a single volume and phase.

Phase 1

In Phase 1, the cortical bone data for volumes 2, 5, 15 and 16 demonstrated a normal distribution and equal variance and were therefore analysed using the parametric one-way ANOVA. Volumes 3, 4 and 6 failed the test of equal variance ($p < 0.05$), while the data for volumes 1 and 7 – 14 was not normally distributed (Shapiro-Wilk $p < 0.05$). As a result, each of these volumes were analysed using the non-parametric Kruskal-Wallis ANOVA on ranks.

The results for each ANOVA are demonstrated in Table 6.33.

*Table 6.33. Results of analysis of variance tests of pelvic and lateral cortical thicknesses at each volume of interest in Phase 1. ◊ Data found to be non-parametric, therefore value is the H statistic. * Significant result (p < 0.05); ** highly significant result (p < 0.01); *** very highly significant result (p < 0.001).*

VOI	F / H$^\lozenge$	DoF	P
1	4.323$^\lozenge$	1	0.038*
2	83.359	1	< 0.001***
3	25.954$^\lozenge$	1	< 0.001***
4	14.547$^\lozenge$	1	< 0.001***
5	10.800	1	0.002**
6	29.268$^\lozenge$	1	< 0.001***
7	29.268$^\square$	1	< 0.001***
8	29.268$^\lozenge$	1	< 0.001***
9	10.803$^\lozenge$	1	< 0.001***
10	29.271$^\lozenge$	1	< 0.001***
11	29.268	1	< 0.001***
12	29.268	1	< 0.001***
13	29.268$^\lozenge$	1	< 0.001***
14	17.129$^\lozenge$	1	< 0.001***
15	60.861	1	< 0.001***
16	13.484	1	< 0.001***

All comparisons of acetabular and pelvic cortical thicknesses were found to be statistically significant. The difference between L.C.Th and P.C.Th in Phase 1 was found to reach the p < 0.05 threshold for significance, while difference observed at VOI 5 was found to be highly significant (p < 0.01). For all other comparisons, the results were found to be very highly significant (p < 0.001).

Phase 2

The VOI comparison data for P.C.Th and L.C.Th in Phase 2 was found to be parametric in all volumes except VOI 2 and 4, which failed the test of normality (Shapiro-Wilk p < 0.05). The parametric data was subjected to one-way analysis of variance, while the non-parametric volumes were subjected to the non-parametric Kruskal-Wallis one-way ANOVA on ranks.

The results of each statistical test are summarised in Table 6.34.

Table 6.34. Results of analysis of variance tests of pelvic and lateral cortical thicknesses at each volume of interest in Phase 2. ◊ Data found to be non-parametric, therefore value is the H statistic. ▫ Power of test below desired level (α < 0.800). * significant result (p < 0.05); ** highly significant result (p < 0.01).

VOI	F / H◊	DoF	P
1	0.385▫	1	0.552
2	0.884◊	1	0.421
3	0.174▫	1	0.175
4	0.0109◊	1	1.000
5	0.000370▫	1	0.985
6	6.509	1	0.034*
7	13.414	1	0.006**
8	1.512▫	1	0.254
9	2.907▫	1	0.127
10	18.942	1	0.002**
11	24.321	1	0.001**
12	3.330▫	1	0.105
13	1.297▫	1	0.288
14	1.251▫	1	0.296
15	1.035▫	1	0.339
16	7.286	1	0.027*

Only five of the sixteen VOI demonstrated significant differences between pelvic and lateral cortical thicknesses. VOI 6 and 16 were found to be significantly different at the level of p < 0.05, while the differences at VOI 7, 10 and 11 were found to be highly

significant (p < 0.01). Volumes 6, 7, 10 and 11 form a single, central group within the ischium which are significantly thicker on the medial aspect than the lateral, while VOI 16 is isolated at the extremity of the ramus.

Phase 3

The phase 3 data comparing lateral and pelvic cortical thicknesses was found to be parametric in volumes 2 – 4, 6 – 8 and 10 – 14, while in volumes 5, 9, 14, 15 and 16 the data was found to be non-parametric (equal variance $p < 0.05$). The volumes that were found to be parametric were analysed using the parametric one-way ANOVA, while the non-parametric volumes were processed with a Kruskal-Wallis one-way ANOVA on ranks. No statistical comparisons were possible for VOI 1 as observations were only available in one specimen.

In stark contrast to the comparisons of P.C.th and L.C.Th in Phase 1, no statistically significant differences were observed between the cortices in any volume [Table 6.35]. The lowest observed p value was found to be 0.333, which did not approximate the level of statistical significance ($p < 0.05$).

Table 6.35. Results of analysis of variance tests of pelvic and lateral cortical thicknesses at each volume of interest in Phase 3. ◊ Data found to be non-parametric, therefore value is the H statistic. ▫ Power of test below desired level (α < 0.800). Significance threshold: p < 0.05.

VOI	F / H$^◊$	DoF	P
1	n/a	n/a	n/a
2	0.0455▫	1	0.841
3	0.178▫	1	0.695
4	0.00751▫	1	0.935
5	0.000$^◊$	1	1.000
6	0.857▫	1	0.407
7	0.697▫	1	0.451
8	0.0116▫	1	0.919
9	0.000$^◊$	1	1.000
10	1.193▫	1	0.336
11	1.110▫	1	0.352
12	0.364▫	1	0.579
13	0.000892▫	1	0.978
14	2.400$^◊$	1	0.333
15	0.600$^◊$	1	0.667
16	2.400 $^◊$	1	0.333

It was noted however that in all parametric tests, the power of the ANOVA fell below the desired level ($\alpha < 0.800$). This indicates that there is a possibility that statistical differences may not be detected where they actually exist, although the closeness of the mean values for each volume supports the absence of notable significant differences.

Chapter 7: Discussion

7.1 Structure of the perinatal ischium

7.1.1 Introduction

The initial growth of skeletal elements in the early juvenile period is primarily driven by the process of bone modelling and remodelling, characterised by the simultaneous deposition and resorption of bone at spatially disparate sites (Parfitt *et al.*, 2000). The conventional long bone model for bone growth dictates that longitudinal growth occurs through the sequential proliferation, hypertrophy and atrophy of chondrocytes in the growth plate, followed by the ossification of residual cartilaginous matrix. Circumferential, or diametric, growth occurs perpendicular to this axis through periosteal apposition and cortical drift (Goldman, 2009). Although not a long bone, it has been noted that growth of the ischium exhibits a similar pattern due to the position of the secondary centres of ossification (Cunningham *et al.*, 2016). Longitudinal growth of the ischium is directed superiorly towards the triradiate unit at the acetabulum, which contains growth cartilage, and inferiorly through the metaphyseal region associated with the ischial tuberosity and ramus. An expansion in volume would then be facilitated by circumferential growth perpendicular to these fronts, primarily through cortical drifting.

7.1.2 Perinatal trabecular architecture

Inferior ischium [VOI 12 – 16]

Following the inferred 'long bone model' of growth (Cunningham *et al.*, 2016), the inferior aspect of the ischium can be considered a region of metaphyseal growth due to the future development of the ischial tuberosity and ramal epiphyses. With the inclusion of progressive ossification of the ischial ramus, this growth acts in two separate planes. Growth is directed anteriorly along the ramus in advance of ischiopubic fusion, while inferoposterior expansion occurs through the growth and

development of the ischial tuberosity metaphysis, which will ultimately fuse to its corresponding epiphysis during adolescence.

The architecture of the inferior ischium demonstrated a transition from a high number of relatively thin trabeculae in the ramal region to a reduced number of thickened trabeculae in the upper inferior region. This transition is consistent with the changes that have been documented previously in regions that are primarily involved in growth, and the subtle change from a region undergoing initial modelling to one that is beginning to exhibit evidence of remodelling.

A similar arrangement was described in the regions adjacent to the anterior iliac crest metaphyseal surface in the neonatal ilium (Cunningham, 2009; Cunningham and Black, 2009b). The volumes immediately adjacent to the growth front were found to consist of a high number of thin, closely packed plate-like trabeculae, while those that were further removed demonstrated a decrease in number but an increase in thickness and separation. It was also suggested that the alignment of trabeculae in these volumes, as indicated by an increased DA, might be a result of the ossification of the cartilaginous septae separating chondrocytes in the growth plate, as these will be predominantly aligned in columns perpendicular to the metaphyseal surface. As both the ischial tuberosity and the iliac crest are convex, three-dimensional surfaces, anisotropy will be lowered as these perpendicular cartilaginous columns may diverge rather than running in parallel to each other.

This proposed architectural transition is also consistent with the observations of Byers *et al.* (2000) when describing the microarchitecture of the primary and secondary spongiosa at the costochondral junction. The primary spongiosa was described as possessing a high number of thin trabeculae that were relatively close together. The secondary spongiosa, which was undergoing remodelling, was found to contain thicker trabeculae that were fewer in number and more sparsely distributed. Although a direct numerical comparison is not advisable due to the regional specificity of trabecular architecture, the observed differences between primary and secondary spongiosa closely mirror the relative changes between the proximal and distal volumes of the inferior ischium. This may indicate that the architecture of VOI 14 and 15 in particular is relatively immature, derived from the process of bone modelling and the

conversion of columnar cartilaginous septae to ossified tissue. The increase in trabecular thickness and separation and concurrent decrease in trabecular number may in turn indicate the beginning of remodelling to adapt the rudimentary primary trabeculae into a more optimal arrangement. This appears to be primarily facilitated through the resorption of the smaller trabeculae that may be surplus to requirement.

Of the three ramal volumes, only the architecture of VOI 16 does not correspond closely with the architecture described for potential primary spongiosa. BV/TV was found to be particularly high as it is the only volume in which mean BV/TV was in excess of 50%, with an elevated trabecular thickness when compared to neighbouring volumes.

This discrepancy may be due to the position of this volume, which does not truly reflect the posteroinferior metaphyseal surface of the ischial tuberosity epiphysis but rather defines the blunted, cone-shaped projection of the perinatal ischial ramus. Although no published accounts of the histology of the ischiopubic synchondrosis, or primary cartilaginous joint, could be found, it is presumed that the cartilage that joins the ischial ramus to the pubic ramus in life contains a region of growth cartilage. Studies that have examined the histology of non-human synchondroses, such as the sphenooccipital synchondrosis in mice (Tsukamoto *et al.*, 2006) and primates (Nakamura *et al.* 1999) and the porcine thoracic neurocentral synchondrosis (Zhou *et al.*, 2014), revealed that a modified form of growth cartilage is present in synchondroses. In each species, a central band of resting and proliferative chondrocytes was identified with anterior and posterior layers of hypertrophic chondrocytes contacting the advancing ossification fronts [Figure 7.01]. This proposed growth front would be expected to present an architecture corresponding to the descriptions of VOI 14 and 15, indicating primary spongiosa. However, the ramus is also likely undergoing circumferential growth via periosteal apposition to expand the relatively thin growing end of the ramus to form a more robust ramal projection. The resorption of pre-existing endosteal surfaces to create the underlying trabecular compartment, called cancellisation, may result in the initial formation of relatively thick trabeculae prior to remodelling (Parfitt *et al.,* 2000). The constrained space in the narrow ramus may result in a higher proportion of peripheral trabeculae being formed from resorbed endosteal bone, rather than thin spicules formed from ossified

cartilaginous septae. This would inflate the mean trabecular thickness, and may also result in the presence of very small trabecular spaces and cavities that would be interpreted as an atypically low SMI.
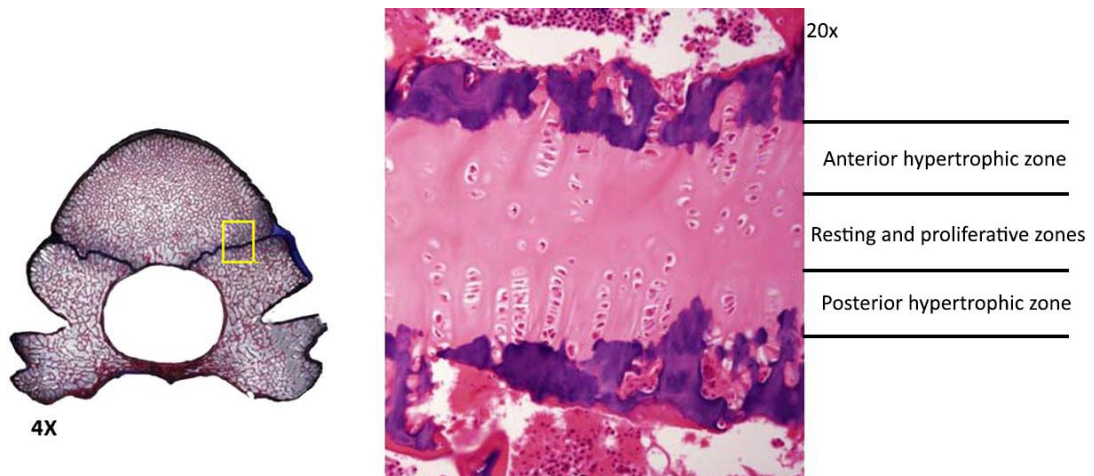
Figure 7.01. Histology of the primate neurocentral synchondrosis, highlighting the dual hypertrophic zones emanating from a central resting zone. Adapted from Nakamura et al. 1999.

Central ischium [VOI 5, 6, 7, 10]

The central core of volumes lies in very close proximity to the centre of ossification and the dominant nutrient foramen on the pelvic aspect of the ischium. These volumes also correspond with the inferior aspect of the developing acetabular margin and lunate surface, as viewed on the lateral surface of the ischium.

The architecture of these volumes corresponds closely to an architectural arrangement previously identified in the neonatal ilium (Cunningham and Black, 2009b), in a region termed the trabecular chiasma. First described radiographically by Macchiarelli *et al.* (1999), the chiasma in the adult appears at the crossing of the sacroischial and iliopubic trabecular bundles, and is represented radiographically by an increase in local intensity in the shape of a saltire cross. In the adult this chiasma is a region of biomechanical significance, representing the crossing point of two primary loading trajectories, and is therefore considered to be a region of increased strength prompted by functional requirement (Macchiarelli *et al.,* 1999; Volpato *et al.*, 2008). However, a similar increase in radiopacity is also evident in fetal and neonatal specimens (Cunningham and Black, 2009a; Macchiarelli *et al.*, 1999), in advance of any notable biomechanical loading related to bipedalism.

Quantitative analysis of the neonatal trabecular chiasma in the ilium revealed an architecture which was comprised of relatively few, thickened trabeculae which were predominantly rod-like in structure (Cunningham and Black, 2009b). The formation of a relatively low volume architecture which was proposed to retain a relatively high strength due to the more mature thickened, rod-like trabeculae was proposed to be a function of duality (Cunningham and Black, 2009b, 2010). The trabecular chiasma closely approximates the primary ossification centre of the ilium and the dominant nutrient foramen, and therefore it likely contains a very high concentration of vascular channels where the nutrient vessels are branching to supply the growing bone (Cunningham and Black, 2010). This would necessitate a decreased BV/TV as two tissues cannot occupy the same space, in a similar manner to the way in which the roots of a geranium displace the surrounding soil as they branch. Those trabeculae that did form between the branches of the vascular network demonstrated an increased thickness and architecturally strong plate-like morphology, indicating a reinforcement of a region which may otherwise be a potential point of failure. This reinforcement through remodelling may also be enhanced by the transmission of retrograde forces from early lower limb movements, as these would be expected to be distributed through the chiasma in a similar manner to ground reaction forces in the adult (Cunningham and Black, 2009b; Macchiarelli *et al.,* 1999).

Similar results have been found for other vascular centres in the juvenile skeleton. Nuzzo *et al.* (2003) observed a low-density central core of high trabecular thickness and very low separation in the fetal lumbar vertebra that transitioned to a region of reduced thickness and greatly decreased trabecular separation. Although not remarked upon by the authors, the region of decreased BV/TV centrally corresponded closely with the ossification centre for the vertebral centra, potentially indicating the position a vascular centre. O'Malley (2013) also quantified a similarly distinctive trabecular architecture in the region of vascular invasion of the juvenile scapula. When the corresponding trabecular volume was rendered in three dimensions, it became apparent that the voids within the architecture formed clear channels indicative of the presence of vascular structures [Figure 7.02].
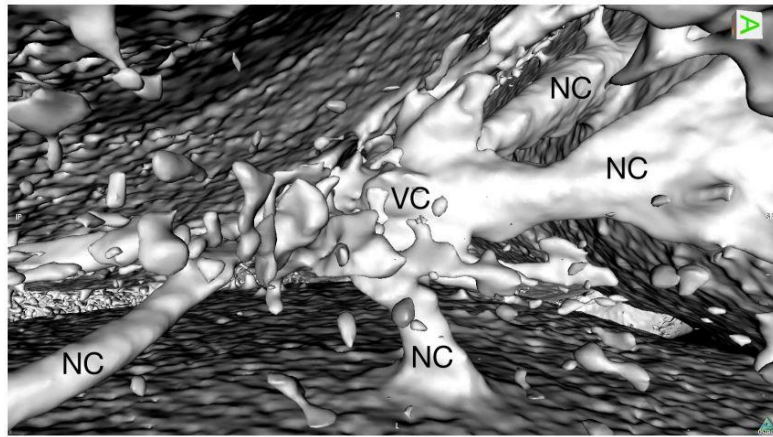
Figure 7.02. Inverted volume rendering of the proposed vascular centre of the neonatal scapula. Rendered object [white] represents the air phase of the trabecular volume. The presence of nutrient canals (NC) joining in a vascular centre (VC) can be observed. Adapted from O'Malley, 2013.

The similarity between the local architecture observed in the central region of the perinatal ischium and potential vascular centres in the ilium, scapula and vertebrae strongly suggests that a similar phenomenon is occurring in the ischium, with the position of trabeculae being dictated by the presence, or absence, of vascular branches within the trabecular compartment.

It was noted, particularly in comparison with the ilium, that trabecular thickness of this region was not as substantially elevated in the ischium. As the increase in trabecular thickness was proposed to be a mechanism for increasing strength in the absence of abundant trabeculae, it is possible that the difference in thickness is a result of the likely diminished force dispersal role of the ischium compared to the ilium. This may be due to the distribution of retrograde forces being directed primarily through the iliac component, if these forces are passing superiorly into the acetabular roof, as there would be a lesser imperative for reinforcement of the ischium. However, Portinaro *et al.* (2001) suggested that *in-utero* forces may also be passed posteriorly into the ischial component due to the flexed position of the femora in the fetal position. It may therefore be more likely that the increased window for remodelling which the ilium is afforded by its earlier ossification allowed for a greater accumulation of trabecular thickness before birth, as it was noted that the range of mean trabecular thicknesses for the ilium (approx. 145 – 220 µm) were notably higher than the mean thicknesses of the ischial trabeculae (approx. 90 – 155 µm).

Acetabular fossa [VOI 3, 4, 8]

The trabecular architecture of the volumes that comprised the non-articular floor of the acetabulum were found to be broadly similar to those of the inferior ischium, and in particular the ramal region, with some minor exceptions. Bone volume fraction was elevated in comparison to the neighbouring volumes, which include the proposed vascular centre. The architecture was defined by an intermediate number of thin, plate-like trabeculae. These volumes also demonstrated the highest degree of anisotropy observed in the ischium.

While the bone volume fraction in these areas was found to be lower than the inferior part of the ischial body, with greater separation between thinner trabeculae, the overall consistency in structure is reminiscent of an area of growth as described previously. That the architecture in this region should be defined by endochondral bone growth is consistent with the anatomical position of these volumes, as they are present along the sites of articulation with the posterior and vertical flange of the triradiate cartilage. The cartilaginous triradiate unit functions as epiphyseal cartilage, with a columnar arrangement of chondrocytes undergoing differentiation, hypertrophy and atrophy (Portinaro *et al.*, 2001). The growth directed towards the vertical flange and the pubis is reportedly the most active region of growth in the acetabulum in the early post-natal period, which facilitates the relatively rapid expansion of the non-articular floor of the acetabulum during the first year of life (Portinaro *et al*., 2001). The postulation that growth in this volume is primarily directed anterosuperiorly to expand the acetabular fossa may be supported by the relatively high degree of anisotropy present, which could be suggestive of recently ossified spicules aligned in the same trajectory as the cartilaginous septae of the growth plate.

Although the anterior volumes of the superior border, VOI 3 and 4, demonstrate an architecture consistent with a region of growth, the posteriorly-positioned volumes present a less distinctive trabecular arrangement.

Posterosuperior border [VOI 1, 2]

VOI 1 and 2 were found to demonstrate an admixture of previously identified trabecular characteristics that are not strongly indicative of a specific function. Bone volume fraction was found to be low, with a similar proportion of bone as the proposed vascular centre extending into neighbouring volumes 5 and 6. However, the trabecular architecture was found to be quite different, characterised by a proliferation of relatively thin, intermediately spaced trabeculae. The trabecular arrangement therefore was not comparable to the relatively mature, thickened trabeculae that defined the vascular centre, but more closely resembled the region of growth observed previously.

It is possible that this apparently peculiar trabecular architecture is indicative of a more restricted region of growth that also contains a relatively high number of vascular elements extending from the inferiorly located vascular centre. The mathematical averaging effect of two conflicting architectures may have prevented either from being clearly expressed. The presence of small foramina around the developing acetabular margin on dry bone specimens supports the presence of vascular elements traversing these volumes, perhaps in part derived from cortical vessels [as indicated in Section 4.51; Figure 4.13]. These vessels may have caused the displacement of trabeculae or a reduction in the available space for trabecular bone. The presence of growth cartilage in the vertical flange of the triradiate, positioned between the ischium and ilium, may however promote the formation of primary spongiosa in the superior periphery of these volumes, and with more mature remodelled secondary trabeculae located inferiorly. The presence of these maturing elements within the height of a single volume may explain the incongruous results which appear to combine elements of each region. It is therefore possible that by subdividing these volumes, two distinctive regions of bone architecture may become identifiable: an inferior region of vascularisation with a more restricted region of growth superiorly.

Peripheral volumes [VOI 9, 11]

As with the posterosuperior border, the peripheral volumes did not present an architecture that was consistent with either growth or vascular influence. The volumes do not lie along a metaphyseal growth front, but rather exist between the secondary spongiosa found in the upper inferior ischium and the vascular centre present in the central region.

The architecture in each of the peripheral volumes is relatively non-descript, with a relatively low number of intermediate thickness trabeculae. This architecture is similar in nature to peripheral regions of the ilium (Cunningham, 2009) and scapula (O'Malley, 2013) that do not contribute to an active metaphyseal region. Rather, it appears the bone in these regions is undergoing a relatively steady process of expansion through periosteal apposition and remodelling of the immature trabecular architecture. As these are single, isolated volumes, there is limited information that can be gained directly from these regions.

7.1.2 Mechanisms of structural alteration

The results of the present study suggest that variations in the trabecular architecture of the perinatal ischium are primarily driven by the number of trabeculae present within a volume of interest. A strong correlation was found between bone volume fraction and trabecular number, and also between trabecular number and separation. A slightly weaker correlation was also observed between bone volume fraction and trabecular separation. This suggests that where there is a decrease in bone volume fraction, it is likely caused by a decrease in trabecular number, which will concurrently increase the distance between the remaining trabeculae. Conversely, no correlations were found between trabecular thickness and either bone volume fraction, trabecular number or trabecular separation.

This observation is in agreement with previous studies of trabecular architecture in the early post-natal period. Fazzalari *et al.*, (1997) noted in their study of the primary and secondary spongiosa of the costochondral junction that the coefficient of variation in trabecular thickness was twice the value for either trabecular surface area or number. The authors proposed that this was perhaps indicative that trabecular thickness, at

least in the early stages of growth, is not under strict biological control, rather changes in architecture are likely brought about by the removal of smaller superfluous trabecular elements from a basic cancellous structure. This action would cause a net increase in mean Tb.Th due to the loss of smaller struts and concurrently result in an increase in Tb.Sp. As the resorption phase of remodelling occurs more rapidly than the subsequent deposition of new bone matrix, it may provide a more rapid mechanism with which to initially alter a rudimentary trabecular microarchitecture (Clarke, 2008; Hadjakis and Androulakis, 2006). However, this is not to suggest that no trabecular thickening occurred in the volumes which are proposed to have undergone remodelling, but rather that this process may not be under strict direction at this stage of development.

The strongest correlation in Phase 1 however, was found between bone volume fraction and structural model index: as BV/TV decreased, SMI was observed to increase, indicating a transition to a more rod-like architecture. It should be noted that while a strong, significant correlation was observed, the final range of SMI values indicated that perinatal SMI fluctuated between a dominant plate-like morphology to an admixture of plate-like and rod-like trabeculae. No volume presented an SMI value which indicated an architecture predominantly formed of rod-like trabeculae.

The range of SMI values in the present study were found to be similar to those established for the perinatal ilium (Cunningham, 2009), with a preference for plate-like structures at the periphery of the bone tending towards a more equal mixture in the regions more closely associated with the primary centre of ossification. It was proposed that this transition was indicative of bone remodelling, perhaps due to the apparent increase in maturity of this region of bone, or functional interactions through fetal and neonatal limb movements. The correspondence between the architecture of the primary ossification site in the ilium and ischium lends weight to the proposal that there may be a temporal relationship with SMI, transitioning from a predominantly plate-like architecture in less mature regions to a more even ratio of rods to plates in more mature regions.

It has been suggested that the SMI is an important indicator for the mechanical strength of bone, with a high degree of correlation between SMI and the elastic

modulus of bone (Liu *et al.*, 2008). This corresponds with observations that regions subjected to increased mechanical loading typically present a more plate-like trabecular structure, while regions experiencing less strenuous loading conditions adopt a more rod-like morphology (Ding *et al.*, 2002; Lazenby *et al.*, 2008). Further, in elements displaying a sandwich construction, such as bones of the innominate, a plate-like trabecular morphology may function as a system to resist shear stresses induced between each cortical surface (Dalstra *et al.*, 1993).

During adulthood, SMI appears to remain relatively consistent within specific skeletal regions, with limited variation in the ratio of rod-like and plate-like trabeculae (Ding and Hvid, 2000; Parkinson and Fazzalari, 2013; Stauber and Müller, 2006). SMI has however been noted to change as a result of degenerative changes in later life, typically beyond 70 years of age, with a significant increase in the number of rod-like structures (Ding and Hvid, 2000). This transition to a more rod-like trabecular architecture has also been found to be one of the most successful predictors of increased fracture risk in post-menopausal women (Melton *et al.*, 2010).

The strength of the linear relationship observed between BV/TV and SMI is not unprecedented in the literature (e.g. Ding and Hvid, 2000; Ding *et al.*, 2002; Hildebrand *et al.*, 1999; Stauber *et al.*, 2006). In the original publication outlining the use of SMI as an indicator of trabecular morphology, it was acknowledged that SMI might be dependent on BV/TV to an extent, particularly in regions with very high BV/TV (Hildebrand and Rüegsegger, 1997b). This is in part due to the calculation failing to account for the effect of trabecular intersections, which are primarily concave in nature, on the surface mesh dilation process through which SMI is calculated. In a recent publication, it was suggested that the use of SMI as a trabecular parameter might be inherently biased by this limitation (Salmon *et al.*, 2015), with increasing BV/TV artificially skewing SMI values towards a rod-like morphology. It was suggested therefore that the results of SMI calculations be treated with caution. However, an earlier study by Liu *et al.* (2006) comparing the results of traditional SMI calculations to those derived using a skeletonisation algorithm demonstrated a strong correlation between the two assessment protocols, which indicates results may be less biased than Salmon *et al.* (2015) have proposed.

Alternative methods of identifying the prevalence of rod-like and plate-like trabeculae have been proposed (e.g. Jennane *et al.*, 2012; Liu *et al.*, 2006; Stauber *et al.*, 2006) which utilise skeletonisation, or volumetric decomposition, to assess trabecular morphology. While there appear to be benefits to the use of such algorithms, including the ability to analyse plate-like and rod-like histomorphometric parameters separately, there is no consensus on which technique provides the most reliable results, and as a result not all techniques are incorporated consistently in histomorphometric software. Further research is therefore required, in addition to greater collaboration and communication to drive forwards this particular component of trabecular analysis.

7.1.3 Phase 1 cortical bone thicknesses

Pelvic cortical surface: modelling-driven growth

When considered in isolation, the mean cortical thickness of measurements of the pelvic cortical surface adopted a gradient emanating from a central point of high thickness in volumes 7, 10 and 11. The volumes that immediately neighbour this high thickness core, both superiorly and inferiorly, demonstrated a consistent, although insignificant, decrease in thickness. As volumes become further removed towards the superior and inferior borders of the ischium, cortical thicknesses were found to be significantly lower than the central VOIs.

The orientation of this gradient is broadly consistent with the anticipated pattern based on dominant modelling activity during early growth of the ischium. The central thickened region corresponds closely with the described position of the primary centre of ossification, located below and behind the acetabulum at the approximate level of the ischial spine (Cunningham *et al.*, 2016). A well-defined nutrient foramen was also noted in close proximity to the intersection between VOIs 7, 8, 10 and 11. This is likely the foramen associated with the dominant nutrient artery of the ischium, which branches from the obturator artery (Beck *et al.*, 2003), and it has been reported that initial nutrient invasion typically occurs in close proximity to the primary ossification centre (Payton, 1934). As the first region to ossify, this high-thickness core would have been permitted the longest period of time in which to accrue mineralised matrix and

increase in thickness through periosteal apposition. Conversely, the peripheral regions of bone, and particularly those at the superior and inferior extremities, would be more recently formed and therefore represent 'new' cortical bone that had little time to increase in thickness.

A similar cortical thickness gradient has been described previously in a comprehensive study of the neonatal ilium (Cunningham and Black, 2009c). A core of high cortical thickness was observed in close proximity to the primary ossification centre, superior to the acetabulum, which decreased towards the periphery of the ilium. It was noted that this gradient radiated outward from the primary centre of ossification, across both the pelvic and gluteal surfaces, with the gradient particularly pronounced towards the iliac crest. This 'radiating' effect was not observed to the same extent in the ischium, rather the gradient appeared to be predominantly oriented towards the superior and inferior poles.

The absence of a distinctive 'radiating' appearance in the ischium is not unexpected due to the difference in both size and gross morphology of the two pelvic elements. The ischium is elongated in the vertical plane and relatively narrow in the horizontal plane, with similarly narrow growth fronts at the acetabulum and ischial tuberosity. Conversely, the ilium is a broad, fan-shaped element that has a particularly elongated superior margin, the metaphyseal surface for the iliac crest epiphyses. This increased surface area and wide growth front would require more rapid radiating growth to ensure that adult proportions are reached and then maintained throughout growth. The more constrained dimensions of the ischium may have allowed the breadth of the ischium to adopt a relatively uniform thickness quickly, which expands slowly through periosteal apposition, with a growth-related gradient only becoming pronounced towards the metaphyseal surfaces of the bone.

Lateral cortical surface

The cortical thickness measurements from the lateral cortical shell were found to be significantly thinner than each corresponding volume on the pelvic surface. Further, the lateral surface did not conform as closely to the proposed radiating growth pattern as the pelvic surface, although a weaker vertical gradient was identifiable. The

diminished presentation of a gradient may in part be a result of the far smaller cortical thickness measurements obtained for the lateral surface, and consequently the more restricted variation in values between volumes of interest. As a result of this reduced range of thicknesses, no significant differences were found between adjacent VOI pairs and only slight variations can be identified across the surface as a whole.

Despite these relatively slight differences, it was possible to identify statistically distinct regions of high thickness in the posterior border of the ischium, centred in VOI's 9 and 10, and low thickness in the most superior and inferior aspects of the ischium.

VOI's 9 and 10 exist on the same plane of the ischium as the proposed centre for ossification on the pelvic aspect of the ischium, and share a similar relative increase in thickness. These volumes may therefore represent the point at which ossification first spreads from the centre of ossification on the pelvic cortex. The cortical thickness in these volumes may also be elevated by local stresses introduced by the proximal attachment of the ischiofemoral ligament, which inserts on the posterior acetabular margin (Standring, 2008). Although the *in-utero* forces associated with the ligaments of the hip are unknown, it is known that in the adult this ligament is activated primarily during internal rotational movements of the hip (van Arkel *et al.*, 2015). Rotational movements are reported to increase in the third trimester as *intra-uterine* space becomes increasingly restricted due to growth (Hayat *et al*, 2015; Nowlan, 2015), which would be supportive of an increased rate of activation of the ischiofemoral ligament. Whether this would be sufficient to influence cortical bone structure is unknown at present, although it should be noted that, while statistically significant, the magnitude of change in the lateral cortical thickness measurements was relatively small.

From this region of slightly elevated cortical thickness, a decrease in thickness was observed passing superiorly and inferiorly as described previously to the regions that statistically presented the lowest thickness values at the superior and inferior metaphyseal surfaces. This mimics the pattern observed on the pelvic surface, although the difference between the extremes is notably diminished, and therefore suggests that a similar temporal relationship with modelling and apposition is occurring. However, VOI 8 presented a relatively high cortical thickness on the lateral

aspect that did not conform with the described gradient effect, as it would be expected to present an intermediary, or low, cortical thickness. This effect is compounded when considering that VOI 8 borders the metaphyseal surface that will ultimately unite with the pubis via ossification and fusion of the vertical flange of the triradiate cartilage. All other metaphyseal regions from both the pelvic and lateral surfaces presented relatively low cortical thicknesses, particularly when compared to the thickness of the more central volumes.

It is possible that this discrepancy is linked to the soft tissues associated with VOI 8, and the potential introduction of mechanical forces. VOI 8 contains the most anterior edge of the ischial acetabular margin, after which it lowers to form the smooth acetabular notch, and also in the neonate comprises a large proportion of the non-articular acetabular fossa. This presents several possible factors that may increase cortical thickness in this region. The border of the acetabular margin provides attachment for the transverse acetabular ligament (TAL), which crosses the acetabular fossa to insert on the most posterior aspect of the pubic acetabular margin (Löhe *et al.*, 1996). It has been suggested that in the adult the TAL is placed under tension by loading of the hip, which causes a small degree of elastic deformation of the acetabulum (Löhe *et al.*, 1996). This ligament alone is unlikely to introduce a high degree of tensile force in the acetabular margin as the hip is not a weight-bearing joint prior to birth. In addition, if the TAL were responsible for the increase in local thickness, it would be expected that an increase in thickness would be continued into VOI 11, which contains a significant proportion of the anterior aspect of the acetabular margin and therefore a component of this insertion site. The TAL also acts to create a small foramen, which can be found between the ligament and the underlying bone, which allows the passage of neurovascular structures into the acetabulum (Palastanga and Soames, 2011).

In addition to the TAL however, the *ligamentum teres* also inserts on the margins of the acetabular notch, blends with the fibres of the TAL and extends to the inferior aspect of the acetabular notch in the adult (Bardakos and Villar, 2009). In the juvenile, this corresponds to the ischial component of the acetabular, which contains the most extensive region of acetabular fossa. In the adult, the role of this ligament is disputed, with reports of its involvement in resisting rotational movements and preventing

dislocation (Bardakos and Villar, 2009; Cerezal *et al.*, 2010). In the juvenile, the function of this ligament has been suggested to be of greater importance as it prevents dislocation of the hip during a period in which the competency and stability of the hip is reduced (Bardakos and Villar, 2009). Brewster (1991) found that the strength of the *ligamentum teres* increased substantially in the final trimester and suggested this was the result of a significant mechanical interaction, likely the action of limiting *in utero* movements of the lower limb and preventing dislocation. The resulting tensile stresses may therefore be partly responsible for stimulating an increase in cortical thickness in this region.

Comparison of pelvic and lateral thicknesses

In each VOI analysed, the pelvic cortical surface was found to be significantly thicker than the corresponding volume on the lateral surface. A significant difference in contralateral cortical surfaces was also observed in the neonatal ilium (Cunningham and Black, 2009c), although in the ilium it was the gluteal surface that was found to be significantly thicker. This was linked to the attachment of the powerful gluteal muscles, which insert across a large proportion of the gluteal surface area, while the pelvic surface lacks any insertions of a similar magnitude (Cunningham and Black, 2009c; Delaere and Dhem, 1999). It has been established that the tensile forces caused by muscular contraction can stimulate the growth of cortical bone (Schoenau, 2006; Schoenau and Fricke, 2008). It has further been suggested that the effects of loading on cortical bone may be exaggerated in the early juvenile period, perhaps due to the increased level of cortical bone modelling during this stage of development (Bass *et al.*, 2002; Kontulainen *et al.*, 2003). Although the pelvis and lower limb are not considered to be weight bearing prior to the beginning of locomotor development, retrograde forces associated with reflexive limb movements *in utero* have previously been suggested to stimulate bone growth and inform future bone strength (Miller, 2005; Nowlan, 2015).

Exploring the discrepancy in thicknesses between the pelvic and lateral aspects of the ischium presents a more complicated scenario. The significant increase in thickness of the pelvic surface does not correspond to any substantial muscle attachment sites, certainly not those equal in magnitude to the gluteal muscles. Only the obturator

internus muscle attaches to the quadrangular plate of the ischium, and it has been observed that this attachment does not cover the entire surface but is rather separated by the presence of a synovial bursa separating the muscle fibres from the periosteal surface inferiorly (Cunningham *et al.*, 2016). Conversely, the lateral aspect of the ischium provides attachment for the ischiofemoral ligament, quadratus femoris muscle and, inferolaterally, the lateral fibres of the semimembranosus and semitendinosus muscles and the adductor magnus (Standring, 2008). It does not seem likely therefore that the increase in thickness of the pelvic cortex can be explained by direct musculoskeletal interactions.

In the first instance, the geometry of the ischium may play a role in informing cortical thicknesses. The lateral surface of the ischium typically demonstrates a convex border when viewed as a transverse slice, expanding laterally towards the acetabular margin. Conversely, the pelvic surface is concave in profile, with a curvature that is at its deepest towards the midline of the posterior border of the obturator foramen. It has been observed that a concave surface is likely to exhibit a greater cortical thickness than either a straight or convex surface (Duan *et al*., 2011; Lazenby, 2002; Simkin *et al.*, 1980), due perhaps to the increased bending strain and introduction of a tensile component on the endosteal surface of the pelvic cortical shell. The increased cortical thickness of the pelvic surface is at its most pronounced in the volumes that correspond with the greatest concavity, and this may suggest a link between the bone curvature and cortical thickness.

It is also possible that the difference in cortical thickness observed between each cortex may be indicative of a directional expansion of ischial volume through asymmetric cortical drift. The relatively low thickness observed across the lateral surface of the ischium is comparable in absolute thickness to the pelvic regions previously associated with growth, i.e. those which fall at the metaphyseal surfaces. This may indicate that the entirety of this surface is undergoing relatively rapid turnover to allow cortical drift, a change in size and shape caused by a simultaneous contralateral resorption and deposition of bone (Gosman *et al.*, 2013; Parfitt *et al.*, 2000). In long bones, this process is responsible for alterations in the cross-sectional shape of the diaphysis from a relatively circular shape to a less uniform structure, while also facilitating an increase in size. The generally accepted pattern in the adult is

that net resorption occurs on the endosteal surface, while net apposition is present on the periosteal surface (Gosman *et al.*, 2013), although it has been demonstrated that this is not true for all bones throughout ontogeny.

Parfitt *et al*. (2000) found that in the developing ilium, the resorptive and appositional surfaces were reversed between the pelvic and gluteal cortices. The gluteal cortical shell followed the 'accepted' pattern described previously, while the pelvic cortical shell demonstrated net apposition on the endosteal surface and net resorption on the periosteal surface. In addition, bone turnover of the gluteal surface was found to be more rapid than that of the pelvic surface, which led to an increase in the trabecular volume of the ilium with age. Goldman *et al.* (2009) noted similar findings in the diaphysis of the femur, which exhibited resorption and deposition on different surfaces around the circumference of the midshaft which induced a posterior and medial drift in infancy. This pattern altered with age however, transitioning to an antero-lateral drift later in childhood as the bone adopted a more adult-like geometry.

It is possible therefore that differential rates and directions of growth are also present in the juvenile ischium. The relatively thin bone observed on the lateral aspect of the ischium may be in part influenced by a continual cycle of periosteal deposition and endosteal deposition to facilitate a lateral expansion of the trabecular bone compartment. A rapid turnover of bone may preclude any distinctive thickening of the cortical shell in this location, particularly with minimal biomechanical drivers requiring an increase in thickness in the perinatal period. Conversely, the concave geometry of the pelvic surface of the ischium, coupled with a rate of apposition and resorption that favoured a net increase in bone mass, may explain the significantly increased thickness.

It was not possible from the present study to determine which bone surfaces were undergoing resorption and apposition. In living individuals this can be ascertained using tetracycline labelling to identify the rate of new bone formation, while resorption can be indicated by visual confirmation of the presence of scalloped resorption lacunae, although these cannot be labelled (Kobayashi *et al.*, 2003; Parfitt *et al.*, 2000; Ott, 2008). Tetracycline labelling requires the extraction of bone biopsies for histological analysis, with research typically utilising transiliac biopsies due to the relative ease of extraction (Vanderoost and van Lenthe, 2014). The identification of

resorption cavities using μCT has been possible only using voxel sizes of 1.4 μm or less (Tkachenko *et al.*, 2009), however this exceeds the technical capabilities of the present study and would require the use of synchatron micro-computed tomography to visualise. Synchatron-based micro-computed tomography (SR-μCT, or nana-CT) is capable of producing very high-resolution images (≤ 1 μm) with minimal interference or artefacts (Bouxsein *et al.*, 2010). However, current technical limitations allow only small-volume samples to be analysed, and therefore would also require the extraction of skeletal tissue biopsies for analysis.

7.2 Architectural changes associated with increasing maturity

7.2.1 Quantifying a decrease in bone intensity

The analysis of radiographic intensity patterns in the juvenile ischium revealed a rapid change in radiopacity following the fetal and perinatal periods. Between the ages of 5 months and 2 years of age, the ischium demonstrated a substantial loss of bone intensity across the entirety of the ischium compared with the relatively high intensity bone observed in the perinatal period. It was hypothesised that this pattern was indicative of a period of bone mineral accrual prior to birth followed and by the rapid resorption and redistribution of this bone in the early post-natal period. However, due to the qualitative nature of the radiographic investigation, it was not possible to determine whether there was a true decrease in the quantity of bone present in the ischium between these developmental phases, whether this loss occurred in the trabecular or cortical compartments, or what effect this may have on the trabecular microarchitecture. The application of quantitative analysis via μCT allowed for the internal architecture to be classified and compared with the architectural patterns previously established for the perinatal cohort.

Of the 8 histomorphometric parameters investigated in the present study, three measurements can be considered to be indicators of the physical quantity of bone present in each VOI: BV/TV, P.C.th and L.C.Th.

A comparison of the data obtained from these three parameters in Phase 1 and 2 confirmed that there was a generalised decrease in local bone quantity within the ischium. The bone volume fraction was found to fall significantly in all volumes of interest, with a loss of up to 60% of Phase 1 BV/TV. It should be noted that as BV/TV is a proportional measurement that relays the percentage of a total tissue volume that is comprised of bone. As such, a decrease in BV/TV does not necessarily translate to an equivalent loss of bone mass if the total volume is increased: the lower BV/TV may be offset to some extent by the redistribution of the trabecular bone within a larger space. However, as a structural parameter, BV/TV is considered one of the primary indicators of the strength of a trabecular network and therefore a decrease such as that observed here may have implications for the mechanical competency of the ischium.

With regards to cortical thicknesses, a significant decrease in pelvic cortical thickness was observed in all volumes except VOI 1 and 16, with a more pronounced decrease in thickness occurring in the central region. The lateral cortical thicknesses conversely did not present a high number of significant differences between Phase 1 and 2. However, lateral cortical surface in Phase 2 was qualitatively thinner than in Phase 1 in all volumes of interest.

These results confirm the hypotheses offered following radiographic analysis, demonstrating a reduction in the overall bone content per volume of interest. This reduction was not specific to either cortical or trabecular bone, but rather appeared to affect both compartments. It was noted that there was a clear disparity in the reduction of cortical thickness between the pelvic and lateral surfaces. However, this apparent increase in resorption on the pelvic cortical surface compared with the lateral surface is perhaps not surprising. The L.C.Th values in Phase 1 were found to be particularly low, therefore any significant loss of bone in Phase 2 may have reduced the thickness to a level at which it lacked any biomechanical competency. The pelvic surface however, with mean thicknesses that reached 2.5 times the equivalent lateral thickness in phase 1, offered a greater proportion of bone that may be considered to be 'in excess'. As a result, the loss of bone from this surface may be more easily accommodated with regards to the mechanical integrity of the ischium.

Possible effects of pathology on trabecular architecture

No external markers indicating skeletal pathology were observed on the specimens included in the present study. However, as the Scheuer Collection is comprised of the remains of juvenile individuals, it is implicit that death was due to illness or pathology, and it is therefore possible that the cause of death or associated morbidity may have influenced skeletal architecture. The possibility that the significant loss of bone observed between specimens in Phase 1 and Phase 2 was in some way influenced by disease processes cannot be wholly excluded. In addition, the bones may be affected by taphonomic changes and post-mortem treatment that could have altered the trabecular and cortical structure.

Unfortunately, the literature which documents the effects of skeletal pathologies on juvenile bone microarchitecture are limited to a small number of studies, therefore little information is available to support whether the changes associated with Phase 2 may be consistent with pathological processes or a true developmental phase. This paucity appears to be driven by a number of factors, including the limited number of specimens, the rarity and variability in these diseases and the difficulties associated with archaeological diagnoses of disease.

The publications that have detailed pathological changes in trabecular and cortical bone structure have however presented a number of potential effects on juvenile skeletal architecture. Conditions such as osteogenesis imperfecta or juvenile idiopathic osteoporosis have been found to cause a significant decrease in bone volume fraction (Rauch *et al.*, 2000a,b) and cortical thickness (Brandi, 2009; Rauch *et al.*, 2000b). In both studies, the decrease in BV/TV was accompanied by a reduction in trabecular number, which is consistent with the present study. However, a significant decrease in trabecular thickness was also observed (Rauch *et al.*, 2000a,b). The opposite change was observed in the ischium in Phase 2, which showed an overall trend towards increased trabecular thickness compared with Phase 1, although this increase was only significant in seven of the 16 volumes analysed.

Diseases of nutritional deficiency such as osteomalacia or rickets have also been found to influence skeletal development (Adams and Hamblen, 2001; Schamall *et al.*, 2003).

However, the most prominent changes appear to be linked to bone morphology and size, rather than bone volume fraction (Schamall *et al.*, 2003). Trabecular morphology was however noted to change, with a significant decrease in trabecular thickness and increase in trabecular number in pathological specimens. As before, these changes are inconsistent with the changes observed in the present study, which demonstrated an increase in trabecular thickness and decrease in trabecular number. This indicates that the relatively rapid alteration of ischial trabecular architecture in the early post-natal period is unlikely to be associated with a pathological nutritional deficiency.

Although presenting only a limited number of pathological scenarios due to a paucity of studies from which to draw comparisons, it appears unlikely that the architectural changes identified between Phase 1 and 2 are the result of pathological changes. However, without further the introduction of more extensive analyses of pathological specimens, this cannot be confirmed for all possible conditions. In the event of future publications regarding pathological changes in trabecular and cortical bone development, the results of the present study should be reassessed to determine whether there are similarities with the new literature that may be of concern.

7.2.2 Changes in trabecular architecture in infancy

While it was possible to identify distinctive regions of characteristic trabecular architecture in the perinatal ischium, the data obtained for Phase 2 and 3 was found to be statistically homogenous. Only a single parameter in each phase presented a suitable number of significant differences to permit the designation of regions of high-, intermediate- and low- mean values, which was not sufficient to segregate regional architectural features within a single phase. As a result, it is not possible to discuss in detail the potential influences acting in different components of the ischium.

It was however noted that, while significant distinctions were not present, there was some similarity in the distribution of mean values for each parameter; for example, the inferior regions of relatively high BV/TV identified in Phase 1 typically retained a qualitatively increased BV/TV in Phases 2 and 3. This suggests that the effects of growth and vascularisation outlined for Phase 1 continue to have at least a residual effect on the trabecular architecture beyond this period.

It was also observed that in Phase 3 there was a significant increase in trabecular number and the degree of anisotropy compared to Phase 2, which was accompanied by a non-significant increase in BV/TV. This transition may be indicative of an increased rate of growth in these regions in advance of ischiopubic fusion, similar to the activity at growth fronts observed in the perinatal ramus.

The fusion of the ischiopubic ramus typically occurs between 5 and 8 years of age, although the onset of fusion has been noted to occur in younger individuals (Cardoso *et al.*, 2013; Herneth *et al.*, 2000). It is therefore possible that the trabecular changes observed in these volumes of interest indicate an increasing rate of growth to extend and expand the ramus to form the heaped, callous-like appearance adopted prior to fusion. The increase in Tb.N and DA is consistent with the changes associated with bone modelling (Byers *et al.,* 2000), although trabecular thickness remains relatively high in these regions. However, it should also be noted that ramal Tb.Th has been persistently higher than might be expected to occur at a growth plate, and it is therefore possible that thickness in Phase 3 continues to be elevated due to the effects of endosteal cancellisation, as was proposed for the same region in Phase 1.

Post-natal ontogenetic changes in ischial architecture

In the adult, BV/TV is considered one of the most reliable indicators of mechanical strength, with an increase in BV/TV correlating with an increase in Young's modulus and material stiffness (Ding *et al.*, 2002; Hildebrand *et al.*, 1999; MacNeil and Boyd, 2007; Maquer *et al.,* 2015; Perilli *et al.*, 2008). Such a significant loss in BV/TV across the entirety of a bone in the adult may therefore be indicative of pathological processes, and may be accompanied by a concurrent decrease in the competency of the trabecular architecture.

However, the ontogenetic relationship with BV/TV is more complex, as skeletal architecture is remodelled from a rudimentary trabecular network rapidly established during growth to a more deliberate, optimised architecture which is functionally viable (Ryan and Krovitz, 2006). The pattern of architectural maturation appears to be highly age- and site-specific, which has been previously suggested to result from functional interactions in the post-natal period (Gosman and Ketcham, 2009).

In the ischium, this pattern of architectural maturation was broadly consistent between Phases 2 and 3. In Phase 2, the typical trabecular network was found to be comprised of relatively few, well-spaced trabeculae which were thicker than those of Phase 1, although the increase was only significant in a limited number of volumes. The structural model index indicated that there was a mixture of rod-like and plate-like trabeculae present, with a greater tenancy towards rod-like trabeculae than was previously observed. No significant difference in BV/TV was noted in the ischium in Phase 3 when compared to Phase 2, however Tb.Th and Tb.Sp continued to increase while Tb.N was found to decrease.

A comparison of the rate of change in parameters between each phase provided some indication as to the underlying imperative. Between Phase 1 and 2, there was a significant decrease in BV/TV, P.C.Th and Tb.N; in order to produce each of these changes, a high rate of bone resorption would be required as these changes are primarily deleterious. While Tb.Th was observed to increase across the ischium, this increase was significant in less than half the volumes examined. The transition between Phase 2 and 3 was reversed: cortical thicknesses were observed to increase in all volumes except VOI 1. Mean BV/TV was also found to increase in ten volumes of interest, although these increases were not statistically significant. Trabecular thickness continued to increase between Phase 2 and 3, with a larger interval than was previously observed between Phase 1 and 2, while the rate of decrease in trabecular number appeared to decrease. These changes suggest that in Phase 3 the net change in bone mass has altered, with either a more rapid rate of bone formation or, perhaps more likely, a reduced rate of bone resorption.

The timing of these transitions coincides with the described time period of the infantile growth spurt, which begins following the perinatal period and continues until approximately 2 – 3 years of age (Ay *et al.,* 2011; Prentice *et al.*, 2006; Ylihärsilä *et al.,* 2008). The apparent increase in the rate of bone resorption in Phase 2 is consistent with the release of the skeletal calcium reservoir, which may be necessary to facilitate the increased rate of bone growth, both of the ischium and perhaps other skeletal elements. This may additionally act to supplement dietary calcium availability during this period, which corresponds with the approximate age at which weaning would be expected. Phase 3 represents the age at which this growth spurt would cease; a

concurrent decrease in bone modelling activity which was necessary to create larger bones may provide greater physiological resources to facilitate bone remodelling, and the architectural reinforcement of the ischium.

Comparison with previous literature

Similar patterns of ontogenetic change have been described previously with regards to the femoral neck (Ryan and Krovitz, 2006), tibia (Gosman and Ketcham, 2009), sacrum (Yusof, 2013), and ilium (Cunningham and Black, 2009b; Glorieux *et al.*, 2000; Hildebrand *et al.*, 1999).

In both the femur (Ryan and Krovitz, 2006) and tibia (Gosman and Ketcham, 2009), bone volume fraction was found to be relatively stable between birth and 4 months of age. By the age of 1 year however, BV/TV in both bones was found to decrease to approximately 50% of its perinatal value, with a concurrent significant decrease in trabecular number. In the tibia, Tb.Th was found to increase at a relatively constant rate despite the decrease in BV/TV (Gosman and Ketcham, 2009), while in the humerus Tb.Th values were found to be more variable, with no clear trend towards either an increase or decrease (Ryan and Krovitz, 2006).

Beyond the age of 1 year, BV/TV and Tb.Th were found to increase steadily until it reached values which were similar to the established adult values, which in each case was found to occur at 7 – 8 years of age. With some interest, it was noted in each case that the stable 'adult' bone volume fraction was markedly lower than the peak observed in the perinatal period, which supports the suggestion that the early increase in BV/TV may be a response designed to maximise calcium storage, rather than a biomechanical response.

A similar post-natal modification of sacral trabecular bone has also been identified (Yusof, 2013). A comparison of two groups, aged 0 – 18 months and 18 months – 3.5 years revealed a significant reduction of BV/TV and Tb.N in the older cohort, and a significant increase in trabecular thickness. It should be noted that the decrease in BV/TV was less severe than previously described in the ischium, femur (Ryan and Krovitz, 2006) and tibia (Gosman and Ketcham, 2009), with a mean decrease of only 7% BV/TV. However, these values represent the totalled sum 14 volumes that defined

the sacral centrum and alae; it is therefore possible that an averaging effect across this larger area may obscure more pronounced transitions between individual regions. The age range of the first cohort was also noted to incorporate the ages at which both the maximum and minimum bone volume fractions were presented in the three bones previously discussed.

While a single comprehensive study of ontogenetic changes in the ilium has not been completed, separate data sources have been published regarding the trabecular architecture of the iliac crest in the neonate (Cunningham and Black, 2009b), between 1.5 and 22.9 years of age (Glorieux *et al.,* 2000) and in the adult (24 – 92 years) (Hildebrand *et al.*, 1999). It should be noted that the data was procured using different experimental techniques: Cunningham and Black (2009b) and Hildebrand *et al.* (1999) utilised µCT imaging, Glorieux *et al*. (2000) applied histological techniques, and therefore a direct comparison of values should be approached with caution. However, three-dimensional imaging modalities have been found to produce comparable data to histological preparations, thus allowing a rudimentary comparison of data (Fajardo *et al.*, 2002; Müller *et al.,* 1998). There are also potential limitations resulting from the discrepancy in spatial resolutions achieved by Cunningham and Black (2009b) and Hildebrand *et al.* (1999), which were approximately 40 µm^3 and 28 µm^3 respectively. The former study is therefore likely to be subjected to a greater degree of partial volume averaging, which may adversely affect the accuracy of histomorphometric analysis. However, in the volumes in question the minimum Tb.Th values were found to be approximately 120 µm, therefore the influence of PVA would likely be relatively low (Cunningham and Black, 2009b).

Of the three datasets, BV/TV was found to be highest in the neonatal period, with mean values of approximately 35 – 40% (Cunningham and Black, 2009b). The architecture was found to consist of a high number of struts of intermediate thickness, which is also consistent with the immature trabecular architecture described for the ischium. The histological bone volume fraction reported for juveniles aged 1.59 – 6.9 years by Glorieux *et al.* (2000) was found to be only 17.7%, representing a substantial decrease over the neonatal state, even allowing for variation in specific anatomical sites and the potential for a degree of shrinkage in the histological specimens (Müller *et al.,* 1998). The lower values of BV/TV observed were caused by an apparent

decrease in both trabecular number and a slight decrease in thickness. With increasing age however, BV/TV and Tb.Th progressively increased while Tb.N did not change significantly (Glorieux *et al.*, 2000).

The adult data presented by Hildebrand *et al.* (1999) was found to present BV/TV, Tb.Th and Tb.N values which were inconsistent with the data recorded for post-pubertal iliac crest samples by Glorieux *et al.* (2000): mean BV/TV in the adult population was found to be only 15.6%, compared with the post-pubertal 27.8 %. Tb.Th was found to be comparable between the adult and post-pubertal groups, while Tb.N was markedly lower in the adult data presented by Hildebrand *et al.* (1999). When these adult values were compared with the neonatal architecture (Cunningham and Black, 2009b), Tb.Th was found to be similar in each group, while Tb.N was reduced by over 50% in the adult group.

While the data presented by Hildebrand *et al*. (1999) was intended to represent the mature trabecular architecture of the iliac crest, it is possible that the age range of the population used negatively influenced the results. Although the age range included individuals between 24 and 92 years of age, the mean age of the sample was 67.3 years, which is tending towards the age at which degenerative changes in trabecular architecture are common (Rupprecht *et al.*, 2006; Stauber and Müller, 2006). These changes can include a loss of BV/TV and concurrent reductions in both trabecular thickness and number with age, particularly beyond the age of 70 years. It is perhaps unwise therefore to treat this data as a true indicator of the optimal architectural arrangement expected in adulthood. Unfortunately, the distribution of values around the presented means with age was not provided, preventing any underlying trends from emerging.

Despite some limitations to comparisons, each of these ontogenetic studies shows similar results regarding early ontogenetic changes. The trabecular architecture of the perinatal and early post-natal period appears to be very different to the architecture which is established during subsequent development, with a rapid alteration in architecture occurring at approximately 1 year of age. This is consistent with changes which have been documented in the ischium in the present study, although data regarding the structure of the ischium beyond the age of 3 years has not been

published, preventing a discussion of its relationship with the adult structure. It is also similar to radiographic changes reported by O'Malley (2013), which were proposed to indicate an architectural rearrangement in the infant period.

Changes that were demonstrated in each study included a dramatic reduction in the bone volume fraction, with a similar decrease in trabecular number. It appears that trabecular thickness does not decrease with age typically, but most frequently shows a relatively steady increase towards values that are similar to adult thicknesses. A strong correlation persisted between BV/TV and Tb.N in the ischium in Phase 2 and 3, indicating a continued relationship between the two parameters.

Perhaps the most important feature to note with regards to the early patterns in trabecular development in each bone for which data is available is that the high BV/TV reported in the perinatal period is typically the peak BV/TV reported for that bone. In the case of the ilium, the neonatal values documented by Cunningham and Black (2009b) are persistently higher than those in the oldest specimens examined by Glorieux *et al.* (2000), and are approximately double the value presented by Hildebrand *et al.* (1999). Whether this is a predetermined, genetically programmed overproduction or a mechanism to reinforce the immature and poorly-optimised trabecular bone structure in the early stages of development is currently unknown. However, as the peak bone volume fraction occurs in advance of major post-natal biomechanical developments such as the attainment of gait, or indeed hands-and-knees crawling, and the period of resorption appears to correspond to the beginnings of infant ambulation when loading may be expected to increase, this may indicate that the peak bone volume achieved in the early post-natal period is surplus to mechanical requirements at the time.

7.3 Potential factors influencing bone mineral accrual

7.3.1 Changes in fetal architecture

It is perhaps surprising that, with frequent indicators of elevated perinatal bone mineral accrual in the form of increased cortical thickness and trabecular bone volume fraction, followed by a substantial resorption and potential redistribution of skeletal

tissues, there is not a greater literature base documenting the early changes in skeletal structure. Those studies that detailed ontogenetic changes emphasised the progressive remodelling changes which increase bone mass and architectural maturity beyond infancy, rather than debating the underlying rationale that led to an apparent excess of tissue prior to this period.

A discussion of changes later in childhood is undoubtedly of importance: for example, the maturation of trabecular architecture in both the femur and tibia appears to coincide with biomechanical milestones (Gosman and Ketcham, 2009; Ryan and Krovitz, 2006). The observed increase in bone volume fraction and trabecular thickness after 1 – 2 years corresponds with habitual bipedal ambulation (Keen, 1993, Sutherland *et al.*, 1980). Further, the architecture appears to broadly stabilise after 8 years in each element, after which histomorphometric parameters more closely approximate the adult structure. This is in accordance with the proposed age at which a mature gait has been established, at around 7 years of age (Beck, 1981; Ryan and Krovitz, 2006; Keen, 1993; Lacquaniti *et al.*, 2012). Certainly, the established literature appears to highlight the importance of bone functional adaptation and the mechanostat hypothesis in controlling skeletal architecture after the early post-natal period.

However, of equal importance is the biological imperative that is responsible for the promotion of early mineral accrual which has been described in the ischium and scapula (O'Malley, 2013), and which has been proposed may be present in the ilium (Cunningham and Black 2009; Glorieux *et al*., 2000), femur (Ryan and Krovitz, 2006) and tibia (Gosman and Ketcham, 2009). However, to understand the pattern this early development follows, the fetal development of trabecular architecture must also be considered.

While quantification of the structure of the fetal ischium has not yet been undertaken, a growing body of literature exists describing changes in other skeletal elements that may reveal potential systemic patterns that may also apply to the ischium. However, the radiographic study conducted previously [see Chapter 4] provided evidence to suggest that the period of bone accrual began during fetal development. Ontogenetic changes in fetal trabecular structure have only been outlined for a small number of

regions, including the femoral metaphysis (Salle *et al.*, 2002), the femoral and humeral diaphyses (Reiss and Abel, 2012) and the vertebral centra (Acquaah *et al.*, 2015; Nuzzo *et al.*, 2003).

Long bone architectural changes

Salle *et al.* (2002) conducted a histological examination of frontal sections of the proximal femur from fetuses between 16 and 41 gestational weeks, examining 36 fields of interest, divided into 8 developmental bands that were positioned progressively further from the growth plate. The results of their analysis demonstrated a significant increase in bone volume fraction across all bands with age, increasing from 24% to 33.6% over the period investigated. This was accompanied by a significant increase in mean trabecular thickness, while no significant change in trabecular number was recorded. Differences were also present between developmental bands: those regions closest to the growth plate, representing the least mature bone, were found to have a very low BV/TV and Tb.Th, but a significantly increased Tb.N compared to the bands further from the growth plate. It was noted by the authors that the apparent rate of change in trabecular thickness in particular was approximately 240 times faster than values previously described in post-natal iliac bone (Glorieux *et al.*, 2000), which indicated the presence of rapid-acting modelling processes rather than remodelling, which typically occurs over a number of months (Clarke, 2008).

The proposal that trabecular architecture *in-utero* is characterised by a progressive increase in bone volume in the fetal period is primarily defined by early modelling processes is consistent with the continuing influence of modelling observed in the juvenile ischium, and the progressive accumulation of radiographic intensity

Reiss and Abel (2012) also examined changes in fetal trabecular architecture in the femur, and also the humerus, using microcomputed tomography. The authors found no significant change in BV/TV in either the femur or humerus between 4 and 9 intrauterine months. Although BV/TV remained constant throughout, complimentary variations in Tb.Th and Tb.N were observed: there was a concurrent significant decrease in Tb.N and significant increase in Tb.Th with age. In addition, although the totalled mean values for Tb.Th and Tb.N were found to differ between the humerus

and femur, no significant differences in histomorphometric parameters were identifiable in any specific age group.

The conflict in results between Salle *et al.* (2002) and Reiss and Abel (2012) may be a result of limitations in the methodology adopted by the latter. Although a three-dimensional imaging modality was applied by Reiss and Abel (2012), data was collected only from two two-dimensional transects, a proximal transect at 10% of the diaphysis length and a distal transect at 90% length. The interceptions with the bone phase were counted and measured and used to determine BV/TV, Tb.Th and Tb.N. In addition, data for the younger specimens was artificially coarsened from 60 μm^2 to 100 μm^2 via resampling to "avoid measurement errors and bias due to the differences in resolution" (Reiss and Abel, 2012). The practice of coarsening resolution has previously been discouraged as it has been found to reduce the accuracy of histomorphometry compared with prospective scanning at the desired resolution (Cooper et al., 2007; Kim et al., 2004). In addition, mean trabecular thickness values presented by Salle et al. (2002) did not exceed 100 μm. The resolution of the resolution of 100 μm^2 utilised by Reiss and Abel (2012) may therefore have been insufficient to resolve the smallest trabecular elements, which would potentially decrease BV/TV and Tb.N, while increasing mean Tb.Th measurements.

Vertebral architectural changes

Ontogenetic changes in fetal vertebral trabecular bone has been shown to follow a similar pattern of change as the fetal femur, as reported by Salle *et al.,* (2002). Nuzzo *et al.* (2003) quantified changes in lumbar BV/TV and Tb.Th between 16 and 24 i.u. weeks. They reported a significant and rapid increase in BV/TV with age, from approximately 30% at 16 weeks to 55% at 24 weeks of age. They did not find any significant variation in trabecular thickness over the same period however, which suggests that this increase in BV/TV was driven by a substantial change in trabecular number. Unfortunately, the authors did not quantify this parameter. It is interesting to note the potential regional distinction in trabecular modification however: where femoral BV/TV appears to be dependent on increased trabecular thickness, it is trabecular number that varies with age in the vertebral centra. It is possible that this discrepancy is due to the relatively rapid rate of change observed in the vertebrae:

such a rapid increase in BV/TV may not provide sufficient time to accrue mineralised bone tissue in the vertebrae.

The pattern of gain in bone volume fraction during fetal development is consistent with the proposed accumulation of bone mass in the ischium, based on the results of the radiographic study. Comparing reported late fetal BV/TV in the femur reveals values which are similar to the reported perinatal and early post-natal architecture, as reported by Ryan and Krovitz (2006), and which are far greater than the values subsequently documented following the loss of bone in the infant period.

Only one study could be identified which had documented progressive changes through the fetal period and into infancy in a single element (Acquaah *et al.,* 2015), which examined histomorphometric data from all vertebrae between C1 and L5 between 6 i.u. months and 2.5 years of age. While some regional variations in the pattern of change, and in absolute values, was observed between vertebral levels, a clear age-related pattern was also present within the data as a whole. Mean bone volume fraction increased significantly between 6 and 7 i.u. months before adopting a relatively stable level until birth. Between birth and 1.2 years, BV/TV decreased significantly to approximately 1/3 of the perinatal level, and no significant change was then observed between 1.2 and 2.5 years of age. The fetal increase in BV/TV was accompanied by a significant increase in Tb.N, and an initial increase in trabecular thickness. It was however noted that between 7 i.u. months and birth, Tb.Th decreased significantly. The decrease in BV/TV following birth was shown to be the result of a simultaneous decrease in both Tb.N, which fell significantly by to 50% of the term trabecular number, and Tb.Th, which continued to decrease significantly between birth and 1.2 years, before showing a significant increase at 2.5 years of age. It should be noted that this increase in Tb.Th did not reach the same thickness level that was present in the fetal vertebrae.

The results of this study are particularly significant, as the authors present not only fetal changes, but also early post-natal changes in the vertebral architecture. It is therefore possible to ascertain whether there are any similarities between the post-natal trabecular development of the ischium and vertebrae. A high degree of consistency was observed between the results of BV/TV and Tb.N, which each showed

a significant decrease in the early post-mortem period. However, it should be noted that, while 120 vertebrae were analysed the authors stated these were drawn from "complete" vertebral columns (Acquaah *et al.*, 2015). With 24 vertebral levels included in the study, this suggests that only 5 individuals were included in the study, although the authors did not directly comment on this. Therefore, extreme caution is advised in interpreting the final data without more extensive investigation.

7.4.2 Recommended terminology for phase designation

Two alternative terminologies have been applied previously to the progression of accrual, resorption and reorganisation of bone mass during early ontogenetic development.

The first known documentation of this ontogenetic pattern, to the author's knowledge, can be credited to O'Malley (2013), who described the pattern of development qualitatively in the juvenile scapula. Due to the novel nature of the descriptions, it was proposed that the period of bone loss in the early post-natal period was an architectural 'reboot' which may have been caused by a conflict between the evolutionary upper limb function as a locomotor apparatus and the prehensile function it fulfils in modern humans. It was proposed that the 'pre-reboot' accumulation of mass was in anticipation of mechanical loading which was ultimately not realised, leading to a 'reboot' to resorb the pre-formed structure and a subsequent 'post-reboot' redistribution of skeletal tissues in a pattern which was better suited to the biomechanical environment of the scapula.

The data presented in the present study, and accumulated through an analysis of previous literature, has revealed that this pattern of development may not be unique to the scapula however, but is rather a widespread phenomenon. Evidence exists to suggest that these changes also occur in the ischium, femur (Ryan and Krovitz, 2006; Salle *et al.*, 2002), the vertebrae (Acquaah *et al.*, 2015; Nuzzo *et al.*, 2003), the ilium (Cunningham and Black 2009a,b; Glorieux *et al.*, 2000) and the tibia (Gosman and Ketcham, 2009). This calls into question the functional basis which underpins the classification of an architectural 'reboot'.

Acquaah *et al.* (2015) proposed that this pattern of change did not represent a conflict, but rather a potential preparatory, protective mechanism designed to support future trabecular adaptation. The authors introduced the terms overproduction, constructive regression and refinement to define the three stages of early trabecular development. It was suggested that overproduction may be a genetic mechanism to create a large reservoir of calcium in advance of rapid post-natal growth to prevent potential calcium deficiencies. During constructive regression, the resorption of bone would release calcium for the purposes of growth and homeostasis, while simultaneously creating a figurative blank slate, into which a biomechanically stable trabecular architecture specific to each element could be etched via bone functional adaptation and the mechanostat model. This process of adaptation could then continue through subsequent refinement by remodelling as the demands on each bone develop with usage.

The proposed model of growth outlined by Acquaah *et al.* (2015) is consistent with the both the qualitative and quantitative patterns of development outlined in the present study. Although the underlying mechanisms driving an early accumulation of bone mass remain unclear, the ages at which each phase of development are active are consistent with the onset and cessation of the juvenile growth spurt, during which there is a substantial increase in ischial size. The post-natal architectural modifications are also consistent with a high rate of bone resorption, which may be the result of a temporary increase in the physiological demand for calcium release. As such, it is recommended that the terminology suggested by Acquaah *et al.* (2015) be adopted with regards to ischial development, therefore reclassifying Phase 1, 2 and 3 as periods of over-production, constructive regression and refinement, respectively.

7.4 Strengths, limitations and future advancement

7.4.1 Study limitations and improvements

Specimen selection

The primary limitations of this study are related to the availability and provenance of specimens available for analysis. These limitations are addressed in Section 1.3.

Although the total number of individuals included in the radiographic study was relatively large for a juvenile study of this nature, the age distribution of specimens was weighted towards the perinatal and pubertal age ranges. As such, there may be significant developmental features that were not observed during this study due to the distribution of data.

The quantitative study was subjected to a similar limitation: there was a substantial age bias towards the Phase 1 individuals (n = 20), with only a small number of Phase 2 and 3 specimens present (n = 5, n = 3 respectively). As such, it is important that this be considered when assessing the weight that can be applied to the present findings. However, it should be noted that the Scheuer Collection is the one of the largest active repositories for juvenile skeletal remains, providing perhaps the greatest opportunity to assess developmental change.

As outlined previously [see Section 1.3], the Scheuer Collection is primarily comprised of undocumented juvenile remains from historic anatomical and archaeological sources, with only a small proportion containing information such as age-at-death or sex. The age guides assigned to each developmental phase are based on age estimations, and therefore these may be affected by any errors in the initial assessment of age. The cause of death and associated morbidity of individuals in the collection is also unknown

Data acquisition

This study is indebted to the Centre for Medical Engineering and Technology, University of Hull, for facilitating the collection of the μCT data that made this research possible. However, the use of a remote third party to complete such a vital stage of the project presented minor limitations during data acquisition, primarily due to the time-consuming nature of specimen transit, μCT scanning and the exchange and examination of the resulting data. As such, the research that could be conducted with regards to optimising conditions for the analysis of the juvenile ischium specifically was restricted.

VOI selection

The present study utilised, and further developed, methodology previously established for the investigation of ontogenetic changes in skeletal architecture (Cunningham, 2009). It represents the first instance where a VOI grid designed to analyse the maximum proportion of the bone in question has been applied across several developmental cohorts, and as such presents an excellent opportunity to review the potential benefits and limitations which apply to this form of analysis.

In the event of further investigations of the architecture of the ischium, it may be useful to experiment with alternative grid arrangements to address questions raised by the present study.

It was noted that, particularly in the region of the acetabulum, the use of only a single VOI to account for the full depth of the ischium was a limiting factor in the subsequent interpretation of skeletal architecture. It engenders the presumption that there is no difference between the trabeculae supporting the pelvic and lateral cortical shells. This decision was driven by necessity as the acetabular margin in the perinate does not project significantly from the lateral surface of the ischium, therefore any volume attempting to exclusively segregate this region would be significantly smaller than other volumes. As the same grid was utilised to quantify each stage of development, it was not possible to impose a division of the volumes associated with the acetabular margin in older developmental cohorts despite its increasing prominence.

In light of the observed disparity in thickness between the pelvic and lateral cortical shells, particularly in Phase 1 specimens, there may be merit in creating a three-dimensional grid that distinguishes pelvic and lateral volumes through the depth of the ischium. This would allow the architecture underlying each surface to be examined with greater distinction, and may provide a better account of the trabecular architecture associated with the acetabular margin.

Degree of anisotropy

Of the histomorphometric parameters analysed during this study, the results of degree of anisotropy provided the least useful information, with high standard deviations and a resulting lack of discernible pattern within the ischium at each stage of development.

This high degree of variability between specimens may be a feature of ischial development; a high DA indicates a preferential loading axis, often associated with regions which experience unidirectional loading, while a low DA is indicative of a less distinct trabecular orientation which may indicate diminished or multi-directional loading (Kim *et al.*, 2013). As the remaining structural parameters did not show a clear indication of discrete biomechanical pathways during the developmental period investigated, variability in the degree of anisotropy may be expected.

However, the results of this parameter may also have been influenced by the size and shape of each volume of interest selected for analysis. The calculation of DA involves the creation of a 'best-fitting sphere' within a designated volume. The use of polygonal volumes of interest contoured to maximise the trabecular volume analysed in each VOI may have caused variability in the size and position of this best fitting sphere between individuals, which could have inflated the variability observed.

The influence of polygonal volumes of interest on DA could be investigated further by conducting a validation study examining the data obtained using several pre-set and polygonal volumes to capture histomorphometric data: the use of a regular geometric shape, such as sphere or cube, to select the VOI may decrease variability in the resulting degree of anisotropy. However, it would also reduce the quantity of bone included in each VOI, particularly those of atypical shape at the periphery of the bone, and any which feature concave cortical surfaces, which may in turn have a detrimental effect on mean trabecular measurements such as thickness and number.

Structural model index

The use of SMI as a parameter for the classification of trabecular architecture as either rod-like or plate-like in nature may also have presented a limitation to the present study. In a recent publication, Salmon *et al.* (2015) outlined a number of concerns with

regards to the implications of SMI as measured by the method of Hildebrand and Rüegsegger 1997b). These concerns centred on the strong dependence on BV/TV and the failure to account for the effects of trabecular intersections during calculations of surface concavity. This limitation is explored further in Section 7.1.2.

Analysis of cortical bone structure

The structural information that can be derived from the three-dimensional imaging of cortical bone structure is unfortunately limited by a dependence on the presence of tissues, or substrata of differing densities. Trabecular bone can be resolved with relative ease due to the phase contrast between bone and non-bone (air) in a structure that is typically predominantly air. Cortical bone porosity is typically less than 5% in the adult, with little change in density to separate the lamellae from which cortical bone is formed.

The methods currently available for the quantification of cortical bone structure using microcomputed tomography are therefore limited to relatively basic measurements of thickness, area and volume. However, microstructural differences have been found to have some potential to determine the presence of remodelling using μCT imaging (Cooper *et al.*, 2006; 2007). Primary, or woven, bone established during modelling is comprised primarily of interstitial lamellae which run parallel to the bone surface (Rauch *et al.*, 2006), which is subsequently converted into Haversian bone through remodelling (Goldman *et al.,* 2009; Rauch *et al.*, 2006). Cortical bone porosity, and the size of the pores, can be used to infer information regarding cortical remodelling: it is possible to identify the voids which are created by the BMU cutting cone (Cooper *et al.*, 2006) and the presence of a central Haversian canal (Cooper *et al.*, 2007) within a three-dimensional dataset, but only if a very high spatial resolution is achieved (< 5 μm). An increase in either of these features could be considered indicative of remodelling processes within the bone. The resolutions achieved in the present study were therefore insufficient to resolve these structures accurately, thus preventing any attempt to quantify features of cortical bone remodelling.

7.4.2 Proposals for technical advancement

The investigation of bone microarchitecture via three-dimensional imaging techniques is primarily limited by technical concerns, including features such as gantry size limitations restricting specimen size, or achieving suitably high spatial resolutions to reduce voxel averaging effects. However, μCT imaging technology is in a state of constant improvement, particularly with regards to the technical capabilities of imaging devices. Several potential improvements are therefore implicit, and would be expected to advance in line with technological improvements over time. These include technical advances which allow for increased spatial resolutions, reduced interference and greater contrast between the bone and air phases would each offer the potential of increased accuracy in μCT analyses.

Perhaps of greater interest is the capacity to image increasingly larger specimens without such a large loss of resolution: in the present study, the voxel size decreased from approximate 12 – 15 μm in Phase 1 to 24 – 32 μm in Phase 3. This restricts the potential developmental periods that can be investigated with sufficiently high resolutions to ensure accurate results, as edge detection and the accuracy of stereological results will decrease with diminished resolution due to the increased influence of partial volume averaging. This would prevent, or at a minimum impede, the analysis of later developmental cohorts and, with regards to the pelvis for example, prevent the accurate documentation of architectural changes during the later stages of gait maturation.

Excluding physical scanning restrictions, the greatest opportunity to further the field of bone histomorphometry is the development and dissemination of automated techniques for the handling, processing and analysis of three-dimensional datasets.

At present, techniques have been investigated to facilitate the automated (or semi-automated) segmentation of bone from non-bone (e.g. de Moura Menses *et al.,* 2011; Polak *et al.*, 2012), and also the automatic differentiation of cortical and trabecular regions (e.g. Buie *et al.*, 2007; Treece *et al.*, 2010). However, while there have been promising results which suggest that automation does not negatively affect the results

of histomorphometric analysis, the techniques often require complex computational steps and the necessary knowledge to understand and apply these.

The development of a single software package, or plug-in to a pre-existing open-source package such as ImageJ, which contains algorithms to apply these automated techniques may ultimately reduce the level of subjectivity and potential for error associated with manual extraction of data. Furthermore, it would provide a platform through which independent groups could conduct widespread validation studies utilising these techniques, including researchers who may lack the computing skills necessary to implement the techniques from the available publications.

Development of a bespoke software application would also allow the introduction of additional features that may similarly reduce the potential for error in histomorphometric studies, or increase the efficiency with which they may be conducted. For example, it would be possible to include a flexible R/VOI selection toolkit similar to that presently available through CTan, which allows the careful adjustment of selected areas, and potentially the ability to select several individual volumes for either simultaneous or sequential analysis, depending on the available computational power. Such a development would ultimately facilitate the more rapid application of a grid-based VOI methodology, allowing researchers to maximise their efficiency and potentially expand the study population or scope or research. The selection of multiple volumes simultaneously would also remove the risk of small overlaps between volumes if they are positioned close together, as they would reveal in real-time the selected volumes of bone.

7.4.3 Future research directions

The present study has successfully quantified early post-natal trabecular and cortical bone changes which occur in the human ischium, and has provided further information in support of emerging reports of a period of constructive regression of bone mass in the literature. It has also further reinforced the potential benefits of examining in detail the full architecture of a single bone, rather than the observation of specific landmarks associated with biomechanical trajectories. However, it has also highlighted

areas that require further investigation beyond the scope of the current investigation, which may assist in resolving wider questions associated with this research.

Further research in the human ischium and pelvis

The research presented regarding the structure of the juvenile ischium represents the first known effort to quantify the internal architecture of this often-neglected component of the innominate at any stage of development. In isolation, there are limits to the applicability of this data, as in life the ischium does not exist and develop in isolation, but as part of the larger innominate. The documentation of the remaining bones of the innominate in the perinatal period would provide a more complete understanding of the early developmental pattern. Literature regarding the neonatal ilium has previously been published (Cunningham, 2009; Cunningham and Black, 2009a, b, c, 2010), therefore only the pubis remains undocumented in the neonatal period. Ontogenetic change from this developmental baseline could then be explored in each of the bones of the innominate throughout juvenile development to track changes which develop as a result of biomechanical, or alternative, stimuli associated with each bone, and with the innominate as a whole: for example, there may be common trabecular pathways which pass between each bone even before fusion, such as the ilioischial and sacropubic trajectories. This investigation would however be dependent on continued development of μCT technology to achieve the high spatial resolutions necessary for trabecular analysis in larger specimens, particularly if stages beyond pelvic fusion events are to be examined.

Support of proposed early ontogenetic patterning

With regards to the study of bone microarchitecture beyond the ischium, this study has reiterated the importance of understanding skeletal changes that occur early in development and the need to explore the subsequent implications for paediatric and adult bone health.

The first stage in understanding these changes is identifying the prevalence and timing of similar periods of constructive regression within the human skeleton, as this may lead to more substantial support for the mechanisms the could control and regulate these changes. In this first instance, the application of the gradient-mapping protocols

to radiographs across a wide range of bones, including axial and appendicular elements, would allow any gross changes in architecture to be established. Due to the pronounced radiographic differences associated with this period in both the ischium and scapula (O'Malley, 2013), and the rapid, cost-effective nature of radiographic imaging, with access to an appropriate skeletal collection such as the Scheuer Collection, this data should be relatively easy to obtain and analyse. The results of this study could then be utilised to direct subsequent quantitative studies, perhaps focusing on a more limited number of skeletal elements and age cohorts to establish the specific architectural changes which occur and their relevance to regions of known biomechanical significance which are well-documented in the adult, such as the femoral neck or the ilium. It can then be investigated whether there it may be necessary to implement clinical practices to attempt to offset a decrease in bone mass, such as calcium supplementation during the resorptive period, and whether there are any implications for current intervention procedures in the juvenile skeleton.

Programmed basis for bone resorption

Perhaps the greatest debate with regards to the correct manner of classification for the changes documented in the present study is the physiological motivation which underpins the early accumulation of bone mass, and whether it is a process which is necessary to support future growth and development, as proposed by Acquaah *et al.*, (2015), or a remnant of a programmed evolutionary blueprint which is no longer applicable to modern man, as suggested by O'Malley (2013).

It has been observed that there is an evolutionary disparity in trabecular architecture between modern humans and both our closest living relatives and our evolutionary ancestors (Chirchir *et al.*, 2015). When bone volume fraction (termed here trabecular bone fraction, or TBF) was assessed in several adult long bone sites in extant primates, hominin fossils and modern human specimens, it was found that TBF was consistently and significantly lower in modern humans than in the other species. The authors related these changes to the relatively recent, and rapid, changes which have occurred in human society, specifically behavioural and societal changes that have led to an increasingly sedentary life, which in turn implies reduced biomechanical demands on the skeleton. No additional architectural parameters were quantified, thereby

restricting further discussion of possible adaptive changes within the architecture which may also account for a reduced TBF.

The proposal that there may have been a relatively recent evolutionary adaptation to trabecular bone architecture in modern humans is consistent with the hypotheses formed by O'Malley (2013) with regards to the scapular reboot. It is possible that the pattern of bone mineral accumulation in other regions of the skeleton is linked to the effects of a changing environment and behaviour pattern. However, it could also be argued that no functional conflict exists in the lower limbs, vertebrae or pelvic girdle, which have each retained a direct role in load bearing: indeed, it could be argued that by passing the full weight of the body through a single axis, the lower extremities may experience a relative increase in strain during loading.

It may be of some benefit to investigate early ontogenetic changes in alternative mammalian species, including extant primates if possible, to establish whether they also present a trend which includes an early period of bone mass accumulation which is followed by a radical loss and reorganisation of the internal architecture. If the observed trend for fetal overproduction followed by post-natal resorption and redistribution is symptom of conflict between evolutionary history and the demands on a modern human skeleton, it would be expected that species which have retained more closely their ancestral behaviours and lifestyle would not follow such a pattern, as there is no genetic-environmental conflict to be resolved.

However, if this proposed transition is a systemic metabolic process designed to maximise bone mineral accrual during gestation to facilitate post-natal growth without introducing a calcium deficit (Acquaah *et al.*, 2015), such a trend may also be present in other extant primate species, and perhaps across mammalian species as a collective group.

7.5 Conclusions

This study presented data on the qualitative and quantitative development of the juvenile ischium.

The qualitative analysis of the juvenile ischium revealed that there are seven radiographically distinct developmental phases identifiable between 28 i.u. weeks and 14 years of age. The fetal and perinatal periods was typified by an overall increase in radiopacity, indicating the accumulation of bone mass in advance of birth. By 5 months of age, however, the intensity of the ischium was found to decrease substantially, despite an increase in bone size over the same period. This period continued until 2 years of age. It was proposed that this apparent decrease in bone mass was related to the concurrent effects of the infant growth spurt and weaning, which would respectively act to increase the demand for calcium to allow new bone formation while reducing the ingested dietary calcium available for incorporation into the skeleton.

Between 1 – 3 years of age, small regions of increased intensity were observed to return the ischium in the region associated with the ischial spine and posterior aspect of the acetabular margin. Following this, a more generalised increase in radiopacity was observed across the ischium, although the intensity of the ramus and acetabular fossa remained relatively low. The position of regions of increased and decreased radiopacity were consistent with those that may be expected following the tenants of bone functional adaptation. For example, regions of high intensity were associated with proposed regions of biomechanical importance following the development of bipedal ambulation. This included the ischial spine, which is placed under strain by the actions of the pelvic floor and sacral ligaments, and the posterior aspect of the ischium, which is proposed to contain the sacroischial trabecular bundle to transmit the weight of the body while seated. It was however noted that the influence of changing external dimensions and proportions may also have an influence on radiopacity, therefore further quantitative investigation was necessary to determine the precise architectural changes associated with these patterns.

The three phases investigated using μCT were selected to incorporate the perinatal increase in radiopacity observed in Phase 1, the loss of bone intensity between 5 months and 2 years of age, or Phase 2, and the subsequent return of intensity in the posterior aspect of the bone in Phase 3. The qualitative analysis of ischial structure in the perinatal period revealed a regional organisation in trabecular architecture and cortical thickness. It is proposed that this is primarily driven by the demands of growth and the dissemination of blood vessels from the vascular centre of the ischium, which is proposed to lie underneath the acetabulum. The metaphyseal regions at the superior and inferior poles of the ischium revealed an immature network similar in structure to primary spongiosa, covered by very thin cortical shells. Towards the vascular centre, this primary architecture demonstrates evidence of remodelling to form a more robust secondary spongiosa around which the vascular elements may be distributed.

The analysis of ischia from Phase 2 confirmed that there was a significant decrease in BV/TV and cortical thickness at 5 months – 2 years of age. A more homogenous architecture was observed, with a reduced number of trabeculae of increased thickness across the ischium. This is consistent with the proposal that the documented changes in radiopacity were driven by a decrease in bone quantity. The architectural transition that accompanied this decrease was consistent with an exaggerated rate of bone resorption over formation, which may have acted to resorb a high number of smaller trabecular elements while thickening those which remained.

Although direct references to this resorptive phenomenon are limited, data presented by other authors in the extant literature regarding infant skeletal development support the postulation that this pattern of development is not exclusive to the ischium, but may also occur in the humerus, femur, ilium, vertebrae and sacrum. It is proposed that the modelling and remodelling interactions which characterise these sequential periods of overproduction, constructive regression and architectural refinement may be indicative of a 'switch' between the predominant genetic control of *in-utero* skeletal development and the post-natal requirement for a functionally-adaptive skeleton which is capable of modification in response to external stimuli. The physiological processes that underpin this transition are unclear and will require further work to address. However, it is proposed that this 'switch' may be linked to the

onset of the infant growth spurt and the calcium demand this likely generates due to the increased resources required for tissue generation. Certainly within the ischium, the rapid decrease in bone mass per volume was accompanied by a large increase in ischial size, and the reversal of the resorptive changes which begins in Phase 3 do not occur until towards the end of this growth period.

With regards to the role of biomechanical stimuli in ischial development, there was relatively little evidence found to support a strong mechanical influence in the age range studied in the quantitative investigation. In Phase 2 and 3, the architecture of the ischium was found to be statistically homogenous, with no clear differentiation of regions which may be placed under strain following the development of a bipedal posture, for example as the volumes associated with the ischial spine, lunate surface of the acetabulum or the hypothetical sacroischial trabecular trajectory. This may be in part due to the relatively diminished weight-bearing role the ischium has when compared to the ilium, or to the lower limb long bones, which have demonstrated a mechanical influence on post-natal development.

The present study represents one of the first investigations to document the developmental patterns of the human ischium specifically, and as such represents an important addition to the developmental osteology literature. Further, through the detailed documentation of the phases of skeletal overproduction and constructive regression within the ischium, this study contributes directly to an advanced understanding of early developmental changes in skeletal architecture. This may have implications for the monitoring of ischial development, and beyond this it may further aid in the identification of the signalling mechanisms and stimuli responsible for directing early skeletal growth and maturation.

References List

Abad, V., Meyers, J.L., Weise, M, Gafni, R.I., Barnes, K.N., Nilsson, O., Bacher, J.D. and Baron, J. (2002). The role of the resting zone in growth plate chondrogenesis. *Endocrinology* **143 (5)**: 1851 – 1857.

Abad, V., Uyeda, J.A., Temple, H.T., De Luca, F. and Baron, J. (1999). Determinants of spatial polarity in the growth plate. *Endocrinology* **140 (2)**: 958 -962.

Abel, R.L., Prime, M., Jin, A., Cobb, J.P and Bhattacharya, R. (2013). 3D imaging bone quality: bench to bedside. *Hard Tissue* **2 (5)**: 1 – 9.

Abitbol, M.M. (1988). Evolution of the ischial spine and of the pelvic floor in the Hominoidea. *American Journal of Physical Anthropology* **75 (1)**: 53 – 67.

Acquaah, F., Robson Brown, K.A., Ahmed, F., Jeffery, N. and Abel, R.L. (2015). Early trabecular development in human vertebrae: overproduction, constructive regression, and refinement. *Frontiers in Endocrinology* **6 (67)**: 1 – 9.

Adams, J.C. and Hamblen, D.L. (2001). Outline of Orthopaedics. Edinburgh: Churchill Livingstone.

Aguirre, J.I., Plotkin, L.I., Stewart, S.A., Weinstein, R.S., Parfitt, A.M., Manolagas, S.C and Bellido, T. (2006). Osteocyte apoptosis is induced by weightlessness in mice and precedes osteoclast recruitment and bone loss. *Journal of Bone and Mineral Research* **21 (4)**: 605 – 615.

Aiello, L. and Dean, C. (1990). An Introduction to Human Evolutionary Anatomy. London: Academic Press Ltd.

Ajube, N.E., Klein-Nulend, J., Alblas, M.J., Burger, E.H. and Nijweide, P.J. (1999). Signal transduction pathways involved in fluid flow-induced PGE_2 production by cultured osteocytes. *American Journal of Physiology – Endocrinology and Metabolism* **276 (1)**: E171 – E178.

Anas, E.M.A., Kim, J.G., Lee, S.Y. and Hassan, M.K. (2011). Comparison of ring artifact removal methods using flat panel detector based CT images. *Biomedical Engineering Online* **10 (72)**: 1 – 25.

Anderson, T.L., Abdelgawad, M.E., Kristensen, H.B., Hauge, E.M., Rolighed, L., Bollerslev, J., Kjærsgaard-Anderson, P. and Deaisse, J.M. (2013). Understanding coupling between bone resorption and formation: are reversal cells the missing link? *The American Journal of Pathology* **183 (1)** 235 – 246.

Arsenault, A.L. and Ottensmeyer, F.P. (1984). Visualisation of early intramembranous ossification by electron microscopic and spectroscopic imaging. *Journal of Cell Biology* **98 (3)**: 911 – 921.

Ay, L., Jaddoe, V.W.V., Hofman, A., Moll, H.A., Raat, H., Steegers, E.A.P. and Hokken-Koelega, A.C.S. (2011). Foetal and postnatal growth and bone mass at 6 months: the Generation R study. *Clinical Endocrinology* **74 (2)**: 181 – 190.

Ayyappa, E. (1997). Normal human locomotion, part 1: basic concepts and terminology. *Journal of Prosthetics and Orthotics* **9 (1)**: 10 – 17.

Aung, H.H., Sakaomoto, H., Akita, K. and Sato, T. (2001). Anatomical study of the obturator internus, gemelli and quadratus femoris muscles with special reference to their innervation. *The Anatomical Record* **263 (1)**: 41 – 52.

Bachrach, L.K. (2001). Acquisition of optimal bone mass in childhood and adolescence. *Trends in Endocrinology and Metabolism* **12 (1)**: 22 – 28.

Bailey, D.A., McKay, H.A., Mirwald, R.L., Crocker, P.R.E. and Faulkner, R.A. (1999). A six-year longitudinal study of the relationship of physical activity to bone mineral accrual in growing children: the University of Saskatchewan bone mineral accrual study. *Journal of Bone and Mineral Research* **14 (10)**: 1672 – 1679.

Baldock, P.A., Thomas, G.P., Hodge, J.M., Baker, S.U.K., Dressel, U., O'Loughlin, P.D., Nicholdson, G.C., Briffa, K.H., Eisman, J.A. and Gardiner, E.M. (2006). Vitamin D action and regulation of bone remodeling: suppression of osteoclastogenesis by the mature osteoblast. *Journal of Bone and Mineral Research* **21 (10)**: 1618 – 1626.

Bano, A., Karantanas, A., Pasku, D., Datseris, G., Tzanakakis, G. and Katonis, P. (2010). Persistent sciatic inducted by quadratus femoris muscle tear and treated by surgical decompression: a case report. *Journal of Medical Case Reports* **4**: 236.

Bardakos, N.V. and Villar, R.N. (2009). The ligamentum teres of the adult hip. *The Journal of Bone and Joint Surgery* **91-B (1)**: 8 – 15.

Barrett, J.F. and Keat, N. (2004). Artifacts in CT: Recognition and avoidance. *RadioGraphics* **24 (6)**: 1679 – 1691.

Barrett, T. and Arthurs, O.J. (2010). Adductor magnus: a post-operative illustration of its dual nerve supply. *Clinical Anatomy* **23 (1)**: 115 – 119.

Bass, S.L., Saxon, L., Daly, R.M., Turner, C.H., Robling, A.G., Seeman, E. and Stuckey, S. (2002). The effect of mechanical loading on the size and shape of bone in pre-, peri- and postpubertal girls: a study in tennis players. *Journal of Bone and Mineral Research* **17 (12)**: 2274 – 2280.

Basso, N. and Heersche, J.N. (2006). Effects of hind limb unloading and reloading on nitric oxide synthase expression and apoptosis of osteocytes and chondrocytes. *Bone* **39 (4)**: 807 – 814.

Beck, M., Leunig, M., Ellis, T., Sledge, J.B. and Ganz, R. (2003). The acetabular blood supply: implications for periacetabular osteotomies. *Surgical and Radiologic Anatomy* **25 (5)**: 361 – 367.

Beck, R., Andriacchi, T.P., Huo, K.N., Fermier, R.W. and Galante, J.O. (1981). Changes in the gait patterns of growing children. *Journal of Bone and Joint Surgery* **63 (9)**: 1452 – 1457.

Becker, I., Woodley, S.J. and Stringer, M.S. (2010). The adult human pubic symphysis: a systematic review. *Journal of Anatomy* **217 (5)**: 475 – 487.

Beltran, L., Ghazikhanian, V., Padron, M. and Beltran, J. (2012). The proximal hamstring muscle-tendon-bone unit: a review of the normal anatomy, biomechanics, and pathophysiology. *European Journal of Radiology* **81 (12)**: 3772 – 3779.

Bergmann, G., Deuretzbacher, G., Heller, M., Graichen, F., Rohlmann, A., Strauss, J. and Duda, G.N. (2001). Hip contact forces and gait patterns from routine activities. *Journal of Biomechanics* **34 (2)**: 859 – 871.

Blair, H.C., Zaidi, M. and Schlesinger, P.H. (2002). Mechanisms balancing skeletal matrix synthesis and degradation. *Biomechemical Journal* **364 (pt 2)**: 329 – 341.

Boas, F.E. and Fleischmann, D. (2012). CT artifacts: causes and reduction techniques. *Imaging in Medicine* **4 (2)**: 229 – 240.

Bondioli, A., Bayle, P., Dean, C., Mazurier, A., Puymerail, L., Ruff, C., Stock, J.T., Volpato, V., Zanolli, C. and Macchiarelli, R. (2010). Technical note: Morphometric maps of long bone shafts and dental roots for imaging topographic thickness variations. *American Journal of Physical Anthropology* **142 (2)**: 328 – 334.

Bonewald, L.F. (2007). Osteocytes as dynamic multifunctional cells. *Annals of the New York Academy of Sciences* **1116 (Pt A)**: 281 – 290.

Bonjour, J. and Chevalley, T. (2014). Pubertal timing, bone acquisition, and risk of fracture throughout life. *Endocrine Reviews* **35 (5)**: 820 – 847.

Bonjour, J., Theintz, G., Law, F., Slosman, D. and Rizzoli, R. (1994). Peak bone mass. *Osteoporosis International* **4 (S1)**: S7 – S13.

Bosscher, D., van Cauwenbergh, R., van der Auwera, J.C., Robberecht, H. and Deelstra, H. (2002). Calcium, iron and zinc availability from weaning meals. *Acta Paediatrica* **91**: 761 – 768.

Bouxsein, M.L., Boyd, S.K., Christiansen, B.A., Guldberg, R.E., Jepsen, K.J. and Müller, R. (2010). Guidelines for assessment of bone microstructure in rodents using micro-computed tomography. *Journal of Bone and Mineral Research* **25 (7)**: 1468 – 1486.

Boyan, B.D., Schwartz., Z. and Swain, L.D. (1990). Matrix vesicles as a marker of endochondral ossification. *Connective Tissue Research* **24 (1)**: 67 – 75.

Boyd, S.K. (2009). Chapter 1. Micro-computed tomography. In: Sensen, C.W. and Hallgrímsson, B. Advanced Imaging in Biology and Medicine. Berlin: Springer Berlin Heidelberg. p 3 – 25.

Brandi, M.L. (2009). Microarchitecture, the key to bone quality. *Rheumatology* **48 (sup. 4)**: iv3 – iv8.

Brewster, S.F. (1991). The development of the ligament of the head of the femur. *Clinical Anatomy* **4 (4)**: 244 – 255.

Brooks, S. and Suchey, J.M. (1990). Skeletal age determination based on the os pubis: a comparison of the Acsádi-Nemskéri and Suchey-Brooks methods. *Human Evolution* **5 (3)**: 277 – 238.

Bruker (N.D.a). Analysis of bone by micro-CT: General information. *Bruker Corporation.* Accessed at: umanitoba.ca/faculties/medicine/units/cacs/sam/media/MN001_Bone_microCT_analysis_general.pdf. Last Accessed: 27-02-17.

Bruker (N.D.b) CT-Analyser and CT-Volume Software: Summary of Capabilities. *SkyScan N.V.* Accessed at: http://bruker-microct.com/next/CTAn02.pdf. Last Accessed: 27-02-17.

Buie, H.R., Campbell, G.M., Klink, J., MacNeil, J.A. and Boyd, S.K. (2007). Automated segmentation of cortical and trabecular compartments based on a dual threshold technique for *in-vivo* micro-CT bone analysis. *Bone* **41**: 505 – 515.

Bsat, S., Frei, H. and Beaulé, P.E. (2016). The acetabular labrum: a review of its function. *The Bone and Joint Journal* **98-B (6)**: 730 – 735.

Burdan, F., Szumilo, J., Korobowicz, A., Farooquee, R., Patel, S., Patel, A., Dave, A., Szumilo, M., Solecki, M., Klepacz, R. and Dudka, J. (2009). Morphology and physiology of the epiphyseal growth plate. *Folia Histochemica et Cytobiologica* **47 (1)**: 5 – 16.

Burger, E.H. and Klein-Nulend, J. (1999). Mechanotransduction in bone – role of the lacuno-canalicular network. *The FASEB Journal* **13 (sup.)**: S101 – S112.

Burghardt, A.J., Kazakia, G.J. and Majumdar, S. (2007). A local adaptive threshold strategy for high resolution peripheral quantitative computed tomography of trabecular bone. *Annals of Biomedical Engineering* **35 (10)**: 1678 – 1686.

Burr, D.B. and Guillot, G.M. (2012). Almost invisible, often ignored: periosteum, the living lace of bone. *Medicographica* **34 (2)**: 221 – 227.

Burra, S., Nicolella, D.P., Francis, W.L., Freitas, C.J., Mueschke, N.J., Poole, K and Jiang, J.X. (2010). Dendritic processes of osteocytes are mechanotransducers that induce the opening of hemichannels. *Proceedings of the National Academy of Sciences* **107 (31)**: 13648 – 13653.

Butte, N.F., Wong, W.W., Hopkinson, J.M., O'Brian Smith, E. and Ellis, K.J. (2000). Infant feeding mode affects early growth and body composition. *Paediatrics* **106 (6)**: 1355 – 1366.

Buzug, T.M. (2008). Computed Tomography: From Photon Statistics to Modern Cone-Beam CT. Leipzig: Springer-Verlag.

Byers, S., Moore, A.J., Byard, R.W. and Fazzalari, N.L. (2000). Quantitative histomorphometric analysis of the human growth plate from birth to adolescence. *Bone* **27 (4)**: 495 – 501.

Cambra-Moo, O., Meneses, C.N., Barbero, M.A.R., Gil, O.G., Pérez, J.R., Rello-Varona, S., D'Angelo, M., Martín, M.C. and Martín, A.G. (2014). An approach to the histomorphological and histochemical variations of the humerus cortical bone through human ontogeny. *Journal of Anatomy* **224 (6)**: 634 – 646.

Cardoso, H.F.V. (2008). Epiphyseal union at the immoninate and lower limb in a modern Portuguese skeletal sample, and age estimation in adolescent and young adult male and female skeletons. *American Journal of Physical Anthropology* **135 (2)**: 161 – 170.

Cardoso, H.F.V., Campanacho, V., Gomes, J. and Marinho, L. (2013). Timing of fusion of the ischiopubic ramus from dry bone observations. *Journal of Comparative Human Biology* **64 (6)**: 454 – 462.

Carter, P.H. and Schipani, E. (2006). The roles of parathyroid hormone and calcitonin in bone remodeling: prospects for novel therapies. *Endocrine, Metabolic and Immune Disorders – Drug Targets* **6 (1)**: 59 – 76.

Cawley, K.A., Dvorak, A.D. and Willmot, M.D. (1983). Normal anatomic variant: scintigraphy of the ischiopubic synchondrosis. *Journal of Nuclear Medicine* **24 (1)**: 14 – 16.

Cerezal, L., Kassarjian, A., Canga, A., Dobado, M.C., Montero, J.A., Llopis, E., Rolón, A. and Pérez-Carro, L. (2010). Anatomy, biomechanics, imaging and management of ligamentum teres injuries. *RadioGraphics* **30 (6)**: 1637 – 1651.

Chang, P.C., Liang, K., Lim, J.C, Chung, M.C. and Chien, L.Y. (2013). A comparison of the thresholding strategies of micro-CT for periodontal bone loss: A pilot study. *Dentomaxillofacial Radiology* **42 (2)**: 1 – 12.

Chirchir, H., Kivell, T.L., Ruff, C.B., Hublin, J.J., Carlson, K.J., Zipfel, B. and Richmond, B.G. (2015). Recent origin of low trabecular bone density in modern humans. *Proceedings of the National Academy of Sciences* **112 (2)**: 366 – 371.

Christensen, A.M., Passalacqua, N.V. and Bartelink, E.J. (2014). Forensic Anthropology: Current Methods and Practice. San Diego: Academic Press.

Cierniak, R. (2011). X-Ray Computed Tomography in Biomedical Engineering. London: Springer-Verlag.

Chuckpaiwong, B., Suwanwong, P. and Harnroongroj, T. (2009). Roof-arc angle and weight-bearing area of the acetabulum. *Injury* **40 (10)**: 1064 – 1066.

Clarke, B. (2008). Normal bone anatomy and physiology. *Clinical Journal of the American Society of Nephrology* **3 (suppl. 3)**: S131 – S139.

Cohn, M.J., Lovejoy, C.O., Wolpert, L. and Coates, M.I. (2002). Branching, segmentation and the metapterygial axis: pattern versus process in the vertebrate limb. *BioEssays* **24 (5)**: 460 – 465.

Cooper, C., Dennison, E.M., Leufkens, H.G.M., Bishop, N. and van Staa, T.P. (2004). Epidemiology of childhood fractures in Britain: a study using the General Practice Research Database. *Journal of Bone and Mineral Research* **19 (12)**: 1976 – 1981.

Cooper, C., Fall, C., Egger, P., Hobbs, R., Eastell, R. and Barker, D. (1997). Growth in infancy and bone mass in later life. *Annals of the Rheumatic Diseases* **56 (1)**: 17 – 21.

Cooper, C., Javaid, K., Westlake, S., Harvey, N. and Dennison, E. (2005). Developmental origins of osteological fracture: the role of maternal vitamin D insufficiency. *The Journal of Nutrition* **153 (11)**: 2728S – 2734S.

Cooper, D.M.L., Thomas, C.D.L., Clement, J.G. and Hallgrĺmsson, B. (2006). Three-dimensional microcomputed tomography imaging of basic multicellular unit-related bone resorption spaces in human cortical bone. *The Anatomical Record* **288 (7)**: 806 – 816.

Cooper, D., Turinsky, A., Sensen, C. and Hallgrimsson, B. (2007). Effect of voxel size on 3D micro-CT analysis of cortical bone porosity. *Calcified Tissue International* **80 (3)**: 211 – 219.

Correia, H., Balseiro, S. and de Areia, M. (2005). Sexual dimorphism in the human pelvis: testing a new hypothesis. *Homo* **56 (2)**: 153 – 160.

Crock, H.V. (1996). An Atlas of Vascular Anatomy of the Skeleton and Spinal Cord. London: Martin Dunitz.

Cunningham, C.A. (2009). A qualitative and quantitative investigation of structural morphology in the neonatal ilium. PhD in Anatomy and Forensic Anthropology, University of Dundee, Dundee. *Available online at: discovery.dundee.ac.uk/portal/files/1307327/Cunningham_phd_2009.pdf*. Last Accessed: 27-02-17.

Cunningham, C.A. and Black, S.M. (2009a). Development of the fetal ilium – challenging concepts of bipedality. *Journal of Anatomy* **214 (1)**: 91 – 99.

Cunningham, C.A. and Black, S.M. (2009b). Anticipating bipedalism: trabecular organisation in the newborn ilium. *Journal of Anatomy* **214 (6)**: 817 – 829.

Cunningham, C.A. and Black, S.M. (2009c). Iliac cortical thickness in the neonate – the gradient effect. *Journal of Anatomy* **215 (3)**: 364 – 370.

Cunningham, C.A. and Black, S.M. (2010). The neonatal ilium – metaphyseal drivers and vascular passengers. *The Anatomical Record* **293 (8)**: 1297 – 1309.

Cunningham, C.A., Scheuer, L. and Black, S.M. (2016). Developmental Juvenile Osteology, 2nd Ed. London: Elsevier Academic Press.

Dalstra, M. and Huiskes, R. (1995). Load transfer across the pelvic bone. *Journal of Biomechanics* **28 (6)**: 715 – 724.

Dalstra, M., Huiskes, R., Odgaard, A. and van Erning, L. (1993). Mechanical and textural properties of pelvic trabecular bone. *Journal of Biomechanics* **26 (4-5)**: 523 – 535.

Daniel, M., Iglič, A. and Kralj-Iglič, V. (2005). The shape of the acetabular cartilage optimizes hip contact stress distribution. *Journal of Anatomy* **207 (1)**: 85 – 91.

Davey, R.A. and Findlay, D.M. (2013). Calcitonin: physiology or fantasy? *Journal of Bone and Mineral Research* **28 (5)**: 973 – 979.

de Moura Meneses, A.A., Giusit, A., de Almeida, A.P., Nogueira, L.P., Braz, D., Barroso, R.C. and de Almeida, C.E. (2011). Automated segmentation of synchrotron radiation micro-computed tomography biomedical images using Graph Cuts and neural networks. *Nuclear Instruments and Methods in Physics Research A* **660 (1)**: 121 – 129.

Decker, R.S., Koyama, E. and Pacifici, M. (2014). Genesis and morphogenesis of limb synovial joints and articular cartilage. *Matrix Biology* **39**: 5 – 10.

Dehao, B.W., Bing, T.K. and Young, J.L.S. (2015). Understanding the ligamentum teres of the hip: a histological study. *Acta Orthopédica Brasileira* **23 (1)**: 29 – 33.

Delaere, O. and Dhem, A. (1999). Prenatal development of the human pelvis and acetabulum. *Acta Orthopaedica Belgica* **65 (3)**: 255 – 260.

Delaisse, J.M. (2014). The reversal phase of the bone-remodeling cycle: cellular prerequisites for coupling resorption and formation. *BoneKEy Reports* **3 (561)**: 1 – 8.

Demirbag, D., Ozdemir, F., Kokino, S. and Berkarda, S. (2005). The relationship between bone mineral density and immobilisation duration in hemiplegic limbs. *Annals of Nuclear Medicine* **19 (8)**: 695 – 700.

Ding, M. and Hvid, I. (2000). Quantification of age-related changes in the structure model type and trabecular thickness of human tibial cancellous bone. *Bone* **26 (3)**: 291 – 295.

Ding, M., Odgaard, A., Danielsen, C.C. and Hvid, I. (2002). Mutual associations among microstructural properties of human cancellous bone. *Journal of Bone and Joint Surgery* **84B (6)**: 900 -907.

Ding, M., Odgaard, A. and Hvid, I. (1999). Accuracy of cancellous bone volume fraction measured by micro-CT scanning. *Journal of Biomechanics* **32 (3)**: 323 – 326.

Drake, R.L., Vogl, A.W. and Mitchell, A.W.M. (eds) (2010). Gray's Anatomy for Students 2nd edition. Philadelphia: Churchill Livingstone.

Duan, C.Y., Orías, A.A.E., Shott, S., Andersson, G.B.J., Hu, J.Z., Lu, H.B. and Inoue, N. (2011). *In vivo* measurement of the subchondral bone thickness of lumbar facet using magnetic resonance imaging. *Osteoarthritis and Cartilage* **19 (1)**: 96 – 102.

Duan, X., Wang, J., Leng, S., Schmidt, B., Allmendinger, T., Grant, K., Flohr, T. and McCollough, C.H. (2013). Electronic noise in CT detectors: Impact on image noise and artefacts. *American Journal of Roentgenology* **201 (4)**: 626 – 632.

Dunnett, C.W. (1964). New tables for multiple comparisons with a control. *Biometrics* **20**: 482 – 491.

Dwek, J.R. (2010). The periosteum: what is it, where is it, and what mimics it in its absence? *Skeletal Radiology* **39 (4)**: 319 – 323.

Ehrlich, P.J. and Lanyon, L.E. (2002). Mechanical strain and bone cell function: a review. *Osteoporosis International* **13 (9)**: 688 – 700.

Eisman, J.A. and Bouillon, R. (2014). Vitamin D: direct effects of vitamin D metabolites on bone: lessons from genetically modified mice. *BoneKEy Reports* **3 (499)**: 1 -6.

Eriksen, E.F., Eghbali-Fatourechi, G.Z. and Khosla, S. (2007). Remodeling and vascular spaces in bone. *Journal of Bone and Mineral Research* **22 (1)**: 1 – 6.

Fajardo, R.J., Ryan, T.M. and Kappelman, J. (2002). Assessing the accuracy of high-resolution x-ray computed tomography of primate trabecular bone by comparisons with histological sections. *American Journal of Physical Anthropology* **118 (1)**: 1 – 10.

Fazekas, I.G. and Kósa, F. (1978). Forensic Fetal Osteology. Budapest: Akadémiai Kiadó.

Fazzalari, N.L., Moore, A.J., Byers, S. and Byard, R.W. (1997). Quantitative analysis of trabecular morphogenesis in the human costochondral junction during the postnatal period in normal subjects. *The Anatomical Record* **248 (1)**: 1 – 12.

Feldkamp, L.A., Goldstein, S.A., Parfitt, A.M., Jesion, G. and Kleerekoper, M. (1989). The direct examination of three-dimensional bone architecture in vitro by computed tomography. *Journal of Bone and Mineral Research* **4 (1)**: 3 – 11.

Feng, X. and McDonald, J.M. (2011). Disorders of bone remodeling. *Annual Reviews of Pathology: Mechanisms of Disease* **6**: 121 – 145.

Ferreira, T. and Rasband, W. (2012). ImageJ User Guide – IJ 1.46. Accessed at https://imagej.nih.gov/ij/docs/guide. Last Accessed: 27-02-17.

Flecker, H. (1932). Roentgenographic observations of the times of appearance of epiphyses and their fusion with the diaphyses. *Journal of Anatomy* **67 (pt 1.)**: 118 – 164.

Forst, S.L., Wheeler, M.T., Fortin, J.D. and Vilensky, J.A. (2006). The sacroiliac joint: anatomy, physiology and clinical significance. *Pain Physician* **9 (1)**: 61 – 67.

Frost, H.M. (1990). Skeletal structural adaptations to mechanical usage (SATMU): 1. Redefining Wolff's law: the bone modeling problem. *The Anatomical Record* **226 (4)**: 403 – 413.

Frost, H.M. (1994). Wolff's law and bone's structural adaptation to mechanical useage: an overview for clinicians. *The Angle Orthodontist* **64 (3)**: 175 – 188.

Frost, H.M. (1996). Perspectives: a proposed general model of the 'mechanostat'. *The Anatomical Record* **224 (2)**: 139 – 147.

Frost, H.M. (1999). On the trabecular "thickness"-number problem. *Journal of Bone and Mineral Research* **14 (11)**: 1816 – 1821.

Gayon, J. (2000). History of the concept of allometry. *American Zoologist* **40**: 748 – 758.

Gamble, J.G., Simmons, S.C. and Freedman, M. (1986). The symphysis pubis: anatomical and pathological considerations. *Clinical Orthopaedics and Related Research* **203**: 261 – 272.

Genant, H.K, Gordon, C., Jiang, Y., Lang, T.F., Link, T.M. and Majumdar, S. (1999). Advanced imaging of bone macro and micro structure. *Bone* **25 (1)**: 149 – 152.

Ghosh, R., Pal, B., Ghosh, D. and Gupta, S. (2015). Finite element analysis of a hemi-pelvis: the effect of inclusion of cartilage layer on acetabular stresses and strain. *Computer Methods in Biomechanical and Biomedical Engineering* **18 (7)**: 697 – 710.

Glinsmann, W.H., Bartholmey, S.J and Coletta, F. (1996). Dietary guidelines for infants: a timely reminder. *Nutrition Reviews* **52 (2)**: 50 – 57.

Glorieux, F.H., Travers, R., Taylor, A., Bowen, J.R., Rauch, F., Norman, M. and Parfitt, A.M. (2000). Normative data for iliac bone histomorphometry in growing children. *Bone* **26 (2)**: 103 – 109.

Golden, N.H. and Abrams, S.A. (2014). Optimising bone health in children and adolescents. *Pediatrics* **134 (4)**: e1229 – e1234.

Goldfield, E.C. (1989). Transition from rocking to crawling: postural constraints on infant movements. *Developmental Psychology* **25 (6)**: 913 – 919.

Goldman, H.M., McFarlin, S.C., Cooper, D.M.L, Thomas, C.D.L. and Clement, J.G. (2009). Ontogenetic patterning of cortical bone microstructure and geometry at the human mid-shaft femur. *The Anatomical Record* **292 (1)**: 48 – 64.

Goodenough, D., Weaver, K., Davis, D. and LaFalce, S. (1981). Volume averaging limitations of computed tomography. *American Journal of Neuroradiology* **2**: 585 – 588.

Gosman, J.H., Hubbell, Z.R., Shaw, C.N. and Ryan, T.M. (2013). Development of cortical bone geometry in the human femoral and tibial diaphysis. *The Anatomical Record* **296 (5)**: 774 – 787.

Gosman, J.H. and Ketcham, R.A. (2008). Patterns in ontogeny of human trabecular bone from SunWatch Village in the prehistoric Ohio Valley: general features of microarchitectural change. *American Journal of Physical Anthropology* **138 (3)**: 318 – 332.

Goulding, A., Cannan, R., Williams, S.M., Gold, E.J., Taylor, R.W. and Lewis-Barned, N.J. (1998). Bone mineral density in girls with forearm fractures. *Journal of Bone and Mineral Research* **13 (1)**: 143 – 148.

Grant, A.D., Sala, D.A. and Davidovitch, R.I. (2012). The labrum: structure, function and injury with femoro-acetabular impingement. *Journal of Children's Orthopaedics* **6 (5)**: 357 – 372.

Greenwald, A.S. and Haynes, D.W. (1972). Weight-bearing areas in the human hip joint. *Journal of Bone and Joint Surgery British Volume* **54 (1)**: 157 – 163.

Greer, F.R. and Krebs, N.F. (2006). Optimising bone health and calcium intakes of infants, children and adolescents. *Paediatrics* **117 (2)**: 578 – 585.

Hadjidakis, D.J. and Androulakis, I.I. (2006). Bone remodeling. *Annals of the New York Academy of Sciences* **1092**: 385 – 396.

Hall, B.K. and Herring, S.W. (1990). Paralysis and growth of the musculoskeletal system in the embryonic chick. *Journal of Morphology* **206 (1)**: 45 – 56.

Hammer, A. (2015). The paradox of Wolff's theories. *Irish Journal of Medical Science* **184 (1)**: 13 – 22.

Hangartner, T.N. (2007). Thresholding technique for accurate analysis of density and geometry in QCT, PQCT and μCT images. *Journal of Musculoskeletal and Neuronal Interactions* **7 (1)**: 9 – 16.

Hanihara, K. and Suzuki, T. (2005). Estimation of age from the pubic symphysis by means of multiple regression analysis. *American Journal of Physical Anthropology* **48 (2)**: 233 – 239.

Hanson, K.M. (1981). Noise and contrast discrimination in computed tomography. In: Newton, T.H and Potts, D.G (eds). Radiology of the Skull and Brain, Vol. 5: Technical Aspects of Computed Tomography. St. Louis: Mosby.

Hara, T., Tanck, E., Homminga, J. and Huiskes, R. (2002). The influence of microcomputed tomography threshold variations on the assessment of structural and mechanical trabecular bone properties. *Bone* **31 (1)**: 107 – 109.

Hayat, T.T.A., Nihat, A., Martinex-Biarge, M., McGuinness, A., Allsop, J.M., Hajnal, J.V. and Rutherford, M.A. (2011). Optimization and initial experience of a multisection balanced steady-state free precession cine sequence for the assessment of fetal behaviour in utero. *American Journal of Neuroradiology* **32**: 331 – 338.

Heaney, R.P., Abrams, S., Dawson-Hughes, B., Looker, A., Marcus, R., Matkovic, V. and Weaver, C. (2000). Peak bone mass. *Osteoporosis International* **11 (12)**: 985 – 1009.

Heino, T.J., Hentunen, T.A. and Väänänen, H.K. (2002). Osteocytes inhibit osteoclastic bone resorption through transforming Growth Factor-β: enhancement by estrogen. *Journal of Cellular Biochemistry* **85 (1)**: 185 – 197.

Henack, C.R., Ellis, B.J., Harris, M.D., Anderson, A.E., Peters, C.L. and Weiss, J.A. (2011). Role of the acetabular labrum in load support across the hip joint. *Journal of Biomechanics* **44 (12)**: 2201 – 2206.

Hentschel, H.G.E., Glimm, T., Glazier, J.A. and Newman, S.A. (2004). Dynamical mechanisms for skeletal pattern formation in the vertebrate limb. *Proceedings of the Biological Society* **271 (1549)**: 1713 – 1722.

Herneth, A.M., Philipp, M.O., Pretterklieber, M.L., Balassy, C., Winkelbauer, F.W. and Beaulieu, C.F. (2004). Asymmetric closure of ischiopubic synchodrosis in pediatric patients: correlation with foot dominance. *American Journal of Roentgenology* **182 (2)**: 361 – 365.

Herneth, A.M., Trattnig, S., Bader, T.R., Ba-Ssalamah, A., Ponhold, W., Wandl-Vergesslich, K. and Steinbach, L.S. (2000). MR imaging of the ischiopubic synchondrosis. *Magnetic Resonance Imaging* **18 (5)**: 519 – 524.

Hetaimish, B.M. and Alshaya, O.S. (2016). Pediatric aneurysmal bone cyst in the ischial region. *Saudi Medical Journal* **37 (7)**: 799 – 803.

Hildebrand, T., Laib, A., Müller, R., Dequeker, J. and Rüegsegger, P. (1999). Direct three-dimensional morphometric analysis of human cancellous bone: microstructural data from spine, femur, iliac crest, and calcaneus. *Journal of Bone and Mineral Research* **14 (7)**: 1167 – 1174.

Hildebrand, T. and Rüegsegger, P. (1997a). A new method for the model-independent assessment of thickness in three-dimensional images. *Journal of Microscopy* **185 (1)**: 67 – 75.

Hildebrand, T. and Rüegsegger, P. (1997b). Quantification of bone microarchitecture with the structural model index. *Computer Methods in Biomechanics and Biomedical Engineering* **1 (1)**: 15 – 23.

Hoff, A.O., Catala-Lehnen, P., Thomas, P.M., Priemel, M., Rueger, J.M., Nasonkin, I., Bradley, A., Hughest, M.R., Ordonez, N., Cote, G.J., Amling, M. and Gagel, R.F. (2002). Increased bone mass is an unexpected phenotype associated with deletion of the calcitonin gene. *Journal of Clinical Investigation* **110 (12)**: 1849 – 1857.

Hogervorst, T., Bouma, H.W. and de Vos, J. (2009). Evolution of the hip and pelvis. *Acta Orthopaedica* **80 (sup 336):** 1 – 39.

Holdsworth, D.W. and Thornton, M.M. (2002). Micro-CT in small animal and specimen imaging. *Trends in Biotechnology* **20 (B)**: S34 – S39.

Holick, M.F. (2007). Vitamin D deficiency. *New England Journal of Medicine* **357 (3)**: 266 – 281.

Holm, N.J. (1980). The internal stress pattern of the os coxae. *Acta Orthopaedica Scandinavia* **51 (3)**: 421 – 428.

Holroyd, C., Harvey, N., Dennison, E and Cooper, C. (2012). Epigenetic influences in the developmental origins of osteoporosis. *Osteoporosis International* **23 (2)**: 401 – 410.

Holzer, G., von Skrbensky, G., Holzer, L.A. and Pichl, W. (2009). Hip fractures and the contribution of cortical versus trabecular bone to femoral neck strength. *Journal of Bone and Mineral Research* **24 (3)**: 468 – 474.

Horton, W.A., Hall, J.G. and Hecht, J.T. (2007). Achondroplasia. *The Lancet* **370 (9582)**: 162 – 172.

Huebner, A.K., Schinke, T., Priemel, M., Schilling, S., Schilling, A.F., Emeson, R.B., Rueger, J.M. and Amling, M. (2006). Calcitonin deficiency in mice progressively results in high bone turnover. *Journal of Bone and Mineral Research* **21 (12)**: 1924 – 1934.

Huiskes, R. (2000). If bone is the answer, then what is the question? *Journal of Anatomy* **197 (pt 2)**: 145 – 156.

Huiskes, R., Ruimerman, R., van Lenthe, G.H. and Janssen, J.D. (2000). Effects of mechanical forces on maintenance and adaptation of form in trabecular bone. *Nature* **405 (8)**: 704 – 706.

Huxley, J.S. and Tessier, G. (1936). Terminology of relative growth. *Nature* **137:** 780-781.

Ipavec, M., Brand, R.A., Pedersen, D.R., Mavčič, B., Kralj-Iglič, V. and Iglič, A. (1999). Mathematical modelling of stress in the hip during gait. *Journal of Biomechanics* **32 (11)**: 1229 – 1235.

Ito, H., Song, Y., Lindsey, D.P., Safran, M.R. and Giori, N.J. (2009). The proximal hip joint capsule and the zona orbicularis contribute to hip joint stability in distraction. *Journal of Orthopaedic Research* **27 (8)**: 989 – 995.

Jain, A., Agarwal, R., Sankar, M.J., Seorari, A. and Paul, V.K. (2010). Hypocalcemia in the newborn. *Indian Journal of Paediatrics* **77 (10)**: 1123 – 1128.

Jamil, N., Sembok, T.M.T. and Bakar, Z.A. (2008). Noise removal and enhancement of binary images using morphological operations. *International Symposium on Information Technology, 2008* **4**: 1 – 6.

Jee, W.S., Tian, X.Y. and Setterberg, R.B. (2007). Cancellous bone minimodeling-based formation: a Frost, Takahashi legacy. *Journal of Musculoskeletal and Neuronal Interactions* **7 (3)**: 232 – 239.

Jennane, R., Almhdie, A., Aufort, G. and Lespessailles, E. (2012). 3D shape-dependent thinning method for trabecular bone characterization. *Medical Physics* **39 (1)**: 168 – 178.

Jilka, R.L. (2001). Biology of the basic multicellular unit and the pathophysiology of osteoporosis. *Medical and Pediatric Oncology* **41 (3)**: 182 – 185.

Jilka, R.L., Noble, B. and Weinstein, R.S. (2013). Osteocyte apoptosis. *Bone* **54 (2)**: 264 – 271.

Jones, G., Riley, M. and Dwyer, T. (2000). Breastfeeding in early life and bone mass in prepubertal children: a longitudinal study. *Osteoporosis International* **11 (2)**: 146 – 152.

Judex, S., Garman, R., Squire, M., Donahue, L.R. and Rubin, C. (2004). Genetically based influences on the site-specific regulation of trabecular and cortical bone morphology. *Journal of Bone and Mineral Research* **19 (4)**: 600 – 606.

Kao, R., Lu, W., Louie, A. and Nissenson, R. (2012). Cyclic AMP signalling in bone marrow stromal cells has reciprocal effects on the ability of mesenchymal stem cells to differentiate into mature osteoblasts versus mature adipocytes. *Endocrine* **42 (3)**: 622 – 636.

Kapandji, A.I. (2011). The Physiology of the Joints Volume 2: The Lower Limb, 6th ed. Edinburgh: Elsevier Ltd.

Karsenty, G. (2001). Chondrogenesis just ain't what it used to be. *Journal of Clinical Investigations* **107 (4)**: 405 – 407.

Kassarjian, A., Tomas, X., Cerezal, L., Canga, A. and Llopis, E. (2011). MRI of the quadratus femoris muscle: anatomic considerations and pathologic lesions. *American Journal of Roentgenology* **197 (1)**: 170 – 174.

Keaveny, T.M., Morgan, E.F., Niebur, G.L. and Yeh, O.C. (2001). Biomechanics of trabecular bone. *Annual Review of Biomedical Engineering* **3**: 307 – 333.

Keen, M. (1993). Early development and attainment of normal mature gait. *Journal of Prosthetics and Orthotics* **5 (2)**: 35 – 38.

Kerr, J.B. (1999). Atlas of Functional Histology. London: Mosby.

Kim, D., Christopherson, G.T., Dong, X.N., Fyhrie, D.P. and Yeni, Y.N. (2004). The effect of microcomputed tomography scanning and reconstruction voxel siZe on the accuracy of stereological measurements in human cancellous bone. *Bone* **35 (6)**: 1375 – 1382.

Kim, J., Shin, J., Oh, S., Yi, W., Heo, M., Lee, S. Choi, S. and Huh, K. (2013). The three-dimensional microstructure of trabecular bone: analysis of site-specific variation in the human jaw bone. *Imaging Science in Dentistry* **43 (4)**: 227 – 233.

Kim, N., Lee, J.G., Song, Y., Kim, H.J., Yeom, J. and Cho, G. (2011). Evaluation of MRI resolution affecting trabecular bone parameters: Determination of acceptable resolution. *Magnetic Resonance in Medicine* **67 (1)**: 218 – 225.

Kini, U. and Nandeesh, B.N. (2012). Physiology of Bone Formation, Remodeling and Metabolism. In: Fogelman, I., Gopinath, G. and van der Well, H., Eds (2012). Radionuclide and Hybrid Bone Imaging. Berlin Heidelberg: Springer-Verlag. pp29 – 57.

Klein-Nulend, J., van der Plas, A., Semeins, C.M., Ajubi, N.E., Frangos, J.A., Nijweide, P.J. and Burger, E.H. (1995). Sensitivity of osteocytes to biomechanical stress *in vitro*. *The FASEB Journal* **9 (5)**: 441 – 445.

Kobayashi, S., Takahashi, H.E., Ito, A., Saito, N., Nawata, M., Horiuchi, H., Ohta, H., Ito, A., Iorio, R., Yamamoto, N. and Takaoka, K. (2003). Trabecular minimodeling in human iliac bone. *Bone* **32 (2)**: 163 – 169.

Kontulainen, S., Sievänen, H., Kannus, P., Pasanen, M and Vuori, I. (2003). Effect of long-term impact-loading on mass, size, and estimated strength of the humerus and radius of female racquet-sports players: a peripheral quantitative computed tomography study between young and old starters and controls. *Journal of Bone and Mineral Research* **18 (2)**: 352 – 359.

Kothari, M., Keaveny, T.M., Lin, J.C., Newitt, D.C., Genant, H.K. and Majumdar, S. (1998). Impact of spatial resolution on the prediction of trabecular architecture parameters. *Bone* **22 (5)**: 437 – 443.

Koulouris, G. and Connell, D. (2005). Hamstring muscle complex: an imaging review. *RadioGraphics* **25 (3)**: 571 – 586.

Kovacs, C.S. (2006). Skeletal physiology: fetus and neonate. In: Favus, M.J., ed (2006). Primer on the Metabolic Dideases and Disorders of Mineral Metabolism, 6th ed. Washington, DC: American Society for Bone and Mineral Research.

Kovacs, C.S. (2009). Calcium and bone metabolism in pregnancy and lactation. *The Journal of Clinical Endocrinology and Metabolism* **86 (6)**: 2344 – 2348.

Kreder, H.J. and Jerome, D. (2010). The hip. In: Lawry, G.V., Kreder, H.J., Hawker, G.A. and Jerome, D., *eds* (2010). Fam's Musculoskeletal examination and joint injection techniques, 2nd Ed. Philadelphia: Mosby Elsevier.

Kroll, M.H. (2000). Parathyroid hormone temporal effects on bone formation and resorption. *Bulletin of Mathematical Biology* **62 (1)**: 163 – 187.

Kryiakou, Y., Prell, D. and Kalander, W.A. (2009). Ring artefact correction for high-resolution micro CT. *Physics in Medicine and Biology* **54**: N385 – N391.

Lacquaniti, F., Ivaneko, Y.P. and Zago, M. (2012). Development of human locomotion. *Current Opinion in Neurobiology* **22 (5)**: 822 – 828.

Lai, Y.M., Qin, L., Yeung, H.Y., Lee, K.K.H and Chan, K.M. (2005). Regional differences in trabecular BMD and micro-architecture of weight-bearing bone under habitual gait loading – A pQCT and microCT study in human cadavers. *Bone* **37 (2)**: 274 – 282.

Landin, L.A. (1983). Fracture patterns in children. *Acta Orthopaedica Scandinavica* **54 (S202)**: 3 – 109.

Lanyon, L.E. (1982). Mechanical function and bone remodelling. In: Sumner-Smith, G., Ed. Bone in Clinical Orthopaedics. Philadelphia: Saunders. pp273 – 304.

Laurenson, R.D. (1963). The chondrification and primary ossification of the human ilium. MD Thesis, University of Aberdeen, Aberdeen.

Laurenson, R.D. (1964a). The chondrification of the human ilium. *Anatomical Record* **148 (2)**: 197 – 202.

Laurenson, R.D. (1964b). The primary ossification of the human ilium. *Anatomical Record* **148 (2)**: 209 – 217.

Lazenby, R.A. (2002). Circumferential variation in human second metacarpal cortical thickness: sex, age and mechanical factors. *The Anatomical Record* **267 (2)**: 154 – 158.

Lazenby, R.A., Angus, S., Cooper, D.M.L. and Hallgrimsson, B. (2008). A three-dimensional microcomputed tomographic study of site-specific variation in trabecular microarchitecture in the human second metacarpal. *Journal of Anatomy* **213 (6)**: 698 – 705.

Lee, M.C. and Eberson, C.P. (2006). Growth and development of the child's hip. *Orthopedic Clinics of North America* **37**: 119-132

Lewis, W.H. (1918). Gray's Anatomy of the Human Body. Philadelphia: Lea and Febiger.

Li, Y.C., Amling, M., Pirro, A.E., Priemel, M., Meuse, J., Baron, R., Delling, G. and Demay, M. (1998). Normalization of mineral ion homeostasis by dietary means prevents hyperparathyroidism, rickets and osteomalacia, but not alopecia in vitamin D receptor-ablated mice. *Endocrinology* **139 (10)**: 4391 – 4396.

Lierse, W. (1987). Applied Anatomy of the Pelvic Girdle. Berlin: Springer-Verlag.

Liu, X.S., Sajda, P., Saha, P.K., Wehrli, F.W., Bevill, G., Keaveny, T.M. and Guo, X.E. (2008). Complete volumetric decomposition of individual trabecular plates and rods and its morphological correlations with anisotropic elastic moduli in human trabecular bone. *Journal of Bone and Mineral Research* **23 (2)**: 223 – 235.

Liu, X.S., Sajda, P., Saha, P.K., Wehrli, F.W. and Guo, X.E. (2006). Quantification of the roles of trabecular microarchitecture and trabecular type in determining the elastic modulus of human trabecular bone. *Journal of Bone and Mineral Research* **21 (10)**: 1608 – 1617.

Liu, X.S., Shane, E., McMahon, D.J. and Guo, X.E. (2011). Individual trabecula segmentation (ITS)-based morphological analysis of microscale images of human tibial trabecular bone at limited spatial resolution. *Journal of Bone and Mineral Research* **26 (9)**: 2184 – 2193.

Löhe, F., Eckstein, F., Sauer, T. and Putz, R. (1996). Structure, strain and function of the transverse acetabular ligament. *Acta Anatomica* **157 (4):** 315 – 323.

Lovejoy, C.O., McCollum, M.A., Reno, P.L. and Rosenman, B.A. (2003). Developmental biology and human evolution. *Annual Review of Anthropology* **32**: 85 – 109.

Lovejoy, C.O., Meindle, R.S., Ohman, J.C., Heiple, K.G. and White, T.D (2002). The Maka femur and its bearing on the antiquity of human walking: applying contemporary concepts of morphogenesis to the human fossil record. *American Journal of Physical Anthropology* **119 (2)**: 97 – 133.

Macchiarelli, R., Bondioli, L., Galichon, V. and Tobias, P.V. (1999). Hip bone trabecular architecture shows uniquely distinctive locomotor behaviour in South African Australopithecines. *Journal of Human Evolution* **36 (2)**: 211 – 232.

Macchiarelli, R., Rook, L. and Bondioli, L. (2001). Comparative analysis of the iliac trabecular architecture in extant and fossil primates by means of digital image processing techniques: implications for the reconstruction of fossil locomotor behaviours. In: De Bonis, L., Koufos, G.D. and Andrews, P. Phylogeny of the Neogene Hominoid Primates of Eurasia. Cambridge: Cambridge University Press. pp60 – 101.

Mackie, E.J., Ahmed, Y.A., Tatarczuch, L., Chen, K.S and Mirams, M. (2008). Endochondral ossification: how cartilage is converted into bone in the developing skeleton. *The International Journal of Biochemistry and Cell Biology* **40 (1)**: 46 – 62.

Maclean, S.J., Black, S.M. and Cunningham, C.A. (2014). The developing juvenile ischium: macro-radiographic insights. *Clinical Anatomy* **27 (6)**: 906 – 914.

MacNeil, J.A. and Boyd, S.K. (2007). Load distribution and the predictive power of morphological indices in the distal radius and tibia by high resolution peripheral quantitative computed tomography. *Bone* **41 (1)**: 129 – 137.

Maes, C., Carmeliet, P., Moermans, K., Stockmans, I., Smets, N., Collen, D., Bouillon, R. and Carmeliet, G. (2002). Impaired angiogenesis and endochondral bone formation in mice lacking the vascular endothelial growth factor isoforms $VEGF_{164}$ and $VEGF_{188}$. *Mechanisms of Development* **111 (1-2)**: 61 – 73.

Maes, C., Kobayashi, T., Selig, M.K., Torrekens, S., Roth, S.I., Mackm, S., Carmeliet, G and Kronenberg, H.M. (2010). Osteoblast precursors, but not mature osteoblasts, move into developing and fratured bones along with invading blood vessels. *Developmental Cell* **19 (2)**: 329 – 344.

Maga, M., Kappelman, J., Ryan, T.M. and Ketcham, R.A. (2006) Preliminary observations on the calcaneal trabecular micro-architecture of extant large-bodied hominoids. *American Journal of Physical Anthropology* **129 (3)**: 410 – 417.

Magee, D.J. (2008). Orthopedic Physical Assessment. Missouri: Saunders Elsevier.

Majumdar, S., Newitt, D., Mathur, A., Osman, D., Gies, A., Chiu, E., Lot, J., Kinney, J. and Genant, H. (1996). Magnetic resonance imaging of trabecular bone structure in the distal radius: relationship with x-ray tomographic microscopy and biomechanics. *Osteoporosis International* **6 (5)**: 376 – 385.

Malagelada, F., Tayar, R., Barke, S., Stafford, G. and Field, R.E. (2015). Anatomy of the zona orbicularis of the hip: a magnetic resonance study. *Surgical and Radiologic Anatomy* **37 (1)**: 11 – 18.

Mann, V., Huber, C., Kogianni, G., Jones, D. and Noble, B. (2006). The influence of mechanical stimulation on osteocyte apoptosis and bone viability in human trabecular bone. *Journal of Musculoskeletal and Neuronal Interactions* **6 (4)**: 408 – 417.

Maquer, G., Musy, S.N., Wandel, J., Gross, T. and Zysset, P.K. (2015). Bone volume fraction and fabric anisotropy are better determinants of trabecular bone stiffness than other morphological variables. *Journal of Bone and Mineral Research* **30 (6)**: 1000 – 1008.

Marenzana, M. and Arnett, T.R. (2013). The key role of the blood supply to bone. *Bone Research* **1**: 203 – 215.

Mariani, F.V. and Martin, G.R. (2003). Deciphering skeletal patterning: clues from the limb. *Nature* **423 (6937)**: 319 – 325.

Marotti, G. (2000). The osteocyte as a wiring transmission system. *Journal of Musculoskeletal Neuronal Interactions* **1 (2)**: 133 – 136.

Martin, T.J. and Sims, N.A. (2005). Osteoclast-derived activity in the coupling of bone formation to resorption. *Trends in Molecular Medicine* **11 (2)**: 76 – 81.

Martinón-Torres, M. (2003). Quantifying trabecular orientation in the pelvic cancellous bone of modern humans, chimpanzees, and the Kebara 2 neanderthal. *American Journal of Human Biology* **15 (5)**: 647 – 661.

Marvaso, V. and Bernard. G.W. (1977). Initial intramembranous osteogenesis *in vitro*. *American Journal of Anatomy* **149 (4)**: 453 – 468.

Mathews, F., Yudkin, P. and Neil, A. (1999). Influence of maternal nutrition on outcome of pregnancy: prospective cohort study. *British Medical Journal* **319 (7206)**: 339 – 343.

Matkovic, V., Jelic, T., Wardlaw, G.M., Ilinch, J.Z., Goel, P.K., Wright, J.K., Andon, M.B., Smith, K.T. and Heaney, R.P. (1994). Timing of peak bone mass in Caucasian females and its implications for the prevention of osteoporosis. Inference from a cross-sectional model *Journal of Clinical Investigations* **93 (2)**: 799 – 808.

McAuley, J.P. and Uhthoff, H.K. (1990). The development of the pelvis. In: Uthoff, H.K. (ed). (1990). *The Embryology of the Human Locomotor System*. Berlin: Springer-Verlag.

McCarthy, J.J., Scoles, P.V. and MacEwen, G.D. (2005). Developmental dysplasia of the hip (DDH). *Current Orthopaedics* **19 (3)**: 223 – 230.

Melton III, L.J., Christen, D., Riggs, B.L., Achenbach, S.J., Müller, R., van Lenthe, G.H., Amin, S., Atkinson, E.J. and Khosla, S. (2010). Assessing forearm fracture risk in postmenopausal women. *Osteoporosis International* **21 (7)**: 1161 – 1169.

Miller, M.E. (2005). Hypothesis: fetal movement influences fetal and infant bone strength. *Medical Hypotheses* **65 (5)**: 880 – 886.

Moester, M.J.C., Papapoulos, S.E., Löwik, C.W.G.M. and van Bezooijen, R.L. (2010). Sclerostin: current knowledge and future perspectives. *Calcified Tissue International* **87 (2)**: 99 – 107.

Moore, K.L. (1983). The Developing Human. *3rd edition*. Philadelphia: Saunders.

Moore, K.L. and Persaud, T.V.N. (1998). The Developing Human, 6th ed. Philadelphia: W.B. Saunders Company.

Moore, K.L., Persaud T.V.N. and Torchia M.G. (2013). Before We Are Born: Essentials of Embryology and Birth Defects, 8th ed. Philadelphia: Elsevier.

Morgan, E.F., Barnes, G.L. and Einhorn, T.A. (2010). Chapter 1. The Bone Organ System: Form and Function. In: Marcus, R., Feldman, D., Nelson, D.A. and Rosen, C.J., Eds. (2010). Fundamentals of Osteoporosis. Burlington: Academic Press. pp1 – 23.

Mortati, R.B., Mortati, L.B., Teixeira, M.S., Takano, M.I. and Borger, R.A. (2014). Avulsion fracture of the iliac crest in a child. *Revista Brasileira de Ortopedia* **49 (3)**: 309 – 312.

Müller, R., Koller, B., Hildebrand, T., Laib, A., Gianolini, S. and Rüegsegger, P. (1996). Resolution dependency of microstructural properties of cancellous bone based on three-dimensional mu-tomography. *Technology Health Care* **4 (1)**: 113 – 119.

Nakamura, T., Noda, K., Kuwahara, Y., Minyeong, L., Tanaka, S., Kawasaki, K and Kobayashi, K. (1999). Magnetic resonance images and histology of the spheno-occipital synchondrosis in young monkeys (*Macaca fuscata*). *American Journal of Orthodontics and Dentofacial Orthopedics* **115 (2)**: 138 – 142.

Nazarian, A., von Stechow, D., Zurakowski, D., Müller, R. and Snyder, B.D. (2008). Bone volume fraction explains the variation in strength and stiffness of cancellous bone affected by metastatic cancer and osteoporosis. *Calcified Tissue International* **83 (6)**: 368 – 379.

Nicholson, P.H.F., Müller, R., Cheng, X.G., Rüegsegger, P., van der Perre, G., Dequeker, J. and Boonen, S. (2001). Quantitative ultrasound and trabecular architecture in the human calcaneus. *Journal of Bone and Mineral Research* **16 (10)**: 1886 – 1892.

Nilsson, O. and Baron, J. (2004). Fundamental limits on longitudinal bone growth: growth plate senescence and epiphyseal fusion. *Trends in Endocrinology and Metabolism* **15 (8)**: 370 – 374.

Nowlan, N.C. (2015). Biomechanics of foetal movement. *European Cells and Materials* **29**: 1 – 21.

Nuzzo, S., Meneghini, C., Braillon, P., Bouvier, R., Mobilio, S. and Peyrin, F. (2003). Microarchitectural and physical changes during fetal growth in human vertebral bone. *Journal of Bone and Mineral Research* **18 (4)**: 760 – 768.

O'Malley, A.S. (2013). A Qualitative and quantitative investigation of the functional morphology of the juvenile scapula. PhD in Anatomy and Human Identification, University of Dundee, Dundee. *Available online at: http://discovery.dundee.ac.uk/portal/files/3191305/O'Malley_phd_2013.pdf*. Last Accessed: 27-02-17.

Osborne, A.C., Lamb, K.J., Lewthwaite, J.C., Dowthwaite, G.P. and Pitsillides, A.A. (2002). Short-term rigid and flaccid paralyses diminish growth of embryonic chick limbs and abrogate joint cavity formation but differentially preserve pre-cavitated joints. *Journal of Musculoskeletal and Neuronal Interactions* **2 (5)**: 448 – 456.

Ott, S.M. (2008). Histomorphometric measurements of bone turnover, mineralisation, and volume. *Clinical Journal of American Society of Nephrology* **3 (suppl. 3)**: S151 – S156.

Palastanga, N. and Soames, R. (2011). Anatomy and Human Movement: Structure and Function, 6th Ed. Edinburgh: Churchill Livingston.

Parfitt, A.M. (1984). The cellular basis of bone remodeling: the quantum concept reexamined in light of recent advances in the cell biology of bone. *Calcified Tissue International* **36 (Suppl. 1)**: S37 – S45.

Parfitt, A.M. (1994). The two faces of growth: benefits and risks to bone integrity. *Osteoporosis International* **4 (6)**: 382 – 398.

Parfitt, A.M. (2010). Chapter 3. Skeletal Heterogeneity and the Purpose of Bone Remodeling: Implications for the Understanding of Osteoporosis. In: Marcus, R., Feldman, D., Nelson, D.A. and Rosen, C.J., eds. (2010). Fundamentals of Osteoporosis. Burlington: Academic Press. pp35 – 53.

Parfitt, A.M., Drezner, M.K., Glorieux, F.H., Kanis, J.A., Malluche, H., Meunier, P.J., Ott, S.M. and Recker, R.R. (1987). Bone histomorphometry: standardization of nomenclature, symbols and units. *Journal of Bone and Mineral Research* **2 (6)**: 595 – 610.

Parfitt, A.M., Travers, R., Rauch, F. and Glorieux, F.H. (2000). Structural and cellular changes during bone growth in healthy children. *Bone* **27 (4)**: 487 – 494.

Parkinson, I.H. and Fazzalari, N.L. (2013). Characterisation of trabecular structure. *Studies in Mechanobiology, Tissue Engineering and Biomaterials* **5 (1)**: 31 – 51.

Payton, C.G. (1934). The position of the nutrient foramen and direction of the nutrient canal in the long bones of the madder-fed pig. *Journal of Anatomy* **68 (pt 4)**: 500 – 510.

Peled. E., Eidelman, M., Katzman, A. and Bialik, M.D. (2008). Neonatal incidence of hip dysplasia *Clinical Orthopaedicas and Related Research* **466 (4)**: 771 – 775.

Perilli, E., Baleani, M., Öhman, C., Fognani, R., Baruffaldi, F. and Viceconti, M. (2008). Dependence of mechanical compressive strength on local variations in microarchitecture in cancellous bone of proximal human femur. *Journal of Biomechanics* **41 (2)**: 438 – 446.

Phillips, A.T., Pankaj, P., Howie, C.R., Usmani, A.S and Simpson, A.H. (2007). Finite element modelling of the pelvis: inclusion of muscular and ligamentous boundary conditions. *Medical Engineering & Physics* **29 (7)**: 739 – 748.

Polak, S.J., Candid, S., Lan Levengood, S.K. and Wagoner Johnson, A.J. (2012). Automated segmentation of micro-CT images of bone formation in calcium phosphate scaffolds. *Computerized Medical Imaging and Graphics* **36 (1)**: 54 – 65.

Portinaro, N.M., Murray, D.W. and Benson, M.K.D. (2001). Microanatomy of the acetabular cavity and its relation to growth. *The Journal of Bone and Joint Surgery* **83-B (3)**: 377 – 383.

Power, M.L., Heaney, R.P., Kalkwarf, H.J., Pitkin, R.M., Repke, J.T., Tsan, R.C. and Schulkin, J. (1999). The role of calcium in health and disease. *American Journal of Obstetrics and Gynecology* **181 (6)**: 1560 – 1569.

Prell, D., Kyriakou, Y. and Kalander, W.A. (2009). Comparison of ring artifact correction methods for flat-detector CT. *Physics in Medicine and Biology* **54**: 3881 – 3895.

Prentice, A. (2001). The relative contribution of diet and genotype to bone development. *Proceedings of the Nutrition Society* **60 (1)**: 45 – 52.

Prentice, A., Schoenmakers, I., Laskey, M.A., de Bono, S., Ginty, F. and Goldberg, G.R. (2006). Symposium on 'Nutrition and health in children and adolescents' Session 1: Nutrition in growth and development: Nutrition and bone growth and development. *Proceedings of the Nutrition Society* **65 (5)**: 348 – 360.

Racic, V., Pavic, A. and Brownjohn, J.M.W. (2009). Experimental identification and analytical modelling of human walking forces: literature review. *Journal of Sound and Vibration* **326 (1-2)**: 1 – 49.

Raggatt, L.J. and Partridge, N.C. (2010). Cellular and molecular mechanisms of bone remodeling. *The Journal of Biological Chemistry* **285 (33)**: 25103 – 25108.

Raisz, L.G. (1999). Physiology and pathophysiology of bone remodeling. *Clinical Chemistry* **45 (8B)**: 1353 – 1358.

Rapillard, L., Charlebois, M. and Zysset, P.K. (2006). Compressive fatigue behavious of human vertebral trabecular bone. *Journal of Biomechanics* **39 (11)**: 2133 – 2139.

Rauch, F., Travers, R and Glorieux, F.H. (2006). Cellular activity on the sever surfaces of iliac bone: a histomorphometric study in children and adolescents. *Journal of Bone and Mineral Research* **21 (4)**: 513 – 519.

Rauch, F., Travers, R., Norman, M.E., Taylor, A., Parfitt, A.M. and Glorieux, F.H. (2000a). Deficient bone formation in idiopathic juvenile osteoporosis: a histomorphometric study of cancellous iliac bone. *Journal of Bone and Mineral Research* **15 (5)**: 957 – 963.

Rauch, F., Travers, R., Parfitt, A.M. and Glorieux, F.H. (2000b). Static and dynamic bone histomorphometry in children with osteogenesis imperfecta. *Bone* **26 (6)**: 581 – 589.

Reiss, D. and Abel, R.L. (2012). Development of fetal trabecular microarchitecture in the humerus and femur. *Journal of Anatomy* **220 (5)**: 496 – 503.

Righetti, L., Nylén, A., Rosander, K. and Ljspeert, A.J. (2015). Kinematic and gait similarities between crawling human infants and other quadruped mammals. *Frontiers in Neurology* **6**: 17 (epub).

Rissech, C., García, M. and Malgosa, A. (2003). Sex and age diagnosis by ischium morphometric analysis. *Forensic Science International* **135 (3)**: 188 – 196.

Rissech, C. and Black, S. (2007). Scapular development from the neonatal period to skeletal maturity: a preliminary study. *International Journal of Osteoarchaeology* **17 (5)**: 451 – 464.

Rissech, C. and Malgosa, A. (2007). Pubis growth study: applicability in sexual and age diagnostic. *Forensic Science International* **173 (2-3)**: 137 – 145.

Roach, H.I. (1997). New aspects of endochondral ossification in the chick: chondrocyte apoptosis, bone formation by former chondrocytes, and acid phosphatase activity in the endochondral bone matrix. *Journal of Bone and Mineral Research* **12 (5)**: 795 – 805.

Roach, H.I. (2007). Bone accrual in children: adding substance to surfaces. *Paediatrics* **119 (supp. 2)**: S137 – S140.

Roach, F. and Glorieux, H. (2004). Osteogenesis imperfecta. *The Lancet* **363 (9418)**: 1377 – 1385.

Roberts, W.E., Huja, S. and Roberts, J.A. (2004). Bone modeling: biomechanics, molecular mechanisms and clinical perspectives. *Seminars in Orthodonics* **10 (2)**: 123 – 161.

Robling, A.G., Duijvelaar, K.M., Geevers, J.V., Ohashi, N and Turner, C.H. (2001). Modulation of appositional and longitudinal bone growth in the rat ulna by applied static and dynamic force. *Bone* **29 (2)**: 105 – 113.

Robling, A.G., Niziolek, P.J., Baldridge, L.A., Condon, K.W., Allen, M.R., Alam, I., Mantila, S.M., Glujak-Heinrich, J., Bellido, T.M., Harris, S.E and Turner, C.H. (2008). Mechanical stimulation of bone *in vivo* reduces osteocyte expression of Sost / sclerostin. *Journal of Biological Chemistry* **283 (9)**: 5866 – 5875.

Roodman, G.D. (1999). Cell biology of the osteoclast. *Experimental Hematology* **27 (8)**: 1229 – 1241.

Rooker, G.D. (1979). The embryological congruity of the human hip joint. *Annals of the Royal College of Surgeons of England* **61**: 357-361

Ruff, C., Holt, B. and Trinkaus, E. (2006). Who's afraid of the big bad Wolff?: 'Wolff's Law' and bone functional adaptation. *American Journal of Physical Anthropology* **129 (4)**: 484 – 498.

Ruimerman, R. and Huiskes, R. (2005). Development of a unifying theory for mechanical adaptation and maintnance of trabecular bone. *Theoretical Issues in Ergonomics Science* **6 (3-4)**: 225 – 238.

Rupprecht, M., Pogoda, P., Mumme, M., Rueger, J.M., Püschel, K. and Amling, M. (2006). Bone microarchitecture of the calcaneus and its changes in aging: a histomorphometric analysis of 60 human specimens. *Journal of Orthopaedic Research* **24 (4)**: 664 – 674.

Ryan, T.M. and Krovitz, G.E. (2006). Trabecular bone ontogeny in the human proximal femur. *Journal of Human Evolution* **51 (6)**: 591 – 602.

Sadler, T.W. (2010). Langman's Medical Embryology, 11th ed. Maryland: Lippincott Williams and Wilkins

Salle, B.L., Rauch, F., Travers, R., Bouvier, R. and Glorieux, F.H. (2002). Human fetal bone development: Histomorphometric evaluation of the proximal femoral metaphysis. *Bone* **30 (6)**: 823 – 828.

Salmon, P.L., Ohlsson, C., Shefelbine, S.J. and Doube, M. (2015). Structural model index does not measure rods and plates in trabecular bone. *Frontiers in Endocrinology* **6 (162)**: 1 – 10.

Sasaki, T., Kim, T.W., Debari, K and Nagamine, H. (1996). Cartilage-bone replacement in endochondral ossification of mandibular condylar heads in young Beagle dogs. *Journal of Electron Microscopy* **45 (3)**: 213 – 222.

Sawamura, C., Takahashi, M., McCarthy, K.J., Shen, Z., Fukai, N., Rodriguez, E.K. and Synder, B.D. (2006). Effect of *in ovo* immobilisation on development of chick hind-limb articular cartilage: an evaluation using micro-MRI measurements of delayed gadolinium uptake. *Magentic Resonance in Medicine* **56 (6)**: 1235 – 1241.

Savli, A.E., Metelli, G.P., Ciriam N. abd Donini, M.T. (2006). Spontaneous healing of an avulsed ischial tuberosity in a young football player: a case report. *Act Orthopaedica Belgica* **72 (2)**: 223 – 225.

Schaefer, M.C. (2008). A summary of epiphyseal union timings in Bosnian males. *International Journal of Osteoarchaeology* **18 (5)**: 536 – 545.

Schaefer, M., Black, S.M. and Scheuer, L. (2008). Juvenile Osteology: A Laboratory and Field Manual. London: Academic Press.

Schaffler, M.B., Cheung, W.Y., Majeska, R. and Kennedy, O. (2014). Osteocytes: master orchestrators of bone. *Calcified Tissue International* **94 (1)**: 5 -24.

Schamall, D., Teschler-Nicola, M., Kainberger, F., Tangl, S., Brandstätter, Patzak, B. and Plenk, H. (2003). Changes in trabecular bone structure in rickets and osteomalacia: the potential of a medico-historical collection. *International Journal of Osteoarchaeology* **13 (5)**: 283 – 288.

Schauberger, C.W. and Pitkin, R.M. (1979). Maternal-perinatal calcium relationships. Obstetrics and Gynecology **53 (1)**: 74 – 76.

Scheuer L. and Black, S.M. (2004). The Juvenile Skeleton. London: Elsevier Academic Press.

Schlonsky, J. and Olix, M.L. (1972). Functional disability following avulsion fracture of the ischial epiphysis: report of two cases. *The Journal of Bone and Joint Surgery* **54 (3)**: 641 – 644.

Schnitzler, C.M., Mesquita, J.M. and Pettifor, J.M. (2009). Cortical bone development in black and white South African children: Iliac crest histomorphometry. *Bone* **44 (4)**: 603 – 611.

Schoenau, E. (2005). From mechanostat theory to development of the 'functional muscle-bone-unit'. *Journal of Musculoskeletal and Neuronal Interactions* **5 (3)**: 232 – 238.

Schoenau, E. (2006). Bone mass increase in puberty: what makes it happen? *Hormone Research in Paediatrics* **65 (suppl. 2)**: 2 – 10.

Schoenau, E and Fricke, O. (2008). Mechanical influences on bone development in children. *European Journal of Endocrinology* **159 (Suppl. 1)**: S27 – S31.

Schwartz, S.M., Parker, A. and Huo, C. (1998). Theoretical and empirical scaling patterns and topological homology in bone trabeculae. *Journal of Experimental Biology* **201 (pt 4)**: 573 – 590.

Seeman, E.G. (1997). From density to structure: growing up and growing old on the surfaces of bone. *Journal of Bone and Mineral Research* **12 (4)**: 509 – 521.

Seeman, E.G. (1998). Editorial: Growth in bone mass and size – are racial and gender differences in bone mineral density more apparent than real? *Journal of Clinical Endocrinology and Metabolism* **83 (5)**: 1414 – 1419.

Seeman, H. (2002). Pathogenesis of bone fragility in women and men. *Lancet* **359**: 1841-1850.

Sellen, D.W. (2001). Comparison of infant feeding patterns reported for nonindustrial populations with current recommendations. *Journal of Nutrition* **131 (10)**: 2707 – 2715.

Serbest, S., Tosun, H.B., Tiftikçi, U., Oktas, B and Kesgin, E. (2015). Anterior inferior iliac spine avulsion fracture: a series of 5 cases. *Medicine (Baltimore)* **94 (7)**: e562.

Shapiro, F. (2008). Bone development and its relation to fracture repair. The role of mesenchymal osteoblasts and surface osteoblasts. *European Cells and Materials* **15**: 53 – 76.

Shim, K.S. (2015). Pubertal growth and epiphyseal fusion. *Annals of Pediatric Endocrinology and Metabolism* **20 (1)**: 8 – 12.

Shingleton, A. (2010) Allometry: The Study of Biological Scaling. *Nature Education Knowledge* **3(10)**:2. Accessed at: http://www.nature.com/scitable/knowledge/library/allometry-the-study-of-biological-scaling-13228439. Last Accessed: 27-02-17.

Shore, E.M. (2012). Fibrodysplasia ossificans progressiva (FOP): a human genetic disorder of extra-skeletal bone formation, or – how does one tissue become another? *Wiley Interdisciplinary Reviews: Developmental Biology* **1 (1)**: 153 – 165.

Simkin, P.A., Graney, D.O. and Fiechtner, J.J. (1980). Roman arches, human joints, and disease. *Arthritis and Rheumatology* **23 (11)**: 1308 – 1311.

Skedros, J.G. and Baucom, S.L. (2007). Mathematical analysis of trabeuclar 'trajectories' in apparent trajectorial structures: the unfortunate historical emphasis on the human proximal femur. *Journal of Theoretical Biology* **244 (1)**: 15 – 45.

Skedros, J.G., Mason, M.W. and Bloebaum, R.D. (2001). Modeling and remodeling in a developing artiodactyl calcaneus: a model for evaluating Frost's mechanostat hypothesis and its corollaries. *The Anatomical Record* **263 (2)**: 167 – 185.

Skedros, J.G., Sorenson, S.M., Hunt, K.J. and Holyoak, J.D. (2007). Ontogenetic structural and material variations in ovine calcanei: a model for interpreting bone adaptation. *The Anatomical Record* **290 (3)**: 284 – 300.

SkyScan (N.D.). Structural Parameters measured by the SkyScan™ CT-analyser software. *SkyScan N.V.*, Accessed at: http://www.skyscan.be/next/ctan_ctvol_02.pdf. Last accessed: 26-11-14. Link no longer active: PDF version included as Appendix R1.

Small, C.G. (1996). The Statistical Theory of Shape. New York: Springer-Verlag.

Sode, M., Burghardt, A.J., Nissenson, R.A. and Mujumdar, S. (2008). Resolution dependence of the non-metric trabecular structure indices. *Bone* **42 (4)**: 728 – 736.

Solomon, L.B., Lee, Y.C., Callary, S.A., Beck, M. and Howie, D.W. (2010). Anatomy of piriformis, obturator internus and obturator externus: implications for the posterior surgical approach to the hip. *Journal of Bone and Joint Surgery* **92 (9)**: 1317 – 1324.

Soma, D.B., Jones, D.B. and Fischer, P.R. (2013). Bone tumors of childhood: benign or malignant? *Consultant for Pediatricians* **12 (5)**: 204 – 208.

Specker, B. (2004). Nutrition influences bone development from infancy through toddler years. *Journal of Nutrition* **143 (3)**: 691S – 695S.

Standring, S. (2008). Gray's Anatomy, 40th ed. Philadelphia: Elsevier.

Standford, C.M. and Brand, R.A. (1999). Toward an understanding of implant occlusion and strain adaptive bone modeling and remodeling. *The Journal of Prosthetic Dentistry* **81 (5)**: 553 – 561.

Stauber, M. and Müller, R. (2006). Age-related changes in trabecular bone microstructures: global and local morphometry. *Osteoporosis International* **17 (4)**: 616 – 626.

Stauber, M. and Müller, R. (2008). Chapter 19. Micro-computed tomography: a method for the non-destructive evaluation of the three-dimensional structure of biological specimens. *In:* Westendorf, J.J. Osteoporosis: Methods and Protocols. New York City: Humana Press. p273 – 292.

Stauber, M., Rapillard, L., van Lenthe, G.H., Zysset, P. and Müller, R. (2006). Importance of individual rods and plates in the assessment of bone quality and their contribution to bone stiffness. *Journal of Bone and Mineral Research* **21 (4)**: 586 – 595.

Suda, T., Takahashi, N., Usagawa, N., Jimi, E., Gillespie, M.T. and Martin, T.J. (1999). Modulation of osteoclast differentiation and function by the new members of the tumor necrosis factor receptor and ligand families. *Endocrine Reviews* **20 (3)**: 345 – 357.

Sundh, D., Mellström, D., Nilsson, M., Karlsson, M., Ohlsson, C. and Lorentzon, M. (2015). Increased cortical porosity in older men with fracture. *Journal of Bone and Mineral Research* **30 (9)**: 1692 – 1700.

Sutherland, D.H., Olshen, R., Cooper, L. and Woo, S.L.Y. (1980). The development of mature gait. *Journal of Bone and Joint Surgery* **62-A (3)**: 336 – 353.

Tan, S.D., de Vries, T.J., Kuijpers-Jagtman, A.M., Semeins, C.M., Everts, V. and Klein-Nulend, J. (2007). Osteocytes subjected to fluid flow inhibit osteoclast formation and bone resorption. *Bone* **41 (5)**: 745 – 751.

Tanck, E., Hannink, G., Ruimerman, R., Buma, P., Burger, E.H. an Huiskes, R. (2006). Cortical bone development under the growth plate is regulated by mechanical load transfer. *Journal of Anatomy* **208 (1)**: 73 – 79.

Tardieu, C., Bonneau, N., Hecquet, J., Boulay, C., Marty, C., Legaye, J. and Duval-Beaupére, G. (2013). How is sagittal balance acquired during bipedal gait acquisition? Comparison of neonatal and adult pelves in three dimensions. Evolutionary implications. *Journal of Human Evolution* **65 (2)**: 209 – 222.

Thelen, E. and Fisher, D.M. (1984). Newborn stepping: an explanation for a disappearing reflex. *Developmental Psychology* **18 (5)**: 760 – 775.

Thelen, E., Fisher, D.M. and Ridley-Johnson, R. (2002). The relationship between physical growth and a newborn reflex. *Infant Behaviour and Development* **7 (4)**: 479 – 493.

Tian, X.Y., Zhang, Q., Zhao, R., Setterberg, R.B., Zeng, Q.Q., Iturria, S.J., Ma, Y.F. and Jee, W.S. (2008). Continuous PGE2 leads to net bone loss while intermettent PGE2 leads to net bone gain in lumbar vertebral bodies of adult female rats. *Bone* **42 (5)**: 914 – 920.

Tkachenko, E.V., Slyfield, C.R., Tomlinson, R.E., Daggett, J.R., Wilson, D.L. and Hernandez, C.J. (2009). Voxel size and measurements of individual resorption cavities in three-dimensional images of cancellous bone. *Bone* **45 (3)**: 487 – 492.

Treece, G.M., Gee, A.H., Mayhew, P.M. and Poole, K.E.S. (2010). High resolution cortical bone thickness measurement from clinical CT data. *Medical Image Analysis* **14 (3)**: 276 – 290.

Tsukamoto, Y., Kajii, T.S., Oonishi, Y., Sugawara-Kato, Y., Hirabayashi, T. and Lida, J. (2006). Histological and histochemical study of the spheno-occipital synchondrosis of the cranial base on BALB/c-bm/bm mouse. *Orthodontic Waves* **65 (4)**: 166 – 172.

Ulrich, D., van Rietbergen, B., Laib, A. and Rüegsegger, P. (1999). The ability of three-dimensional structural indices to reflect mechanical aspects of trabecular bone. *Bone* **25 (1)**: 55 – 60.

Uthoff, H.K. and Carey, T. (1990). The development of the hip. In: Uthoff, H.K. (ed). (1990). The Embryology of the Human Locomotor System. Berlin: Springer-Verlag.

van Arkel, R.J., Amis, A.A., Cobb, J.P. and Jeffers. J.R.T. (2015). The capsular ligaments provide more hip rotational restraint than the acetabular labrum and the ligamentum teres: an experimental study. *The Bone and Joint Journal* **97-B (4)**: 484 – 491.

van Oers, R.F.M., Ruimerman, R., Tanck, E., Hilbers, P.A.J. and Huiskes, R. (2008). A unified theory for osteonal and hemi-osteonal remodelling. *Bone* **42 (2)**: 250 – 259.

Vanderoost, J. and van Lenthe, G.H. (2014). From histology to micro-CT: measuring and modeling resorption cavities and their relation to bone competence. *World Journal of Radiology* **6 (9)**: 643 – 656.

Verbruggen, S.W., Vaughan, T.J. and McNamara, L.M. (2012). Strain amplification in bone mechanobiology: a computational study of the *in vivo* mechanics of osteocytes. *Journal of the Royal Society Interface* **9 (75)**: 2735 – 2744.

Vezeridis, P.S., Semeins, C.M., Chen, Q. and Klein-Nulend, J. (2006). Osteocytes subjected to pulsating fluid flow regulate osteoblast proliferation and differentiation. *Biochemical and Biophysical Research Communications* **348 (3)**: 1082 – 1088.

Vleeming, A., Schuenke, M.D., Masi, A.T., Carreiro, J.E., Danneels, L. and Willard, F.H. (2012). The sacroiliac joint: an overview of its anatomy, function and potential clinical implications. *Journal of Anatomy* **221 (6)**: 537 – 567.

Volpato, V., Viola, T.B., Nakatsukasa, M., Bondioli, L.B. and Macchiarelli, R. (2008). Textural characteristics of the iliac-femoral trabecular pattern in a bipedally trained Japanese macaque. *Primates* **49 (1)**: 16 – 25.

von Meyer, G.H. (1867). Die architektur der spongiosa. *Archiv für Anatomie, Physiologie und Wissenschaftliche Medicin* **34**: 615 – 628. Translated by: Amundson, P.K., Skedros, J. and Brand, R. (2011). The classic: the architecture of the trabecular bone. *Clinical Orthopaedics and Related Research* **469 (11)**: 3079 – 3084.

Waarsing, J.H., Dayy, J.S. and Weinans, H. (2004). An improved segmentation method for *in vivo* μCT imaging. *Journal of Bone and Mineral Research* **19 (10)**: 1640 – 1650.

Wagner, C.L. and Greer, F.R. (2008). Prevention of rickets and vitamin D deficiency in infants, children and adolescents. *Pediatrics* **122 (5)**: 1142 – 1152.

Wagner, F.V., Negrão, J.R., Campos, J., Ward, S.R., Haghighi, P., Trudell, D.J. and Resnick, D. (2012). Capsular ligaments of the hip: anatomic, histologic, and positional study in cadaveric specimens with MR arthrography. *Radiology* **263 (1)**: 189 – 198.

Walker, J.M. (1991). Musculoskeletal development: a review. *Physical Therapy* **71 (12)**: 878 – 889.

Wallace, I.J., Middleton, K.M., Lublinksky, S., Kelly, S.A., Judex, S., Garland, T. Jr. and Demes, B. (2010). Functional significance of genetic variation underlying limb bone diaphyseal structure. *American Journal of Physical Anthropology* **143 (1)**: 21 – 30.

Watson, P.J., Dostanpor, A., Fagan, M.J. and Dobson, C.A. (2017). The effect of boundary constraints on finite element modelling of the human pelvis. *Medical Engineering and Physics* **43 (1)**: 48 – 57.

Webb, P.A.O. and Suchey, J.M. (1985). Epiphyseal union of the anterior iliac crest and medial clavicle in a modern multiracial sample of American males and females. *American Journal of Physical Anthropology* **68 (4)**: 457 – 466.

Weise, M., De-Levi, S., Barnes, K.M., Gafni, R.I., Abad, V. and Baron, J. (2001). Effects of estrogen on growth plate senescence and epiphyseal fusion. *Proceedings of the National Academy of Sciences* **98 (12)**: 6871 – 6876.

White, T.D., Black, M.T. and Folkeins, P.A. (2005). Human Osteology, 3rd Ed. San Diego: Elsevier Academic Press.

Whitehead, M., Lane, G., Young, O., Campbell, S., Abeyasekera, G., Hillyard, C.J., MacIntyre, I., Phang, K.G. and Stevenson, J.C. (1981). Interrelations of calcium-regulating hormones during normal pregnancy. *British Medical Journal* **283**: 10 – 12.

WHOMGRS (2006). WHO motor development study: windows of achievement for six gross motor development milestones. *Acta Paediatrica Supplement* **450**: 86 – 95.

Wimmer, W., Gerber, N., Guignard, J., Dubach, P., Kompis, M., Weber, S., Caversaccio, M. (2015). Topographic bone thickness maps for Bonebridge implantations. *European Archives of Oto-Rhino-Laryngology* **272 (7)**: 1651 – 1658.

Wolff, J. (1870). Ueber die innere architectur der knochen und ihre bedeutung *für* die frage vom knochenwachsthum. *Virchows Archiv fur Pathologische, Anatomie und Physiologe* **50**: 389 – 450. Translated by: Heller, M.O., Taylor, W.R., Aslanisis, N and Duda, G.N. (2010). The classic: on the inner architecture of bones and its importance for growth. *Clinical Orthopaedics and Related Research* **468 (4)**: 1056 – 1065.

Wolff, J. (1873). Zur lehre von der fracturenheilung. *Deutsche Zeitschrift für Chirurgie* **2 (6)**: 546 – 551. Translated by: Heller, M.O., Taylor, W.R., Aslanidis, N. and Duda, G.N. (2010). The classic: on the theory of fracture healing *Clinical Orthopaedics and Related Research* **468 (4)**: 1052 – 1055.

Wolff, J. (1892). Das Gesetz der Transformation der Knochen. Verlag von August Hirschwald: Berlin. Translated by Maquet, P. and Furlong, R. (1986). The Law of Bone Remodeling. Springer-Verlag, Berlin Heidelberg.

Woodley, S.J. and Kennedy, E. (2005). Anatomy in practice: the sacrotuberous ligament. *New Zealand Journal of Physiotherapy* **33 (3)**: 91 – 94.

World Health Organisation (1994). An evaluation of infant growth: the use and interpretation of anthopometry in infants. *Who Working Group on Infant Growth.* Accessible online at: http://apps.who.int/iris/bitstream/10665/49678/1/bulletin_1995_73(2)_165-174.pdf. Date accessed: 16.03.16.

World Health Organisation (2002). Infant and young child nutrition. *Fifty-fifth World Health Assembly, 16th April 2002.* Available online at: http://apps.who.int/gb/archive/pdf_files/WHA55/ea5515.pdf?ua=1. Accessed: 09-04-2016.

Yang, Y.Q., Tan, Y.Y., Wong, R., Wenden, A., Zhang, L.K. and Rabie, A.B.M. (2012). The role of vascular endothelial growth factor in ossification. *International Journal of Oral Science* **4 (2)**: 64 – 68.

Yiming, A., Baqué, P., Rahili, A., Mayer, J., Braccini, A.L., Fontaine, A., Leplatois, A., Clavé, A., Bourgeon, A. and de Peretti, F. (2002). Anatomical study of the coxal bone: radiological and clinical application. *Surgical Radiologic Anatomy* **24 (1)**: 81 – 86.

Ylihärsilä, H., Kagantie, E., Osmond, C., Forsén, T., Barker, D.J.P. and Eriksson, J.G. (2008). Body mass index during childhood and adult body composition in men and women aged 56 – 70. *American Journal of Clinical Nutrition* **103 (3)**: 1769 – 1775.

You, J., Yellowley, C.E., Donahue, H.J., Zhang, Y., Chen, Q. and Jacobs, C.R. (2000). Substrate deformation levels associated with routine physical activity are less stimulatory to bone cells relative to loading-induced oscillatory fluid flow. *Journal of Biomechanical Engineering* **122 (4)**: 387 – 393.

Yusof, N.A. (2013). The development and anatomy of the sacrum in relation to the ilium and the sacroiliac joint. PhD in Anatomy and Forensic Anthropology, University of Dundee, Dundee. *Available online at: http://discovery.dundee.ac.uk/portal/files/4391254/Yusof_phd_2013.pdf*. Last Accessed: 27-02-17.

Yusof, N.A., Soames, R.W., Cunningham, C.A. and Black, S.M. (2013). Growth of the human ilium: the anomalous sacroiliac junction. *The Anatomical Record* **296 (11)**: 1688 – 1694.

Zaman, G., Pitsillides, A.A., Rawlinson, S.C., Suswillo, R.F., Mosley, J.R., Cheng, M.Z., Platts, L.A., Hukkanen, M., Polak, J.M. and Lanyon, L.E. (1999). Mechanical strain stimulates nitric oxide production by rapid activation of endothelial nitric oxide synthase in osteocytes. *Journal of Bone and Mineral Research* **14 (7)**: 1123 – 1131.

Zelazo, P.R., Zelazo, N.A. and Kolb, S. (1972). "Walking" in the newborn. *Science* **176 (4032)**: 314 – 315.

Zhou, X., Zhang, H., Sucato, D.J. and Johnston, C.E. (2014). Effect of dual screws across the vertebral neurocentral synchondrosis on spinal canal development in an immature spine. *The Journal of Bone and Joint Surgery* **96 (17)**: e146.1 – e146.6.

Zhu, K. and Prince, R.L. (2012). Calcium and bone. *Clinical Biochemistry* **45 (12)**: 936 – 942.